



Sixth International Symposium on Space Terahertz Technology



JPL

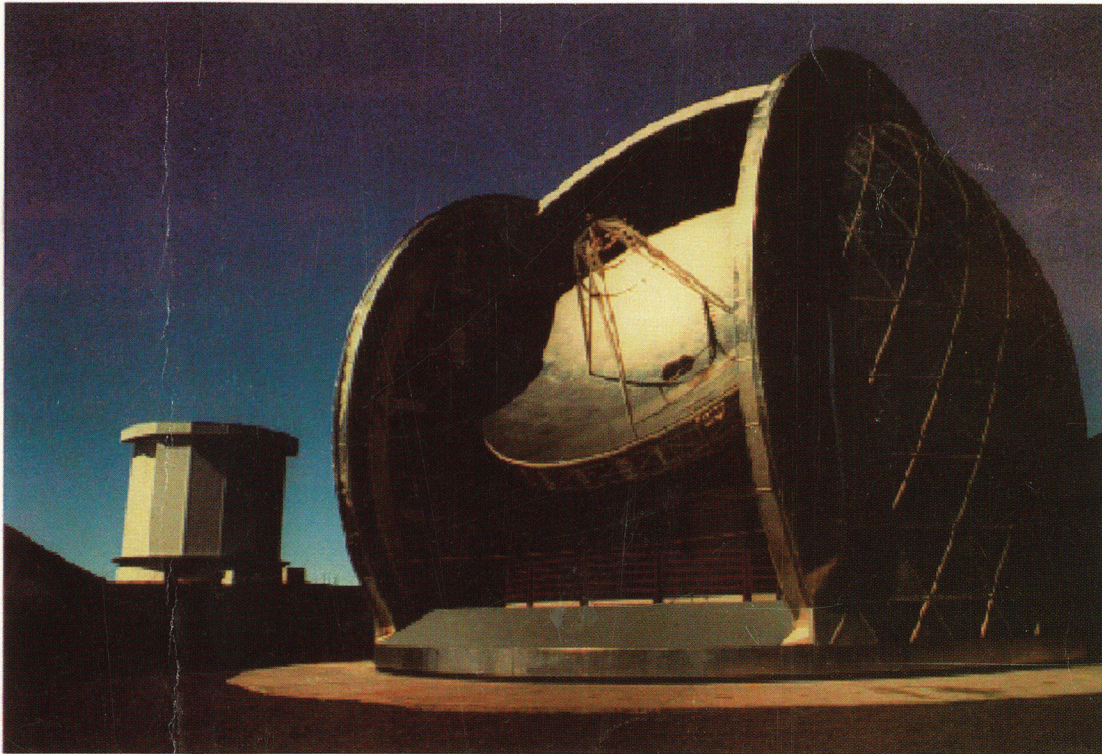
March 21-23, 1995



Beckman Institute Auditorium
California Institute of Technology
Pasadena, California

IEEE

SYMPOSIUM PROCEEDINGS



Caltech Submillimeter Observatory on Mauna Kea, Hawaii

Sponsored by: NASA Office of Advanced Concepts and Technology, University Space Engineering Research Centers Program.

Co-sponsored by: IEEE Microwave Theory and Techniques Society.

Organized Jointly by: California Institute of Technology, The University of Michigan's NASA Center for Space Terahertz Technology, and JPL's Center for Space Microelectronics Technology.

PROCEEDINGS
of the
**SIXTH INTERNATIONAL SYMPOSIUM ON
SPACE TERAHERTZ TECHNOLOGY**

Tuesday-Thursday, March 21-23, 1995

Beckman Institute Auditorium
California Institute of Technology
Pasadena, California

Sponsored by: NASA Office of Advanced Concepts and Technology, University Space Engineering Research Centers Program, and co-sponsored by the Microwave Theory and Techniques Society of IEEE.

Organized Jointly by: California Institute of Technology, The University of Michigan's NASA Center for Space Terahertz Technology, and JPL's Center for Space Microelectronics Technology.

Organizing Committee

Symposium Co-chairs:

Jonas Zmuidzinas, Caltech
Gabriel M. Rebeiz, University of Michigan

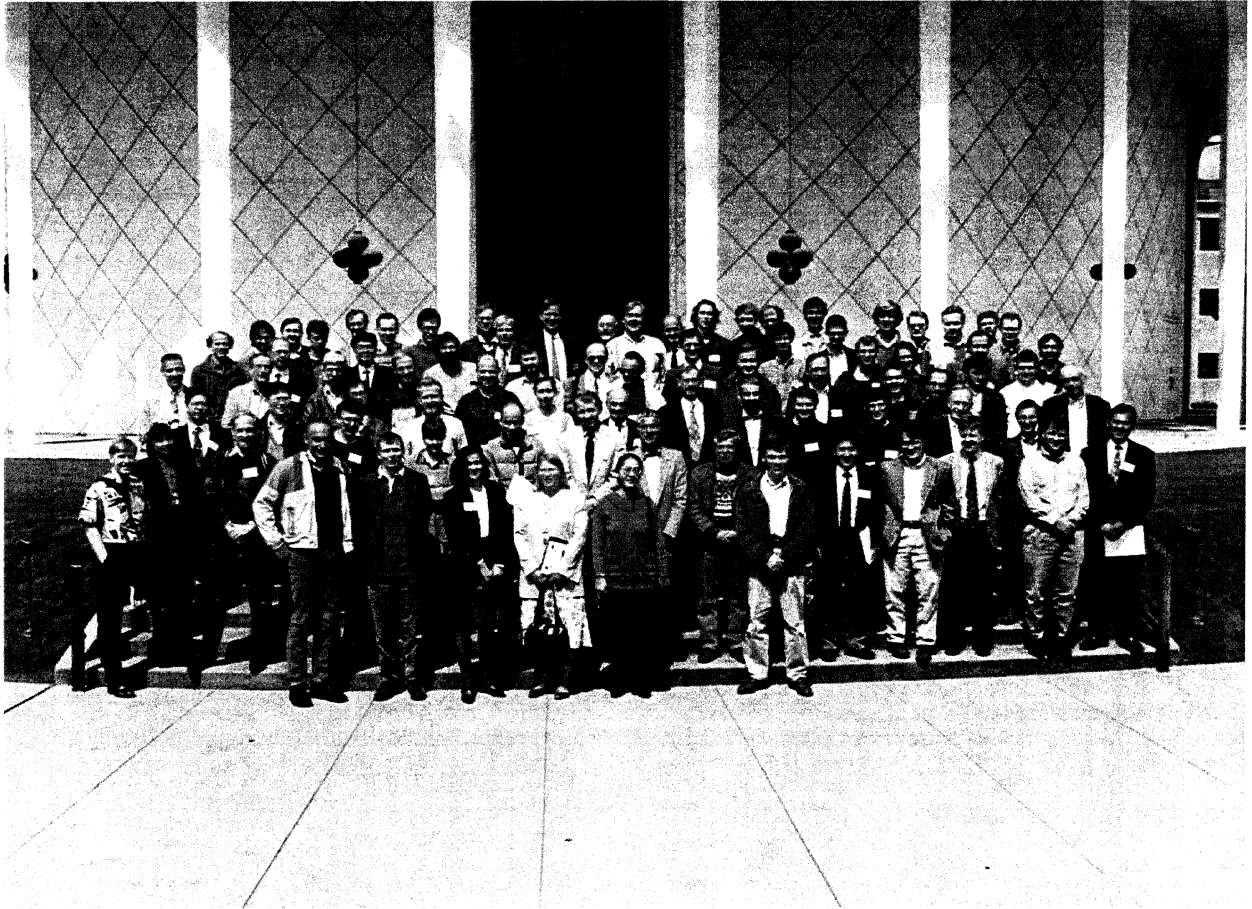
Technical Co-chair:

William R. McGrath, Jet Propulsion Laboratory

Arrangements:

Vilia Zmuidzinas, Caltech
Timothy Brice, Jet Propulsion Laboratory
Janice Rosan, University of Michigan

GROUP PHOTO



PREFACE

The Sixth International Symposium on Space Terahertz Technology was held at the California Institute of Technology in Pasadena, California, on March 21–23, 1995. The Symposium was attended by approximately 110 scientists and engineers from the U. S., Europe, Russia, and Japan. The theme of the Symposium centered on the generation, detection, and manipulation of radiation in the terahertz spectral region for space applications including astronomy and remote sensing of the Earth's atmosphere. The program included eleven sessions covering a wide variety of topics including Schottky, SIS, and hot electron bolometer mixers; local oscillators including fundamental sources and varactor frequency multipliers; and various techniques involving optics, antennas, and micromachining. In addition, several invited presentations outlined the recent progress and future opportunities in ground-based, airborne, and space observatories for submillimeter astronomy.

The Symposium was sponsored by the NASA Office of Advanced Concepts and Technology, University Space Engineering Research Centers Program, and was organized jointly by California Institute of Technology, The University of Michigan's NASA Center for Space Terahertz Technology, and JPL's Center for Space Microelectronics Technology. The Microwave Theory and Techniques Society of IEEE served as a cooperative sponsor of the Symposium.

The Seventh International Symposium on Space Terahertz Technology will be held at the University of Virginia in Charlottesville, Virginia on March 12–14, 1996.

Jonas Zmuidzinis, Caltech
Gabriel Rebeiz, University of Michigan
Fawwaz T. Ulaby, University of Michigan
Carl Kukkonen, Jet Propulsion Laboratory

For more information on the next Symposium please contact:

Prof. Robert M. Weikle
Dept. of Electrical Engineering
Thornton Hall
University of Virginia
Charlottesville, VA 22903
Telephone: (804) 924-3362
Fax: (804) 924-8818
E-mail: rmw5w@virginia.edu

CONTENTS

DAY 1 - TUESDAY, MARCH 21

Opening Session

Chair: Jonas Zmuidzinas

Welcoming Remarks	Carl Kukkonen	JPL (*)
The Submillimeter Wave Astronomy Satellite (SWAS): Current Status	G. Melnick	Harvard-CfA (*)
SOFIA: The Stratospheric Observatory for Infrared Astronomy	E. Erickson	NASA/Ames Research Center (*)

Session 1: Schottky Diodes and Receivers

Chair: Tom Crowe

2.5 THz Airborne Heterodyne System for Measurement of Stratospheric OH	R. Titz, M. Birk, D. Hausamann, R. Nitsche, F. Schreier, J. Urban, H. Kullmann, and H.P. Roser	DLR Oberpfaffenhofen; U-Bremen; DLR Berlin 1
A Novel Micron-Thick Whisker Contacted Schottky Diode Chip	A. Grüb, A. Simon, H. L. Hartnagel, J. Bune, M. Raum, and H. Brand	TH Darmstadt; U-Erlangen-Nürnberg 4
An All Solid-State 1 THz Radiometer For Space Applications	R. Zimmermann, T. Rose, and T. Crowe	Radiometer Physics; U-Virginia 13
A Practical Schottky Mixer for 5 THz	A. L. Betz	U-Colorado 28

Session 1 (cont'd): Schottky Diodes and Receivers

Chair: Robert Mattauch

The Design, Construction, and Evaluation of a 585 GHz Planar Schottky Receiver	J. L. Hesler, T. W. Crowe, R. F. Bradley, S. K. Pan, R. M. Weikle, and G. Chattopadhyay	U-Virginia; NRAO 34
Low-Noise MOVPE-Grown Planar InGaAs Mixer Diodes	P. Marsh, H. Kong, and D. Pavlidis	U-Michigan 45
Electrolytic Deposition Techniques for the Fabrication of Submicron Anodes	A. Grüb, C. Lin, and H. L. Hartnagel	TH Darmstadt 54

(*) - presentation only.

Session 2: SIS Receivers I**Chair: Ray Blundell**

A 1 THz Nb SIS Heterodyne Mixer with Normal Metal Tuning Structures	<u>H. Van de Stadt</u> , A. Baryshev, P. Dieleman, T. Klapwijk, S. Kovtonyuk, G. de Lange, I. Lapitskaya, J. Mees, R. Panhuyzen, G. Prokopenko, and H. Schaeffer	SRON; U-Groningen; 66 IREE-Moscow
An 800 GHz Receiver Using Nb/Al ₂ O ₃ /Nb SIS Junctions	<u>C. E. Honingh</u> , K. Jacobs, D. Hottgenroth, S. Haas, and J. Stutzki	U-Cologne 78
The Development of an 850 GHz Waveguide Receiver Using Tuned SIS Junctions on 1 μ m Si ₃ N ₄ Membranes	<u>J. W. Kooi</u> , M. S. Chan, M. Bin, B. Bumble, H. G. LeDuc, C. K. Walker, and T. G. Phillips	Caltech; JPL; U-Arizona . 86 [†]
Theoretical and Experimental Studies of Nb-Based Tuning Circuits for THz SIS Mixers	<u>V. Yu. Belitsky</u> , S.W. Jacobson, L.V. Filippenko, and E.L. Kollberg	IREE-Moscow; Chalmers- . . 87 U
NbN Mixers and Tuning Circuits for 630 GHz: Design and Preliminary Measurements	<u>M. Salez</u> , P. Febvre, W.R. McGrath, J.A. Stern, and H.G. LeDuc	JPL; DEMIRM-Paris 103

Session 2 (cont'd): SIS Receivers I**Chair: Karl Jacobs**

Noise Properties of a Mixer with SIS NbN Quasiparticle Tunnel Junctions	<u>A. Karpov</u> , B. Plathner, K.H. Gundlach, M. Aoyagi, and S. Takada	IRAM 117
A Fixed Tuned SIS Receiver for the 450 GHz Frequency Band	<u>R. Blundell</u> , C.-Y.E. Tong, D. C. Papa, J. W. Barrett, S. Paine, X. Zhang, J.A. Stern, and H. G. LeDuc	Harvard-CfA; JPL 123
An Integrated SIS Mixer and HEMT IF Amplifier	<u>S. Padin</u> , D.P. Woody, J.A. Stern, H.G. LeDuc, R. Blundell, C.-Y.E. Tong, and M.W. Pospieszalski	Caltech/OVRO; JPL; 134 Harvard-CfA; NRAO
On Using the Shot Noise in SIS Tunnel Junctions for Characterizing IF Amplifiers	<u>D. P. Woody</u> , S. Padin, H.G. LeDuc, and J. A. Stern	Caltech/OVRO; JPL 140

[†] - abstract only.

DAY 2 - WEDNESDAY, MARCH 22

New Submillimeter Observatories

Installation of the Antarctic Sub-mm Telescope and Remote Observatory (AST/RO)	Antony Stark	Chair: Jonas Zmuidzinas Harvard Smithsonian CfA . . . 150
The Submillimeter Telescope Observatory (SMTO): Current Status	Robert Martin	Steward Observatory; U- . . . (*) Arizona
HHT Instrumentation – Present and Future	Rolf Güsten	Max-Planck Institut für 155 Radioastronomie

Session 4: Local Oscillator Sources

Tunable p-Ge Laser in the Frequency Range from 1 to 4.5 THz	<u>E. Brundermann</u> and H.P. Roser	Chair: Neal Erickson DLR-Berlin 159
InP Gunn Devices and GaAs TUNNETT Diodes as Low-Noise High-Performance Local Oscillators in Fundamental Mode	<u>H. Eisele</u> and G. I. Haddad	U-Michigan 167
115-145 GHz Stable Depletion Layer Second-Harmonic Transferred Electron Oscillators	M. F. Zyburu, <u>S. H. Jones</u> , J.E. Carlstrom, and J. D. Crowley	U-Virginia; Caltech; 176 Litton

Session 4 (cont'd): Local Oscillator Sources

345 GHz Radiation from a Quasioptical Josephson Oscillator	<u>M. J. Wengler</u> , B. Guan, and E. K. Track	Chair: Steve Jones U-Rochester; HYPRES . . . 190 [‡]
A Waveguide Tripler for 720-880 GHz	<u>N. Erickson</u> and J. Tuovinen	U-Mass. Amherst; Helsinki- 191 U
Terahertz Grid Frequency Doublers	<u>J.-C. Chiao</u> , A. Markelz, Y. Li, J. Hacker, T. Crowe, J. Allen, and D. Rutledge	Caltech; UCSB; U- 199 Virginia; Bellcore
Effect of the Increased Number of Diodes on the Performance of Oscillators with Series- Connected Tunnel Diodes	<u>O. Boric-Lubecke</u> , D.-S. Pan, and T. Itoh	UCLA 207

[‡] – abstract only.

(*) – presentation only.

Session 5: Hot Electron Bolometer Mixers**Chair: Tony Kerr**

Hot Electron Bolometer Mixers for Submillimeter Wavelengths: an Overview of Recent Developments	<u>W. R. McGrath</u>	JPL 216
Analysis of the Noise Performance of a Hot-Electron Superconducting Bolometer Mixer	<u>B. S. Karasik</u> and A.I. Elantev	Moscow State Ped.-U 229
Performances of Hot-Electron Superconducting Mixer for Frequencies Less than the Gap Energy: NbN Mixer for 100 GHz Operation	O. Okunev, A. Dzardanov, <u>G. Gol'tsman</u> , and E. Gershenson	Moscow State Ped.-U 247
NbN Hot-Electron Mixer Measurements At 200 GHz	<u>J. Kawamura</u> , R. Blundell, C.-Y.E. Tong, <u>G. Gol'tsman</u> , E. Gershenson and B. Vorinov	Harvard-CfA; Moscow State Ped.-U 254

Session 5 (cont'd): Hot Electron Bolometer Mixers**Chair: Rob McGrath**

Noise Temperature and IF Bandwidth of a 530 GHz Diffusion-Cooled Hot-Electron Bolometer Mixer	<u>A. Skalare</u> , W.R. McGrath, B. Bumble, H.G. Leduc, P.J. Burke, A.A. Verheijen, and D.E. Prober	JPL; Yale-U 262
Noise Temperature of NbN Hot-Electron Quasioptical Superconducting Mixer in 200-700 GHz Range	<u>G. N. Gol'tsman</u> , B. S. Karasik, S. I. Svechnikov, E. M. Gershenson, H. Ekström and E. Kollberg	Moscow State Ped.-U; Chalmers-U 268 [†]
350 GHz NbN Hot Electron Bolometer Mixer	<u>H. Ekström</u> , B. Karasik, E. Kollberg, <u>G. Gol'tsman</u> , and E. Gershenson	Chalmers-U; Moscow State Ped.-U 269
Hot Electron Detection And Mixing Experiments in NbN at 119 Micrometer Wavelength	E. Gerecht, C.F. Musante, R. Schuch, C.R. Lutz, Jr., <u>K.S. Yngvesson</u> , E.R. Mueller, J. Waldman, <u>G. N. Gol'tsman</u> , and E. M. Gershenson	U-Mass. Amherst; U-Mass. Lowell; Moscow State Ped.-U 284

[†] - abstract only.

DAY 3 - THURSDAY, MARCH 23

Session 6: SIS Receivers II

Chair: Dave Woody

Analytical Treatment and Optimum Parameters for DSB SIS Receivers	<u>P. Febvre</u>	DEMIRM-Paris 294 [†]
A Fixed Tuned Low Noise SIS Receiver For The 600 GHz Frequency Band	<u>C.-Y.E. Tong</u> , R. Blundell, D.C. Papa, J. W. Barnett, S. Paine, X. Zhang, J.A. Stern, and H.G. LeDuc	Harvard-CfA; JPL 295
Design and Characterization of Two-Junction Tuning Circuits for Submillimeter SIS Mixers	<u>M. C. Gaidis</u> , M. Bin, D. Miller, J. Zmuidzinis, H.G. LeDuc, and J.A. Stern	Caltech; JPL 305
A Circular Waveguide SIS Receiver for 600-720 GHz	<u>P. A. Jaminet</u> , J.A. Stern, H.G. LeDuc, S. Shepard, J. Kawamura, and X. Zhang	Harvard-CfA; JPL 314

Session 6 (cont'd): SIS Receivers II

Chair: Rick LeDuc

A Superconducting Planar Integrated Receiver for the Frequency Range 430-480 GHz	<u>S. V. Shitov</u> , V. P. Koshelets, I. L. Lapitskaya, L. V. Filippenko, A. M. Baryshev, T. de Graauw, H. Schaefer, H. van de Stadt, and W. Luinge	IREE-Moscow; SRON 324
A 16-Element SIS Receiver for 455-495 GHz for the Heinrich Hertz Telescope	<u>M. A. Scherschel</u> , G.A. Ediss, R. Güsten, K.H. Gundlach, H. Hauschildt, C. Kasemann, A. Korn, D. Maier, and G. Schneider	MPIfR-Bonn; IRAM 338
Low Noise Mixer with the Nb-Al Oxide-Al-Nb Tunnel Junctions for a Multibeam 345 GHz Receiver	<u>A. Karpov</u> , D. Maier, J. Blondel, B. Lazareff, and K.H. Gundlach	IRAM 344
180-500 GHz Low Noise SIS Waveguide Receivers Employing Tuned Nb/Al-Oxide/Nb Tunnel Junctions	<u>J. W. Kooi</u> , M. Chan, B. Bumble, H. G. LeDuc, M. Bin, and T. G. Phillips	Caltech; JPL; 355 [†]

Session 7: Varactor Devices

Chair: Antti Räsänen

A Self-Biased Antiparallel Planar Varactor Diode Monolithic Nonlinear Transmission Line	<u>N. Erickson</u> <u>W-M. Zhang</u> , X. Qin, F. Jiang, G. Song, Y. Li, C.W. Domier, and N.C. Luhmann, Jr.	U-Mass. Amherst 356 UCLA; UC Davis 365
60 GHz Monolithic Schottky Varactor Transmission Beam Switching Array	<u>X. Qin</u> , W-M. Zhang, C.W. Domier, N.C. Luhmann, Jr., W. Berk, S. Duncan, and D.W. Tu	UCLA; UC Davis; Martin Marietta 371 [†]

[†] - abstract only.

Session 8: Optics, Antennas, and Micromachining		Chair: Peter Siegel
Micromachined Millimeter-Wave SIS-Mixers	<u>G. de Lange</u> , B.R. Jacobson, and Q. Hu	MIT 372
Integrated Silicon Micromachined Waveguide Circuits for Submillimeter Wave Applications	<u>J. Wright</u> , B. Bumble, H. LeDuc, W. McGrath, and Y. Tai	Caltech; JPL; 387
Tolerance Analysis of a 500 GHz Amplitude Hologram	<u>Taavi Hirvonen</u> , Jussi Tuovinen, and Antti Räsänen	Helsinki-U 397
Off-Axis Beam Patterns of Extended-Hemispherical Dielectric Lens Antennas: Theory and Experiment at 250 GHz	<u>G. Gauthier</u> , D. Filipovic, S. Raman, and G. M. Rebeiz	U-Michigan 407 [‡]

Session 9: Varactor Device Theory		Chair: Margaret Frerking
Effect of Voltage Modulation on the Shape of the Depletion Layer of a Submillimeter Wave Schottky Varactor	<u>Jyrki T. Louhi</u> and Antti V. Räsänen	Helsinki-U 408
Self Consistent Physics-Based Numerical Device and Harmonic Balance Circuit Analysis of Heterostructure Barrier and Schottky Barrier Varactors Including Thermal Effects	<u>J. R. Jones</u> , S. H. Jones, and G. B. Tait	U-Virginia; USMA West Point .. 423
Monte Carlo Simulation of Schottky Barrier Mixers and Varactors	<u>J. East</u>	U-Michigan 442
Submicron Schottky-Collector AlAs/InGaAs Resonant Tunnel Diodes	S. C. Martin, R. E. Muller, K. Nummila, <u>R. P. Smith</u> , M. Reddy, M. J. Mondry, M. J. W. Rodwell, D. H. Chow, and J. N. Schulman	JPL; UCSB; Hughes Research Laboratories; 458

[‡] - abstract only.

2.5 THZ AIRBORNE HETERODYNE SYSTEM
FOR MEASUREMENT OF STRATOSPHERIC OH

R. Titz, M. Birk, D. Hausmann, R. Nitsche, F. Schreier

Institute of Optoelectronics, DLR Oberpfaffenhofen, D-82230 Wessling

J. Urban, H. Küllmann,

Institute of Environmental Physics, University of Bremen, D-28334 Bremen

H. P. Röser

Institute for Space Sensor Technology, DLR Berlin-Adlershof, D-12484 Berlin

Abstract

A 2.5 THz heterodyne system originally designed for astronomical purposes [1] was modified and further developed for atmospheric measurements. In several flights it was successfully used aboard the research aircraft FALCON at flight altitudes between 11km and 12 km and with pointing angles between 5° and 20° versus horizon. The thermal emission of the hydroxyl radical OH at 2.514 THz was received. The latest results show a sufficient signal-to-noise ratio that OH concentration profile can be retrieved.

Introduction

The hydroxyl radical OH is involved in all main catalytic ozone destruction cycles. For remote observation of OH the most sensitive spectral range is the far infrared (FIR). The lowest rotational transitions of this short life molecule are in the THz range, where the triplet at 2514.3 GHz is best suited for remote sensing with a heterodyne system [2]: it is strong, interference with lines of other atmospheric species is weak and the frequency is accessible with state-of the art heterodyne technique.

Airborne Heterodyne System

The scheme and the specifications of the airborne heterodyne system are given in Fig. 1 and Tab. 1. The essential parts are the optically pumped far infrared laser used as local oscillator (LO), the GaAs Schottky barrier mixer diode and the acousto-optical spectrometer (AOS).

The FIR laser is designed as a ring resonator, pumped by 20 W of the discharge CO₂ laser. With methanol as laser gas it emits around 10mW FIR output power at 2.522 THz, enough to drive the GaAs Schottky diode mixer in an open structure mount. The atmospheric signal and the FIR laser are spatially overlapped with a double sideband diplexer (Martin-Puplett type). The diode, the diplexer and the other optical components including the pointing mirror are fixed to the optical plate which is mounted at the level of the aircraft window. The position of the pointing mirror determines the angle at which the atmospheric signal is received, furthermore the mirror can be switched to a hot and a cold calibration load. An off-axis parabolic mirror focuses the radiation into the main beam of the 4λ whisker antenna (10dB beam width: 26°). The Schottky diodes of type 1112 and 1T15 were used, designed and fabricated by the University of Virginia [3]. The intermediate frequency at 8.5 GHz is first amplified with a 33dB low noise HEMT amplifier at liquid nitrogen temperature. In a second mixer stage the signal is downconverted a second time to adopt it to the center frequency of the acousto-optical spectrometer (AOS). In the first flight campaigns the AOS of the University of Bremen was used with 0.995 GHz center frequency, 840 MHz bandwidth and a resolution of 1.5 MHz, for the last flight an AOS of MAN Technology (center frequency: 2.1 GHz, bandwidth: 1400 MHz, resolution: around 1 MHz) was used.

Results

The system has been successfully operated from aboard the DLR jet aircraft FALCON at flight altitudes between 11km and 12km over Germany [4].

The first measurement was performed in June 1994 at a flight altitude of 11.3km, observation angle 20° and a system noise temperature of 68000K (diode: 1112). Temperature recording outside the aircraft indicated that we were above the tropopause. In Fig. 2a the spectrum is shown which results out of 245sec OH net observation time. During the second flight in September 1994 the flight altitude of 11.9km was still in the tropopause. The observation angle was 22°. The net observation time for OH was 314 sec. The system noise temperature was improved to 18000K (diode: 1T15), which yields a less noisy baseline comparing (a) and (b) in Fig. 2. In Fig. 2a and b calculated spectra are given

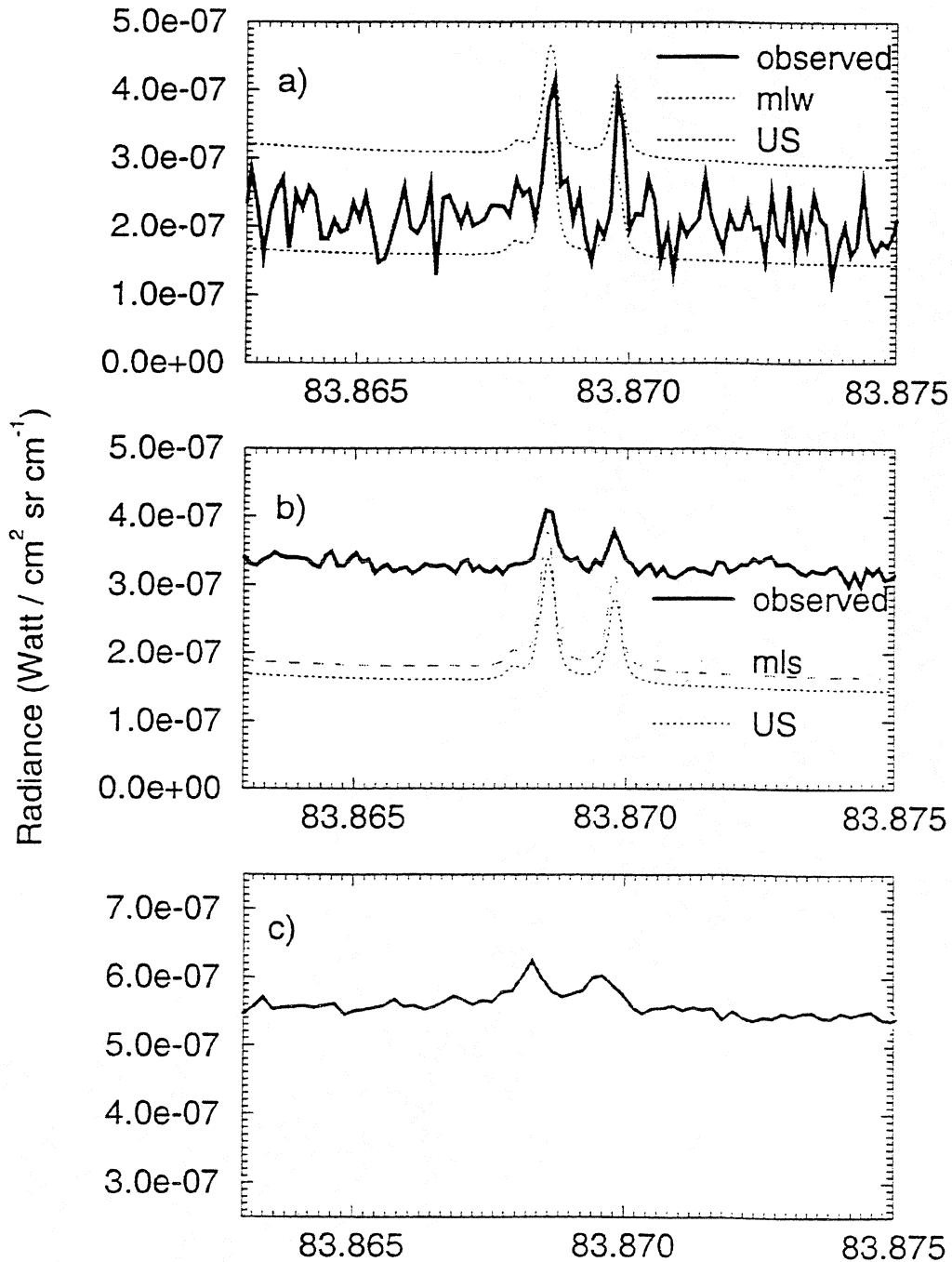


Fig. 3: Spectra of stratospheric OH measured aboard the FALCON aircraft
 a) June 1994, observation angle: 20°, $T_{\text{sys}}= 68000$ K, altitude: 11.3 km, above tropopause, OH observation time: 254 sec.
 b) September 1994, angle: 22°, $T_{\text{sys}}= 18000$ K, altitude: 11.9 km, in the tropopause, OH observation time: 314 sec.
 c) March 1995, angle: 10°, $T_{\text{sys}}= 18000$ K, altitude: 10.7 km, in the tropopause, OH observation time: 831 sec.

with respect to the flight conditions and different atmospheric models. For the June measurements the model of midlatitude winter (mlw) seems to fit best, for September the midlatitude summer (mls) model was closest to the measurements, in both figures the forward calculation with the US standard atmosphere is also given.

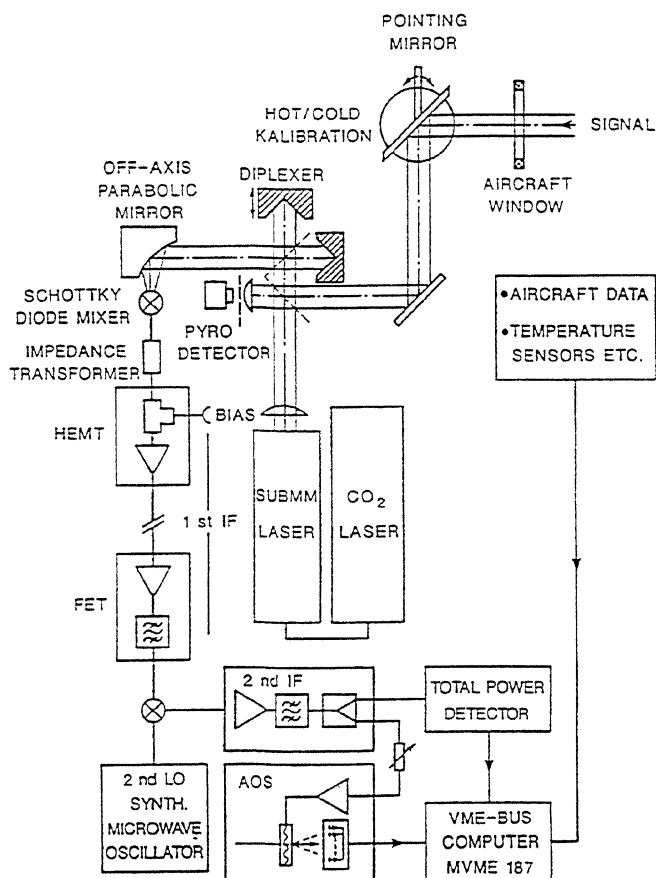
In February/March 1995 we participated in the Second European Stratospheric Arctic and Mid-latitude Experiment (SESAME). In Fig. 2c a spectrum is shown which was obtained at 10.7 km with an observation angle of 10° during a flight from Stockholm to Munich. The system noise temperature with a 1T15 diode was around 18000K. Because of a further improved system, especially with respect to the optically pumped laser, the time for measuring the atmospheric signal could be increased to 831 sec during one flight hour.

Conclusion

A heterodyne system at 2.5THz has been used to measure the thermal emission of upper stratospheric OH in several flights. The system was improved steadily, the latest results yield spectra which can be inverted in order to obtain OH concentration profiles. This seems to be a promising step towards the space qualification of a THz heterodyne system.

References:

- [1] S. Miller, M. Birk, F. Schreier, D. Hausmann, Int J Infrared and Millim Waves **13**, 1241-1268 (1992)
- [2] H.P. Röser, J. Schmid-Burgk, G. W. Schwaab, R. U. Titz, Proc. 29th Int Astrophysical Coll , Liège, Belgium, 3-5 July 1990, ESA SP-314 (1990)
- [3] T.W. Crowe, R. J. Mattauch, H.P. Röser, W.L. Bishop, W.C.B: Peatman, X. Liu, Proc. IEEE, **80**, 11 (1991)
- [4] R. Titz, M. Birk, D. Hausmann, R. Nitsche, F. Schreier, J. Urban, H. Küllmann, H.P. Röser, Infrared Phys (accepted for publication 1995)



Mixer	GaAs Schottky Diode in a open structure mount Type: 1112 and 1T15
Local Oscillator	Optically pumped gas laser at 2522 GHz with 10mW output power
1st IF	8.46 GHz
2nd LO	Synthesizer: 7.475 GHz /6.55 GHz
AOS	2048 channels
center frequency	0.995 GHz / 2.1 GHZ
resolution	1.5 MHz / 1MHz
bandwidth	±420 MHz / ±700 MHz
Sensitivity (1T15)	Tsys (DSB)= 18000 K

Tab. 1: Specifications of the heterodyne system. First value for the measurements with the AOSof University of Bremen, second one with the MAN Technology AOS.

Fig. 1: Airborne heterodyne system

A Novel Micron-Thick Whisker Contacted Schottky Diode Chip

A. Simon^{*}, A. Grüb^{*}, M. Rodriguez-Gironés^{*}, H.L. Hartnagel^{*},
J. Brune⁺, M. Raum⁺, H. Brand⁺, R. Zimmermann[#]

** Institut für Hochfrequenztechnik, TH Darmstadt, Merckstr. 25, 64283 Darmstadt, Germany*

+ Lehrstuhl für Hochfrequenztechnik, U Erlangen-Nürnberg, Cauerstr. 9, 91058, Erlangen, Germany

RPG - Radiometer Physics GmbH, Bergerwiesenstr. 15, 53340 Meckenheim, Germany

Abstract

Although planar diode technology recently has improved significantly, whisker contacted Schottky diodes are required for applications above 1 THz. This paper presents a novel whiskered substrate-less diode chip which exhibits a significantly reduced DC series resistance. Due to the extremely small chip geometries, these diodes are also expected to be more suitable for operation at THz frequencies than the conventional diode chips because of the reduced skin effect resistance.

The novel diode chip consists of a 100-250 μm wide gold foil with a 10-30 μm wide and 3 μm high GaAs mesa on it. The typical honeycomb-array of anodes is located on top of the mesa. The diameters of the gold foil and the GaAs mesas can be varied according to the mixer geometry.

Up to now, diode chips with 0.8 μm and 0.5 μm anodes have been fabricated and compared to conventional diode chips with identical epi-layers and anode diameters. The novel device shows a DC series resistance which is reduced by $\sim 3 \Omega$.

The fabrication process for these devices is presented which requires a number of additional steps compared to the conventional devices.

Introduction

A number of optimisation approaches for whiskered Schottky diodes have improved the performance of heterodyne receivers for use at frequencies as high as 2.5 THz. The traditional chip structure consists of a chip which is typically 100-200 μm square and 80-100 μm thick, with ohmic contacts on the back and a honeycomb anode array on top.

The optimisation of a diode covers the following items:

- reduction of the zero-bias junction capacitance and the series resistance which mainly determine the high-frequency performance
- GaAs growth and fabrication techniques for a high-quality Schottky contact which mainly determines the noise behaviour
- layer design according to the application
- structuring of the entire chip

With respect to a decrease in zero-bias junction capacitance of less than one fF the anode diameters have been reduced to 0.25-0.5 μm [1]. Plating techniques for a high-quality Schottky metal deposition providing an oxide-free contact have been investigated [2,3]. The quality of the epitaxial layers has improved significantly and the structure of the layers have been optimised with regard to the specific needs of the radiometer developers [4,5]. In this paper we investigate the optimisation and fabrication of improved chip structures with respect to THz applications. There are several reasons why the structure of the entire chip could be optimised:

- at highest frequencies the skin effect adds significant parasitic resistance to the diode which degrades the receiver sensitivity
- the diode chip is mounted in different embedding circuits and the ideal chip shape might differ.

Diode Design

The skin effect confines the current within a few microns of the outer boundary of the chip for frequencies higher than a few hundred gigahertz. Fig. 1 shows the skin effect resistance vs. diode diameter at 600 GHz, 1 THz and 2.5 THz [6] for a traditional diode chip geometry indicating that at highest frequencies the skin effect becomes an important factor. Especially at 2.5 THz, the most important frequency for the investigation of the OH molecule, the skin effect adds 8 Ω ($d = 0.5 \mu\text{m}$) to the series resistance and therefore decreases the receiver sensitivity.

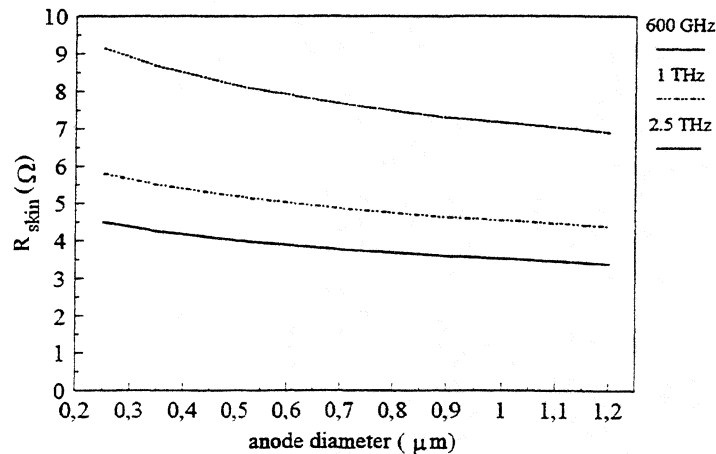


Fig. 1 skin effect resistance vs. diode diameter for several operating frequencies

In a first attempt Seidel and Crowe [7] calculated and fabricated a membrane diode with a thickness of about 2 microns which should be capable to reduce the series resistance. Using an improved finite difference calculation Bhapkar and Crowe [8] have shown that a reduction of the substrate significantly reduces the influence of the skin effect. Neglecting the ohmic contact, the series resistance should be reduced by more than 30 % at 1 THz compared to a traditional diode chip if the thickness of the substrate does not exceed the skin depth. Taking into account reasonable specific ohmic contact resistivities, a substrate thickness of at least 2 microns has been proposed. At 2.5 THz even with a thickness of two microns most of the current is forced to flow in the outer boundaries of the chip and therefore the benefit of a thin substrate is reduced.

As a second approach to reduce the influence of the skin effect the diameter of the chips can be reduced. Kelly et al. [9] fabricated 30 μm diameter cylindrical Schottky diode chips which should result in a decrease of the skin resistance of about 10 %.

To reduce the influence of the Skin effect most effectively we decided to fabricate devices which are drastically reduced in height and width illustrated in Fig. 2. With a substrate thickness of 2 - 3 microns a reasonable effective ohmic contact area still is provided. In combination with a diode chip diameter of 15 - 35 microns the influence of the skin effect is significantly reduced. Such diode chips would be extremely difficult or maybe impossible to handle. Therefore, the diode is located on top of a metal disk which is providing the ohmic contact. The diameter of this disk is 120 - 250 microns with a thickness of at least 10 microns to obtain mechanical stability of the whole structure and to guarantee a facilitated soldering of the diode into a mixer mount.

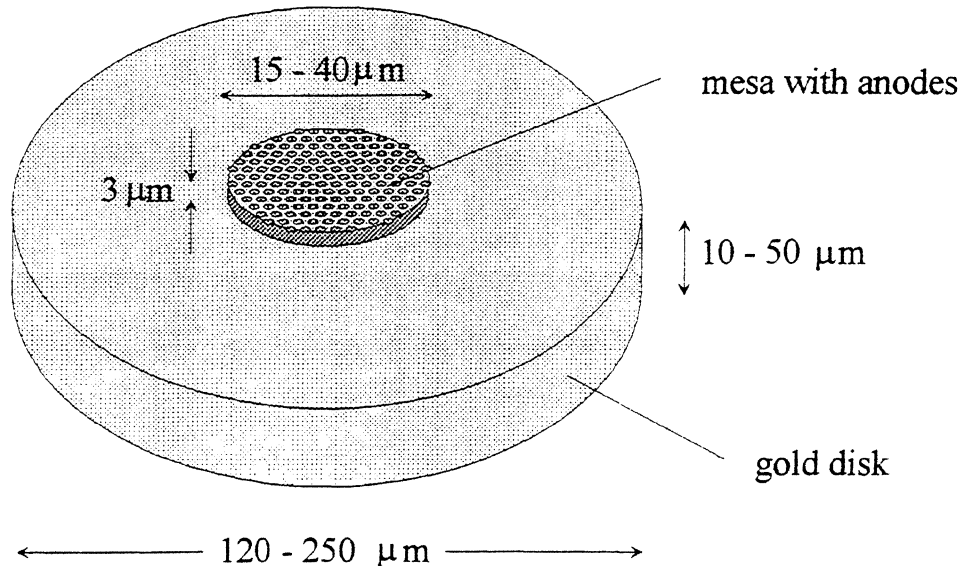


Fig. 2 "Substrateless" diode chip

Device Fabrication Process

The material is composed of four layers. A 1 μm $\text{Ga}_{0.45}\text{Al}_{0.55}\text{As}$ - layer is grown on top of a semi insulating GaAs substrate to incorporate an etchstop layer into the structure. A 3 μm n^+ GaAs with a doping level of $N_D = 3 \times 10^{18} \text{ cm}^{-3}$ is used to create the ohmic back-side contact. A 50-100 nm ($N_D = 3 \cdot 10 \times 10^{17} \text{ cm}^{-3}$) n-GaAs active layer completes the structure. A 300 nm layer of SiO_2 , which is necessary for the definition of submicron anodes, is deposited on the active layer. The wafers are lapped to a thickness of about 100-120 μm. With a selective via-hole etching using $\text{H}_2\text{O}_2 / \text{NH}_4\text{OH}$ (pH = 7.9) and a modified spray etching technique, small holes with diameters of $\varnothing = 120 - 250 \text{ μm}$ are defined from the backside. The AlGaAs layer is etched selectively with $\text{J}_2:\text{KJ}:\text{H}_2\text{O}$. Ohmic contacts which have been formed at the original interface between GaAs and AlGaAs often offered a high contact resistance. Therefore, prior to the deposition of a Ni/AuGe/Ni contact 100-200 nm of this interfacial layer is removed with a nonselective etchant. A rapid thermal annealing step with a subsequent electroplating of the contact areas to a thickness of 10 - 30 μm completes the backside fabrication steps.

The fabrication processes for the anode definition are the same as utilised for conventional whiskered diode chips. For the formation of the anodes the samples are processed by standard contact UV lithography. The honeycomb pattern is transferred to the oxide

by reactive ion etching. To achieve near ideal electrical and noise performance a homogeneous metal/semiconductor contact, free of interfacial layers, is required. Using anodic pulse etching in a Pt- electrolyte some nm of the epitactical layer are removed. Within the same electrolyte 100 - 150 nm of Pt is deposited [10]. A final 150 nm Au overlayer deposition completes the anode formation.

The mesas are defined by a two-step etch process: Firstly, the SiO_2 mesh regions between the mesas is etched in buffered HF. Finally, with an $\text{H}_2\text{O}_2 / \text{NH}_4\text{OH}$ (pH = 7.9) etchant small mesas remain on the Au backside metallisation. The mesas then are covered with wax and the remaining substrate is removed using $\text{H}_2\text{O}_2 / \text{NH}_4\text{OH}$ (pH = 8.4).

Fig. 3 shows a mesa with a diameter of 16 μm and 1 μm anodes on top of a 120 μm metal disk prior to the substrate removal. This shows that very small mesa and metal disk diameters are possible. The main limitation for these geometrical aspects is not the fabrication technology but the handling of the devices and the contacting of the anodes. In Fig. 4 a 35 μm diameter mesa with 0.5 μm anodes is shown. Fig. 5 shows a device with seven diode mesas after substrate removal. Devices with only one mesa utilize less than 1 % of the wafer surface. Therefore, our recent devices have been fabricated with seven mesas. The Au-disc and the mesas offer high mechanical stability and the handling is even easier as with the traditional chips.

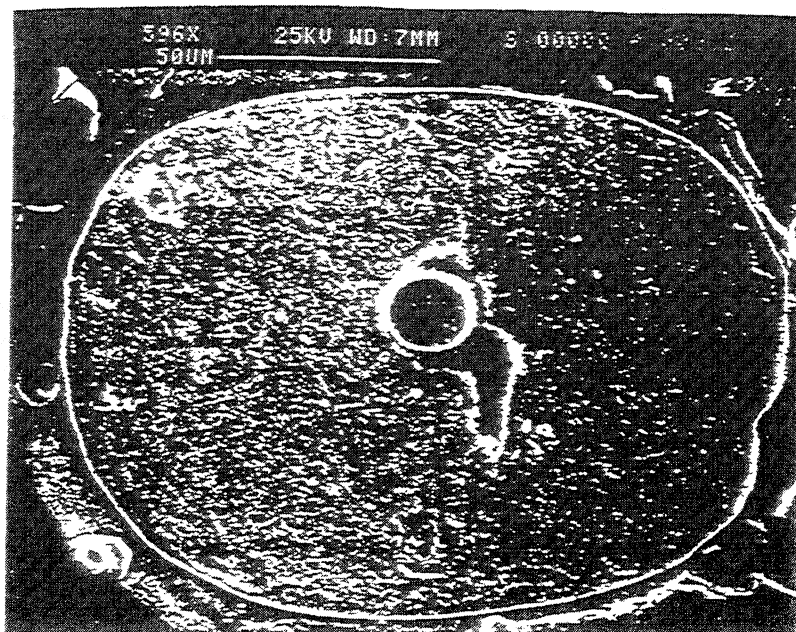


Fig. 3 mesa. $\varnothing=16 \mu\text{m}$ with 1 μm anodes on top of a $\varnothing=120 \mu\text{m}$ Au-disc

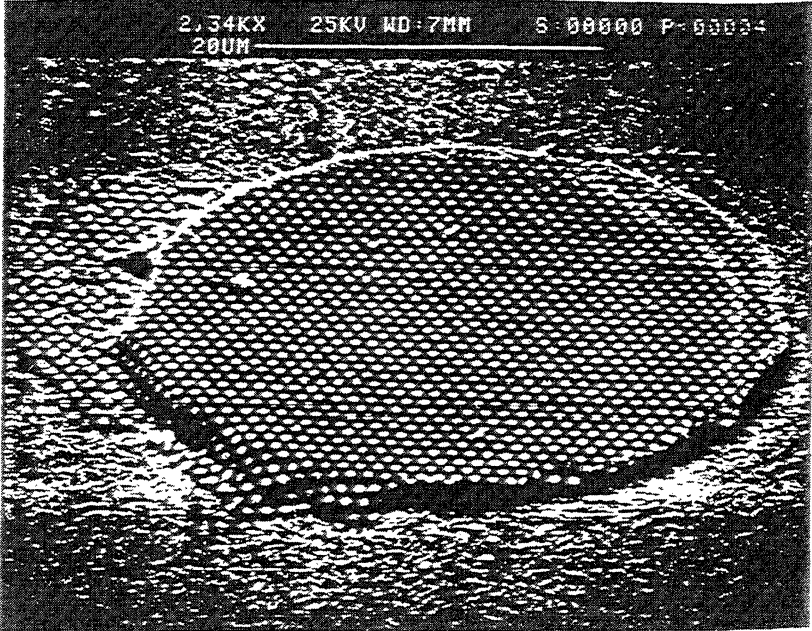


Fig. 4 mesa, $\varnothing = 35 \mu\text{m}$ with $0.5 \mu\text{m}$ anodes

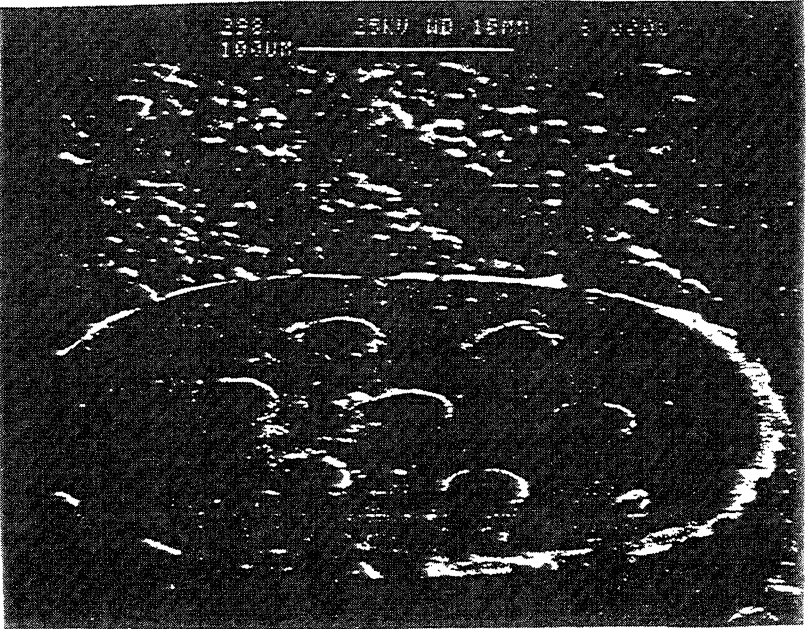


Fig. 5 device with seven mesas

Device Characteristics

A batch of prototype diodes has been fabricated with different epi-layer doping concentrations and anode diameters. Table I shows a comparison of a conventional chip and four substrateless devices.

	DA560	DASL038	DASL037	DASL055	DASL107
parameter					
type	conventional	substrateless	substrateless	substrateless	substrateless
$N_{\text{epi}} (\text{cm}^{-3})$	3×10^{17}	3×10^{17}	3×10^{17}	5×10^{17}	1×10^{18}
$d_{\text{anode}} (\mu\text{m})$	0.8	0.8	0.6-0.7	0.5-0.6	0.7
$R_s (\Omega)$	13	10	20	30	30
C_{j0} (fF)	1	1	(0.6)	(0.5)	(1)
η	1.1	1.1	1.12	1.21	1.32

Table 1 DC characteristics of different diodes

The first substrateless diode, the DASL038 offers the same barrier characteristics of the corresponding standard whiskered diode DA560 (also fabricated at TH Darmstadt) but a 3Ω lower series resistance. Assuming that the crystal quality of the wafers is the same and with the prospect of a reduced skin resistance the high frequency results performance of the new devices is very likely to be even better. First results (measured at RPG) are shown below. At 545 GHz a mixer noise temperature of $T_M=1300$ K has been achieved. There is only one result with a conventional whiskered diode (DA560 at 570 GHz) which has achieved a better performance.

Although devices with 0.5-0.7 micron anodes have shown low series resistances there is no striking decrease in DC series resistance compared to traditional chips. To classify these devices in Fig. 6 the plot of $\log(I)$ against V and the differential resistance against V of the DASL055 and the IT12 and IT6 from the University of Virginia are shown. The IT12 and IT6 which have shown excellent performance [11], are the most established half-micron whiskered diodes with nearly the same doping levels as the DASL055. It can easily be seen that the three diodes exhibit almost identical I/V curves. Small differences occur in the R_s curves which are probably due to variations in the anode diameters. Taking into account the prospect of reduced dependence on the skin effect the substrateless devices offer very promising DC- characteristics.

	Freq (GHz)	L(dB)	T_{Svs} (K)	T_M (K)
DA560	570	6	1550	1250
DASL055	545	6.1	1680	1300

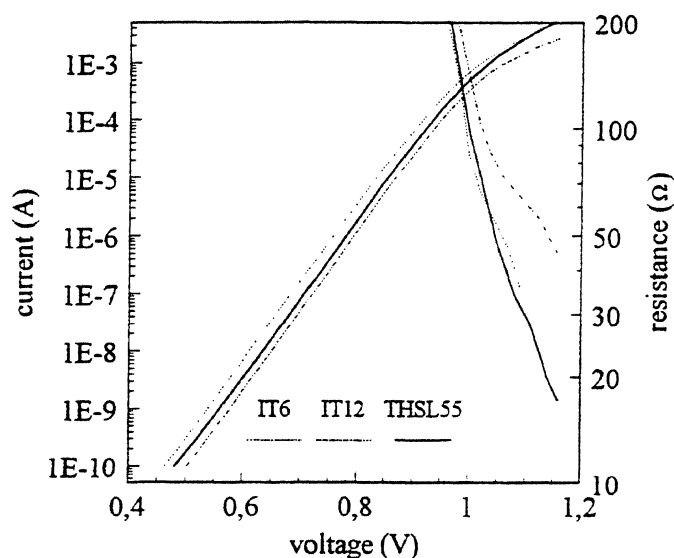


Fig. 6 DC-characteristics of the DASL055, IT12 and IT6

Besides these pros there are some serious cons, which will however be overcome in the future. The uniformity of different batches and even diodes on different mesas still show some variations. There are several reasons for this:

- the quality of available wafers varies much more than that for standard diodes
- the AlGaAs etchstop layer creates dislocations in the following grown GaAs layers which are essential for good diode performance
- the formation of a good ohmic contact is much more difficult

Therefore, the fabrication has not yet achieved the maturity of standard devices and up to now there are only prototype chips available. To obtain a higher reproducibility we will substitute the AlGaAs by an InGaP etchstop layer. InGaP can be grown lattice matched and due to its higher selectivity a reduced layer thickness can be chosen. Both aspects should positively affect the crystal quality and therefore the performance of the diodes.

Conclusion

A fabrication process for Schottky barrier diodes with reduced overall dimensions has been developed. These devices should offer a drastically reduced influence on skin effect and therefore could offer advantages in the THz frequency range. Prototype devices have been fabricated and the DC characteristics show that the same or even slightly reduced series resistance values and the same ideality factors with respect to traditional diode chips can be achieved.

The fabrication has not yet achieved the maturity of the standard whiskered chips. This is mainly due to the AlGaAs etchstop layer which decreases the quality of the essential layers significantly and makes the formation of a reasonably good ohmic contact much more difficult.

Acknowledgement

The authors would like to express their acknowledgements to Dr. H. Grothe and Dr J. Freyer, both from the Technical University of Munich, Germany, for supplying the high-quality epitaxial material.

References

- [1] P. A. D. Wood, D. W. Porterfield, W. L. Bishop, T. W. Crowe, "GaAs Schottky Diodes for Atmospheric Measurements at 2.5 THz", Fifth International Symposium on Space Terahertz Technology, pp 355-367, 1994
- [2] T. W. Crowe, "GaAs Schottky Barrier Mixer Diodes for the Frequency Range 1-10 THz", Int. Journal IR and Millimeter Waves, Vol. 10, No. 7, pp.765 -777, 1989
- [3] A. Grüb, C. Lin, H.L. Hartnagel, "Electrolytic Deposition Techniques For The Fabrication Of Submicron Anodes", this proceedings
- [4] A. Jelenski, A. Grüb, V. Krozer, H. L. Hartnagel, "New Approach to the Design and Fabrication of THz Schottky Barrier Diodes", IEEE Tans. Microwave Theory Tech., Vol 41, No. 4, pp. 549-557, 1993.
- [5] A. Grüb, V. Krozer, A. Simon, H.L. Hartnagel, "Reliability and Micro-Structural Properties of GaAs Schottky Diodes for Submillimeter-Wave Applications", Solid-State Electronics, Vol 37, No. 12, pp 1925-1931, 1994
- [6] L.E. Dickens, "Spreading Resistance as a Function of Frequency", IEEE Transactions, Vol. MTT-15, No. 2, pp 101-109, Feb. 1967
- [7] L.K.Seidel, T. W. Crowe, "Fabrication and Analysis of GaAs Schottky Barrier Diodes Fabricated on Thin Membranes for Terahertz Applications", Int. Journal IR and Millimeter Waves, Vol. 10, No 7, pp. 779-787, 1989
- [8] U. V. Bhapkar, T. W. Crowe, "Analysis of the High Frequency Series Impedance of GaAs Schottky Diodes by a Finite Difference Technique", IEEE Trans. Microwave Theory Tech., Vol. 40, No.5, pp. 886-894, 1992
- [9] W. M. Kelly, S. Mackenzie, P. Maaskant, "Novel Chip Geometries For THz Schottky Diodes", Fifth International Symposium on Space Terahertz Technology, pp. 404-408, 1994
- [10] A. Grüb, R. Richter, H. Hartnagel, "Electrolytic Processes for Etching and Metal Deposition towards Nanometre Quantum Structures", Electr. Letters, vol. 27, no.4 pp. 856-857, 1991
- [11] W. C. B. Peatman, T. W. Crowe, "Design and Fabrication of 0.5 Micron GaAs Schottky Barrier Diodes for Low-Noise Terahertz Receiver Applications", Int. Journal IR and Millimeter Waves, Vol. 11, No. 3, pp. 355 -365, 1990

AN ALL-SOLID-STATE - 1 THz - RADIOMETER FOR SPACE APPLICATIONS

Rüdiger Zimmermann *, Thomas Rose *,
Thomas W. Crowe **, Thomas W. Grein **,

*RPG Radiometer-physics , Bergerwiesenstr. 15, 53340 Meckenheim, Germany

** Semiconductor Device Laboratories, U. of Virginia, Charlottesville, USA

SUMMARY

A heterodyne receiver at 1 THz is described, whose components are waveguide mixer and frequency multipliers with Schottky-diodes as mixing and multiplying elements.

Most important is the breakthrough in local-oscillator development:

The power at the fundamental frequency is generated by an InP-Gunn-Oscillator which delivers 70 mW at 111.22 GHz. The output power from two cascade triplers (at the 9th-harmonic) was 60 μ W (min.)

Coupling of signal- and L.O.-power is achieved by a Martin-Puplett Interferometer. System noise temperature was determined with absorbers at room temperature and 77 K yielding $T_{\text{sys}} = 8800$ K (DSB) and total conversion loss = 13dB. Atmospheric losses appear to account for half of the noise temperature and 3dB conversion loss. The mixer is prepared for cooling to liquid nitrogen from which we hope for a further reduction in system noise of approximately a factor of two.

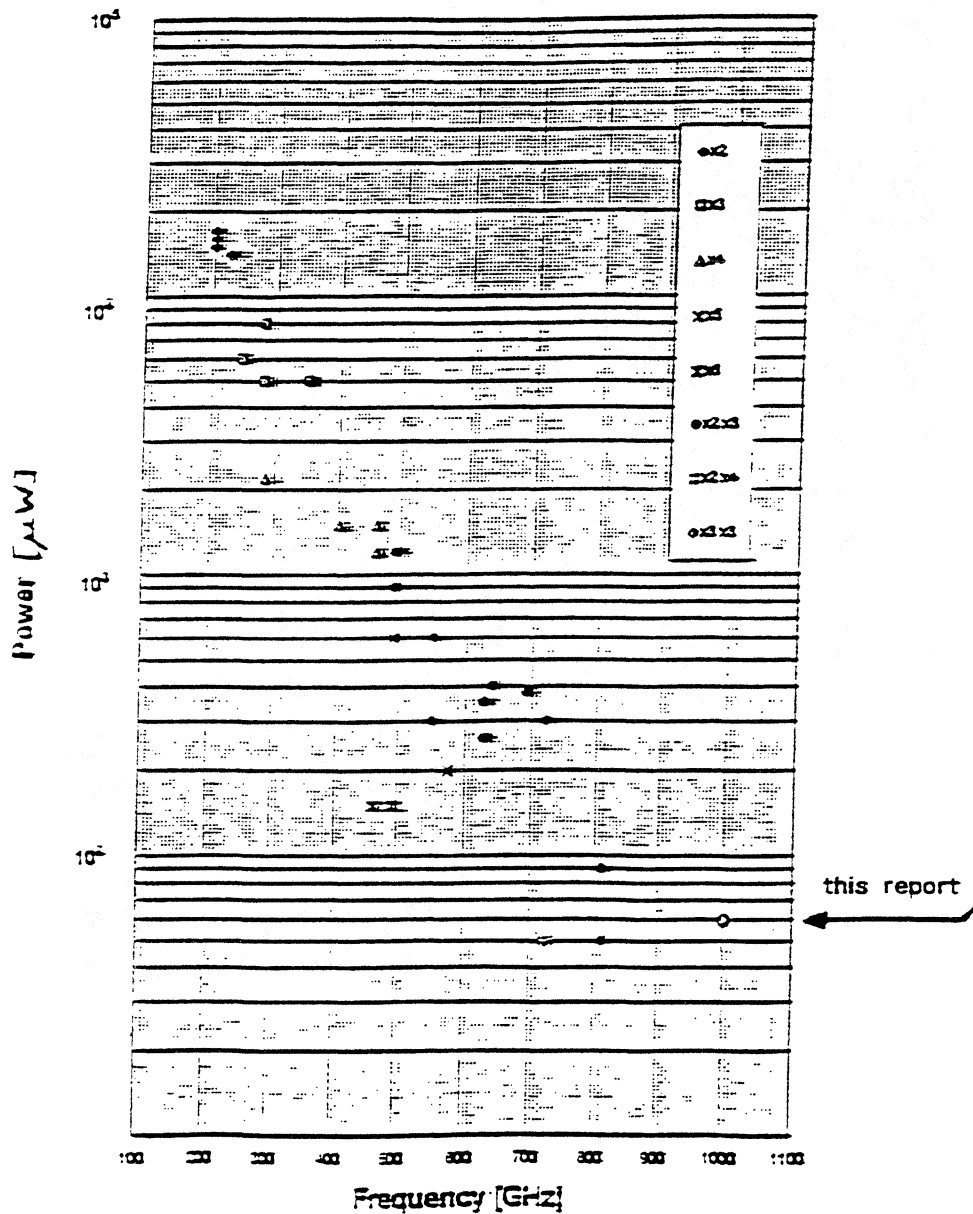
INTRODUCTION

A study for the FIRST - project of the European Space Agency requires submm-receivers up to 1200 GHz for a spaceborne mission, with low weight, low power consumption and high receiver sensitivity. Despite considerable improvements in SIS-receivers over the past years, their performance at and above 1000 GHz is

SIS-receivers over the past years, their performance at and above 1000 GHz is unknown and their liquid helium requirement could be a drawback for space operation.

Schottky-receivers could be operated in space with closed-cycle refrigerators at 80 K, but up to now only carcinotrons or lasers have been suitable as LO-sources. Recent improvements in solid-state oscillators up to 800 GHz (see Figure1) have indicated that all-solid-state LO's will be usable to above 1 THz.

Figure 1: Output Power of Local Oscillator sources



LOCAL OSCILLATOR DESIGN CONSIDERATIONS

From practical experience with receivers at 550 GHz and 650 GHz [1,2] we estimate that a cooled Schottky diode requires approximately 100 μ W output power, in order to achieve lowest conversion loss. Since this is the most critical step in building an all Solid-state-Schottky-receiver, we describe how the final L.O. design was chosen by employing a varactor-diode multiplier driven by a solid-state fundamental oscillator.

As fundamental oscillators we considered gunn-oscillators in the range 100-125 GHz, due to their excellent spectral properties and space compatibility. In 1991, 50 mW was obtainable at 111 GHz and 25 mW at 125 GHz, today the figures are (respectively) 70 mW and 50 mW.

The basic theory of frequency multiplication by varactor-diodes is given by Penfield and Rafuse [3] and has been used to create a multiplier analysis program by Siegel, Kerr and Hwang [4]. On the basis of this program we evaluate which multiplication factor might produce the highest efficiency.

The selection of suitable varactor diodes commenced by taking the parameters given by the manufacturer. Table 1 lists the principal parameters: series resistance (R_s), junction capacitance (C_j) and breakdown voltage (V_{Br}) in the reverse direction.

Unfortunately the key parameter in varactor applications, the capacitance modulation, is not given. It determines the figure-of-merit or the dynamic cut-off-frequency (f_c)

$$f_c = \frac{S_{\max} - S_{\min}}{2 \pi R_s}$$

where S_{\max} and S_{\min} are maximum and minimum values of the junction elastance (= capacitance⁻¹) over one cycle of the pump waveform. Measurements at RPG yield capacitance modulation results also shown in Table 1.

TABLE 1

Diode	R_s []	C_j [fF]	V_{Br} [V]	f_c [GHz]
VD 011*	10.6	12.3	16.5	1370
VD 012*	14.7	9.3	15.0	1440
6P4 **	8	19	20	2200
2T2 **	12.4	5.6	10.8	4800
2T8 **	14.7	4.0	10	n.m.

* Farran Technology

**University of Virginia ,Semiconductor Devices Lab

Generally the diode with the highest cutoff frequency leads to the highest efficiency , but the input power is restricted by the breakdown voltage in the reverse direction and the maximum safe current in the forward direction. Since high input power and reliability is required for effective operation, the 6P4 was chosen for the first multiplier stage. For the second stage, and generally speaking for higher input frequencies, the 2T2 was the diode of choice due to the high-cutoff frequency and low capacitance.

In principle multiplication can be achieved in a single diode, but the efficiency for x8, x9 or x10 is very low. In addition there would be the difficulty of implementation due to the many idlers which have to be correctly terminated. Hence we considered cascaded multipliers of x2x2x2, x2x4, x2x5 and x3x3, using the diagrams for efficiency in [3] and the multiplier program [4].

The results are shown in Table 2.

TABLE 2

Multiplicat. factor	Input frequ. (GHz)	Cutoff frequ. (GHz)	Input power (mW)	Efficiency (%)	Output power (mW)
1.) x2	125	1400	25	25	5.5 (2.75)
x4	250	2000	2.75	0.5	<0.002
2.) x2	125	1400	25	22	5.5 (2.75)
x2	250	2000	2.75	15	0.4 (0.2)
x2	500	2000	0.2	1	0.002
3.) x3	100	1400	50	30	15 (7.5)
x5	200	2000	7.5	0.2	<0.015
4.) x3	111	2200	50	26	13 (6.5)
x3	333	2000	6.5	5,5	0.36 (0.18)

Values in parantheses are for estimated 3 dB mount losses

It can be seen:

- a.) the octupler combinations x2x4 and x2x2x2 deliver output power of only 2 μ W. This does not change significantly even if the fundamental power is raised to 50 mW.
- b.) The x2x5 suffers from the problem that the efficiency of the second stage (quintupler) is too low.
- c.) The x3x3 combination produces the most output power, whereby the first stage can deliver as much as 6.5 mW and the second stage up to 180 μ W.

The calculations do not consider the velocity saturation effects as theoretically described in [5], and thus it is expected that the actual output powers will be significantly lower than predicted. However, it is hoped that the analyses are accurate enough to compare the various multiplier designs and justify our choice of a x3x3 multiplier chain.

Table 3 shows the predicted performance of a tripler to 990 GHz with a 2T2 when velocity saturation effects are neglected and when the diode current is clipped at 23 mA to simulate these effects. With 10mW of input power assumed, the result is a drop in output power from 1.2 mW ($\eta = 11.6\%$) to 0.06 mW ($\eta = 0.6\%$).

TABLE 3 from [5]

Table 3: Calculated performance of 990 GHz Schottky Barrier Diode Varactor (2T2) Multiplier.

	P_{in} (mW)	i_{RF} (mA)	$\bar{a}W/\alpha$ 10^5 (m/s)	η	R_s (Ω)	a
3x330	2	24	2.3	4.1	12	-
GHz	10	53	4.6	11.6	12	-
i_{sat}	2	23	2.0	2.3	$R(i)$	$1.53 \cdot 10^9$
23 mA	10	31	2.9	0.6	$R(i)$	$1.53 \cdot 10^9$

An accurate analysis of a submillimeter wavelength multiplier circuit, including all of the embedded impedances at the fundamental and important harmonics, and an accurate model of the electron transport in the Schottky diode has not yet been developed. This is partially due to the extreme nonlinearity of the circuit. However, the complex nature of the electron transport in the diode also complicates such an analysis. Traditional multiplier analyses use the measured low frequency series resistance, junction capacitance and breakdown characteristics to generate a diode equivalent circuit that is assumed to be accurate at very high frequencies. As was initially pointed out by Kollberg, this is generally not a valid assumption. Charge carrier inertia and velocity saturation certainly affect multiplier performance and must be accurately incorporated into the analyses. Furthermore, the difficulty of modeling the diode's reverse breakdown due to avalanche multiplication in such a non-dc situation is also considerable. Attempts are now being made to develop more complete analyses of high frequency multipliers which will take these effects into account [6,7].

Due to these theoretical limitations, we chose simultaneously to pursue an experimental path toward varactor diode optimization. For example, it seems clear that diodes with thinner and more heavily doped epitaxial layers should be less likely to suffer from velocity saturation effects. This appears to have been confirmed in a recent publication [8] which compared two diodes, UVa 6P4 and 5T1, in a 100-200 GHz doubler. Both of these diodes are described in Table 4 and the newer diode (5T1) was also used in the first stage tripler for this paper.

Since velocity saturation effects become more critical at higher frequencies, the second stage tripler is even more challenging. Up to the present, two diodes, UVa 2T2 and 2N1, have been used in this system. However, only the 2N1 diode, with its higher doping density and thinner epitaxial layer, has yielded significant output power.

Table 4 also presents the characteristics of a variety of newer varactor diodes that have been fabricated with doping densities as high as $4 \times 10^{17} \text{ cm}^{-3}$ and zero-bias capacitances in the range from 3 to 6 fF. The trade-offs are clearly evident in this data: As the doping is increased the series resistance is reduced for a given zero-bias capacitance level, but the breakdown voltage is reduced. Thus, greater efficiency is expected but at the cost of reduced power handling ability.

However, this appears to be a necessary trade-off for THz frequency multipliers.

TABLE 4

Nominal Parameters for Some Schottky Varactor Diodes							
Diode Batch	Epitaxial Doping Density (cm^{-3})	Epitaxial Thickness (μm)	Anode Diameter (μm)	Series Resistance (Ω)	Breakdown Voltage (V)	Zero-bias Capacitance (fF)	Capacitance at Breakdown (fF)
6P4	3.5×10^{16}	1.0	6.3	9.5	20	20	5
5T1	1×10^{17}	0.6	4.7	5.3	10	22	7.5
2T2	1×10^{17}	0.6	2.5	11.5	10.7	5.5	1.9
2T3	1×10^{17}	0.6	2.5	11.5	10.7	5.5	1.9
2N1	2×10^{17}	0.26	1.8	9	9.8	5.3	2.4
2T12	2.3×10^{17}	0.24	2.1	7.2	8.2	5.5	—
2T13	4×10^{17}	0.16	1.8	5	5.9	6.2	—
2T14	2.3×10^{17}	0.24	1.7	8.5	7	4	—
2T15	4×10^{17}	0.16	1.4	8.5	6	3.3	1.6

LOCAL OSCILLATOR CONSTRUCTION

The local Oscillator comprises of a Gunn-oscillator, coupler, the tripler-tripler cascade and an output feedhorn (s. fig. 2).

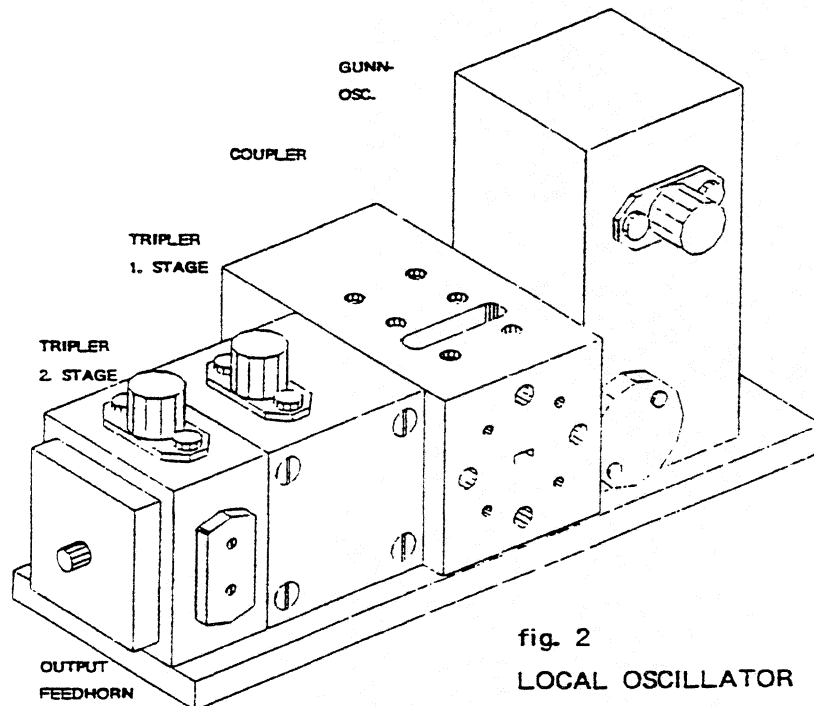


fig. 2
LOCAL OSCILLATOR

Contrary to the usual multiplier design, whereby input- and output-waveguide are at 90° to each other (crossguide), we have developed an in-line-construction. This considerably simplifies construction when two or more multipliers have to be cascaded.

The principal details of the tripler mounts are shown in Fig.3.

These mounts consists of three parts:

The UPPER BLOCK contains the bias connector, a rejection filter to prevent leakage of the fundamental frequency and the input waveguide. The MIDDLE BLOCK contains the coupling structure for the fundamental frequency to the diode and is simultaneously a rejection filter for the harmonics. The LOWER BLOCK contains the output waveguide, idler cavity and the whisker post.

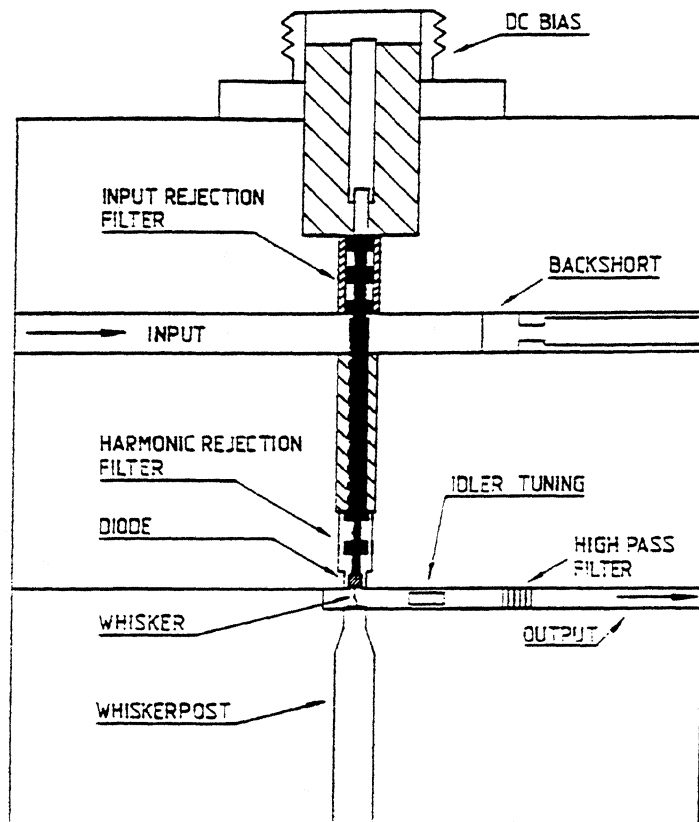


fig. 3 MULTIPLIER SCHEMATIC

Critical features of the design are:

a.) Input power coupling structure

This includes the waveguide and a low pass-filter with low losses at the fundamental frequency and high rejection at all higher harmonics. The waveguide is single moded and reduced in height to provide efficient coupling to the coaxial probe, which is part of the filter. The waveguide bends 90° around this probe. The backshort is of the contacting loop-type, as this results in best performance up to the highest frequencies.

b.) Harmonic rejection-filter and diode

This filter is in-line with the coaxial probe, and is constructed in coaxial airline technique being held by a macor spacer.

This has the following advantages over microstrip:

- 1.) Lower dissipative losses
- 2.) If changes are required during multiplier development these can be achieved more rapidly.

The dimensions have to be kept very small, to prevent the excitation of the first coaxial waveguide mode, whose cutoff-wavelength is given by

$$\lambda = \pi (a + b) / 2$$

(a , b = inner and outer diameter of coaxial section)

At 1000 GHz the first section a + b should be ≤ 0.19 mm, which can be achieved with a = 0.07 mm, b = 0.12 mm. In addition, excellent coaxial alignment is essential, particularly when the inner section becomes wider.

The filter was originally from a Tchebycheff design and was then modified for best performance by modelling between approx. 2 and 20 GHz.

c.) output section

This consists of the whisker, idler tuning circuits, high-pass filter and output waveguide.

The whisker is a further key element for good multiplier performance. Firstly it provides a DC-contact to the diode and should provide an ohmic contact without adding any series-resistance. Secondly the whisker length and diameter are critical since they determine the inductance in series with the diode.

The output waveguide was chosen to be cutoff for idler and fundamental frequencies. It was matched to the diode-whisker idler circuit by a moving backshort.

The dimensions of the output-waveguide became as small as 0.27x0.05mm to prevent losses into higher modes.

LOCAL OSCILLATOR RESULTS

The output power of the gunn-oscillator at 111.22 GHz was measured with a Hughes Thermistor Mount. The result was $70 \text{ mW} \pm 5\%$.

With 70 mW input power the output power of the first tripler was 7 mW. This was measured with a TK-powermeter * in a quasioptical setup, no corrections for possible inaccuracy of beam-matching or atmospheric losses are applied. We estimate the accuracy of this measurement in the range $\pm 10\%$.

Though the result in itself is quite acceptable, the achieved efficiency of 10% is low compared to the prediction of 26%. At present it is not clear whether the discrepancy is due to dissipative or mismatch losses or to the velocity saturation effect.

The second tripler, delivered a minimum output power of $60 \mu\text{W}$. This was again measured with a TK-power meter. The accuracy of this result is difficult to estimate due to the problem of atmospheric absorption. The variations during the measurement indicate higher power.

An indication about the atmospheric losses at 1000 GHz is given by a measurement of rectified power at a mixer diode: when the mixer-feedhorn was placed against the multiplier output feedhorn, the increase in mixer current was three times more than when the mixer feedhorn was illuminated through the quasioptical path in the receiver. From our experience in building receivers with low loss quasioptical components we estimate that most of the loss was due to atmosphere: we estimate 3 dB.

QUASIOPTICS AND MIXER

Signal and local oscillator were coupled into the waveguide mixer through a Martin Puplett polarisation diplexer [9] and a dual-mode horn [10]. The coupler consisted of $10 \mu\text{m}$ tungsten wires with $60 \mu\text{m}$ spacing.

*Thomas Keating Ltd, Station Mills, Billingshurst, England

Two elliptical mirrors served as beam matching devices to mixer and multiplier feedhorn respectively.

The mixer is a scaled version as described in [11] with a waveguide cross-section $270 \times 50 \mu\text{m}$. The mixer diode chip, a 1T15 from Semiconductor Device Lab. of Univ. of Virginia was mounted on a four-section coaxial filter protruding through the middle of the broad wall of the waveguide. This diode is described in detail in [12] and was specially designed for terahertz use. The epitaxial layer doping density was $1 \times 10^{18} \text{ cm}^{-3}$ and the anode diameter was 0.25 microns. The measured DC series resistance was roughly 25 Ohm and the zero-bias capacitance was 0.25fF, yielding a figure-of-merit cut-off frequency of 25 THz ($1/2\pi R_s C_j$). The whisker-wire was eight microns in diameter with a sharply pointed tip. This diode has been specifically developed for THz mixing applications and has already yielded excellent results in corner-cube mixers at 2.5 THz [13]. At 1 THz it is not expected to be the most sensitive mixer diode available, but was chosen for this work because of its low local oscillator power requirement.

The output of the coaxial filter was matched to the IF amplifier by a transformer centred at 1.4 GHz.

RECEIVER RESULTS

A schematic of the receiver is shown in fig. 4 . The mixer is mounted in a dewar in preparation for later cooling to liquid nitrogen. The IF amplifier was centred at 1.4 GHz with 100 MHz bandwidth, and had a noise temperature of 35 K.

System noise temperature was measured by the Y-factor method, using absorbing material (Emerson and Cumings AN-72) at 77 K and ambient temperature. No corrections are made for non-ideal absorbtivity (exact value not known) and errors due to assuming the Rayleigh-Jeans approximation (about 10 K, at this frequency).

REFERENCES

- [1] 550GHz mixers for ODIN, Swed. Space Project, results at
RPG-Radiometer-physics
- [2] 650GHz receiver: Development of Limb Sounder Critical Receiver
Technologies, ESA contract No. 2292/89/NL(PB), results at
RPG-Radiometer-physics
- [3] Penfield and Rafuse, Varactor Applications
MIT Press, 1962
- [4] P.H. Siegel, A. R. Kerr, W. Herang,
Topics in the Optimization of Millimeter-Wave-Mixers
NASA Technical Paper 2287, March 1984
- [5] E.L. Kollberg, T.J. Tolmunen, M.A. Frerking and J.R. East,
“ Current Saturation in Submillimeter Wave Varactors,“
IEE Trans. Microwave Theory Tech., Vol. MTT-40,
No. 5, pp. 831-838, May 1992
- [6] J.R. Jones, S.H. Jones, G.B. Tait, and M.F. Zybura
“Heterostructure Barrier Varactor Simulation Using an Integrated
Hydrodynamic Device/Harmonic-Balance Circuit Analysis Technique“
IEEE Microwave and Guided Wave Lett., Vol. 4, No. 12, p. 1-4,
Dec. 1994
- [7] J.R. Jones, S.H. Jones, and G.B. Tait
“Self-Consistent Physics-Based Numerical Device / Harmonic-Balance
Circuit Analysis of Heterostructure Barrier and Schottky Barrier Varactors
including Thermal Effects.“ This proceedings
- [8] T.W. Crowe, W.C.B. Peatman, R. Zimmermann, and R. Zimmermann
“ Consideration of Velocity Saturation in the Design of GaAs Varactor
Diodes“
IEEE Microwave and Guided Wave Letters, Vol. 3, No. 6,

- pp. 161-163, June 1993
- [9] D.H. Martin
Polarizing Interferometric Spectrometers for the
Near- and Submm-Spectrum
Infrared and MM-waves, Vol. 6, Ed. by K.J. Button
Academic Press
- [10] M.H. Picket, J.C. Hardy, J. Farhoomand
Characterization of a Dual Mode Horn for Submm-Wavelength,
IEEE, MTT-32, 1984 (936-937)
- [11] R.R. and P. Zimmermann
All-Solid-State Radiometers for environmental studies to 700GHz
Third Int. Symp. on Space Terahertz Technology
March 1992, Univ. of Michigan, Ann Arbor
- [12] W.C.B. Peatman, T.W. Crowe, G. Lundershausen, and
H.P. Roser
“ A Quarter-Micron GaAs Schottky Barrier Diode with High Video
Responsivity at 118 μm “
Appl. Phys. Lett. 61 (3), July 1992
- [13] P.A.D. Wood, D.W. Porterfield, W.L. Bishop and T.W. Crowe
“ GaAs Schottky Diodes for Atmospheric Measurements at 2.5 THz“
Proc. Fifth Intl. Symp. Space THz Tech., Ann Arbor, May 1994

A Practical Schottky Mixer for 5 THz

A. L. Betz and R. T. Boreiko
Center for Astrophysics and Space Astronomy
University of Colorado, Boulder

I. SCIENTIFIC MOTIVATION

The wavelength band between 60 and 120 μm is particularly important for observations of the interstellar medium, for it is here that the cores of galactic molecular clouds radiate most of their energy. Both continuum radiation from warm dust grains and line radiation from ions, atoms, and molecules are important cooling mechanisms for material warmed by the intense UV radiation from newly formed stars. Velocity gradients within the clouds are so small that the resolving power of the spectrometer should exceed 10^6 , if the intrinsic line shapes (and the information they contain) are not to be degraded. Heterodyne receivers capable of such resolution have so far only been operated at wavelengths $>118 \mu\text{m}$ (2.5 THz) [1]. Of particular interest to astronomers are observations of the fine structure line from neutral oxygen (O I) at 63 μm (4.75 THz). This transition is the major cooling line for the "warm" ($T = 200 \text{ K}$) and "dense" ($n \geq 10^6 \text{ cm}^{-3}$) gas in the cloud core. Of course this radiation cannot penetrate the earth's atmosphere, so all observations must be done above the tropopause with aircraft or space-borne instruments. To date only grating and Fabry-Perot spectrometers have been successfully used for observations of the oxygen line, albeit with far less spectral resolution than that possible with heterodyne techniques.

We can estimate some of the line parameters for the oxygen line by comparison with another fine structure line emitted by these

clouds: the 158 μm line of ionized carbon (C II). This longer wavelength line has been observed with a laser heterodyne spectrometer aboard NASA's Kuiper Airborne Observatory (KAO) for over 7 years now [2]. Heterodyne observations at 3 MHz (0.5 km s^{-1}) spectral resolution have shown that the C⁺ emission may in some sources be optically thick, in which case its function as a major cooling mechanism is somewhat impaired. For the conditions expected in cloud cores, emission from the 63 μm line should be even more optically thick (saturated), but no direct spectroscopic evidence exists. Up to now most theoretical analyses of excitation temperatures in photodissociated gas have been based simply on the observed intensity ratio of unresolved 158 μm carbon and 63 μm oxygen lines, which are assumed to be optically thin. Therefore the derived excitation temperatures (and element abundances) could be erroneous if either line is optically thick. A better way to determine the gas excitation temperature would be to measure the peak brightness temperatures of resolved O I and C II lines. If a case for optically thick emission can be made, then the peak temperature yields the excitation temperature directly.

Fabrication of a mixer for 63 μm using either waveguide or a standard 4λ antenna corner-reflector design [3] would be an exercise in tedium and disappointment. Fortunately, a practical solution exists within the corner reflector design model, and that is to use an antenna length much greater than 4λ .

Our plan is to use an antenna length in the range of $20-30\lambda$ for observations at $63\mu\text{m}$, and thereby to avoid some of the tight technical constraints imposed by a shorter antenna length. Another constraint is the time schedule – the only available observational platform, the KAO aircraft, will likely no longer be in service after September, 1995.

II. TECHNICAL PLAN

(A) Background on Corner Reflector Mixers

Heterodyne receivers using GaAs Schottky diodes and far-infrared lasers as local oscillators (LOs) have proven themselves to be practical instruments for astronomical spectroscopy at wavelengths between 400 and $118\mu\text{m}$. Although their dominance for ultra-high resolution observations ($\lambda/\delta\lambda > 10^5$) arises primarily from the lack of practical competing technologies, it should be borne in mind that they are still sensitive enough for a number of problems of astronomical interest, in particular the study of the strongest FIR lines which dominate the cooling of molecular clouds. Although SIS mixers undoubtedly will prove superior to Schottky diodes at the longer FIR wavelengths ($> 330\mu\text{m}$) sometime soon, there is still a future for Schottkys and laser-LOs at the shorter FIR wavelengths.

The advance of Schottky mixers to sub-millimeter and FIR wavelengths began with the introduction of the open resonator corner-reflector mixer design. Most corner reflector mixers now in use are similar to the original design of Krautle *et al.* [3] in that they have a 4λ “long-wire” antenna spaced a distance of 1.2λ from the apex of a 90° roof-type reflector. The tip of the antenna contacts the anode of a small ($< 1\mu\text{m}$) GaAs Schottky diode, which is the active mixer element. There is nothing magic about the 4λ antenna length, but it does yield a main beam with good symmetry in the E- and H-planes, with an $f/3$ divergence which is easily matched to the telescope. Further work on this general design

showed that although a better main beam efficiency can be achieved with a shorter antenna length of 1.35λ (spaced 0.9λ) [4], antenna lengths much longer than 4λ could be effectively used if the reflector spacing is appropriately chosen [5].

The principal advantage of the open-structure corner-reflector design is that it is simple and has relatively few critical dimensions, all of which are larger than λ . Consequently, in comparison with the more traditional waveguide structure with its sub- λ dimensions and three-dimensional constraints, corner-reflector mixers are much easier to fabricate and generally have lower losses. The long-wire character of the antenna, however, does introduce more sidelobe structure to the beam pattern than does a single-mode waveguide mixer, but the penalty of about 3 dB in main-beam efficiency for the “long-wire” seems worth the price when the alternative may be no mixer at all.

As we go to ever shorter wavelengths, the 4λ antenna itself becomes difficult to fabricate and position accurately. At $158\mu\text{m}$ where the important C II fine-structure line occurs, the 4λ antenna is only 0.63 mm long, and for the equally important $63\mu\text{m}$ O I line the length is only 0.25 mm. In an attempt to keep the mixer dimensions much larger than common machining tolerances, we have investigated the efficiency of higher order antennas with lengths of 10 to 30λ . For the $63\mu\text{m}$ O I line, a 25λ antenna length is physically identical to a 4λ design for $370\mu\text{m}$, which we know from experience to be mechanically practical.

The efficacy of antenna lengths longer than 4λ is demonstrated by our observations of the $158\mu\text{m}$ C II line, where we used an antenna length of 9.7λ [2]. As will be shown below, for any antenna length $> \lambda/2$, most of the radiation can be confined to a single main lobe if the distance s between the reflector apex and the antenna wire is correctly adjusted. For the 9.7λ antenna mentioned above, $s = 1.7\lambda$.

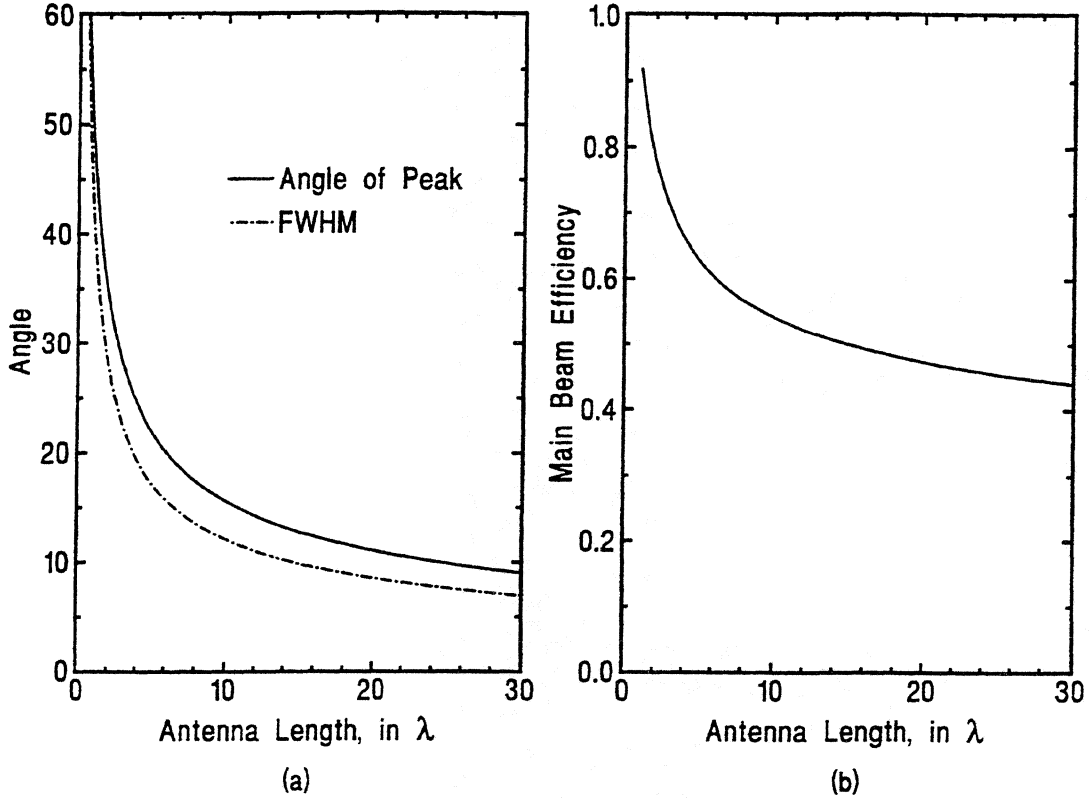


Figure 1: Peak angle, width, and efficiency of a long wire antenna

The apex spacing s increases slowly with antenna length, as will be shown later, and for this reason we still need to be careful about dimensional tolerances for the short wavelength mixers. A 25λ mixer for $63\mu\text{m}$, for example, will have an apex spacing $s = 3\lambda$, which is $189\mu\text{m}$. For best operation this distance should be accurate to $\lambda/2$, which is 16% of s .

(B) Mixer Description

The discussion which follows is adapted from Zmuidzinas *et al.* [5], with emphasis on the parameters of antennas with lengths of $20\text{--}30\lambda$.

(1) Long Wire Antennas

The antenna's radiation pattern is that of a long wire with a traveling-wave excitation. For such an antenna (assuming equal current and phase velocities) the far-field pattern is given by:

$$E_{\theta}(\theta) \propto \sin \theta \left[\frac{\sin[(\pi L/\lambda)(1 - \cos \theta)]}{(\pi L/\lambda)(1 - \cos \theta)} \right], \quad (1)$$

where L/λ is the length of the wire in wavelengths and θ is the angle between the wire and the direction of peak radiation. If there are no obstructions, the radiation pattern is symmetric about the wire axis (independent of the azimuthal angle ϕ). The power radiated by the long wire antenna can be computed from the square of the E-field given in the equation above. The intensity in the higher order lobes dies away because of the $\sin^2\theta$ term in the power dependence, and is exactly zero by $\theta = 180^\circ$. We are interested in the fundamental lobe of the response. For antennas with lengths $\geq 4\lambda$, the angle θ_{max} at which the response is maximized is given approximately by:

$$\theta_{max} \approx \cos^{-1}(1 - 0.37101(\lambda/L)), \quad (2)$$

where L is the length of the antenna. Figure 1a illustrates this equation and also shows the 3 dB beamwidth as a function of antenna length. Figure 1b shows the fraction

of the total power radiated (or received) in the main lobe as a function of L/λ (where the integral around the symmetry axis of the antenna has been performed). As we go to longer antennas, the power in the main lobe drops, but not rapidly. As can be seen in Figure 1b, a 25λ wire is 70% as efficient as a 4λ wire in coupling power into the fundamental lobe, and therefore is quite attractive for work at the shortest wavelengths. From these graphs we can deduce three things: (1) antenna lengths of $4\text{--}30\lambda$ have nominally similar efficiencies, (2) antenna lengths can be chosen to synthesize a beamwidth well matched to the telescope optics, and (3) the beam angle and width of the antenna response is approximately proportional to $\sqrt{\lambda/L}$ and hence not a strong function of the antenna length for $L > 10\lambda$.

(2) Corner Reflectors

The placement of the corner reflector in the path of an incoming beam will produce standing waves in the vicinity of the reflector. For optimum coupling, the antenna should be located at the first standing-wave peak produced by radiation incident on the symmetry axis of the corner reflector ($\phi = \pi/4$) and at the angle θ_{max} . For the specific case of a 90° corner reflector, the optimum spacing s of the antenna to the reflector apex is given by:

$$s = \lambda/2 \sin \theta_{max} . \quad (3)$$

This equation is plotted in Figure 2, where θ_{max} is solved for exactly and not by the approximation given before. From the figure we see that for a 4λ antenna $s = 1.2\lambda$, whereas for a 25λ wire $s = 3\lambda$.

Figure 3 shows the calculated E-plane beam patterns (in the plane of the antenna wire and reflector apex) for 4λ and 30λ mixers with the corner reflector in place. The increased sidelobe content of the longer wire is evident, but the main-beam response is well formed in both cases. The cross-power (H-plane) response has a similar beamwidth and is free

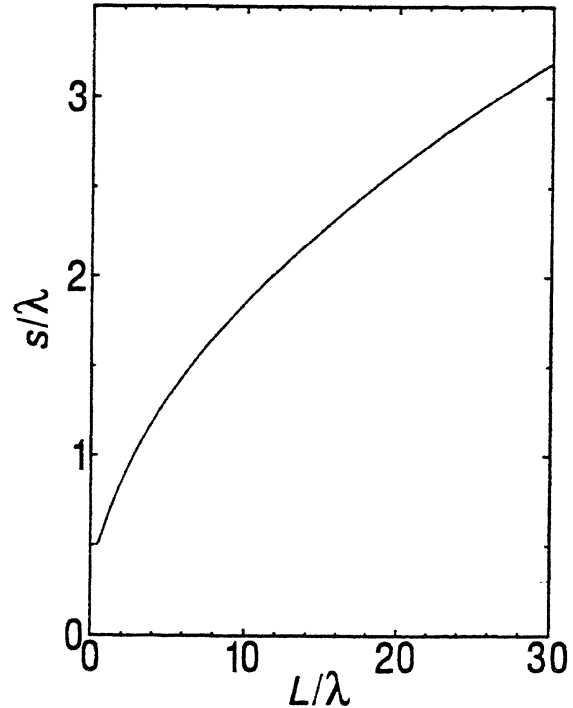


Figure 2: Optimum reflector spacing s as a function of antenna length L

of sidelobe structure for $\theta = \theta_{max}$. The off-axis response, on the other hand, contains considerable sidelobe structure, but nothing larger than -6 dB relative to the peak response. The mixer beamwidths are slightly smaller than those of long-wire antennas in free space because of the interaction of the reflectors. Notice that some low level E-plane sidelobes of a free-space antenna are significantly reduced after the reflectors are positioned. Our measurements of beam patterns for 4 and 9.7λ mixers confirm these predicted response patterns, and give us confidence that the $20\text{--}30\lambda$ mixers will perform to expectations. Our first measurements for the E-plane response of a mixer with a 25.2λ antenna are shown in Figure 4, along with the calculated (smooth curve) values. These measurements were done at $\lambda = 86\ \mu\text{m}$ (3.5 THz), because the particular mount used could not be ad-

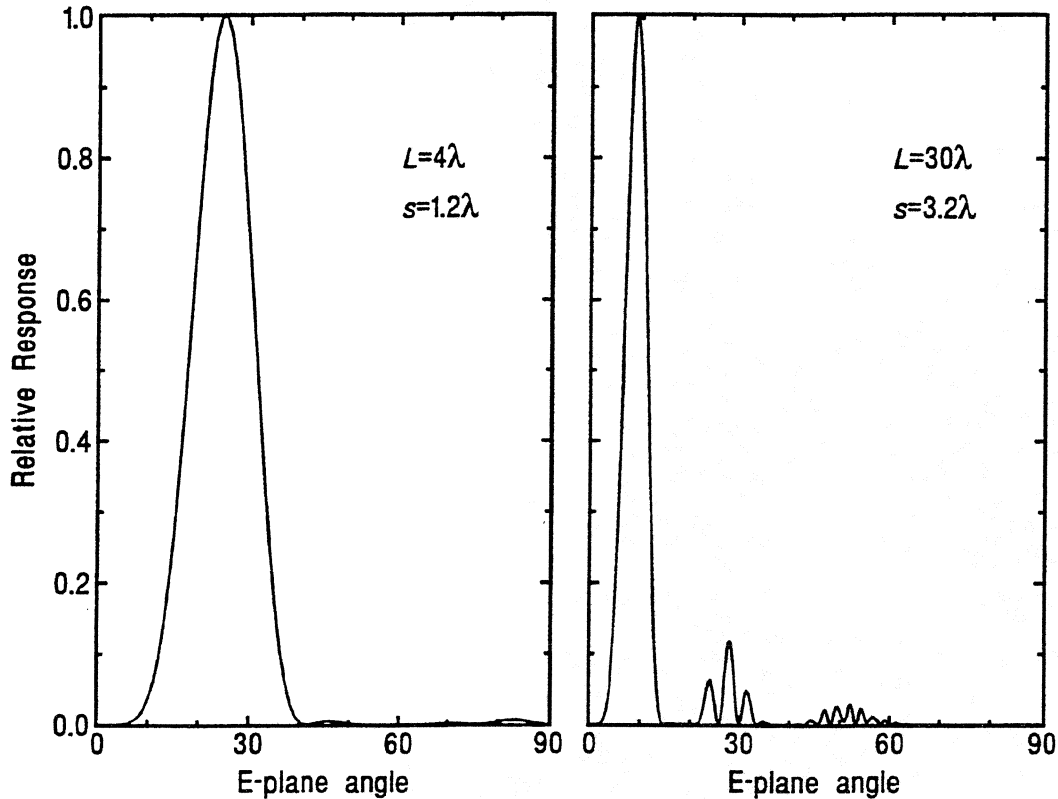


Figure 3: E-plane beam patterns for 4λ and 30λ antennas with optimally spaced corner reflectors

justed for shorter wavelengths. The excess response measured at 30° is thought to be the result of the observed tilt of the antenna whisker relative to the apex line of the corner reflector, and can be improved with further work. Regardless, the agreement between the measured and calculated responses of the mixer in the vicinity of the main lobe is quite good.

(C) Sensitivity Measurements

Our experience with mixers with antenna lengths between 4 and 10λ leads us to expect receiver noise temperatures <5000 K (DSB)/THz between 2.5 and 5 THz. Although we have achieved a receiver noise temperature of 5000 K (DSB) at 1.9 THz (C II line), our best noise temperature at 2.53 THz ($118\mu\text{m}$) was $12,000$ K (DSB) 2 years ago with cooled 1T11 and 1T15 Schottky devices from the Univ. of Virginia Semiconductor Device Lab. It seems that cooled devices with anode

sizes $<0.4\mu\text{m}$ (and concomitant R_S values of 30 - 40 ohms at room temperature) show an increase in R_S upon cooling that limits the coupling efficiency into a 50 ohm IF amplifier.

The mixer of Figure 4 produced a system noise temperature of $15,000$ K (DSB) at 3.5 THz ($86\mu\text{m}$). The mixer uses a type 1T15 GaAs Schottky diode and was tested at room temperature, but the 6 GHz IF amplifier was cooled to 77 K where it achieves $T_N = 35$ K. (Note that 6 GHz is the IF needed for observations of the oxygen line at $63\mu\text{m}$ with the fixed frequency of the laser LO line.) No data are currently available on conversion loss, but measurements are continuing, especially at 4.75 THz ($63\mu\text{m}$) where our goal is $T_{\text{sys}} = 25,000$ K (DSB). This modest performance will be more than adequate to yield S/N ratios better than 100 on many sources of the interstellar $63\mu\text{m}$ O I line.

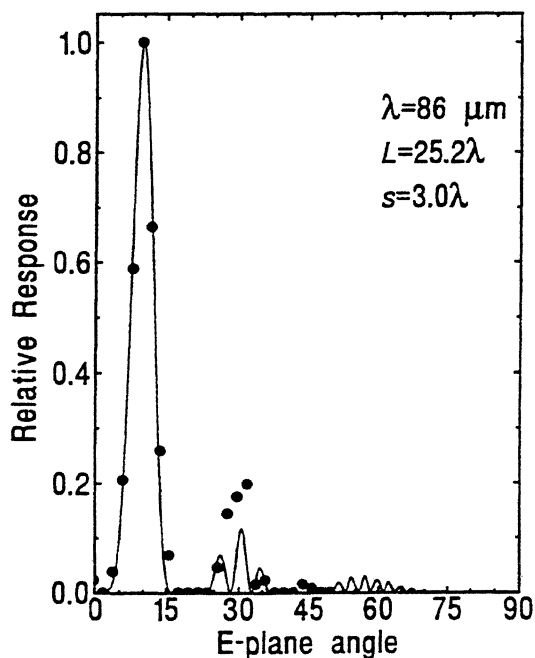


Figure 4: Calculated and measured E-plane response of a 25.2λ antenna with optimally spaced reflectors

- [5] Zmuidzinas, J., Betz, A. L., and Boreiko, R. T., "A Corner-Reflector Mixer Mount for Far-Infrared Wavelengths", *Infrared Physics*, **29**, 119-131 (1989).

References

- [1] Boreiko, R. T. and Betz, A. L., "Heterodyne Spectroscopy of the J=22-21 CO Line in Orion", *Ap. J. (Letters)*, **346**, L97-L100 (1989).
- [2] Boreiko, R. T., Betz, A. L., and Zmuidzinas, J., "Heterodyne Spectroscopy of the 158 Micron C II Line in M42", *Ap. J. (Letters)*, **325**, L47-L51 (1988).
- [3] Kräutle, H., Sauter, E., and Schultz, G. V., "Antenna Characteristics of Whisker Diodes Used as Submillimeter Receivers", *Infrared Physics*, **17**, 477-483 (1977).
- [4] Grossman, E. N., "The Coupling of Submillimeter Corner-Cube Antennas to Gaussian Beams", *Infrared Physics*, **29**, 875-885 (1989).

The Design, Construction and Evaluation of a 585 GHz Planar Schottky Mixer

Jeffrey L. Hesler and Thomas W. Crowe
Department of Electrical Engineering
University of Virginia
Charlottesville, VA 22901

Richard F. Bradley and Shing-Kuo Pan
National Radio Astronomy Observatory*
Charlottesville, VA 22903

Goutam Chattopadhyay
Division of Engineering and Applied Science
California Institute of Technology
Pasadena, CA 91125

Abstract

The design, construction and testing of a room temperature 585 GHz fundamentally pumped planar Schottky waveguide receiver are presented. Microwave modeling of the planar diode and circuit structure are discussed. Preliminary receiver tests have yielded a double sideband receiver noise temperature of 4100 K and total conversion loss of 10.0 dB using less than 0.5 mW of LO power.

Introduction

There is a need for sensitive receivers at submillimeter wavelengths for such applications as radio astronomy, atmospheric studies, plasma diagnostics, molecular spectroscopy and compact range radars. Receivers based on SIS junctions have achieved record sensitivity to frequencies as high as about 800 GHz and are the technology of choice for radio astronomy at millimeter and submillimeter wavelengths. However, many applications, particularly those which involve space based receivers, require a technology which does not require cryogenic cooling. GaAs Schottky diodes have the advantage of operating well at either cryogenic or room temperatures, although not with the sensitivity of SIS receivers. The best reported Schottky receiver at 500 GHz has a receiver noise temperature of only 550K (DSB) at 20K operating temperature [1]. Unfortunately, the best Schottky receivers have used whisker contacted diodes, which

*The National Radio Astronomy Observatory is operated by Associated Universities, Inc. under cooperative agreement with the National Science Foundation.

makes the receiver design and assembly quite expensive, and complicates the space qualification process. This research is an investigation of the use of new planar Schottky diodes [2,3] in waveguide receivers which are optimized through the use of modern circuit simulators and design tools, with the goal of achieving the same level of performance that has already been demonstrated with whisker contacted Schottky diodes.

This paper describes our design, fabrication and initial testing of a 585 GHz waveguide receiver which utilizes state-of-the-art planar Schottky diodes. The design of the mixer, including numerical modeling of the diode and circuitry with Hewlett Packard's High Frequency Design Software is described. These design tools allow us to fully understand the mixer performance and draw important conclusions about the fundamental limits of these receivers in terms of sensitivity and maximum operating frequency. The results of preliminary testing with several mixer configurations are also presented, and future improvements to the receiver are discussed.

Mixer Configuration

The mixer block, shown schematically in Fig. 1, was originally designed for use with an SIS junction. The primary modification was the redesign of the microstrip circuitry which includes the waveguide transition, solder pads for the diode, IF filter structure and bonding pads for the IF output and DC/IF return. The LO and RF signals are coupled into an 8x16 mil waveguide by a diagonal feedhorn. The waveguide transition to microstrip was designed using a scale model at 3.3-4.9 GHz. The measured return loss of the transition was better than 25 dB over the full waveguide band. The design was also verified using Hewlett Packard's High Frequency Structure Simulator (HFSS). The IF and DC return to ground is provided by a 1 mil gold wire bonded to the microstrip which is shorted in indium at the end of a quarter wave side channel. The diode, a UVa SC1T5-S20 diode with 20 μm finger length and 1 μm anode diameter, is mounted across a gap in the microstrip. The distance between the gap and the low pass filter is used for tuning.

Diode Modeling

The equivalent circuit of Schottky junctions has been extensively investigated and is rather well understood. However, the parasitic impedances created by the diode chip structure can also have a great impact on receiver performance. To determine these circuit elements HFSS was used to solve for the fields of the diode mounted in the microstrip channel. The two port S-parameters generated by HFSS were then compared with the equivalent circuit model shown in Fig. 2. The circuit element values were determined by using the optimization routines available in Hewlett Packard's Microwave Design System (MDS) to match the S-parameters with those of the equivalent circuit.

In order to determine the effect of the diode's semi-insulating GaAs substrate, the equivalent circuit for a chip without a substrate was also determined. With the diode

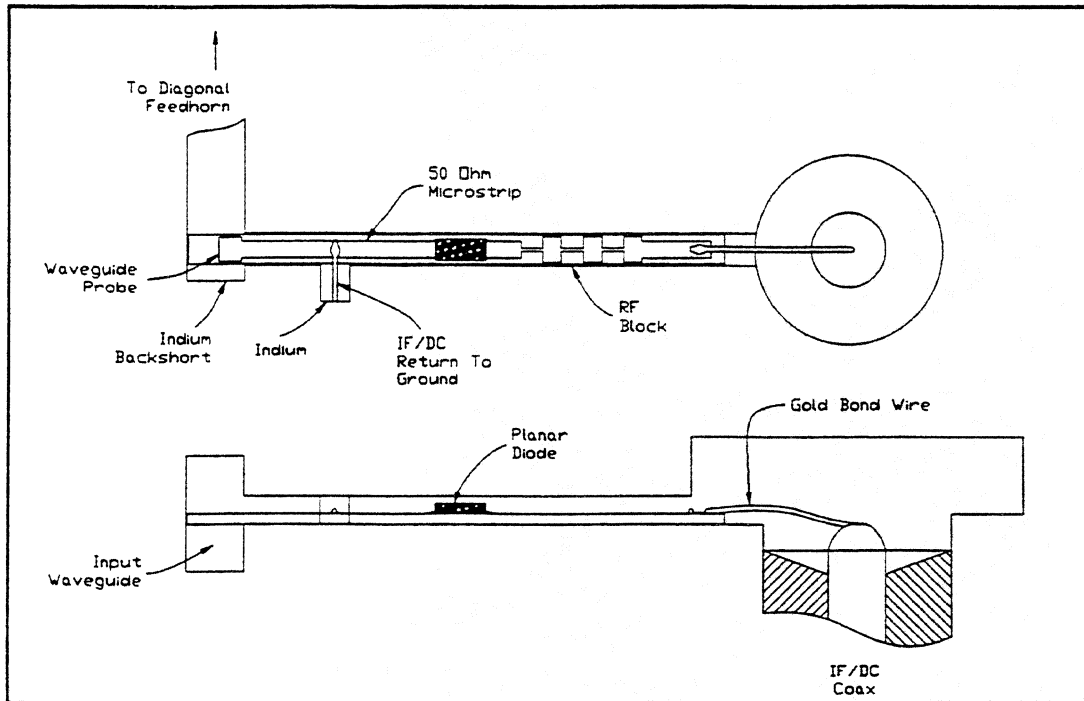


Fig. 1. Schematic of the interior of the 585 GHz mixer block, with quartz choke and diode mounted in block.

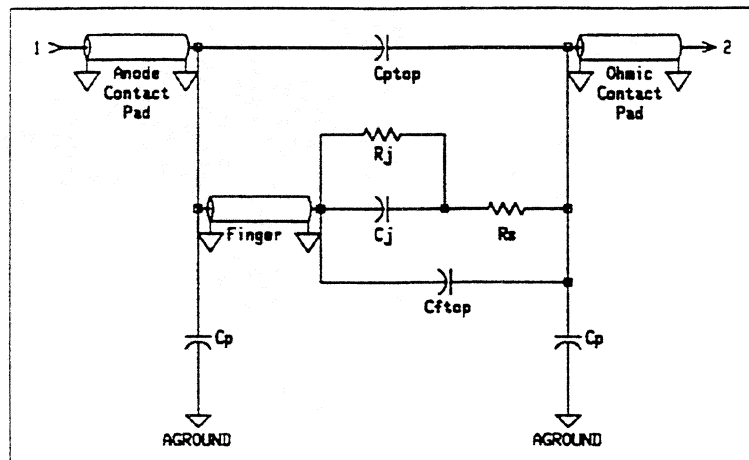


Fig. 2. Equivalent circuit model of SC1T5 planar diode.

substrate in place the pad-to-pad capacitance, C_{pp} , is the dominant parasitic capacitance. However, after substrate removal C_{pp} is significantly decreased and the finger-to-pad capacitance, C_{fp} , becomes the dominant element. Table 1 gives a summary of the equivalent circuit modeling results.

The equivalent circuit model is useful because it gives insight into the relative importance of the various parasitic elements related to the diode's geometry. However, at 585 GHz the lumped element circuit model begins to break down because the geometric features of the diode (e.g. surface channel width) are significant compared to a wavelength. By adding a small coaxial probe near the anode and solving for the fields, the embedding impedance can be determined more directly. Fig. 3 shows a schematic of the area near the anode with a coaxial probe inserted to determine embedding impedance.

In order to compare the two methods, the embedding impedance at the anode is calculated by each method for the circuit of Fig. 4 with Z_{source} and Z_{match} equal to 50 Ω . Fig. 5 shows the variation in embedding impedance for both methods as the distance between the diode and the low pass filter (L_{match}) is varied.

Microstrip Circuit Design

Once the variation of the diode's embedding impedance with system parameters was determined, the harmonic balance routines in MDS were used to design RF coupling structures for the diodes. Typical diode parameters for an SCIT5 diode are: $R_s = 15 \Omega$, $\eta = 1.16$, $I_{sat} = 3E-17$ A, and $C_{fp} = 1$ fF. The values for R_s , η and I_{sat} were determined by a least squares fit of the measured diode I-V to the non-linear diode equation. The mixer simulations include plasma resonance and skin effect by the addition of a complex series resistance. The predicted locations of the conversion loss minimum (L_{opt}) and noise temperature minimum (T_{opt}) for the SCIT5 diode with no parasitics are indicated in the impedance Smith chart shown in Fig. 6.

A schematic of the basic mixer microstrip configuration is shown in Fig. 4. On one side of the diode is a length of transmission line, L_{match} , between the diode and the low pass filter. The low pass filter presents an open circuit at its input to the LO and RF. On the other side of the diode is a length of microstrip line running to the waveguide transition. This mixer circuit design thus offers 3 main variables for tuning: Z_{source} , Z_{match} and L_{match} . Changing L_{match} loops the embedding impedance around the Smith chart in a circle (see Fig. 6). Varying Z_{match} alters the sensitivity of Z_{embed} to changes in both L_{match} and frequency. Finally, varying Z_{source} changes the size of the loop on the Smith chart. The gap which the diode is mounted across can also significantly affect the embedding impedance presented to the diode. This is because the diode's pads alter the transmission line into the nonlinear diode and thus alter Z_{embed} .

The microstrip circuit on which the diode is mounted should be designed to give the proper Z_{embed} while also being broadband in frequency and insensitive to variations in diode mounting. The designs that have been tested to date have had both Z_{source} and Z_{match} of 50 Ω . Harmonic balance simulations indicated that this mixer design is

Diode Type	C_{pp} (fF)	C_{fp} (fF)	C_p (fF)	Z_{finger} (Ω)	θ_{finger} ($^\circ$)
SC1T5-S5	2.9	1.2	0.5	193	6.9
SC1T5-S5 (no substrate)	0.8	1.9	0.3	198	6.4
SC1T5-S20	1.8	1.3	1.0	194	18
SC1T5-S20 (no substrate)	0.3	1.7	0.7	199	17

Table 1. Summary of the equivalent circuit modeling results for the SC1T5 diode.

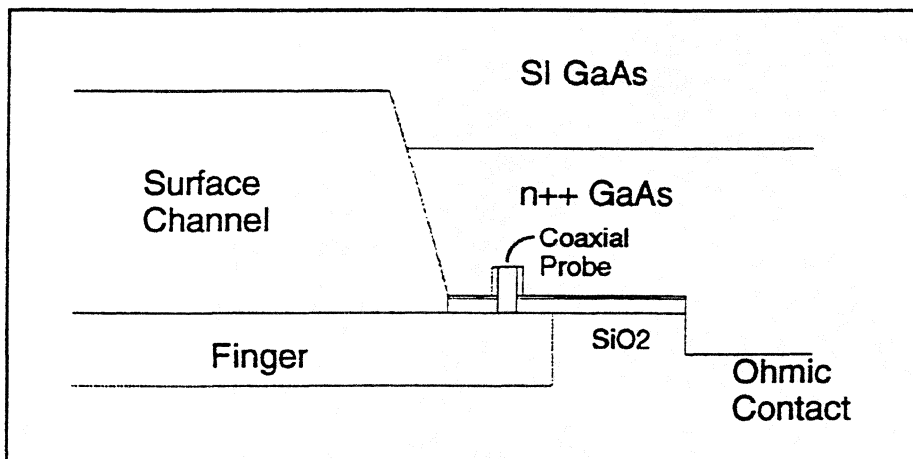


Fig. 3. Schematic of diode near anode for coaxial probe method.

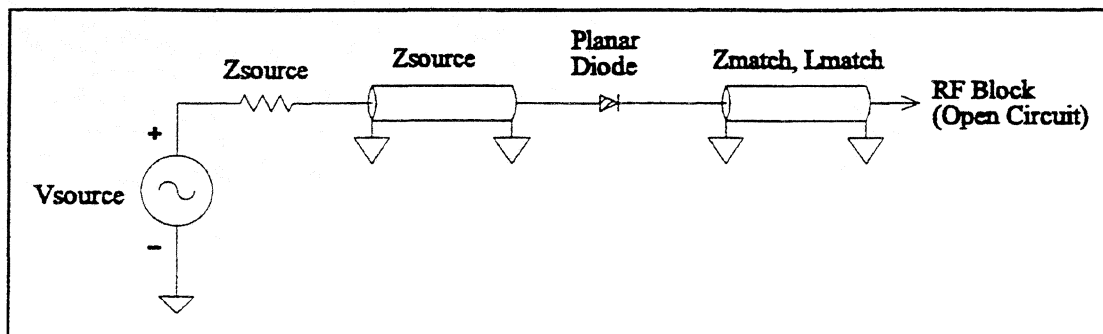


Fig. 4. Simplified schematic of the mixer microstrip configuration.

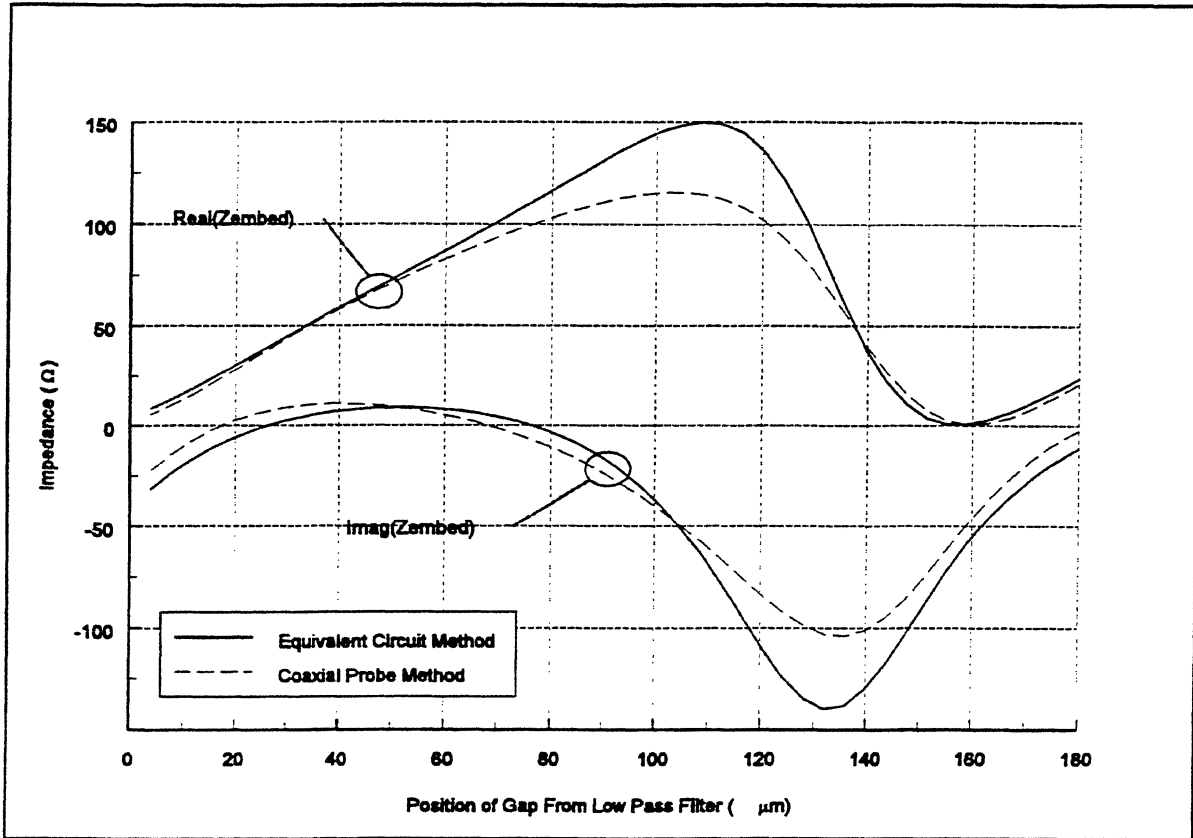


Fig. 5. Variation of embedding impedance with distance between the diode and the low pass filter for equivalent circuit and coaxial probe methods. The curves shown are for a choke with Z_{source} and Z_{match} equal to 50 Ω .

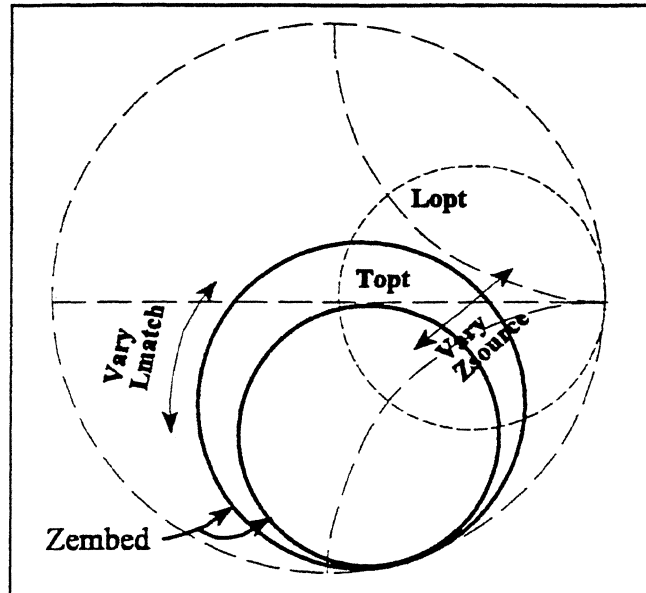


Fig. 6. Z-Smith chart showing variation of Z_{embed} with choke parameters. L_{opt} and T_{opt} indicate points of minimum conversion loss and noise temperature.

broadband, with a 3 dB conversion loss bandwidth of approximately 160 GHz.

The microstrip circuits were fabricated on 1.5 mil quartz substrates. The thin quartz wafer was mounted with wax on a silicon support wafer, allowing the use of standard photolithography techniques to fabricate the circuitry. The quartz wafer was then diced into individual circuits before being removed from the silicon carrier. The IF/DC connection wires were then bonded onto the choke and the diode was soldered across the gap. Finally the quartz structure was mounted into the mixer block and held in place by the wires which were pressed into indium. A picture of a quartz choke mounted in a mixer block is shown in Fig. 7.

Performance of the Diagonal Feed Horn

A diagonal feed horn based on the design discussed in [4] is used to couple power into the mixer block. With proper quasi-optical design this horn should capture 84% of the power from a Gaussian beam. Fig. 8 shows a contour plot of the measured antenna pattern of the diagonal feed horn. This pattern was measured using the video response of a diode mounted in the block. Using this data we calculated the beam waist to be 0.67 mm, which is very close to the design value of 0.7 mm.

Receiver Measurements

A schematic of the receiver test setup is shown in Fig. 9. A Martin-Puplett diplexer [5] and an off-axis parabolic mirror with a focal length of 60 mm are used to couple the LO and RF power into the feed horn. The LO power is supplied by an FIR gas laser which is in turn pumped by a CO₂ gas laser.

The first mixer block tested was made at NRAO, and the best results to date in this block are 4400K double sideband receiver temperature and 10.1 dB conversion loss. A new mixer block with a shorter input waveguide and an integrated feedhorn was fabricated by Rutherford Appleton Laboratory (RAL). Preliminary testing in the RAL block has yielded a slight improvement in performance. The best results to date with this block are a double sideband receiver noise temperature of 4100 K and total conversion loss of 10.0 dB. The mixer required less than 0.5 mW of LO power to achieve this performance. Fig. 10 shows a plot of receiver temperature versus LO power incident on the parabolic mirror. These results are discussed in further detail in the next section.

Comparison of Simulations with Measured Results

The harmonic balance simulations indicated that the double sideband conversion loss for the SC1T5-S20 diode mounted on a choke with Z_{source} and Z_{match} equal to 50 Ω should be 3.4 dB, not including waveguide and horn conductor losses. Conductor losses are hard to estimate for real waveguide surfaces which have significant roughness. To approximate these losses we have chosen to assume that they are twice as large as would be measured with ideal smooth surfaces but finite conductivity. For the NRAO block, the losses are: 1.8 dB for microstrip channel, 1.2 dB for the waveguide, and 1.0 dB for

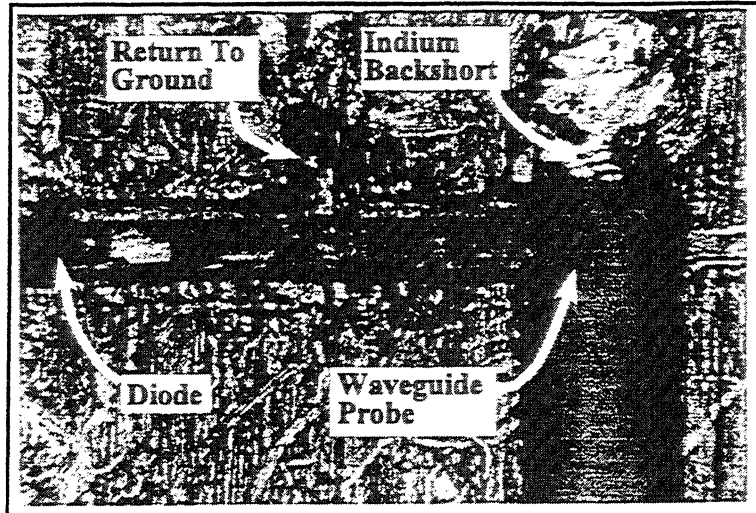


Fig. 7. Choke mounted in mixer block channel.

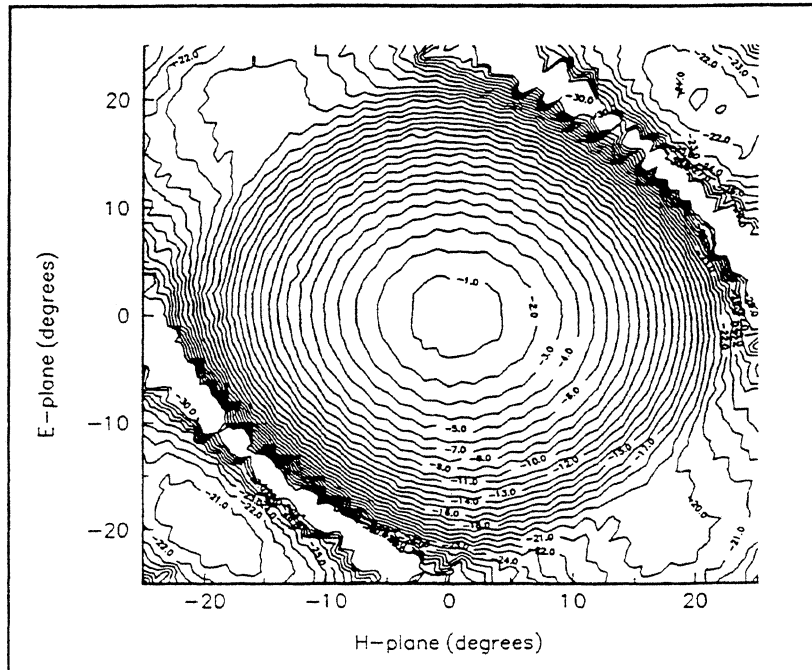


Fig. 8. Antenna map of diagonal feed horn.

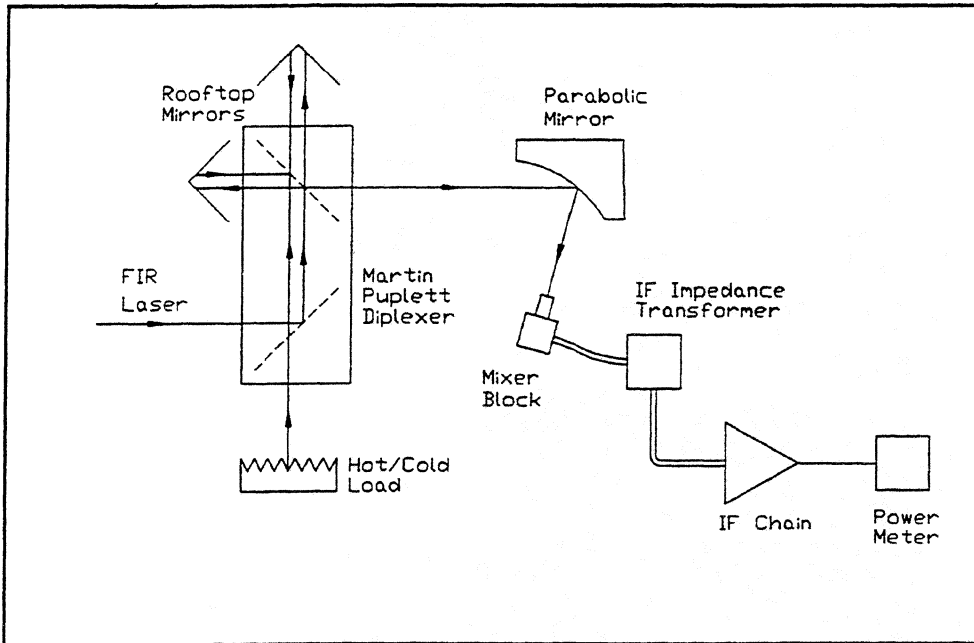


Fig. 9. Schematic of quasi-optical receiver test setup.

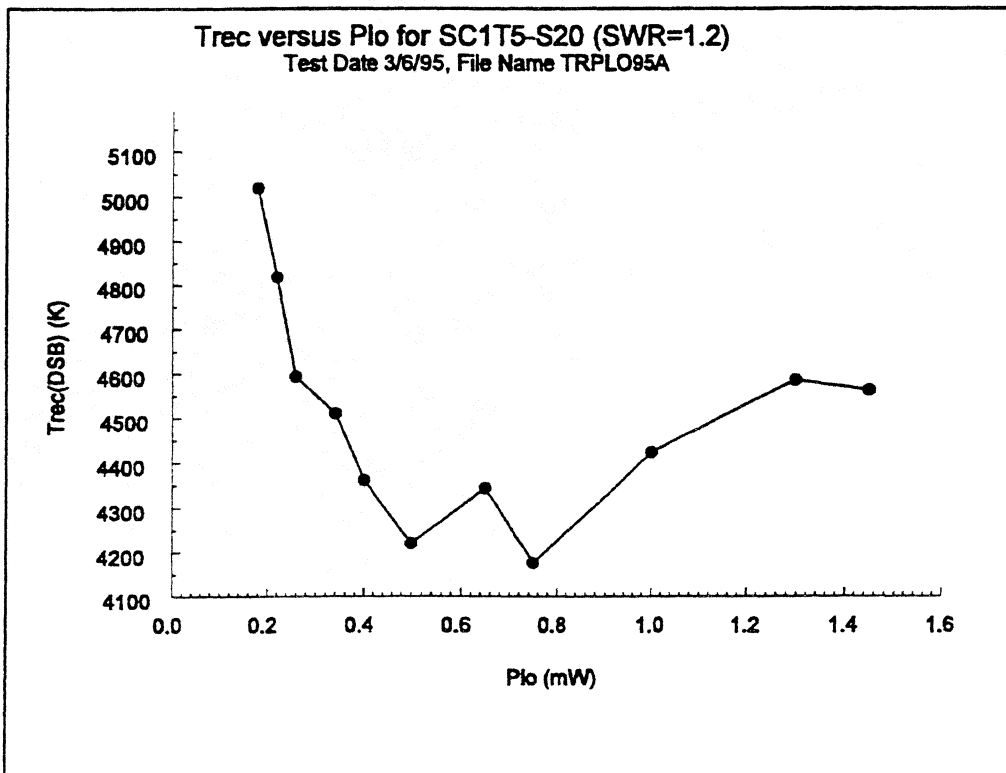


Fig. 10. T_{rec} versus P_{LO} for the SC1T5-S20 diode.

horn. The total expected loss for the receiver with this diode in the NRAO block is 7.4 dB. The RAL block has similar losses, except that the 1.2 dB waveguide loss is eliminated, yielding a predicted conversion loss of 6.2 dB. The measured conversion loss of 10.0 dB leaves a 2.6 dB discrepancy for the NRAO block, and 3.8 dB for the RAL block. These discrepancies may be attributed to problems with either the design or the assembly of the mixer.

We have performed extensive testing with the NRAO block, and have tested a number of diodes mounted on the same choke design. We have not tested the RAL block as extensively. Also, the microstrip channel on the RAL block was machined deeper than expected, thus making choke mounting difficult. Future testing using quartz chokes with the proper thickness is expected to show the improvement in mixer performance that should occur because of the reduced waveguide loss of the RAL block.

Future testing will also be performed with diodes that have their semi-insulating GaAs substrate removed after mounting on the circuit. This will reduce the shunt capacitance, and according to the harmonic balance simulations could reduce the diode's conversion loss by an additional 1.0 - 1.5 dB. Finally, testing with new choke structures with different Z_{source} will be performed. It is our expectation that with these improvements the performance of this receiver will approach that of the best whisker contacted diode receiver at this frequency.

Acknowledgments

The authors would like to acknowledge the assistance of William L. Bishop and Frank Li in the fabrication of the diodes used in this research and Hewlett Packard for the donation of their High Frequency Design System software to the University of Virginia. This research has been supported by the U.S. Army National Ground Intelligence Center through grant DAHC90-91-C-0030.

References

- [1] J. Hernichel, R. Schieder, J. Stutzki, B. Vowinkel, G. Winnewisser, and P. Zimmermann, "A 492 GHz Cooled Schottky Receiver for Radio-Astronomy," Third Int. Symp. on Space THz Tech., Ann Arbor, MI, pp. 724-730, March 24-26 1992.
- [2] W.L. Bishop, K. McKinney, R.J. Mattauch, T.W. Crowe and G. Green, "A novel whiskerless diode for millimeter and submillimeter wave applications," 1987 IEEE MTT-S Int. Mic. Sym. Digest, pp. 607-610, June 1987.
- [3] W.L. Bishop, E. Meiburg, R.J. Mattauch, T.W. Crowe and L. Poli, "A micron-thickness, planar Schottky diode chip for terahertz applications with theoretical minimum parasitic capacitance," 1990 IEEE MTT-S Int. Mic. Sym. Digest, pp. 1305-1308, May 1990.
- [4] J. Johansson and N.D. Whyborn, "The diagonal horn as a sub-millimeter wave antenna" IEEE MTT, pp. 795-800, May 1992.
- [5] D.H. Martin and E. Puplett, "Polarised interferometric spectrometry for the millimetre and submillimetre spectrum," *Infrared Phys.* 10, pp. 105-109, 1966.

Low-Noise MOVPE-Grown Planar InGaAs Mixer Diodes

P. Marsh, D. Pavlidis, and K. Hong

Solid State Electronics Laboratory, Department of Electrical Engineering and Computer Science,
The University of Michigan, Ann Arbor, MI 48109-2122

Abstract

InGaAs lattice-matched to InP is an excellent candidate for applications requiring high mobility and conductivity. Schottky junctions on InGaAs exhibit barriers (ϕ_b) in the neighborhood of 0.25eV and high mobility contributes to the low n+ sheet resistances of 2.0-5 Ω/\square for 1 μm n+ InGaAs layers ($n_s = 1.5 \times 10^{19}/\text{cm}^3$, $\mu_n = 1800 \text{cm}^2/\text{volt}\cdot\text{sec}$) grown with our in-house Metalorganic Vapor Phase Epitaxy (MOVPE) system. This material is therefore well suited for high-performance THz diodes since it provides low ϕ_b , as necessary for low required LO power and has low specific contact resistance needed for reduced losses and high-frequency operation.

The design, material growth, fabrication, and characterization of InGaAs planar mixers is reported. These mixers demonstrated a state-of-the-art performance of 261K DSB noise temperature (T_{mix}) with a corresponding conversion loss (L_{mix}) of 5.4dB at LO, RF, and IF frequencies of 92GHz, 92GHz \pm 1.4GHz, and 1.4GHz respectively. Planar mixer diodes were produced using a novel chemical dice process that performs all lithography and wafer thinning steps before airbridge fabrication, thus greatly reducing the possibility of damage to airbridge and anodes. The mixer diodes were quasi-optically tested while mounted on spiral antennae.

II. Introduction

Planar mixer diodes have traditionally relied on GaAs material systems to achieve high performance at submillimeter and THz frequencies and have shown performance comparable to whisker-contacted Schottkys [1]. In recent years, improvements in growth technology have made it feasible to utilize the performance advantages offered by the InP-based material systems. The high mobility of InGaAs enables the reduction of access resistance (R_s). For example, a 1 μm thick n+ ($n > 10^{19}/\text{cm}^3$) InGaAs layer showed a sheet resistance on the order of 2-5 Ω/\square . The low barrier heights (ϕ_{be}) of mixers using InGaAs Schottky junctions are especially useful in reducing LO power (P_{LO}) requirements, particularly under zero-bias conditions as required in simple antiparallel subharmonic mixer designs [2]. The InP-based system also allows for a highly-

controlled HCl wet etch that virtually eliminates undercut in the $0\bar{1}1$ and $01\bar{1}$ directions, thus allowing for the repeatable chemical dicing obtained for the discrete mixers. Another advantage of the InP-based system is the availability of high-performance HEMT technology which can potentially be integrated with the diodes. Platinum plating is used here to produce anodes having good ideality, high ϕ_{bc} and low reverse leakage.

This paper covers the fabrication, characterization, and performance of planar InGaAs mixers. Section III covers mixer layer structure, fabrication and mounting. Section IV describes the test setup and extraction of mixer performance. Section V describes dc characteristics and compares measured against modeled RF performance.

III. Layer Structure, Fabrication, and Mixer Mounting

Mixer diodes were grown at 570°C via in-house MOCVD using TMG, TMI, and AsH_3 precursors

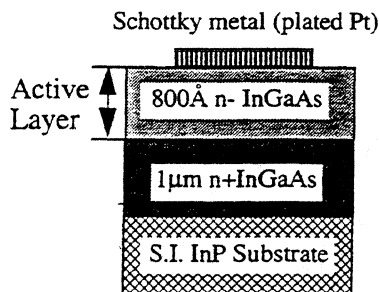


Figure 1. Layer structure of the mixer diodes. The n+ InGaAs layer provides low sheet and ohmic contact resistance. The n- layer is Si doped to $2 \times 10^{17}/\text{cm}^3$. A plated Pt anode improves Schottky quality.

with Si (disilane) doping. Figure 1 shows the layer structure of the mixer diodes characterized here. The $1\mu\text{m}$ n+ layer is doped to approximately $2 \times 10^{19}/\text{cm}^3$ and the 800\AA active layer is doped to $2 \times 10^{17}/\text{cm}^3$. The authors' previous InP-based mixer designs made use of an InP or InAlAs layer beneath the Schottky contact to raise ϕ_b and reduce reverse leakage [3]. However, mixers having active layers consisting completely of InGaAs gave much lower series resistance than InGaAs-InP or InGaAs-InAlAs

structures but also had much higher leakage. The use of plated Pt Schottkys has since greatly reduced reverse leakage while preserving the benefits of an all-InGaAs structure.

Discrete devices are fabricated using a process similar to that covered in [3]-[5]. First, ohmic and interconnect metal are deposited as shown in Figure 2A. Optionally, ohmic metal alone may be deposited in place of the interconnect - as was the case here. Next, the wafer frontside is attached to a cover glass using black wax. The wafer is then thinned to $50\mu\text{m}$, using concentrated HCl (37%) in a process similar to that of [4], [5]. To continue processing, it is necessary to attach the thinned wafer to a silicon substrate (Figure 2B). Wafer attachment is accomplished using Norland NOR 121[®] glue, spun on the wafer backside and oven-cured. The cover glass and black wax are removed using concentrated HF and trichloroethylene (TCE) respectively. Next, pillar photoresist (P.R.) is spun on. Pillars and anode regions are opened. Then the anodes are Pt plated using

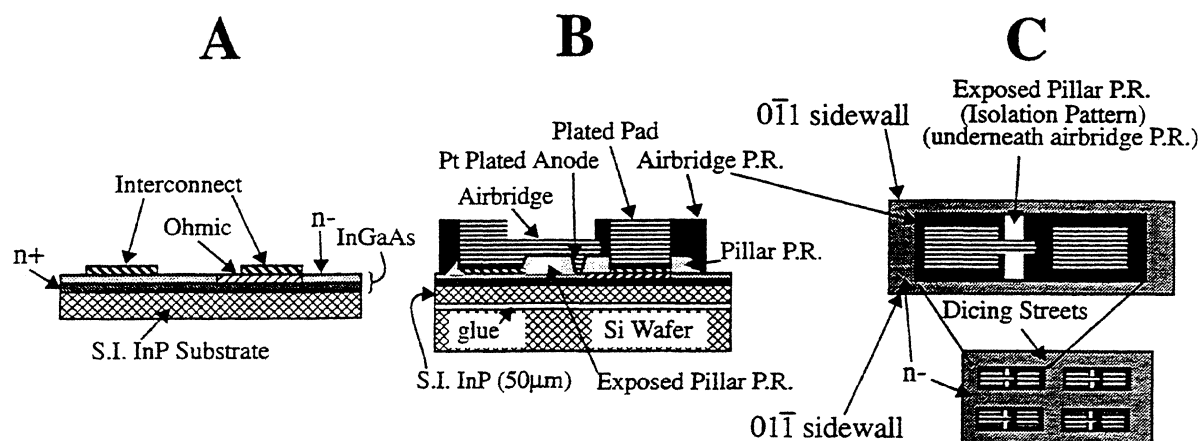


Figure 2. Discrete mixer fabrication process. The wafer is thinned after the ohmic and interconnect steps. Here, the interconnect and ohmic were both deposited as ohmic metal to save a step. Multiple exposures of both pillar and airbridge photoresist (P.R.) allow for definition of the dicing streets. The possibility of damage to the anode contacts is greatly reduced by performing all lithography before forming the airbridges. Contact pads are plated thicker than the airbridges to further increase mechanical ruggedness.

Enthone Platanex III[®] Pt plating solution. Dicing streets are then opened in the pillar P.R., followed by a contour bake. A final exposure of the pillar P.R. defines the isolation pattern (Figure 2B). Development of the isolation pattern is delayed until the end of the process to allow the isolation etch to then remove n+ between the diode pads. Ti/Au/Ti pillar metal is then deposited and 3 μ m airbridge P.R. is spun on. The interconnect mask is used to open the pad areas, allowing them to receive a thick Au plate. Subsequently, the airbridge areas are exposed but not immediately developed. After heavily plating the pad areas, the airbridge regions are developed and the dicing streets are exposed into the airbridge P.R. Airbridges are then formed via Au plating. Development of the dicing streets follows. A combination of wet etch and ion milling then removes the pillar metal from the dicing streets, exposing bare n- InGaAs. Dicing is then subsequently performed by first removing the InGaAs with H₂O:H₂O₂:H₃PO₄ (8:1:1) then using 37% HCl to etch the 50 μ m thick InP, down to the Si wafer. During this dicing process, the pillar P.R. and anode regions are well-protected by the airbridge P.R. and dicing is carried out through a mask of InGaAs covered by photoresist. The InGaAs mask virtually eliminates undercut in the 0 $\bar{1}1$ and 0 $1\bar{1}$ directions and gives vertical 0 $\bar{1}1$ /0 $1\bar{1}$ sidewalls. Undercut occurring at the ends of the device is very predictable. Profiles resulting from the chemical dicing enhance the handling and mountability of the devices. The process continues with flood exposure and development of the airbridge resist. The remaining pillar metal is removed via wet etching and ion milling. At this point the InP wafer becomes a set of discrete diodes held on the Si wafer by the Norland[®] glue. Finally, a development step removes the previously exposed pillar P.R. beneath the airbridge to enable electrical separation of the diode pads via the isolation etch of the InGaAs. The isolation

etch yields operational, discrete mixer diodes. These diodes may be readily plucked from the Si wafer after soaking them in acetone for about 24 hours.

A spiral antenna topology [6] eases mixer characterization by virtue of broadbanded performance, predictable impedance, and ease of coupling both LO and RF signals with predictable losses. Spiral antennae for the discrete mixers are fabricated on mechanical-grade semiinsulating (S.I.) GaAs. The antennae are Au plated to improve contacting. Diodes are mounted in a flip-chip fashion as illustrated in Figure 3. Excellent electrical and mechanical bonding are provided by pressing the diode pads into indium pieces placed onto the antenna terminals. This room-temperature process avoids possible heat damage and/or high resistance that might occur from the use of conductive epoxies or solder.

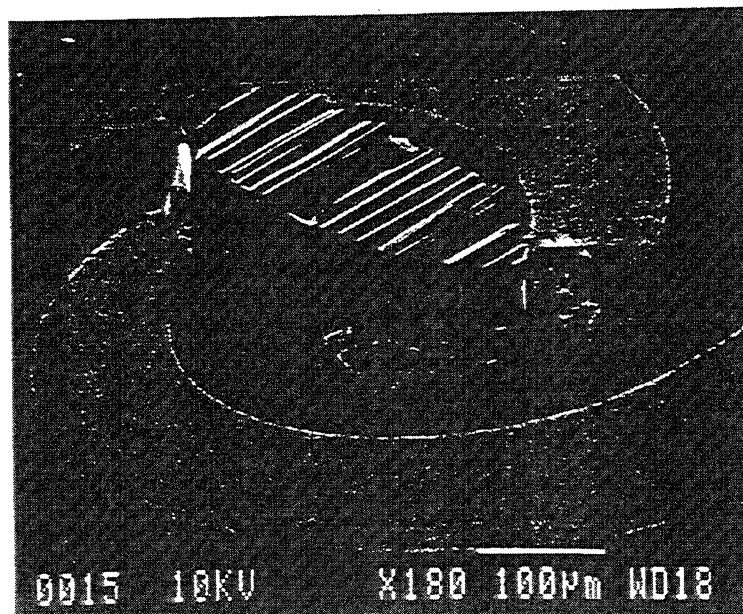


Figure 3. SEM shot of a discrete mixer, having the diode flip-chip mounted onto the spiral antenna with indium.

The antenna wafer is positioned with its backside contacting a silicon substrate lens such that the antenna lies at the lens' focal point. IF is taken off at the ends of the antenna terminals.

IV. Test Setup and Extraction of Mixer Performance

Measurement results are reported here for two planar InGaAs mixers, namely: 7c6 and 7b3 having anode diameters of $1.9\mu\text{m}$ and $3.5\mu\text{m}$ respectively. Mixer performance is defined by the double sideband (DSB) RF port noise temperature, T_{mix} , and single sideband (SSB) RF to IF conversion loss, L_{mix} . T_{mix} is defined as the temperature of a noiseless mixer's blackbody RF load such that it would produce the same noise power at its IF port as the actual mixer under test with an RF load at 0K. T_{mix} and L_{mix} are evaluated using the quasi-optical setup shown in Figure 4. The mixer's spiral antenna couples well to both horizontal and vertical polarizations which serves to simplify the simultaneous coupling of LO and blackbody RF radiation to the mixer diode. A polarization grid of closely-spaced wires reflects the vertically-polarized LO signal into the mixer Si lens while the horizontal component of the RF signal passes through the polarizer. The Si lens is aligned by pulsing the LO and detecting the pulsed signal at the IF port. The IF chain is calibrated to enable measurement of the uncorrected IF noise temperature T_{im} . T_{i} , the equivalent

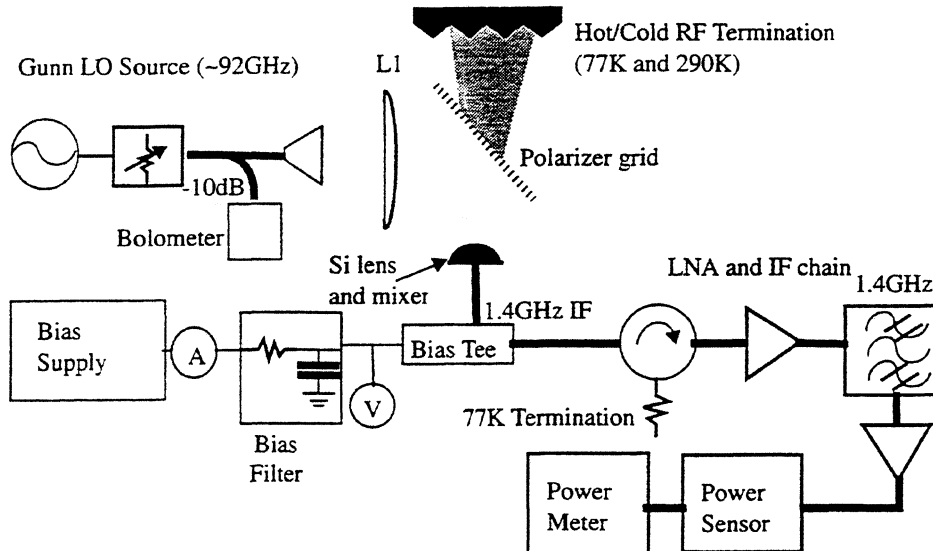


Figure 4. Quasi-optical test setup for evaluation of mixer performance. A low-noise IF chain is calibrated to measure the mixer's IF noise temperature (T_i). The mixer's performance is then extracted from known system losses and the variation of T_i as a function of the RF load temperature (T_r).

matched IF noise temperature, is extracted via the relation: $T_i = \frac{T_{im} - T_c \cdot \Gamma_i^2}{1 - \Gamma_i^2}$ Where T_c is the effective temperature of the circulator termination and Γ_i is the IF reflection coefficient.

Therefore:

$$G_m = \frac{\Delta T_{im}}{(1 - \Gamma_i^2) (1 - \Gamma_r^2) G_a G_p \Delta T_r} \quad \text{and}$$

$$T_{mix} = \frac{T_i}{G_m} - \underbrace{(1 - G_a) T_o}_{\text{Si lens}} + \underbrace{(1 - G_a) \Gamma_r^2 T_o G_a}_{\text{Polarization Grid}} + \underbrace{(1 - G_p) (1 - \Gamma_r^2) T_o G_a + (1 - \Gamma_r^2) G_a G_p T_{rh}}_{\text{RF Load}}$$

Noise contributions

Where $G_m = 2/L_{mix}$, $T_o = 290\text{K}$ (room temperature), $G_a = 0.871$ = reciprocal of the Si lens loss due to backside radiation and dielectric loss, $\Gamma_r = 0.555$ = reflection coefficient of the Si lens, $G_p = 0.5$ which represents the RF coupling loss due to insertion of a linearly-polarized RF signal into a spiral antenna, $T_{rh} = 295\text{K}$ = hot RF load temperature, and $\Delta T_r = 295\text{K} - 77\text{K}$ = difference between hot and cold RF load temperatures. Here, T_{im} is measured with a room temperature RF load. LO power (P_{LO}) was determined by obtaining it from a use of a harmonic balance program [7] used with the measured diode I-V, current, and dc bias voltage under LO drive. The P_{LO} extracted this way was found to be $3.5\text{dB} \pm 1.5\text{dB}$ lower than that read by the bolometer, i.e. about 4-6dB lower than that accounted for from the quasi-optical setup losses. However, confidence is inspired by the consistency of the discrepancy between the bolometer readings and extracted P_{LO} across nearly all bias, P_{LO} , and anode diameters measured; for both preliminary unreported results and the results reported here.

IF reflection, polarization losses, and Si lens losses and reflections were removed from the calculations of measured T_{mix} and L_{mix} . No attempt was made to remove the effect of the mismatch between diode and antenna.

V. Measured Performance

Figure 5 illustrates dc characteristics of the mixer diodes. At 0.22-0.28eV, ϕ_b is considerably below that of GaAs diodes (0.8-0.9eV), thus lowering P_{LO} . The ideality factor (η) is good at 1.2 and the highest cutoff frequency ($f_c = 1/(2\pi R_s C_{j0})$) is $> 7\text{THz}$. The zero-bias capacitances, C_{j0} , were estimated from depletion-layer thickness calculations based on the $2 \times 10^{17}/\text{cm}^3$ doping of the n- InGaAs layer. The series resistance, R_s ; ideality, η ; and Schottky barrier height, ϕ_b ; and reverse saturation current, I_s , were determined from the I-V curves.

Diode Designation	Wafer Designation	Diameter (μm)	C_{j0} (fF)(est.)	R_s (Ω)	η	ϕ_b (eV)	I_s (μA)	f_c (THz)
7c6	U423 (discrete)	1.9	7.4	5.5	1.2	0.27	0.25	3.9
7b3	U423 (discrete)	3.5	27.85	0.8	1.2	0.22	5.5	7.14

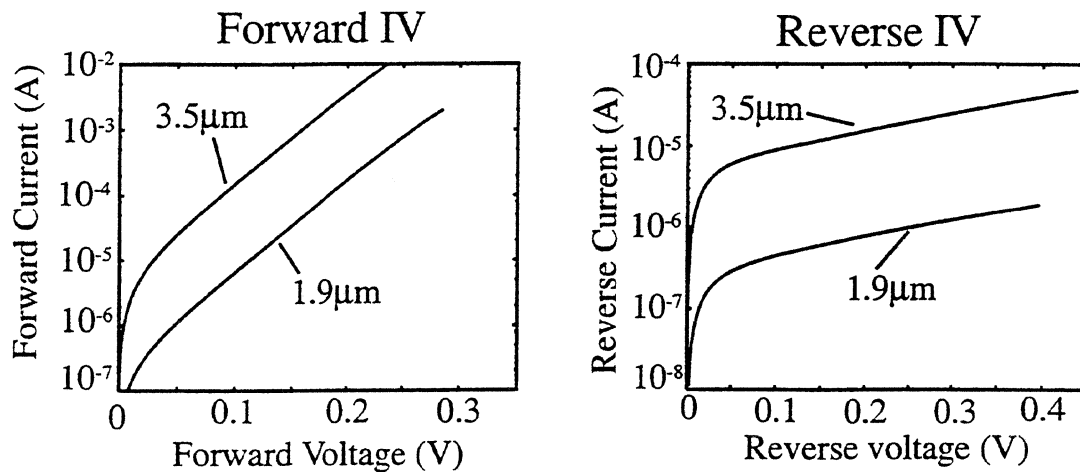


Figure 5. DC Characteristics of the measured mixer diodes. Diodes exhibit low ϕ_b with low η and low reverse leakage (for 1.9 μm diodes).

Figure 6, illustrates measured performance of mixers 7c6 and 7B3 compared against the corresponding harmonic-balance simulated results based on the mixer simulator of [7]. DC bias was set to optimize noise temperature. The simulator was loaded with the diodes' dc values of R_s ; C_{j0} ; η ; and reverse saturation current, I_s . This simulator obtains noise calculations exclusively from shot and R_s 's thermal noise. Since the theoretical and measured data agree well, especially for diode 7c6, it appears that the real diodes are relatively free of significant noise due to hot electron effects, trapping, or other sources. Insignificant levels of hot electron noise allow these diodes to obtain excellent performance ($T_{\text{mix}} < 500\text{K}$) over a 1:5 range of P_{LO} . Other measurements showed a weakened dependency of noise performance and P_{LO} for $P_{\text{LO}} > 440\mu\text{W}$. Zero-bias performance for the 1.9 μm diode (7c6) is excellent, $T_{\text{mix}} < 500\text{K}$ for $P_{\text{LO}} > 220\mu\text{W}$.

The smaller anode device (7c6) performs better largely due to its RF and LO impedances being closer to the antenna impedance of 71Ω .

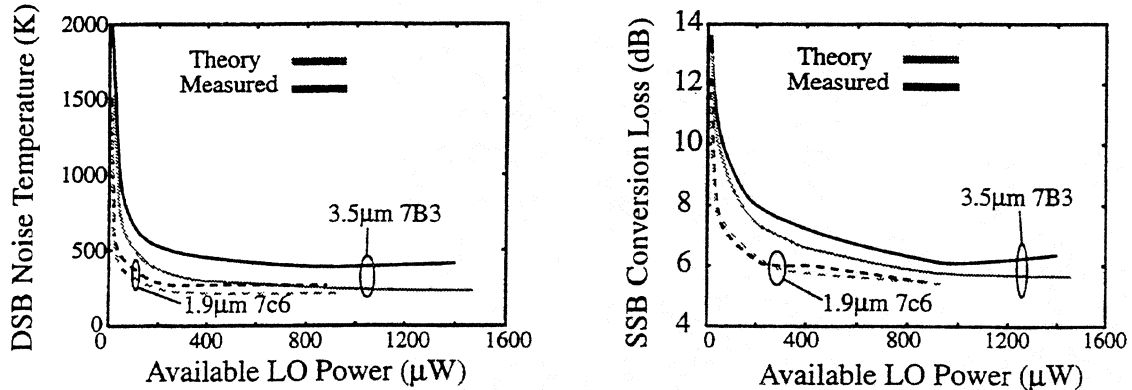


Figure 6. Measured vs. modeled performance for mixers. DC bias was set to minimize the mixers' noise temperature. Noise temperature approaches its minimum value for $P_{LO} > 180\mu\text{W}$. Good agreement of measured and modeled performance indicates a low level of hot electron and trap noise.

VI. Conclusions

Planar InGaAs mixers having state-of-the-art noise performance have been fabricated and demonstrated at 92GHz. Pt plated Schottkys have been shown effective at achieving low ($\sim 0.25\text{eV}$) ϕ_b while maintaining low reverse currents on the $n = 2 \times 10^{17}/\text{cm}^3$ InGaAs. DSB noise temperature (T_{mix}) and SSB conversion loss (L_{mix}) were 261K and 5.4dB respectively @ $P_{LO} = 891\mu\text{W}$ for a mixer (7c6) having a $1.9\mu\text{m}$ anode diameter. This mixer gave $T_{\text{mix}} = 451\text{K}$, and $L_{\text{mix}} = 8\text{dB}$ @ $P_{LO} = 44\mu\text{W}$; $T_{\text{mix}} = 271\text{K}$, and $L_{\text{mix}} = 6\text{dB}$ @ $P_{LO} = 223\mu\text{W}$; and a zero-bias performance of $T_{\text{mix}} \sim 450\text{K}$, and $L_{\text{mix}} = 8\text{dB}$ @ $P_{LO} = 225\mu\text{W}$. These InGaAs mixers show very little hot electron or trap noise contribution to T_{mix} . Therefore, they have demonstrated very low noise performance over a 1:5 range of P_{LO} . Performance appears to depend on the matching of the mixers' RF impedance to that presented by the spiral antenna, i.e. 71Ω . This likely was the reason the $1.9\mu\text{m}$ diode outperformed the $3.5\mu\text{m}$ diode. For $P_{LO} > 220\mu\text{W}$ and an anode diameter of $1.9\mu\text{m}$, the mixer's performance is only a weak function of dc bias. These InGaAs mixer results compare favorably to that of state-of-art planar GaAs mixers [1] in waveguide fixtures.

These results indicate that InGaAs mixers hold promise in submillimeter and THz receiver applications. Their low ϕ_b and consequently low P_{LO} requirements reduce the problem of supplying LO at high frequencies. The low hot electron noise is expected to have a large impact on submillimeter and THz noise performance. The etch and undercut controllability of InGaAs-masked InP points to possible micromachining of waveguides etc. in the InP substrates. Finally the availability of high-performance HEMTs and HBTs on InP-based systems could facilitate integration of RF and IF functions on the same InP wafer.

Acknowledgments:

The authors wish to thank Gildas Gauthier, Dan Filipovic, and Professor Gabriel Rebeiz for technical advice and assistance in setting up the optics for the quasi-optical system.

References:

- [1] D. Garfield, R. J. Mattauch, S. Weinreb, "RF Performance of a Novel Planar Millimeter-Wave Diode Incorporating an Etched Surface Channel", *IEEE Transactions on Microwave Theory and Techniques*, Vol 39, No. 1, Jan 1991.
- [2] U.V. Bhapkar, T.A. Brennan, and R.J. Mattauch, "InGaAs Schottky Barrier Mixer Diodes for Minimum Conversion Loss and Low LO Power Requirements at Terahertz Frequencies", *Second International Symposium on Space Terahertz Technology*, Jet Propulsion Laboratory, Pasadena, CA, February 26-28, 1991, pp. 371-388.
- [3] P. Marsh, Pavlidis, and K. Hong, "Planar Varactor and Mixer Diodes Fabricated Using InP-Based Materials", *Fifth International Symposium on Space Terahertz Technology*, The University of Michigan, Ann Arbor, MI, May 10-12, 1994, pp. 514-523.
- [4] P. Marsh, G.I. Ng, D. Pavlidis, and K. Hong, "InAlAs/InGaAs Varactor Diodes with THz Cutoff Frequencies Fabricated by Planar Integrated Technology", *Proceedings of the Sixth International Conference on Indium Phosphide and Related Materials*, Santa Barbara, CA, March 28-31, 1994.
- [5] P. Marsh, G.I. Ng, D. Pavlidis and K. Hong, "Air-Bridge Anode Process for High-Performance Planar Schottky Diodes", Presented at the *1994 US Conference on Gallium Arsenide Manufacturing Technology*, Las Vegas NV, May 1994, pp. 159-162.
- [6] J. Dyson, "The Equiangular Spiral Antenna", *IRE Transactions on Antennas and Propagation*, April 1959, pp. 181-187.
- [7] P. H. Siegel, A. R. Kerr, and W. Hwang, "Topics in the Optimization of Millimeter-Wave Mixers", *NASA Technical Paper 2287*, 1984.

Electrolytic Deposition Techniques For The Fabrication Of Submicron Anodes

A. Grüb, C.I. Lin, H.L. Hartnagel

*Institut für Hochfrequenztechnik, TH Darmstadt, Merckstr. 25,
64283 Darmstadt, Germany*

Abstract

Small-area anodes of whisker contacted Schottky diodes as well as planar Schottky diodes usually are deposited by electroplating techniques. With shrinking anode areas, the physical structure of the deposited metal becomes increasingly important. Therefore, it is essential to investigate the influence of the deposition parameters on the diode performance in order to be capable of fabricating submicron anodes with improved electrical performance.

A comparison of DC- and pulse-plating techniques is presented and the influence of parameters such as deposition temperature, current density, and metal film thickness on the diode I/V characteristics is experimentally investigated. It is shown that non-optimized deposition parameters lead to degraded diode performance, especially with small anode diameters. Therefore, the influence of the diode diameter is also taken into account for the optimization of the electrolytic deposition. A number of experiments demonstrate that variations of the plating process especially affect the ideality factor and the series resistance of the diodes.

1. Introduction

Contacts to semiconductors have been a topic of interest for more than five decades [1]. Especially for applications at high frequencies, the nonlinear space charge properties of metal-semiconductor contacts are utilized in MeSFET's, HEMT's and Schottky mixer and varactor diodes for a large variety of applications [2]. It is a matter of fact that the quality of the metal-semiconductor interface determines the electrical performance and the reliability of the devices. When device operation at submillimeter wavelengths is envisaged, the required area of the metal-semiconductor contacts are so small that only optimized metal deposition techniques enable the reliable fabrication. GaAs Schottky mixer diodes for THz operation have anode diameters between 0.8 μm and 0.25 μm , which means contact areas between 0.5 μm^2 and 0.05 μm^2 [3]. Due to a number of advantages, electrolytic deposition techniques are used for the fabrication of the anodes.

The requirements for THz Schottky diodes with such small anodes from the electrical point of view are near-ideal I/V characteristics and low-noise performance. Another item of great importance is of course the reliability of the contacts and the yield during fabrication. Especially for planar diodes where only one anode per device is available, in contrast to whiskered devices with thousands of anodes per chip, this item is of major importance. It has already been shown earlier that small deviations from a near-ideal I/V characteristic caused by non-optimized Schottky metal deposition lead to a reduced device reliability [4].

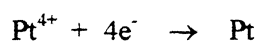
This paper presents results on Schottky contacts fabricated by DC- and pulse plating techniques. The influence of the most important deposition parameters on the device characteristics is investigated and an optimized process for the fabrication of submicron Pt anodes is described.

2. Experimental

The fundamentals of electrodeposition of metals on semiconductors are well understood for some decades and the metal growth generally is considered as a simple cathodic reduction [5,6].



which reads in the case of Pt as follows:



It is the large number of electrochemical and chemical reactions and side reactions in connection with the possible deposition parameters which makes this field extremely difficult

for the theoretical investigation of realistic structures [7]. Therefore, this study concentrates on experimental results. In the literature three approaches for the electrodeposition of metals on semiconductors are described:

- Current at a controlled potential (potentiostatic technique) [7,8]
- Electrode potential under constant current (galvanostatic technique) [4]
- Pulse-plating techniques [9,10]

Because of their importance for the fabrication of whiskered and planar Schottky diodes, this work concentrates on galvanostatic and pulse plating techniques.

We have used a number of different wafers for the investigations with doping concentrations between $2 \cdot 10^{16} \text{ cm}^{-3}$ and $1 \cdot 10^{18} \text{ cm}^{-3}$ and an epi-layer thickness between 300 nm and 50 nm, respectively, such as commonly utilized for the fabrication of mixer and varactor diodes. The anode diameters have been varied between 7 μm and 0.5 μm . All anodes were fabricated according to our standard diode process [11]. This means that the GaAs surface is electrochemically etched prior to the platinum deposition. This etch technique results in a smooth and oxide-free interface [12] because etching and Pt deposition are performed in-situ in the Pt electrolyte. The Pt solution¹ is based on sulfuric and phosphoric acid with a pH-value of 0.2 and 2 g Pt/l. The recommended current density for the galvanostatic deposition is 0.4 mA/mm². The pulse generator for the pulse plating generates voltage pulses with an amplitude between 0-20 V, pulse width 0.2 -10 μs , and pulse rate 1-4 ms.

The fabricated Pt/GaAs diodes have been electrically characterized by I/V- and C/V-measurements. Usually, the Schottky anodes consist of a Pt/Au contact. The Pt layer forms the Schottky contact to the GaAs and determines the diode performance whereas the Au layer only provides a good contact to the whisker wire or to the airbridge. Therefore, all diodes fabricated in the course of this work only have a Pt layer. This allows additionally the investigation of the deposited Pt layers with the SEM.

3. Results and Discussion

3.1 DC-plating

For a given Pt solution, the DC-plating deposition parameters are the electrolyte temperature T_{Pt} and the current density during the deposition J_{DC} . Fig. 1 shows the influence of T_{Pt} on the forward I/V characteristics of Schottky diodes (anode diameter 6.7 μm , epi-layer doping $1 \cdot$

¹ Platinbad D. DODUCO, Germany

10^{17} cm^{-3}). At very small diode currents ($I_D < 1 \text{ nA}$) occurs a deviation from the ideal diode behavior. This deviation (excess current) is more pronounced at $T_{\text{Pt}} = 40 \text{ }^\circ\text{C}$ and reduces with increasing T_{Pt} . This could be explained that with increasing electrolyte temperature also the thermal energy of the metal ions increases. This causes a more homogeneous distribution of the Pt^{4+} -ions on the GaAs surface. A further increase of T_{Pt} has led to a very inhomogeneous deposition. The reason is that the anodic pulse etching which is performed prior to the Pt deposition at high T_{Pt} preferably takes place at surface crystal defects. So at some areas at the free GaAs surface the epi-layer is removed with a high etch rate which subsequently leads to a preferred Pt deposition on these areas. Therefore, the combined pulse etching and DC-plating process is limited to a T_{Pt} of $60 \text{ }^\circ\text{C}$. The diodes fabricated at $60 \text{ }^\circ\text{C}$ also exhibit a slightly better n-value (1.13) and smaller series resistance ($20 \text{ } \Omega$) compared to the deposition at lower T_{Pt} ($n=1.17$, $R_S=23 \text{ } \Omega$). Therefore, all subsequent experiments have been carried out at $T_{\text{Pt}} = 60 \text{ }^\circ\text{C}$.

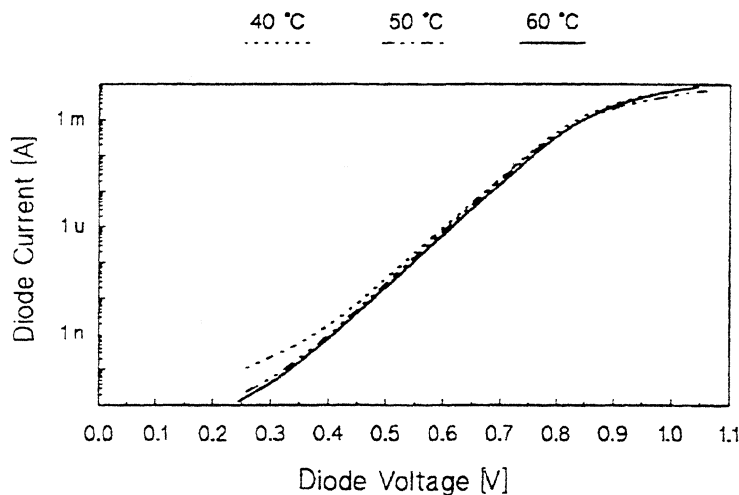


Fig. 1: DC-plating: Influence of the deposition temperature on the diode I/V characteristics

The influence of the deposition current density on the diode characteristics is discussed in fig. 2 (anode diameter $6.7 \text{ } \mu\text{m}$, epi-layer doping $1 \cdot 10^{17} \text{ cm}^{-3}$). Generally, the current density J_{DC} is the deposition parameter which has the strongest effect on the metallurgical quality of the deposited metal film. If J_{DC} is too high, hydrogen ions contribute considerably to the ion current and are incorporated into the deposited film which must be avoided because it leads to Pt films with reduced adhesion and higher brittleness. On the other hand, if J_{DC} is too small the number of Pt growth centers on the GaAs surface decreases which leads to a reduced homogeneity. The best results in our study have been obtained with deposition current densities J_{DC} between 2 and 3 mA/mm^2 . The deposition at 2.4 mA/mm^2 leads to a reduction of n to 1.09 compared to 1.11 for a current density of 1.2 mA/mm^2 . More pronounced is the reduction of the series resistance which is in the order of $3\text{-}4 \text{ } \Omega$. Since the higher current density also leads to a higher Pt growth rate, the deposition time t_{DC} was chosen such that the thickness of the Pt was identical for all samples ($J_{\text{DC}} \cdot t_{\text{DC}} = \text{const.}$).

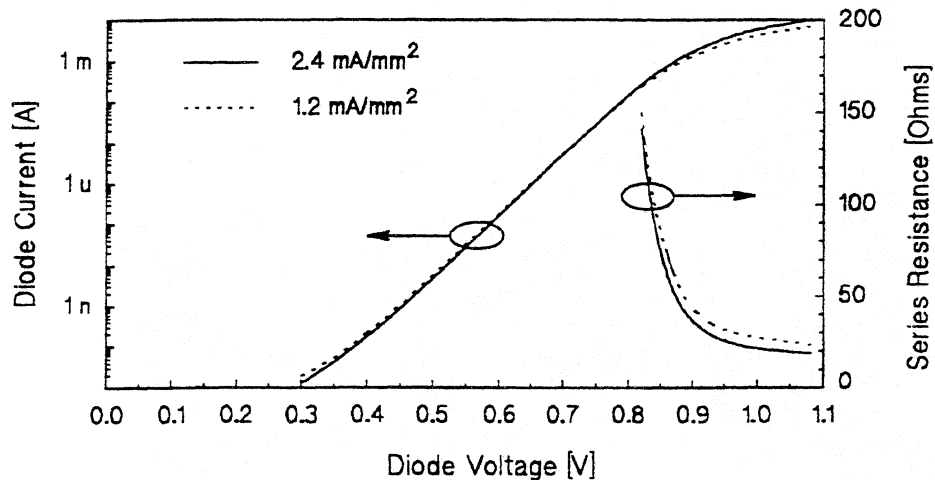


Fig. 2: DC-plating: Influence of the deposition current density on the diode I/V characteristics

The experiments have shown that DC-Plating should be carried out at $T_{Pt} = 60\text{ }^{\circ}\text{C}$ and $J_{DC} = 2\text{-}3\text{ mA/mm}^2$. Additionally, it has been revealed that all DC-plated anodes exhibit a small excess current at small bias which is the more pronounced the smaller the anode diameter is. However, the fabrication of homogeneous Pt anodes with diameters smaller than $1.5\text{ }\mu\text{m}$ requires due to the small contact area a larger density of Pt growth centers (nuclei). This can be achieved by an increase of J_{DC} but as demonstrated, J_{DC} is limited to a certain range in order to grow Pt films with sufficiently good quality. Therefore, pulse plating techniques should be applied for the fabrication of submicron anodes [10].

3.2 Pulse plating

Up to now, there exists only very few insight in which way the pulse parameters influence the deposited films and the diode performance. The following paragraph therefore shows in how far the pulse parameters (pulse width Δt_p , pulse amplitude V_p , number of pulses N_p) affect the diode performance.

Fig. 3 (anode diameter $6.7\text{ }\mu\text{m}$, epi-layer doping $2 \cdot 10^{16}\text{ cm}^{-3}$, exponentially increasing towards the substrate) shows the current dependent diode ideality factor n as a function of the pulse amplitude. Best results have been achieved with $V_p=17\text{ V}$. These diodes exhibit an ideal behavior with a minimum n of 1.08 down to currents of less than 40 pA . This demonstrates already the difference to dc-plated diodes which even with optimized deposition parameters (see above) have a small excess current (\Rightarrow slightly increased ideality factor) at pA-currents.

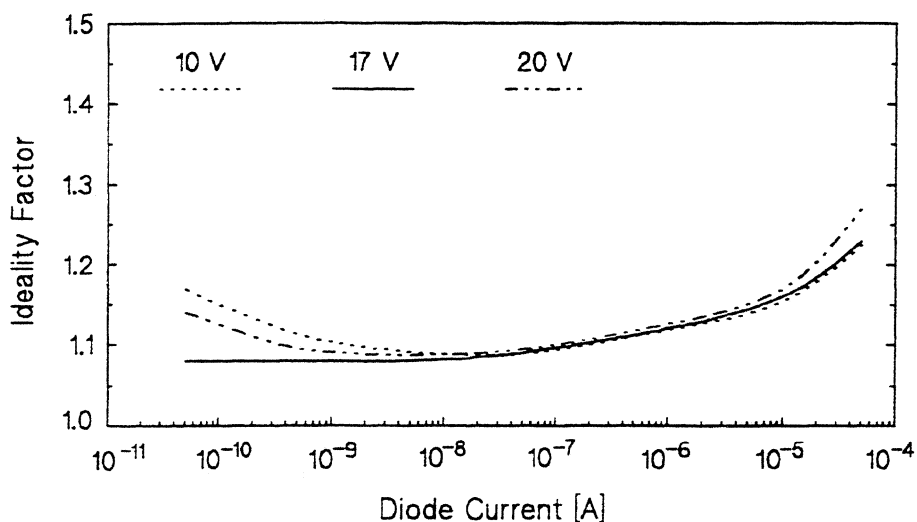


Fig. 3: Pulse plating: Influence of the pulse amplitude on the diode ideality factor

The next parameter which has to be investigated is the pulse width. The utilized pulse generator delivers pulse widths from 200 ns to 10 μ s. For the anodic pulse etching prior to the Pt deposition the pulse width has to be as short as possible in order to achieve a resolution of 1 nm /pulse. This is required for the controlled etching of thin epi-layers. The experiments have revealed that for the subsequent cathodic deposition a pulse width of about 1 μ s seems to be optimum. Fig. 4 (anode diameter 6.7 μ m, epi-layer doping $2 \cdot 10^{16}$ cm⁻³, exponentially increasing towards the substrate) shows the ideality factor and series resistance as a function of the diode current for a pulse width of 1 μ s and 10 μ s. It can be seen that the minimum ideality factor is the same for both curves ($n=1.07$). A slight deviation occurs in the current range above 10 μ A where the series resistance begins influence the I/V curve. This behavior is also expressed in the curves for the series resistance. The diode fabricated by application of 1 μ s-pulses exhibits a series resistance which is approx. 2 Ω smaller than that of the 10 μ s-pulses diode. This could be explained by the assumption that for pulse widths > 10 μ s saturation effects at the electrolyte/GaAs surface start to play a role. Of course, also pulse widths shorter than 1 μ s can be utilized but since the generation of such pulses is more difficult there is no need to do so.

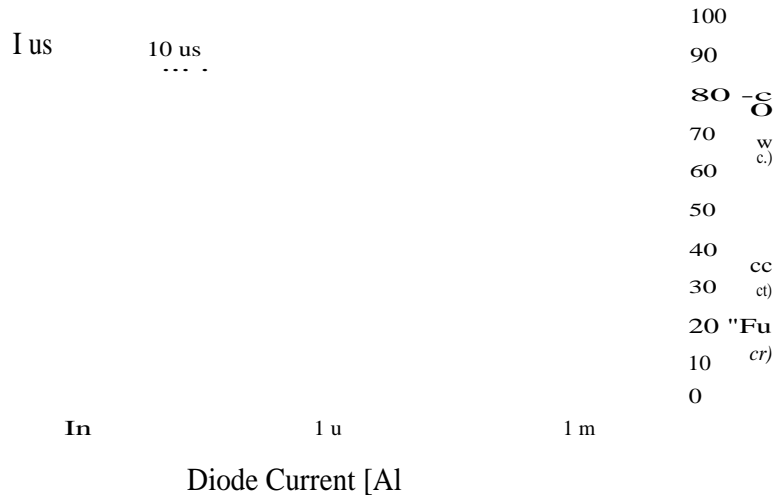


Fig. 4: Pulse plating: Influence of the pulse width on the diode ideality factor and series resistance

The influence of the Pt thickness i_s illustrated in fig. 5 (anode diameter 6.7 μm , epi-layer doping $2 \cdot 10^{16} \text{ cm}^{-3}$, exponentially increasing towards the substrate). One diode chip with -varactor diodes has been fabricated for this test. In a first step 50 pulses of Pt plating have been applied. Subsequently, the IN characteristics was measured. Then the diode chip was again immersed into the Pt solution and another 70 pulses were applied. Thus, plating pulses were applied and IN curves measured until stable curves were obtained. It clearly can be stated that already after a small number of pulses the Schottky barrier i_s stable and is not affected by a further growth of the Pt layer. This is obvious due to the constant ideality factor of 1.08 which could be measured for all curves. However, a significant change occurs in the series resistance which decreases with the increasing number of pulses, shown in fig. 6 (120 $^{\circ}\text{C}$ for 50 pulses, 20 $^{\circ}\text{C}$, for 8000 pulses). For $N_p > 2000$ the series resistance decreases very slowly and for $N_p > 5000$ it remains constant at a minimum value. This means that at least 5000 plating pulses should be applied which corresponds to a Pt thickness of approximately 50 nm.

Diode Voltage [V]

Fig. 5: Pulse plating: IN characteristics as a function of the number of pulses

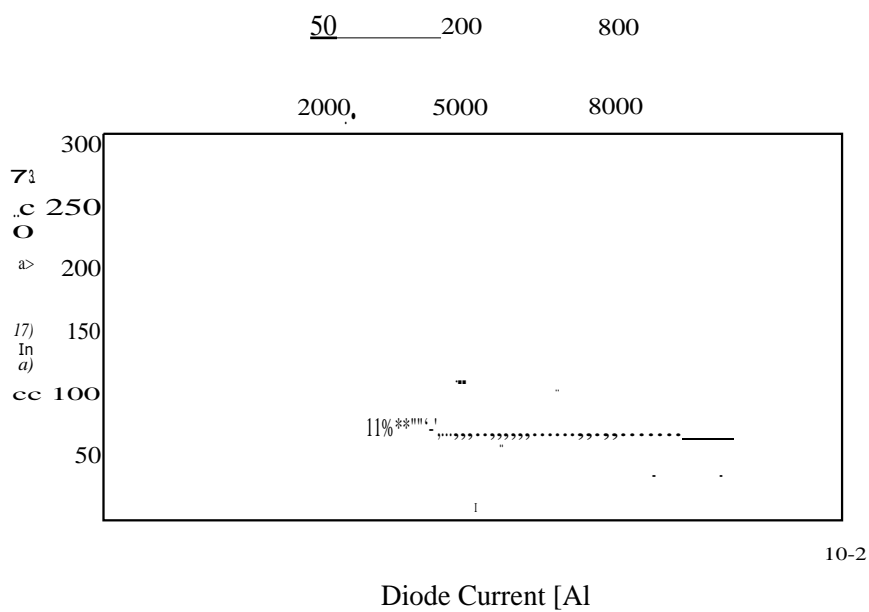


Fig. 6: Pulse plating: Series resistance as a function of number of pulses

It is commonly accepted that with decreasing mode diameter the minimum ideality factor increases but no investigations on this have been made. The higher n values of small area contacts is due to the increasing influence of edge effects [13] but also due to the increasing influence of the anode homogeneity [14,15]. This behavior also can be seen in fig. 7 where the ideality factor versus the current density with the anode diameter as parameter is depicted. Diodes with diameters varying between 6.7 μm and 0.7 μm have been fabricated simultaneously on the same chip. The 6.7 μm -diodes behave almost ideal with a n of 1.06 and no excess currents at small bias. With shrinking diameter the minimum n increases and additionally the behavior at small currents becomes more non-ideal. Since the diodes have been fabricated with the optimized pulse plating process which delivers very good results even for 0.5 μm -diodes (see fig. 8), this tin of 0.08 between 6.7 μm and 0.7 μm -anodes can be a contribution due to the increasing influence of edge effects. The fact that at high current densities the n values of the large diodes increase faster is due to the influence of the series resistance at mA-currents. This demonstrates that even with an optimized fabrication process diodes with diameters smaller than approximately 1.5 μm exhibit a higher ideality factor which cannot be reduced.

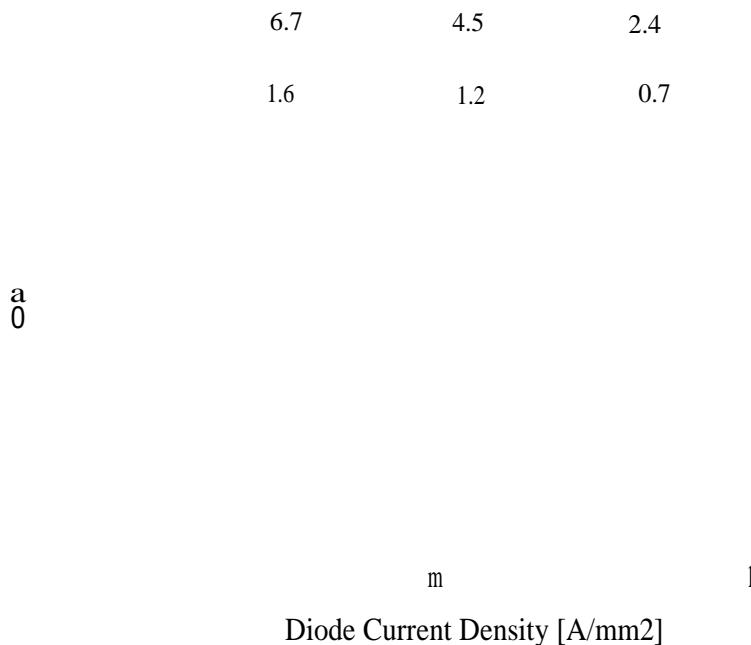


Fig.7: Pulse plating: Area dependence of the ideality factor

Fig. 8 finally shows a SEM photograph of a $0.5\mu\text{m}$ Schottky diode fabricated according to the optimized pulse plating process with the following parameters: $V_p=17\text{ V}$, $\Delta t_p=1\ \mu\text{s}$, $N_p=8000$, $T_p=60\ ^\circ\text{C}$. This diode chip has an $\text{In}_{0.02}\text{Ga}_{0.48}\text{As}$ epi-layer with a doping concentration of $1 \cdot 10^{18}\text{ cm}^{-3}$. The measured diode parameters are as follows: $C_{j0}=0.9\text{ fF}$, $n=1.28$, $R_s=20\ \Omega$, $V_{br}=-2.9\text{ V}$.

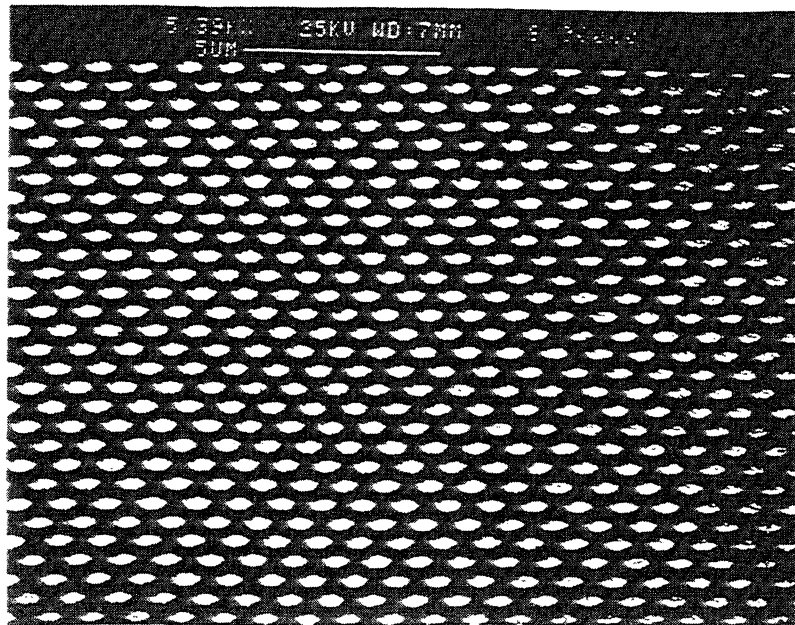


Fig. 8: SEM-photograph of a $0.5\mu\text{m}$ Schottky diode

4. Conclusions

The reliable fabrication of whiskered and planar submicron Schottky diodes with near-ideal electrical performance is still a technological challenge. Therefore, the Pt deposition process has to be investigated. This paper shows the influence of plating parameters on the I/V characteristics of diodes with varying diameters. It is demonstrated that submicron anodes should be fabricated with a pulse plating process.

5. Acknowledgments

The authors want to thank Drs. J. Freyer and H. Grote, Technical University of Munich, Germany, for supplying the high quality MBE material. This work has been funded by the Deutsche Forschungsgemeinschaft (DFG).

6. References

- [1] J. Brillson (Editor): *Contacts to semiconductors: Fundamentals and technology*, Noyes Publications, New Jersey, 1993.
- [2] S.A. Maas: *Microwave Mixers*, Artech House Inc., 2. edition, 1993.
- [3] T.W. Crowe, R.J. Mattauch, H.P. Röser, W.L. Bishop, W.C.B. Peatman: GaAs Schottky diodes for THz mixing applications, *Proc. IEEE*, Vol. 80, no. 11, 1992.
- [4] A. Grüb, V. Krozer, A. Simon, H.L. Hartnagel: Reliability and micro-structural properties of GaAs Schottky diodes for submillimeter-wave applications, *Solid-State Electronics*, Vol. 37, No. 12, 1925-1931, 1994.
- [5] F.C. Walsh, M.E. Herron: Electrocrystallization and electrochemical control of crystal growth: fundamental considerations and electrodeposition of metals, *J. Phys: D. Appl. Phys*, Vol. 24, 217-225, 1991.
- [6] P. Allongue, E. Souteyrand: Metal electrodeposition on semiconductors, *J. Electroanal. Chem.*, Vol. 286, 217-237, 1990.
- [7] W. Davison, J.A. Harrison: The electrochemical growth of three dimensional nuclei during a potentiostatic pulse: A simulation, *Electroanalytical Chemistry and Interfacial Electrochemistry*, Vol. 44, 213-219, 1973.
- [8] P. Allongue, E. Souteyrand: Schottky barrier formation of various metals on n-GaAs(100) by electrochemical deposition, *J. Vac. Sci. Technol. B5*, 1644-1649, 1987.
- [9] C.A. Burrus: Pulse electroplating of high-resistance materials, poorly contacted devices, and extremely small areas, *J. Electrochem. Soc.*, Vol. 118, No. 5, 833-834.

- [10] M. McColl, A.B. Chase, W.A. Garber: Extremely uniform electrodeposition of submicron Schottky contacts, *J. Appl. Phys.*, Vol. 50, No. 12, 8254-8256, 1979.
- [11] V. Krozer, A. Grüb: A novel fabrication process and analytical model for Pt/GaAs Schottky barrier mixer diodes, *Solid-State Electronics*, Vol.37, No. 1, 169-180, 1994.
- [12] T. Hashizume, H. Hasegawa, T. Sawada, A. Grüb, H.L. Hartnagel: Deep level characterization of submillimeter-wave GaAs Schottky diodes produced by a novel in-situ electrochemical process, *Jpn. J. Appl. Phys.*, Vol. 32, Part I, No. 1B, 486-490, 1993.
- [13] A.J. Willis: Edge effects in Schottky diodes, *Solid-State Electronics*, Vol. 33, No. 5, 531-536, 1990.
- [14] M.V. Schneider, A.Y. Cho, E. Kollberg, H. Zirath: Characteristics of Schottky diodes with microcluster interface, *Appl. Phys. Lett.*, Vol. 43, No. 6, 558-560, 1983.
- [15] J.H. Werner, H.H. Güttler: Barrier inhomogeneities at Schottky contacts, *J. Appl. Phys.*, Vol. 69, No. 3, 1522-1533, 1991.

A 1 THZ Nb SIS HETERODYNE MIXER WITH NORMAL METAL TUNING STRUCTURE.

H. van de Stadt*, A. Baryshev^{□‡}, P. Dieleman[□], Th. de Graauw*, T.M. Klapwijk[□], S. Kovtonyuk^{□‡}, G. de Lange^{□‡}, I. Lapitskaya^{□‡}, J. Mees*, R.A. Panhuyzen[□], G. Prokopenko^{□‡}, H. Schaeffer*.

* Space Research Organization of the Netherlands, PO Box 800, 9700 AV Groningen, The Netherlands.

□ Department of Applied Physics and Materials Science Center, University of Groningen, Nijenborgh 4, 9747 AG Groningen, The Netherlands.

† Present addr: Research Laboratory of Electronics, MIT, 02139 Cambridge MA, U.S.

‡ Permanent address: Institute for Radio Engineering and Electronics, Russian Academy of Sciences, Mochoyova str. 11, Moscow 103907, Russia.

1. Introduction.

The use of niobium SIS mixers with integrated tuning structures for frequencies above the gap frequency is described. From model calculations for integrated striplines one can predict lower losses at high frequencies if one replaces a niobium tuning structure by one of normal metal. This idea has been tested in waveguide mixers for frequencies between 0.5 and 1.1 THz.

2. Model Calculations.

Superconductive striplines have shown to be of major importance in the coupling of high frequency signals to SIS quasiparticle mixers. Räisänen et al. [1] proposed the use of on chip superconductive striplines as tuning elements at 100 GHz and several groups now successfully employed niobium integrated tuning elements at frequencies up to 800 GHz [2,3].

In principle an SIS junction can be used for mixing at frequencies up to twice the gap frequency, which lies around 700 GHz for niobium. However, already at frequencies just above the gap frequency the sensitivity of the device decreases due to losses in the integrated tuning structure and to a lesser extent, losses in the antenna and the junction itself.

To calculate the losses and the effect on the behaviour of the entire mixer, the mixer is modelled by an equivalent RF circuit. For the case of an endloaded stripline this consists of the stripline impedance in series with the parallel circuit of the junction's nonlinear tunnel resistance and its capacitance. If we define the total incident power as P_{in} , the reflected power as P_r , and the absorbed power in the junction and the tuning as $P_{abs}=P_j+P_{tun}$, then we have $P_{in}=P_r+P_j+P_{tun}$. The relative power coupled to the junction and the stripline, $\{P_j+P_{tun}\}/P_{in}$, is shown as the dashed lines in figures 2.1 and 2.2, the fraction of the absorbed power coupled to the junction, $\{P_j/(P_j+P_{tun})\}$, is represented by the dotted lines and the fraction of incident power coupled to the junction, $\{P_j/P_{in}\}$, is given as the continuous lines. Results for Nb and Al striplines are shown in figures 2.1 and 2.2, where we assumed striplines of 43 μm length and 10 μm width. For the case of a normal metal stripline we assumed a conductivity of $3 \cdot 10^{10} (\Omega\text{m})^{-1}$. From the figures it can be seen that the fall-off of the efficiency of the Al stripline at high frequencies is less severe than in the case of the Nb stripline. The expected higher transmission of power to the junction is the reason that we decided to implement aluminum striplines.

Fig 2.1: RF power coupling into a Nb SIS junction with Nb stripline.
 Fig 2.2: RF power coupling into a Nb SIS junction with aluminum stripline.

3. Measurements.

3.1: Waveguide mixers.

For our measurements we use two waveguide mixers based on the original design by C.E. Honingh et al.[4] for 345 GHz. One mixer is scaled to a center frequency of 700 GHz and has been tested extensively by G. de Lange et al.[3] up to a frequency of 760 GHz. This mixer was successfully used in airplane campaigns by J. Mees et al[5] to measure atmospheric C10, NCI, N₂O and O₃ lines at frequencies between 625 and 650 GHz. The other mixer is scaled to a center frequency of 900 GHz. Both mixers use a contacting mechanical backshort tuner. Instead of an E-plane tuner we use integrated tuning elements to achieve the desired matching between the junction and its environment. Characteristics of the two mixers are summarized in the following table:

	0.7 THz mixer	1 THz mixer
waveguide size	150x300 gm	120x240 pan
cut-off frequency	500 GHz	625 GHz
substrate channel	100x100 gm	90x75 GHz
substrate thickness	50	40 μm

An impression of the waveguide losses in the 1 THz mixer can be obtained by measuring the LO coupling as a function of backshort position. This was done at a frequency of 1013 GHz by moving the backshort over a distance of 3.0 mm. This covers more than 13 half periods of the guide wavelength. There appeared to be no strong decrease of the coupling efficiency. In figure 3.1 we show data taken at 912 GHz over a distance of about 1.0 mm together with a sinusoidal best fit to the data. These measurements suggest that waveguide losses are small, even for a crosssection as small as 120 x 240 micrometer.

Fig 3.1: Coupling as a function of backshort position.

3.2. Optics.

Both mixers use diagonal horns with a plastic lens in front. Our lenses have one flat and one curved, aspherical surface, where the asphericity is used to compensate for spherical aberration of the high focal ratio lens. The 1 THz mixer uses essentially the optics as described by G. de Lange et al[3] with a horn of 11° cone angle and a HDP lens. The antenna beam pattern is shown in figure 3.2; it shows good symmetry, sidelobes lower than 15 dB and good Gaussian behaviour. But the measured beam angle is larger than the expected value by about 10%. The horn-lens combination of the 0.7 THz mixer uses a horn with 7° cone angle and a PTFE lens.

For injection of the LO beam we do not use an interferometer-diplexer, but a thin beamsplitter under 45° angle of incidence. We use mylar sheets of different thicknesses and the inherent loss in the signal beam for various thicknesses and frequencies is calibrated with good accuracy. Therefore we present not only our actually measured noise temperatures but also the values after correction for the beamsplitter loss.

Fig 3.2: Antenna beam pattern of 1 THz mixer.

3.3. Local oscillators.

For the various frequencies we use different carcinotrons and BWCY s (Backward Wave Oscillator), sometimes in combination with a doubler, as local oscillators. In this way we can cover a nearly continuous range from 520 to 1090 GHz. The only gap in the frequency range, where we have no suitable LO available, runs from about 760 to 840 GHz,

3.4. Nb SIS junctions with aluminum striplines.

For the fabrication of Nb junctions with aluminum striplines we use a modification of the SNOEP process described by Dierichs et al [6]. In the usual SNOEP process the trilayer is defined by lift-off and the junctions are made via an overetch (the letters OE in SNOEP) process. In this way the junctions are formed in the top layer of the trilayer and usually have areas of $1.0 \mu\text{m}^2$. In the modified process for the fabrication of aluminum striplines we apply the lift-off process to the trilayer with an extra aluminum underlayer of 100 nm thickness. A second modification is that the junctions are defined by etching through the whole trilayer by using an extra RF sputter etching step in addition to the usual RIE etching. A third modification is the use of an extra 100 nm thick aluminum layer underneath the niobium wiring layer. In this way we obtain a configuration where all conducting structures in the RF filters as well as in the integrated tuning elements consist of a combination of aluminum and niobium layers. The details of the process were developed by one of us (S.Kovtonyuk). A similar process with some modifications seems to be possible for copper instead of aluminum in order to achieve an even better conductivity.

In figure 3.3 we present the pumped and unpumped I-V curves of a Nb junction with an aluminum- stripline of 40 μm length mounted in the 0.7 THz mixer block and used at a temperature of 2 K. The pump frequency is 1056 GHz and we can deduce the following parameters:

Gap Voltage:	$V_{\text{gap}}=2.80 \text{ mV}$	Gap smearing:	$\Delta V=0.31 \text{ mV}$
Normal R:	$R_N=38.6 \text{ E}2$	Subgap R:	$R_S=3.3 \text{ ka}$
Photon step:	$V_{\text{ph}}=4.31 \text{ mV}$	Resistance ratio:	$R_S/R_N=85$
Junction Area:	$A= 1.1 \mu\text{m}^2$		

The gap voltage of 2.80 mV corresponds to a gap frequency is 678 GHz and the operating frequency of 1056 GHz, as reported in the next section, means that we are at 1.56 times the gap frequency.

We also want to draw your attention to the fact that the widths of the photon steps below and above the gapvoltage are almost equal, indicating that almost no heating occurs, in contrast to what we see with niobium striplines. We attribute the good heat conductivity to the use of aluminum, which is in contact with all niobium structures.

Fig 3.3: Pumped and unpumped I-V curves of a Nb junction with aluminum stripline of 40 μm length.

3.5. Measurements with the 0.7 THz mixer.

We have investigated several junctions with different kinds of tuning structures. We report here the results of so-called endloaded striplines of 10 μm width and three different lengths: 60, 50 and 40 micrometer, mounted in the 0.7 THz mixer.

First we present in figure 3.4 the values of IF power and Y-factor as a function of bias voltage for the junction with the shortest stripline and used at 1056 GHz. For reference we include also the I-V curves of figure 3.3. The Y-factor is measured with a chopped hot-cold

blackbody source as an incoherent signal and is given in arbitrary units. Note that we detect only a heterodyne response over the bias region with non-overlapping photon steps, i.e. from about 1.5 to 2.6 mV. Similar curves were obtained for other frequencies and for other junctions.

Fig 3.4: IF power and Y-factor curves at 1056 GHz.

In figures 3.5, 3.6 and 3.7 we present system noise temperatures versus frequency for end-loaded junctions with three different lengths of striplines, as measured in the 0.7 THz mixer block. Since we use a mylar beamsplitter under 45° with known loss, DSB noise temperatures are given as actually measured values as well as after correction for the beamsplitter loss. We have not applied a correction for the Rayleigh-Jeans approximation. It is obvious that the longest stripline of 60 micron has its best response at lower frequencies ranging from about 640 to 740 GHz.

In figure 3.5 we show results from the 0.7 THz mixer block with junctions with a 60 long Al stripline. Note that we use different local oscillators for the frequencies below and above 680 GHz and that data below 680 GHz refer to a detector temperature of 4.2 K, while above that frequency we have also 2.0 K.

Figure 3.6 gives measured noise temperatures for a junction with a 50 gm long stripline. We have no data between 740 and 840 GHz due to the lack of a local oscillator for these frequencies. However, the wideband FTS (Fourier Transformer Spectrometer) data presented in figure 3.8, indicate that we can expect a continuous behaviour of T_{syst} .

In figure 3.7 we show measured values of T_{syst} for a junction with a 40 long stripline. Measured values increase from a lowest value of 1,966 K at 660 GHz to a value of 6,140 K at WOO GHz and 10,650 K at 1056 GHz. These last frequencies are at 1.5 times the gapfrequency.

The spectral response in the case of Al striplines of 40, 50 and 60 microns length was measured with a Fourier Transform Spectrometer (FTS). In figure 3.8 we present the spectra in each of the three cases with the same relative magnitude and for different settings of the backshort. For each backshort setting we see peak sensitivities at several different frequencies. We could draw a line through the maxima and obtain a good impression of the maximum sensitivity curve for each junction. The 60 micron long stripline provides the best sensitivity at a frequency of 690 GHz, the 40 micron stripline shows a rather wideband response, but it has a dip at frequencies around 900 GHz. In all cases the FTS response agrees well with the heterodyne response, as can be seen by comparing figure 3.8 with 3.5, 3.6, and 3.7.

3.5. Measurements with the 1.0 THz mixer.

In figure 3.9 we show results measured with the 1.0 THz mixer block, using a series of two $2.0 \mu\text{m}^2$ area Nb junctions with 43 gm long Al striplines. The parameters of this junction were used in the calculations shown in Fig 2.2. The heterodyne data of the 1.0 THz mixer block have been measured only over a limited frequency range from 832 GHz to 1000 GHz. As shown, we measure a lowest value for the DSB noise temperature of 1,340 K at 846 GHz and a value of 3,349 K at 1000 GHz. Note that these values have been corrected for the loss in the 60 beamsplitter.

4. Discussion.

In this section we mention some aspects that influence the sensitivity of SIS junctions with aluminum striplines in our 0.7 and the 1.0 THz mixers.

The resistance ratio for the unpumped I-V curve is pretty high (see Fig 3.3), indicating that we have a good quality barrier with low leakage current. The gap smearing of 0.31 mV seems rather high and may be caused by impurities in the niobium of the trilayer. The resistivity of the aluminum of the stripline is higher than that of bulk aluminum due to impurities. The last two factors may be improved in the future.

In figure 3.3 we also see an important feature: the photon steps below and above the gap voltage are equal. As mentioned earlier, this indicates that almost no heating occurs.

Pumping on the Helium in our dewar in order to reduce the temperature from 4.2K to 2.0 K is less effective than observed for Nb striplines. This is because the conductivity of aluminum does not increase when lowering the temperature. In general the lower physical temperature reduces T_{syst} by about 25%.

For the 0.7 THz mixer there is a frequency range around 900 GHz with reduced sensitivity. This is not only seen in the heterodyne measurements, but also in the wideband FTS measurements. The precise reason for this is not well understood. The fact that the backshort adjustment at these frequencies is not very effective, indicates that we have an absorptive or a reflective effect at the junction substrate around these frequencies.

5. Conclusions.

We calculated the behavior of superconducting Nb SIS detectors with aluminum striplines for frequencies above the bandgap. When compared to Nb tuning structures we expect a better sensitivity for frequencies in the THz regime. So we developed and implemented a new process for the fabrication of Nb SIS junctions with Al tuning structures.

The resulting devices have been tested in waveguide mixers designed for center frequencies of 0.7 and 1.0 THz. For frequencies above 900 GHz our measured noise temperatures compare favourably with results from similar devices with niobium striplines, for which we measured a best DSB noise temperature of 18,100 K at 945 GHz.

In the 0.7 THz mixer block the measured DSB noise temperature of a single junction with a stripline of 40 micron length gradually increases from a lowest value of 1,966 K at 660 GHz to values of 6,140 K at 1000 GHz and 10,650 K at 1056 GHz. The last frequencies are at about 1.5 times the gapfrequency.

Data of the 1.0 THz mixer block are available at this moment only over a limited frequency range of 832 GHz to 1000 GHz. Using a double junction with 43 μm long Al stripline we measure a lowest value of 1,340 K at 846 GHz and a value of 3,349 K at 1000 GHz. These values have been corrected for the loss in the beam splitter, as shown in figure 3.9.

Acknowledgements.

We are indebted to E. Armandillo of ESTEC, Noordwijk, for stimulating this research during many years. We wish to acknowledge the support of J.R.Gao, Van Duc Nguyen, N.Whyborn and Hans Golstein and we benefitted from useful advise and V.Koshelets and S.Shitov of the IREE Institute, Moscow.

We acknowledge the financial support of the European Space Agency via contract No. 7898/88/NL/PB(SC) and the Stichting for Technische Wetenschappen contract GTN 33.2971.

References.

- [1] A.V. Räisänen, W.R. McGrath, P.L. Richards, and F.L. Lloyd, *IEEE Trans. Microwave Theory Techn. MTT-33*, 1495 (1985).
- [2] T.G. Büttgenbach, H.G. LeDuc, P.D. Parker and T.G. Philips, "A Fixed Tuned Broadband Matching Structure for Submillimeter Astronomy," *IEEE Trans. Appl. Superconductivity*, **2**, 165, 1992.
- [3] G.de Lange, C.E. Honingh, J.J. Kuipers, H.H.A. Schaeffer, R.A. Panhuyzen, T.M. Klapwijk, H.van de Stadt, Th.de Graauw, "Heterodyne mixing with Nb tunnel junctions above the gap frequency", *Appl.Phys.Lett*, **64**, 3039, 1994.
- [4] C.E. Honingh, J.J. Wezelman, M.M.T.M. Dierichs, G.de Lange, H.H.A. Schaeffer, T.M. Klapwijk and Th.de Graauw, "Extensive test of the three-port quantum mixer theory on 345 GHz superconductor-insulator-superconductor mixers," *J.Appl.Phys*, **74**, 4762, 1993.
- [5] J. Mees, S. Crewell, H. Nett, G.de Lange, H.van de Stadt, J.J. Kuipers and R.A. Panhuyzen, "An airborne SIS-receiver for atmospheric measurements of trace gases at 625 to 720 GHz," *Proc. of Fifth Int. Symp. on Space THz Technology*, PP.142-156, Ann Arbor, 1994.
- [6] M.M.T.M. Dierichs, R.A. Panhuyzen, C.E. Honingh, M.J. de Boer, and T.M. Klapwijk, "Submicron niobium Junctions for submillimetre-wave mixers using optical lithography," *Appl.Phys.Lett*. **62**, 774 (1993)

Calculated coupling for 43 μm Nb stripline

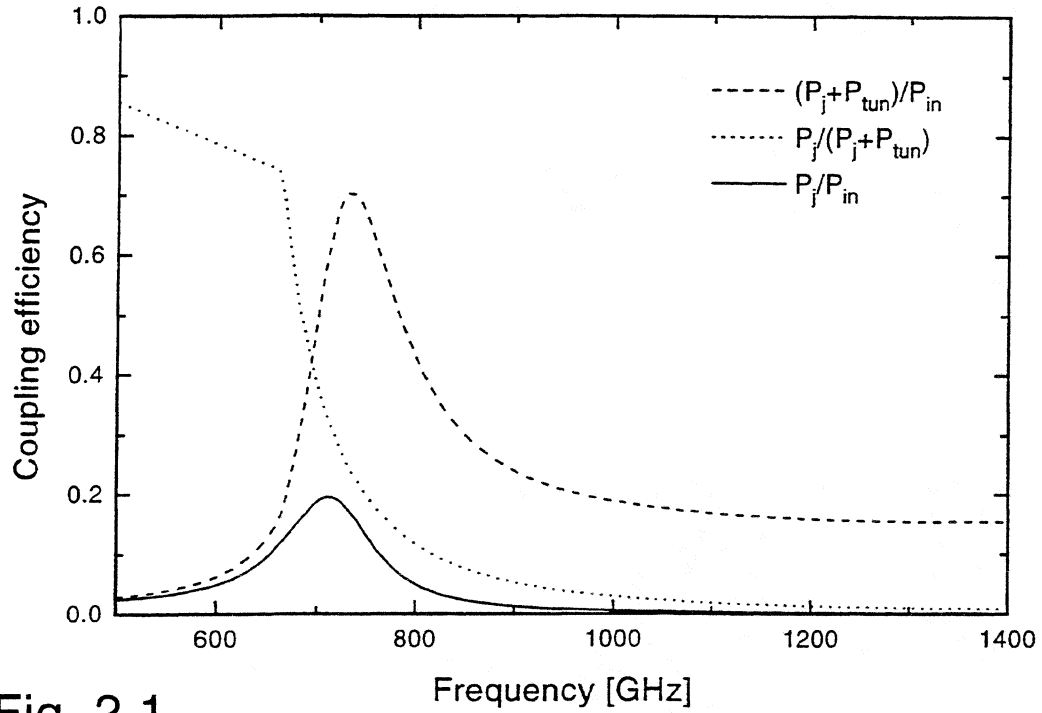


Fig. 2.1

Calculated coupling for 43 μm Al stripline

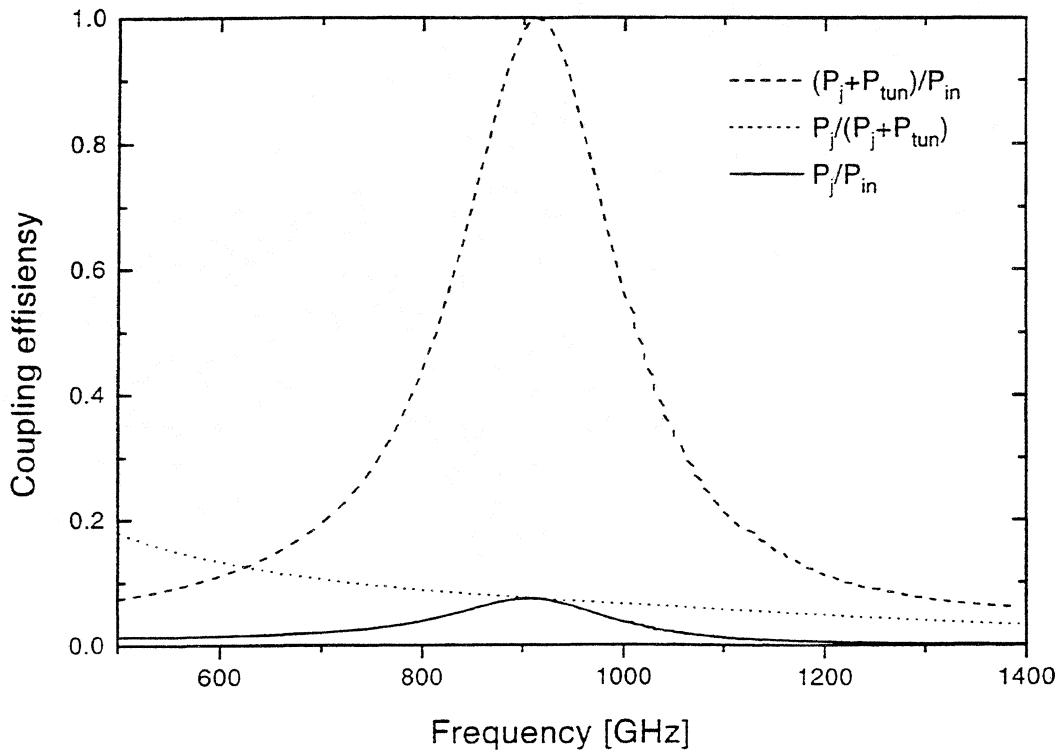


Fig. 2.2

Coupling as a function of backshort position for 1THz mixer.

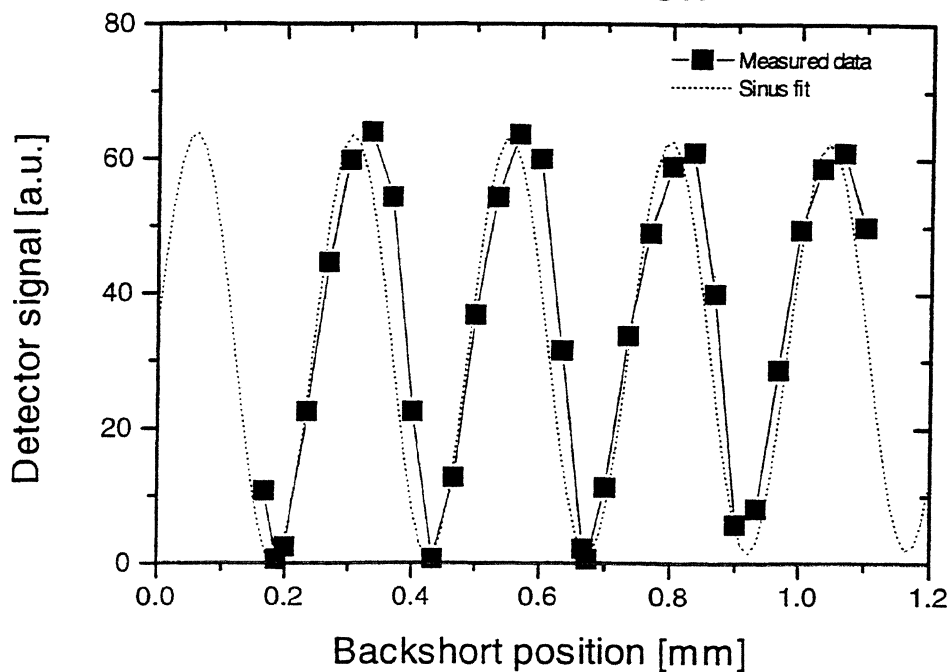


Fig. 3.1

Beam pattern of 1 THz mixer.

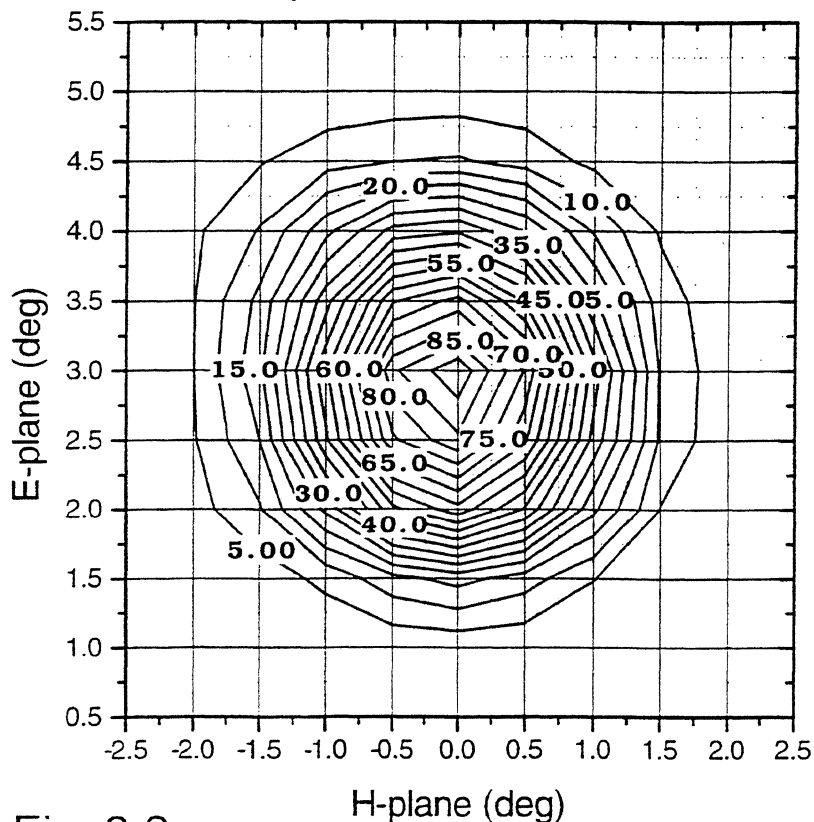


Fig. 3.2

Pumped and unpumped IV-curves @ 1056 GHz

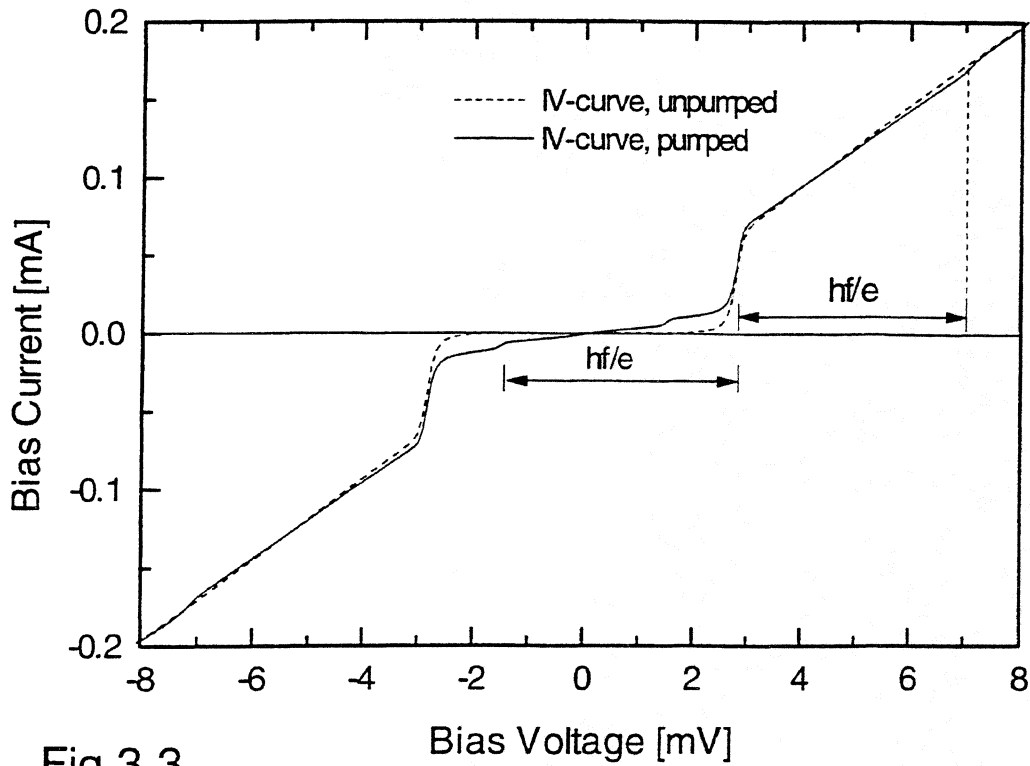


Fig.3.3

Nb SIS junction with 40 μm long normal metal stripline @ 1056 GHz

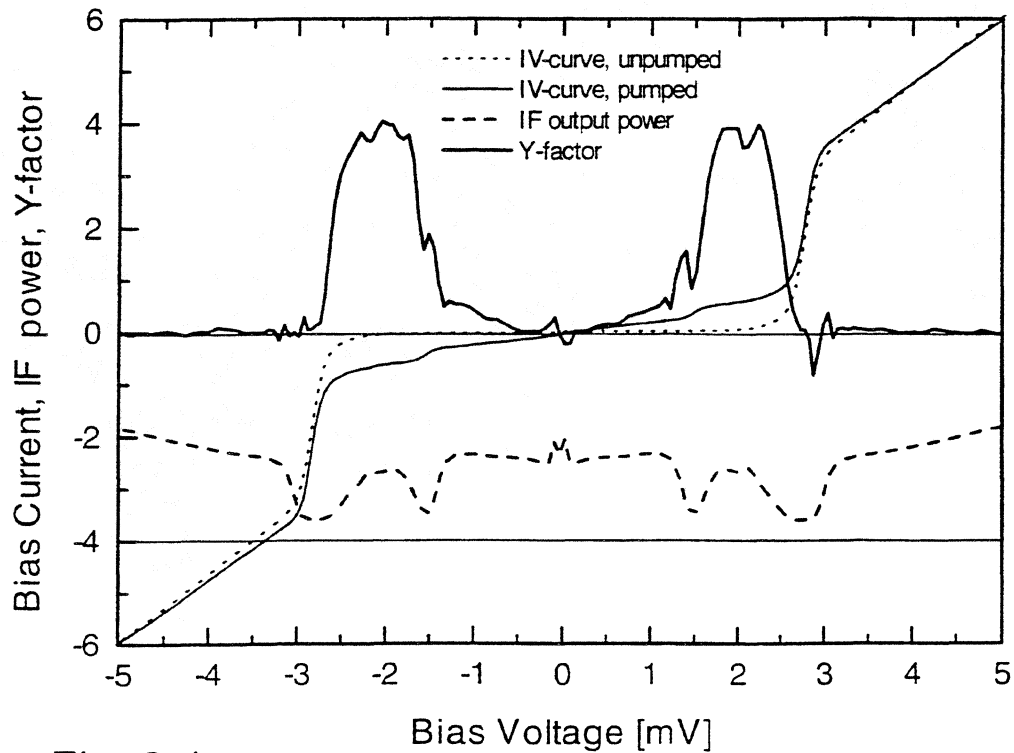


Fig. 3.4

Nb SIS junction with 60 μm long Al stripline.

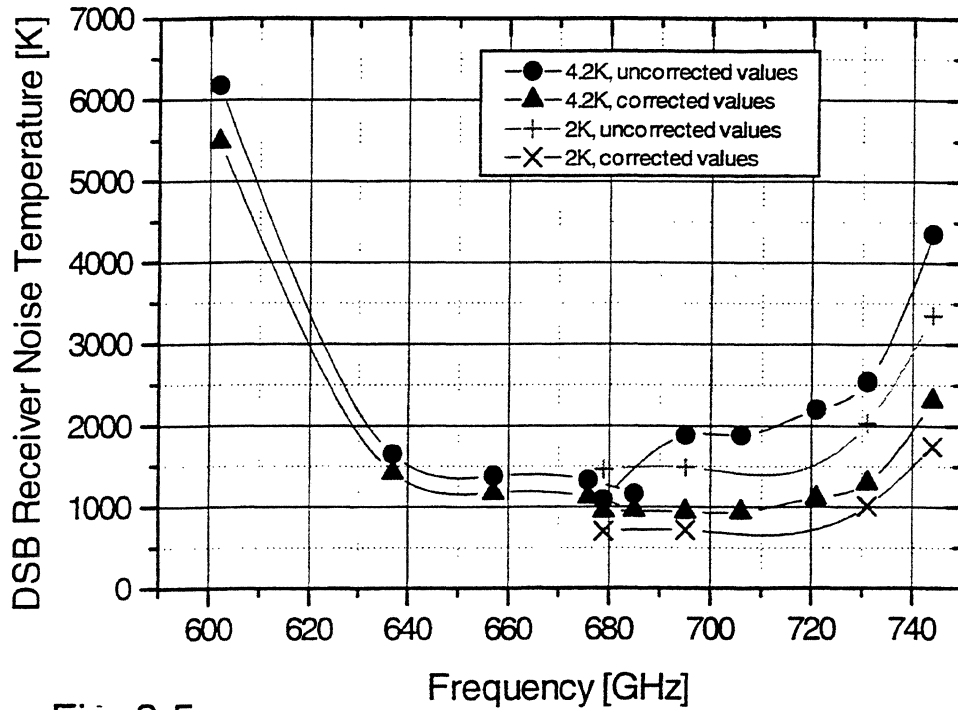


Fig. 3.5

Nb SIS junction with 50 μm long Al stripline.

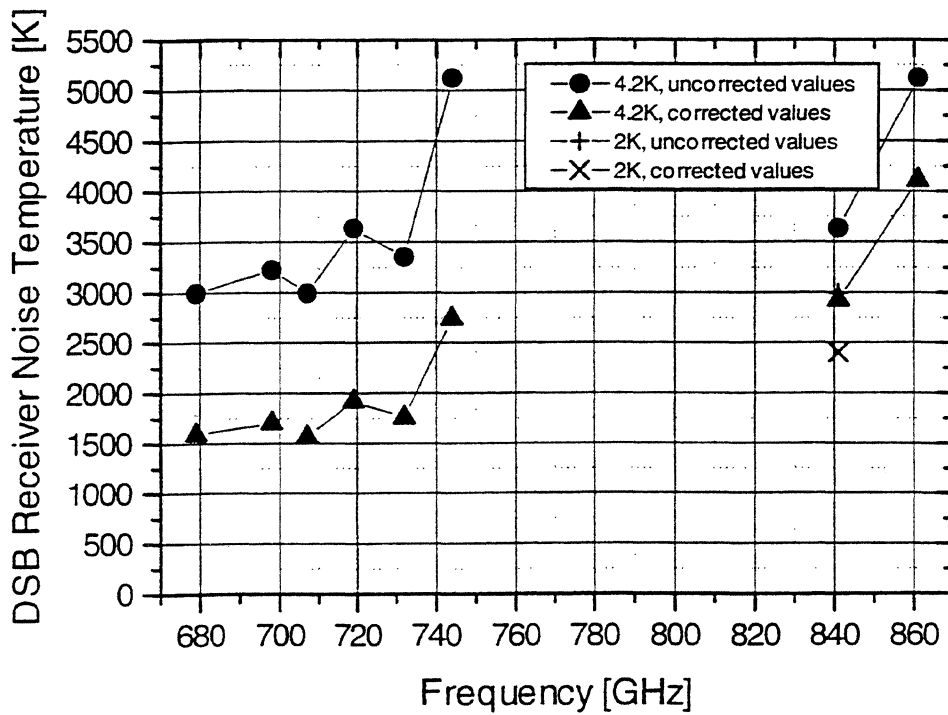


Fig. 3.6

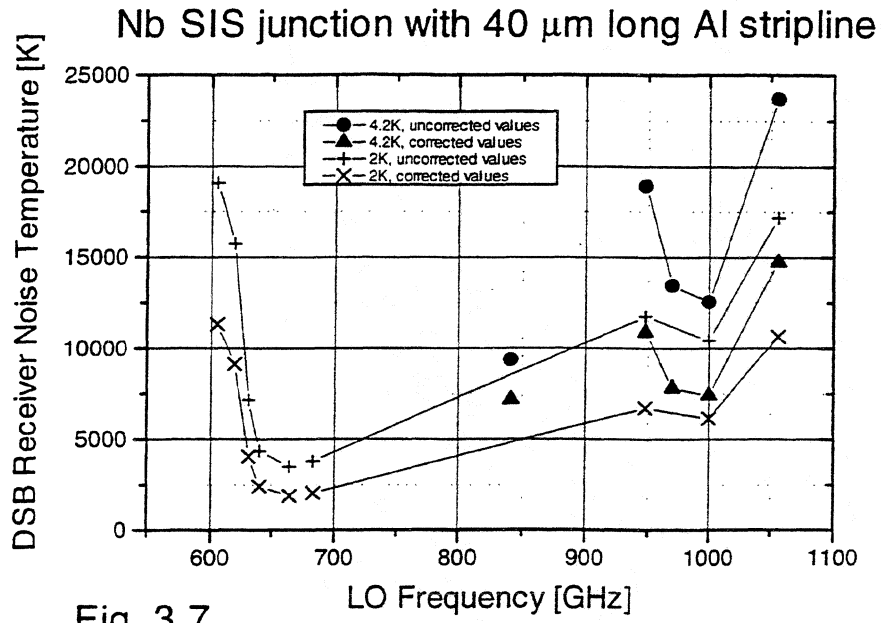


Fig. 3.7

FTS Video Response of 0.7 THz mixerblock

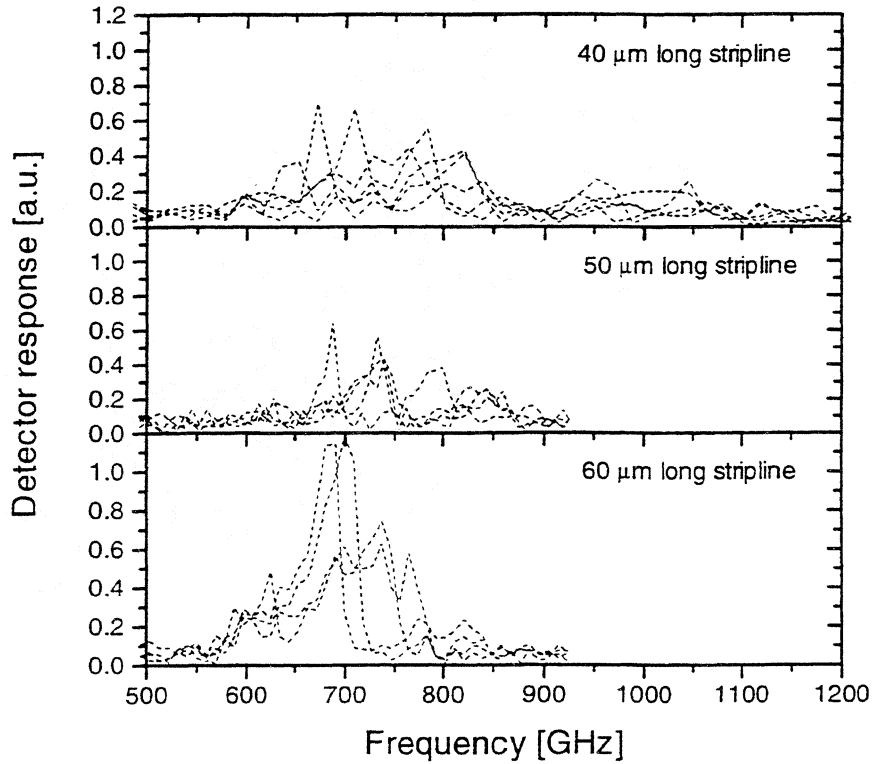


Fig. 3.8

T_{sys} for Nb SIS junction with 43 μm Al stripline.

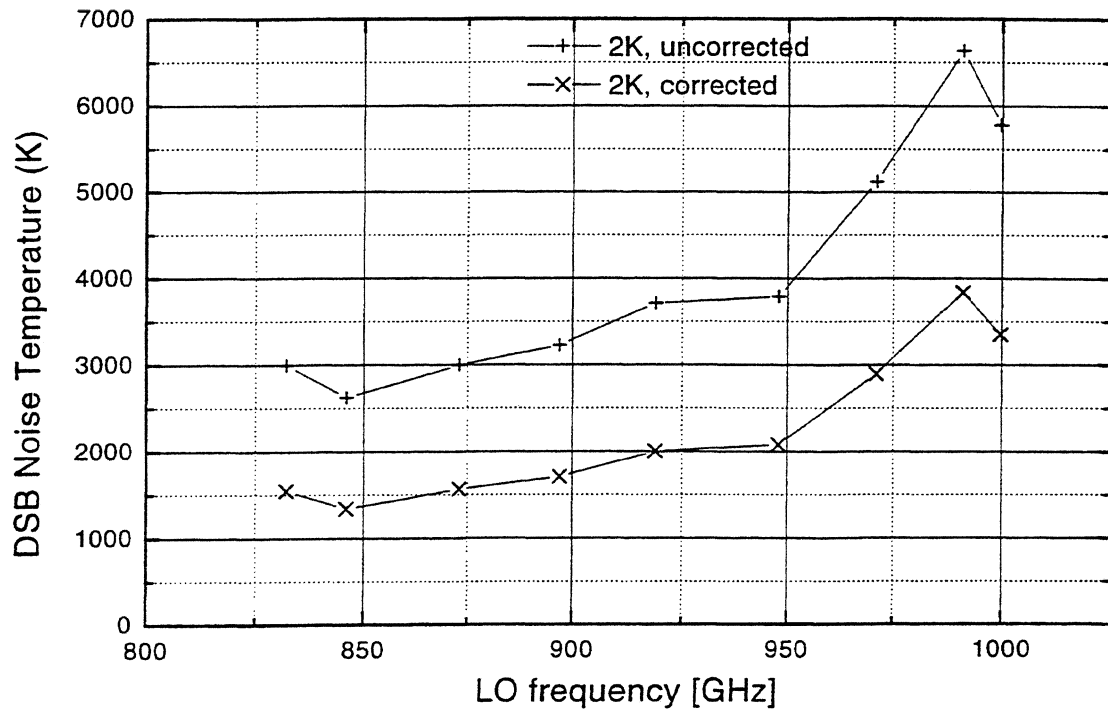


Fig. 3.9

An 800 GHz SIS mixer using Nb-Al₂O₃-Nb SIS junctions

C.E.Honingh, K.Jacobs, D. Hottgenroth, and S.Haas.



KOSMA

*I. Physikalisches Institut der Universität zu Köln
Zùlpicher Str. 77
D-50937 Köln
Germany*

Introduction

The development of an 800 GHz mixer is part of a project to build a dual channel SIS receiver for submillimeter frequencies to be used at a ground based telescope. The two channels are integrated in one hybrid liquid helium dewar, and are each fed by one polarization of the incoming signal. Since most mixers are sensitive to one polarization only a factor of two in observing time is gained. Also the simultaneous observation at two frequencies improves the calibration accuracy of the two sets of data with respect to each other. This is especially important in observing spectral lines in molecular clouds of which the relative intensity at two frequencies is crucial to determination of their properties. The receiver will have one channel just for 450GHz-500 GHz, while the other channel can be used alternatively for 650-700 GHz or 800-820 GHz.

For the two lower frequencies superconductor-insulator-superconductor (SIS) quasi-particle mixers are the obvious choice. In the past few years there has been a rapid development of SIS mixers towards use at higher frequencies, and various groups have shown sensitivities as good as five to ten times the quantum limit in both bands.[1-5]. This development has been possible because high quality, high current density Nb-Al₂O₃-Nb SIS junctions became available, with areas small enough to be useful at higher frequencies.

A typical current density at 700 GHz is 10 kA/cm², with a leakage current below the gap voltage smaller than 10 μ A. The area of the junction that is used depends on the method that is chosen to tune out the geometrical capacitance of the junction. A tuning that depends solely on adjustable tuners has been used up to 750 GHz [5]. The tuning of this type of mixer usually has to be adjusted at every frequency. Generally mixers that have a larger instantaneous bandwidth use a microstrip tuning structure integrated with the junction. The microstrip metallization is also made of niobium. This makes the tuning structures almost lossless (below the gap frequency of niobium), which is crucial to their excellent performance. This types of tuning allows somewhat larger junction areas, typically 1 μ m² around 700 GHz, than the former type.

For the 800-820 GHz band the noise temperatures reported so far are about a factor of 10 higher than at 700 GHz. It has been shown [5], using a waveguide mixer with two mechanically

adjustable tuners and a junction with an area of $0.25 \mu\text{m}^2$, that above the gap frequency of niobium (700 GHz) the Nb-Al₂O₃-Nb junctions still function very well as mixing elements. The tuning of the geometrical capacitance of the junction however is more complicated because integrated tuning structures will have losses and this rapidly deteriorates the sensitivity of the mixer [6].

1 Design considerations

SIS junctions and tuning

For the SIS junction we will take a simple equivalent circuit consisting of its normal state resistance (R_j) parallel to its geometrical capacitance (C_j). Apart from all other considerations the current density of an SIS junction to be used at 800 GHz should be equal or higher than 12 kA/cm² to have an $\omega R_j C_j$ product below 7. This is among the highest current densities shown so far, in junctions that still have a good SIS barrier. At even higher current densities the barrier becomes so thin that microshorts may occur, which potentially increase the shotnoise production of the junction.

The value of $\omega R_j C_j$ makes some kind of tuning necessary. Low loss waveguide tuners alone will not be sufficient. Although an E-beam lithography facility has been set up recently as part of this project, as a first approach we had to work with junctions that we could fabricate with standard UV lithography. This results in junction areas not much smaller than $1 \mu\text{m}^2$ which require some kind of integrated tuning. We used traditional integrated tuning circuits, made of niobium, similar to those used below the gap frequency. In general the integrated tuning structures can be split in two types. Parallel resonant structures which connect an inductance parallel to junction capacitance, and series resonant structures, which put a small inductor in series with the junction. These latter structures are usually followed by a transformer to transform the very low impedance to a value that can be matched better to an antenna.

A quick estimate of the effect of a parallel resonant structure with a lossy inductor can be obtained from a lumped element equivalent circuit, given in Fig. 1A. Around the resonance frequency the loss in series (R_s) with the inductor (impedance X_s) can be transformed into a resistor (R_p) parallel to the junction resistance via $R_p = (Q^2 + 1)R_s$, where $Q = X_s/R_s$. The real and imaginary part of the inductive impedance are calculated from an ordinary transmission line model for lossy transmission lines.

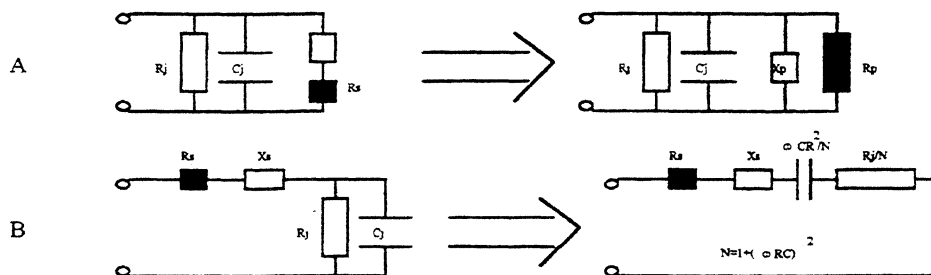


Fig. 1 Lumped element equivalent of a parallel and a series resonant circuit for an SIS junction R_j/C_j , with a lossy inductor ($R_s + iX_s$).

For a junction with area $0.95 \mu\text{m}^2$, $j_c = 10 \text{ kA/cm}^2$ and $C_j = 70 \text{ fF}$, R_p lies somewhere between 3.5 and 4.3Ω , depending on the exact estimate of the loss in niobium. The transmission line is $4 \mu\text{m}$ wide, on a 200 nm thick SiO dielectric. The 4.3Ω result from the Mattis Bardeen (MB) [7] theory in the extreme anomalous limit, which is certain to give a too low estimate of the loss [6, 8]. The MB calculation is made with a normal state conductivity of niobium of $1.25 \times 10^7 (\Omega \text{ m})^{-1}$, an energy gap 1.45 meV at zero Kelvin, and a critical temperature of 9.2 K . The 3.5Ω are found if the loss is taken 2.5 times as large. Comparing these resistances values with the junction normal state resistance of 23Ω gives a maximum coupling to the junction of approximately 16%. Also the resonance frequency depends on the loss in the structure. Between the two extremes of loss that are used here the difference in resonance frequency is about 35 GHz . The situation can be improved by increasing the current density of the junction. To first order this reduces R_j without changing C_j , thus improving the ratio between R_p and R_j . Also the junction area can be made smaller, which reduces C_j , and leads to a higher value of R_p at resonance. Because R_j also increases the effect is not very large. For a junction with area $0.6 \mu\text{m}^2$, $j_c = 12 \text{ kA/cm}^2$ and $C_j = 45 \text{ fF}$, a maximum coupling between 20% and 26% is calculated this way.

For a series resonance, shown in Fig. 1B, a similar reasoning is possible. The SIS junction is now taken as a series circuit of a capacitance and a resistance. For a junction with area $0.95 \mu\text{m}^2$, $j_c = 10 \text{ kA/cm}^2$ and $C_j = 70 \text{ fF}$, this resistance is 0.33Ω . A resonating series stub will have an impedance with a real part between 0.22 and 0.55Ω for the two extremes of loss mentioned above. This leads to a coupling to the junction between 37% and 60%, much better than with the parallel stub. Unfortunately the resulting impedance is so low that a quarter wave transmission line transformer has to be used to transform the impedance to a reasonable level. This line attenuates the power by a factor $\exp(2\alpha l)$, where α is the real part of the complex propagation constant along the line and l is the length of the transformer. The extra factor 0.5 to 0.8 leads to a total coupling between 20 % and 50 %.

As mentioned above, the transformed impedances have to be matched to a receiving antenna. Also the resulting embedding impedance of the junction, which determines its conversion and noise properties has to be evaluated. In Fig. 2 the embedding impedance and the (complex conjugate of) the transformed junction impedance are shown for a parallel(A) and series resonant(B) tuning circuit for a junction with area $0.95 \mu\text{m}^2$, $j_c = 10 \text{ kA/cm}^2$ and $C_j = 70 \text{ fF}$. As antenna impedance we chose the impedance of a standard waveguide mount. The loss in the tuning structure has the unavoidable effect that in the case of a series resonance structure the matching between the transformed junction impedance and the waveguide impedance is better than the parallel one, but the embedding impedance is worse. This leads to the question which effect has stronger influence on the overall receiver performance, the embedding impedance of the junction or the coupling between the waveguide and the junction.

Since the quantum theory of mixing [8] seems to predict mixer performance rather accurately even well above the gap frequency [6], we used the embedding impedance and the coupling efficiency shown above to calculate the overall receiver performance. The result is similar for the two structures and both temperatures lie between 1400 K and 1800 K , assuming an IF frequency of 1.5 GHz , an IF noise temperature of 10 K and an IF input impedance of 50Ω .

Accordingly we have implemented both types of tuning structures on the fabrication mask. An additional advantage of the series resonance structure might be that it is not as sensitive to alignment accuracy, with a length of around $30 \mu\text{m}$ and a width of 5 to $8 \mu\text{m}$. The parallel

structure needs a narrower line, almost as short as it is narrow, and an open circuited section to create an RF-short for which we used both radial and straight stubs. Because this last line section is much wider line its additional contribution to the loss is small. The resonance frequencies of both structures are dependent on the actual loss in the circuit. To reach receiver noise temperatures below 1000 K, assuming the same losses in the niobium tuning structure, we tentatively put some junctions with an area of approximately $0.6 \mu\text{m}^2$ on the mask to be fabricated with a current density of $12 \text{ kA}/\text{cm}^2$.

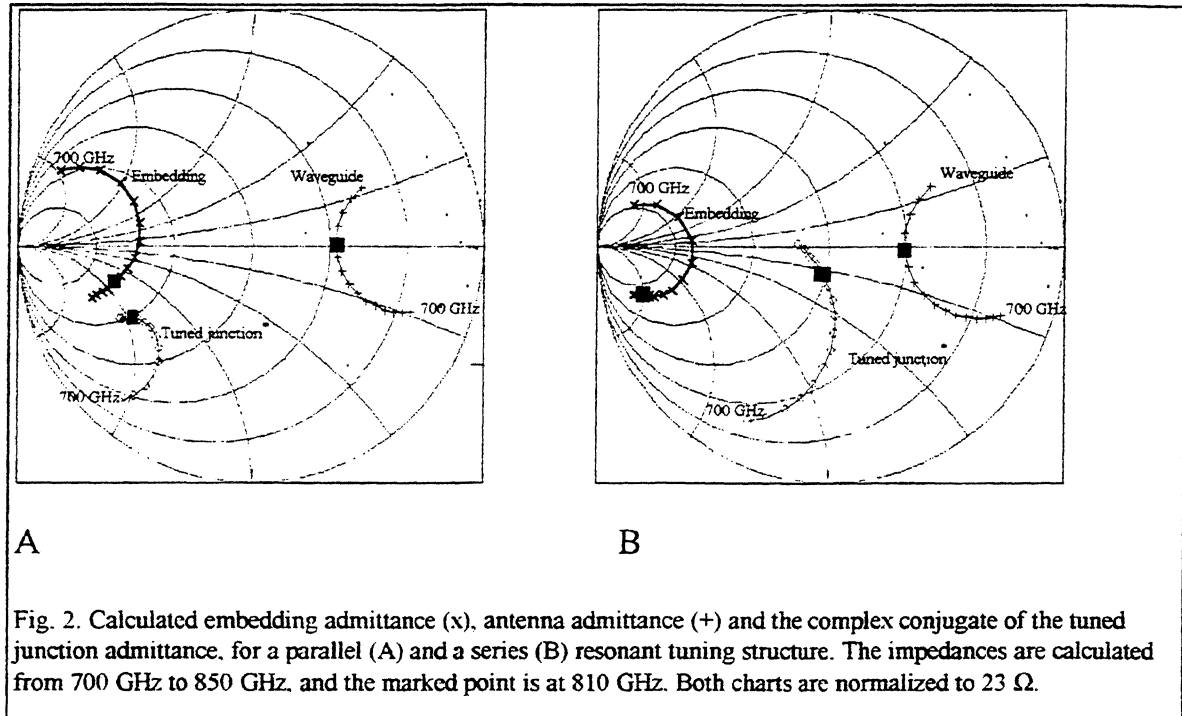


Fig. 2. Calculated embedding admittance (x), antenna admittance (+) and the complex conjugate of the tuned junction admittance, for a parallel (A) and a series (B) resonant tuning structure. The impedances are calculated from 700 GHz to 850 GHz, and the marked point is at 810 GHz. Both charts are normalized to 23Ω .

Mixerblock

We use a traditional waveguide mixer block. A block with a backshort as well as an E-plane tuner would have been optimal, especially to reach the low impedance created by a parallel resonant tuning structure. To avoid the complication of fabricating a mixerblock with two perpendicular tuners, we built a block similar to the 500 GHz mixer [1] with a single backshort. The waveguide dimensions are $330 \mu\text{m} \times 95 \mu\text{m}$, and those of the substrate channel $100 \mu\text{m} \times 95 \mu\text{m}$. The block is fabricated in split block technique to minimize the loss in the waveguide due to imperfect contact between the two halves. The waveguide and the substrate channel have been sawed into the brass mixer block, using a carbon hardened saw blade with a width of $95 \mu\text{m}$.

The junction is fabricated on a fused quartz substrate with integrated RF blocking filters. The substrate is glued in the substrate channel with Crystal Bond in such a way that the junction is placed in the center of the waveguide, facing its narrow wall. Electrical contact with the end of the RF filters is made by wire bonding. A simple IF matching circuit is implemented in the mixer block. The reflection of the RF blocking filters is adapted to reach low waveguide impedances also

with one backshort. We use an integrated diagonal horn machined directly in line with the waveguide as described in Ref. [1].

2 Measurements

The DC IV-curve of the junction used in the measurements is shown in Fig. 3. The junction is fabricated at Cologne University, it has an area of $0.95\mu\text{m}^2$ and a notably high current density of 15 kA/cm^2 . The leakage current is about $20\ \mu\text{A}$. For mixer measurements a solid state local oscillator (Gunn + multiplier, 800-820 GHz) [9] is coupled to the mixer using a Martin-Puplett diplexer. The pumped curve is also shown in Fig. 3. It is taken at the maximum output power of the oscillator, which is $30\ \mu\text{W}$ at 810 GHz according to the manufacturer. The junction used in the experiment had a simple parallel tuning structure, consisting of a short stub $4\mu\text{m}$ wide and $5\mu\text{m}$ long, followed by an open ended line of $18\ \mu\text{m}$ wide and $20\ \mu\text{m}$ long. This structure had a resonance in the DC IV curve at a bias voltage corresponding to approximately 780 GHz.

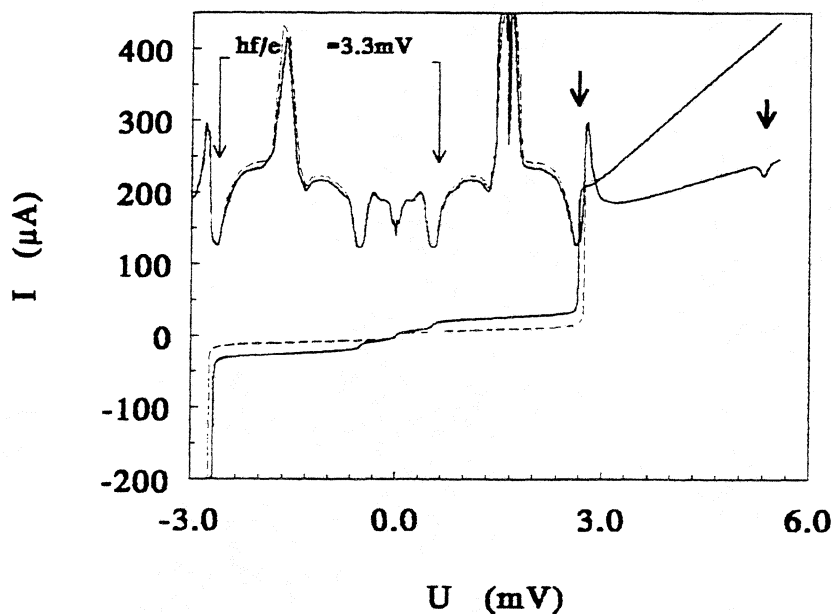


Fig. 3 DC IV-curve of the junction without and with 810 GHz radiation (quasi-particle pump step width is 3.3 mV). Notice the smaller step width above the gap voltage. The corresponding IF-output power at a 300K and a 77K input is given on the same voltage axis.

The mixer response to a hot and cold load is also shown in Fig. 3. The Josephson effect is suppressed as good as possible by a magnetic field. The receiver noise temperature calculated from this measurement is 4000 K DSB. Other junctions, also with parallel tuning structures using a radial stub, or slightly different line length and width have also been tested. The best noise temperatures all were between 3800K and 4200 K DSB at 810 GHz. At

the other frequencies (800GHz to 820 GHz) the output power of the oscillator is lower. As can be seen in Fig. 3, the pump level at 810 GHz is already rather low for optimum mixer performance, so at the other frequencies the performance is probably worse due to LO-starvation. Junctions with series resonant tuning structures were unfortunately not available for measuring.

In all measurements there was a rather sharp dependence of the maximum input coupling on the backshort position. The slope of the pump step was not changed by the backshort setting. We

have however observed different pump step slopes for different tuning structures, indicating that the integrated tuning structures have some effect.

To get an impression of the quality of the tunnel barrier, the IF output power of a junction was measured as a function of bias voltage at 1.4 GHz in a 100 MHz bandwidth. The result is given Fig. 4, together with the IF output calculated from the measured unpumped DC IV-curve. For the IF-amplifier a noise temperature of 10 K is determined. Apparently the junction does not show additional shotnoise below the gap voltage. At half the gap voltage a clear structure is observed, which is not affected by a magnetic field.

In a measurement to determine the cross polarization of the diagonal horn we found to our surprise that the mixer receives both polarizations equally well. For a standard diagonal horn a cross polarization detection level of 10-15 % is expected [10]. Scale model measurements at 100

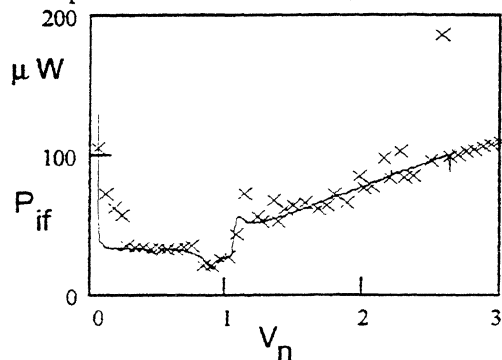


Fig. 4 Measured (solid line) and calculated (crosses) IF output power of the unpumped SIS junction as a function of normalized bias voltage.

GHz subsequently showed that a small misalignment, especially at the apex of the horn, destroys the symmetry of the horn in such a way that high cross polarization levels are easily achieved.

The misalignment in the scale model corresponds to 10 to 20 μm in the 800 GHz mixerblock, which was indeed observed. But even with a better alignment, tested in the 500 GHz mixerblock, we still observed a crosspolarization detection of 25-30% of the copolarization.

3 Discussion

The calculated noise temperature for the junction shown in Fig. 3 is approximately 1500 K.

This temperature is calculated using an estimation for the actual losses in the superconducting microstrip lines obtained from DC measurements. The resonance frequency of 40 different parallel resonant tuning circuits was determined from the bias voltage at which the current rise due to the AC-Josephson effect was observed in the DC IV curve at 4.2 K. Under the assumption that the current density is uniform over the whole wafer, the area of the junctions was calculated from the measured normal state resistance. For a specific junction capacitance of $75 \text{ fF}/\mu\text{m}^2$ the average loss in the stripline lies between 2 and 2.5 times the value calculated from MB, taking the material parameters mentioned in paragraph 1.

With this loss the embedding impedance of the junction is calculated from the geometry of the tuning structure, adapting the actual length of the tuning stub to the resonance frequency measured in the DC-IV curve. (the typical adaption of the length is smaller than $1 \mu\text{m}$, which is within the alignment accuracy)

Because the coupling of the LO and the signal are made with a polarizing diplexer, the high cross polarization level of the horn has an effect on the receiver noise temperature. If a loss of 40% is included in the signal path, the calculated noise temperature increases to 2000 K. Other influences, like the somewhat low pump level or the slight heating of the pumped curve, have only a small effect on the noise temperature.

We are still investigating various effects that might explain the measured noise temperature of 4000K. For example possible losses in the niobium RF-filters could influence the waveguide impedance. Equating the output power of the LO-source with the pump step height shows that only approximately 5 % of the available LO-power is coupled to the junction. We have not fitted an embedding impedance from the measured pumped IV-curve, but the flat slope of the pumped step indicates that the junction capacitance is at least partly tuned out. On the other hand the heating of the pumped IV-curve, as can be clearly seen from the reduction of the gap voltage, might be a sign of bad matching. Badly matched junctions at frequencies below the gap frequencies show a similar gap reduction

Even if we would have measured the theoretically predicted noise temperature however, the result is still only comparable with the best Schottky receivers at this frequency. A definite improvement can only be achieved if the loss in the tuning is reduced. It might be necessary to build a waveguide mixer with two tuners [5]. Aluminum electrodes might be better than niobium at frequencies above 800 GHz [6], and have the advantage that they require no drastic changes in the fabrication process. The propagation velocity along normal metal lines is different, which leads to a little bit longer structures. Really low loss tuning structures at these high frequencies can probably only be made of niobium nitride (NbN). In that respect the mixer results at 350 GHz [11], measured at IRAM, are very promising. A disadvantage of NbN is that the length of the tuning structures is even shorter than that of the Nb stubs. This makes the alignment during fabrication very critical.

An alternative might be the use of a superconducting hot electron bolometer mixer, which is not limited by the gap frequency of the superconductor. It has a negligible capacitance, so no resonant tuning circuits are required. The noise temperature of this device is expected to be independent of frequency. Skalare et al.[12] reported a noise temperature of 650K DSB at 533 GHz at an IF frequency of 1.5 GHz.

We are currently working towards fabricating smaller junctions and superconducting hot electron bolometers to replace the present junctions. A new mixerblock is fabricated, which will have a corrugated horn or a Potter horn. Via a collaboration with IRAM [11] that has been set up two years ago for the development of NbN fabrication technology, we hope to get low loss tuning structures.

Acknowledgements

We would like to thank Stephan Wulff for technical assistance and Dirk Diehl and Jürgen Stutzki for valuable discussions. This work is supported by the Bundesministerium für Forschung und Technologie, Verbundforschung Astronomie, grant 05-KU134(6) and the Deutsche Forschungsgemeinschaft, grant SFB301.

References

- [1] K. Jacobs, U. Müller, U. Schwenk, D. Diehl, C.E. Honingh, and S. Haas, "SIS receivers with large instantaneous bandwidth for radio astronomy", Proc. Fifth Int. Symp. on Space Terahertz Tech., pp. 60-72, 1994

- [2] R. Blundell, C.-Y. E. Tong, J.W. Barrett, R.L. Leombruno, S. Paine, D.C. Papa, X. Zhang, J.A. Stern, H.G. LeDuc, and B. Bumble, "A 400-500 GHz receiver", Proc. European SIS user meeting, 1994
- [3] P. Febvre, W.R. McGrath, P. Batelaan, B. Bumble, H.G. LeDuc, S. George, P. Feautrier, "A low noise SIS receiver measured from 480 GHz to 650 GHz using Nb junctions with integrated RF tuning circuits", Int. J. IR & MM Waves, **15**, pp. 943-965, 1994
- [4] J. Zmuidzinas, N.G. Ugras, D. Miller, M. Gaidis, H.G. LeDuc, and J.A. Stern, "Low noise slot antenna SIS mixers", to appear in IEEE Trans. on Appl. Supercond., 1995
- [5] J.W. Kooi, C.K. Walker, H.G. LeDuc, P.L. Schaffer, and T.G. Phillips, "A low noise 565-735 GHz waveguide receiver", Proc. Fifth Int. Symp. on Space Terahertz Tech., pp. 126-141, 1994
- [5] G. de Lange, C.E. Honingh, J.J. Kuipers, H.H.A. Schaeffer, R.A. Panhuyzen, T.M. Klapwijk, H. van de Stadt, and M.W.M. de Graauw, "Heterodyne mixing with Nb tunnel junctions above the gap frequency", Appl. Phys. Lett., **64**, pp. 3039-3041, 1994
- [6] D.C. Mattis, and J. Bardeen, "Theory of the anomalous skin effect in normal and superconducting metals", Phys. Rev., **111**, pp. 412-417, 1958
- [7] R. Pöpel, "Surface impedance and reflectivity of superconductors", J. Appl. Phys., **66**, pp. 5950-5959, 1989
- [8] J.R. Tucker, and M.J. Feldman, "Quantum Detection at MM Wavelengths", Rev. Mod. Phys., **57**, pp. 1055-1113, 1985
- [9] Radiometer Physics, Meckenheim, Germany
- [10] J.F. Johansson, and N.D. Whyborn, "The diagonal horn as a sub-millimeter wave antenna", IEEE Trans. Microwave, Theory and Tech., **40**, pp. 795-800, 1992
- [11] A. Karpov, B. Plathner, K.H. Gundlach, M. Aoyagi, and S. Takada, "Noise properties of a mixer with SIS NbN quasiparticle tunnel junctions", to appear in these proceedings.
- [12] A. Skalare, W.R. McGrath, B. Bumble, H.G. LeDuc, P.J. Burke, A.A. Verheijen, and D.E. Prober, "A heterodyne receiver at 533 GHz using a diffusion cooled superconducting hot electron bolometer mixer", to appear in IEEE Trans. on Appl. Supercond., 1995

**The Development of an 850 GHz Waveguide Receiver using Tuned
SIS Junctions on $1\mu\text{m}$ Si_3N_4 Membranes.**

*J. W. Kooi¹, M.S Chan¹, M. Bin¹, Bruce Bumble²,
H. G. LeDuc², C. K. Walker³ and T.G. Phillips¹*

1- Caltech Submillimeter Observatory

Division of Physics, Mathematics and Astronomy

California Institute of Technology, Pasadena, California 91125

2- Center for Space Microelectronics Technology, Jet Propulsion Laboratory

3- University of Arizona, Tuscon, Arizona

ABSTRACT

We report preliminary development work on a 850 GHz SIS heterodyne receiver employing a tuned niobium tunnel junction on a $1\mu\text{m}$ Si_3N_4 supporting membrane. Since the mixer is meant to be operated well above the superconducting gap frequency of niobium ($2\Delta/h \approx 690$ GHz) special care has been taken to minimize transmission line loss. We have therefore used junctions with an integrated radial stub RF matching network to tune out the large shunt susceptance of the junction and minimize the niobium film absorption loss. Scale model measurements of the waveguide embedding impedance have been made to aid in the design of the choke structure and RF matching network. Detailed Fourier Transform Spectrometer measurements of tuned junctions on both SiO_2 and silicon nitride membranes show response up to 1100 GHz and indicate that the absorption loss in the niobium film is in the order of 4-7 dB at 850 GHz, in fairly good agreement with the theoretical loss calculated from the Mattis-Bardeen theory. The junctions have a center frequency of 800 GHz which presents a 6% downshift from the designed value.

THEORETICAL AND EXPERIMENTAL STUDIES OF Nb-BASED TUNING CIRCUITS FOR THz SIS MIXERS.

V.Yu. Belitsky[†], S.W. Jacobsson[‡], L.V. Filippenko[†], E.L. Kollberg[‡].

[†] Institute of Radio Engineering and Electronics RAS, 103907, Mokhovaja St. 11,
Moscow, Russia.

[‡] Department of Microwave Technology, Chalmers University of Technology,
S-412 96, Göteborg, Sweden.

Abstract

Three Nb-AlO_x-Nb SIS mixers tuned to operate in the 400-550, 550-700 and 600-750 GHz frequency bands have been investigated by modeling and experimentally by employing Fourier Transform Spectrometer (FTS) technique and mixer measurements. The mixers were of quasi-optical type with spiral antennas and twin junction tuning circuits integrated onto the apex area of the antenna arms. Modeling was employed for optimizing the tuning circuits and evaluating its performance. The comprehensive model for the SIS mixer bases on Tucker-Feldman theory of quasiparticle SIS mixer and Mattis-Bardeen theory of anomalous skin-effect. Very good agreement between modeling, FTS measurements and mixer experiment results was achieved. Accuracy in prediction of the tuning band and the coupling efficiency for the tuning circuits is better or about 15% within 400-1000 GHz band.

Introduction

The SIS mixer optimum performance can be reached when the intrinsic capacitance of the SIS junction is tuned out. Different integrated on chip tuning circuits have been developed for waveguide and open structure (quasi-optical) Nb-AlO_x-Nb SIS mixers for 100—820 GHz band [1-6] providing broadband low-noise operation of the receivers [7-11]. These tuning circuits mainly utilize different microstrip lines, made from Nb with SiO or SiO₂ insulator, to resonate out SIS junction capacitance.

The focus of this work is theoretical (by modeling) and experimental investigation of twin junction tuning circuit [4-6] for frequency band about 400-1000 GHz. Mattis-Bardeen theory was employed for the tuning circuit modeling. Fourier Transformer Spectrometer technique as well as mixer measurements of developed SIS mixers were used to determine tuning circuits performance, to compare experimental data and results of modeling.

At the first step of the tuning circuit development simplified free-of-loss model has been employed for evaluating of the tuning circuit behavior and its optimization [11,19]. The coupling efficiency of the spiral antenna output and the tuning circuit input was used as a quality parameter for loss-free circuitry (Fig. 1). However Fourier Transform Spectrometer (FTS) measurements of the tuning circuits [19] have shown noticeable discrepancy between tuning circuit coupling efficiency at above the gap frequency and model predicted performance. This associated with loss in Nb microstrip tuning circuitry.

Near the gap frequency of Nb material (~690 GHz for film) the Nb based microstrip lines become dispersing [12, 13] and above this frequency having increasing losses [14, 15]. Mattis-Bardeen theory [16] of skin anomalous effect describes behavior of a superconductor at these frequencies in terms of complex conductivity σ :

$$\sigma = \sigma_1 - j \cdot \sigma_2, \quad (1)$$

where real σ_1 and imaginary σ_2 components translate directly into the normal-electron and Cooper currents in a superconductor. Following fundamental paper of R.L. Kautz [14] these components above can be presented in integral form:

$$\frac{\sigma_1}{\sigma_n} = \frac{2}{h\omega} \int_{\Delta}^{\infty} d\varepsilon [f(\varepsilon) - f(\varepsilon + h\omega)] \frac{\varepsilon^2 + \Delta^2 + h\omega\varepsilon}{(\varepsilon^2 - \Delta^2)^{1/2} [(\varepsilon + h\omega)^2 - \Delta^2]^{1/2}} +$$

$$+ \frac{1}{h\omega} \int_{\Delta}^{h\omega - \Delta} d\varepsilon [1 - 2f(h\omega - \varepsilon)] \frac{h\omega\varepsilon - \Delta^2 - \varepsilon^2}{(\varepsilon^2 - \Delta^2)^{1/2} [(h\omega - \varepsilon)^2 - \Delta^2]^{1/2}}, \quad (2)$$

and

$$\frac{\sigma_2}{\sigma_n} = \frac{1}{h\omega} \int_{\Delta(T) - h\omega, -\Delta}^{\Delta(T)} d\varepsilon [1 - 2f(\varepsilon + h\omega)] \frac{\varepsilon^2 + \Delta^2 + h\omega\varepsilon}{(\varepsilon^2 - \Delta^2)^{1/2} [(\varepsilon + h\omega)^2 - \Delta^2]^{1/2}}, \quad (3)$$

where T is the temperature [K], σ_n is the conductivity of a superconductor just above the critical temperature T_c , $\Delta = \Delta(T)$ is the energy gap parameter [eV], $f(\varepsilon) = 1/(1 + \exp(\varepsilon/kT))$ is Fermi function, ω is the angular frequency. The first integral of σ_1 represents conduction of thermally excited normal electrons, while the second integral of σ_1 introduces generation of quasiparticles by incoming radiation. The lower limit on the integral for σ_2 becomes $-\Delta$ when the frequency exceeds the gap frequency.

In [14] the relation between material parameters of a superconductor defines as below:

$$\lambda_o = \sqrt{\frac{h}{\pi\mu_o\sigma_n\Delta}} \quad (4)$$

where μ_o is the permeability of vacuum, h is the reduced Plank's constant and λ_o is the London penetration depth.

The specific surface impedance Z_s per unit of length of the superconducting film with thickness d is expressed as follow:

$$Z_s(\omega) = (j\omega\mu_o/\sigma)^{1/2} \coth[(j\omega\mu_o/\sigma)^{1/2}d], \quad (5)$$

Microstrip line parameters, *e.g.* propagation constant γ and the characteristic impedance Z_o with series impedance Z and admittance Y of a unit of line are:

$$\gamma = \sqrt{ZY}, \quad (6)$$

$$Z_o = \sqrt{\frac{Z}{Y}}. \quad (7)$$

Hence for particular superconducting microstrip-line with specific geometrical inductance L and capacitance C per unit length of line, Z should include Z_s (Fig. 2) that introduces additional frequency dependent inductance and surface loss. At frequencies about 600 GHz the SIS junction of μm size has to be considered as a distributed element; we assumed microstrip line model with superconducting electrodes for such junction, where the tunnel barrier is considered as insulator. Along with mentioned Z_s we add a conductance representing quasiparticle loss $G = 1/R_{\text{rf}}$, (Fig. 2), where R_{rf} is input quantum impedance for signal frequency ω for unit of SIS junction line at some bias voltage U and LO power (normalized parameter $\alpha = eV_{\text{rf}}/h\omega$ with LO signal amplitude across the junction V_{rf}).

Quasi-optical SIS mixer. Tuning circuit

Three SIS mixers tuned for operation in the 400-550, 550-750 and 650-800 GHz bands have been investigated. The mixers utilize equiangular spiral antennas that were designed for operation between 230-850 GHz (inner radius of the antenna 13 μm , and outer radius 480 μm) for the 500 GHz mixer and between 350-1000 GHz (7 μm , and 315 μm , respectively) for the 600 and 700 GHz mixers. The antenna has real and frequency independent impedance 114 Ω when it is mounted onto the flat side of an extended hyperhemispherical crystal quartz lens [17]. The SIS junctions and the tuning circuit were placed at the apex of the antenna Fig. 3.

The tuning circuit [4] connects two identical (twin) SIS junctions through a microstrip transmission line, so that the reactance of the first junction is transformed to cancel the reactance of the second junction, *i.e.* the transmission line conjugates the impedance of the first junction. Then, the resulting impedance is transformed by another transmission line to match the impedance of the antenna (Fig. 4). Both junctions assumed to have identical junction areas, A , normal state resistance, R_n , as well as the same DC bias, signal and LO levels. The length of the impedance conjugator section can be chosen to compensate the reactance at one specific frequency. However, the dimensions of the two transmission lines can be adjusted to give an increased bandwidth at the expense of a ripple in the pass band (Fig. 1). The particular shape of the coupling band is a compromise between bandwidth and ripples in the pass band. The mixers for 600 and 700 GHz are scaled versions of the 500 GHz one, *i.e.* different $R_n A$ products ($20 \Omega \mu\text{m}^2$ ($J_c=10 \text{ kA/cm}^2$) and $25 \Omega \mu\text{m}^2$ ($J_c=8 \text{ kA/cm}^2$) respectively) and circuit dimensions. The realization of the detector tuning circuitry is limited by the available Nb technology. For instance, we have to use SIS junctions with $R_n A \geq 20 \Omega \mu\text{m}^2$ to keep the quality parameter $R_i/R_n \geq 10$, where R_i is the sub gap resistance, and the gap voltage $V_g = 2.5 - 2.75 \text{ mV}$. Furthermore, the SiO insulation has to be thicker than $\approx 140 \text{ nm}$ to prevent shorts between the microstrip and its ground plane. Due to technology limitations coupling efficiencies less than 100% for the 600 and 700 GHz mixers are the results of compromises between broadband operation and good coupling efficiencies (Fig. 1). The circuit design in more details discussed in [11,19]. Table 1 lists SIS junction parameter values as well as Table 2 lists the dimensions of the optimized tuning circuits assuming loss-free tuning circuitry.

For the twin junction tuning circuitry with loss RF power distributed from output of the antenna has to be carefully estimated for both outermost and furthestmost SIS junctions; total power from the two junctions related to optimum matched power for given source impedance to evaluate quality parameter for the circuitry with loss.

Modeling of the mixer performance

Model for the Nb film

At the gap frequency Nb superconductor surface impedance dramatically changes. The gap frequency is $\omega_g = \Delta/\hbar$ and the gap energy Δ according to BCS theory depends on the temperature. The gap energy at zero temperature $\Delta(0)$ is directly related to the critical temperature of superconductor [15]. In our model we used measured the gap voltage (energy). Empirically it was found to correspond to the voltage of 10% quasiparticle current onset (Fig. 5) at given temperature (4.2 K) for the best model fitting. Expression (5) then was used to evaluate the conductivity σ_n and BCS dependence of Δ was employed to estimate $\Delta(0)$. Table 3 lists material parameters used in our modeling to describe the Nb film quality. Calculated real and imaginary components σ_1, σ_2 for the Nb films (presented in Table 3) and plotted vs. frequency $f = \omega/2\pi$ in Fig. 6.

Model for SIS junction

In the modeling of the SIS junction we used a piece-wise linear approximation of the SIS junction's current-voltage curve (IVC) (Fig. 5). The RF impedance of the SIS junctions was calculated for given α (LO power level) and U_{bias} (usually at the middle of the first quasiparticle step) according to Tucker-Feldman theory for quantum mixing in SIS tunnel junctions. Since the SIS junction quantum susceptance is small compared with the intrinsic junction capacitance the former was neglected in the modeling. The SIS junction capacitance was calculated according to [18] for measured R_n and estimated junction area, A , taking into account junction window over-etching.

At frequencies about 600 GHz we consider SIS junctions of μm size as distributed elements, assuming microstrip line model with superconducting electrodes for such junction, where tunnel barrier is considered as insulator. The SIS junction impedance components of $2 \mu\text{m}$ width and $1.5 \mu\text{m}$ length are presented in Figure 7 (for the junction as a lumped and distributed element). In the 600 and 700 GHz mixers SIS junction size along the microstrip was set to $1 \mu\text{m}$ to eliminate effect of distributing.

Model for Nb microstrip line

Parasitic reactance in the tuning circuit caused by steps in the strip widths and SiO insulator thicknesses have been neglected. Fig. 8 presents calculated transmission loss vs. frequency for transformer section lines of the tuning circuits for 500, 600 and 700 GHz mixers those have quarter-wave-length at the center frequencies of the tuning bands. At the transformer sections of the tuning circuit the condition $t \ll W$, where t is SiO insulator thickness and W is strip width, is not valid (see Table 2). Therefore the fringing field should be taken into account correcting the microstrip impedance with about 10-15%. Fig. 9 displays a family of transmission loss curves at different ambient temperatures for the transformer section of the 600 GHz mixer. Three regions with different performance of the line could be distinguished: *i.* below $\approx (0.8-0.9)\omega_g$ the line is loss free; *ii.* in the band $\approx (0.8...0.9-1.4)\omega_g$ the line has increasing losses with a strong temperature dependence of the loss; *iii.* above $1.4\omega_g$ the Nb superconducting line has high transmission loss.

Model for superconducting spiral antenna

In a real mixer it is difficult to separate loss contribution from the antenna between RF optic loss, the mixer loss, *etc.* In our modeling we have tried to estimate this component of loss presenting the antenna as an equivalent microstrip line.

Spiral equiangular antenna is a traveling wave antenna, *i.e.* the antenna can be represented as a segment of transmission line with propagating electromagnetic wave along it. Spiral antenna has a continuously changing arm width. We re-presented the antenna as a microstrip line with characteristic impedance corresponding to that of the antenna onto crystal quartz hemispace (114Ω). The strip width at distance L_1 is equal to the actual dimension of the antenna arm at the same distance L_1 along the arm from the apex of the antenna. Keeping the impedance of this equivalent line to be 114Ω leads to increase of the insulator thickness for peripheral parts of the equivalent line as the antenna arm width increase. Wide-band log-spiral antenna at every frequency has active area about $\lambda\pi$ in diameter [20], where λ is current wavelength. However for modeling we set this dimension (related with length of the equivalent line) to be 0.4λ . It gives us about 25% overestimation of loss. Furthermore we also neglected that in the real antenna RF current rapidly decreases along the antenna arms so that loss contribution from outer parts of the spiral antenna is less than from inner. Fig. 10 shows the calculated loss vs. frequency for the equivalent line of the spiral antenna for 600/700 GHz mixers.

For optimized model, *i.e.* the model that provides the best fitting to measured data, no *additional* changes have been done for any samples, batches, *etc.* The input measured parameters for the model are: *i.* for Nb film — T_c or/and V_g at 4.2 K, λ_0 ; *ii.* for SIS junctions — R_n , V_g , A , junction dimensions; *iii.* for the tuning circuit — strip dimensions and layer thicknesses.

Measuring technique and results

The three mixers, *e.g.* tuned for 500, 600 and 700 GHz, have been measured using Fourier Transformer Spectrometer technique, operating as direct detectors to evaluate tuning bands and coupling efficiency (relative). In our experiments the mixers were measured in identical as possible conditions with FTS operated in frequency range 400 — 1500 GHz and with resolution about 4 GHz. No any response above ≈ 940 GHz were observed. The 500 GHz detector was also operated as a mixer. The 500 GHz mixer measurements have shown that cooling the mixer below 4.2 K temperature may be very advantageous for decreasing the receiver noise temperature [7]. To investigate temperature behavior of the tuning circuits and coupling efficiency all mixers were FTS tested at 4.2 and about 3.1 K temperatures. Measuring set-ups, technique in details described in [7,11,19].

Figures 11, 12 and 13 present results of FTS measurements of 500, 600 and 700 GHz mixers correspondingly at temperatures 4.2 and 3.1 K. At these figures the results of modeling for the mixers at the same temperatures are plotted as well; all data normalized. Figure 14 shows compiled measurements for all mixers with original scale and the model predicted direct detector responses. At Figure 15 the 500 GHz receiver measured noise temperatures (DSB) are plotted

with FTS data and model predicted curve for coupling efficiency vs. frequency (two latter curves are inverted and normalized by the receiver noise temperature at 480 GHz).

Discussion and conclusion

Our FTS and mixer measurements and theoretical investigations by modeling of the quasi-optical SIS mixers comprising superconducting spiral antenna, SIS junctions and tuning circuitry show excellent agreement of tuning bands and coupling efficiency at frequencies below the gap and very good agreement above the gap frequency for Nb material. The model of the mixer describes temperature dependence of the direct detector response correct. Although for frequencies above the gap the measurements of direct detector response show more changes with temperature than the model predicts. We believe it can be explained by presence of "critical points" in superconducting circuitry, that are beyond the model consideration, and where high DC current and dissipating power (close to SIS junction) may lead to local increasing of ambient temperature and degrading of the superconductor film. Additional cooling dramatically improves performance at these critical points.

While optimizing of the model, presentation of SIS junction as lumped element has shown better fit to the experimental data than the distributed model. We suppose that it can be explained by the fact that SIS junction introduces very sharp discontinuity for the electromagnetic wave (in its dimensions, impedance, etc.), so that RF current penetrates perpendicularly to the SIS junction rather than along it. Furthermore our modeling of the SIS junction with distributed line shows extremely high losses appearing at this junction line above the gap frequency. This fact explains the absence of Josephson resonance in long junctions and tuning circuitry [12,13] above the gap.

Accurate estimation of RF loss in the spiral antenna requires detail knowledge of electromagnetic field distribution in this complicated strip-slot spiral structure and complete analysis has not been done so far. Our modeling of the superconducting spiral log-periodical planar antenna, based on the equivalent line presentation, shows that RF loss in such antenna produced from superconductor at above the gap frequency not exceed $\approx 14\%$ (with overestimation). This offer using pure superconducting Nb circuitry for THz SIS mixers without suggested in [21] replacing Nb film for normal metal and associated with it technological problems.

To the conclusion, the introduced modeling based on Mattis—Bardeen skin anomalous effect theory and Tucker-Feldman theory of quasiparticle mixing provides very good agreement of tuning bands and coupling efficiencies (within 15%) with mixer and FTS measurements of the twin junction tuning circuitry for the spiral antenna SIS mixers at 400 — 1000 GHz band. The model includes all important parts of the SIS open structure mixer, *i.e.* SIS junctions, microstrip tuning circuitry and spiral antenna. The experimental results and modeling show good prospects of the twin compensation circuit for frequencies up to 700 GHz.

Acknowledgments

C. Holmstedt is greatly acknowledged for very useful technical assistance. Photomasks for producing investigated mixers were made by S.L. Muratov ("Sapphire", Moscow).

This work has been supported by grants from the European Space Agency (ESA) under contracts 7898/88/NL/PB, Russian Program of Fundamental Research (contract 92-02-3484) and Russian State Scientific Program "Superconductivity" (contract No 91009), Royal Swedish Academy of Sciences, The Swedish Board for Space Activities and The Swedish National Board of Industrial and Technical Development. The Swedish Institute is acknowledged for the support of Dr. V.Yu. Belitsky during his visit at Chalmers University of Technology.

References

- [1] M. J. Wengler, "Submillimeter-Wave Detection with Superconducting Tunnel Diodes," *Proc. of the IEEE*, vol. 80, pp. 1810-1826, 1992.
- [2] R. Blundell, C.-Y. E. Tong, "Submillimeter Receivers for Radio Astronomy," *Proc. of the IEEE*, vol. 80, pp. 1702-1720, 1992.
- [3] A. R. Kerr, S.-K. Pan, and M. J. Feldman, "Integrated tuning elements for SIS mixers," *Int. J. IR and MM Waves*, vol. 9, pp. 203-212, 1988.

- [4] V. Yu. Belitsky and M. A. Tarasov, "SIS junction reactance complete compensation," *IEEE Trans. on Magnetics*, vol. MAG-27, Part. 2, pp. 2638-2641, 1991.
- [5] V. Yu. Belitsky, S.W. Jacobsson, L.V. Filippenko, S.A. Kovtonjuk, V.P. Koshelets and E.L. Kollberg, "0.5 THz SIS Receiver with Twin Junction Tuning Circuit," Proc. of the 4th Int. Symp. on Space Terahertz Technology, UCLA, Los Angeles, p.538, 1993.
- [6] J. Zmuidzinas, H. G. LeDuc, J. A. Stern, and S. R. Cypher, "Two-Junction Tuning Circuits for Submillimeter SIS Mixers," *IEEE Trans. on MTT*, vol. 42, pp. 698-706, 1994.
- [7] S. W. Jacobsson, V. Y. Belitsky, L. V. Filippenko, S. A. Kovtonjuk, V. P. Koshelets, and E. L. Kollberg, "Quasi-optical 0.5 THz receiver with twin junction tuning circuit," in proceedings of the 18th International conference on Infrared and Millimeter Waves, pp. 267-268, Colchester, UK, 1993.
- [8] P. Febvre, W.R. McGrath, P. Btelaan, B. Bumble, H.G. LeDuc, S. George and P. Feautier, "A Low-Noise SIS Receiver Measured from 480 GHz and 650 GHz Using Nb Junctions with Integrated RF Tuning Circuits", *Int. Journal of Infrared and Millimeter Waves*, vol.15, No.6, pp.943—966, June 1994.
- [9] G. de Lange, C. E. Honingh, J. J. Kuipers, H. H. A. Schaeffer, R. A. Panhuyzen, T. M. Klapwijk, H. van de Stadt, and M. M. W. M. de Graauw, "Heterodyne mixing with Nb tunnel junctions above the gap frequency," *Appl. Phys. Lett.*, vol. 64, pp. 3039-3041, 1994.
- [10] J. Zmuidzinas, N.G. Urgas, D. Miller, M. Gaidis, H. G. LeDuc, J.A. Stern, "Low-Noise Slot Antenna SIS Mixer", submitted to *IEEE Trans. on Applied Superconductivity*.
- [11] V. Yu. Belitsky, S.W. Jacobsson, L.V. Filippenko, E.L. Kollberg, "Broad band Twin junction tuning circuit for submillimeter SIS mixers," in preparation.
- [12] G. S. Lee and A. T. Barfknecht, "Geometrical and Material Dispersion in Josephson Transmission Lines," *IEEE Trans. on Appl. Superconductivity*, vol. 2, pp. 67-72, 1992.
- [13] H. H. S. Javadi, W. R. McGrath, B. Bumble, and H. G. LeDuc, "Onset of Dispersion in Nb Microstrip Transmission Lines," in proceedings of the III Int. Symp. on Space Terahertz Technology, pp. 362-381, Univ. Of Michigan, Ann Arbor, USA, 1992.
- [14] R. L. Kautz, "Picosecond pulses on superconducting striplines," *J. Appl. Phys*, vol. 49, pp. 308-314, 1978.
- [15] R. Pöpel, "Surface impedance and reflectivity of superconductors," *J. Appl. Phys*, vol. 66, pp. 5950-5957, 1989.
- [16] D.C. Mattis and J. Bardeen, *Phys. Rev.* 111, p.412, 1958
- [17] T. G. Büttgenbach, H. G. LeDuc, P. G. Maker, and T. G. Phillips, "A Fixed Tuned Broadband Matching Structure for Submillimeter SIS Receivers," *IEEE Trans. on Appl. Supercond*, vol. 2, pp. 165-175, 1992.
- [18] V. Y. Belitsky, S. W. Jacobsson, S. A. Kovtonjuk, E. L. Kollberg, and A. B. Ermakov, "100 GHz Mixer with Vertically Integrated (stacked) SIS Junction Array," *Int. J. of Infrared and Millimeter Waves*, vol. 14, pp. 949-957, 1993.
- [19] V. Y. Belitsky, S. W. Jacobsson, L. V. Filippenko and E. L. Kollberg, "Fourier transform spectrometer studies (300 - 1000 GHz) of Nb-based quasi-optical SIS detectors," *Accepted for publication in IEEE Trans. on Applied Superconductivity*, Dec. 1994
- [20] G.T. Markov, D.M. Sazonov: *Antennas*, Power Publisher (in Russian), Moscow 1975.
- [21] G. de Lange, Ph.D. thesis: *Quantum limited heterodyne detection of 400-840 GHz radiation with superconducting Nb tunnel junctions*: Department of Physics, Rijksuniversiteit Groningen, The Netherlands, 1994.

Tables

Table 1

Parameter:	500 GHz mixer	600 / 700 GHz mixers
Normal state resistance R_N (two junctions in parallel) [Ω]	6	5
Junction area [μm^2]	4	2
Leakage resistance R_N (two junctions in parallel) [Ω]	60	50
Gap voltage [mV]	2.5 – 2.7	2.7 – 2.8
Gap width [mV]	10% of V_g	10% of V_g
Critical current density [kA/cm ²] / junction capacitance [pF]	8 / 0.38	10 / 0.2

Table 2

Dimensions [μm]	500 GHz mixer		600 / 700 GHz mixers	
	Conjugator	Transformer	Conjugator	Transformer
Length	12	56	6 / 4.5	41 / 37
Width	8	3	3	2.5
Top electrode thickness	0.35	0.35	0.4	0.4
SiO insulator thickness	0.15	0.3	0.33	0.33
Ground electrode thickness	0.2	0.2	0.2	0.2

Table 3

Nb material critical temperature T [K]	8.1	8.4	9.0
Normal state conductivity $\sigma_N \times 10^{-7}$ [$\Omega^{-1}\text{m}^{-1}$]	1.74	1.67	1.57
Gap voltage [mV] at temperatures T = 0 K/4.2 K	2.65/2.53	2.75/2.65	2.95/2.85
Penetration depth λ_0 [μm]	0.86	0.86	0.86

Figures

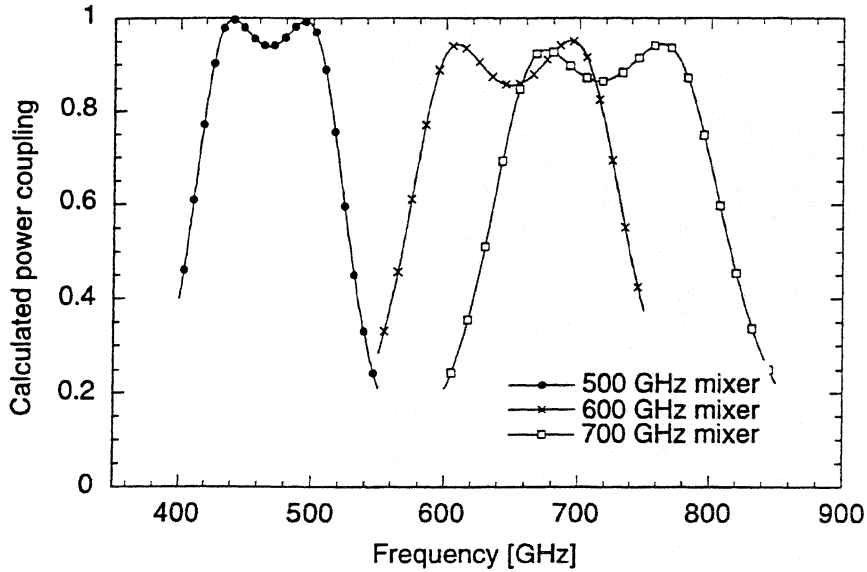


Figure 1 Modeled performance of the investigated mixers. Modeling was made assuming loss-free microstrip lines. The fabricated 600 and 700 GHz samples were measured to have their best coupling located at higher frequencies than those of the modeled circuits. The reason was found to be improper thickness of the SiO layer in the microstrip transmission line between the junctions.

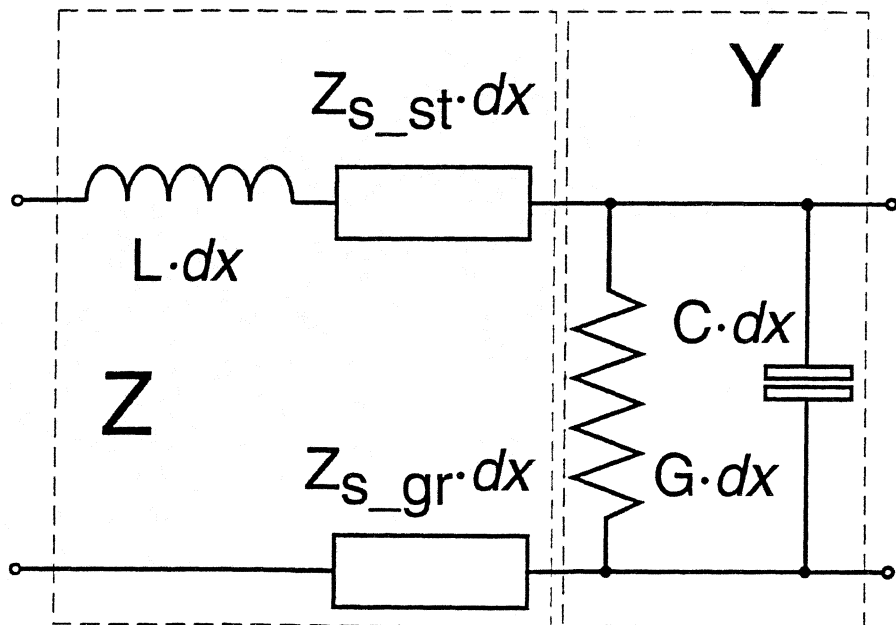


Figure 2 Circuit diagram for cell of superconducting microstrip line. L , C are specific geometrical inductance and capacitance per unit of length; Z_{s_st} , Z_{s_gr} are surface resistance of microstrip and ground electrodes correspondingly defined according to (5); $G=1/R_f$ is quasiparticle quantum non-linear conductance of a unit of SIS junction line.

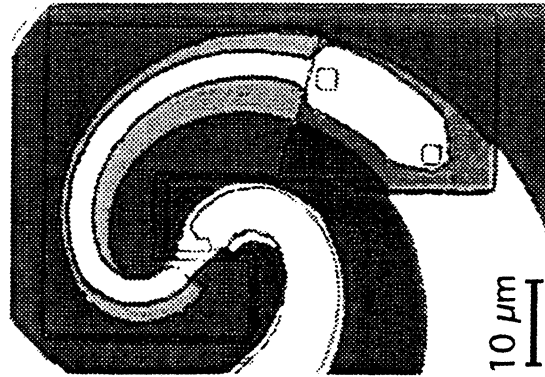


Figure 3 Photo of the 500 GHz mixer chip. SIS junctions and the tuning circuit located at the apex of the spiral antenna. The two squares in the upper right part of the figure are the $2\ \mu\text{m} \times 2\ \mu\text{m}$ area SIS junctions. The equivalent circuit diagram is shown in figure 4.

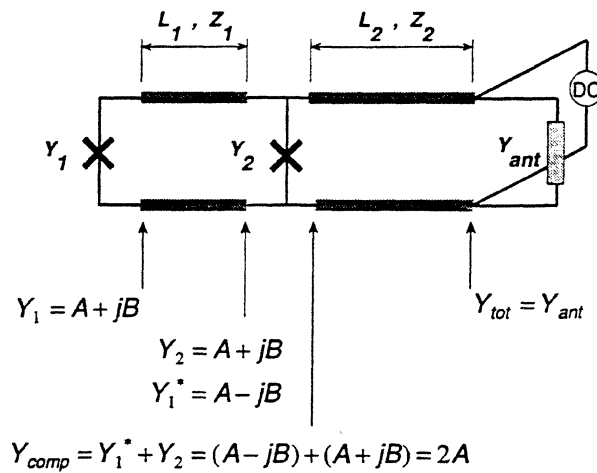


Figure 4 Principle of the twin junction tuning circuit. The SIS junctions (represented by the admittances Y_1 and Y_2) are connected via a short transmission line with impedance Z_1 . The length, L_1 , of this transmission line is such that the conjugate of Y_1 is obtained at the position of the second SIS junction. Then, the resulting real admittance is matched to the antenna admittance by a second transmission line, with impedance Z_2 and length L_2 . Both junctions are DC-biased in parallel.

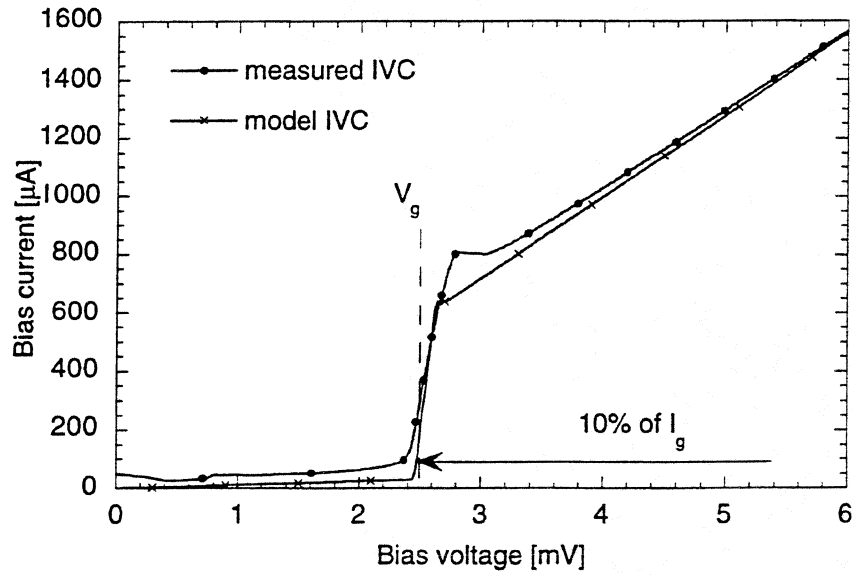


Figure 5 Model IV curve approximation of real measured IVC. Gap voltage defines as the bias voltage at 10% current onset for evaluation of Nb material parameters.

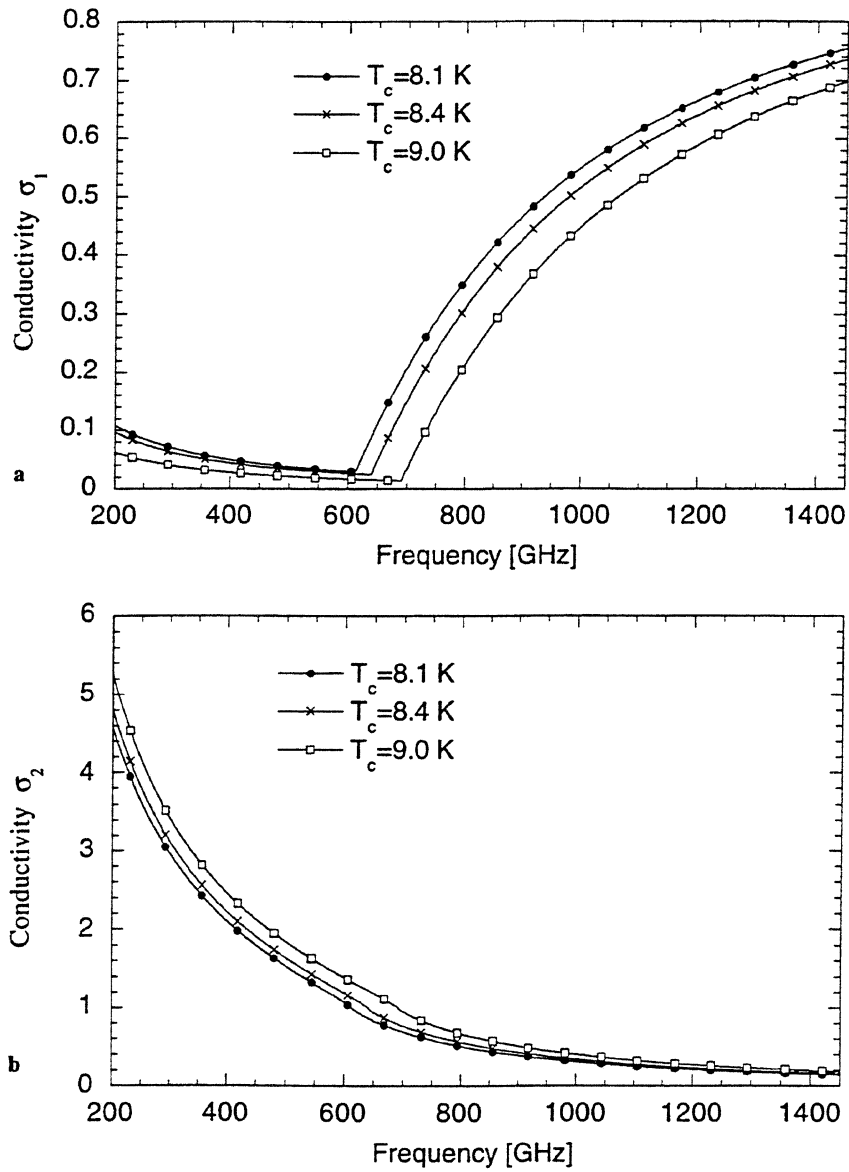


Figure 6 a,b Calculated real and imaginary components σ_1 , σ_2 for the Nb films presented in Table 3 vs. frequency .

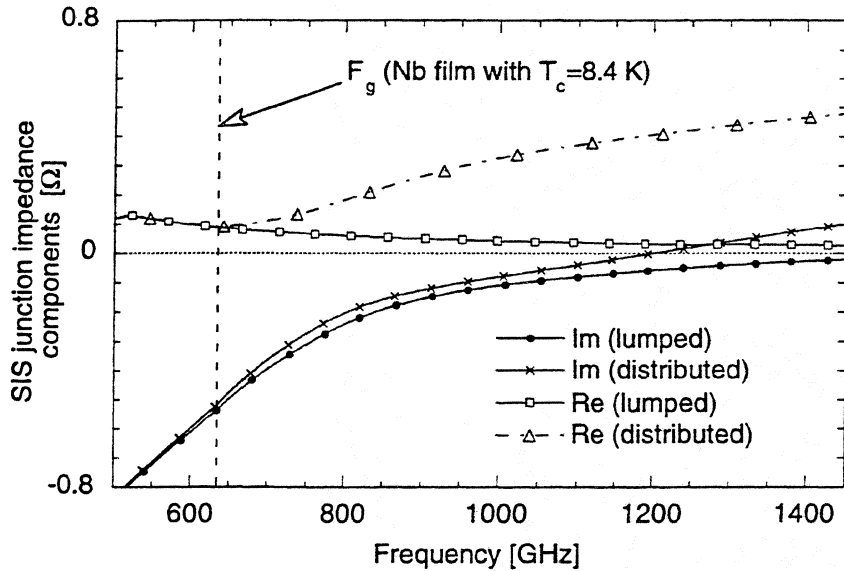


Figure 7 Modeling of SIS junction as distributed and lump circuit (R//C). Plotted results for SIS junction of 2 μm (width) and 1.5 μm (length), $R_n=6.7 \Omega$. Here Nb material was assumed to have $T_c=8.4 \text{ K}$ (see Table 3). U_{bias} was set at the middle of the first quasiparticle step with LO power level to be $\alpha=0.97$

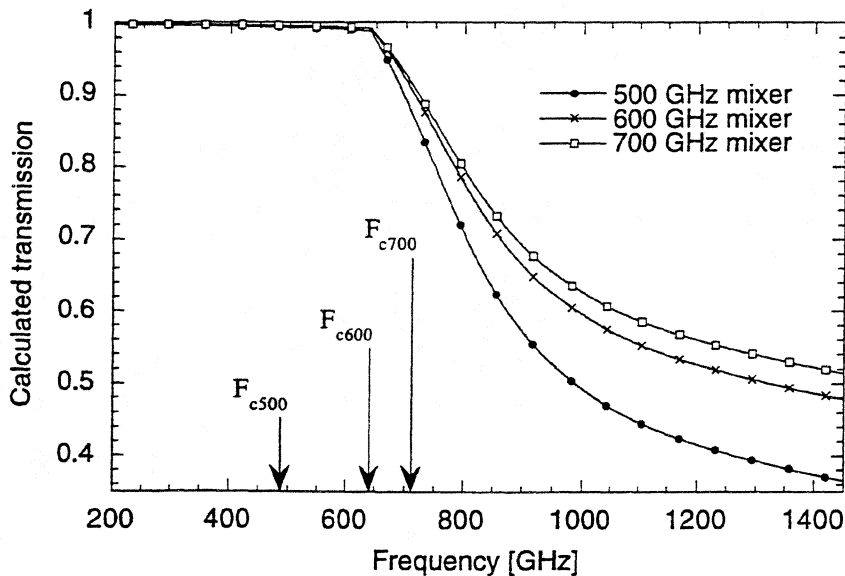


Figure 8 Calculated transmission of the transformer sections for the studied mixers; here Nb material was assumed to have $T_c=8.4 \text{ K}$ (see Table 3), ambient temperature set to 4.2 K. Arrows indicate center of the tuning bands, where the transformers have quarter—wave lengths.

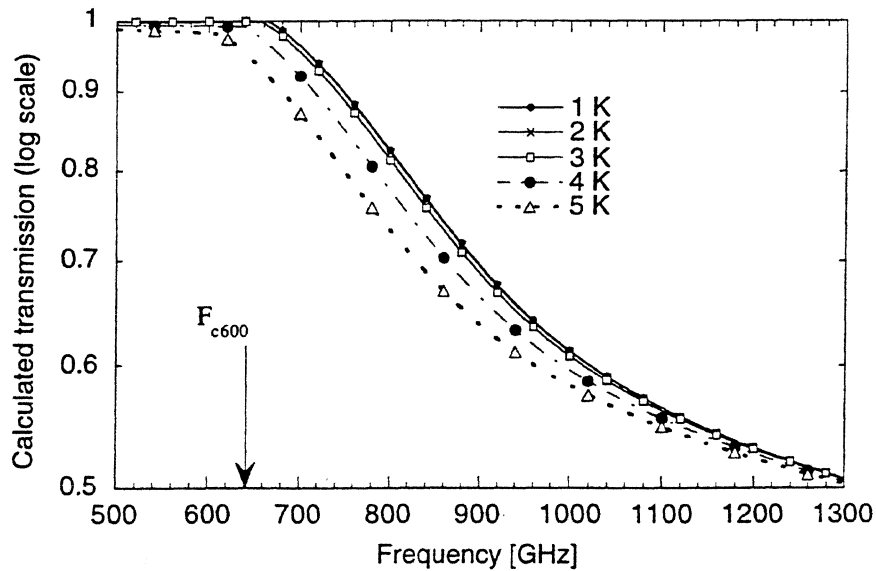


Figure 9 Calculated transmission of the transformer section for the 600 GHz mixer; Nb material was assumed to have $T_c=8.4$ K (see Table 3), plotted for ambient temperatures 1-5 K. The arrow indicates center of the tuning band, where the transformer has quarter—wave length.

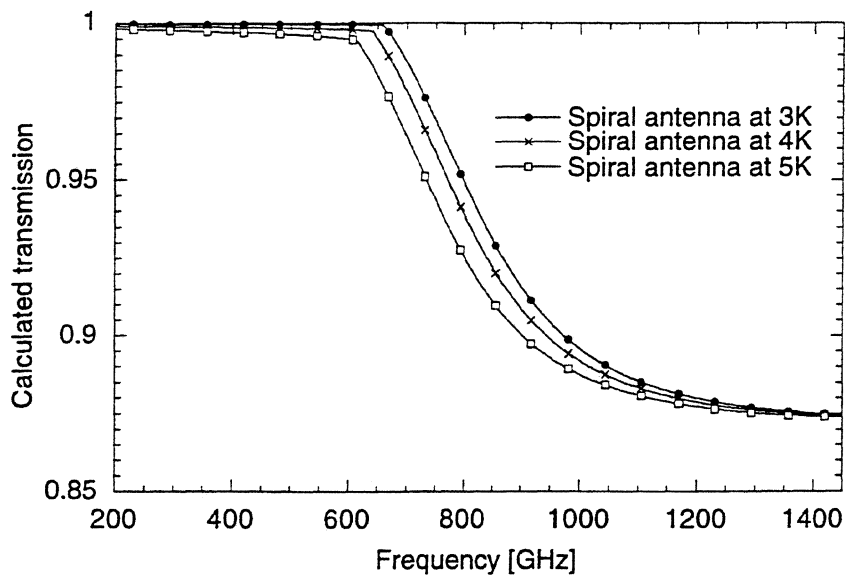


Figure 10 Transmission of the equivalent line for the spiral antenna of 600/700 GHz mixers (inner radii $7 \mu\text{m}$ and outer radii $315 \mu\text{m}$) at different ambient temperatures. The equivalent line current length in modeling corresponds to the active area of antenna 0.4λ in diameter.

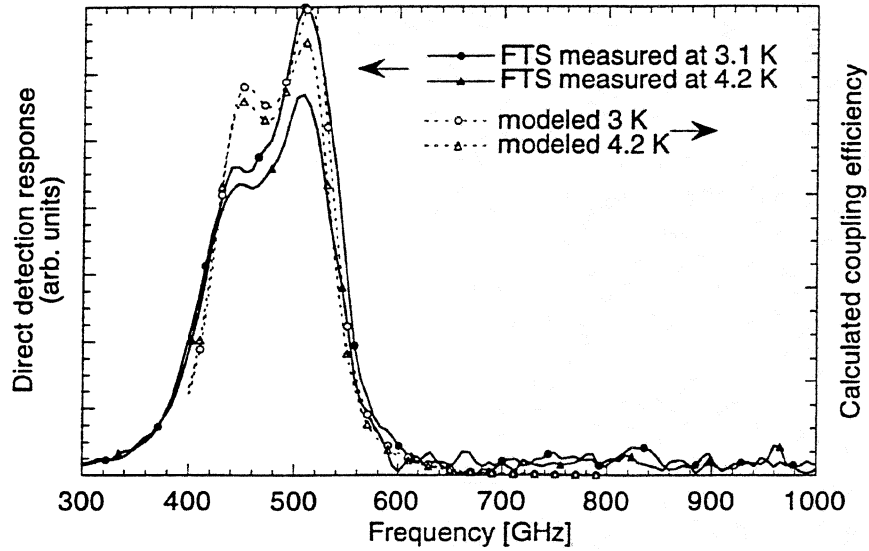


Figure 11 The 500 GHz mixer: FTS measured direct detector responses and modeled coupling efficiencies at different ambient temperatures, i.e. 3 K and 4.2 K. Modeling was done for the measured sample parameters R_n , V_g , $T_c=8.4$ K, etc.

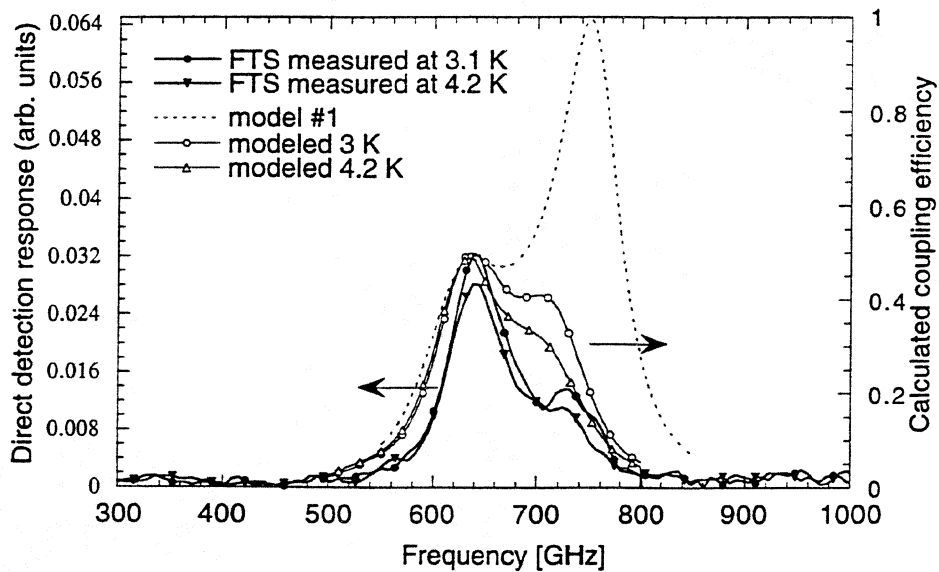


Figure 12 The 600 GHz mixer (real circuit measured to be tuned to higher frequency than presented in Figure 1 because of improper SiO insulator thickness in conjugator): FTS measured direct detector responses and modeled coupling efficiencies are presented. Model #1 is the result of modeling for loss-free tuning circuitry, other curves at different ambient temperatures, i.e. 3 K and 4.2 K are for model including loss. Modeling was done for the measured sample parameters R_n , V_g , $T_c=8.4$ K, etc.

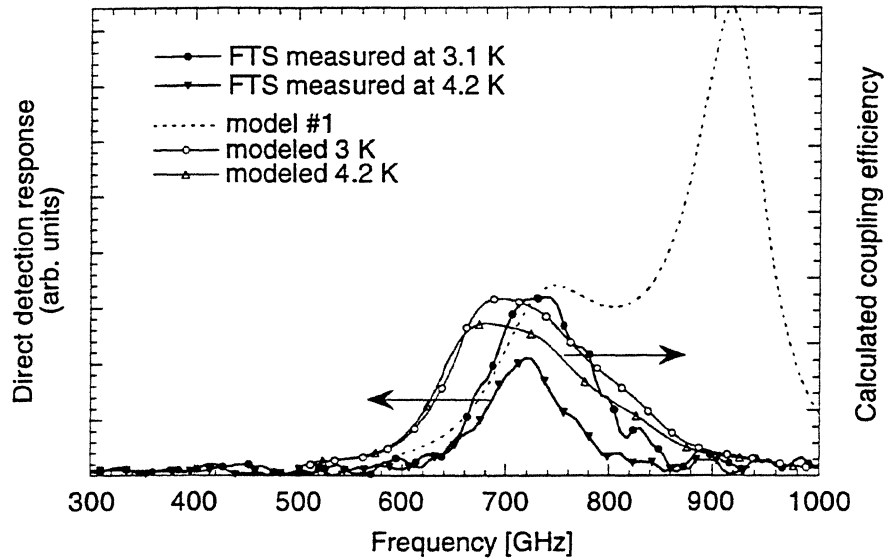


Figure 13 The 700 GHz mixer (real circuit measured to be tuned to higher frequency than that presented in Figure 1 because of improper SiO insulator thickness in conjugator): FTS measured direct detector responses and modeled coupling efficiencies are presented. Model #1 curve is the result of modeling for loss-free tuning circuitry, other curves at different ambient temperatures, i.e. 3 K and 4.2 K are for model including loss. Modeling was done for the measured sample parameters R_n , V_g , $T_c=8.4$ K, etc.

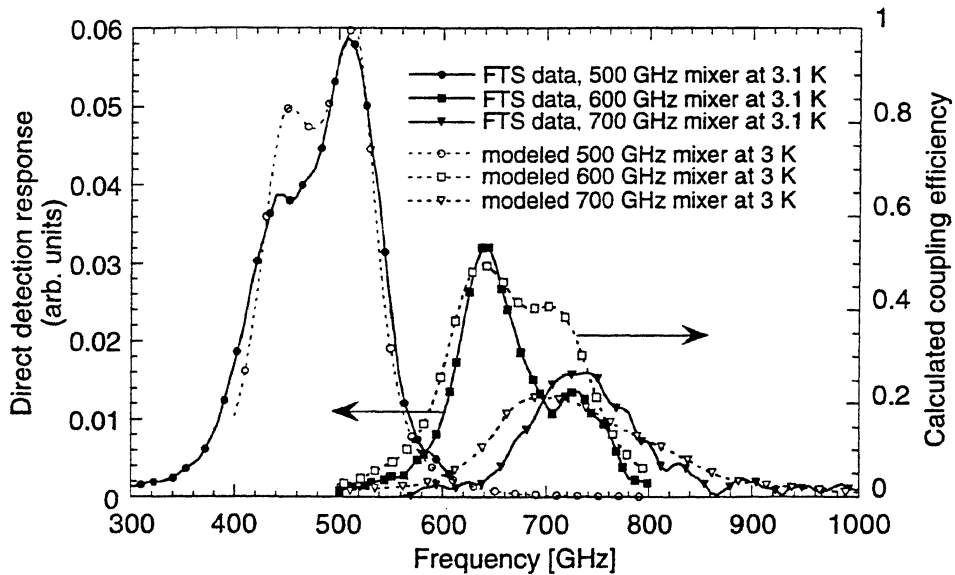


Figure 14 The compiled data for 500, 600 and 700 GHz in original FTS measured scale and results of modeling. Accuracy of the tuning bands and coupling efficiencies is better or about 15% over the 400-1000 GHz band.

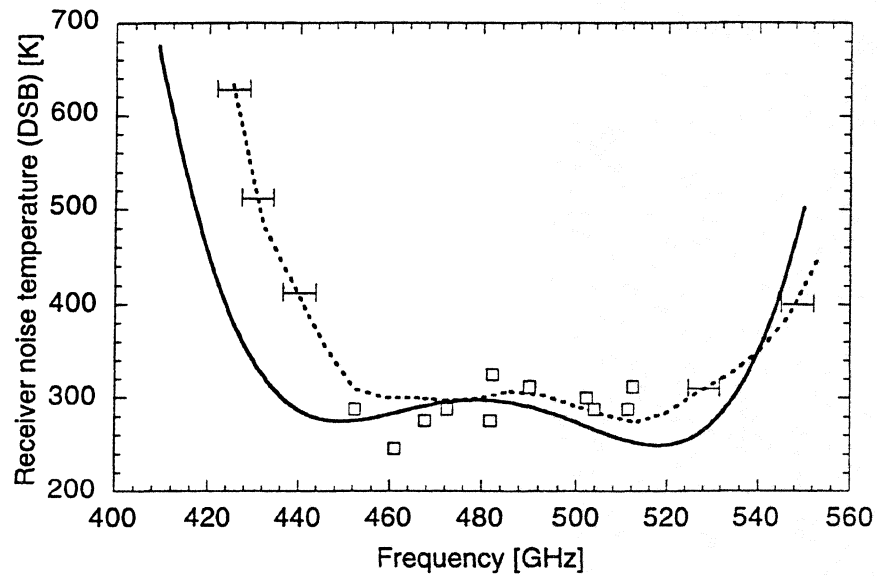


Figure 15 The 500 GHz receiver measured noise temperatures (DSB) (\square). The dashed curve is FTS measured direct detector response for the same sample and the solid line is the result of modeling (coupling efficiency) for measured R_n , V_g , etc. The two latter curves are inverted and normalized to the measured receiver noise temperature at 480 GHz.

NbN MIXERS AND TUNING CIRCUITS FOR 630 GHz: DESIGN AND PRELIMINARY MEASUREMENTS

M. Salez, J.A. Stern, W.R. McGrath, H.G. LeDuc
*Center for Space Microelectronics Technology, Jet Propulsion Laboratory,
California Institute of Technology, 4800 Oak Grove Drive, 91109 Pasadena*

P. Febvre
DEMIRM-Observatoire de Paris, 61 avenue de l'Observatoire, 75014 Paris, France

ABSTRACT

At frequencies above the gap frequency of niobium (710 GHz), the performance of Nb/AlO_x/Nb SIS mixers degrades and the losses in the niobium films of the superconductive Nb/SiO/Nb microstrip circuits used to provide a good RF impedance match severely limit the performance. Therefore, we are investigating the properties of NbN mixers, and in particular of NbN/SiO/NbN microstrip circuits integrated with submicron NbN/MgO/NbN tunnel junctions. The very large penetration depth of NbN (3000-4000 Å) makes the circuit design difficult and also puts critical constraints on alignment during fabrication. We present here the design of several rf tuning circuits for 630 GHz including novel symmetric designs which ease the alignment tolerances. In addition, a new approach for determining experimentally the penetration depth in the NbN films is presented.

I. INTRODUCTION

It has been shown both theoretically and experimentally that SIS mixers work well at frequencies up to the gap frequency of the superconductor used, and less well above that frequency [1-3]. In the case of Nb-based mixers, this frequency is about 710 GHz, the gap frequency of niobium. One reason for this performance degradation is the overlap of photon steps from opposite voltage branches of the tunnel junction's *I-V* curve, which yields a mixer noise increase of up to 50%. This has been investigated with Nb-based mixers from 490 GHz to 650 GHz [4]. Probably, the most impeding factor for the use of SIS mixers above the gap frequency is the exceedingly large rf losses in the superconductive films, as predicted by the Mattis-Bardeen theory. With such high losses, the integrated circuit which should be a purely reactive impedance transformer becomes a highly resistive device dissipating a major fraction of the rf power available to the overall mixer.

A potential solution for building SIS mixers at frequencies above 700 GHz is to use another superconductor with a higher gap energy for the tunnel junction and its integrated tuning circuits. Since NbN has a gap energy about twice as large as that of Nb, NbN-based SIS mixers should in principle work up to 1400 GHz. We are therefore investigating the use of submicron NbN/MgO/NbN tunnel junctions integrated with NbN/SiO/NbN microstrip tuning circuits. The present work focuses on operation near 630 GHz to facilitate the comparison between the well-characterized performance of Nb mixers at this frequency [5] and that of

a similar NbN mixer with identical integrated tuning circuits, when both are used in a waveguide receiver.

II. NbN/SiO/NbN MICROSTRIP TUNING CIRCUITS

A. Circuit Design

NbN films offer the advantage over Nb and lead-alloy films of an energy gap about twice as large, $2\Delta=5$ meV, so that in theory they become lossy for frequencies higher than 1200 GHz. The fabrication process of NbN/MgO/NbN tunnel junctions has been described elsewhere [6]. The submicron ($0.4 \times 0.4 \mu\text{m}^2$) tunnel junctions are patterned by electron-beam lithography, while the integrated microstrip circuits are produced by photolithography. The NbN layers are deposited by DC magnetron sputtering, while the MgO barrier layer is produced by rf magnetron sputtering, with an oxygen glow discharge to cure potential pinholes in the barrier. A gold layer is added on top of the counterelectrode layer to avoid oxydation. The penetration depth of the NbN films has been measured via SQUID measurements [7]. It has been found to depend on the temperature of the substrate at the time of deposition. When the substrate is heated to 300 °C during film deposition the transition temperature increases from 14 K to 16 K, with the corresponding penetration depth λ varying from 3800 Å to 2800 Å. For our circuit design calculations, a value of 3200 Å was assumed, and the variations in each design should allow for at least ± 300 Å. A critical current density of $j_c = 20$ kA/cm² was chosen for the tunnel junctions, corresponding to $R_n \cdot A = 20 \Omega \mu\text{m}^2$. These junctions are characterized by $R_n=125 \Omega$ and $C=16$ fF, yielding $\omega R_n C = 7.5$ at 600 GHz.

The integrated NbN/SiO/NbN superconductive microstrip circuits have been designed to match these junctions to a typical impedance that the mixer mount should provide, i.e with a real part comprised between 25 Ω and 150 Ω . The transmission line properties have been calculated using the Wheeler formulation [8] for the fringing fields which leads to an effective width, effective characteristic impedance, and effective dielectric constant (see reference [11] for a detailed discussion of the circuit design formulas). We have taken the superconductive behavior of the films into account [9] using an effective permeability μ_{eff} given by:

$$\mu_{\text{eff}} = 1 + \lambda t_d (\coth(t_1/\lambda) + \coth(t_2/\lambda)) \quad (1)$$

where t_d and ϵ_r are the thickness and dielectric constant of the SiO layer respectively, and t_1 and t_2 are respectively the thickness of the base and top electrodes of the microstrip. All the microstrip circuits use $t_1=3000$ Å, $t_2=5000$ Å, $t_d=2000$ Å, $\epsilon_r=5.5$, and the normalized propagation velocity v/c varies between 0.195 and 0.215, depending on the width of the microstrip. For certain circuits, the effect of large step discontinuities had to be calculated, using the Oliner inductance formula [10], so as to modify the actual length of a transmission line section to obtain the correct electrical length. The $4\mu\text{m} \times 4\mu\text{m}$ pad formed by the wiring layer around the junction adds 4 fF to the junction capacitance. The

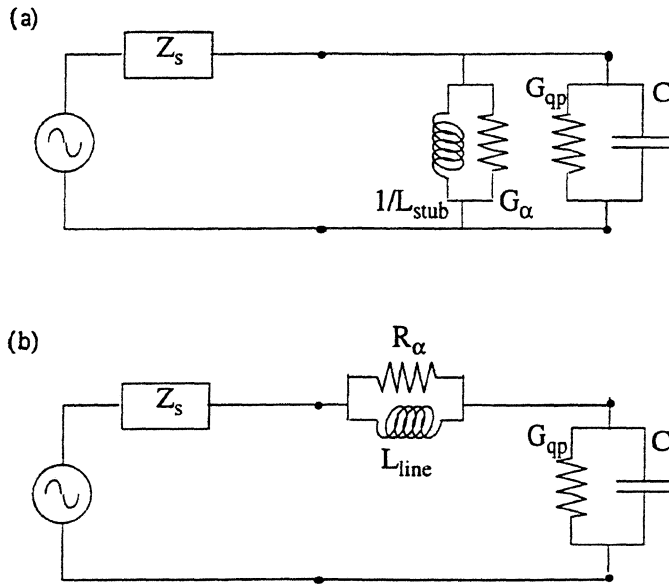


Fig. 1. Schematic diagram of a tunnel junction represented by the admittance $G_{qp} + j.C\omega$, where G_{qp} is the quasiparticle tunneling conductance and C is the geometric capacitance, matched to the source of impedance Z_s with (a) parallel and (b) series tuning circuits. L is the tuning circuit inductance, and G_α and R_α represent resistive losses.

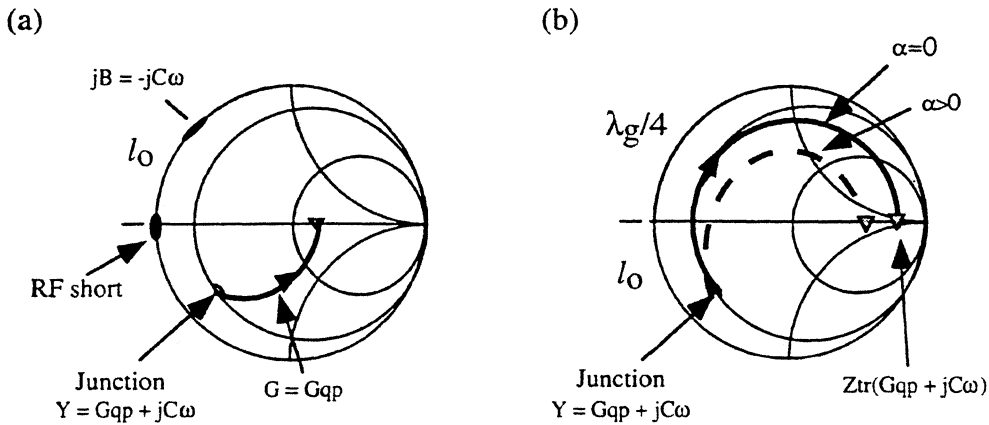


Fig. 2. Illustration on a Smith chart normalized to the source impedance of (a) a parallel tuning circuit and (b) a series tuning circuit, realised by means of distributed elements. In both (a) and (b) l_0 is the length of the section of transmission line required to transform the junction admittance $Y = G_{qp} + jC\omega$ into a purely real load (left on the real axis of the Smith chart). In (a) this is also the length of transmission line that transforms a short (the radial stub) into an admittance whose reactive part jB is the complex conjugate of the junction susceptance, $jC\omega$. Hence, the junction and the radial stub in parallel have an impedance $1/G_{qp}$. In (b), the low-impedance load produced by the l_0 long transmission line loaded by the junction is further transformed by a $\lambda/4$ section of line into a high-impedance load, easier to match with a waveguide mixer mount. The dashed line indicates the effect of rf losses ($\alpha > 0$).

performance of all the circuits has been evaluated in terms of the return loss at the input of the junction/tuning circuit device, for an assumed source impedance provided by the mixer mount of about 50Ω .

The circuits can be split in two categories, depending on whether they are parallel circuits or series transformers (see Fig. 1). The principle of their operation is shown on Smith's charts in Fig. 2 and discussed in more detail below.

Parallel circuits:

Radial stubs. Parallel circuits which provide an inductance in parallel with the junction capacitance have been used for many years. Figure 3(a) shows a microstrip implementation of this type of tuning circuit. A radial stub provides a broadband rf short which is transformed into the proper inductance by a short section of microstrip line (for simplicity, we refer to the stub and microstrip line as a "radial stub" tuning circuit). Both radial stubs and conventional quarter-wave stubs have been used at 600 GHz and have yielded good mixer performance [5, 13]. Radial stubs usually provide the broadest frequency response, around 75 GHz for $S_{11} = -10$ dB. The difficulty of scaling the radial stub design used with Nb to the NbN material lies in the very short physical lengths associated with the large penetration depth. Errors of only $1 \mu\text{m}$ in the length of the microstrip line have an enormous effect on the stub response, shifting its central frequency by as much as 30 GHz. A solution to this alignment issue is discussed in II.C below.

Twin-junction transformers. These transformers use two junctions separated by a short section of transmission line, in such a way that the complex impedance of one junction, transformed by the line, acts as a reactive element that exactly compensates for the capacitance of the other [12]. This approach has been used successfully up to 700 GHz [12,14]. Such a transformer must be understood as a parallel stub of a particular type, which instead of using a broad rf short uses the complex impedance of another junction to provide the inductance $1/\omega C$ that is needed to resonate out C. Because it relies on a highly reactive load (the junction capacitance), it can be expected that these 'stubs' achieve a bandwidth narrower than those using a broadband rf short. The bandwidth is maximized for $Z_C \gg R_N$, where Z_C is the characteristic impedance of the transmission line. Calculations show that even for a relatively large junction area ($0.8 \times 0.8 \mu\text{m}^2$) and narrow line ($2 \mu\text{m}$), the -10 dB bandwidth is only 40-50 GHz at 600 GHz or about 7%. However, this circuit offers two advantages: First, it requires a smaller area of NbN film since it avoids the need for a wide radial stub or quarter-wave stub. This can be of interest if the losses in NbN films prove to be prohibitive for the use of large stubs. Second, the distance between the two junctions, which determines the amount of induction connected in parallel, does not suffer from possible misalignments as does the section of line linking the junction to the rf short.

Series transformers:

Tchebychev two-pole transformers. These circuits have been used [13,15] and achieve the largest bandwidth. The junction complex impedance is transformed by a short microstrip line of length l_0 into a purely resistive load, which is then

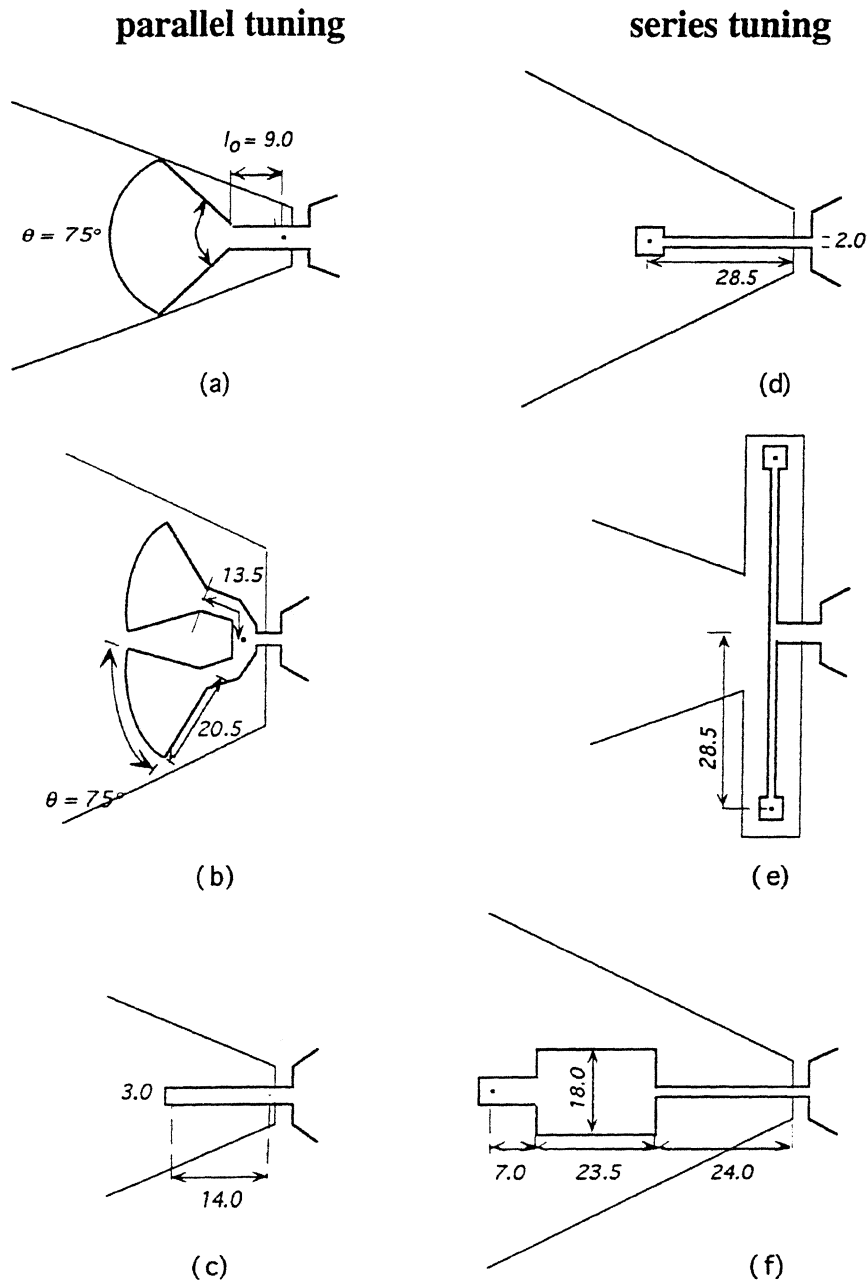


Fig. 3. Summary of the tuning circuits investigated: (a) single radial stub; (b) twin radial stub; (c) twin-junction transformer; (d) single-section transformer; (e) twin single-section transformer; (f) two-section Tchebychev transformer.

transformed to $\approx 50 \Omega$ by a transformer consisting of two nearly quarter-wave microstrips of well-defined characteristic impedances. As previously discussed [16], the purely real impedance which has to be transformed is extremely small (a few ohms) in the lossless case, which requires a low-impedance (wide) microstrip line as the first $\lambda/4$ section and a large transformation ratio (around 25). The rf losses may improve this situation by increasing the resistance at the transformer input. Our calculations show that S_{11} can be lower than -10 dB over more than 100 GHz bandwidth for small losses ($\alpha=10^{-3}/\mu\text{m}$), and up to 200 GHz for moderate losses ($\alpha=10^{-2}/\mu\text{m}$). Therefore, even in the worst case, the bandwidth is adequate for many receiver applications, and uncertainties in λ and in the junction capacitance have a negligible effect. Errors in the length of the first section of microstrip line, like those due to misalignments, have also no effect.

Single-section transformers. These are the simplest transformers. They consist of a single section of microstrip line which transforms the junction complex impedance into a purely real impedance in the high impedance region of the Smith's chart (see Figs. 2(b) and 3(d)). The microstrip length is $l_0 + \lambda/4$, where l_0 is the length defined above. Depending on losses in the microstrip, the value of the impedance varies between 20 and 100 Ω . The -10-dB bandwidth in the lossless case is about 150 GHz.

B. Microwave Losses

Although calculations based on the Mattis-Bardeen theory predict that rf losses in NbN are negligible near 600 GHz, there is experimental evidence [17] that NbN-based microstrip tuning circuits are much lossier than Nb-based ones, perhaps as an effect of grain boundaries in the NbN superconductive films. Hence, in addition to using the Mattis-Bardeen formulas, we have included the rf losses via a range of empirical values for the absorption per unit length. From previous measurements of the quality factor associated with the Josephson resonance seen in the I - V curves of NbN tunnel junctions integrated with open-ended stubs in the low-coupling limit induced by a magnetic field, an absorption of about $10^{-2}/\mu\text{m}$ has been derived. In our calculations of the tuning circuits properties, we have taken into account absorption factors varying from $10^{-3}/\mu\text{m}$ to $10^{-1}/\mu\text{m}$. We believe those two numbers to be respectively optimistic and pessimistic values for the range of losses that could occur in the NbN films at 600 GHz.

Two effects of these losses can be distinguished depending on whether one deals with a parallel-type or a series-type impedance transformer. In the parallel circuits, rf losses appear as a parasitic conductance G_α branched in parallel with the junction capacitance and quasiparticle conductance G_{qp} . In the series transformers, rf losses can be modelled by a resistance in series with the junction, which modifies the impedance transformation ratio and cause the power reaching the tunnel junction to be smaller than the power available at the input to the transformer. In the following, the junction parameters are taken to be $R_n=125 \Omega$ and $C=21 \text{ fF}$.

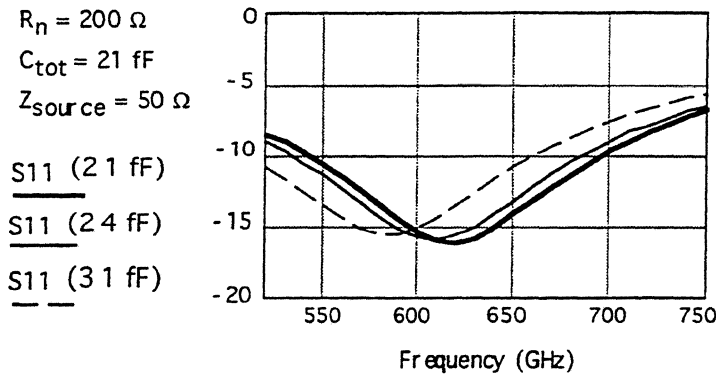


Fig. 4. Reflection coefficient at the input of a single-section end-loaded transformer, for a mixer mount source impedance of $Z_S=50 \Omega$. The different curves show the consequence of errors on the junction capacitance.

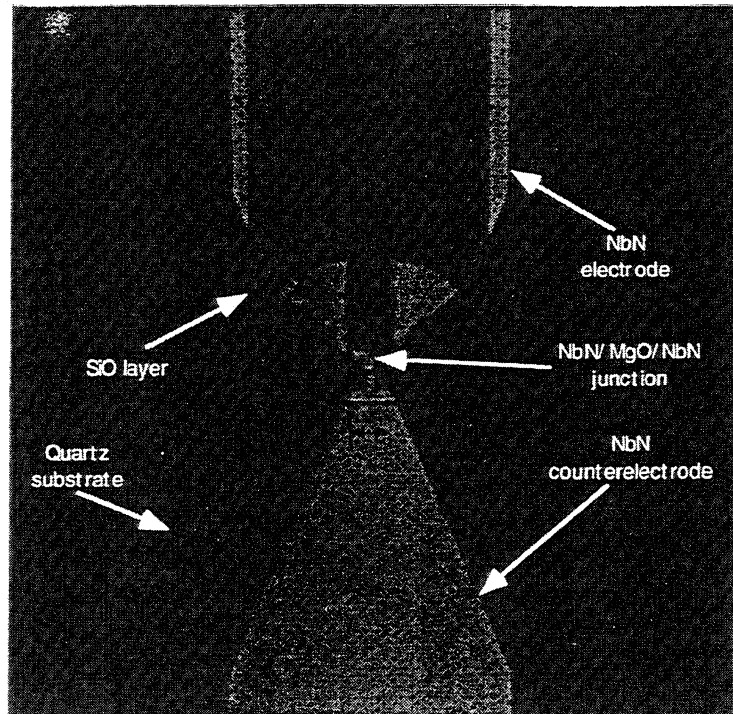


Fig. 5. Photograph of a twin-radial stub.

Parallel stubs. At the resonance frequency of the junction-stub circuit, the input impedance presented by the combination is:

$$Z_{\text{mixer}} = 1/(G_\alpha + G_{qp}) \quad (2)$$

In the case of very high losses ($\alpha=10^{-1}/\mu\text{m}$), G_α can be as large as $17 / R_n$. This implies about 13 dB loss in the rf power actually coupled into the junction, along

with a real part of the equivalent input impedance as low as 7Ω . For $\alpha = 5 \times 10^{-3}/\mu\text{m}$, the numbers above become 4 dB and 70Ω . Hence losses in the NbN films can have a substantial effect in terms of an unpredicted mismatch and a large derivation of the rf power away from the quasiparticle nonlinearity. While a suitable amount of tunability of the mixer mount may cope with the former effect, there is no means of avoiding the poor coupling due to the latter effect. The $\alpha=10^{-1}/\mu\text{m}$ case which we believe is a more realistic assumption leads to a real impedance of 42Ω , an impedance easily matched by the mixer mount, and to an additional 6-dB of rf losses, which should not overwhelmingly impede the mixer operation.

Series transformers. The consequences of rf losses in the films are less dramatic here than in the case of parallel tuning. For α between $5 \times 10^{-3}/\mu\text{m}$ and $10^{-1}/\mu\text{m}$, the equivalent impedance measured at the transformer input varies between 20Ω and 100Ω for the single-section transformer, and between 22Ω and 50Ω for the Tchebychev transformer. Our waveguide mixer mount is, in theory, capable of matching any real impedance in this range. One notes that the single-transformer is the only tuning circuit that may lead, in the lossless limit, to an impedance possibly too high for the mixer mount to match. Any rf losses then act in a positive way, since it reduces the real part of the transformed impedance as one moves away from the junction to finally intersect the real axis on the Smith chart (see Fig. 2(b)). However, assuming a good impedance match provided by the waveguide mount, rf losses also decrease the fraction of the power coupled into the junction. This fraction can be written

$$\Delta P / P_{\text{in}} = 1 - e^{-2\alpha l} \quad (3)$$

where l is the transformer line length, P_{in} is the power available at the input to the transformer, and ΔP is the power coupled into the junction. Using this simple model, in the case of the single-section transformer, $\Delta P / P_{\text{in}} = 0.85$ for $\alpha=10^{-2}/\mu\text{m}$ and $\Delta P / P_{\text{in}} = 0.92$ for $\alpha=5 \cdot 10^{-3}/\mu\text{m}$. This means that the power loss is smaller than 1 dB for $\alpha < 10^{-2}/\mu\text{m}$. For higher absorption rates, however, the loss of power in the transformer itself quickly becomes prohibitive. For $\alpha=10^{-1}/\mu\text{m}$, the power loss in the tuning circuit reaches 7 dB. In the case of the Tchebychev transformer, the larger size of the tuning circuit makes the effect of α more severe, leading to typical $\Delta P / P_{\text{in}} = 0.5$ for $5 \times 10^{-3}/\mu\text{m} < \alpha < 10^{-2}/\mu\text{m}$. In addition, the whole of the incident power would be dissipated within the microstrip circuit for α around $10^{-1}/\mu\text{m}$.

C. Sensitivity to Alignment

Our earlier work at 600 GHz with NbN junctions tuned with NbN/SiO/NbN open-ended microstrip stubs showed that the extreme sensitivity of the frequency response to the stub physical length made the issue of misalignment during photolithography critical. The resonance frequency was measured in the I - V curves for several stub physical lengths ranging from $23 \mu\text{m}$ to $38 \mu\text{m}$ with

increments of $0.5 \mu\text{m}$. The measurements were in good agreement with the predictions of multi-mode resonance theory, and showed the large frequency shift of the resonance per physical length increment. Although radial stubs have broader bandwidths than open-ended stubs, a $1\text{-}\mu\text{m}$ alignment error along the transmission line connected to the radial stub still causes the central frequency to shift by about 30 GHz, which is comparable to the circuit bandwidth.

We solve this problem by introducing into the circuit design a twin-symmetry, rendering them fairly insensitive to alignment errors as large as $2 \mu\text{m}$. The idea is to use whenever possible two identical sections of transmission line instead of one, in a geometry such that an excess of electrical length in one section due to misalignment is automatically compensated by an equivalent lack of electrical length in the other section. This principle can be applied to either parallel-type circuits such as the radial stubs (see Fig. 3(b)) or series-type circuits such as the single-section transformers (see fig. 3(e)). Figure 6 shows the effects of misalignment for both a simple radial stub and a twin-radial stub. In the case of the Tchebychev two-section transformer, there is no need for such a symmetric design since the following two quarter-wave sections naturally tend to wash out $1\text{-}2 \mu\text{m}$ alignment errors. Although the bandwidth achievable with the symmetric circuits is reduced, the usefulness lies in the insensitivity to alignment errors, which is critical for NbN.

Figure 3 summarizes all the rf tuning circuits for our NbN mixers. About 5 variations were designed for each to account for variations in junction capacitance and penetration depth.

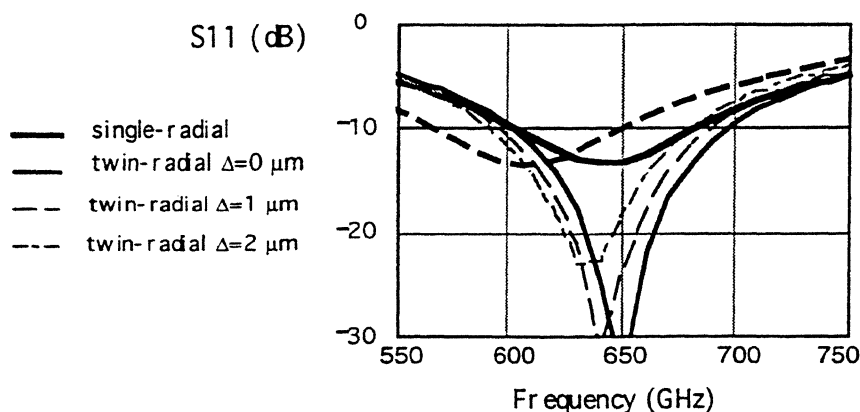


Fig. 6. Compared effects of 1 and $2 \mu\text{m}$ alignment errors on the tuning achieved by a simple radial stub (heavy lines) and a twin-radial stub (thin lines). The solid curves correspond to a perfect alignment while the dashed curves indicate the frequency-shifted response for a given amount of misalignment.

III. DC MEASUREMENTS

A. Devices Fabricated

One batch of $0.4 \times 0.4 \mu\text{m}^2$ NbN/MgO/NbN junctions have been fabricated, with $R_{\text{N.A}}$ around $50 \Omega \cdot \mu\text{m}^2$ and $V_{\text{gap}} = 4.95 \text{ mV}$. Figure 6 shows one junction integrated with the twin-radial stubs introduced earlier. A typical I - V curve is shown in Fig. 7. The corresponding critical current density is $7\text{-}10 \text{ kA/cm}^2$. The subgap-to-normal resistance ratio is around 5, and the subgap current is much reduced in comparison with previous batches with higher critical current densities. In particular, a bump-like half-gap feature which appears in all NbN tunnel junctions becomes small at low current densities, which is expected if this feature results from two-particle tunneling in a highly non-uniform oxide barrier [18]. The normal resistance of nearly 200Ω is higher than the nominal value of 125Ω assumed for the calculations. However, deviation from the optimum value is less critical for the normal resistance than for the geometric capacitance or the film penetration depth, which drastically modify the length of transmission line required for tuning.

B. Josephson Resonances

The DC characteristics of several circuits have been investigated, and the voltages at which Josephson resonances occur in the I - V curves have been measured. From such measurements, it is possible to deduce the frequency at which a parallel tuning stub resonates out the junction's capacitance [13,17]. In the case of a series-type transformer, it is more difficult to correlate the DC Josephson resonance to the actual mixer circuit behavior, since the impedance seen by the tunnel junction is a function of the rf source impedance supplied by the waveguide mount. Two-section Tchebychev transformers, however, can at least tell us at what frequency the two poles resonate, providing information on the rf properties of the superconductive microstrips. Similarly, although the simpler transformers provide little or no information on the propagation velocity in the lines, their symmetric counterparts do. This is because the two end-loaded sections of transmission line make an ideal microstrip resonator, whose modes can be excited by the AC Josephson currents of each junction at the ends. This microstrip resonator is also a useful feature of the design since it traps additional magnetic flux to cancel the Josephson effect during mixer operation.

The resonances described above have been measured in the radial, twin-radial and twin-transformers (see Fig. 3(a), (b), and (e)). There is good agreement between the resonance frequencies measured in the I - V curves and the calculated resonances using the actual $R_{\text{N.A}}$ product and the measured penetration depth. More work needs to be done, however, before an exhaustive comparison between theory and experiment can be made. Twin-radial stubs and twin-transformers have shown DC resonances indicating nominal operation near 500-650 GHz, and these devices are currently being tested.

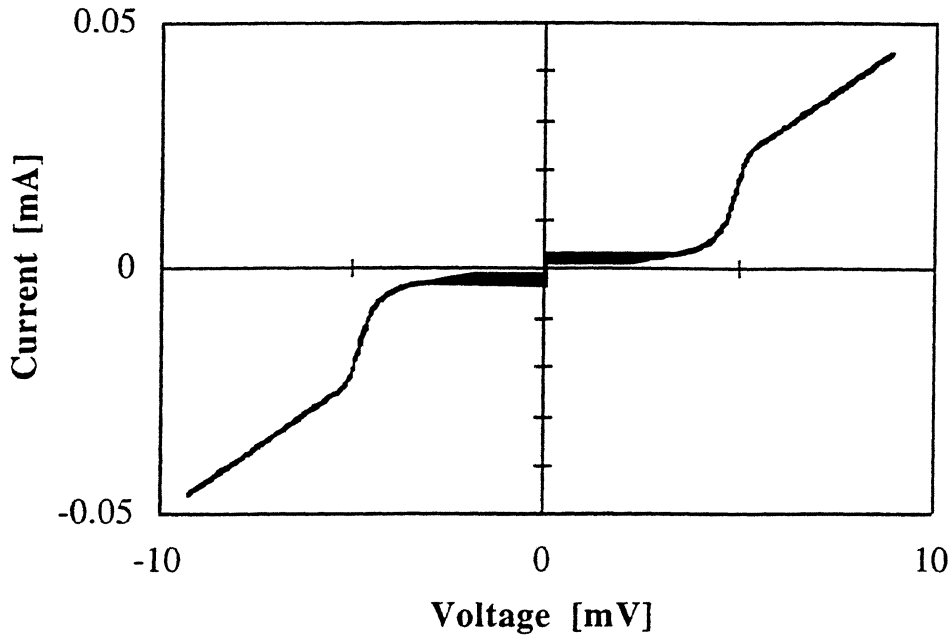


Fig. 7. Measured I - V curve of a 0.4×0.4 - μm^2 NbN/MgO/NbN tunnel junction with $R_{\text{n,A}} = 50 \Omega \cdot \mu\text{m}^2$.

C. Penetration Depth Derivation using Long Tunnel Junctions

Accurate values of the penetration depth of the superconductor used for the electrodes of the microstrip circuits is crucial for the design. A well-established method to derive this penetration depth uses the amount of magnetic flux which can penetrate between the two superconductive strips of a SQUID [7]. This method is accurate to $\sim 10\%$. We suggest the use of long (in-line) Josephson junctions (LJJ) to deduce the penetration depth in the superconductive electrodes. A tunnel junction is considered 'long' (see Fig. 8(a)) when its length is several times its width and the Josephson length λ_J , defined as:

$$\lambda_J = (\Phi_0 / 4\pi \mu_0 j_c \lambda)^{1/2} \quad (4)$$

where Φ_0 is the flux quantum and j_c is the critical current density. Then, in the in-line configuration represented in Fig. 8, the density of current flowing through the oxide barrier peaks at the two ends of the LJJ, and decreases toward the center as $e^{-\lambda_J}$. Owens and Scalapino [19] have shown that for junctions long enough ($L/\lambda_J > 5$) the maximum supercurrent is independent on the length and is only a function of the critical current density and the junction's width, w :

$$I_{\text{max}} = 4w \cdot \lambda_J j_c \quad (5)$$

This maximum supercurrent can be measured with high accuracy in zero magnetic field, allowing the Josephson length to be derived. Equation (4) can then be used to derive λ .

The LJJs not only provide a way to investigate the penetration depth in the films. They also can be used to measure the specific capacitance of the tunnel junctions. It is possible to measure accurately in the I - V curves the voltage of the zero-field steps, V_{ZFS} , indicating the resonant motion of flux quanta trapped in the oxide barrier and accelerated by the bias current. Their velocity v is given by

$$v = 2L.V_{ZFS} / \Phi_0 \tag{6}$$

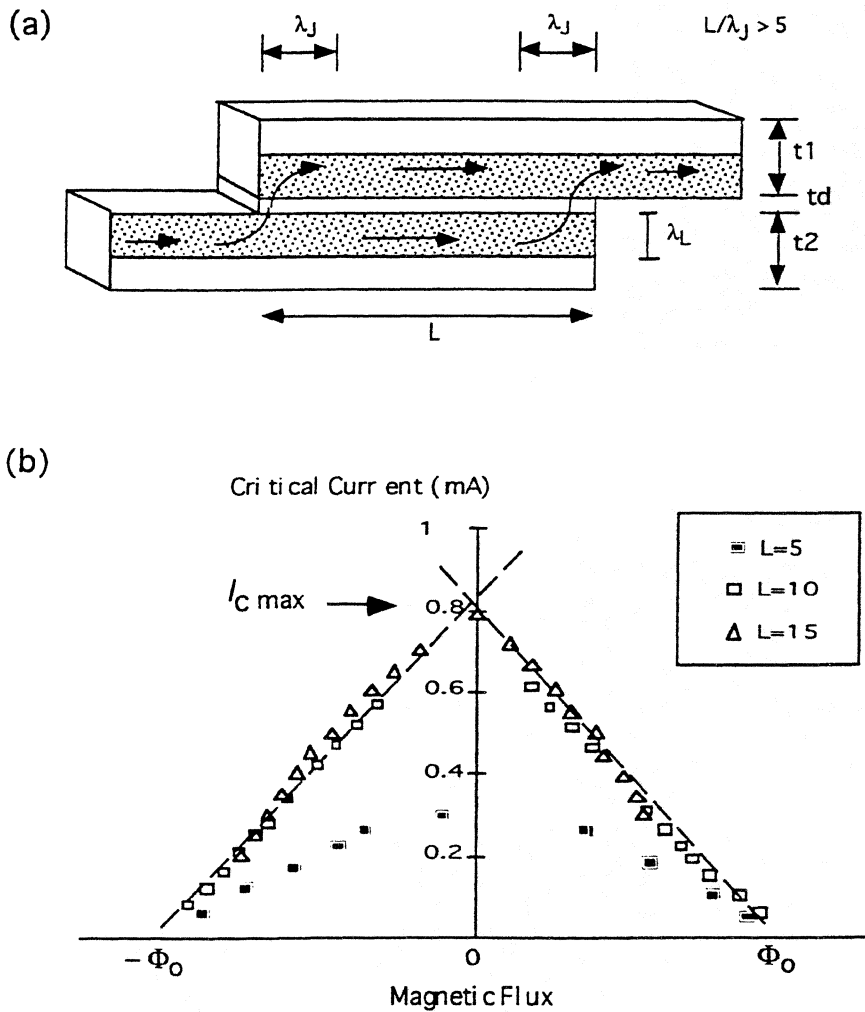


Fig. 8. (a) Schematic drawing of a 'long' Josephson junction showing the confinement of the supercurrent to the edges; (b) measured maximum supercurrent in 5, 10 and 15- μm long junctions versus the applied magnetic flux. Because they are both much longer than the Josephson length ($\approx 2 \mu\text{m}$), the 10- μm and the 15- μm junctions are LJJs and hence exhibit the same total supercurrent.

and is also the speed of light in the oxide barrier, of thickness d and of dielectric constant ϵ_r , that is:

$$v = c (d/2\lambda \epsilon_r)^{1/2} \quad (7)$$

Hence by measuring in the same device the penetration depth and the soliton speed, one has also measured the ratio d/ϵ_r on which depends the specific capacitance of the junction:

$$C/A = \epsilon_0 \epsilon_r/d \quad (8)$$

The I - V curves of NbN/MgO/NbN LJJs with $w = 0.7, 1 \mu\text{m}$, $L = 5, 10$ and $15 \mu\text{m}$ have been measured. The criterion of length is satisfied for $L = 10 - 15 \mu\text{m}$ since $\lambda_j \approx 2.1 \mu\text{m}$, and about the same maximum supercurrent could be measured for junctions of either length. While SQUID measurements have given $\lambda \approx 3500 \text{ \AA} \pm 400 \text{ \AA}$ for NbN, the LJJ method has provided numbers around $3200 \text{ \AA} \pm 500 \text{ \AA}$. The zero-field steps have been measured in all junctions, giving $v/c \approx 0.018$ and $C/A \approx 90 \text{ fF}/\mu\text{m}^2$, which is consistent with values deduced previously [7].

This new approach has been tried successfully with NbN and could be used with any other superconductor. The scattering in the method is mostly due to scattering in the measurements of the critical current density in small junctions and of the maximum current in the LJJs, which may occasionally be reduced by trapped flux in the NbN electrodes. This source of scattering disappears with type I superconductors such as Nb.

IV. CONCLUSION

Several NbN/SiO/NbN microstrip rf tuning circuits for NbN-based SIS mixers have been designed, fabricated and will soon be evaluated in a waveguide receiver at 630 GHz. Calculations of these circuits include the effects of fringing fields, strip-width discontinuity, and rf losses in the superconductive films. These circuits take into account design difficulties specifically associated with the potentially higher rf losses in NbN films. Novel symmetric circuits designs have been introduced to address the extreme sensitivity to microfabrication tolerances which result from the long magnetic penetration depth in NbN. In addition, a new method for deriving experimentally the penetration depth of the NbN films using in-line long tunnel junctions has been used and has given results compatible with previous SQUID measurements. This method could be used for other superconductors as well.

ACKNOWLEDGEMENTS

This research described in the paper was performed by the Center for Space Microelectronics Technology, Jet Propulsion Laboratory, California Institute of Technology, and was sponsored by the National Aeronautics and Space Administration, Office of Space Access and Technology. Morvan Salez is currently sponsored by the Research Associateship Program of the National Research Council.

REFERENCES

- [1] M.J. Feldman, *Internat. J. of Infrared and Millimeter Waves* **8**, 1287 (1987).
- [2] G. DeLange, C.E. Honingh, M.M.T.M. Dierichs, H.H.A. Schaeffer, H. Kuipers, *Proc. 4th Internat. Symp. on Space Terahertz Technology*, p. 41, UCLA, CA (1993).
- [3] J. Zmuidzinas, N.G. Ugras, D. Miller, M. Gaidis, H.G. LeDuc, and J.A. Stern, *ASC'95*, Boston, MA (1994).
- [4] P. Febvre, M. Salez, W.R. McGrath, B. Bumble, and H.G. LeDuc, to appear in *Applied Physics Letters* (1995).
- [5] M. Salez, P. Febvre, W.R. McGrath, B. Bumble, H.G. LeDuc, *Internat. J. of Infrared and Millimeter Waves* **15**, (6) 349 (1994).
- [6] J.A. Stern, B.D. Hunt, H.G. LeDuc, A. Judas, W.R. McGrath, S.R. Cypher, and S.K. Khanna, *IEEE Trans. on Magn.*, **25**, 2, 1054 (1989)
- [7] J.A. Stern and H.G. LeDuc, *IEEE Trans. on Magn.*, **27**, 2, 3196 (1991)
- [8] H.A. Wheeler, *IEEE Trans. Microwave Theory Tech.*, **MTT-25**, 631 (1977)
- [9] J.C. Swihart, 1961, *J. Appl. Phys.* **32**, 441 (1961).
- [10] A.A. Oliner, *IRE Trans. Microwave Theory Tech.*, **MTT-3**, 134, (1955)
- [11] P. Febvre, W.R. McGrath, B. Bumble, H.G. LeDuc, S. George, G. Ruffie, G. Beaudin, *Proceedings of the 24th. European Microwave Conference*, Palais des Festivals, Cannes, France, September 5-8, 1994.
- [12] V.Yu. Belitzky, M.A. Tarasov, S.A. Kovtonjuk, L.V. Filippenko, and O.V. Kaplunenko, *Internat. J. of Infrared and Millimeter Waves* **13**, 389 (1992)
- [13] P. Febvre, W.R. McGrath, P. Batelaan, B. Bumble, H.G. LaDuc, S. George, and P. Feautrier, *Internat. J. of Infrared and Millimeter Waves* **15**, 943 (1994)
- [14] J. Zmuidzinas, H.G. LeDuc, J.A. Stern, and S.R. Cypher, *IEEE Trans. Microwave Theory Tech.*, **42**, 698 (1994)
- [15] R. Blundell, C. Tong, J.W. Barrett, R.L. Leombruno, S. Paine, D.C. Papa, X. Zhang, J.A. Stern, H.G. LeDuc, and B. Bumble, *Proceedings of the European SIS User Meeting*, KOSMA, Koln, Germany (1994)
- [16] J.W. Kooi, M. Chan, B. Bumble, H.G. LeDuc, P.L. Schaeffer, and T.G. Phillips, *Internat. J. of Infrared and Millimeter Waves* **15**, 783 (1994)
- [17] W.R. McGrath, J.A. Stern, H.H.S. Javadi, S.R. Cypher, B.D. Hunt, and H.G. LeDuc, *IEEE Trans. Mag.*, **MAG-27**, 2650 (1991)
- [18] J.R. Schrieffer and J.W. Wilkins, *Phys. Rev. Lett.*, **10**, 17 (1962)
- [19] C.S. Owens and D.J. Scalapino, *Phys. Rev.*, **164**, 538 (1967)

NOISE PROPERTIES OF A MIXER WITH SIS NbN QUASIPARTICLE TUNNEL JUNCTIONS.

A. Karpov*, B. Plathner*, K. H. Gundlach*, M. Aoyagi**, S. Takada**

* IRAM, 300 rue de la Piscine, F - 38406 St. Martin d'Hères, France.

** Electrotech. Lab. 1-1-4 Umezono, Tsukuba - shi Ibaraki, 305 Japan.

Abstract

We present an analysis of the noise properties of a mixer with the full NbN tunnel junctions. Our work is based on experiment in 120 -180 GHz range with SIS mixer with the NbN-MgO-NbN tunnel junctions. Mixer circuit is totally in NbN. The mixer operates at 5.4 K temperature unacceptable with Nb junctions. Minimum DSB receiver noise temperature is about 65 K at 160 GHz and approaches the Nb SIS mixer performance in mm band. In the whole 50 % band receiver noise varied between 65 and 150 K with the middle value about 80 K.

It has been found that noise sources in the NbN junctions are comparable to the Nb junctions and that the receiver noise with the NbN SIS mixer may be only few times more than the quantum limit of noise in the frequency range below the gap frequency. Output noise of the SIS mixer has been found constant in a wide frequency band and within an important range of the local oscillator amplitudes.

Introduction

Progress of the millimeter and submillimeter ultra low noise receiver required for the radioastronomy programs and for the atmosphere monitoring was provided with the development of the new generation of the low noise Superconductor- Insulator- Superconductor (SIS) mixers with Nb-Al oxide-Nb quasiparticle tunnel junctions [1,2]. The upper frequency limit of Nb SIS devices about 700 GHz is settled by the increase of the loss behind the gap frequency of superconductor. The further progress in frequency of the SIS devices was currently related to the NbN junctions with the highest gap frequency around 1200 GHz. Only one experimental investigation was performed in the mm band with a full NbN SIS mixer at 200 - 208 GHz [3]. Up-to-date noise performance of the SIS NbN mixers was out of concurrence with the Nb devices. Presented in [3] receiver DSB noise was about 460 K and a minimum available mixer noise was estimated as 145 K. Origin of such a high noise in the NbN junctions was not clear. The aim of this work is to demonstrate a low noise operation of a SIS mixer with NbN tunnel junctions and to understand mixer noise properties.

NbN - Mg Oxide - NbN junctions

NbN-MgO-NbN junctions used in this work was produced with the tri-layers coming from the Electrotechnical Laboratory. Tri-layer deposition technology was presented in [4]. Junction etching and the deposition of the NbN wiring layer was performed in IRAM. Critical temperature of NbN used in our experiments is about 15 K and the gap voltage of the junction is about 5 mV.

Optimum $R_N\omega C$ for the use in the quasiparticle tunnel NbN junctions in the mm and submm mixers

Optimum $R_N\omega C$ for the Nb junctions is discussed in [5,6]. If the local oscillator frequency is well below the gap frequency of Nb ($F \ll \Delta/h$) and if the junction I-V curve is sharp the optimum is about or below $R_N\omega C = 4/F$, where F is the frequency in 100 GHz [5].

In the same conditions a similar relation may be outlined for the NbN junctions. This relation may be based on the estimation of the optimum RF impedance of the SIS junction $R_{RF OPT}$. Optimum coupling to the external circuit of the junction presented by a parallel connection of RF resistance and small junction reactance is expected when $R_{RF OPT} = |X_{RF}|$. Junction RF resistance may be estimated in the case $F \ll \Delta/h$ as $R_{RF} = 2h\nu R_N / eVg$, leading to the expression for the optimum junction parameter $R_N\omega C = eVg / 2h\nu$. In the case of the tunnel junction with the Nb

electrodes it gives a known expression $R_N\omega C=3.5/F[100 \text{ GHz}]$. In the case of the NbN junction with $V_g=5 \text{ mV}$ we arrive to:

$$R_N\omega C=6/F[100 \text{ GHz}] \quad (1)$$

This relation gives an approximate value of the optimum $R_N\omega C$ for the use of the NbN junction in a mixer. As in the case of the Nb junctions, optimum $R_N\omega C$ of the NbN junctions approaches 1 if I-V curve is not sharp or if the operation frequency comes closer to Δ/h .

Mixer design

SIS mixer comprises a multi layer NbN printed circuit with two tunnel junctions and a mixer block. It is a single backshort mixer block with a reduced height waveguide. An L-C microstrip impedance transformer is integrated with each junction as a part of the interconnection layer in the junction fabrication process. Printed circuit of the mixer was optimized for the individual junction normal resistance about 30 Ohm and $R_N\omega C=6$. The junctions available for the test have $R_N\omega C=50$ resulting in extra loss in the mixer circuit. Backshort position of this mixer with a relatively large junction $R_N\omega C$ product have to be adjusted at each frequency.

Experimental set - up

Experiments with the NbN SIS mixer were hold in the receiver developed for the SIS Nb mixers. Receiver comprises a liquid helium cryostat, SIS mixer, cooled HEMT IF amplifier, ambient temperature amplifier and the local oscillator. Local oscillator consists of the Carlstrom Gunn oscillator and a doubler developed in IRAM by F. Mattiocco. Local oscillator power is injected at the mixer input by a commercial cooled waveguide coupler. Receiver input window is in milar and an infrared filter in expanded polystyrene form is fixed at the 77 K shield. Temperature at the mixer block in experiment with NbN junctions was about 5.4 K. This temperature is not acceptable with the Nb junctions but in the case of the NbN junction is still below $0.4 T_c$.

Operation of the SIS receiver with the NbN tunnel junctions in the mixer

Current-voltage characteristics (CVC) of the two NbN SIS junction array with and without local oscillator power (P_{LO}) are presented in Fig. 1. Normal resistance of the two junction array is 260 Ohm and the Josephson critical current density is about 1.3 KA/cm^2 . The subgap resistance of these junctions is about 4 time larger then the normal state resistance. Junction CVC may be compared with a "Dull" characteristic used in [6] for the calculation of the SIS mixer performance. Conversion gain -5 dB is predicted in [6] for a mixer with the dull CVC at 150 GHz, corresponding to 0.12 of the NbN gup frequency.

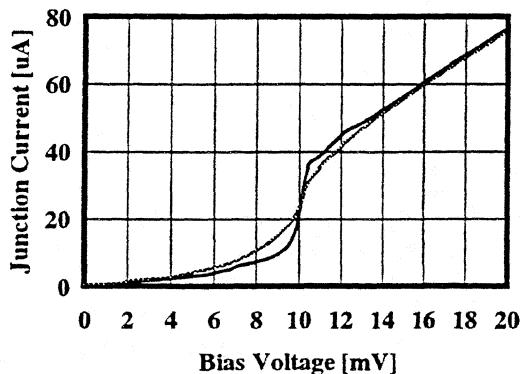


Figure 1. Current-Voltage characteristics of the two NbN SIS junction array. Black line - without local oscillator power; gray line - with P_{LO} .

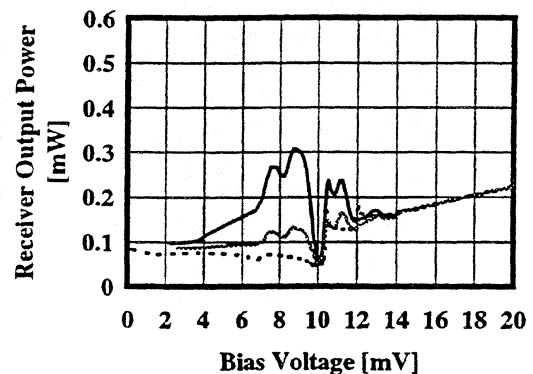


Figure 2. Output power of the SIS receiver versus junction bias voltage. Dotted line - without P_{LO} . The gray line is measured with P_{LO} and with a nitrogen temperature load; black line - with P_{LO} with an ambient temperature load.

Tien - Gordon steps are not obvious at the CVC in the presence of the local oscillator power (gray curve in Fig. 1). It may be a common effect of a very smooth CVC and of a relatively low frequency of operation in our experiment. The quantum structures are better visible in the curves of the output power of receiver versus bias voltage presented in Fig. 2. Output power of the receiver is measured in the 500 MHz band around 1500 MHz with an ambient and nitrogen temperature loads in front of receiver (black and gray lines in Fig. 2 respectively). Dotted line in Fig. 2 presents the receiver output power without local oscillator.

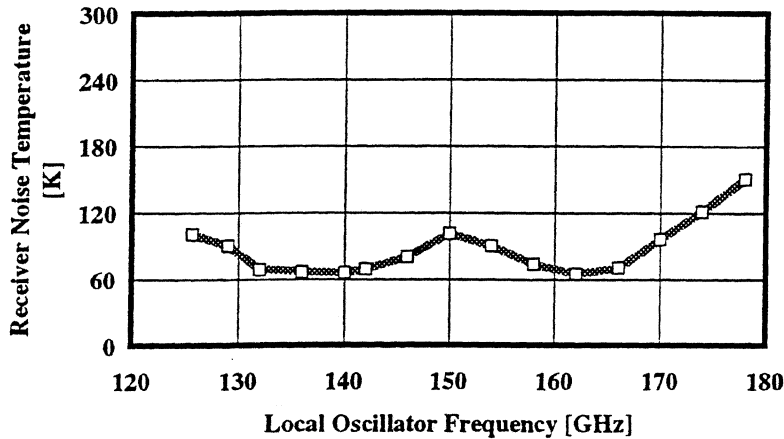


Figure 3. DSB receiver noise temperature with the NbN SIS junctions in the mixer.

Receiver noise temperature is measured in the standard nitrogen and ambient temperature load experiments. Mixer was tuned at each frequency. Minimum DSB receiver noise temperature is 65 K when the average noise in the 125 - 180 GHz band is about 80 K (Fig.). The noise level of this receiver is comparable with the performance of a receiver with the Nb SIS junctions.

Below we discuss the sources of the receiver noise using a standard relation for the receiver double sideband noise temperature:

$$T_{\text{Rec}} = T_{\text{RF}} + \frac{T_{\text{M}}}{G_{\text{RF}}} + \frac{T_{\text{OUT}} + T_{\text{IF}}}{2G_{\text{M}} \cdot G_{\text{RF}}} \quad (2)$$

Here T_{RF} , T_{M} , T_{OUT} and T_{IF} are respectively the noise temperatures of the receiver input section, of the mixer, the output mixer temperature and the IF amplifier temperature. Terms G_{RF} and G_{M} denote the gains of the receiver input section and the mixer respectively. Receiver conversion gain is $G_{\text{R}} = G_{\text{RF}}G_{\text{M}}$.

Receiver and mixer conversion gain

Receiver gain was measured in situ in the hot and cold load experiments. Receiver IF chain was calibrated with the shot noise of the junction normal resistance biased behind the gap voltage according to [6]. Receiver conversion gain versus bias current (bias voltage is fixed) is presented in Fig. 4. Maximum gain between the receiver input window and the output of the IF isolator of the mixer is about 0.25 (-6 dB). In this receiver we used the junctions with the $R_{\text{N}}\omega\text{C}$ parameter more than 10 times large the optimal value. Analysis of the mixer circuit shows that at least 2 dB of loss may be explained by the junction mismatch.

Measured IF chain noise temperature is 6.5 K.

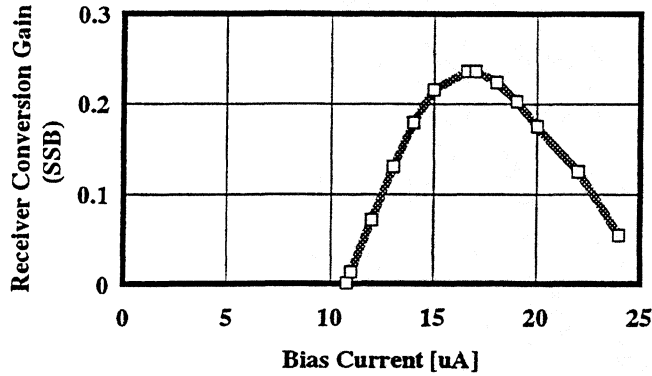


Figure 4. Receiver conversion gain versus bias current at 166 GHz. This curve is measured with the bias voltage fixed at 9 mV and with the different levels of the local oscillator power.

Noise of the input section of the SIS receiver

Input section noise of this receiver was determined according to [7, 8] in the experiment with a SIS mixer with Nb junctions. It has been found that $T_{FE} + T_M / G_{FE}$ is about 7 K. Here we present in Fig. 5 SIS NbN receiver gain versus receiver loss dependence measured at 166 GHz with at the different local oscillator power levels between zero and a level superior to the optimum working P_{LO} . Experimental points are situated on the straight line. This behavior corresponds to a constant output mixer noise temperature if T_{IF} , T_{FE} and T_M are constant. In this experiment mixer CVC does not change significantly with the P_{LO} and we can expect constant SIS junction coupling to the mixer circuit at RF and IF. Extrapolation of the measured data to zero conversion loss gives according to expression (2): $T_{FE} + T_M / G_{FE} = 8$ K. Receiver front end section noise measured with NbN and Nb junctions are identical.

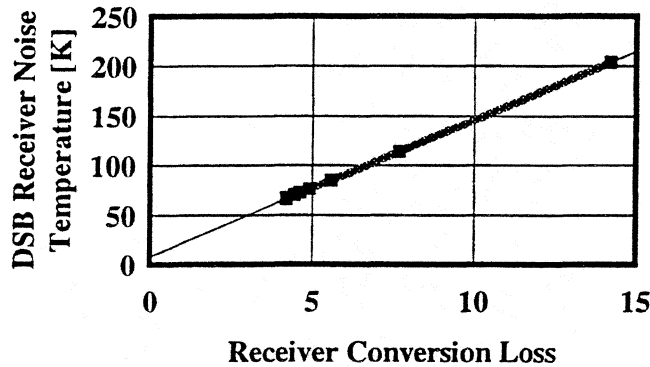


Figure 5. Receiver DSB noise temperature versus conversion loss measured at the different levels of the local oscillator power. Experimental points are located on a straight line.

Output noise of the mixer with NbN SIS junctions

Output noise of the mixer was determined according to (2) as:

$$T_{OUT} = (T_{Rec} - T_{FE})2G_{Rec} - T_{IF} \quad (3)$$

Measured output noise versus bias current is presented in Fig. 6. Minimum receiver noise was measured with a 17 μ A current. Output mixer noise is perfectly stable up to 20 μ A current, superior to the optimum level. In this experiment mixer tuning was fixed and bias current was changed by P_{LO} . Observed in our experiment Constant

output noise at the different amplitudes of the local oscillator is in a good accord with the theoretical prediction in [9] for the low P_{LO} level.

Frequency dependence of the output mixer noise is presented in Fig. 7. Mixer tuning and P_{LO} are optimized at each frequency. Output noise is stable in the 50% frequency band, except some points with a difficult tuning. Frequency independent output noise of the SIS mixer was predicted in [6, 9].

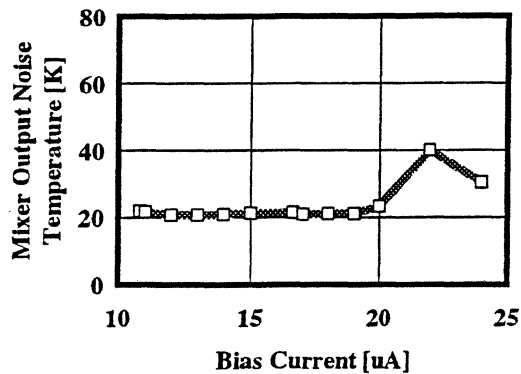


Figure 6. SIS mixer output noise dependence on the bias current measured at 166 GHz local oscillator frequency. Mixer tuning is fixed and the bias current changes with the local oscillator power.

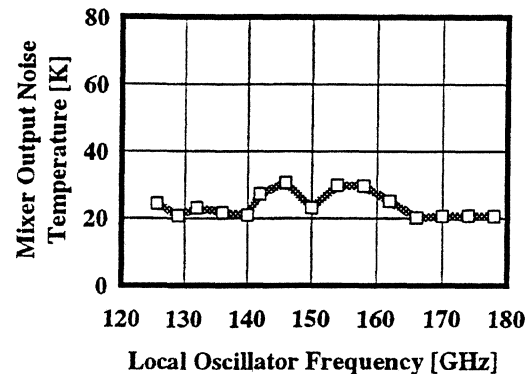


Figure 7. SIS mixer output noise temperature versus frequency. Mixer tuning and local oscillator power are optimized at each frequency.

Conclusion

We demonstrated for the first time the low noise operation of the SIS mixer with a full NbN tunnel junction. Minimum receiver noise temperature of 65 K was measured at 162 GHz. Average noise temperature over all the 125 - 180 GHz band is about 80 K. Presented in this paper receiver noise with the NbN tunnel junctions in the mixer is comparable with the typical results with Nb junctions.

In our experiment the NbN SIS junction was at 5.4 K temperature unacceptable with the Nb devices. Introduction of the low noise NbN mixers may simplify the receiver cryogenics, especially the closed-cycle refrigerators.

For operation in the mixer the optimum $R_N\omega C$ NbN junction product is different from the Nb junctions. The optimum with NbN is $R_N\omega C=600\text{GHz}/F$ if the junction current-voltage characteristic is not smooth and if the frequency of operation does not approach to the gap frequency. In our experiment the junctions with $R_N\omega C=50$ have been used. A further improvement in the receiver noise with NbN tunnel junctions is possible with the progress in the junction parameters and mixer circuit design.

It has been demonstrated that in a good agreement with the theoretical prediction [6,9] the SIS mixer output noise is nearly independent on frequency and on the local oscillator power. Relative frequency band in our experiment was 50%; local oscillator power was between zero and optimum working level. According to our experiment the output noise level may be used as a basic characteristic of a SIS mixer.

References:

1. G Philips and J. Keene, "Submillimeter astronomy", Proceedings of the IEEE, Vol. 80, No. 11, pp. 1662-1678, November 1992.
2. R. Blundell and C.-Y. E. Tong, "Submillimeter receivers for radioastronomy", Proceedings of the IEEE, Vol. 80, No. 11, pp. 1702-1720, November 1992.
3. W. R. McGrath et al, "Performance of NbN superconductive tunnel junctions as SIS mixers at 205 GHz", IEEE Transactions on Magnetics, Vol. 27, No. 2, pp. 2650-2653, March 1991.

4. M. Aoyagi, H. Nakagawa, I. Kurosava and S. Takada, "NbN/MgO/NbN Josephson junctions for integrated circuits", *Jpn. J. Appl. Phys.*, Vol. 31, Part 1, No. 6A, pp. 1778-1783, June 1992.
5. A. R. Kerr and S.-K. Pan, "Some recent developments in the design of SIS mixers", *International Journal on Infrared and Millimeter Waves*, Vol. 11, pp. 1169-1187, October 1990.
6. Q. Ke, and M. Feldman, "Source conductance scaling for high frequency superconducting quasiparticle receivers", *Proceedings of the Third International Symposium on Space Terahertz Technology*, pp. 538-547, March 24-26, 1994, Ann Arbor, MI, USA.
7. R. Blundell, R. E. Miller, and K. H. Gundlach, "Understanding noise in SIS receivers", *Int. J. IR and MM* 13. Woody, R. E. Miller and M. J. Wengler, "85-115 GHz receivers for radio astronomy", *IEEE Trans. Microwave Theory Tech.*, vol. MTT-33, pp. 90-95, 1985.
8. Q. Ke, and M. Feldman, "A technique for accurate noise temperature measurements for the superconducting quasiparticle receiver", in *Proceedings of the Fourth International Symposium on Space Terahertz Technology*, 1993, Los Angeles, US, pp. 33-40.
9. Q. Ke, and M. Feldman, "Constant output noise temperature of the superconducting quasiparticle mixer", *IEEE Transactions on Applied Superconductivity*, Vol. 3, No. 1, pp. 2245-2249, March 1993.

A Fixed Tuned SIS Receiver for the 450 GHz Frequency Band

**R. Blundell, C.-Y. E. Tong, J. W. Barrett, J. Kawamura,
R. L. Leombruno, S. Paine, D. C. Papa and X. Zhang**
Harvard-Smithsonian Center for Astrophysics,
60, Garden Street, Cambridge, MA 02138, USA

J. A. Stern, H. G. LeDuc and B. Bumble
Center for Space Microelectronics Technology,
Jet Propulsion Laboratory,
California Institute of Technology,
Pasadena, CA 91109, USA

Abstract

We report on the development of a heterodyne receiver designed to cover the frequency range 400 - 500 GHz. This receiver incorporates mixer technology used in a wide band, fixed-tuned SIS receiver developed for the Submillimeter Array of the Smithsonian Astrophysical Observatory. The mixer employs a Nb SIS tunnel junction that has a current density of about 7.5 kA/cm² and is about 0.6 μm^2 in area. On-chip tuning is provided by a short inductor section followed by a microstrip transformer. Double sideband receiver noise temperatures, determined from experimental Y-factor measurements, are about 100 K across the majority of the desired operating frequency band. A single-sideband mixer, for operation at 460 and 490 GHz, has also been tested in the same receiver set-up. In this case, the receiver noise is about twice the double-sideband value.

I. Introduction

The Submillimeter Array (SMA), a six-element interferometer presently under construction by the Smithsonian Astrophysical Observatory, is designed to operate in the major atmospheric windows from below 200 GHz to above 900 GHz. In Figure 1 we show a plot of atmospheric transmission, typical of a high altitude site selected for submillimeter wavelength radioastronomy [1]. Also shown in the Figure are the rotational transitions of the CO molecule and the fine structure transitions of the Cl atom, both of considerable astrophysical interest. Heterodyne receiver development in this wavelength range has generally taken place around 115, 230, and 345 GHz.

More recently a good deal of attention has been focussed on developing receivers for higher frequency operation [2,3,4,5]. Referring to Figure 1, the frequency band 380 - 520 GHz is discontinuous for reasonable atmospheric transmission and contains two particularly interesting spectral lines, CO ($J = 4 \rightarrow 3$) and Cl ($2P^2 = {}^3P_1 \rightarrow {}^3P_0$) at 461.0408 GHz and 492.1607 GHz, respectively. While it is generally desirable for a radioastronomy receiver to cover as wide a frequency range as possible, it is essential that high efficiency operation at these frequencies be provided. Furthermore, single side band (SSB) receiver operation may offer some advantages over double side band (DSB) operation, both in terms of reducing excess atmospheric noise and the strength of unwanted spectral lines from the image sideband.

II. Mixer design

The mixer block, shown schematically in Figure 2, is made in two pieces: a corrugated horn feed, and a shorted section of reduced-height waveguide. The fused quartz substrate carrying the SIS tunnel junction is sandwiched between the two pieces in a suspended configuration. The suspended stripline circuit containing the SIS tunnel junction and low-pass filter structures for IF output and dc bias faces the corrugated horn feed.

The waveguide dimensions, shown in Figure 2, were determined by simply scaling those of an existing lower frequency mixer [6]. The length of the shorted section of waveguide was determined experimentally to be 0.16 mm for wideband DSB operation and 4.43 mm for SSB operation at 461 and 492 GHz. The dimensions of the suspended stripline filter, shown in Figure 3a, were also determined by simple scaling from the lower frequency unit.

The SIS tunnel junctions used in this work were fabricated using standard Nb trilayer technology developed at the Jet Propulsion Laboratory. In order to achieve the required junction size, $\sim 0.7 \mu\text{m}^2$, e-beam lithography was used [7]. For wideband operation a thin film microstrip matching network was inserted between the center of the suspended stripline filter and the SIS tunnel junction. This consists of a two-section impedance transformer followed by a short inductive line, and is shown in Figure 3a. Shown in Figure 3b is the calculated match between the 35Ω impedance presented by the waveguide circuit and an SIS junction with nominal characteristics ($R_N \sim 22 \Omega$, $A \sim 0.7 \mu\text{m}^2$, $J_C \sim 10 \text{ kAcm}^{-2}$). From the Figure, a reasonably good match, better than -12 dB, is obtained over 120 GHz bandwidth.

III. Receiver noise measurements

In all receiver noise measurements, the mixer was cooled in a liquid helium filled cryostat equipped with a liquid nitrogen cooled radiation shield. Signal input to

the mixer was via a 0.5 mm thick room-temperature Teflon vacuum window and a 1.2 mm thick Zitex film, cooled by the radiation shield, that acted as an infrared block [8]. A Teflon lens, cooled to 4.2 K, provided additional infrared filtering. Local oscillator (LO) power was provided by a Gunn oscillator and solid-state frequency multipliers, and was coupled to the receiver via either a Martin-Puplett interferometer or a simple wire grid polarizer. The intermediate frequency (IF) was 5 GHz, and the IF bandwidth, either 1 or 2.5 GHz, was selected using filters external to the cryostat. In all cases, the receiver noise was calculated from Y-factor measurements using room-temperature and liquid nitrogen cooled loads at 295 K and 77 K respectively, and no corrections were made for losses in front of the receiver.

IV. Double sideband receiver performance

In Figure 4 we show the receiver noise temperature, measured over a 2.5 GHz instantaneous bandwidth, for three different SIS junctions cooled to 4.2 K in the same mixer block. In each case the integrated microstrip tuner was identical, but the junction area and normal resistance, were varied from 0.65 to 0.5 μm^2 and 40 to 50 Ω , respectively. A Martin-Puplett interferometer was used to couple LO and signal to the receiver. From the Figure, the receiver noise is approximately 150 K over about 100 GHz bandwidth and the region of low receiver noise extends to higher frequencies as the junction area is reduced. Recalling that the nominal mixer design calls for an SIS junction with $A \sim 0.65 \mu\text{m}^2$ and $R_N \sim 22 \Omega$, these results are encouraging.

In Figure 5, the receiver noise is plotted, for two IF bandwidths, as a function of LO frequency from about 350 to 500 GHz. For the 2.5 GHz IF bandwidth the receiver noise is approximately 130 K from about 350 to 500 GHz. The receiver noise is about 20 K lower for the reduced IF bandwidth (1 GHz). This reduction is due to a small reduction in IF amplifier noise and a reduction in input noise from the Martin-Puplett interferometer used to combine signal and LO. In Figure 6 we display current-voltage and IF response curves, measured at selected LO frequencies, for the same receiver configuration with an SIS junction with improved characteristics. At each frequency, the Josephson currents were easily suppressed by the application of a small magnetic field.

V. Single sideband receiver performance

In radioastronomy, particularly for single-dish spectral line observations, SSB receiver operation is often preferred. This is usually achieved through mechanical means: by tuning an SSB filter placed at the receiver input or by detuning the mixer backshort. We have built a fixed tuned SSB receiver for observing the spectral lines CO ($J = 4 \rightarrow 3$) and CI ($2P^2 = {}^3P_1 \rightarrow {}^3P_0$) (at 461.0408 GHz and 492.1607 GHz, respectively) using the latter approach. In this case the length of the shorted section of waveguide that acts as a fixed backshort tuner was calculated to be 4.42 mm, and

experimentally determined to be 4.43 mm. Figure 7a shows the raw interferogram of the SSB receiver when coupled to a Fourier Transform Spectrometer (FTS) designed for use in the 200 - 2000 GHz frequency range. The Fourier transform of this, giving the receiver response as a function of input frequency, is shown in Figure 7b. Clearly the receiver responds well to signals at 461 and 492 GHz and offers reduced response to 471 and 502 GHz, the corresponding image frequencies for lower sideband operation for our receiver IF of 5 GHz.

We have measured the lower sideband to upper sideband gain ratio $G_{\text{LSB}}/G_{\text{USB}}$ of this receiver, over the frequency range 450 to 500 GHz, using a Martin-Puplett interferometer as an SSB filter. This is a laborious process, as each data point requires tuning of the receiver LO, and calibration and tuning of the SSB filter. The results of these measurements are given in Figure 8. Also shown in the Figure are the sideband gain ratios calculated directly from the receiver's FTS response shown in Figure 7b. Clearly there is excellent agreement between the measured data and that calculated from the FTS response. Referring to Figure 8, the sideband gain ratio $G_{\text{LSB}}/G_{\text{USB}} \sim 7$ indicates that LSB operation is preferred at LO frequencies of 466 and 497 GHz.

In order to compare SSB and DSB receiver performance, we have determined the receiver noise from Y-factor measurements made using the same SIS junction in the two receiver configurations. A wire grid polarizer was used to combine LO and signal at the receiver input. Figure 9 shows the receiver noise data obtained from measurements over a 1 GHz IF bandwidth. From the Figure, the SSB receiver noise is approximately twice that of the DSB receiver for LO frequencies of 466 and 497 GHz. For a perfectly transparent atmosphere, spectral line observations of CO ($J = 4 \rightarrow 3$) and CI ($2P_2 = {}^3P_1 \rightarrow {}^3P_0$) made with either receiver offer approximately equal sensitivity. However, the SSB receiver has the advantage of reducing the intensity of spectral lines falling in the image sidebands. For an atmosphere with significant attenuation in the image sidebands, the SSB receiver also offers an improvement in sensitivity over the DSB equivalent.

VI. Summary

We have developed a fixed-tuned SIS receiver for the frequency range 350 to 500 GHz. This receiver combines high sensitivity with wide IF bandwidth. A single sideband version of this receiver offers improved performance for spectral line observations of CO ($J = 4 \rightarrow 3$) and CI ($2P_2 = {}^3P_1 \rightarrow {}^3P_0$) at 461 GHz and 492 GHz respectively.

Acknowledgement

We thank M. J. Smith for his superior technical assistance in developing the mixers used in this work.

References.

- [1] R. N. Martin, P. A. Strittmatter, J. H. Black, W. F. Hoffman, C. J. Hogan, C. J. Lada, and W. L. Peters, *in: "A proposal to the National Science Foundation for partial funding of the Submillimeter Telescope,"* University of Arizona, Steward Observatory, 1989.
- [2] R. Blundell, and C.-Y. E. Tong, "Submillimeter receivers for radioastronomy," *Proc. IEEE*, vol. 80, pp. 1702-1720, 1992.
- [3] J. W. Kooi, C. K. Walker, H. G. LeDuc, P. L. Schaffer, and T. G. Phillips, "A low noise 565 - 735 GHz SIS waveguide receiver," *in: Proc. 5th Int. Symp. Space Terahertz Tech.*, Ann Arbor, MI, pp. 126-141, 1994.
- [4] Zmuidzinas, H. G. LeDuc, J. A. Stren, and S. R. Cypher, "Two junction tuning circuits for submillimeter SIS mixers," *IEEE Trans. Microwave Theory Tech.*, vol. MTT-42, pp. 698-706, 1994.
- [5] G. de Lange, J. J. Kuipers, T. M. Klapwijk, R. A. Panhuyzen, H. van de Stadt, and M. W. M. de Graauw, "Superconducting resonator circuits at frequencies above the gap frequency," *J. App. Phys.*, vol. 77, pp. 1795-1804, 1995.
- [6] R. Blundell, C.-Y. E. Tong, D. C. Papa, R. L. Leombruno, X. Zhang, S. Paine, J. A. Stern, H. G. LeDuc and B. Bumble, "A Wideband Fixed-Tuned SIS Receiver for 200 GHz Operation," *in: Proc. 5th Int. Symp. Space Terahertz Tech.*, Ann Arbor, MI, pp. 27-37, 1994.
- [7] H. G. LeDuc, B. Bumble, S. R. Cypher, A. J. Judas, and J. A. Stern, "Submicron area Nb/AlOx/Nb tunnel junctions for submillimeter mixer applications," *in: Proc. 3rd Int. Symp. Space Terahertz Tech.*, Ann Arbor, MI, pp. 408-418, 1992.
- [8] Zitex A, a product of Norton Performance Plastics, Wayne, NJ.

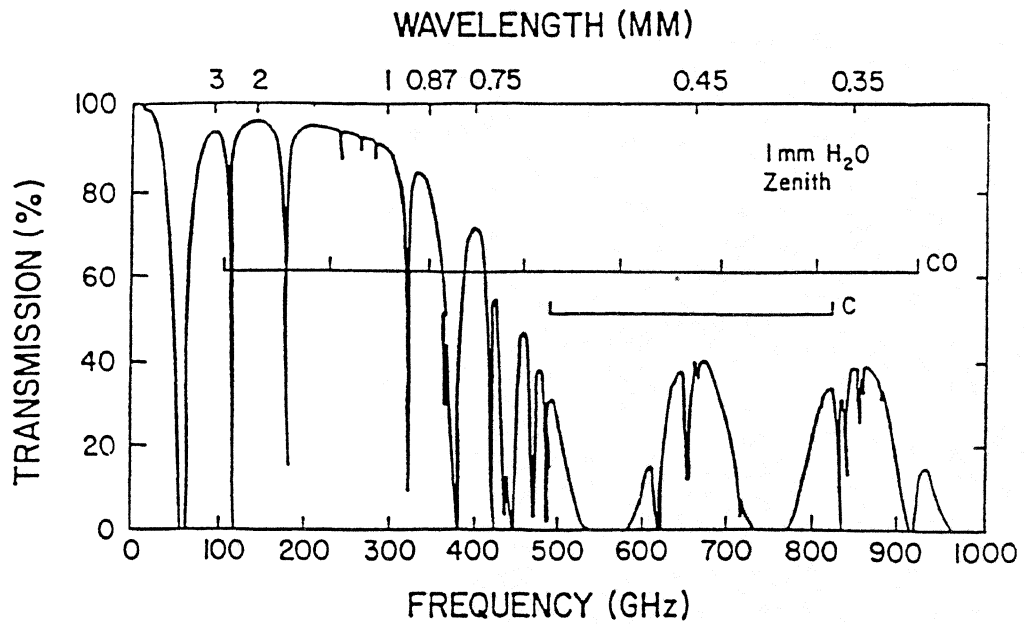


Figure 1: Atmospheric transmission at millimeter and submillimeter wavelengths from the altitude of Mt. Graham (Arizona, USA) for 1mm precipitable water along the line of sight.

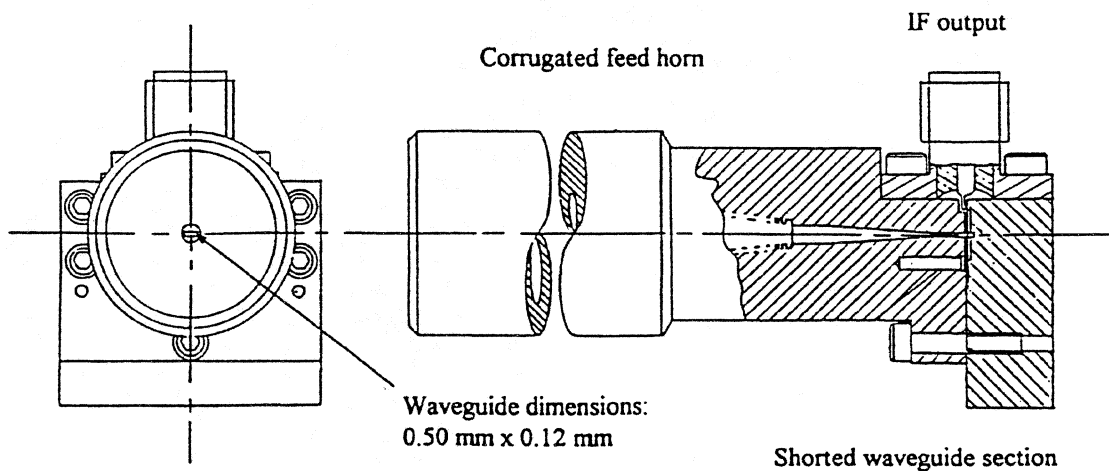


Figure 2: Mixer block detail showing the corrugated horn feed and the shorted section of reduced-height waveguide.

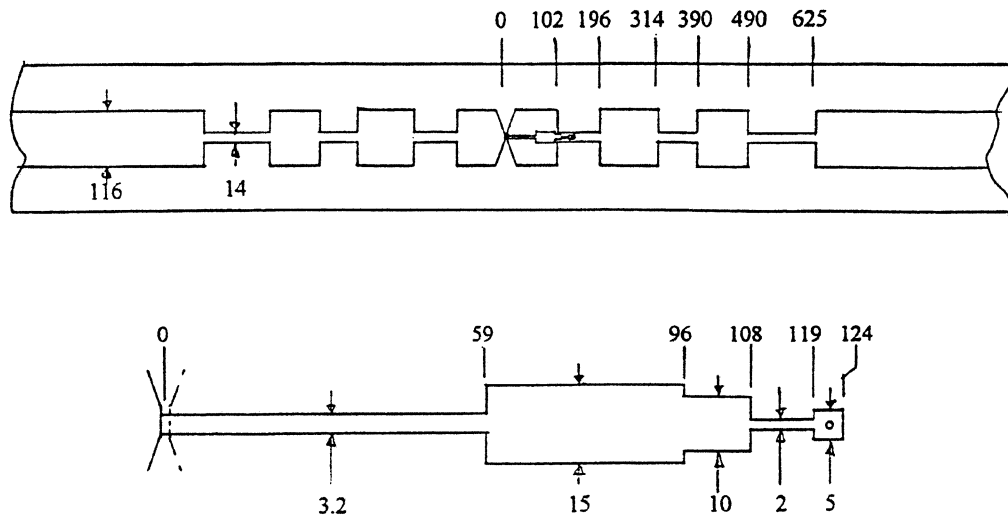


Figure 3a: Layout of the suspended stripline filter and the thin film microstripline matching network showing the SIS junction, the short inductive line and the two-section impedance transformer (dimensions in microns).

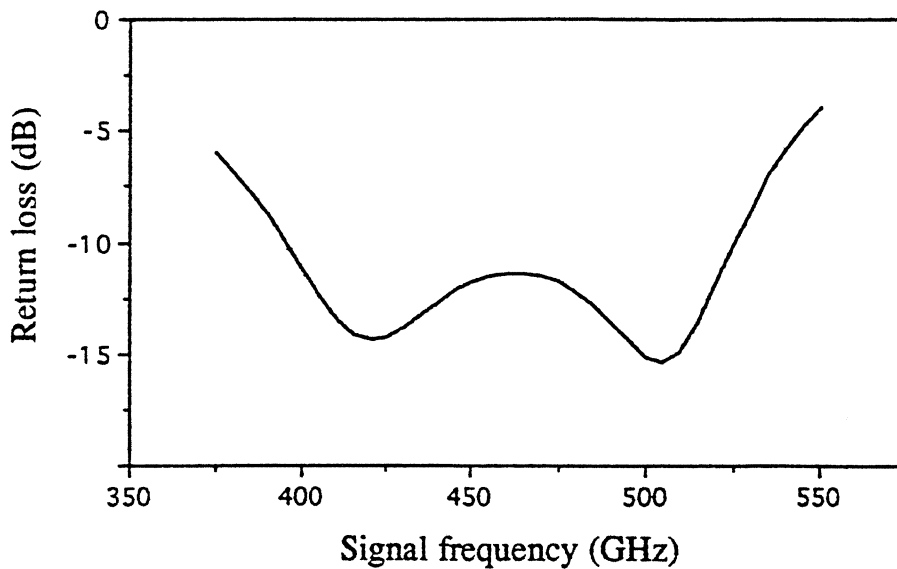


Figure 3b: Calculated match between the SIS junction and waveguide embedding circuit.

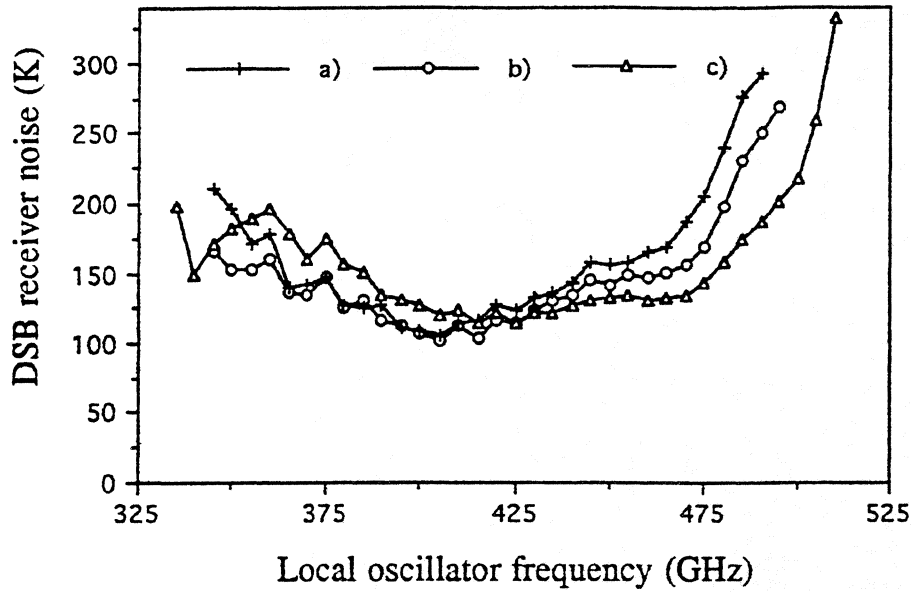


Figure 4: The DSB receiver noise is plotted as a function of LO frequency for a receiver with a mixer using SIS junctions of different sizes: a) $0.65 \mu\text{m}^2$, b) $0.58 \mu\text{m}^2$, c) $0.5 \mu\text{m}^2$.

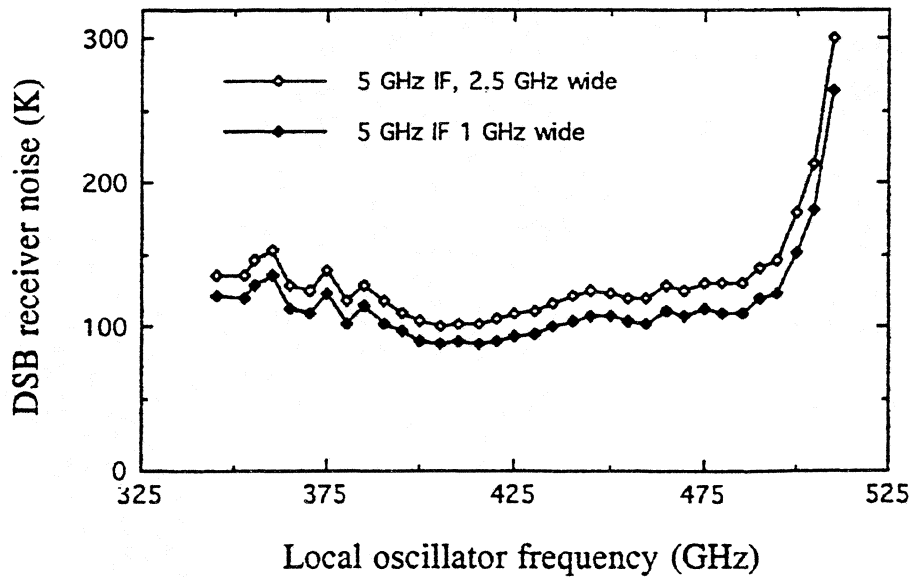


Figure 5: The DSB receiver noise as a function of LO frequency for two IF bandwidths.

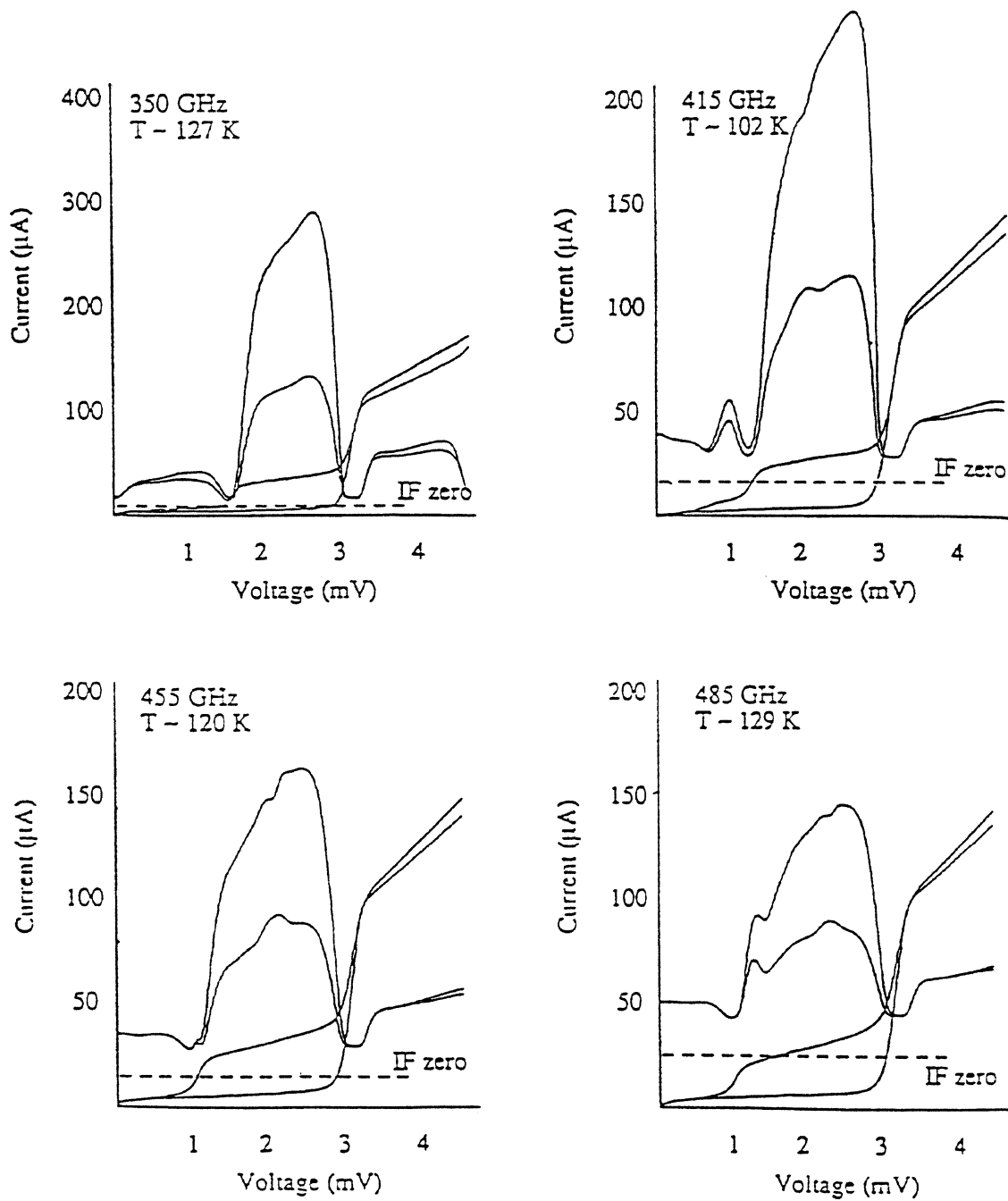


Figure 6: Current-voltage curves, pumped and unpumped, are given as a function of LO frequency. Also shown is the receiver's response to hot, 295 K, and cold, 77 K, input loads.

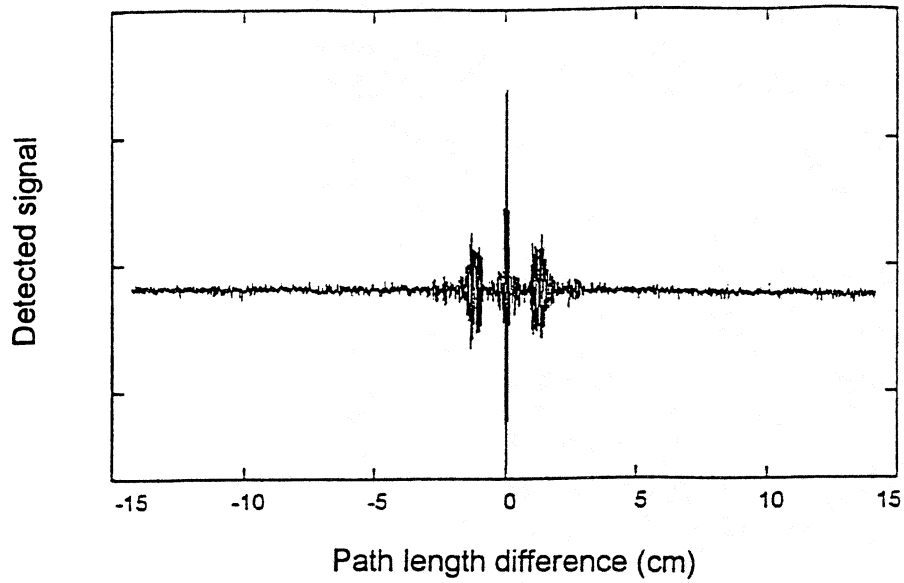


Figure 7a: FTS output interferogram of the SSB mixer receiver.

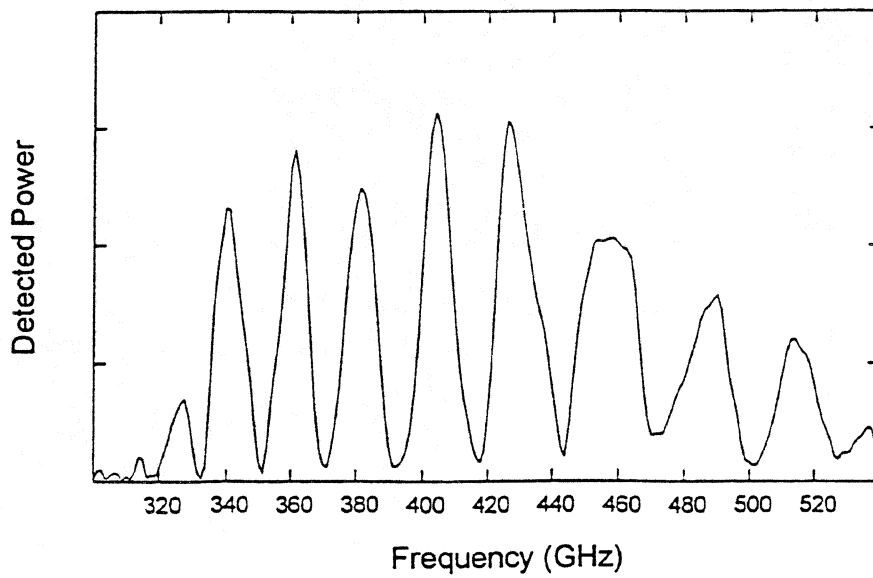


Figure 7b: Corresponding receiver response as a function of signal frequency.

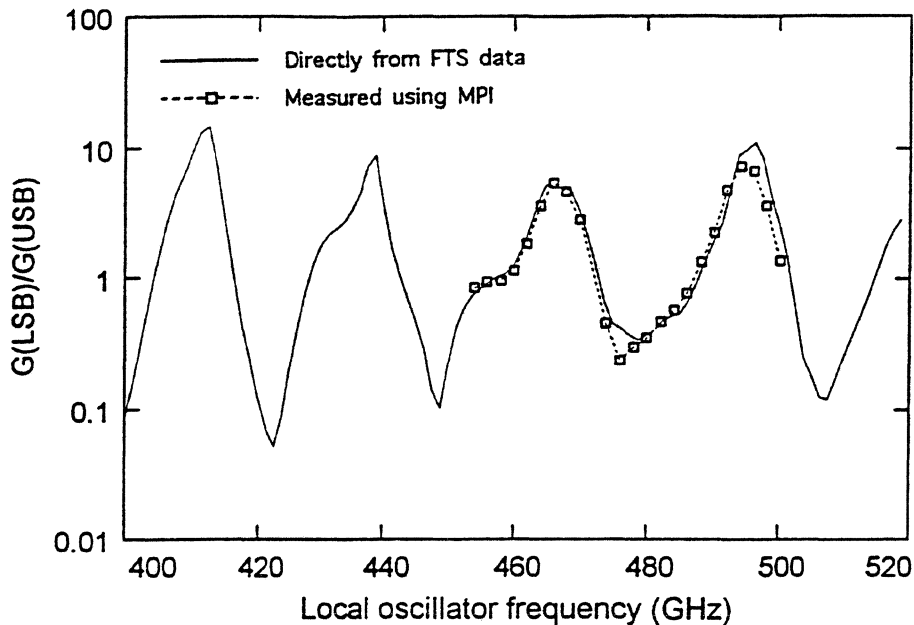


Figure 8: LSB to USB gain ratio as a function of LO frequency for the SSB receiver.

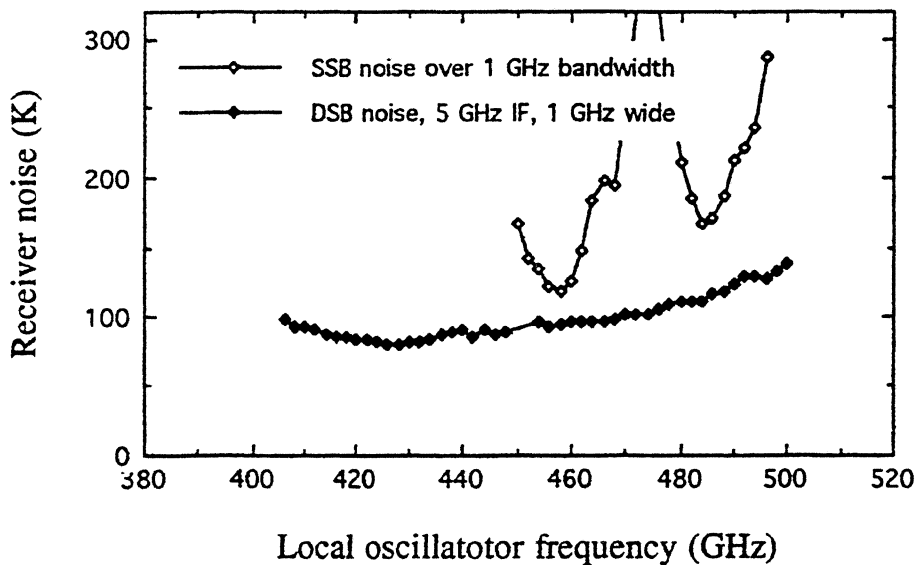


Figure 9: SSB and DSB receiver noise, calculated from Y-factor measurements, as a function of LO frequency from SSB and DSB mixers using the same SIS junction.

An Integrated SIS Mixer and HEMT IF Amplifier

S. Padin, D.P. Woody, J.A. Stern, H.G. LeDuc,
R. Blundell, C.-Y.E. Tong and M.W. Pospieszalski

Abstract— Design details are given for a 205-270 GHz fixed-tuned SIS receiver in which the SIS mixer and HEMT IF amplifier are integrated into a single compact unit. The mixer and IF amplifier are connected with an inductor which provides the reactive part of the optimum input impedance for the HEMT. This simple coupling circuit gives an IF bandwidth of ~ 4 GHz. The receiver has a DSB noise temperature in the range 35-80 K over the 205-270 GHz local oscillator band and 0.5-4.5 GHz IF band.

I. INTRODUCTION

In a millimeter-wave SIS receiver, the SIS mixer and HEMT IF amplifier are usually separate units connected with a $50\ \Omega$ coaxial line. The mixer is attached to the 4 K stage of a refrigerator while the IF amplifier is typically mounted ~ 10 cm away on the 12 K stage [1, 2, 3]. The mixer may have an isolator at its IF port or a matching network which transforms the mixer IF port impedance to $50\ \Omega$ [4]. The IF amplifier also has a matching network which transforms $50\ \Omega$ to the optimum input impedance for a HEMT [5].

SIS mixers usually operate with conversion loss so the IF contribution to the receiver noise is significant. IF amplifier noise temperatures increase roughly linearly with frequency and low-noise amplifiers typically have bandwidths of about an oc-

tave [6]. This leads to a compromise between receiver noise and IF bandwidth which is responsible for the popularity of the 1-2 GHz IF band. Increasing the receiver IF bandwidth requires the development of either a wideband low-noise IF amplifier or a mixer with enough gain to precede a noisier amplifier. The first approach is difficult because it requires a low-loss network to simultaneously match a HEMT input to $50\ \Omega$ and provide the optimum input impedance for the HEMT over a bandwidth of several octaves. Increasing the mixer gain also causes problems because SIS mixers with gain tend to saturate [7].

We have explored a new approach in which the SIS mixer and first IF amplifier are integrated into a single unit with a very simple coupling network between the two circuits. In this case there is no impedance transformation through $50\ \Omega$. The mixer is designed to provide an IF port impedance that is real and equal to the real part of the optimum input impedance for a HEMT at a particular IF. The imaginary part of the required input impedance is provided by an inductor. This simple coupling network provides the HEMT with a generator impedance which is close to the minimum noise impedance (Z_{opt}) over a wide range of frequencies. In the standard receiver configuration the coupling network contains a coaxial line and this severely limits the bandwidth of "noise matching" of the SIS junction and HEMT.

The simple coupling circuit in the integrated receiver has lower loss than the isolator, $50\ \Omega$ line and IF amplifier input matching network in the standard receiver configuration. This reduces the IF contribution to the receiver noise in the integrated receiver. Also, in the integrated receiver the IF amplifier is cooled to 4 K which gives some improvement in noise compared with a receiver where the IF amplifier is at 12 K. Integrating the mixer and IF amplifier substantially reduces the size of the receiver and this is an important advantage for multiple receiver systems such as dual polarization receivers and focal plane arrays. The main disadvantage of the integrated approach is that the mixer and IF amplifier

This work was supported by the National Science Foundation under Grant AST 93-14079 and by NASA Grant NAGW 4030.

S. Padin and D.P. Woody are with the California Institute of Technology, Owens Valley Radio Observatory, Big Pine, CA 93513 USA.

J.A. Stern and H.G. LeDuc are with the Jet Propulsion Laboratory, California Institute of Technology, Pasadena, CA 91109 USA.

R. Blundell and C.-Y.E. Tong are with the Harvard-Smithsonian Center for Astrophysics, Cambridge, MA 02138 USA.

M.W. Pospieszalski is with the National Radio Astronomy Observatory, Charlottesville, VA 22903 USA.

cannot be tested separately with the correct load and source impedances. As a result, the development of an integrated receiver relies heavily on modelling. We used programs written by Wengler [8] to calculate admittance and noise parameters for the SIS junction and the MMICAD [9] microwave circuit design program was used to model the integrated receiver.

II. SIS MIXER



Figure 1 – Photograph of the mixer section of the integrated receiver. This is a split block with a fixed backshort in one half and a transition to the feedhorn in the other. The photograph shows the backshort block with the mixer chip suspended in a channel across the waveguide. The waveguide dimensions are 9.2 x 37 mil. The block was made in a Tree 325 CNC milling machine [17] and the waveguides were punched in the same machine using a rectangular titanium-nitride-coated high-speed-steel die.

The SIS mixer is a copy of a 176-256 GHz mixer designed by Blundell [10] but scaled for a center frequency of 245 GHz. It is a fixed-tuned waveguide design with a corrugated feedhorn and a single SIS junction. The junction is fabricated on a thin-film chip which is suspended across the waveguide as shown in Fig. 1. The chip has a waveguide to microstrip transition and a 3-section microstrip transformer which is designed to present the SIS junction with the optimum impedance for minimum noise. The original mixer achieved a DSB noise temperature of 30-40 K over the 180-250 GHz band at 1.5 GHz IF with a $1.3 \mu\text{m}^2$ 7.5 kAcm^{-2} SIS junction with a normal state resistance of 22Ω .

Bias for the SIS junction is provided through a 45 nH spiral chip inductor connected to the mixer IF port as shown in Fig. 2. The inductor is mounted

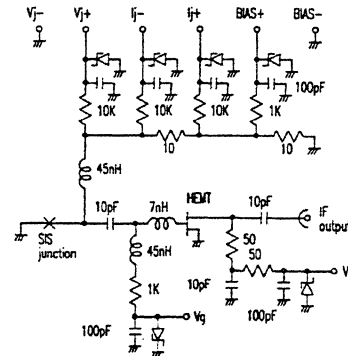


Figure 2 – Circuit diagram of the integrated receiver.

on a 50 mil thick quartz slab to move its parallel resonant frequency above the top of the IF band. The bias network has differential connections for voltage and current monitoring and provides 20Ω shunt resistance across the SIS junction to prevent the bias supply from oscillating when the junction has negative resistance.

For the integrated receiver work, the SIS junction was modelled as a 3-port device (signal, image and IF ports) with admittance and noise parameters computed from a typical I-V curve. MMICAD can only handle 2-port noise parameters so the 3-port junction was synthesized from a triangular array of 2-ports. The mixer model consists of the junction, an image termination, a transformer to simulate the signal port impedance and an IF port circuit which contains the junction capacitance, the various microstrip and suspended stripline sections on the thin film chip and the bias network. The model is primarily a description of the mixer at IF but it can also be used to investigate different signal and image port impedances. For double sideband operation, an SIS junction with a normal state resistance of 22Ω has optimum signal and image port impedances of $\sim 13 \Omega$. The corresponding IF port impedance is $\sim 200 \Omega$ which is close to the real part of the optimum input impedance for a $200 \mu\text{m}$ HEMT at L-band.

III. IF AMPLIFIER

The IF amplifier is a HEMT with very simple input and output networks as shown in Fig. 2. The input network is just a dc blocking capacitor and a 7 nH spiral chip inductor. This inductor and the mixer IF port resistance provide close to the optimum in-

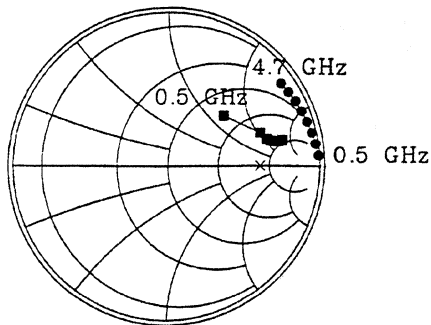


Figure 3 – The impedance presented to the HEMT gate in the integrated receiver (squares) and the optimum input impedance for best noise for an FHR02X HEMT (circles). The points are at 600 MHz intervals. The cross indicates the mixer IF port impedance for an SIS junction with a normal state resistance of 22Ω and the optimum signal impedance. All the calculations were made using MMICAD with an integrated receiver model including parasitics for the chip components and wirebonds. The HEMT model was developed by Pospieszalski [18].

put impedance for the HEMT. The bandwidth of the amplifier is determined by the inductor which forms a low-pass filter with the HEMT gate capacitance. A $200 \mu\text{m}$ HEMT has a gate capacitance of $\sim 200 \text{ fF}$ so a 7 nH gate inductor gives a bandwidth of $\sim 4 \text{ GHz}$. Fig. 3 shows model calculations of the optimum input impedance for an FHR02X $200 \mu\text{m}$ HEMT [11] and the impedance presented to the HEMT gate in the integrated receiver. The impedance at the HEMT gate is slightly less reactive than optimum but a 7 nH inductor gives a good compromise between IF amplifier bandwidth and noise. Below $\sim 500 \text{ MHz}$, the increasing reactance of the dc blocking capacitor reduces the gain of the IF amplifier and moves the HEMT input impedance far from optimum. With just a single inductor at the HEMT gate, deviations from optimum input impedance increase with the mixer IF port capacitance. To reduce this capacitance, the dc blocking capacitor and chip inductor are mounted on a 50 mil quartz slab (which also supports 45 nH inductors for the SIS junction and HEMT gate bias circuits). The mixer IF port capacitance is then dominated by the microstrip transformers on the mixer chip. The quartz slab also serves as a thermal shunt to prevent the HEMT from heating the SIS junction. The HEMT

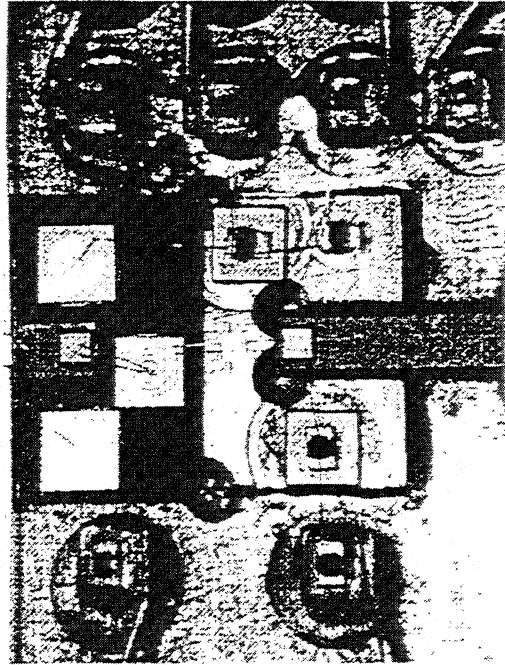


Figure 4 – Photograph of the IF section of the integrated receiver. The HEMT is glued to the pedestal in the center of the photograph. On the left is the 50-mil thick quartz slab which carries the input network and the 45 nH inductors in the bias circuits. The SIS junction bias circuit is at the top of the photograph and the HEMT bias circuit is at the bottom. The small black chips with metallized pads at each end are resistors. These have a wrap-around contact on one side so they can be glued directly to chip capacitors or to the block.

drain has a 50Ω shunt resistor which guarantees unconditional stability and provides a convenient connection for the drain bias. The source is connected directly to ground with short wirebonds.

The IF amplifier and SIS junction bias network are built on a separate sub-block in the integrated receiver. This is shown in Fig. 4. The chip components are soldered to the block or glued with conductive epoxy and connected with 1 mil aluminium wirebonds. Wirebonded chip construction was chosen to minimize parasitics with a view to making the integrated receiver model easier to construct and more accurate. The IF sub-block can be tested in a 50Ω system and while this presents a lower impedance than the mixer IF port the test provides a useful comparison with the IF section of the re-

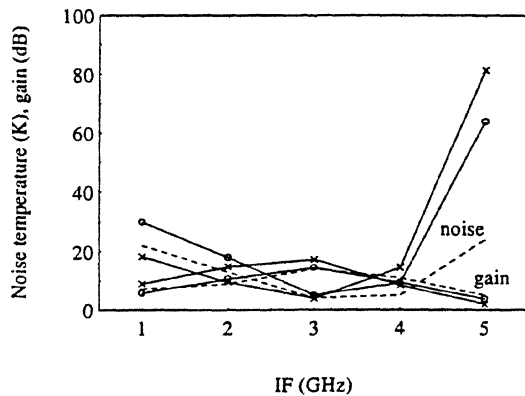


Figure 5 – IF block gain and noise temperature measured with 50Ω input impedance. The circles are for an FHR02X $200 \mu\text{m}$ GaAs HEMT and the crosses are for a $300 \mu\text{m}$ InP HEMT. Noise and gain measurement errors are ~ 2 K and ~ 0.2 dB. The dotted lines are model predictions for an FHR02X HEMT.

ceiver model. To facilitate testing, a plate with a coaxial connector can be attached to the IF sub-block in place of the mixer. Fig. 5 shows the gain and noise temperature for IF blocks with FHR02X and $300 \mu\text{m}$ InP [12, 13] HEMTs along with predictions from the receiver model. The measurements were made at 12 K using a cooled 20 dB attenuator at the input of the IF block [5]. The IF block can also be tested using shot noise from the SIS junction biased above the gap [2]. This yields the amplifier noise temperature with an input impedance equal to the junction normal state resistance ($\sim 22 \Omega$) and provides another test of the receiver model.

IV. INTEGRATED RECEIVER PERFORMANCE

The integrated receiver was tested at 4.2 K in a cryostat with a closed-cycle helium refrigerator [14]. The cryostat has an expanded polyethylene vacuum window and an expanded styrofoam infra-red block. Local oscillator signals were injected using a 1-mil thick mylar beamsplitter. Noise temperature measurements were made using room and liquid nitrogen temperature loads. The receiver gain and 2nd IF amplifier noise contribution were obtained from additional measurements with room and liquid nitrogen temperature coaxial loads at the input to the 2nd IF amplifier.

Fig. 6 shows the noise temperature and gain for several different integrated receivers at 3 GHz IF.

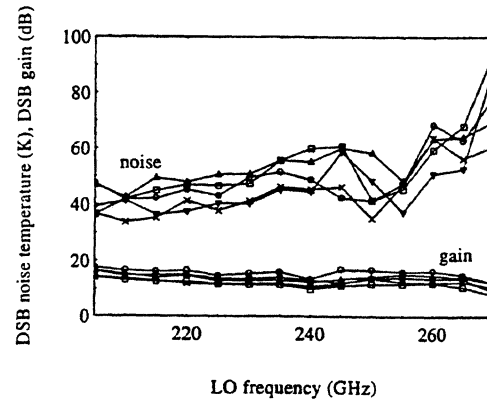


Figure 6 – Noise temperature and gain for several different integrated receivers at 3 GHz IF. The circles indicate a receiver with a $300 \mu\text{m}$ InP HEMT. All the other receivers have FHR02X HEMTs. The noise contribution from the 2nd IF amplifier has been subtracted and noise and gain measurement errors are ~ 5 K and ~ 0.2 dB.

The noise temperature increases from about 35 to 80 K across the 205-270 GHz band. Measurements of the IF output power with hot and cold loads at the receiver input and different local oscillator power levels were used to calculate the noise contribution due to optical and RF coupling losses [15]. For all the receivers measured, the input noise is ~ 20 K at 230 GHz. Fig. 7 shows the receiver noise temperature and gain across the IF band for receivers with FHR02X and InP HEMTs. The receiver with an InP HEMT has approximately flat gain and noise at IFs down to ~ 0.5 GHz but the receiver with an FHR02X HEMT shows a significant increase in noise at the bottom of the IF band. This is because the mixer IF port resistance is much lower than predicted so at low IF the impedance presented to the HEMT gate is far from optimum. Fig. 8 shows typical I-V curves for a receiver. On the 1st photon step, where the junction is generally biased, the resistance is only $\sim 80 \Omega$ instead of the expected $\sim 200 \Omega$. As a result, the IF amplifier noise is similar to that measured with a 50Ω input instead of being roughly constant across the IF band. Fig. 5 shows much better performance for an InP HEMT IF amplifier with a 50Ω input and this explains the lower noise temperature at low IF for the receiver with the InP HEMT. The low mixer IF port resistance is probably caused by a signal impedance that is not optimum.

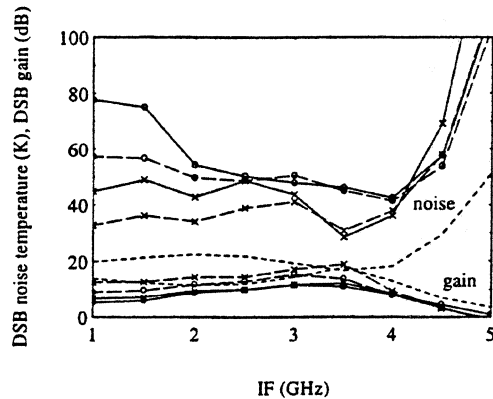


Figure 7 - Receiver noise temperature and gain across the IF band at 230 GHz (circles) and 250 GHz (crosses). The solid lines are for an FHR02X HEMT and the dashed lines are for a 300 μm InP HEMT. The same mixer was used for all the measurements so these results provide a direct comparison of the different IF amplifiers. The noise contribution from the 2nd IF amplifier has been subtracted and noise and gain measurement errors are ~ 5 K and ~ 0.2 dB. The dotted lines are model predictions. Note that these do not include the mixer input loss which contributes ~ 20 K at 230 GHz.

V. CONCLUSIONS

We have demonstrated an integrated SIS mixer and HEMT IF amplifier with good noise performance over a 4-GHz IF bandwidth. In addition to being sensitive, the receiver is fixed-tuned, small and easy to construct, all of which are big advantages for systems with many receivers. The present version of the integrated receiver has just a single IF stage so the gain is small and the receiver must be followed by a low-noise amplifier. A second integrated IF stage could be included and the inter-IF coupling network designed to compensate the passband variations in the single IF stage receiver. The IF bandwidth could also be increased further. This would require a smaller HEMT with a lower gate capacitance to increase the cut-off frequency of the low-pass filter at the IF amplifier input. Providing the optimum input impedance for the smaller HEMT would require a mixer with a very low IF port capacitance so the tuning structures would not use microstrip. With a 50 μm InP HEMT and a coplanar waveguide mixer chip designed by Kerr [16], our receiver model predicts an IF bandwidth of ~ 8 GHz.

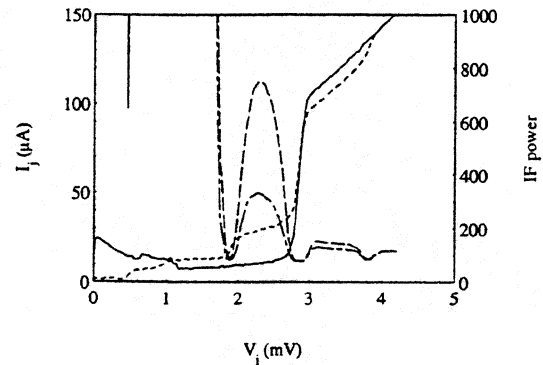


Figure 8 - I-V and IF power curves for a typical integrated receiver. The solid line is the dc I-V response of the unpumped SIS junction and the dotted line is for the junction pumped at 230 GHz with the optimum local oscillator power for minimum noise. The junction normal state resistance is 25Ω and the resistance on the first photon step is 79Ω . The dashed lines show the IF response (arbitrary units) at 1.5 GHz with room temperature (295 K) and cold (74 K) loads.

REFERENCES

- [1] B.N. Ellison, P.L. Schaffer, W. Schaal, D. Vail and R.N. Miller, "A 345 GHz Receiver for Radio Astronomy," *Int. J. IR & MM Waves*, vol. 10, pp.937-948, 1989.
- [2] D.P. Woody, R.E. Miller and M.J. Wengler, "85-115 GHz Receivers for Radio Astronomy," *IEEE Trans. Microwave Theory Tech.*, vol. 33, no. 2, pp. 90-95, February 1985.
- [3] T.H. Buttgenbach, R.E. Miller, M.J. Wengler, D.M. Watson and T.G. Phillips, "A Broad-Band Low-Noise SIS Receiver for Submillimeter Astronomy," *IEEE Trans. Microwave Theory Tech.*, vol. 36, no. 12, pp. 1720-1726, December 1988.
- [4] J.W. Kooi, M. Chan, T.G. Phillips, B. Bumble and H.G. LeDuc, "A Low Noise 230 GHz Heterodyne Receiver Employing $0.25 \mu\text{m}^2$ Area Nb/ AlO_x /Nb Tunnel Junctions," *IEEE Trans. Microwave Theory Tech.*, vol. 40, no. 5 pp. 812-815, May 1992.
- [5] S. Padin and G.G. Ortiz, "A Cooled 1-2 GHz Balanced HEMT Amplifier," *IEEE Trans. Mi-*

- crowave Theory Tech.*, vol. 39, no. 7, pp. 1239-1243, July 1991.
- [6] M.W. Pospieszalski, "Ultra-Low-Noise Receivers for the 1 to 120 GHz Frequency Range," *Proc. 23rd European Microwave Conference*, 1993, pp. 73-79.
- [7] J.R. Tucker and M.J. Feldman, "Quantum Detection at Millimeter Wavelengths," *Rev. Mod. Phys.*, vol. 57, no. 4, pp. 1055-1113, October 1985.
- [8] M.J. Wengler, "Heterodyne Detection with Superconducting Tunnel Junctions," Ph.D. thesis, California Institute of Technology, Pasadena, June 1987.
- [9] Optotek Ltd., Kanata, Ontario, K2K 2A9, Canada.
- [10] R. Blundell, C.-Y.E. Tong, D.C. Papa, R.L. Leombruno, X. Zhang, S. Paine, J.A. Stern, H.G. LeDuc and B. Bumble, "A Wideband Fixed-Tuned SIS Receiver for 200 GHz Operation," *Proc. Fifth Int. Symp. Space Terahertz Tech.*, 1994, pp. 27-37.
- [11] Fujitsu Compound Semiconductor Inc., San Jose, CA, 95131, USA.
- [12] M.W. Pospieszalski, L.D. Nguyen, M. Lui, T. Liu, M.A. Thompson and M.J. Delaney, "Very Low Noise and Low Power Operation of Cryogenic AlInAs/GaInAs/InP HFETs," *Proc. 1994 IEEE MTT-S Int. Microwave Symp.*, San Diego, CA, pp. 1345-1346, May 1994.
- [13] M.W. Pospieszalski, W.J. Lakatos, L.D. Nguyen, M. Lui, T. Liu, M. Le, M.A. Thompson and M.J. Delaney, "Q- and E-Band Cryogenically-Coolable Amplifiers Using AlInAs/GaInAs/InP HEMTs," *Proc. 1995 Int. Microwave Symp.*, Orlando, FL, May 1995, in press.
- [14] D.P. Woody, C.J. Giovanine and R.E. Miller, "Dual Channel 115 and 230 GHz SIS Receivers in Operation at the Owens Valley Radio Observatory," *IEEE Trans. Magnetism*, vol. 25, no. 2, pp. 1366-1370, March 1989.
- [15] R. Blundell, R.E. Miller and K.H. Gundlach, "Understanding Noise in SIS Receivers," *Int. J. IR & MM Waves*, vol. 13, no. 1, pp. 3-14, 1992.
- [16] A.R. Kerr, S.-K. Pan, A.W. Lichtenberger and D.M. Lea, "Progress on Tunerless SIS Mixers for the 200-300 GHz Band," *IEEE Microwave and Guided Wave Letters*, vol. 2, no. 11, pp.454-456, November 1992.
- [17] Tree Machine Tool Company Inc., Racine, Wisconsin, USA.
- [18] M.W. Pospieszalski, "Modelling of Noise Parameters of MESFETs and MODFETs and Their Frequency and Temperature Dependence," *IEEE Trans. Microwave Theory Tech.*, vol. 37, no. 9, pp. 1340-1350, September 1989.

On using the shot noise in SIS tunnel junctions for characterizing IF amplifiers

David Woody, Steve Padin
California Institute of Technology
Owens Valley Radio Observatory, Big Pine, CA 93513 USA

Henry LeDuc and Jeff Stern
Jet Propulsion Laboratory, California Institute of Technology, Pasadena, CA 91109 USA.

Abstract--The IF amplifier in SIS heterodyne mixers can represent a major contribution to the receiver noise. Achieving quantum limited performance of SIS receivers will require accurate measurement and characterization of this noise contribution. A standard method for in situ characterization of the IF amplifier uses the shot noise from the SIS tunnel junction biased above the gap voltage as a calibrated noise source. This provides an accurate measurement of the IF amplifier noise and gain for source impedances equal to the normal state resistance of the junction, R_n . This paper describes an extension of this technique to determine the 2-port noise and gain parameters of the IF amplifier by using the junction as a noise source over its full dc bias range. Measuring the IF output power over the full bias range (with no LO applied) samples the IF amplifier response for source impedances ranging from zero to $>10R_n$. The IF amplifier characteristics are obtained by fitting the measurements to a six parameter model of the IF amplifier system. Although there is insufficient data to accurately determine the standard noise and gain parameters, the contribution from the IF system to the receiver noise is accurately determined.

This method of characterizing the IF system references the noise and gain parameters to the plane of the tunnel junction and includes the effect of the circuitry between the junction and the IF amplifier. This is particularly useful for receivers which don't use standard 50 ohm amplifiers with cooled isolators. This paper describes the IF noise and gain model together with the fitting procedure. Examples of this technique applied to the receivers used on the Owens Valley Radio Observatory millimeter array are presented. These receivers include mixers with integrated IF transformers and mixers with integrated HEMT amplifiers.

I. Introduction

An important step in improving the performance of low noise radio astronomy receivers is identifying and quantifying the various noise contributions. Although many of the contributions can be estimated from calculations or laboratory measurements of individual components it is important to be able to make in situ measurements of the noise sources. The IF amplifier is a major source of noise in SIS heterodyne receivers and its contribution must be determined before the mixer noise and other noise sources can be evaluated. Several techniques have been developed for characterizing the IF system using specialized laboratory instrumentation such as that employed by Kerr et al. [1]. But these laboratory instruments often are not appropriate for use on operating telescopes either because of inconvenience or some sacrifice in performance necessitated by installation of special test devices. Thus it is important to develop methods for accurately measuring the IF noise in receivers using a minimum of extra equipment.

*This work was supported by the NSF under Grant AST 91-00306 and by NASA Grant NAGW 2196.

The noise in a heterodyne receiver can be written as the sum of two basic components,

$$T_{rec} = T_{rf} + T_{if}^* \quad (1)$$

T_{rf} includes the noise associated with the optical losses in front of the mixer and the mixer noise. T_{if}^* is the noise present at the mixer's IF-port even in the absence of any LO or mixing but referred to the receiver's input under normal operating conditions. It is given by

$$T_{if}^* = L(T_{if} + T_{I0}), \quad (2)$$

where L is the mixer's conversion loss, T_{if} is the noise temperature of the IF amplifier chain and T_{I0} is the noise arising from the linear component of the leakage current in the SIS tunnel junction.

One method for estimating T_{if}^* is to use lab measurements of the IF system. The conversion loss can be determined from the standard hot and cold load receiver measurements used to measure T_{rec} if the gain of the amplifier system is known and T_{if} can be measured separately using a noise test fixture. These characterizations usually apply to 50ohm source impedances and corrections based upon a circuit model must be made for non-50ohm impedances. These corrections can be significant and accurate values for the full set of 2-port noise and gain parameters are often not available. In addition the IF circuit inside the mixer block is often poorly characterized making it difficult to properly include in the circuit model.

Another method is to use the shot noise from the SIS tunnel junction biased above the gap voltage as a calibrated noise source [2]. This yields T_{if} and IF gain for a source impedance equal to the normal state resistance of the junction, including the effects of any IF circuitry in the mixer block. But you still have to estimate the change in IF parameters in going from R_n to actual IF impedance.

Blundell et al. have developed a method for determining T_{rf} using hot and cold load measurements at low LO levels [3]. This method is based upon the graphical method of determining T_{rec} by plotting the IF output power, P_{if} , as a function of load temperature, T_{load} . The hot and cold load data provide two points through which a straight line is drawn. The line intersects the $P_{if}=0$ line at $-T_{rec}$. They found that the set of lines for a series of low LO measurements crossed at a common point. The T_{load} coordinate of this point is $-T_{rf}$. This is referred to as the "intersecting lines" technique. By including the LO off case (a horizontal line) it is seen that this technique is equivalent to subtracting the P_{if} value measured with the LO off from the raw hot and cold data. The mixer noise contribution to T_{rf} is a function of the LO power and thus T_{rf} under normal operating conditions will differ from the value derived from the intersecting lines technique derived using low LO levels.

Both the junction shot noise and intersecting lines technique are easy to apply and have been successfully used for characterizing SIS receivers. This paper extends the junction shot noise calibration technique to incorporate the IF response for the junction biased over the full range from zero to above the gap voltage. The method described in this paper was used as part of a technique for separating the optical loss and mixer noise contributions to T_{rf} [4]. The theory of 2-port noise and gain characterization is applied to the IF system and a generalized formulation of the IF output noise is developed in section II. Section III describes how to derive the IF parameters from the measured data and gives examples using the 1mm receivers used by the Owens Valley Millimeter Array (OVMA). Section IV discusses how accurately these parameters are determined and in particular it is shown why the intersecting lines technique works so well. It is also shown that the LO dependence of T_{rf} can be determined using this technique.

II. Generalized Formulation of the IF output Power

A complete characterization of an IF amplifier requires measuring the four real noise parameters and the four complex S-parameters or their equivalents [5]. The typical IF amplifier chain has several amplifiers in series ending in a power detector. For such a system the load termination is fixed and the reverse gain, S12, and the phase of the forward gain, S21, can be set to zero. Thus the IF system is characterized by seven real parameters which are functions of frequency; four noise parameters, input conductance and susceptance and gain for a matched load. We will use the following standard formulation for the IF system noise temperature [6,7],

$$T_{if} = T_{\min} + T_d \frac{(G_{opt} - G_s)^2 + (B_{opt} - B_s)^2}{G_s G_{opt}}, \quad (3)$$

where $Y_s = G_s + jB_s$ is the source admittance. The IF system output power is given by

$$P_{out} = 2G_{11}g_0 \frac{\langle i_s^2 \rangle + 4kBG_s [T_{\min} + \frac{T_d [(G_s - G_{opt})^2 + (B_s - B_{opt})^2]}{G_s G_{opt}}]}{(G_s + G_{11})^2 + (B_s - B_{11})^2}. \quad (4)$$

where $\langle i_s^2 \rangle$ is the mean square source noise current and B the predetection bandwidth. $Y_{11} = G_{11} + jB_{11}$ is the input admittance for the IF chain and g_0 is the net IF gain for a matched load. The second term in the numerator is the equivalent noise current from the IF system noise.

We will define the mixer IF-port for the SIS mixer as being at the tunnel junction. The junction capacitance and other parasitics associated with the junction chip and mixer block will be included as part of the IF system. The IF-port admittance of an SIS junction will in general be real and equal to the dc differential conductance for low IF's. This is the case in the absence of RF or LO power and for double sideband receivers. At higher frequencies, determined by the sharpness of the current vs. voltage characteristics, there is a quantum susceptance which peaks at the gap voltage [8,9]. The quantum susceptance is negligible at frequencies much below $e\delta V/h$, where δV is the width of the voltage transition from the "off" to the "on" state at the gap voltage. The devices used for millimeter and submillimeter receivers have transition widths of $\sim 50\mu V$, corresponding to $e\delta V/h \sim 10\text{GHz}$. Thus the effect of the quantum susceptance at the IF-port can be neglected for SIS heterodyne receivers with IF's below $\sim 5\text{GHz}$.

Ideally, in the absence of LO or RF power, the noise current associated with quasiparticles tunneling through an SIS junction is just the shot noise associated with the dc current [8]. This has been quantitatively verified by Dubash et al. for the types of devices used for low noise heterodyne receivers [10, 11]. Extra noise can arise from the ac Josephson effect in high current density (low capacitance) junctions at low bias voltages. Another possible deviation from shot noise can occur in devices which have pin-hole shorts across the tunnel barrier. The junctions used for this work show no indications of such micro-shorts or excess noise when biased above $\sim 1.5\text{mV}$. Thus the mean square current noise is given simply by $\langle i_s^2 \rangle = 2eI_{dc}B$.

We are initially interested in the output power from the IF system in the absence of any LO or RF power. For this purpose we can set the source susceptance, B_s , equal to zero and use the shot noise formula for source current noise, then equ. 4 can be written as

$$P_{out}(G_s, I_{dc}) = g \frac{2eI_{dc} + aG_s^2 + bG_s + c}{(G_s + G_{11})^2 + B_{11}^2}. \quad (5)$$

The bandwidth, B, has been incorporated into g, e.g. $g = 2G_{11}g_0B$. The coefficients a, b, and c have the following dependence on the noise parameters;

$$a = \frac{4kT_d}{G_{opt}}, \quad (6)$$

$$b = 4k(T_{min} - 2T_d), \text{ and} \quad (7)$$

$$c = \frac{4kT_d(G_{opt}^2 + B_{opt}^2)}{G_{opt}}. \quad (8)$$

We hope to determine the six parameters G_{11} , B_{11} , g, a, b, and c by using the SIS tunnel junction as a variable conductance and variable noise source. In high quality junctions, the differential conductance varies by more than a factor of a thousand and the dc current changes by more than a factor of fifty as the bias is increased from the "off" state below the gap voltage to the "on" state above the gap voltage. The junction also serves as a perfect short when biased at zero voltage and zero current. The large range of conductance and noise current should make the SIS tunnel junction an excellent tool for probing the IF system gain and noise parameters. Measuring the IF output power as the dc bias voltage is varied from zero to well above the gap voltage should allow us to determine the six parameters by using equ. 5 to fit the data. Once the parameters are determined, then the IF noise contribution and gain can be determined for any real IF-port admittance for the SIS heterodyne receiver. The case of negative admittance can be handled with proper definition of the noise parameters, but will not be dealt with here since such mixers are notoriously noisy [12].

The three equations 6, 7 and 8 are insufficient to uniquely determine the four IF system noise parameters from the values for the coefficients a, b, and c. But physical constraints can be used to limit the range of possible values. It can be shown that $T_{min} < 4T_d$ [13] and if we force $G_{opt} > 0$ then the range of solutions to this set of equations are

$$0 \leq B_{opt} \leq \sqrt{\frac{c}{a}}, \quad (9)$$

$$\left| \frac{b}{2a} \right| \leq G_{opt} \leq \sqrt{\frac{c}{a}}, \quad (10)$$

$$\left| \frac{b}{8k} \right| \leq T_d \leq \frac{\sqrt{ac}}{4k}, \text{ and} \quad (11)$$

$$\frac{(b + |b|)}{4k} \leq T_{min} \leq \frac{b + 2\sqrt{ac}}{4k}. \quad (12)$$

It is also required that $a > 0$, $c > 0$, and $b^2 < 4ac$ for a physically a realizable IF system. Using a priori information to limit any one of the noise parameters will also limit the range of the others. You can treat B_{opt} as a free parameter and write G_{opt} , T_d , and T_{min} as functions of a, b, c and B_{opt} . Then the allowed

solutions for a given set of a , b , and c is a parametric line in the 3-dimensional space of (G_{opt}, T_d, T_{min}) . A particularly powerful constraint is to require $Y_{opt} = Y_{11}$ as is the case for systems employing cooled isolators with 50ohm transmission lines ending at the junction. The noise from an isolator cooled to 4K can be significant compared to the extremely low noise IF amplifiers currently available [14] and the IF circuitry in the mixer block can result in the power match no longer being equal to the noise match, e.g. $Y_{opt} \neq Y_{11}$.

The usefulness of this method for determining the standard noise parameters, as opposed to just the noise contribution as a function of source admittance, will depend upon the actual values of the three coefficients and what additional IF system data is available. At this point we have not dealt with how accurately the six parameters in equ. 5 can be determined from real data. These issues will be discussed in the following section.

III. Measurements on Radio Astronomy Receivers

Three examples of the measured and calculated output power vs. bias voltage are shown in fig. 1. The first example, mixer block R4/2A, is one of the standard 1mm band receivers in use on the OVMA [15]. It utilizes a backshort tuner and incorporates a 160ohm to 50ohm IF transformer [16] before feeding a 1-2GHz balanced amplifier [17]. The other two examples are from mixer block M3 which is a tunerless mixer based upon the design of Blundell et al. [18] with a .5-4.5GHz HEMT amplifier integrated into the block [19]. The middle data set is for the 1.0-1.2GHz section of the IF band while the last data set is for the 1.84-1.96GHz section of the IF band. These mixers operate in the 200-270GHz band and utilize scalar feed horns with transitions to .98x.49mm waveguide. The SIS devices are single $\sim 1\mu\text{m} \times 1\mu\text{m}$ Al-AlOx-Al tunnel junctions [20]. The device in mixer R4/2A is a simple junction without any on chip RF or IF circuitry while the junction in M3 incorporates an RF matching circuit and an RF blocking filter for the IF-port on the chip [18].

The data in fig. 1 were obtained in an automated receiver test fixture which measures the output power for ambient and liquid nitrogen temperature loads as a function of the bias voltage. Although no LO was applied there was a measurable direct detection dc current and IF response below the voltage gap at 2.9mV. The IF response is most likely a result of "self-mixing" of the thermal noise power in these broad band mixers. The absorbed power from the thermal loads can approach 1nW for mixers with large instantaneous RF bandwidths which is sufficient to produce measurable mixing of the noise with itself. This mechanism would produce a response proportional the square of the noise power. Although the effect is small, it can influence the deduced IF system parameters and the data shown in fig. 1 has been extrapolated to an effective load temperature of 0K.

A hybrid procedure is employed to fit equ. 5 to the measured IF power. The input admittance (G_{11}, B_{11}) is determined from a raster search over the Smith Chart with a linear least squares fit for g , a , b , and c at each raster point. At each raster point the data yield unique well defined values for g , a , b , and c but these values and the RMS residual vary as you move across the Smith Chart. Fig. 2 shows the contour plots of the RMS residuals for the same three data sets displayed in fig. 1. The minimum RMS residuals are 2-3% of the average IF power. The values of $G_{11}, B_{11}, g, a, b,$ and c at the minimums are used in equ. 4 to calculate the best fit IF power plotted in fig. 1.

The fit faithfully reproduces the details in the P_{if} vs. V_{dc} data over the full bias range, including the superconducting short at $V_{dc}=0$ and the structure at V_{gsp} . The measurements cover more than three decades of conductance and more than a factor of fifty in source noise current. The largest errors in the technique are a result of inaccuracies in determining the differential conductance, dI_{dc}/dV_{dc} , from the discretely sampled current and voltage data. The I_{dc} data have been smoothed to reduce the errors in calculating dI_{dc}/dV_{dc} .

Table 1
Valid ranges for IF system parameters

parameter	R4/2A	M3 1.84-1.96Ghz IF	M3 1.0-1.2Ghz IF
G ₁₁ [1/ohm]	.0006-.008	.01-.08	.008-.02
B ₁₁ [1/ohm]	0-.008	0-.06	0-.01
g [Hz/(Aohm) ²]	.0002-0004	.003-.007	.0003-.0006
G _{opt} [1/ohm]	.001-.003	.006-.06	.007-.03
B _{opt} [1/ohm]	0-.003	0-.06	0-.03
T _n [K]	2.4-25	1.1-13	7-32
T _m [K]	0-9.1	0-4.7	7-23

The fits are equally good over vertical strips in the Smith Chart which extend almost to the edges of the chart. Thus the parameter values are not accurately determined by the data. Table 1 lists the ranges of gain and noise parameter values consistent with the data without using any a priori information. The ranges given in table 1 incorporate eqs. 9-12 along with the range of parameter values within the lowest contours in fig. 2. The parameters in table 1 are consistent with the expected values derived from the IF circuit designs, in particular, the IF transformer in mixer R4/2A was designed to give a $G_{opt}=G_{11}=.006\text{mhos}$ [16] and the change in G_{opt} and G_{11} for mixer M3 between 1.1 and 1.9GHz is predicted by the MMICAD circuit model of the GaAs HEMT integrated into the mixer block. The parameters can't be separately varied within these ranges since they are interdependent, but it is clear that the standard IF gain and noise parameters are poorly determined using this method without another method for constraining some of the parameters.

IV. Discussion

The poor determination of the standard noise parameters limits the usefulness of this technique for locating minor problems in the IF circuitry but it can point to gross errors in design or fabrication. The situation is considerably improved for determining the IF system's contribution to the receiver noise. This just requires determining what fraction of the IF power originates from the IF chain. Fig. 3 plots the calculated output power as a function of G_s for several different parameter sets spanning the allowed range of parameter values. The gain and IF noise temperature have the expected dependence on G_s . But the net output power which is the product of the gain and noise temperature is relatively flat. This is a consequence of $G_{opt} \sim G_{11}$ as is the case for many IF amplifiers. Also notice that the fractional spread in net power is less than the spread in gain or noise temperature. Thus the output power from the IF system as a function of G_s is well determined despite the poor determination of the standard amplifier noise and gain parameters. The errors in determining the conversion loss and IF amplifier noise separately can be larger than a factor of two for low IF-port conductances. But their net contribution to the receiver noise can be determined to better than 20%.

The itemized contributions to the receiver noise as a function of the LO induced dc current for mixer M3 operating at 230GHz is shown in fig. 4. At each LO level G_s was obtained from the differential dc conductance at the bias voltage used for measuring T_{rec} . The IF output power from the leakage noise, P_{I0} , was calculated from equ. 5 using the best fit parameter values for G_{11} , B_{11} and g , $a=b=c=0$, and the value for I_{dc} at the same bias voltage with the LO off. This was normalized by the measured hot and cold load response to convert P_{I0} to an equivalent temperature at the receiver input, e.g. LT_{I0} in equ. 2. The IF amplifier contribution, LT_{IF} in equ. 2, was similarly obtained using the same G_{11} , B_{11} and g plus the best fit parameter values for a , b , and c and $I_{dc}=0$. T_{rf} was obtained by subtracting the sum of these contributions from T_{rec} .

The receiver noise temperature initially decreases with increasing LO level as the conversion efficiency improves, as expected for a receiver dominated by IF noise. T_{rf} approaches a constant values at low LO levels as expected. The optical losses are independent of LO level and the mixer noise which is inversely proportional to the quantum efficiency reaches a maximum limiting value as the LO approaches zero [21]. T_{rf} degrades as the LO level increases and the quantum efficiency (the efficiency with which incident photons are converted to quasiparticle carriers) decreases. Note that the effect of increasing mixer noise shows up before the conversion loss, L , begins to degrade and increase the contributions from the leakage current and IF amplifier noise. As seen from the flatness of the leakage and IF amplifier contributions, the conversion loss is nearly constant over a large LO range. Thus it is the mixer noise and hence the quantum efficiency which sets the upper limit on the LO for low noise performance.

The limiting value for T_{rf} is the same value obtained using the intersecting lines technique [3]. The flatness of the net IF power curves in fig. 3 explains why this technique works so well. To first order, the IF amplifier's noise contribution to the IF power is independent of the IF-port conductance. Also the IF power contributed by the shot noise in the leakage current will scale as the gain divided by G_s and thus will be relatively flat for the low IF-port conductances seen at low LO levels or with the LO off. The contribution of the IF system noise plus the leakage shot noise can be obtained by simply measuring the IF output power with the LO off. Calculating the receiver noise after subtracting this LO off power from the raw hot and cold load measurements for low LO levels then yields T_{rf} directly.

V. Summary

The gain and noise contributions of the IF system have been formulated as a function of the IF-port conductance with six free parameters. The relationship between these parameters and the standard noise and gain parameters is also derived. A procedure is described for determining the values for the six parameters from measurements of the IF output power vs. bias voltage with the LO off. The technique does not use any special equipment or setup and can be applied to any SIS heterodyne receiver. It also does not rely on the often incorrect assumption that the IF-port conductance is equal to the normal state conductance nor does it assume that the IF system contribution to the noise is the same as the noise with the LO off at the same V_{dc} .

Several examples of the procedure are given for the millimeter band receivers used on the OVMA. It is shown that although the standard noise and gain parameters are poorly determined, the net contribution of the IF amplifier noise and leakage current, T_{if}^* , to the receiver noise is accurately determined. This allows the sum of the optical loss and mixer noise, $T_{rf} = T_{rec} - T_{if}^*$, to be determined even for the case of large LO power.

References

- [1] A.R. Kerr, S.-K. Pan, M.J. Feldman, and A. Davidson, "Infinite available gain in a 115 GHz SIS mixer," *Physica* vol. 108B, pp. 1369-1370, 1981.
- [2] D.P. Woody, R.E. Miller, and M.J. Wengler, "85-115GHz receivers for radio astronomy," *IEEE Trans Microwave Theory Tech.*, vol. MTT-42, pp. 90-95, 1985.
- [3] R. Blundell, R.E. Miller, and K.H. Gundlach, "Understanding noise in SIS receivers," *Int. J. Infrared and Millimeter Waves*, vol. 13, pp. 3-14, 1992.
- [4] D. P. Woody "Measurement of the noise contributions to SIS heterodyne receivers" *IEEE Trans Microwave Theory Tech.* in press.

- [5] H. Rothe and W. Dahlke, "Theory of noisy fourpoles," *Proc. IRE*, vol. 44, pp. 811-818, 1956.
- [6] IRE Subcommittee 7.9 on Noise: "Representation of noise in linear two-port," *Proc IRE*, vol. 48, pp. 69-74, 1960.
- [7] J. Lange, "Noise characterization of linear two-ports in terms of invariant parameters," *IEEE J. Solid-State Circuits*, vol. SC-2, pp. 37-40, 1967.
- [8] J.R. Tucker, "Quantum limited detection in tunnel junction mixers," *IEEE Quant. Elect.*, vol. QE-15, pp. 1234-1258, 1979.
- [9] J.R. Tucker and M.J. Feldman, "Quantum detection at millimeter wavelengths," *Rev. Mod. Physics*, vol. 57, pp. 1055-1123, 1985.
- [10] N.B. Dubash, M.J. Wengler, and J. Zmuidzinis, "Shot noise and photon-induced correlations in 500GHz SIS detectors," *IEEE Trans Microwave Theory Tech.* in press.
- [11] N.B. Dubash, G. Pance, and M.J. Wengler, "Photon induced noise in the SIS detector," *IEEE Trans Microwave Theory Tech.*, vol. MTT-42, pp. 715-725, 1994.
- [12] L.R. D'Addario, "Noise parameters of SIS mixers," *IEEE Trans Microwave Theory Tech.*, vol. MTT-36, pp. 1196-1206, 1988.
- [13] M.W. Pospieszalski, "On the measurement of noise parameters of microwave two-ports," *IEEE Trans Microwave Theory Tech.*, vol. MTT-34, pp. 456-458, 1986.
- [14] M.W. Pospieszalski, "Ultra-low-noise receivers for the 1 to 120 GHz frequency range," *Proc. 23rd European Microwave Conference*, pp. 73-79, 1993.
- [15] D.P. Woody, C.J. Giovanine, and R.E. Miller, "Dual channel 115 and 230 GHz SIS receivers in operation at the Owens Valley Radio Observatory," *IEEE Trans Mag.*, vol. M-25, pp. 1366-1370, 1989.
- [16] J.W. Kooi, M. Chan, T.G. Phillips, B. Bumble, and H. G. LeDuc, "A low noise 230GHz heterodyne receiver employing .25 μm^2 area Nb/AlOx/Nb tunnel junctions," *IEEE Trans Microwave Theory Tech.*, vol. MTT-40, pp. 812-815, 1992.
- [17] S. Padin and G.G. Ortiz, "A cooled 1-2 GHz balanced HEMT amplifier," *IEEE Trans Microwave Theory Tech.*, vol. MTT-39, pp. 1239-1243, 1991.
- [18] R. Blundell, C.-Y.E. Tong, D.C. Papa, R.L. Leombruno, X. Zhang, S. Paine, J.A. Stern, H.G. LeDuc, and B. Bumble, "A wideband fixed-tuned SIS receiver for 200 GHz operation," *Fifth Int. Symp. Space Terahertz Tech.*, pp. 27-37, 1994.
- [19] S. Padin, D.P. Woody, J.A. Stern, H.G. LeDuc, R. Blundell, C.-Y.E. Tong, and M.W. Pospieszalski, "An integrated SIS mixer and HEMT IF amplifier," this proceedings.
- [20] H.G. LeDuc, B. Bumble, S.R. Cypher, and J.A. Stern, "Submicron area Bb/AlOx/Nb tunnel junctions for submillimeter wave applications," *Third Int. Symp. Space Terahertz Tech.*, pp. 1253-1256, 1990.
- [21] M.J. Wengler and D.P. Woody, "Quantum noise in heterodyne detection," *IEEE J. Quant. Elect.*, vol. QE-23, pp. 613-622, 1987.

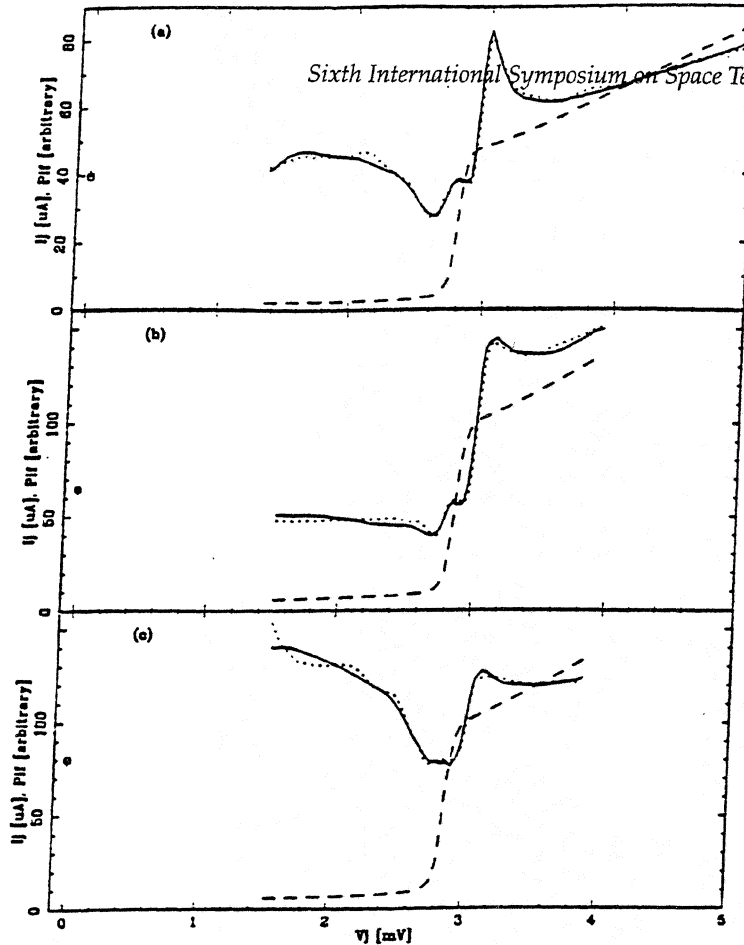


Fig. 1. I_{dc} (dashed line), measured P_{if} (solid line), and calculated P_{if} (dotted line) as a function of V_{dc} . (a) is mixer R4/2A with best fit parameter values of $G_{11}=.0035$, $|B_{11}|=.0063$, $g=.00029$, $a=70.$, $b=-.19$ and $c=.0034$. (b) is mixer M3 1.84-1.96GHz IF, with best fit parameter values of $G_{11}=.044$, $|B_{11}|=.036$, $g=.0037$, $a=65.$, $b=.72$ and $c=.11$. (c) is mixer M3 1.0-1.2GHz IF, with best fit parameter values of $G_{11}=.013$, $|B_{11}|=.0003$, $g=.00043$, $a=65.$, $b=1.2$ and $c=.016$. The circles are the measured and '+'s are the calculated P_{if} with the dc bias off, e.g. $V_{dc}=0$ and $I_{dc}=0$.

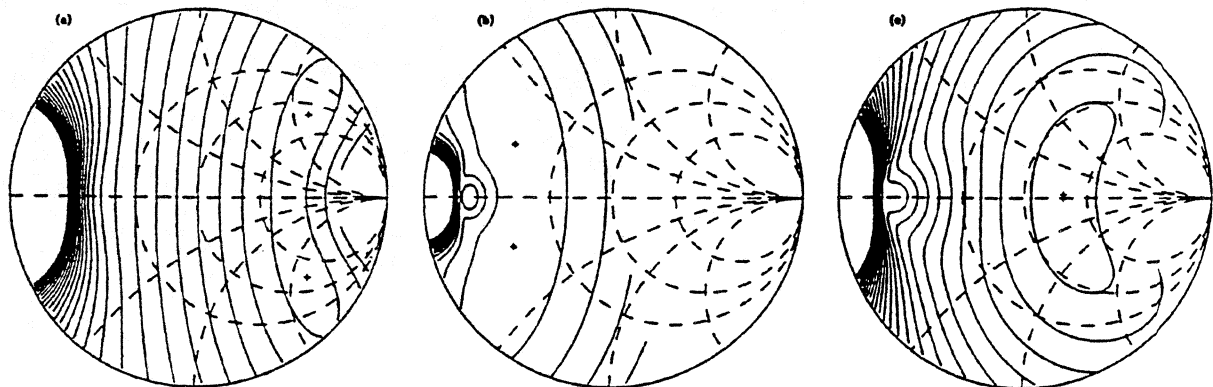


Fig. 2. Contour plots over the Smith Chart for IF system input impedance, $Z_{11}/50\Omega$, of the RMS residuals for fitting equ. 5 to the measured P_{if} data in fig. 1. The contour intervals are .5% of the average IF power and the conjugate pair of points with the smallest residuals are indicated by '+'s.

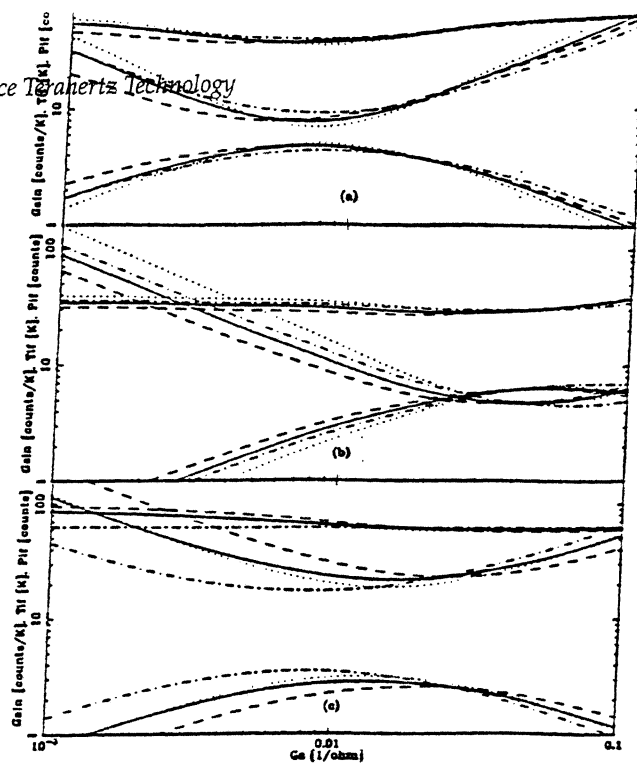


Fig. 3. Plot of the calculated gain, T_{if} , and P_{if} for the same mixers displayed in fig. 1. In each plot the lower set of the lines are the gain, middle set T_{if} and top set P_{if} . The parameter sets used for calculating the lines span the range of values consistent with the measured data in fig. 1 and listed in table 1.

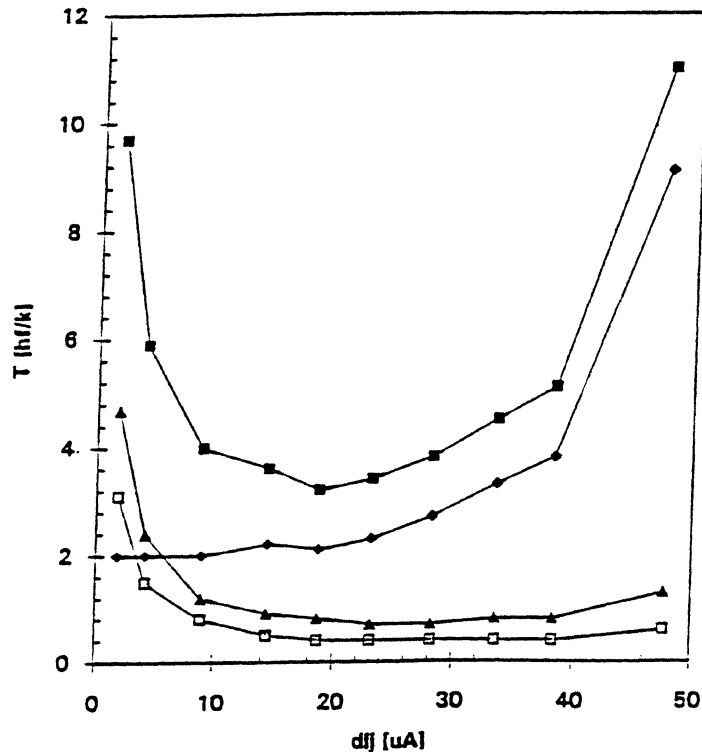


Fig. 4. Contributions to T_{rec} for mixer M3 in the 1.84-1.96GHz IF band at 230 GHz as a function of LO induced dc current. Filled squares: T_{rec} measured using hot and cold loads. Open squares: leakage current noise contribution, LT_{I0} , and triangles: IF amplifier noise contribution, LT_{if} . These values were obtained using equ. 5 with the best fit parameter values and the measured G_s . Diamonds: T_{if} calculated by subtracting $T_{if}^* = (LT_{I0} + LT_{if})$ from T_{rec} .

Installation of the Antarctic Sub-mm Telescope and Remote Observatory (AST/RO)

Antony A. Stark

*Harvard-Smithsonian Center for Astrophysics,
60 Garden St.; Cambridge, MA 02138, USA**

Abstract. Atmospheric measurements by various observers indicate that the Antarctic Plateau is the best submillimeter-wave observatory site ever tested. AST/RO, a 1.7 m diameter telescope for astronomy and aeronomy studies at wavelengths between 200 and 2000 μm , was installed at the South Pole during the 1994-95 Austral summer, after some logistical difficulties were overcome. The instrument is now operational with four heterodyne receivers and three acousto-optical spectrometers. The optical design is Gregorian, offset in both azimuth and elevation, with the exit pupil at the chopping tertiary mirror: this arrangement provides for low switched-power offsets even when the beam is thrown several degrees. There is a Coudé focus in a warm, spacious receiver room and also a Nasmyth focus with optical and mechanical properties similar to the KAO.

Submillimeter-wavelength astronomy can be pursued only from extremely cold and dry sites, where the atmosphere contains less than 1 mm of precipitable water vapor. Water vapor is the dominant source of opacity at these wavelengths, although many other atmospheric molecules, both rare and common, also make contributions (1, 2). Measurements from the South Pole reported by Pajot *et al.* (3) and Dragovan *et al.* (4) indicate that the broad-band atmospheric opacity in the 650 μm window is typically $\tau_{\text{zenith}} \sim 0.2$. Chamberlin and Bally (5, 6) measured the 225 GHz opacity at the South Pole several times a day throughout 1992, using an NRAO tipping radiometer. These observations show that the $\lambda 1.3\text{mm}$ sky opacity at the South Pole exceeds 0.1 only fifteen days a year, significantly better than Mauna Kea where this value is exceeded about half the time. The atmospheric opacity at the South Pole changes only slowly, unlike Mauna Kea where diurnal effects are significant and the submillimeter-wave opacity may change significantly in less than an hour.

AST/RO is a 1.7-m diameter telescope at the South Pole (7). The immediate scientific goals of this instrument are heterodyne spectroscopy of galactic atomic and molecular clouds and molecular lines in the earth's stratosphere at wavelengths near 600 μm , but the telescope was designed to be a general-purpose instrument for the millimeter, submillimeter and far-infrared. The 1.7-m aperture yields a beamsize of $96''(\lambda/600\mu\text{m})$, large enough to

*Also associated with the Center for Astrophysical Research in Antarctica (CARA)

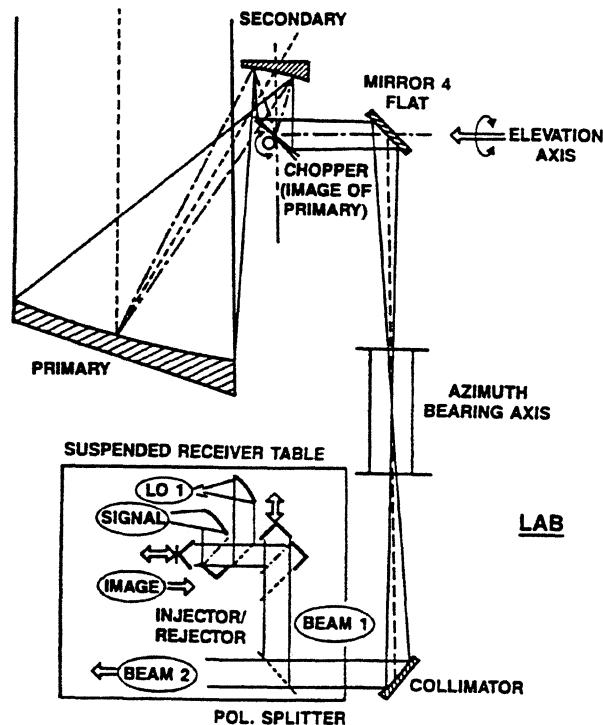


Figure 1: Schematic of the AST/RO optical system. For purposes of representation, the beam path has been flattened and the reader should imagine that the primary and secondary mirrors are rotated by 90° out of the plane of the page around a vertical line passing through the center of the secondary. The azimuth bearing is at the level of the building roof.

allow large-scale mapping programs, yet small enough to map distant clouds in the Galaxy and to just resolve hundreds of external galaxies. It is not small enough, however, to study distant galaxies or to study protostellar regions in any detail. The telescope was designed to be transported to the South Pole in a few large pieces and re-assembled on-site. It happened, however, that the amount of on-site work required was much greater than planned.

All of the optics in AST/RO are offset for high beam efficiency and avoidance of inadvertent reflections and resonances (8). Figure 1 shows the optical arrangement in its Coudé form. The primary reflector is made of carbon fiber and epoxy with a vacuum-sputtered aluminum surface having a surface roughness of $6\mu\text{m}$ and an rms figure of about $9\mu\text{m}$ (9). The Gregorian secondary is a prolate spheroid, and its offset angle was chosen using the method of Dragone (10), so that the Gregorian focus is aplanatic. The diffraction-limited field-of-view is 3° in diameter at $\lambda 3\text{mm}$ and $30'$ in diameter at $\lambda 200\mu\text{m}$. The chopper can make full use of this field-of-view, because it is located at the exit pupil and so does not change the illumination pattern on the primary while chopping. Note in Figure 1 that rays diverging from a point on the primary mirror reconverge at the tertiary mirror, since the tertiary is at the exit pupil of the instrument. Optimizing the optics this way requires that

the primary mirror be cantilevered away from the elevation axis: this is accomplished with a truss of Invar rods which hold the primary-to-secondary distance invariant with temperature. When the fourth mirror shown in Figure 1 is removed, the telescope has a Nasmyth focus where the beam passes through an elevation bearing which has a 0.2m diameter hole. This focus is almost identical in its optical properties to the bent Cassegrain focus on the Kuiper Airborne Observatory, except for a larger field-of-view. Array detectors of various types could be used at this focus in the future.

Currently, there are four heterodyne receivers mounted on an optical table suspended from the telescope structure in a spacious, warm Coudé room:

- a 230 GHz SIS receiver, 500 K SSB noise temperature (11);
- a 460-500 GHz Schottky-barrier diode receiver, 950 K DSB (this receiver will work without a liquid Helium supply) (12);
- a 492 GHz SIS waveguide receiver, 340 K DSB with the current SIS junction (13);
- a 492 GHz SIS quasi-optical receiver, 170 K DSB (14, 15).

The laboratory space under the telescope holds three racks of electronics, including two 1.2-GHz wide acousto-optical spectrometers and one high-resolution acousto-optical spectrometer (16), cryogenic equipment, laboratory benches, and storage for tools. Other rooms in the AST/RO building are used for telescope control monitors, data analysis, additional laboratory space, and storage. The entire system is highly automated to reduce to a minimum the need for operator intervention and can be operated over the Internet.

The AST/RO telescope was fabricated between 1990 and 1992 at AT&T Bell Laboratories, Crawford Hill, NJ, and at the Scientific Instrument Facility at Boston University. In 1993 and 1994, it was installed at a test site in Boston and used for observational tests (17). In August 1994, this entire working observatory was packed into crates and shipped. Unfortunately, the truck carrying all the equipment was involved in a serious accident. Some of the parts which had been critically positioned in the shop during telescope assembly, such as the encoders, were knocked out of position. When mounted on the AST/RO building at the Pole, the telescope can be enclosed in a retractable cloth and aluminum "baby-buggy" cover. This sheltered working environment allowed an unplanned partial disassembly and realignment of the critical components, demonstrating that even delicate mechanical work can be accomplished on the Polar plateau.

The first observations from the South Pole were made in January 1995. Figure 2 shows a spectrum of the 492 GHz line of neutral atomic carbon toward the galactic center molecular cloud Sagittarius A taken by AST/RO. As of this writing (April 1995), AST/RO winter-over scientist Richard Chamberlin is carrying out engineering tests and observations. All

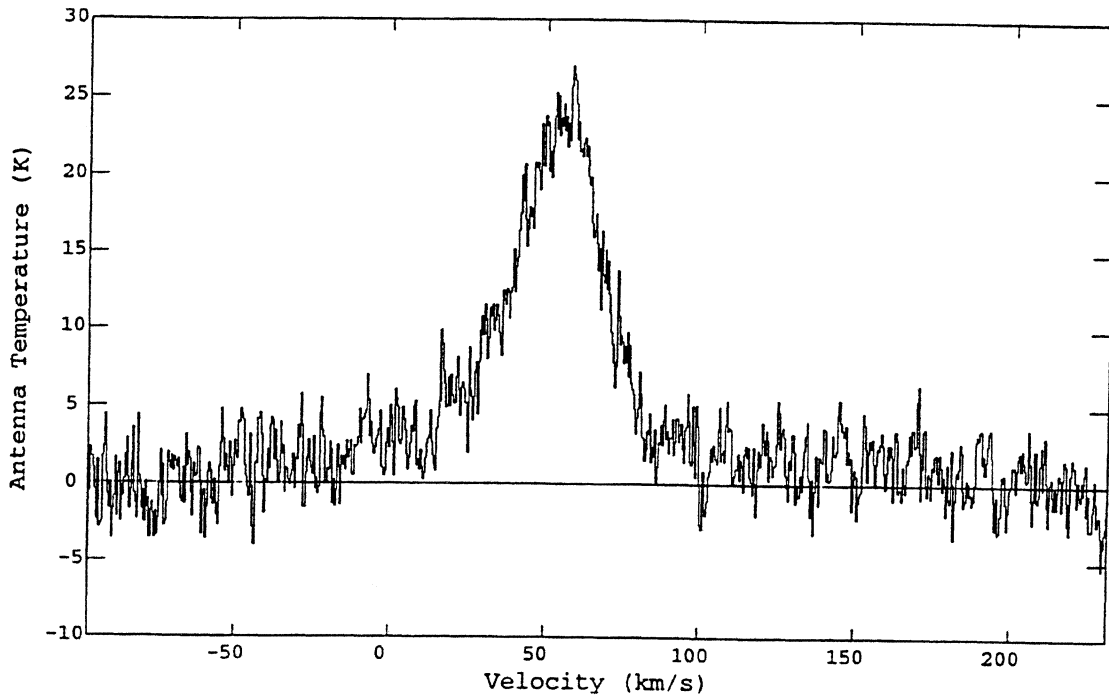


Figure 2: The 492 GHz line of neutral atomic carbon, in the direction of the galactic center molecular cloud Sagittarius A, taken by the AST/RO telescope from the South Pole. The calibration of the vertical scale is preliminary.

four receivers are operational. The liquid helium supply is expect to last for most of the winter season. Skydips at 492 GHz are made regularly and will be used to characterize the quality of the winter sky.

The AST/RO group is grateful for the logistical support of the National Science Foundation (NSF), Antarctic Support Associates, and CARA during the 1994-95 expedition. We also thank Rick LeDuc and Bruce Bumble at JPL for making SIS junctions and Jacob Kooi and Tom Phillips at Caltech for making them available to us. This work was supported in part by National Science Foundation grant DPP88-18384, and by the Center for Astrophysical Research in Antarctica and the NSF under Cooperative Agreement OPP89-20223.

REFERENCES

1. Waters, J. W., Wilson, W. J. & Shimabokuro, F. I. 1976. *Science*, **191**, 1174.
2. Bally, J. 1989. In *Astrophysics in Antarctica*, ed. D. J. Mullan, M. A. Pomerantz & T. Stanev (AIP Press: New York) , p. 100.

3. Pajot, F., Gispert, R., Lamarre, J. M., Puget, J. L., Pomerantz, M. A. & Peyturaux, R. 1989. In *Astrophysics in Antarctica*, ed. D. J. Mullan, M. A. Pomerantz & T. Stanev (AIP Press: New York) , p. 93.
4. Dragovan, M., Stark, A. A., Pernic, R. & Pomerantz, M. 1990. *Appl. Optics*, **29**, 463.
5. Chamberlin, R. & Bally, J. 1994. *Appl. Optics*, **33**, 1095.
6. Chamberlin, R. & Bally, J. 1995 *Int. J. of IR & MM Waves*, in press.
7. AST/RO is the result of a successful proposal to the United States National Science Foundation by A. A. Stark, J. Bally and R. W. Wilson of AT&T Bell Laboratories, T. M. Bania and A. P. Lane of Boston University, and K.-Y. Lo of the University of Illinois.
8. Stark, A. A. 1989. In *Astrophysics in Antarctica*, ed. D. J. Mullan, M. A. Pomerantz & T. Stanev (AIP Press: New York), p. 106.
9. Fabricated by Dornier GmbH, Friedrichshafen, Germany.
10. Dragone, C. 1982. *IEEE Trans. Antennas and Propagation*, Vol. AP-30, p.p. 331-339
11. This receiver was made in 1989 at AT&T Bell Laboratories by J. Bally.
12. Made by Radiometer Physics, GmbH, Meckenheim, Germany.
13. Made at the University of Arizona by C. Walker.
14. Engargiola, G. , Zmuidzinas, J., and Lo, K.-Y. 1994. A 492 GHz Quasioptical SIS Receiver for Submillimeter Astronomy. *Reviews of Scientific Instruments.*, 65:1833.
15. Zmuidzinas, J. and LeDuc, H. G. 1993. Quasi-optical slot antenna SIS mixers. *IEEE Transactions on Microwave Theory and Techniques.*, 40:1797.
16. Schieder, R., Tolls, V. and Winnewisser, G. 1989. The Cologne Acousto-optical Spectrometers. *Experimental Astronomy.*, 1:101.
17. Stark, A. A., Lane, A. P., Balm, S., Rumitz, M., Bania, T., Chamberlin, R., Huang, M., Ingalls, J., Jackson, J., Castro, E., Engargiola, G., Lo, K.-Y., Bally, J., Wilson, R. W., Wright, G., Mumma, D., Schieder, R., Stutzki, J., Staguhn, J. 1995. *Antarctic J. of the U. S.*, in press.

HHT Instrumentation – Present and Future

Rolf Güsten and Nigel Keen

Max-Planck-Institut für Radioastronomie

Auf dem Hügel 69, 53121 Bonn, F.R.G.

Abstract

A brief review of receiving systems for the Heinrich-Hertz-Telescope over the next few years is presented. Spectroscopic and continuum detectors will increasingly be focal-plane arrays. Two such system, a 37-element bolometer-array for operation at $350\mu\text{m}$ and a 16-element $625\mu\text{m}$ heterodyne-array, including a broadband autocorrelator, are under construction at the MPIfR.

First-Generation Facility Instrumentation

Current plans are to make the Heinrich-Hertz-Telescope (HHT) available to the astronomical community after the summer 1995 shutdown. The prime atmospheric submillimeter windows should then be covered by state-of-the-art receivers. Preliminary 'test' receivers, currently used for commissioning the telescope, will successively be replaced by the facility obligations outlined in the Memorandum of Understanding between the two partner institutes (MPIfR and Steward Observatory).

Heterodyne Detectors. Table I summarizes the facility SIS frontends expected to be operating by September 1995. All mixers are currently in full-height waveguides, with two tuning elements. Junctions have been provided by and/or produced in cooperation with the SIS laboratories of IRAM (345 & 690 GHz) and JPL (250 & 480 GHz). The upgraded dual-channel systems delivered by the MPIfR will come with newly developed hybrid dewars, with Helium hold-times of up to two weeks. Once the broader band spectrometers are available (see below), the bandwidth of the IF chain will be increased to 2 GHz. To ease on-site operation of the instruments, intrinsically wideband-tunerless mixers and junctions will be installed as soon as possible.

Table I. First-Generation SIS Frontends

Tuning Range	Polarization	IF Bandwidth	Responsibility
220–270 GHz	single	1 GHz	SO
310–370 GHz	single	1 GHz	MPIfR
	dual	1 GHz	MPIfR
450–500 GHz	single	1 GHz	SO
660–690 GHz	dual	2 GHz	MPIfR

NOTES: initial single-channel units, currently used for commissioning the telescope ($T_{Rx} \sim 125$ K at 345 GHz; $T_{Rx} \sim 75$ K across the 1.3mm band), will be replaced by dual-polarization units. To permit heterodyne observations at $350\mu\text{m}$, prior to the completion of the SIS receivers under development at both institutes (SO, MPIfR), a Schottky-diode open-structure receiver can be made available in coordination with H.P.Röser (MPIfR/DLR).

Spectrometers. Two broadband (1 GHz, each) and one high-resolution (250 MHz) acousto-optical spectrometer will be available (Table II). The physical arrangement of the receivers in one of the Nasmyth cabins allows simultaneous observation at two different sky frequencies (with perpendicular polarizations). A Martin-Puplett interferometer will serve as single-sideband filter and for proper calibration. A *taumeter* has been installed for continuous monitoring of the atmospheric transmission at 225 GHz.

Table II. Spectrometer Backends (MPIfR)

Unit	Bandwidth	Channels	Resolution
AOS#1	1 GHz	2048	1.2 MHz
AOS#2	1 GHz	2048	1.2 MHz
AOS#3	240 MHz	2048	250 kHz

Bolometers (MPIfR). Two single-channel bolometers, currently operating in the 1300 and 350 μm windows for commissioning, will be replaced by a four-color instrument (with filters for 0.35, 0.45, 0.87 and 1.2 mm wavelength) in Fall 1995. The four channels will be operated in parallel, with spatially displaced beams on the sky. The multi-channel digital backend *Drumbeat* can currently handle up to 8 continuum channels simultaneously, but for operation of the future bolometer arrays the unit can easily be upgraded for up to 64 channels.

Software. The operation of the facility instruments will be remotely controlled (selection and control of receivers, thermal calibration, SSB filtering). The observer's interface is patterned after the IRAM-30m telescope; data acquisition and analysis is within the GAG-software environment. At a later date an environment similar to that of the NRAO 12-m telescope is envisaged too, and additional software packages may be provided. For processing continuum observations a NOD-based algorithm will be available.

Development Projects

The dynamical range of current submillimeter observations is seriously limited by the rather low atmospheric transmission and its temporal fluctuations. Allowing dedicated observing modes and correlation algorithms, large focal-plane arrays will make better use of rare submm observing conditions, thus providing intrinsically much improved image quality. In 1993 the SMTO Council recommended the development of coherent and incoherent focal-plane arrays for operation at the HHT. We restrict our discussion to those systems under development and with approved funding.

- At the MPIfR (PI: E.Kreysa) a large bolometer array with 37 elements for operation in the 350 μm atmospheric window is being built, based on the experience gained with the 7 and 19-channel prototypes, which have been operated successfully at the IRAM 30m-telescope at 1.2mm wavelength. The beams of the diffraction limited array will be in a hexagonal packed arrangement with individual sky-pixels separated by $2 \times \Theta_{\text{HPFW}}$.

- Construction of a 16-element heterodyne array for operation in the 625 μm window, including a flexible spectrometer backend, commenced in 1994 (PI: R.Güsten). Details of the development will be presented elsewhere in this conference (Scherschel et al.), so we only briefly summarize the system definition:
 - the array consists of 16 elements with the closest feasible spacing of the pixels on the sky ($\sqrt{2} \times \Theta_{\text{HPFW}}$),
 - the performance of the individual modules should be state-of-the-art. In particular we require:
 - mixer & junction to be ‘tunerless’,
 - $T_{\text{Rx}} \leq 150$ K over the LO-tuning band of 455 – 495 GHz
 - minimum instantaneous bandwidth of 1.5 GHz.

All the major phase I project goals have now been achieved: reduced-height mixers and competitive 480 GHz junctions with integrated tuning structures have been designed, manufactured and successfully tested; the layout of the system has been designed, based on detailed Gaussian optics calculations and scale-model measurements; broad-band low-noise HEMTs (IF: 2–4 GHz) have been developed. By the summer of this year, a 5-element array prototype will be constructed to test the optics and LO-distribution scheme. By the end of 1995 the array dewar with the first of the two sub-arrays will be finalized. Commissioning of the complete instrument at the telescope is foreseen for winter 96/97.

- A 2-bit hybrid-autocorrelator, based on the new correlator chips of the University of New Mexico is under development (PI: W.Wiedenhoefer). The maximum bandwidth will be 2 ($\times 1$) GHz for each of the 16 modules, each with 2048 effective channels. In the high-resolution mode, 500 MHz of bandwidth will be covered by 8192 channels with 61 kHz spectral resolution.

**TUNABLE p-Ge LASER
IN THE FREQUENCY RANGE FROM 1 TO 4.5 THz**

E. Bründermann and H.P. Röser

DLR, Institute for Space Sensor Technology, Rudower Chaussee 5,
D-12489 Berlin, Germany
Email: WS2T@ARZVS1.RZ.BA.DLR.DE

Paper: STT-95-32

Space THz conf. 3/21/95 - 3/23/95

Length of paper: 7 pages
with 1-1/2" borders

TUNABLE p-Ge LASER IN THE FREQUENCY RANGE FROM 1 TO 4.5 THz

E. Bründermann and H.P. Röser

DLR, Institute for Space Sensor Technology, Rudower Chaussee 5,
D-12489 Berlin, Germany
Email: WS2T@ARZVS1.RZ.BA.DLR.DE

ABSTRACT

We have studied the pulsed p-type Ge laser to build a tunable local oscillator source for the THz frequency range. We have used the heterodyne technique to reveal the fine structure of the emission spectrum on the MHz scale that was only resolved on the GHz scale. The heterodyne measurements using a ring gas laser as local oscillator and a Schottky diode as mixer revealed an absolute line width of the p-Ge laser of 25 MHz due to heating of the active Ge sample. Self mixing of the p-Ge laser modes gives a line width which is only determined by the pulse length and can be as small as 0.9 MHz. The emission is broad band but it can be confined in one laser mode, concentrating the total power by using a lamellar grating in high orders. The pulse duration is in the order of 10 μ s while the repetition rate can reach a few tens of Hz which results in a low duty cycle. We present some ideas to improve the laser performance and to reach continuous wave operation.

INTRODUCTION

We have used a heterodyne receiver for many years on the Kuiper Airborne Observatory (NASA) to study rotational transitions of molecules in starforming regions. The receiver signal and laser beam are overlaid in a Martin-Puplett type diplexer and directed onto a Schottky diode. The resulting intermediate frequency is improved by low noise amplifiers and can be analyzed by an acousto-optical spectrometer which resolves a 1 GHz band simultaneously with 1 MHz [1]. Due to the limited bandwidth of those amplifiers, it is necessary to find a laser transition close to the signal frequency.

In the present receiver we use an optically pumped, continuous wave, ring gas laser as the local oscillator that can be filled with different laser gases, e.g., CH_2F_2 and CH_3OH , which generate laser radiation on discrete frequencies. A further improvement of the device would be a tunable laser source based on a semiconductor especially if space qualifications have to be fulfilled. This could open new possibilities in astronomical observations [2] and also for atmospheric research [3]. The only possible material in the THz frequency range with reasonable output power is the far infrared pulsed p-type Ge laser.

The p-Ge material can operate in various configurations as a laser source and is already intensively studied since its invention in 1984 [4,5,6]. Recently, the p-Ge laser has been considered as a useful tool for spectroscopy due to the wide tuning range [1,7]. We would like to concentrate here on the p-Ge laser in crossed electric and magnetic fields in the Faraday configuration meaning the radiation detection and the resonator longitudinal axis are in the direction of the magnetic field.

p-Ge LASER MECHANISM

The crystals are normally cut and polished in a rectangular shape. The surfaces are parallel within $30''$ so that the crystal can already operate on internal reflection modes in a Fabry-Perot cavity due to the high refractive index of Ge ($n_{\text{Ge}} \approx 4$). Typical lengths of the samples are between 30 and 60 mm and cross sections vary between 3×4 and 6×8 mm². The acceptor doping concentration which allows laser action covers a range of nearly two orders from 6×10^{12} cm⁻³ up to 5×10^{14} cm⁻³ [6].

There are two processes which provide laser action. The first involves intervalence band (IVB) transitions between the light and heavy hole bands where the magnetic field is in the range of 0.25-2.5 T. In the second type a higher magnetic field 1.5-4.5 T separates the bands significantly into Landau levels, and then cyclotron resonance (CR) lasing transitions within the light hole band occur. The essential difference between the two is that in the CR mode a single line is produced while IVB transitions can give a multiline output.

To obtain IVB lasing it is necessary to induce an inversion between the light and heavy hole bands, and the first requirement is a lattice temperature below 20 K which is achieved by immersing it into liquid Helium at 4.2 K. Then acoustical lattice scattering is negligible and optical lattice scattering is not possible. Excitation by a high electric field between 0.33 and 3.5 kV/cm then accelerates holes above the optical phonon energy leading to strong backscattering into the valence band. The electric field of 0.33 kV/cm defines the onset of heavy hole streaming motion. If at the same time a magnetic field is applied, the light holes can be 'trapped' into an orbit where the maximum energy is always less than the optical phonon energy of 37 meV, while at the same time the heavy holes exceed this energy and scatter by a 4% chance into the light hole band. Thus, a situation is created where the lifetime of the light holes (upper laser level) is much longer than that of heavy holes (lower laser level) and inversion is produced. This results in an emission in the range of 1-4.5 THz [8].

In the CR mode the inversion which is built up between the light hole levels is even more sensitive to the heavy hole motion, so that a specific crystallographic orientation of the applied fields has to be taken into account. The CR line is tunable by the magnetic field in the frequency range from 0.9-2.7 THz due to the CR transition frequency $e \cdot B / (2 \cdot \pi \cdot m) = B$ [T] $\cdot 0.6$ THz, where e is the electron (hole) charge, m the light hole effective mass which is a factor of 22 smaller than the free electron mass, and B the magnetic field. The output power within the pulse is less than 0.3 W [9].

The IVB laser has an output power of 1-10 W and is homogeneously broadened [10]. This allows the concentration of the total power in one frequency forced by an external resonator condition [11].

While the crystals are long in one direction, the easiest way to mount the sample in a homogeneous magnetic field is in Faraday configuration although the Voigt configuration seems to be preferable for laser emission [12]. For this configuration a larger bore superconducting magnet is used and the radiation is detected perpendicular to the magnetic field axis. An easier way to mount the sample in this configuration would be two permanent magnets which could be laid onto the side faces of the crystal. The magnetic field can then be tuned by varying the spacing between the two magnets. Although this method is restricted to low magnetic fields it might be useful for applications. In the following we concentrate on the IVB laser.

MODE FINE STRUCTURE OF THE p-Ge LASER

We have used grating spectroscopy to analyze the laser spectrum on the GHz scale, the heterodyne system to study in detail the emission characteristics on the MHz scale, and we measured frequency tunability, frequency and amplitude stability and line width.

The first attempt to measure the line width by self (homodyne) mixing of the p-Ge laser modes in a Schottky diode [13] revealed a small mixing product line width in the order of 10 MHz which was spaced by 633 MHz due to the cavity length of the laser. This can be easily calculated by $c/(2 \cdot n_{Ge} \cdot L)$, c velocity of light, n_{Ge} refractive index of Ge and the crystal length L . This encouraged us to think of a narrow line source in the order of the acousto optical spectrometer resolution which we use in the heterodyne receiver. Later we have shown by using a Schottky diode that the homodyne line width is only pulse length dependent, e.g., the smallest line width was achieved with a full width at half mean of 900 kHz for a 3.7 μ s long laser pulse [14].

By using mesh outcouplers which were developed for the gas laser [15], we were able to increase the IVB laser emission range in respect to the parameters E and B , electric and magnetic field, which is an indication for a high quality cavity [16].

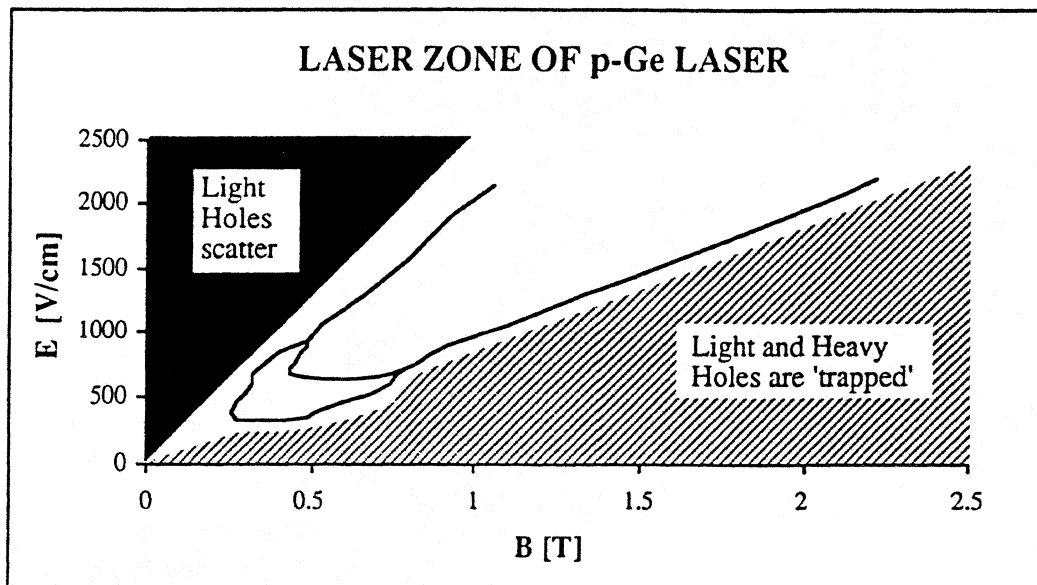


Fig. 1: IVB laser emission zone of a Ga doped Ge laser for different electric and magnetic fields. The sample size is $35 \times 7 \times 5 \text{ mm}^3$ with a Ga acceptor concentration of $7 \times 10^{13} \text{ cm}^{-3}$. The electric field E is applied in the [1-10] direction and the magnetic field B in the [110] direction. The line in-between areas divides a low frequency emission part around 1.5 THz and a high frequency part above 2.5 THz. The frequencies 1.5-2.5 THz are absorbed by the impurity transitions in the C and D lines of Ga. Due to the sensitivity of the Ge photoconductive detector which we used, those parts can be easily separated by their intensity and their time dependence during the laser pulse. For higher electric fields the laser zone is closed, usually around 2.5 T and 3.5 kV/cm. The lower electric field value of 0.33 kV/cm defines the onset of heavy hole streaming motion.

In the heterodyne mixing experiment we have shown that the absolute line width of a laser mode is about 25 MHz due to sample heating during the applied voltage pulse. The heating changes the optical length of the sample so that all laser modes move in the same

direction. Therefore the homodyne mixing experiment cannot sense this temperature effect while difference frequencies do not change. As a result only pulse length limited line widths are measured. This suggests an extremely narrow emission line if stable temperature conditions are fulfilled or in continuous wave operation where an equilibrium temperature can evolve. The relative mode frequency positions for different resonators follow closely the calculated values [17]. Tunability of the emission is possible by shifting the apparatus function of a lamellar grating in high orders across the resonator mode pattern. Due to the homogeneously broadened medium the total power can be concentrated in one single line [11,17].

In addition we started preliminary heterodyne experiments to study the CR laser (in cooperation with W. Heiss, TU Wien) which has a line width of 6 GHz resolved by a tunable detector with the same resolution [9]. This line width should consist of several finer modes on the MHz scale spaced in the order of one GHz due to the sample size.

FUTURE IMPROVEMENTS

While the orbits of heavy and light holes are centered at the drift velocity E/B , we find the necessary condition for inversion and trapping of light holes in a semiclassical approach. The maximum energy is reached when the velocity of the holes is $2E/B$, and for the light holes this has to be lower than the optical phonon energy $E_{op} = 37$ meV. The light hole effective mass $m = 0.046m_e$ and the heavy hole effective mass $M = 0.35m_e$, m_e free electron mass, have a ratio of $M/m \approx 7.6$.

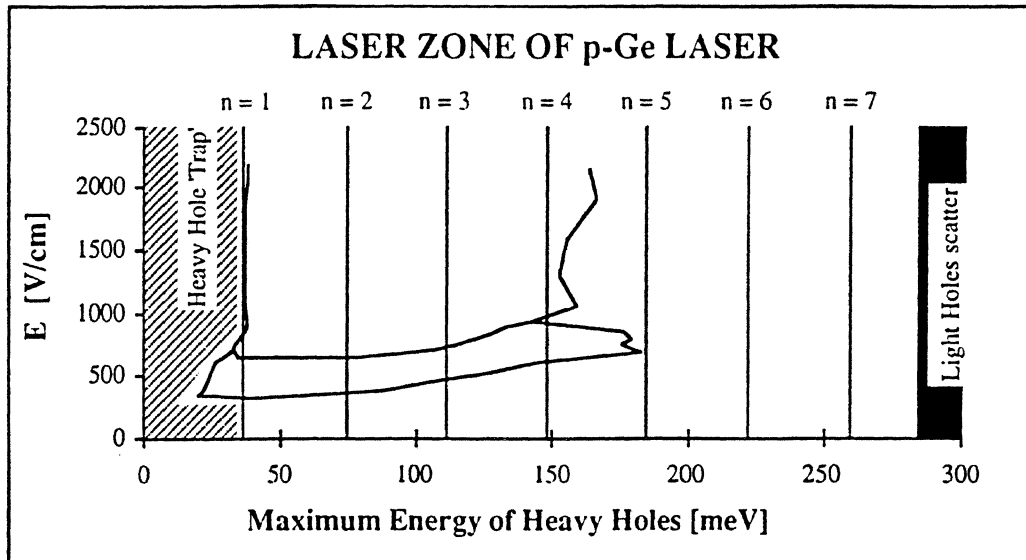


Fig.2: Laser zone of p-Ge laser from Fig.1. The maximum heavy hole energy follows from $2E/B$. Clearly the emission is not found below $E_{op} = 37$ meV, except for high magnetic and low electric fields. The reason might be a different heavy hole mass while in a more exact approach the total electric field in the crystal is made up by the applied field and a Hall component which can change the direction of the total field versus the crystallographic axis. The maximum gain is usually found between 74 meV and 111 meV, close to 74 meV (9.7 meV for light holes). Emission can be found up to $n = 4$, e.g., 148 meV. Light holes are below 37 meV if heavy holes are below 280 meV.

If the energy of the light holes is less than 37 meV, or $E/B < 2.7 \text{ kV}/(\text{cmT}) = 2.7 \times 10^5 \text{ m/s}$, the heavy holes can still scatter not only by emission of one optical phonon but up to seven optical phonons. We find that the laser power peaks if the maximum phonon energy of the heavy holes is equal to $n \cdot E_{\text{op}}$ or $E/B = (\sqrt{n}) \cdot 0.96 \text{ kV}/(\text{cmT})$, where $n = 1, 2, 3, 4$.

The maximum at $n = 1$ is very rare while the stream of heavy holes is not infinitely thin but already broadened by the scattering. Therefore some heavy holes have closed orbits below the optical phonon energy so that they are lost for populating the light hole band via this scattering mechanism. Especially with further reduction of E/B below 0.96 kV/(cmT) the lasing is not possible because all heavy holes stay below 37 meV. We find clear maxima for $n = 2$ and 3 which corresponds to $E/B = 1.36 \text{ kV}/(\text{cmT})$ and $1.67 \text{ kV}/(\text{cmT})$ with the highest peak in most cases close to $n = 2$ (more exactly at $E/B = 1.42 \text{ kV}/(\text{cmT})$ which is also found in Monte-Carlo simulations [6]). We propose that in this picture the shift is due to the doping itself. If we calculate the maximum light hole energy for $E/B = 1.36 \text{ kV}/(\text{cmT})$, we obtain 9.7 meV while for $E/B = 1.42 \text{ kV}/(\text{cmT})$ we obtain 10.5 meV.

In the emission spectrum of the p-Ge laser it was found that impurities play an important role especially by self-absorption due to transitions between the impurity ground state and excited impurity states [18,19]. In an absorption spectrum the transitions can be recognized as several narrow lines labeled A, B, C, D, E, G. The result is the absence of emission lines in the IVB laser range of 1.6-2.1 THz because of strong absorption at the B, C and D transitions. Recently, additional proof has been given with a Tl-doped crystal which differs drastically in these transitions [20].

The transitions for Ga, the most commonly used acceptor in p-Ge lasers, correspond to energies of 9.8 meV, 9.2 meV and 8.4 meV (B, C and D). This leads to a reduction of the light hole population due to impurity scattering and hole capture when the pumping from the heavy holes into the light hole band at 74 meV is most efficient. In this respect, one improvement of the p-Ge lasers could be the introduction of group II acceptors or deep level acceptors. While we found that laser radiation can be detected with group III acceptors (so far we tested Ga, Al, Tl), this might be a major step forward to a continuous wave laser. Our experience showed also that the crystal performance varied drastically from crystal to crystal, e.g., a 50 mm long sample which should have a higher gain operated in a smaller range of E and B values than a 35 mm long sample although the preparation and the doping level were the same. Due to the low level of doping we assume an inhomogeneity of doping across the sample and also different compensation levels.

Therefore we would like to use Neutron Transmutation Doping (NTD) of isotopically engineered Ge which is already used to fabricate Ge bolometers. This method enables a control of the compensation ratio and a statistical distribution of the doping atoms [21]. In addition we will change the usually used method of forming ohmic contacts for p-Ge lasers. Diffusing of Al or In into the crystals lateral surfaces will be substituted by implantation of Boron ions which are also used as low noise contacts for Ge bolometers or Ge photoconductors [21,22].

The main problem for a useful device in time-limited experiments on satellites or in airplanes is the pulsed operation. Preliminary experiments have shown that the repetition rate is mainly determined by the input energy of the applied electric field. The field heats the crystal adiabatically resulting in a hot crystal of about 20 K when laser action breaks down. High repetition rates produced a lot of He gas which in our experiments led to a local heating of the superconducting magnet and quenching. We believe that a He gas cloud covers the surface of the sample and limits the repetition rate. We have used superfluid liquid helium at 2 K to increase the repetition rate but this resulted in no major

improvement possibly still due to the local gas cloud attached to the sample. Otherwise we found a reduction in the pulse peak power and a reduced pulse length down to 70% compared to 4.2 K [23]. This seems to be in agreement with a better performance of the p-Ge lasers in 4.2 K liquid helium if the repetition rate is increased and the lattice mean temperature rises slightly above 4.2 K. This is probably connected to a higher mobility of the carriers.

In a more detailed study for different p-Ge lasers, we show that the electric input power P is connected to the geometry of the sample [24]. The power P can be easily calculated by $P = U \cdot I \cdot \Delta t \cdot f$ with the applied voltage U , the current I through the sample, the applied voltage duration Δt and the repetition rate f . The current is a result of the acceptor concentration N_a and the drift velocity E/B . The latter tends to saturate at 1/2 of the velocity which corresponds to heavy holes with an energy of $E_{op} = 37$ meV ($v_{op} = 1.9 \times 10^5$ m/s). With several measurements of different laser crystals, we found a very accurate relation to determine the current through the crystal: $I = A \cdot N_a \cdot e \cdot E / (2 \cdot B)$, where A is the ohmic contact area. We assume that it is possible to design a continuous wave laser by using the high quality cavity based on a lamellar grating with a mesh outcoupler and by using our results about the electric input power and crystal geometry which already increased the duty cycle due to a high repetition rate by an order in comparison to reported values [6].

CONCLUSION

Due to the high output power, the single mode operation possibility, the tunability over a wide frequency range from 1 to 4.5 THz and the narrow spectral width of the laser modes on the MHz scale, this laser will be a very useful spectroscopic source. If continuous wave operation is possible, then the device will be also usable in space applications, e.g., as the local oscillator in a heterodyne spectrometer. In addition the fine tunable source can lead to an exchange of Schottky diode mixers by Ge photoconductors which are not practical with gas lasers due to their small bandwidth of a few tens of MHz.

Acknowledgements - We would like to thank W. Heiss and E.E. Haller for inspiring discussions. Also we like to gratefully acknowledge the contributions of A.V. Muravjov, S.G. Pavlov and V.N. Shastin in cooperation and discussions.

REFERENCES

- [1] H.P. Röser, *Infrared Phys.* **32** (1991) 385-407
- [2] B.H. Kaldeich (Ed.), Proc. ESA SP-314 (1990)
- [3] R. Titz et al., this issue
- [4] A. Andronov et al., *Sov. Phys.-JETP Lett.* **40** (1984) 804-807
- [5] S. Komiyama et al., *Appl. Phys. Lett.* **47** (1985) 958-960
- [6] E. Gornik, A.A. Andronov (Eds), *Optical and Quantum elec., Special issue* **23**(2) (1991) S111-S349
- [7] E. Gornik et al., *Infrared Phys. Technol.* **1** (1995) 113-122
- [8] E. Bründermann et al., *Laser und Optoelektronik* **25**(1) (1993) 48-60 (in german/english)
- [9] P. Pfeffer et al., *Phys. Rev.* **B47** (1993) 4522-4531
- [10] F. Keilmann et al., *Appl. Phys. Lett.* **58** (1991) 2205-2207
- [11] A.V. Murav'ev et al., *Quantum Electron.* **23**(2) (1993) 119-124
- [12] I. Hosako, S. Komiyama, *Semicond. Sci. Technol.* **7** (1992) B645-B648
- [13] H.P. Röser et al., *Digest of the 15th Int. Conf. on IR&MM Waves*, SPIE Vol. **1514** (1990) 720-722
- [14] V.N. Shastin et al., *Digest of the 17th Int. Conf. on IR&MM Waves*, SPIE Vol. **1929** (1992) 182-183

- [15] R. Densing et al., *Infrared Phys.* **33** (1995) 219-226
- [16] R. Densing et al., *Laser und Optoelektronik* **25**(6) (1993) 46-53 (in german/english)
- [17] E. Bründermann et al., *Infrared Phys. Technol.* **1** (1995) 59-69
- [18] C. Kremser et al., *Appl. Phys. Lett.* **60** (1992) 1785-1787
- [19] S.V. Demihovsky et al., *Semicond. Sci. Technol.* **7** (1992) B622-B625
- [20] W. Heiss et al., *Semicond. Sci. Technol.* **9** (1994) 638-B640
- [21] K.M. Itoh et al., *Appl. Phys. Lett.* **64** (1994) 2121-2123
- [22] J.W. Beeman, E.E. Haller, *Infrared Phys. Technol.* **35** (1994) 827-836
- [23] E. Bründermann, PhD thesis, MPI for Radioastronomy, Bonn (1994) (in german)
- [24] E. Bründermann, W. Heiss, (in preparation)

INP GUNN DEVICES AND GAAS TUNNETT DIODES AS LOW-NOISE HIGH-PERFORMANCE LOCAL OSCILLATORS IN FUNDAMENTAL MODE

H. Eisele and G. I. Haddad

**Solid-State Electronics Laboratory
Department of Electrical Engineering & Computer Science
2231 EECS Building
The University of Michigan
Ann Arbor, Michigan 48109-2122**

Abstract

Improved fabrication technologies significantly increased the RF power levels that are available from GaAs TUNNETT diodes and InP Gunn devices. RF power up to 100 mW around 105 GHz and more than 100 mW around 132 GHz were obtained from TUNNETT diodes and Gunn devices, respectively. Corresponding dc-to-RF conversion efficiencies reach 6 % in TUNNETT diodes and 2.5 % in Gunn devices. Free-running oscillators with both types of devices exhibit excellent noise performance up to the highest power levels and typical phase noise, measured at a frequency off-carrier of 500 kHz, is below -94 dBc/Hz for TUNNETT diodes and below -100 dBc/Hz for Gunn devices. At lower power levels, TUNNETT diodes show the best noise measure (< 20 dB) of any two-terminal devices.

1. Introduction

Low-noise fundamental sources in the 100-170 GHz range with significantly increased RF output power are required to drive high-power high-efficiency multiplier stages and are one key element in reaching RF power levels of more than 0.1 mW at 1 THz. The RF power output of most two-terminal devices at millimeter-wave frequencies is limited by the tolerable active-layer temperature, and diamond with its high thermal conductivity is a preferred heat sink material. As shown in Figure 1, a simple analysis [1] indicates that the thermal resistance of GaAs-based (and similarly InP-based) devices is reduced by at least a factor of two on diamond heat sinks [2]. Therefore, devices on diamond heat sinks can handle more than twice the dc input power at the same operating active-layer temperature, and this is expected to more than double the available RF output power. To demonstrate this potential, a selective etching technology originally developed for GaAs IMPATT diodes was adopted and modified for various GaAs and InP-based two-terminal devices. The design of the devices and additional theoretical investigations were published

previously [3-5] and are not repeated here. Not only the power capabilities but also excellent noise properties at the maximum available power are required for their use in low-noise receivers. Therefore, the spectra of free-running oscillators were monitored from intermediate up to the highest power levels, and the FM noise measure was extracted from these measurements.

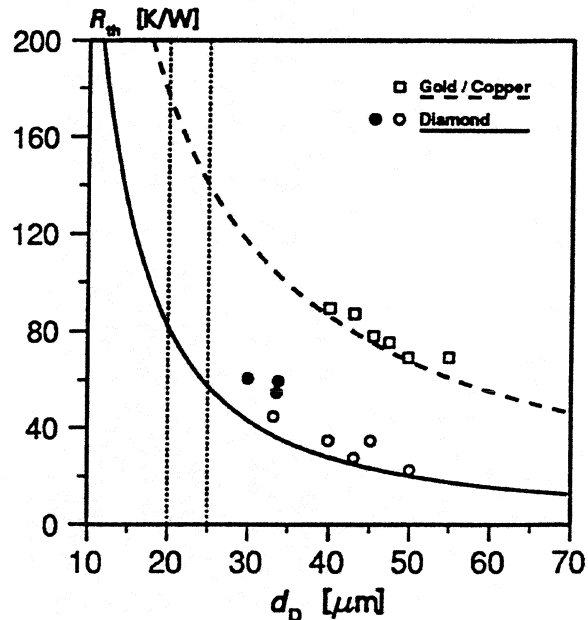


Figure 1: Predicted thermal resistances of diodes on diamond heat sinks (—) and integral heat sinks (- -) as a function of the diode diameter. Measured thermal resistances of GaAs W-band (●), V-band (○) IMPATT diodes on diamond heat sinks, and GaAs V-band IMPATT diodes on integral heat sinks (□).

2. Device Technology

The selective etching technology for devices to be mounted on diamond heat sinks was originally developed for GaAs W-band IMPATT diodes [6] and was subsequently modified for different device structures [2,7] in both GaAs and InP material systems. The basic steps are as follows:

- The epitaxial side of the entire sample is coated with the metal layers for the ohmic contact (Ti/Pt/Au for p type and AuGeNi/Ti/Au for n type).
- A supporting grating is selectively electroplated onto the metallization for mechanical support during the final processing steps.
- The sample is glued on a carrier epitaxial side down, and the substrate is removed in the first selective etch.

- The etch-stop layer is removed in the second selective etch (obligatory for AlGaAs/GaAs, optional for InGaAs/InP).
- The metal layers for the n ohmic contact (AuGeNi/Ti/Au) are deposited and selectively electroplated with a few microns of gold.
- The device mesa is etched and the sample is removed from the carrier.
- The ohmic contacts are annealed on a hotplate in a nitrogen atmosphere.
- The sample is diced into individual devices, and single devices are thermocompression bonded onto metallized diamond heat sinks.

In order to obtain from one wafer InP Gunn devices with either orientation of the grading [8], the order of the first five steps had to be reversed.

3. RF Performance

The GaAs TUNNETT diodes were evaluated in the WR-10 waveguide version of a standard full-height waveguide resonant-cap cavity [9] and the InP Gunn devices, in the WR-6 waveguide version [2]. Only a back short at one flange of the cavity was used to tune for maximum RF output power, and no other tuning elements such as an E-H tuner were found necessary for TUNNETT diodes and Gunn devices. Figure 2 summarizes the results of ten GaAs TUNNETT diodes on diamond heat sinks with power levels up to 100 mW between 100 GHz and 105 GHz and dc-to-RF conversion efficiencies above 5 % around 105 GHz. Figure 3 summarizes the results of the best InP Gunn in fundamental mode with RF power levels of more than 100 mW and dc-to-RF conversion efficiencies up to 2.5 % around 132 GHz. Most devices were evaluated at up to seven different frequencies and RF power levels of more than 40 mW around 150 GHz and more than 15 mW at 159 GHz were obtained from the best devices on diamond heat sinks. To the authors' knowledge, these are the highest values reported to date and they exceed those of InP Gunn devices in second-harmonic mode around 140 GHz [10]. Figure 4 shows the performance of one InP Gunn device as a function of the dc bias. The position of the back short was tuned for maximum RF output power (> 100 mW) at maximum bias and kept fixed throughout the measurement. For input power levels between about 3 W and 4.2 W, the device operates in a stable single mode, and the oscillation frequency drops monotonically by more than 250 MHz. This allows simple electronic tuning through the bias in a phase-locked loop. The insert of Figure 3 also shows the nominal doping profile of the n^+nn^+ epitaxial layers. At maximum applied bias, the frequency tuning range of the backshort was measured for the same Gunn device. As can be seen from Figure 5, fundamental-mode operation allows smooth tuning with the backshort as the only tuning element. No mode jumps occur and the drop in RF output power remains below 2 dB between 131 GHz and 135.5 GHz. Over a smaller tuning range of about 3 GHz, the RF power decreases by less than 1 dB.

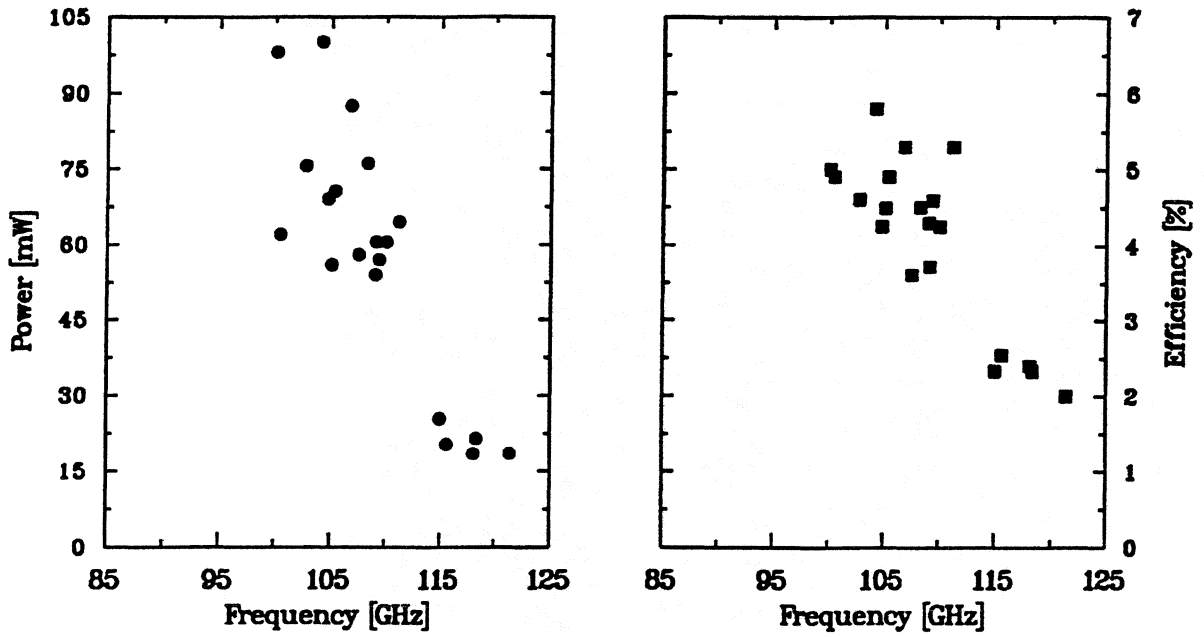


Figure 2: Output power (●) and efficiency (■) versus oscillation frequency in W-band for different GaAs TUNNETT diodes on diamond heat sinks.

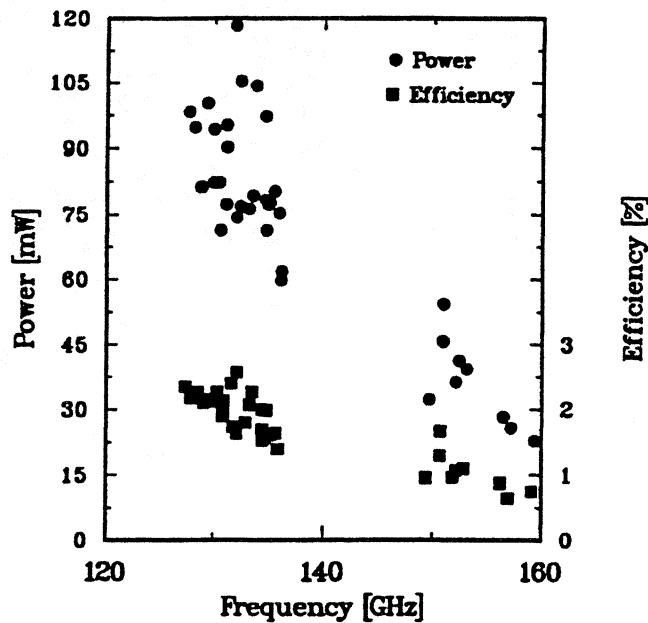


Figure 3: Output power (●) and efficiency (■) versus oscillation frequency in D-band for different InP Gunn devices on diamond heat sinks.

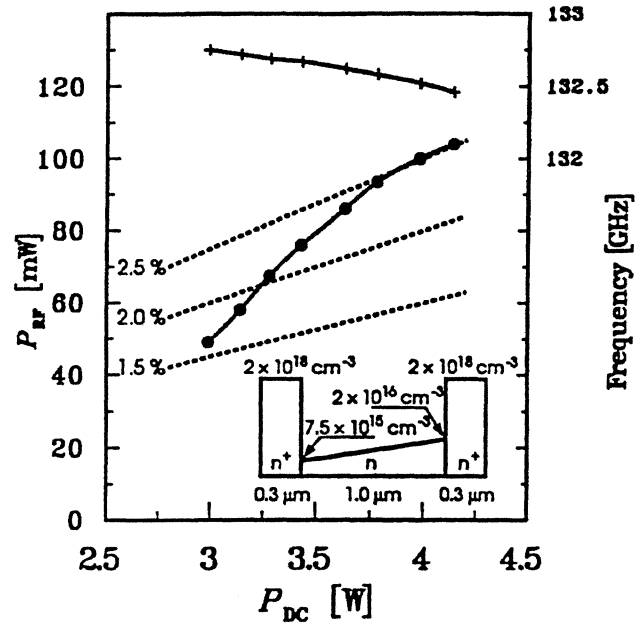


Figure 4: Bias-dependent RF characteristics of a D-band InP Gunn device (●: output power, +: oscillation frequency, ---: lines of constant efficiency).

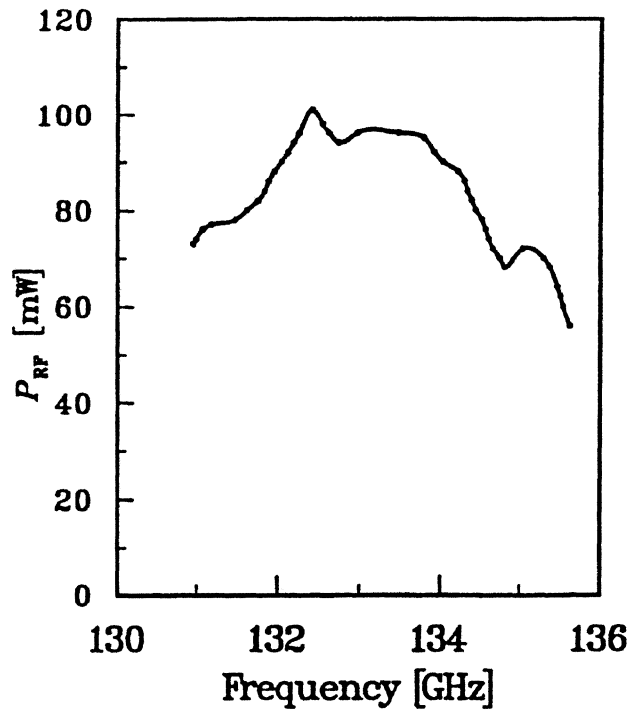


Figure 5: Tuning characteristics of a D-band InP Gunn device at maximum dc bias.

4. Noise Performance

Free-running oscillators with either TUNNETT diodes or Gunn devices exhibit clean spectra up to the highest RF output power. Typical phase noise is below - 94 dBc/Hz for TUNNETT diodes and - 100 dBc/Hz for Gunn devices both at a frequency off-carrier of 500 kHz. Figures 6 and 7 show examples for a TUNNETT diode with an RF output power of 40 mW at an oscillation frequency of 109.047 GHz and for a Gunn device with 41 mW at 134.791 GHz. The noise measure M

$$M = \frac{\Delta f_{\text{rms}}^2 Q_{\text{ex}}^2}{f_o^2 k T_0 B} P_{\text{RF}}$$

allows a better comparison between different types of devices. The effective frequency deviation Δf_{rms} at the frequency off-carrier f_m is derived from the phase-noise-to-carrier ratio N/C above

$$\Delta f_{\text{rms}}^2 = 2(N/C) f_m^2 ,$$

and the loaded Q value (Q_{ex}) is determined using a self-injection locking technique with a directional coupler (measured coupling value 21 dB) and a tunable short [11]. The noise measure of TUNNETT diodes at high RF power levels ranges from 22 dB to 27 dB, and examples are 22 dB at 60 mW and 111.15 GHz, 24 dB at 76 mW and 108.33 GHz, and 26 dB at 55 mW and 109.56 GHz. Loaded Q values range from 32 to 64. Lower values for M were obtained at intermediate power levels, *e.g.*, 20 dB at 5.2 mW and 102.46 GHz and below 18 dB at 11 mW and 104.05 GHz. To the authors' knowledge these are the best values for any oscillator with two-terminal devices in this frequency range and they confirm that tunneling is the dominant mechanism in the carrier injection of these TUNNETT diodes. Examples for the noise measure of Gunn devices at high RF power levels are 25 dB at 44 mW and 132.38 GHz and 23 dB at 35 mW and 134.82 GHz [7] with loaded Q values ranging from 60 to 120. Noise data are quite sparse at D-band frequencies, are limited to transit-time diodes and mainly cover the typically better small-signal case [12-14]. These D-band InP Gunn devices show better noise performance than present transit-time diodes with high multiplication factors (IMPATT and MITATT diodes in GaAs and Si) [12-14] and, probably due to easier impedance matching, offer higher RF power levels and dc-to-RF conversion efficiencies than present GaAs single-drift IMPATT and MITATT diodes [13-15] at these D-band frequencies. They even approach the RF performance of Si double-drift IMPATT diodes [16-17].

The $1/f$ corner frequency in Δf_{rms} is on the order of 100 kHz (< 500 kHz) for the investigated TUNNETT diodes and Gunn devices, and the phase noise typically reaches the noise floor of the spectrum analyzer

with the harmonic mixer around 1 MHz for TUNNETT diodes and Gunn devices. Therefore, it is not clear at this point whether the higher values in the noise measure of TUNNETT diodes are caused by $1/f$ (flicker) noise components. The phase noise of the best Gunn device in Figure 4 reaches the noise floor below a frequency off-carrier of 500 kHz and, therefore, its noise measure is assumed to be well below 25 dB for the highest power levels around 132 GHz.

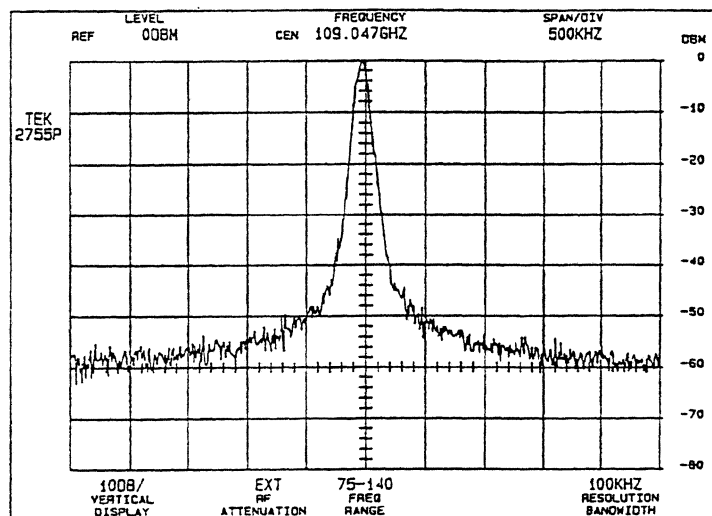


Figure 6: Spectrum of a GaAs W-band TUNNETT diode free-running oscillator, power level 40 mW, center frequency 109.047 GHz, vertical scale 10 dB/div, horizontal scale 500 kHz/div, BW 100 kHz.

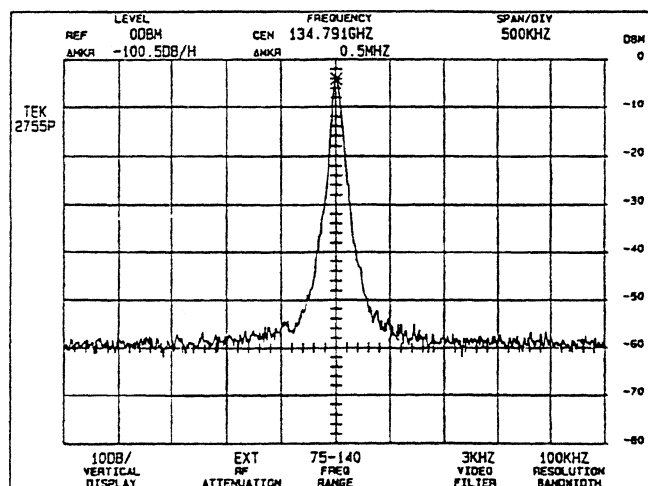


Figure 7: Spectrum of an InP D-band Gunn device free-running oscillator, power level 41 mW, center frequency 134.791 GHz, vertical scale 10 dB/div, horizontal scale 500 kHz/div, BW 100 kHz, VBW 3 kHz.

5. Conclusion

GaAs TUNNETT diodes and InP Gunn devices in fundamental mode reach the highest power levels of any GaAs- and InP-based two-terminal devices. Their excellent noise performance makes them ideally suited for local oscillators and drivers for multiplier chains. Still higher power levels and oscillation frequencies can be expected from more optimized devices.

Acknowledgment

Part of the work was supported by the Center for Space Terahertz Technology under contract No. NAGW 1334. The authors are indebted to Jim Morgan for machining some of the waveguide and other mechanical parts with excellent skill.

References

- [1] Holway, L. W., Adlerstein, M. G.: "Approximate Formulas for the Thermal Resistance of IMPATT Diodes Compared with Computer Calculations", *IEEE Transactions on Electron Devices*, ED-24(2), 1977, pp. 156-159.
- [2] Eisele, H., Haddad, G. I.: "GaAs TUNNETT Diodes on Diamond Heat Sinks for 100 GHz and Above", *IEEE Transactions on Microwave Theory and Techniques*, MTT-43(1), 1995, pp. 210-213.
- [3] Kamoua, R., Eisele, H., Haddad, G. I.: "D-Band (110 GHz - 170 GHz) InP Gunn Devices", *Solid-State Electronics*, 36, 1993, pp. 1547-1555.
- [4] Eisele, H., Kidner, C., Haddad, G. I.: "A CW GaAs TUNNETT Diode Source for 100 GHz and Above", *Proceedings of the 22nd European Microwave Conference*, August 24-27, 1992, Helsinki, Finland, pp. 467-472.
- [5] Eisele, H., Chen, C-C., Mains, R. K., Haddad, G. I.: "Performance of GaAs TUNNETT Diodes as Local Oscillator Sources", *Proceedings of the Fifth International Symposium of Space Terahertz Technology*, May 10 - May 13, 1994, Ann Arbor, Michigan, pp. 622-628.
- [6] Eisele, H.: "Selective Etching Technology for 94 GHz GaAs IMPATT Diodes on Diamond Heat Sinks", *Solid-State Electronics*, 32(3), 1989, pp. 253-257.

- [7] Eisele, H., Haddad, G. I.: "D-Band InP Gunn Devices with Second-Harmonic Power Extraction up to 290 GHz", *Electronics Letters*, **30**, 1994, pp. 1950-1951.
- [8] Eisele, H., Haddad, G. I.: submitted for publication.
- [9] Eisele, H., Haddad, G. I.: "Enhanced Performance in GaAs TUNNETT Diode Oscillators Above 100 GHz through Diamond Heat Sinking and Power Combining", *IEEE Transactions on Microwave Theory and Techniques*, **MTT-42(12)**, 1994, pp. 2498-2503.
- [10] Crowley, J. D., Hang, C., Dalrymple, R. E., Tringali, D. R., Fank, F. B., Wandinger, L., Wallace, H. B.: "140 GHz Indium Phosphide Gunn Diode", *Electronics Letters*, **30**, 1994, pp. 499-500.
- [11] Kurokawa, K.: "Noise in Synchronized Oscillators", *IEEE Transactions on Microwave Theory and Techniques*, **MTT-16**, 1968, pp. 234-240.
- [12] Wenger, J., Huber, S.: "Low-Noise D-Band IMPATT Oscillators", *Electronics Letters*, **23**, 1987, pp. 475-476.
- [13] Tschermitz, M., Freyer, J., Grothe, H.: "GaAs Read-Type IMPATT Diodes for D-Band", *Electronics Letters*, **30**, 1994, pp. 1070-1071.
- [14] Pöbl, M., Bogner, W., Gaul, L.: "CW GaAs IMPATT Source on Copper Heat Sink up to 160 GHz", *Electronics Letters*, **30**, 1994, pp. 1316-1317.
- [15] Eisele, H., Haddad, G. I.: "GaAs Single-Drift Flat-Profile IMPATT Diodes for CW Operation in D Band", *Electronics Letters*, **28**, 1992, pp. 2176-2177.
- [16] Lee, D. H., Ying, R. S.: "Ion-Implanted Complementary IMPATT Diodes for D-Band", *Proceedings of the IEEE*, **62**, 1974, pp. 1295-1296.
- [17] Chang, K., Thrower, W. F., Hayashibara, G. M.: "Millimeter-Wave Silicon IMPATT Sources and Combiners for the 110-260 GHz Range", *IEEE Trans. Microwave Theory and Tech.*, **MTT-29**, 1981, pp. 1278-1284.

115-145 GHz STABLE DEPLETION LAYER SECOND-HARMONIC TRANSFERRED ELECTRON OSCILLATORS

M.F. Zybura, S.H. Jones, J.E. Carlstrom[†], and J.D. Crowley[‡]

Applied Electrophysics Laboratories
Department of Electrical Engineering
University of Virginia
Charlottesville, VA 22903-2442

[†]Department of Astrophysics
California Institute of Technology
Pasadena, CA 91125

[‡]Litton Solid State
Santa Clara, CA 95054-3095

Abstract

The aim of this paper is to demonstrate and clarify the superior performance of Transferred Electron Devices utilizing current limiting contacts. These devices operate in a novel Stable Depletion Layer mode characterized by an oscillating stable depletion layer rather than an unstable propagating accumulation layer or dipole. A small-signal model is offered to explain the stable small-signal resistance of the device over a broad frequency range. Large-signal analysis is completed using a hydrodynamic device simulator employing the temperature-dependent drift/diffusion equation and Poisson's equation combined with a novel harmonic-balance circuit analysis technique. Analysis of the electric fields, electron concentration, and device temperature is included for steady-state large-signal operation. Embedding impedances are extracted for a broadband cavity using the High Frequency Structure Simulator from Hewlett Packard. Comparisons are made with experimental data for a Stable Depletion Layer oscillator in the above mentioned broadband continuously tunable cavity with excellent correlation, demonstrating at least 30 mW from 115-145 GHz. High reliability operation and as much as 60 mW of output power at 140 GHz is achievable.

1 Introduction

Presently, the state-of-the-art performance in Transferred Electron Devices (TEDs) is dominated by current limiting devices demonstrating 60 mW at 140 GHz [1]. In comparison to typical TEDs, current limiting TEDs offer increased output power, reliability, and improved frequency stability with temperature variation. The salient feature of these devices is a current limiting contact applied directly to the active layer of the device. The resulting shallow barrier contacting interface establishes a depletion layer at the cathode in the active region; the magnitude of this depletion layer governs the operating mode of the device. As a result of the cathode depletion, these devices operate in a novel Stable Depletion Layer (SDL) mode characterized by an oscillating stable depletion layer rather than an unstable propagating accumulation layer or dipole. This phenomena was first described by Kroemer [2], but its application to high performance oscillators was not fully recognized at that time. Essentially, the SDL mode is a stable negative resistance mode which is rich in both fundamental and second-harmonic frequency components. Since the output power is no longer limited by the formation of large charge instabilities, a higher frequency of operation is possible. Current limiting TEDs also exhibit much lower operating current densities, temperatures, and thus higher reliability performance.

2 Small-Signal Analysis

The approximate behavior of current limiting TEDs can be obtained through a small-signal analysis [2] of the commercially available Litton Solid State second-harmonic InP TED of reference [1]. The device structure consists of a current limiting contact applied to a 1.8 μm InP active region uniformly doped at $1 \times 10^{16} \text{ cm}^{-3}$, followed by an n^+ anode region. Typical d.c. bias points range from $-10 \text{ V} \leq V_{d.c.} \leq -7 \text{ V}$. Each physical quantity characterizing the semiconductor is written as a sum of a time-independent term and a small oscillating term:

$$\begin{aligned} E &= E_o + E_1 e^{i\omega t}, \\ n &= n_o + n_1 e^{i\omega t}, \end{aligned}$$

$$v = v_o + v_1 e^{i\omega t}, \quad (1)$$

where E , n , v , and ω , are the electric field, the electron concentration, the electron velocity, and the angular frequency, respectively. If higher order terms are neglected, the continuity equation for the oscillating part of the total current can be written as

$$\begin{aligned} J_1 &= q(n_1 v_o + n_o v_1) + i\omega \epsilon E_1 \\ &= \epsilon v_o \frac{\partial E_1}{\partial x} + (\sigma + i\omega \epsilon) E_1 = \text{constant}, \end{aligned} \quad (2)$$

where σ is the small-signal differential conductivity, ϵ is the dielectric permittivity, and Poisson's equation is used to generate the first term to the right of the equality. The oscillating current density at the cathode, $x = 0$, is given by

$$J_1(0) = [\sigma(0) + i\omega \epsilon] E_1(0), \quad (3)$$

and the cathode small-signal differential conductivity, $\sigma(0)$, is approximated as

$$\begin{aligned} \sigma(0) &= \frac{\partial J_c(0)}{\partial E_1} \\ &\simeq \frac{\partial}{\partial E_1} q \mu E n(0) \left[\exp\left(\frac{qV}{kT}\right) - 1 \right] \\ &\simeq -q \mu n(0), \end{aligned} \quad (4)$$

for transport across shallow metal-semiconductor barriers (< 300 meV) [3]. The exponential term in equation (4) has been neglected since the diode is strongly reverse biased under normal operating conditions. In this equation, μ , k , and T are the electron mobility, Boltzmann's constant, and the lattice temperature, respectively. The electron concentration at the cathode, $n(0)$, is given by

$$n(0) = N_c \exp\left(-\frac{q\phi_b}{kT}\right), \quad (5)$$

where N_c is the effective density of states in the conduction band, and ϕ_b is the barrier height. To complete the analysis, several approximations are needed. An average carrier velocity, \bar{v} , is defined as $\bar{v} = (v_{peak} + v_{sat})/2$. This average velocity is employed since the applied d.c. bias results in an electric field profile which is approximately equal to that of the peak field at the anode and substantially greater

than the peak field at the cathode. The small-signal differential conductivity, σ , of (2) is assigned an average value

$$\bar{\sigma} = q\bar{n}_o \overline{\frac{dv}{dE}} \quad (6)$$

where

$$\bar{n}_o = \frac{n(0)}{2} \left(1 + \frac{v_{sat}}{v_{peak}}\right), \quad (7)$$

and $\overline{dv/dE}$ is approximated as the value midway between the peak and saturation velocities. The solution of (2) subject to the boundary condition (4) is

$$E_1(x) = \frac{J_1}{\bar{\sigma} + i\omega\epsilon} \left[1 - \frac{\sigma(0) - \bar{\sigma}}{\sigma(0) + i\omega\epsilon} e^{i\Gamma x}\right], \quad (8)$$

where

$$\Gamma = -\frac{\bar{\sigma} + i\omega\epsilon}{\epsilon\bar{v}}. \quad (9)$$

The impedance then is found to be

$$\begin{aligned} Z &= \frac{1}{J_1} \int_0^l E_1 dx \\ &= \frac{l}{\bar{\sigma} + i\omega\epsilon} \left[1 - \frac{\sigma(0) - \bar{\sigma}}{\sigma(0) + i\omega\epsilon} \frac{e^{\Gamma l} - 1}{\Gamma l}\right] (\Omega - cm^2). \end{aligned} \quad (10)$$

There are two distinct contributions to Z , a uniform field contribution, and a space-charge wave contribution proportional to $\sigma(0) - \bar{\sigma}$. The small-signal resistance and reactance for the InP TED of reference [1] are shown in Figures 1 and 2, respectively, for several cathode barrier heights.

As illustrated in Figure 1, both the magnitude and region of negative resistance is greatly dependent on the cathode barrier, ϕ_b . With a cathode barrier of 110 meV, there exists a large region of negative resistance from 25 to 85 GHz to support fundamental oscillations. As the cathode barrier is increased such regions quickly are damped to near zero resistance over the frequency range of interest. The small-signal reactance is primarily capacitive with a slight oscillatory behavior. As the cathode barrier height is increased, the magnitude of the reactance is skewed to a lower frequency with smaller oscillations at the higher frequencies. Although not shown, changing the active region length provides further control over the region and magnitude of negative resistance. For example, a $1.5\mu\text{m}$ active region results in a

negative resistance domain ($\leq -1\Omega$) from 25-100 GHz, while a $1.9\mu\text{m}$ active region yields negative resistance from 21-75 GHz. While approximations to the average velocity and conductivity here are quite crude, similar trends are predicted by the large-signal simulator, described below, under small-signal a.c. drive.

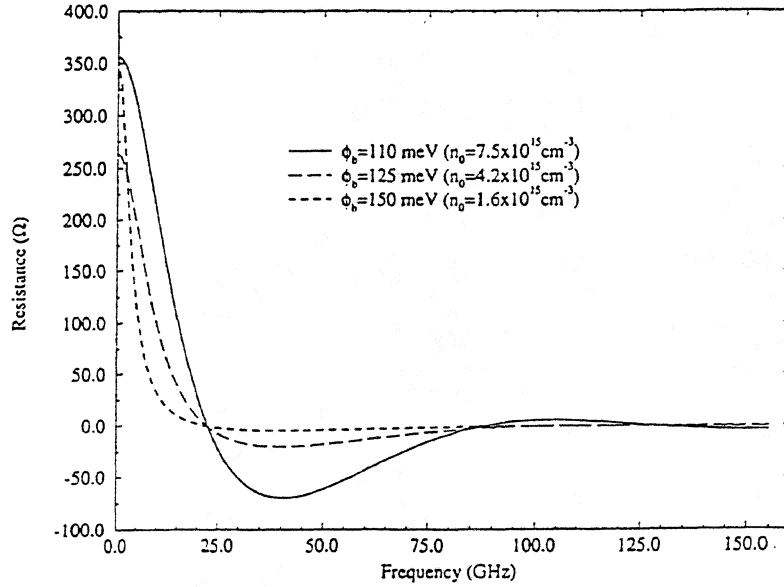


Figure.1: Small-signal resistance versus frequency for the Litton second-harmonic InP TED.

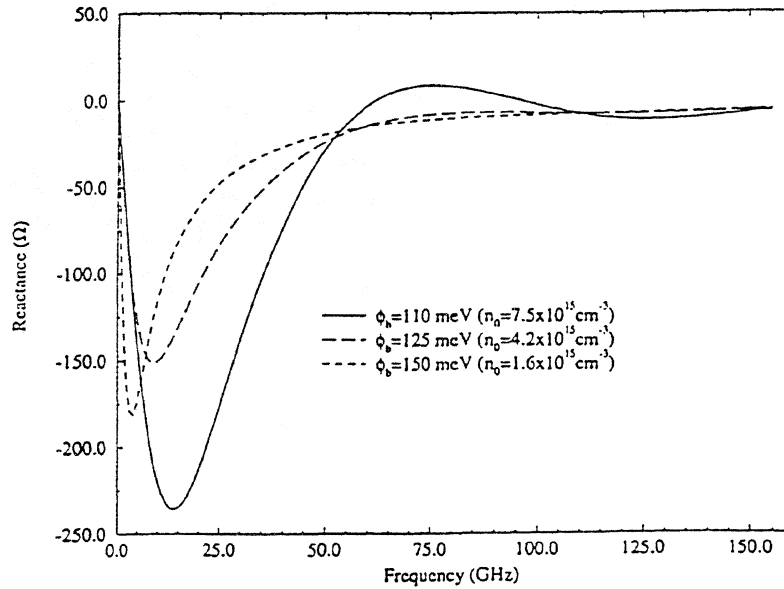


Figure 2: Small-signal reactance versus frequency for the Litton second-harmonic InP TED.

3 Combined Drift and Diffusion/Harmonic-Balance Large-Signal Simulation

A dynamic understanding of current limiting contact TEDs can be obtained through combined Drift and Diffusion/Harmonic-Balance (DDHB) simulations of the Litton InP second-harmonic TED mounted in a broadband cavity (H63) similar to that of reference [4]. The embedding impedances of the circuit have been extracted using the High Frequency Structure Simulator (HFSS) [5], and comparisons with experimental results have been made. The DDHB analysis used here employs an efficient fixed-point iteration method [6] derived from the multiple-reflection technique [7], facilitating the use of a hydrodynamic device simulator using the temperature-dependent drift/diffusion equation and Poisson's equation [8]. The drift and diffusion equation utilizes both field- (0.1-100 kV/cm) and temperature- (300-500 K) dependent mobility and diffusivity extracted from Monte Carlo simulations, and is coupled to a thermal analysis that includes all regions of the packaged device [9]. Complex frequency-dependent parasitic impedances, external to the active region of the device and similar to those of [10], are included in the analysis as additional contributions to the linear device embedding circuit. The Dirichlet boundary condition for electron concentration at the cathode, $n(0)$, is adjusted according to the current limiting contact barrier height for the SDL TEDs (see equation 5).

Figure 3 shows the current and voltage waveforms for the second-harmonic InP TED at 140 GHz in the H63 cavity where $\phi_b \approx 110$ meV, $n(0) \approx 7 \times 10^{15} \text{ cm}^{-3}$. Since the fundamental oscillation (70 GHz) is cutoff and terminated in an essentially reactive load, the fundamental voltage is large, and the corresponding fundamental output power is near zero. At 140 GHz second-harmonic operation, the magnitude of the fundamental voltage is 8.8 V, and the fundamental embedding impedance is $Z_1^{ckt} = 0.1 + i12.3\Omega$. The second-harmonic embedding impedance, extracted from HFSS simulations at 140 GHz for the optimal backshort positions, is $Z_2^{ckt} = 12.0 + i3.8\Omega$. The third-harmonic embedding impedance remains fairly stable at $Z_3^{ckt} = 0.2 + i59.9\Omega$ throughout the frequency range of interest. The optimal d.c. bias ($-10 \leq V_{d.c.} \leq -7$

V) is nearly twice that of a conventional Gunn diode of similar length, and the resultant d.c. current is more than three times smaller. Consequently, the SDL TED operating temperature over the active layer is nearly 100°C cooler than a companion (n^+nn^+) Gunn diode, leading to both better reliability and performance.

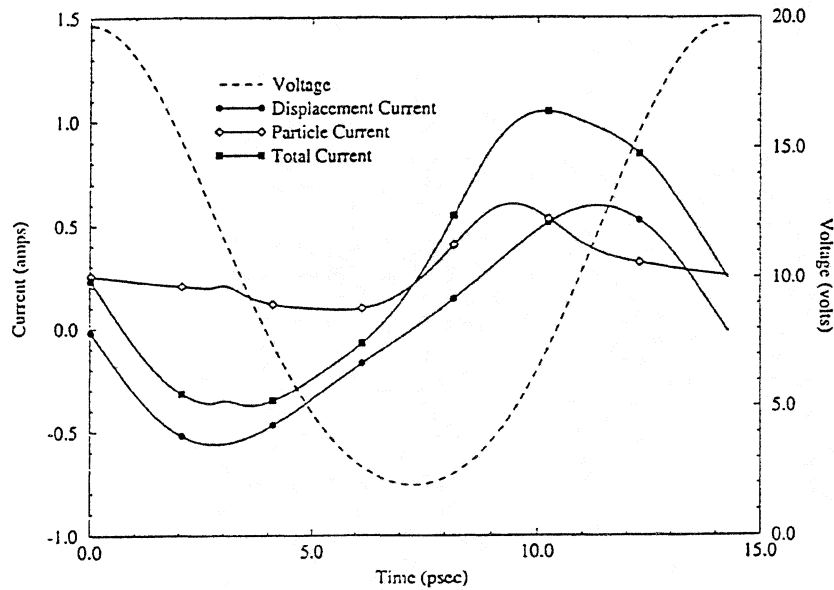


Figure 3: Current and voltage waveforms for the Litton second-harmonic InP SDL TED at 140 GHz. ($V_{d.c.} = -10V$, $Z_1^{ckt} = 0.17 + i12.3\Omega$, $Z_2^{ckt} = 12.0 + i3.8\Omega$)

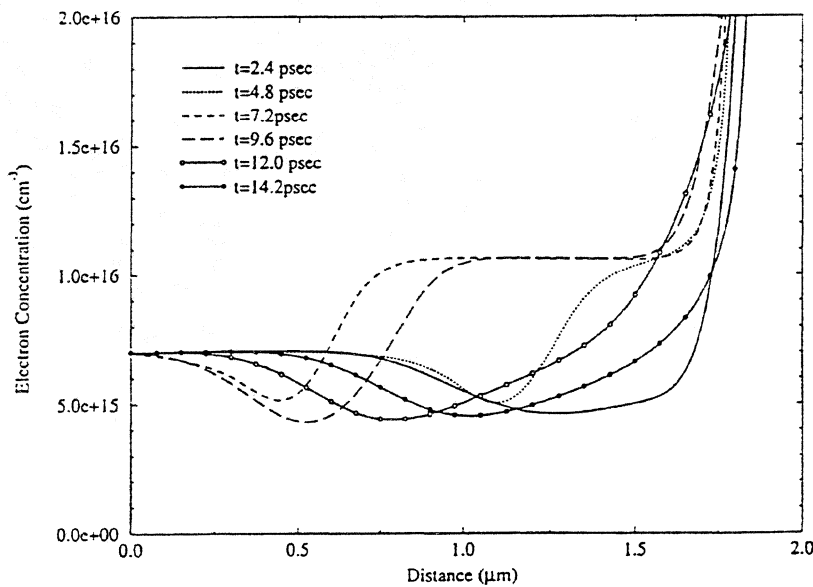


Figure 4: Electron concentration (positive electron charge) versus distance and time for the Litton second-harmonic InP SDL TED at 140 GHz. ($V_{d.c.} = -10V$, $Z_1^{ckt} = 0.17 + i12.3\Omega$, $Z_2^{ckt} = 12.0 + i3.8\Omega$)

Figures 4 and 5 show the corresponding electron concentration and electric field versus distance and time. The positive space charge associated with the partial electron depletion at the cathode leads to a decreasing electric field with increasing distance from the cathode and, thus, no possibility of accumulation layer formation. Like Gunn diodes, the method of power generation is a combined transferred electron and transit time effect. The power is generated by the transferred electron effect which serves to offset the current and voltage phase relation; the depletion layer transit time effect reduces the power dissipation by suppressing the particle current during the decreasing voltage cycle. As the applied voltage increases from its minimum, the particle current is quenched due to the transferred electron effect since, at this point, the entire electric field profile across the active region moves above the peak field ($E_{peak}^{InP} \approx 12 \text{ kV/cm}$). This occurs approximately 9.5ps into an oscillation cycle and is shown in Figures 3 and 5. The reduction in particle current is further aided by the

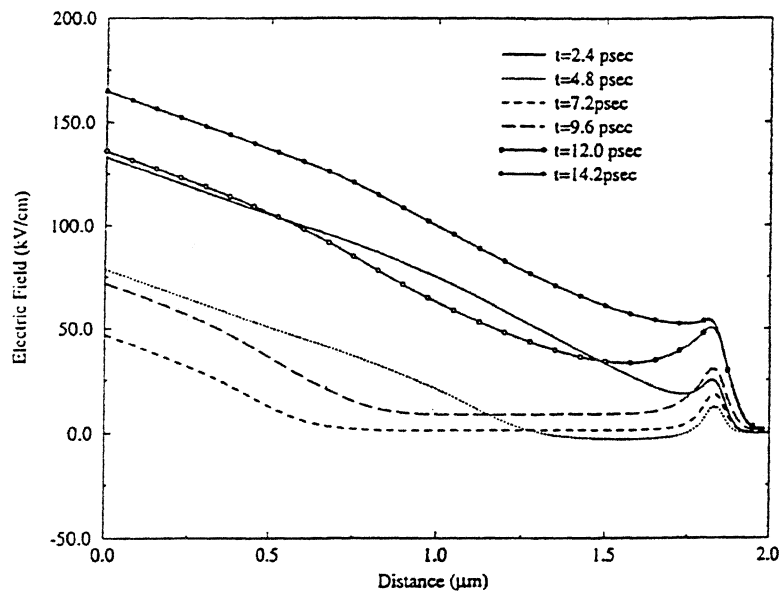


Figure 5: Electric field (positive electron charge) versus distance and time for the Litton second-harmonic InP SDL TED at 140 GHz. ($V_{d.c.} = -10V$, $Z_1^{ckt} = 0.17 + i12.3\Omega$, $Z_2^{ckt} = 12.0 + i3.8\Omega$)

onset of the partial depletion of the entire active region; this occurs at approximately 13ps into an oscillation cycle, and is maintained until midway between the peak and trough of the decreasing voltage waveform (3ps). As shown in Figure 4, a slight rise in particle current is seen at this point associated with the re-emergence of the depletion region from the anode. However, due to the large back diffusion of carriers from the anode, a minimal particle current is preserved. The resultant asymmetry in the current waveform provides excellent power generation at both the fundamental and second-harmonic.

Comparisons with experimental results have been made for the Litton second-harmonic InP SDL TED mounted in a broadband (115-145 GHz) cavity. More than 30 mW of CW output power can be obtained experimentally over the entire band. The cavity, shown in Figure 6, is similar to that of reference [4], with the diode embedded in a fundamental frequency resonator, and the second-harmonic power coupled out through half-height WR-8 waveguide having a cutoff frequency below the fundamental frequency (67.5-73.5 GHz). The fundamental resonator consists of a disk

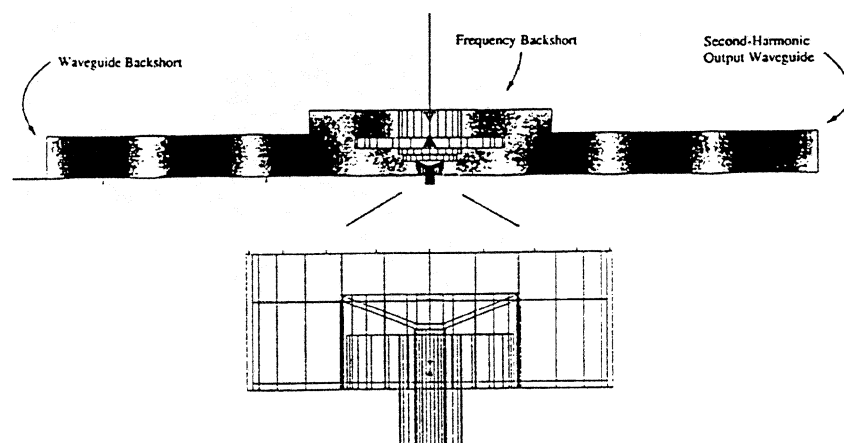


Figure 6: An HFSS schematic of the H63 115-145 GHz second-harmonic cavity and corresponding electric field profiles for 140 GHz operation. The package and coaxial probe are shown in the expanded region.

and post structure with a mechanically adjustable post length. An adjustable waveguide backshort is also provided to optimize the second-harmonic output power. Also shown in Figure 6 is a snapshot of the resultant electric field intensity at 140 GHz, and an expanded view of the diode package. For HFSS simulations, the cavity is characterized as a three port system in which both the second-harmonic output and backshort waveguides are modelled as matched loads. Excitations representing those generated by the diode occur through the third port via a coaxial line whose inner dimension is precisely that of the TED. Since the frequency backshort is adjacent to large evanescent fields, it is modelled physically by adjusting the height of the fundamental resonator according to experimental settings. The variable waveguide backshort is modelled through the use of the Microwave Design System (MDS) [11] using the simulated HFSS S-parameters. A variable length of matched transmission line, terminated in an electrical short, is added, and the input impedance at the diode port is extracted through standard transformation of the S-parameter matrix. Figure 7 shows the simulated 140 GHz second-harmonic embedding impedance ver-

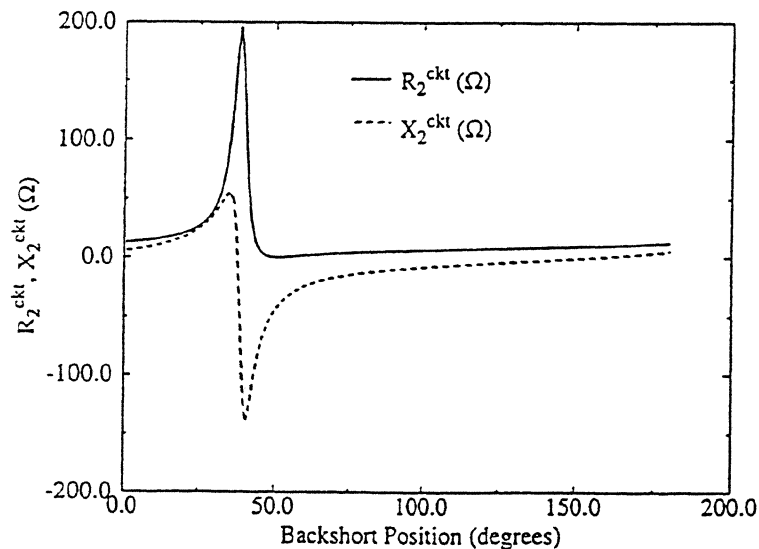


Figure 7: Simulated 140 GHz second-harmonic embedding impedances versus waveguide backshort position for the H63 broadband cavity.

sus waveguide backshort position for the H63 cavity. Besides a resonance at $\sim 40^\circ$, the resistance, R_2^{ckt} , and reactance, X_2^{ckt} , remain quit low ($\leq 20\Omega$) throughout the tuning range. Both capacitive and inductive reactances can be presented to the diode at the second harmonic; substantially better performance is obtained with the latter. Combined drift and diffusion/harmonic balance simulations have been performed employing optimal backshort positions as derived from HFSS, and the results are shown in Table 1. It is important to note that this commercially available device outperforms conventional research oriented Gunn [12], IMPATT [13], and TUNNET [14] diodes even when presented with a wide range of second-harmonic embedding impedances associated with a broadband cavity. Experimentally, as much as 60 mW has been achieved at 140 GHz with optimal embedding impedances [1].

Frequency	125 GHz		130 GHz		140 GHz	
	Experiment	Simulation	Experiment	Simulation	Experiment	Simulation
$V_{d.c.}$ (V)	10	10	10	10	10	10
$I_{d.c.}$ (mA)	~ 220	279	~ 220	281	~ 220	278
$Z_1^{ckt}(\Omega)$	NA	$0.13 + j13.9$	NA	$0.13 + j13.1$	NA	$0.17 + j12.3$
$Z_2^{ckt}(\Omega)$	NA	$4.1 + j9.5$	NA	$10.9 + j6.8$	NA	$12.0 + j3.8$
Power (mW)	42	59	33	39	31	26

Table 1: 120-140 GHz second-harmonic InP SDL TED simulations versus experimental results from the H63 cavity ($Z_3^{ckt} = 0.2 + j59.9\Omega$)

4 Conclusion

A novel Stable Depletion Layer TED operating mode representing state-of-the-art performance in low noise millimeter-wave power generation has been identified. In comparison to other solid-state millimeter-wave sources, SDL TEDs provide increased output power, reliability, and improved frequency stability with temperature variation. The small-signal negative resistance of SDL TEDs has been calculated, and large-signal simulations have provided a dynamic insight into the operation of this device. It has been shown that the SDL mode is a hybrid transferred electron/transit

time process. The phenomena and analysis reported here may also explain the behavior recently reported [15, 16] for low to high energy bandgap heterojunction cathode TEDs. Furthermore, simulations have been performed to show that significantly higher frequency (10 mW at 210 GHz) operation is possible since the output power is no longer limited by the formation of electron accumulation charge instabilities.

5 Acknowledgement

The authors would like to thank Dr. G. B. Tait of the United States Military Academy and Dr. D. Wilt of Nasa Lewis for stimulating discussions regarding TEOs and current limiting contacts. This work has been supported by NSF grant ECS-9202037.

References

- [1] J. D. Crowley, C. Hang, R. E. Dalrymple, D. R. Tringali, F. B. Fank, L. Wandinger and H. B. Wallace, "140 GHz indium phosphide Gunn diode," *Electronics Lett.*, **30**, 6 (1994), pp. 499-500.
- [2] H. Kroemer, "The Gunn Effect Under Imperfect Boundary Conditions," *IEEE Trans. Electron Devices*, vol. ED-15, No. 11, (1968), pp. 819-837.
- [3] S. M. Sze, *Physics of Semiconductor Devices*. New York, NY: John Wiley & Sons, Inc. 1981.
- [4] J. E. Carlstrom, R. L. Plambeck, and D. D. Thornton, "A Continuously Tunable 65-115-GHz Gunn Oscillator," *IEEE Trans. Microwave Theory Tech.*, vol. MTT-33, (1985) pp. 610-619.
- [5] High Frequency Structure Simulator, Hewlett-Packard Co., Network Measurements Division, Santa Rosa, CA, 1992.
- [6] G. B. Tait, "Efficient Solution Method for Unified Nonlinear Microwave Circuit and Numerical Solid-State Device Simulation," *IEEE Microwave and Guided Wave Let.*, Vol. 4, No. 12, (1994), pp. 420-422.
- [7] P. H. Siegel, A. R. Kerr, and W. Hwang, "Topics in the Optimization of Millimeter-Wave Mixers," *NASA Tech. Paper*, No. 2287, March 1984.
- [8] M. F. Zybura, S. H. Jones, G. B. Tait, and J. R. Jones, "100-300 GHz Gunn Oscillator Simulation Through Harmonic Balance Circuit Analysis Linked to a Hydrodynamic Device Simulator," *IEEE Microwave and Guided Wave Let.*, Vol. 4, No. 8, (1994), pp. 282-284.
- [9] M. F. Zybura, S. H. Jones, G. B. Tait, and J. M. Duva, "Efficient Computer Aided design of GaAs and InP Millimeter Wave Transferred Electron Devices Including Detailed Thermal Analysis," *Solid-State Electronics*, Vol. 38, (1995), pp. 873-880.
- [10] S. A. Maas *Nonlinear Microwave Circuits*: Artech House, Norwood, MA, 1988, Ch. 2, pp. 49-51.
- [11] Microwave Design System, Hewlett-Packard Co., Network Measurements Division, Santa Rosa, CA, 1990.
- [12] A. Rydberg, "A Contribution to the Design of Wideband Tunable Second Harmonic Mode Millimeter-Wave InP-TED Oscillators Above 110 GHz," *Intl. Journ. of Infrared and Millimeter Waves*, Vol. 11, No. 3, (1990), pp. 383-404.
- [13] M. Tschernitz and J. Freyer, "Design and Realization of GaAs D-Band IMPATT Oscillators", *Proc. Fifth Intl. Symp. on Space THz Tech.*, Ann Arbor, Mi. May 10-12 (1994), pp. 611-621.

- [14] H. Eisele and G. I. Haddad, "GaAs TUNNET Diodes on Diamond Heat Sinks for 100 GHz and Above," *IEEE Trans. Microwave Theory Tech.*, Vol. 43, No. 1, (1995), pp. 210-213.
- [15] M. R. Friscourt, P. A. Rolland, and M. Pernisek, "Heterojunction Cathode Contact Transferred-Electron Oscillators," *IEEE Elec. Dev. Lett.*, Vol. 6, No. 10, (1985), pp. 497-499.
- [16] R. Kamoua, "Heterojunction Cathode Injectors for D-Band InP Gunn Devices," *Solid-State Electronics*, Vol. 38, No. 2, (1995), pp. 269-274.

345 GHz RADIATION FROM A QUASIOPTICAL JOSEPHSON OSCILLATOR

Michael J. Wengler, Boran Guan

Electrical Engineering Department, University of Rochester, NY 14627

and

Elie K. Track, *HYPRES, Inc., 175 Clearbrook Rd., Elmsford, NY 10523*

At 345 GHz, 0.7 μ W has been detected from an 24×116 array of Josephson junctions fabricated using Hypres's standard niobium process. The power is radiated directly into free space above the surface of the two-dimensional array of junctions. Detection is made by a commercial bolometer in a separate cryostat from the one which cools the array to 4.2 K. The junctions in the array are closely spaced in the y-dimension, but spaced by more than one-half wavelength in the x-direction. This asymmetry results in mutual phase-locking between adjacent junctions suitable for the production of y-polarized radiation. Microwave models show that this array geometry presents a low antenna impedance which favors efficient coupling from the junction to free-space radiation.

The design of the 345 GHz array is very close to a two-times scaling of an array reported at the 1994 THz Symposium.¹ In particular, the horizontal and vertical spacing between junctions in the array is half as much in the 345 GHz array as in the previously reported 190 GHz array. Since the total area of the two arrays, 3×3 mm, is about the same, the 345 GHz array includes about 4 times as many junctions as the 190 GHz array. At least for this factor of two, scaling has worked approximately as follows: half the spacing horizontally and half the spacing vertically result in 4 times as many junctions, oscillating at twice the frequency, emitting twice the power. This result is quite encouraging towards the possibilities of further frequency and power increases through further reduction of vertical and horizontal spacing in a future array.

Fabrication of this array was supported by the Ballistic Missile Defense Organization through a Phase I SBIR award to HYPRES. Testing and analysis of the results were supported by HYPRES and the Electrical Engineering Department at the University of Rochester.

¹Wengler, Guan, and Track, "190 GHz Radiation from a Quasioptical Josephson Junction Array," *IEEE Trans. on Microwave Theory and Techniques*, vol. 43, April, 1995, in press.

A Waveguide Tripler for 720-880 GHz

Neal R. Erickson
Department of Physics and Astronomy
University of Massachusetts
Amherst, MA 01003

Jussi Tuovinen
Radio Laboratory
Helsinki University of Technology
Otakaari 5 A, FIN-02150 Espoo, Finland

Abstract

A tripler has been built for the frequency range 720-880 GHz using a novel style of construction intended to minimize the machining difficulties associated with devices at such high frequencies. The performance has been tested with a Gunn oscillator/doubler source producing 4-6.5 mW in the 238-294 GHz range. The maximum output power is $110\mu W$ with an efficiency of 1.7%. The bandwidth of operation covers the full input range tested, and is consistent with the design expectations, although the center frequency is slightly shifted.

Introduction

Triplers have been built throughout the millimeter range, and well into the submillimeter, using a technique in which waveguides, filters and mechanical supports are machined and assembled into relatively thin wafers, which are then stacked up to form the complete device [1,2,3]. While this method has the advantage that each part is fairly simple, machining tolerances are considerable and the relative alignment of the wafers is critical. It is particularly difficult to measure the outer diameter of the coaxial filter coupling the two waveguides, or the concentricity of the coaxial center pin passing through them. This means that there is no way to ensure that the impedances of the coaxial sections are at the design values. This is a major problem in the fabrication of wideband devices, particularly those designed to have fixed backshort tuning. There are other problems associated with the wafer style design, such as maintaining the required flatness to the rather thin parts, and cutting the diode chip into a nearly round shape so that it will fit the outer conductor shape. All these problems become more severe as the frequency increases, and eventually require a new approach. The tripler described here is an effort to solve these problems, and is largely successful.

While the basic electrical design is the same as previous devices using a stack of wafers, this new structure is built from only two blocks which are split along the E-plane center-line of the input and output waveguides. Most features are machined in a single step, making

it easier to maintain the needed alignment. A design constraint was that all features could be machined with conventional tools, without requiring the use of electroforming. While machining of the overall structure is not really easier than for the previous designs, it is far easier to verify dimensions, and to assemble this new design.

Electrical Design

The goal of the microwave design was to produce a tripler which could operate over the 750-900 GHz range, with minimal tuning of the backshorts. Only one tuner in each waveguide is used, and over the midband, they are intended to remain fixed. Such fixed tuned triplers have worked well at lower frequencies where fractional bandwidths of up to 26% may be covered [4]. The electrical design follows closely upon this principal, one critical element of which is the coaxial resonator in the output waveguide which adds the necessary inductance at the input circuit for a wideband match. However, splitting the circuit in the E-plane of the waveguides requires a complete re-evaluation of many of the design features.

Mechanical and electrical constraints required that critical features be split between the halves in the following manner:

- Waveguides are split near the centerline in the E plane for lowest loss. The split line was not exactly on center for the output waveguide because of the asymmetry in the coaxial sections.
- The smallest coaxial sections were machined entirely in one half of the block to avoid problems with the mutual alignment, and to ensure that the most delicate features of the center pin were well protected during assembly.
- The larger coaxial sections partially extend into the mating half of the block in order to maintain coaxial symmetry.
- The center pin of the coaxial resonator (with the whisker attached) is fixed in a channel in the main block with a good electrical contact to ground at the end of the reduced diameter section.
- The diagonal horn was split on the centerline since this horn requires symmetry and this is the only way to machine it.

The inside of the block is shown in Fig.1. The input WR-3 waveguide and output horn are on opposite sides of the block, while the tuners are on the remaining two sides. The coaxial filter uses cross sections having a square outer conductor and a round inner conductor. The center conductor is supported by a ceramic block at one end, with air dielectric throughout the filter sections. The center conductor of the section adjacent to the output waveguide is comprised of the varactor diode chip, which is cut into a square. Since the outer conductor is square, no further shaping is needed. These details are shown in Fig. 2.

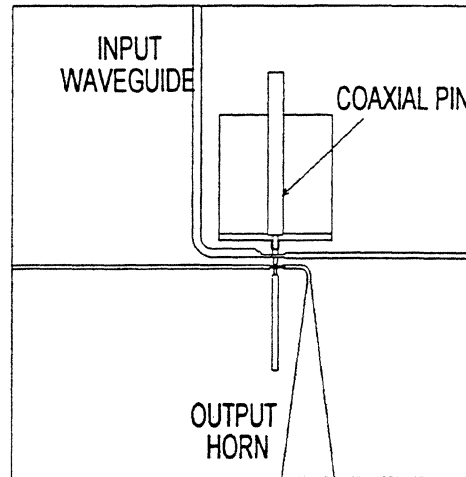


Fig.1. Internal view of the tripler block showing the overall features of the waveguides and horn.

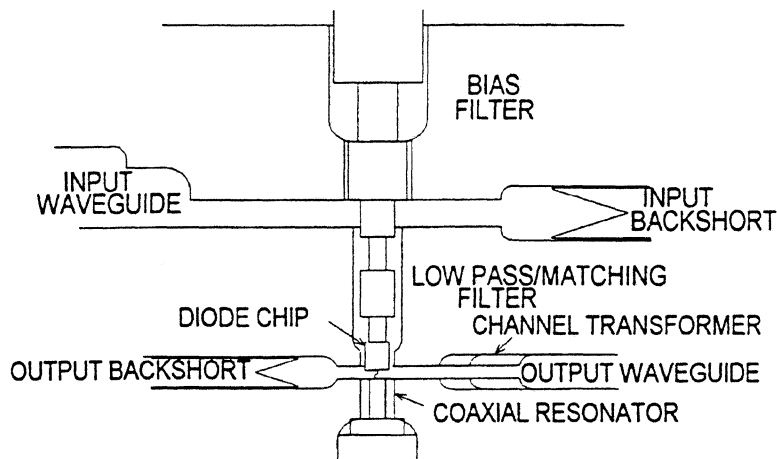


Fig. 2. Details of the waveguides and filters within the tripler, greatly magnified from above.

The design was refined through extensive use of the finite element program HP-High Frequency Structure Simulator (HFSS). This was necessary because of the unconventional cross sections and discontinuity effects involved and eliminated any need for scale modeling except as a final check. The particular problem areas were:

- The output waveguide "channel" transformer, particularly discontinuity capacitances at the steps.

- The off-center mounting of the diode in the output waveguide. This arises because of the near-center waveguide split and the off-center coax split.
- The discontinuity capacitances at the steps in the unconventional coax.
- Higher mode excitation in the coaxial filter at the junction with the output waveguide.
- Expected backshort locations, to position the steps up to the backshort sections.

Details of these areas are covered in the later sections. The individual pieces were designed with a linear circuit simulator (Touchstone), with the behavior of details and verification of the complete circuit provided by HFSS. The final design verification was performed using a scale model. In this model, minor but critical differences were seen relative to the HFSS predictions. To resolve these, the predicted vs. measured behavior were compared using a circuit simulator. This made it clear that a simple modification would correct the problem, involving just an increase in the size of the diode chip. No complete explanation has been found to resolve the source of the difference.

Coax to output waveguide transition

The size of the coaxial line needed to ensure single mode propagation at 900 GHz is too small for accurate fabrication or assembly, particularly with the use of the square coax at the waveguide junction. An alternative approach which has been found to work well is to use a larger cross section, but to ensure that higher modes are not excited. In this case, the maximum possible coax size was desired so HFSS was used to predict the excitation of the next order mode in the coax. Excitation of this waveguide mode is found to be greatest near its mode cutoff and diminishes to a small value at higher frequencies. If this cutoff frequency is set near 690 GHz, it should have little effect on the operation of the tripler in the 780-900 GHz range. This cutoff frequency is achieved with an outer conductor 0.14 mm square and an inner conductor 0.86 mm square. The impedance of this section is 24Ω . In the following sections, the size is enlarged further, since there is little tendency to excite higher modes.

Square outer/round inner coax

The choice of cross section for the coax is purely for ease of machining, and has no circuit advantages. In fact, this cross section tends to have a higher impedance, higher loss and a lower higher mode cutoff than circular coax of similar dimensions. The minimum practical impedance with reasonable clearance is 15Ω . The high impedance sections are 56Ω . Discontinuity effects are very similar to those in comparably sized circular coax.

Waveguide transformers

The waveguides are cut using slitting saws, in order to produce the required reduced height sections. The input waveguide is transformed to full height WR-3 using a conventional $\lambda/4$ step transformer. The reduced height section of the output waveguide is $50 \times 250\mu\text{m}$ and may be cut with a saw, while the full height section is $150 \times 300\mu\text{m}$ and may be machined with an end mill. However, there is no tool available which can machine the transition section using conventional rectangular waveguide. A solution to this problem has been devised in a cross section called channel waveguide [5]. While the original approach was to saw the

transition as a long taper, the same cross section may be machined as a step transformer using an end mill. A usual problem with this type of transformer is that the cutoff frequency increases within the transformer by an amount dependent upon the impedance ratio being transformed. This is actually an advantage in the present use because the cutoff helps to suppress the radiation of the second harmonic.

Designing such a transformer with steps is difficult because the impedance of a given cross section may not be chosen independently from its cutoff frequency, and no closed form method of solution exists. In nearly all cases, practical solutions do exist although they may involve more steps than might initially be expected. In this case a two step transformer proved to work well.

Waveguide backshorts

The very low height of the waveguides was expected to cause serious problems with tunable backshorts, particularly in the output waveguide. This problem was expected to be particularly severe if the halves of the waveguide did not line up perfectly. Backshorts will work equally well in waveguides of enlarged cross sections, but their tuning tends to be more critical. However, if the location of the backshort may be predicted in advance, the waveguide may step to greater height at a distance $\lambda_g/4$ away, and so approximate an open circuit at this point. In this case, the backshort tuning becomes much less critical. This approach was used in both waveguides.

Performance

The pump source for all these tests was a Gunn oscillator in the 119-147 GHz range [6] with 35-45 mW output power. This source drives a balanced doubler [3] using a pair of UVa 2T2 whisker contacted varactors ($C_j(0) = 6fF$, $R_s = 15\Omega$). The output power of this source is 4-6.5 mW across the band of interest. This doubler was designed for the 300-370 GHz band, and is far from optimum at lower frequencies. The intended source is a planar diode doubler which has been tested in the correct band [7], but presently has less output than the whiskered doubler. While the optimized power is expected to be $>10\text{mW}$, diodes with the needed performance are still under development.

The tripler uses a UVa 2T8 varactor with $C_j(0) = 4.5fF$, $R_s = 15\Omega$ and $V_b = 10V$. The contact whisker is $3\mu\text{m}$ diameter NiAu wire with a total length of $38\mu\text{m}$. The tripler is found to operate over the entire range that may be tested with the above source. The optimum bias voltage varies from 0.7-2V (in the reverse direction) with a forward current of $500\mu\text{A}$ at the lowest frequencies, decreasing to $10\mu\text{A}$ at the highest. This operation is consistent with the designed varactor mode of operation, and is similar to that of devices at lower frequency. Despite the lack of any isolation between the tripler and doubler, the power coupling is good at all frequencies tested, with a fixed spacing between the devices and only backshort tuning. The maximum output power is $110\mu\text{W}$ at 790 GHz, where the input power is 6.3 mW, yielding an efficiency of 1.7%. This compares favorably to an efficiency of 3.5% measured for the same diode design in a tripler for 474 GHz [3]. The measured output power across the band is shown in Fig. 3. The variation in the output power is due to a combination of the available input power and the inherent properties of the tripler, so the details of the

curve are not significant. The drop in power at both ends of the band is apparently due to the tripler, since the pump source shows no similar trend. At all frequencies, the varactor is underdriven, judging from the bias voltage, which is well below the optimum value of $0.35 V_b$, typical of most varactors. Thus we may expect the output power to increase with increasing input power, perhaps by a factor of two or more. Some increase in efficiency is also expected. Usually, the high end of the band is most sensitive to low input power, so the greatest gain may be seen here. The measured tuning curve is offset slightly from the design range, but this type of problem is expected with small variations in dimensions.

The performance is not yet optimized, and a variety of minor refinements in the internal geometry are possible. In addition, better varactors are now available from UVA, and will be installed in the near future. The design was intended to require minimal backshort tuning across the band, but the data in Fig. 3 involved peaking at each frequency. It is not certain if true fixed tuned operation is possible with this unit, or if the waveguide steps to full height in the backshort sections are placed correctly. However, this has not proven to be a liability because the backshorts work very smoothly and reliably. There is no tendency for the shorts to lift metal flakes from the waveguide walls as is the usual case, because the shorts do not need to fit tightly to work well.

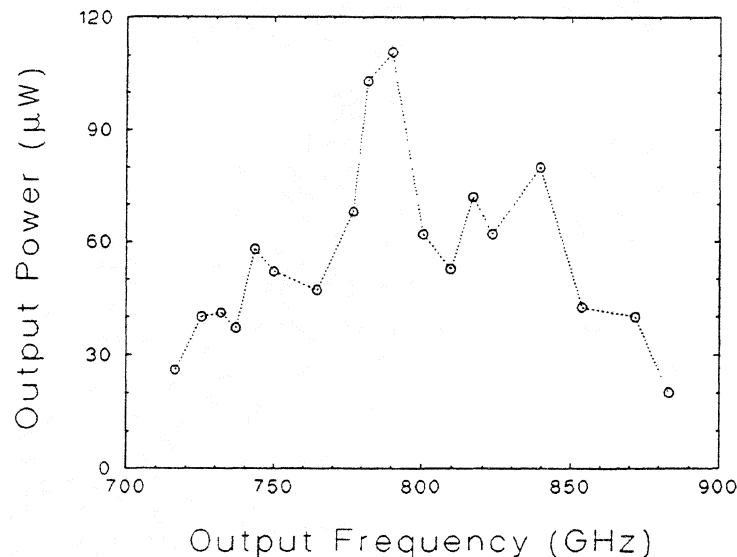


Figure 3. Tripler output power vs. frequency.

Calibration

Accurate power measurements of devices at such high frequencies is quite a challenge because there are few power sensors sensitive enough to detect low power having any reliable calibration. For use in this work, a waveguide calorimeter was constructed which is sensitive enough to detect $1\mu W$, and which may be accurately calibrated. This calorimeter uses very thin wall stainless steel WR-10 waveguide on the input, with a very low mass absorbing

element. It has a VSWR $< 1.2:1$ in the WR-10 band, and the match improves with increasing frequency, although nothing is known about its behavior well into the submillimeter. The time constant is about 20 sec, which is not a serious problem because the sensor is so stable. The coupling to the tripler output is via a taper from 3.0 mm diameter circular waveguide to WR-10, which is placed against the horn aperture.

Calibration is a combination of measuring the sensor power responsivity using dc heating of a resistor mounted on the sensor, plus a correction for the input waveguide loss (which is frequency dependent). This loss may be determined by adding a second section of waveguide to the input having characteristics identical to those of the internal waveguide (a 35mm length of gold plated SS waveguide), and measuring the decrease in indicated power. It is found that the waveguide attenuation is much higher than expected for the lowest order mode, probably due to a combination of higher than theoretical surface resistivity, and the excitation of many higher modes in the horn coupling power out of the tripler, and the taper into the calorimeter. In this case the internal loss plus that estimated for the waveguide taper is about 2 dB. The actual internal loss may be higher, since the SS waveguide used to estimate the loss has better quality gold plating than the section used within the calorimeter. This method of calibration has been verified at 147 GHz where the corrected power measured with the calorimeter is within 0.1 dB of the power measured with an Anritsu sensor calibrated using other means.

Conclusions

A tripler has been built which tunes from 720-880 GHz with a minimum output power of $25\mu W$ and a typical power of $60\mu W$. The tuning range is very similar to the design value, with an error of only 3% in center frequency. This validates the method of construction, which is intended to permit the design of wide band multipliers in the submillimeter with predictable performance. The efficiency compares favorably with that of a device at much lower frequency using the same varactor diode. This multiplier should provide adequate LO power over nearly the full bandwidth of an SIS receiver.

Acknowledgments

The authors wish to thank Ronna Erickson for her help in assembling the tripler, and Ron Grosslein and Joe Janes for their help in assembling the calorimeter. This work was supported by JPL under contract 959206.

References

- [1] Erickson, N.R., "A high efficiency frequency tripler for 230 GHz," Proc. 12th European Microwave Conf. (Helsinki), p. 288, 1982.
- [2] Erickson, N.R., "A very low noise single sideband receiver for 200-260 GHz," IEEE Trans. Microwave Theory Tech., vol. 33, p. 1179, 1985.

- [3] Erickson, N.R., "High efficiency submillimeter frequency multipliers," 1990 IEEE MTT-S Int'l. Microwave Symp., p. 1301.
- [4] Erickson, N.R., Goldsmith, P.F., Novak, G., Grosslein, R.M., Viscuso, P.J., Erickson, R.B., and Predmore, C.R., "A 15 element focal plane array for 100 GHz," IEEE Trans. Microwave Theory Tech., vol. 40, p. 1, 1992.
- [5] Siegel, P.H., Peterson, D.W., and Kerr, A.R. , "Design and analysis of the channel waveguide transformer," IEEE Trans. Microwave Theory Tech., vol. 31, p. 473, 1983.
- [6] Zybura, M.F. Jones, S.H., Carlstrom, J.E., and Crowley, J.D., "120-145 GHz stable depletion layer second harmonic transferred electron oscillators," this conference proceedings.
- [7] Erickson, N.R., Tuovinen, J., Rizzi, B.J., and Crowe, T.W., "A balanced doubler using a planar diode array for 270 GHz," Proc. Fifth Int'l. Symposium on Space THz Tech. (1994), p. 409.

TERAHERTZ GRID FREQUENCY DOUBLERS

Jung-Chih Chiao¹, Andrea Markelz², Yongjun Li³, Jonathan Hacker⁴,
Thomas Crowe³, James Allen², and David Rutledge¹

¹Department of Electrical Engineering, California Institute of Technology, Pasadena, CA 91125

²Department of Physics, University of California at Santa Barbara, Santa Barbara, CA 93106

³Department of Electrical Engineering, University of Virginia, Charlottesville, VA 22903

⁴Bellcore Communications Research, Red Bank, NJ 07701

Abstract – A terahertz quasi-optical grid frequency doubler has been developed. This frequency doubler is a planar bow-tie grid structure periodically loaded with planar Schottky diodes. This is the first experimental result with quasi-optical grid frequency multipliers in the terahertz frequency range. A peak output power of $330 \mu\text{W}$ was measured at 1 THz for $2.42 \mu\text{s}$ 500-GHz input pulses with a peak power of 3.3 W.

INTRODUCTION

The demand for solid-state local oscillators in the THz frequency range has been steadily increasing for applications in radio astronomy and remote sensing of the atmosphere [1,2]. The interest for THz applications has fostered a strong need for submillimeter-wave receivers, mixers and sources, especially tunable high-power sources used as the local oscillators for heterodyne submillimeter-wave receivers. For example, the local-oscillator output-power requirement at 1 THz for NASA's SMMM (Submillimeter Moderate Mission) is at least $50 \mu\text{W}$ [3]. Traditional high-power sources in the THz region such as gas lasers and vacuum-tube oscillators are not suitable for this purpose due to their large size, high-voltage supplies, short lifetime

and small tuning ranges. However, frequency multipliers and upconverters like Schottky diode multipliers can be used to generate the required terahertz frequencies from lower-frequency solid-state tunable signal sources such as Gunn-diode oscillators.

APPROACH

Current diode multipliers have mostly been single-diode structures typically consisting of a Schottky varactor diode placed in a waveguide with a whisker contact. Rydberg, Lyons and Lidholm have demonstrated a Schottky varactor diode frequency tripler with a measured output power more than $120 \mu\text{W}$ at 803 GHz [4]. Erickson and Tuovinen presented a waveguide tripler with an output power of $110 \mu\text{W}$ at 800 GHz [5]. Zimmermann, Rose and Crowe have demonstrated an output power of $60 \mu\text{W}$ at 1 THz by using a cascade of two whisker contacted Schottky varactor frequency triplers [6]. One approach to overcome the low power of solid-state devices in the submillimeter-wave band is to combine a large number of devices together [7,8]. A grid of planar diodes quasi-optically coupled in free space does not require the construction of single-mode waveguides and can potentially overcome the power limits of conventional single-diode multipliers [9]. Using this approach, H.-X. Liu has demonstrated a frequency

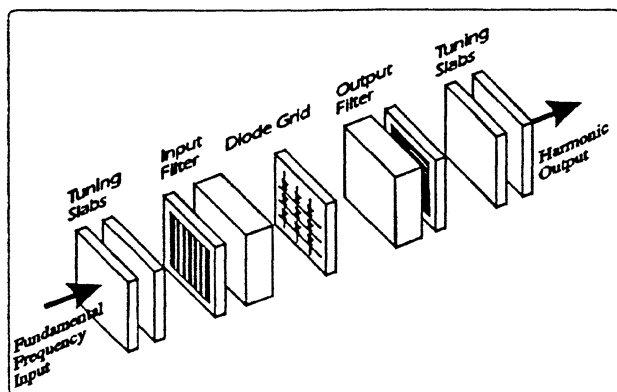


Fig. 1. The grid-multiplier concept [8]. The fundamental wave enters on the left as a beam, passes through a filter, and is incident on the diode grid. The grid acts as a nonlinear surface and produces a beam at the harmonic frequencies, which passes through filters on the right.

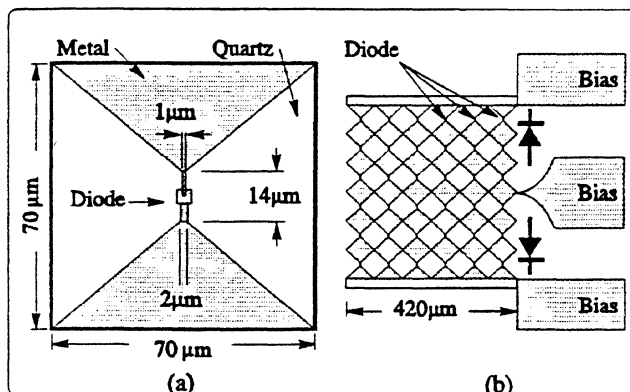


Fig. 2. The grid frequency doubler. (a): the unit cell, (b): the entire 6×6 array. The diode symbols indicate the polarity. Three diodes are in series from the top or bottom bias line to the center bias line. The bow-ties in two adjacent columns are not connected except the ones in the center row for biasing.

tripler consisting of 3,100 Schottky-quantum-barrier varactor diodes to produce 5 W pulsed output power at 99 GHz [10].

The multiplier concept is shown in Fig. 1. The input beam at the fundamental frequency enters from the left. The first element is a pair of dielectric tuning slabs that act to transform the impedance of the input wave to one appropriate for the multiplier grid. Typically inductive reactance is needed to cancel capacitance of the diodes in the grid. In addition, the free-space wave impedance, 377Ω , is inconveniently high and needs to be reduced. Next the beam passes through a low-pass filter that passes the fundamental frequency, but reflects harmonics. Then the beam hits the grid. The grid acts as a nonlinear surface which results from the nonlinearity of I-V or C-V characteristics of diodes and generates harmonics. This harmonic beam radiates both forward and backward, but the

backward beam reflects off the low-pass filter. The forward beam passes through the high-pass filter, and then through another pair of tuning slabs. One important feature is that the tuning slabs are outside the filters, so that the input and output can be tuned independently. The entire structure is quite compact, only a few wavelengths thick. The design is also suitable for cascading, so that even higher harmonics could be produced. The multiplication process preserves the beam shape. Therefore, a focused beam could be used so that different sizes of multiplier grids could be cascaded.

In this paper, the tuning slabs were not used for experimental simplicity.

PLANAR SCHOTTKY DIODE GRID

These grid multipliers were fabricated by monolithic technology on a $30\text{-}\mu\text{m}$ thick fused-quartz substrate at the University of Virginia [11]. Figure 2(a) shows the bow-tie-shaped metal pattern used for the unit cell. The Schottky diode junction is located at the center of the unit cell. The size of a unit cell is $70\text{ }\mu\text{m} \times 70\text{ }\mu\text{m}$. Figure 2(b) shows the entire 6×6 array. The active area is $420\text{ }\mu\text{m} \times 420\text{ }\mu\text{m}$. Three diodes are in series from the top or bottom bias line to the center bias line. The adjacent bow-ties are not connected except the center row. The diodes in the top and bottom halves of the grid have opposite polarity. This is because the grid was originally designed as a sideband generator[7]. When the grid is used as a frequency multiplier, the polarity change causes an undesired null in the middle of the beam.

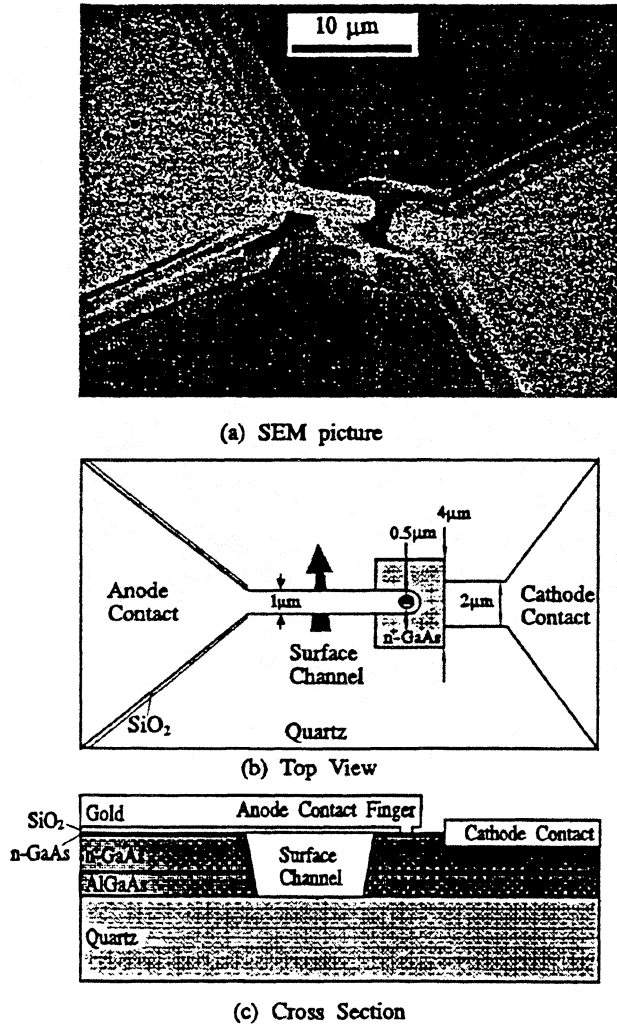


Fig. 3. (a) The SEM picture, (b) the top view and dimensions, and (c) the cross section of the Schottky diode.

Figure 3(a) shows an SEM picture of the planar Schottky diode located between the metal fingers of the bow-tie structure. Figure 3(b) and 3(c) show the top view and the cross section of the planar Schottky diode. The anode has a diameter of $0.5\text{ }\mu\text{m}$. The n-GaAs layer has a thickness of $0.1\text{ }\mu\text{m}$ and a doping concentration of $4 \times 10^{17}\text{ cm}^{-3}$.

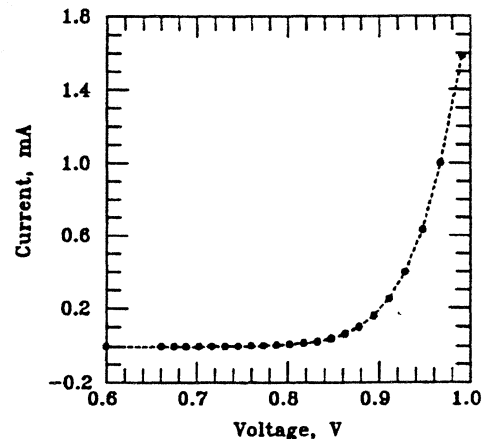


Fig. 4. Typical measured DC I-V curve.

The n^+ -GaAs layer has a thickness of $3\ \mu\text{m}$ and a doping concentration of $5 \times 10^{18}\text{cm}^{-3}$. The AlGaAs layer has a thickness of $1.5\ \mu\text{m}$. A surface channel was etched away underneath the anode contact finger to reduce the shunt capacitance. The diodes have a measured DC series resistance of $14\ \Omega$ and an estimated junction capacitance of $0.6\ \text{fF}$ at zero bias. Figure 4 shows a typical I-V curve measured on one of the diodes.

MEASUREMENT ARRANGEMENT

The measurements use the free-electron laser (FEL) as the input source in the Quantum Institute at the University of California, Santa Barbara. The free-electron laser generates kilowatts of polarized radiation tunable from 120 GHz to 4.8 THz [12]. The pulse width is $2.42\ \mu\text{s}$ with a period of 1.3 s. The measurement setup is shown in Fig. 5. All the optical components were aligned using a He-Ne laser. Half of the input power at the fundamental frequency in the incident beam was split off into a reference detector. We used a pyroelectric detector as the reference detector. The radiation from the FEL was then focused by a parabolic mirror with an f-number of 1.6 and a focal length of 15 cm. We varied the input power by inserting plexiglass attenuators in front of the beam splitter.

The harmonic radiation from the grid was collimated by an f/1 parabolic mirror with a focal length of 11 cm. A metallic-mesh Fabry-Perot interferometer in the collimated beam was used to measure the frequency content. The diameter of the interferometer is 15 cm so that it covers the

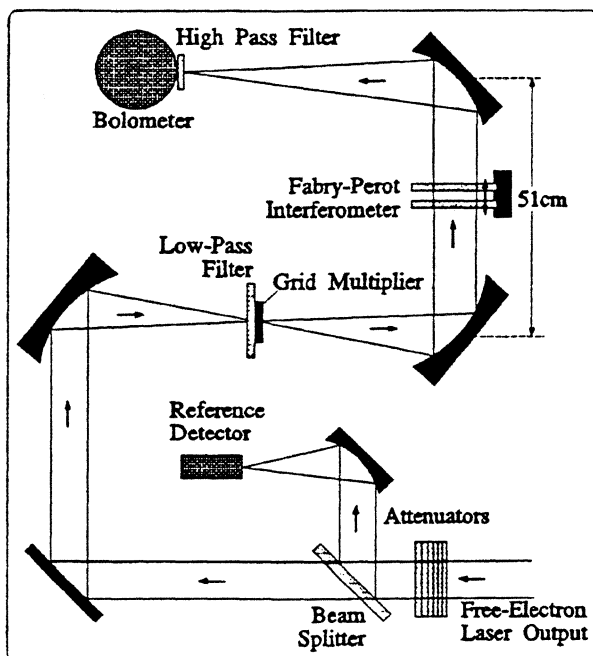


Fig. 5. Experimental arrangement.

entire collimated beam. Then the collimated beam was refocused onto a liquid-helium-cooled Germanium bolometer by another f/1 parabolic mirror with a focal length of 12.8 cm.

An 8-layer metal-mesh filter was used as a low-pass filter on the input side. It has an attenuation more than 60 dB at 1 THz. A circular-waveguide array filter was used as a high-pass filter on the output side of the grid. The waveguide array filter was attached to the window of the bolometer. The circular waveguides have a diameter of $200.7\ \mu\text{m}$ and a length of 1.02 mm. The diameter of the array is 5.1 mm. Figure 6 shows the measured transmittance of the high-pass filter from 300 GHz to 1.5 THz. The transmittance at 1 THz is 0.76 and the attenuation is more than 60 dB at 500 GHz.

MEASUREMENT

Several different diode grids have been tested. These diode grids are glued on the edges of microscope glass slides and suspended in air. Bonding wires connect the bias lines on the substrate to the contact pads on the slides for DC biasing.

Figure 7 shows time responses of the bolometer voltage as a function of input power level. Each curve is an average of 4 pulses. The solid lines show the outputs with the multiplier grid in the path and with four different input power levels which have 0 dB, 3.8 dB, 5.8 dB and 7 dB attenuations. The dashed line was measured without the multiplier in the path and 0 dB input power attenuation. This measurement shows the harmonics are radiated from the multiplier grid instead of harmonic contamination from the free-electron laser. The 0 dB attenuation reference was

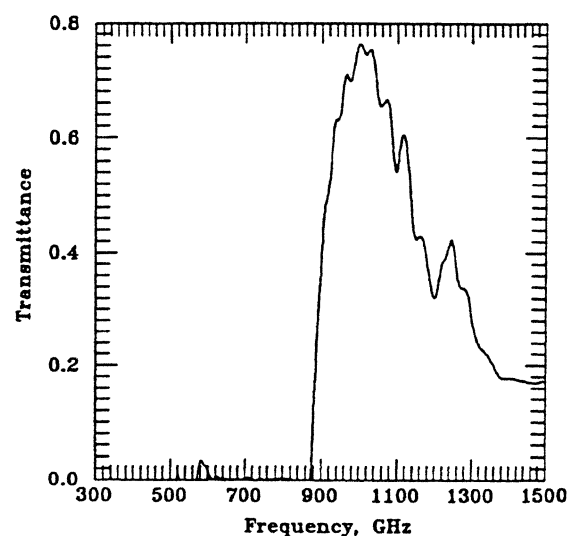


Fig. 6. Measured transmittance of the high-pass waveguide cutoff filter as a function of frequency.

actually set with enough sheets of plexiglass in front of the beam splitter so that there was no output signal detected by the bolometer without the multiplier in the optical path. Then extra attenuation was added to measure the time responses for different input signal levels.

Another way to show that the THz radiation comes

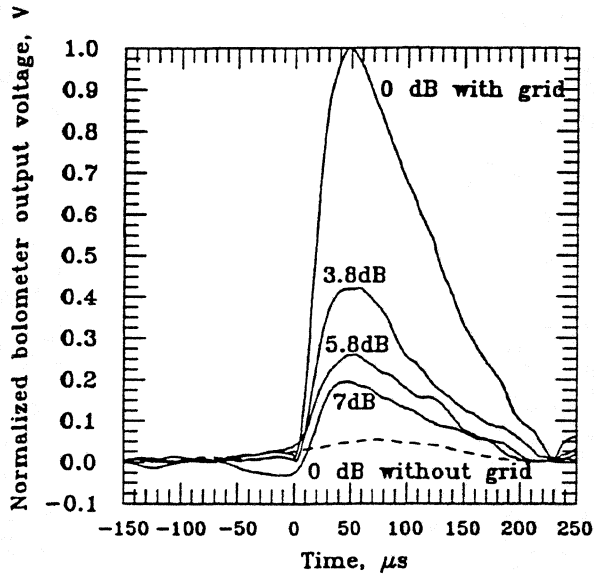


Fig. 7. Normalized time responses of bolometer voltage as a function of input power level. The dashed line was measured with 0 dB attenuation of the input power but without the multiplier in the path. The solid lines were measured with the multiplier in the path and with different attenuation of the input power.

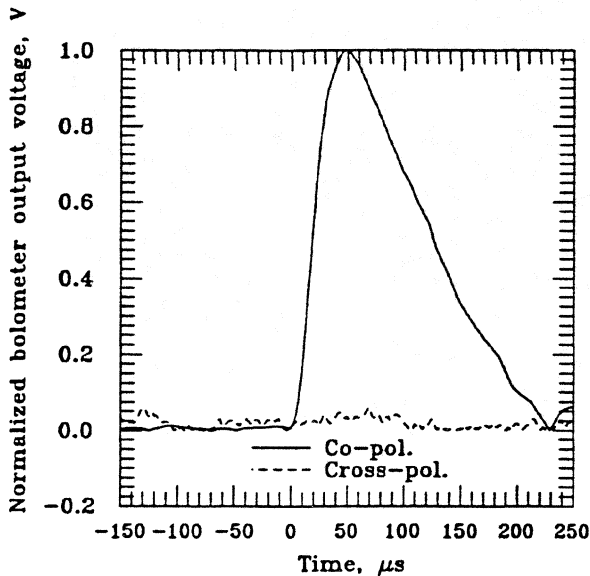
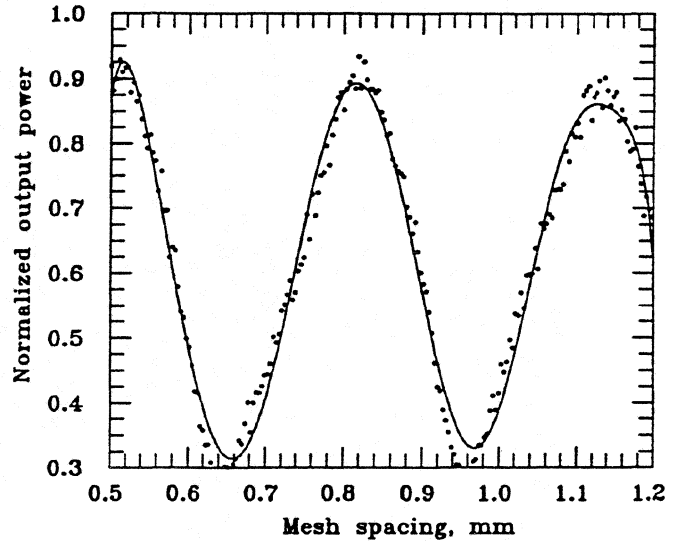
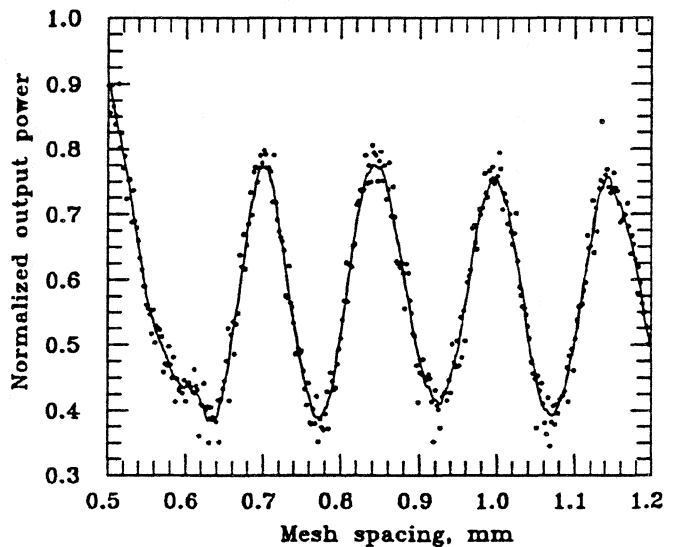


Fig. 8. Normalized time responses of bolometer voltage with different grid orientations. The solid line indicates the electric field parallel to the diode and the dashed line indicates that the electric field perpendicular to the diode.

from the grid rather than the laser is to rotate the grid by 90° and measure the cross-polarized signal. Figure 8 shows the time responses. The solid line was measured with the electric field parallel to the diodes and the dashed line was measured with the electric field perpendicular to the diodes. This result shows that: (1) The bow-tie metal structures on the grid work as linearly-polarized antennas and couple the signal into the diodes. The harmonic signal is not generated by just pumping high energy on GaAs in the device. (2) The harmonic signal does not come from the free-electron laser.



(a)



(b)

Fig. 9 Normalized output power as a function of the metal-mesh spacing in the Fabry-Perot interferometer. (a) Measurement of 500-GHz input signal and (b) measurement of 1.00 THz output signal.

A Fabry-Perot interferometer was used to measure the signal frequencies. The metal-mesh plates could be positioned in $0.7 \mu\text{m}$ increments. Figure 9 shows (a) the fundamental frequency from the free-electron laser after passing the low-pass filter but without the high-pass filter, and (b) the output frequency from the grid after passing the high-pass filter. Figure 9(a) and 9(b) only show parts of the measured curves. The average distance between two peaks in the output-frequency measurement is $301 \mu\text{m}$ over 14 peaks. This indicates the output frequency is 1.00 THz . No higher harmonics have been detected. The average distance between two peaks in the input-frequency measurement is $603 \mu\text{m}$ over 9 peaks. This indicates the input frequency is 500 GHz .

POWER

Figure 10 shows the power dependence of the first multiplier with normal incidence. This grid has diodes with an anode diameter of $0.56 \mu\text{m}$ and 100% yield. The dashed line indicates a square-power relationship. A peak output power of $330 \mu\text{W}$ at 1 THz was achieved when the diode grid was pumped by a peak input power of 3.3 W at 500 GHz . With low input power, the data do not follow the square-power relationship, possibly due to measurement noise. It should be noticed that these diodes have not yet saturated. We tried to increase the input power in order to investigate the saturation conditions. However, some of the diodes were damaged when the input power reached 13 W . These damaged diodes are open-circuited, verified by a curve tracer.

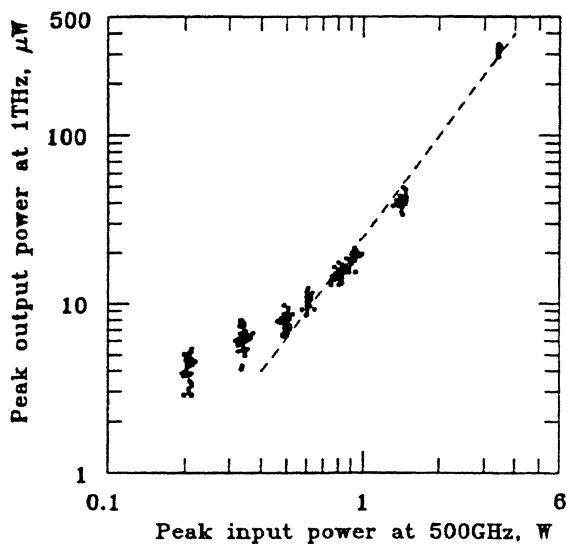


Fig. 10. Measured peak power dependence of the first multiplier grid. The dashed line indicates a square-power relationship. The diodes were not biased.

We improved the data acquisition method to investigate the power dependence with low input power. Each pulse was integrated to reduce noise effect. Because some of the diodes got damaged in the first grid, we used a new device. Figure 11 shows the power dependence of the second multiplier with normal incidence in a linear scale. This grid has diodes with an anode diameter of $0.5 \mu\text{m}$ and 100% yield. The solid line indicates a square-power relationship. With an input power of 800 mW , this multiplier generated a peak output power of $45 \mu\text{W}$. These diodes have not saturated yet and some of the diodes were damaged when the input power was increased to 4 W . It should be noticed that the data with low input power follows the square-power relationship after reducing the noise effect.

PATTERN

The diodes in the top and bottom halves of the grid have opposite polarities because the grid was designed for a sideband generator. When the grid is used as a frequency doubler, this causes an undesired null in the middle of the beam. The output pattern was measured to verify the existence of the null. The measurements were done by rotating the grid itself. In Figure 12, the solid curve shows the measured output pattern with a peak input power of 300 mW . Peaks appear at 42° and 26° from the center with a power of 3.2 times and 2.3 times bigger than the power in the null, respectively. The accuracy of this measurement is limited by the uncertainty in the position of the rotating axis. The asymmetry of the output pattern may be caused by the off-axis rotating effect or by the fact that the diodes in one array are not completely identical. The bolometer

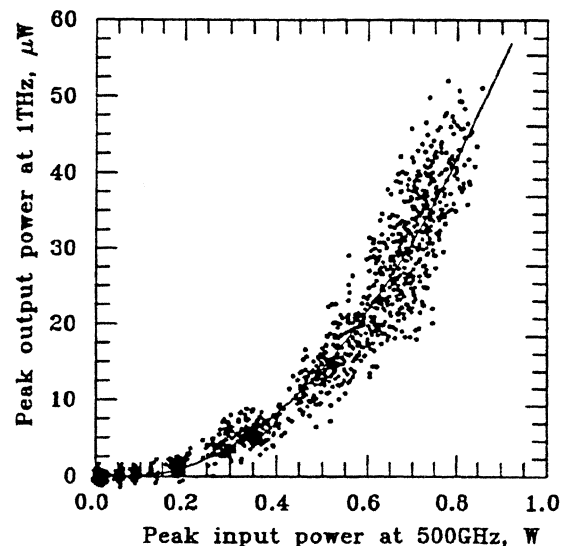


Fig. 11. Measured peak power dependence of the second multiplier grid. The solid line indicates a square-power relationship. The diodes were not biased.

has a limited acceptance angle ($\pm 14^\circ$) and only 10% of the total radiated power is accepted at normal incidence. The dashed curve in Fig. 12 shows a calculated one-dimensional output pattern. Three infinitesimal current elements on the left are assumed to have an opposite phase from the other three elements on the right of a linear array and the spacing between elements is $70 \mu\text{m}$. The normalized array factor is determined by [13]

$$A(\theta) = \left[\frac{\sin(\frac{3k_0 d}{2} \sin \theta)}{\sin(\frac{k_0 d}{2} \sin \theta)} \right]^2 \cdot \left[\sin(\frac{3k_0 d}{2} \sin \theta) \right]^2 \quad (1)$$

where θ is the angle, d is the spacing and the propagation constant $k_0 = 2\pi / \lambda_0$ where λ_0 is the wavelength, $300 \mu\text{m}$. The receiving horn in the bolometer has an acceptance angle of $\pm 14^\circ$. Therefore, taking both the antenna array factor and the finite acceptance-angle effect into account, the output pattern is calculated by

$$P(\phi) = \int_{\phi-14^\circ}^{\phi+14^\circ} A(\theta) d\theta \quad (2)$$

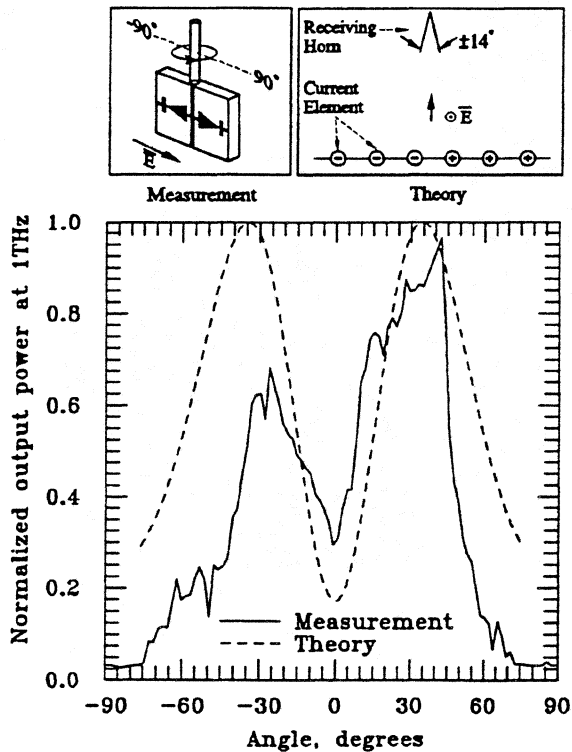


Fig. 12. Output pattern. The measurements were done by rotating the grid from -90° to $+90^\circ$ with the electric field parallel to the diodes. The solid line is a calculated output pattern considering the antenna array factor and the acceptance angle of the receiving horn. The null was caused by the opposite polarities of the diodes in two halves of the grid.

BIASING

Traditionally, Schottky diode multipliers are reverse-biased to increase the frequency multiplying efficiency since the diodes are designed as varactors. However, these diodes were originally planned for use as sideband generators and were designed to be used under forward bias. Thus, these diodes have very thin epitaxial layers and the capacitance does not change significantly with reverse bias. Therefore, the frequency multiplication in these grids probably results from varistor multiplication, that is to say, from the nonlinear I-V relationship. C-V curves with 1 MHz RF frequency were measured by probing each diode in an array when other diodes were still connected to the one probed. The capacitance of the diodes on the edge of the array stayed the same (about 10 fF) when the bias changed from 0.4 V to -6 V. The capacitance of the diodes in the center of the array varied from 19.2 fF to 18.4 fF as the bias changed from 0.4 V to -6 V. These capacitances are much bigger than the estimated junction capacitance which is 0.6 fF at zero bias. The discrepancy is due to the fact that these diodes are still connected and therefore the measured capacitance is a result of all shunt capacitance in the array and the junction capacitance is not significant enough to change it when the bias changes.

Power dependence was measured under different biasing conditions. The grid was rotated to the angle where the maximum output power appeared. The maximum point of the output pattern should be more sensitive to the bias than the null in the center (with normal incidence) due to that the null is caused by a cancellation of electric fields from the two halves of the diodes. Figure 13 shows the

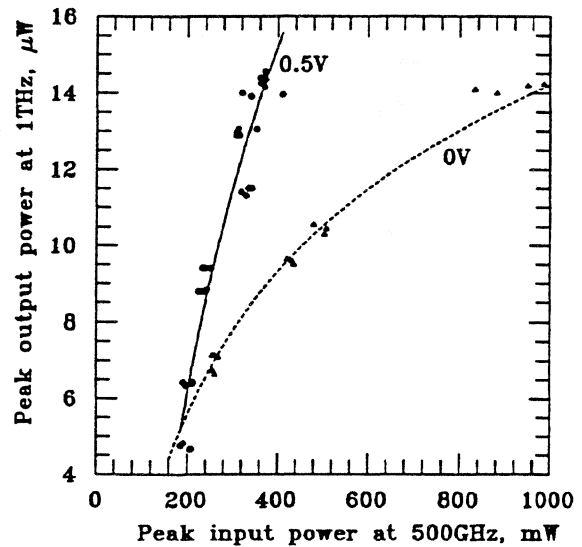


Fig. 13. Measured power dependence with bias 0 V and 0.5 V. The grid was rotated by 30° for the bolometer to receive signal from the peak angle of the output pattern.

measured power dependence with bias 0 V and 0.5 V. Each data point is an average of 60 pulses. The frequency doubling efficiency with a $14 \mu\text{W}$ output power was increased from 1.5×10^{-5} with zero bias to 3.9×10^{-5} with 0.5 V bias. It should be noticed that these diodes become saturated with high input power when the diodes are biased at 0 V. This measurement verifies that the frequency multiplication results from varistors.

Peak output power was measured as a function of bias with a peak input power of 400 mW (Fig. 14). The maximum peak output power is $17 \mu\text{W}$ with a bias of 0.375 V. Comparing with a peak output power of $13 \mu\text{W}$ which was measured with the open-circuited bias line, it seems biasing only makes a small improvement in the output power. One possible reason is that these diodes are self-biased when the bias lines are open-circuited.

CONCLUSION

Terahertz quasi-optical grid frequency doublers have been investigated by using Schottky diode-grids which are originally designed as sideband generators. A peak output power of $330 \mu\text{W}$ was measured at 1 THz without any impedance tuning for $2.42 \mu\text{s}$ 500-GHz input pulses with a peak power of 3.3 W. The relationship between the input power at 500 GHz and the output power at 1 THz follows a square-power law. The polarity of the diodes designed for sideband-generator application results in a null in the center of the output beam for multiplier application. Measurements shows that only 10% of the total radiated power is received by the detector due to the null in the output beam. A grid with diode-orientation appropriate for a mul-

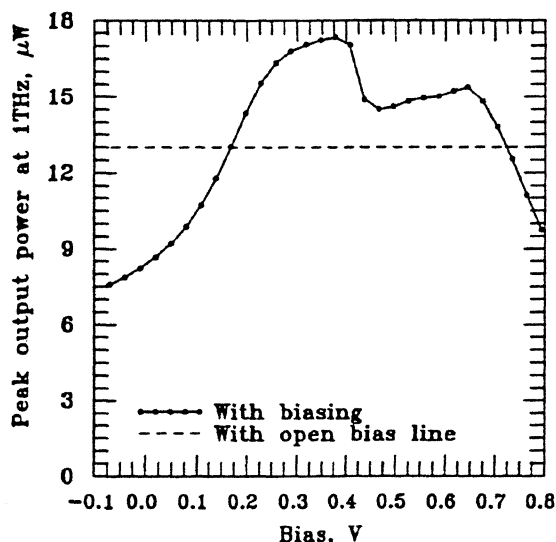


Fig. 14. Measured peak output power as a function of bias. The peak input power is 400 mW. The dashed line was measured with open-circuited bias lines.

tiplier application should improve the output pattern and increase the output power. Biasing tests verify that the frequency multiplication results from varistors. It should be possible to increase the output power and the conversion efficiency since these diodes are not saturated yet when no bias is applied.

ACKNOWLEDGMENTS

We appreciate the support from the Jet Propulsion Laboratory and the Army Research Office. We would like to thank Jeffery Hesler and Dr. William Bishop for their help on fabrication at University of Virginia. We would also like to thank David Enyeart and the staff of the Center for Free-Electron Laser Studies for their help on operating the laser at University of California, Santa Barbara. We are grateful to Kent Potter for his help building the measurement components and Michael DeLisio for valuable discussion at California Institute of Technology.

REFERENCES

- [1] T.G. Phillips, "Developments in Submillimeterwave Astronomy," *The 19th International Conference on Infrared and Millimeter Waves*, Sendai, Japan, Oct. 1994.
- [2] J.W. Waters and P.H. Siegel, "Applications of Millimeter and Submillimeter Technology to Earth's Upper Atmosphere: Results To Date and Potential for the Future," *The 4th International Symposium on Space Terahertz Technology*, Los Angeles, CA, March 1993.
- [3] M.A. Frerking, "The Submillimeter Mission Heterodyne Instrument," *The Proceeding of the 2nd International Symposium on Space Terahertz Technology*, pp. 17-31, 1991.
- [4] A. Rydberg, B.N. Lyons and S.U. Lidholm, "On the Development of a High Efficiency 750 GHz Frequency Tripler for THz Heterodyne Systems," *IEEE Trans. on Microwave Theory and Tech.*, vol. 40, No. 5, pp. 827-830, May 1992.
- [5] N. Erickson and J. Tuovinen, "A Waveguide Tripler for 800-900 GHz," *The 6th International Symposium on Space Terahertz Technology*, Pasadena, CA, March 1995.
- [6] R. Zimmermann, T. Rose and T. Crowe, "An All Solid-State 1 THz Radiometer for Space Applications," *The 6th International Symposium on Space Terahertz Technology*, Pasadena, CA, March 1995.
- [7] Jonathan B. Hacker, "Grid Mixers and Power Grid Oscillators," *Ph.D. Dissertation*, California Institute of Technology, 1994.
- [8] J.B. Hacker, R.M. Weikle II, M. Kim, M.P. DeLisio, D.B. Rutledge, "A 100-Element Planar Schottky Diode Grid Mixer," *IEEE Trans. Microwave Theory Tech.*, vol. 40, no. 3, pp. 557-562, March 1992.

- [9] C.F. Jou, W.W. Lam, H.Z. Chen, K.S. Stolt, N.C. Luhmann, Jr. and D.B. Rutledge, "Millimeter-Wave Diode-Grid Frequency Doubler," *IEEE Trans. on Microwave Theory and Tech.*, vol. 36, No. 11, pp. 1507-1514, Nov. 1988.
 - [10] H-X.L. Liu, L.B. Sjogren, C.W. Domier, N.C. Luhmann, Jr., D.L. Sivco and A.Y. Cho, "Monolithic Quasi-Optical Frequency Tripler Array with 5-W Output Power at 99 GHz," *IEEE Electron Device Letters*, vol. 14, No. 7, pp. 329-331, July 1993.
 - [11] T.W. Crowe, R.J. Mattauch, H.P. Röser, W.L. Bishop, W.C.B. Peatman and X. Liu, "GaAs Schottky Diodes for THz Mixing Applications," *Proceedings of the IEEE*, vol. 80, No. 11, pp. 1827-1841, Nov. 1992.
 - [12] S.J. Allen, K. Craig, B. Galdrikian, J.N. Heyman, J.P. Kaminski, K. Campman, P.F. Hopkins, A.C. Gossard, D.H. Chow, M. Lui and T.K. Liu, "Materials Science in the Far-IR with Electrostatic Based FELs," presented at *FEL 94*, Stanford, CA, August 1994.
 - [13] D. Cheng, "Field and Wave Electromagnetics," *Addison-Wesley Pub. Co.*, Chap. 11, 1983.
-

EFFECT OF THE INCREASED NUMBER OF DIODES ON THE PERFORMANCE OF OSCILLATORS WITH SERIES-CONNECTED TUNNEL DIODES

Olga Boric-Lubecke, Dee-Son Pan and Tatsuo Itoh

Department of Electrical Engineering, University of California at Los Angeles
405 Hilgard Avenue, Los Angeles, CA 90095, USA

ABSTRACT

Connecting several tunneling devices in series was proven to be an effective method to increase the oscillator output power. However, there are several difficulties associated with the series connection. The phase shift between the devices and the length of the series connection may be quite considerable. Therefore, connecting diode in series is not strictly the device level power combining, but the circuit level power combining as well. The design procedure, as well as the experimental results for the oscillators with two, three, and four series connected tunnel diodes at 2 GHz will be presented here. A multimode operation, characteristic for the circuit level power combining, was observed for the four diode oscillator.

INTRODUCTION

The resonant tunneling diode (RTD) is currently the fastest solid state source, but with a very low output power [1]. An RTD and a tunnel diode, even though physically quite different, are electrically almost identical. They share the same equivalent circuit, and except for the high frequency cutoff, there is no difference in behavior of oscillators with either tunneling device. Series connection of tunnel diodes was proposed by Vorontsov and Polyakov in 1965 to increase the oscillator output power at low frequencies [2]. Series integration of RTD's was proposed by Yang and Pan in 1992 in order to increase the output power at millimeter wave frequencies [3]. Because of DC instability of the series connection, design and excitation of an oscillator with series connected tunneling diodes is much more complex than for a single diode oscillator. A simple DC battery alone is not sufficient for successful biasing, and there is an oscillation amplitude cutoff and a low

frequency cutoff [2,3]. The oscillation amplitude cutoff and the low frequency cutoff make the occurrence of low frequency spurious oscillations associated with the bias circuitry highly unlikely. This is an important advantage over a single diode oscillator. A series connection of tunneling diodes is not expected to solve all power problems, however it may be used as a unit device in a power combining grid, which would greatly reduce probability of subharmonic oscillations and chaotic behavior such as reported in [4]. Oscillators with two tunnel diodes in series have been successfully designed and tested so far [7,8]. Connecting several tunneling devices in series was proven to be an effective method to increase the oscillator output power, and both fundamental and subharmonic RF excitation were demonstrated [7,8].

If packaged diodes are used, a distance between the diodes is limited by the package dimensions. The diode separation must be taken into account for the impedance calculation. Due to the diode package, impedance of the series connection is not simply the sum of impedances of the individual diodes. Therefore connecting diodes in series is not strictly the device level power combining, but the circuit level power combining as well. For more diodes connected in series, the circuit level power combining effect is more pronounced. A series integrated device, such as proposed in [3], should not be affected by this problem, since diodes can be placed very close to each other. The design procedure as well as the experimental results for oscillators with series connected, packaged tunnel diodes at 2 GHz will be presented here. Multimode operation, characteristic for circuit level power combining [5], was observed for one four-diode oscillator.

SINGLE DIODE IMPEDANCE

Low peak current (back) tunnel diodes, manufactured by Metelics Co., were used for the experiment. Fig. 1. shows the diode equivalent circuit model. Values of the series resistance R_S (6.5 Ω), junction capacitance C_j (0.32 pF), bonding wire inductance L_S (0.1 nH), and package capacitance C_p (0.23 pF) are provided by the manufacturer, and are considered constant. Negative differential conductance G is a strong function of both the DC bias voltage and the oscillation amplitude, and can be calculated from the DC I-V curve using the procedure described in [6]. The diode DC I-V curve and the negative differential conductance and output power as a function of the oscillation amplitude are shown in [7]. Fig. 2. shows the diode impedance plot for the negative differential conductance of -0.5 mS and -1.7 mS, in the frequency range from 1 GHz to 8 GHz.

SERIES CONNECTION IMPEDANCE

Fig. 3. shows the series connection schematically. The diode package length l_p is 2.25 mm, and the separation between packages l_s 0.75 mm. At 2 GHz, the length of the package is about one fortieth of the wavelength. Oscillators with two diodes reported in [8] were designed assuming that diodes are lumped elements separated by the distance of 0.75 mm. However, it was found later that increased separation resulted in a more accurate design. Since a single diode impedance is in a region of a Smith chart where a small phase delay causes a large difference in the impedance value (Fig. 2), even a small separation between the diodes greatly affects the total impedance of the series connection. Fig. 4. shows the impedance of two, three and four diode connected in series, for negative conductance of 1.7 mS, at 2 GHz, and for three separation lengths. The separation between diodes is modeled as a piece of a transmission line in microstrip configuration, 0.75 mm wide, on a substrate with a dielectric constant of 2.33. The separation of 0.75 mm, which is a physical distance between two packages, brings about 10 %, 20 % and 30 % reduction in the negative resistance for two, three and four diodes respectively. The separation of 3 mm, which is a distance between centers of two packages brings a much more drastic reduction in the negative resistance, specially for four diodes, where it is over 50 %.

EXPERIMENTAL RESULTS

Several oscillators with two, three and four tunnel diodes in series were designed in a one-port microstrip configuration described in [7,8], for the oscillation amplitude of 0.154 V (slightly above the amplitude cutoff) and 0.176 V (slightly below the amplitude at which negative differential conductance vanishes). Fig. 5. shows oscillators with two, three, and four diodes, designed for the oscillation amplitude of 0.176 V. For three and four-diode oscillators, the length of the series connection is considerable compared to the length of the whole circuit, which is about half-wavelength at 2 GHz. The experimental set-up described in [7,8] was used to test the oscillators, and the fundamental RF excitation to initialize them.

Oscillators with three and four diodes were much more difficult to design and excite than two-diode oscillators. It was found that the separation of 3 mm was optimum for the design of the two-diode oscillators. With this separation included in impedance calculation, two-diode oscillator performance improved significantly from what was reported in [8]. For the oscillation amplitude of 0.154 V, the oscillation frequency was 1.979 GHz, and the output power -18.6 dBm. For the oscillation amplitude of 0.176 GHz, the oscillation frequency

was 1.99 GHz, with the output power of -28 dBm, and successive triggering was possible. For three and four diode oscillators, additional impedance compensation was required (inductive stub was assumed to be about 1 mm longer than what it really was), probably due to errors in determining the impedance of the series connection. Switching was occurring, but stable oscillation was not possible for the amplitude of 0.154 V in case of three and four-diode oscillators. For the oscillation amplitude of 0.176 V, signal in three and four-diode oscillators existed only for a very limited bias voltage range, successive triggering was not possible, and the output power was barely increased as compared to the two-diode oscillators. For the best three-diode oscillator, the oscillation frequency was 2.001 GHz, with the output power of -27.5 dBm.

The four-diode oscillator designed for the oscillation amplitude of 0.176 V exhibited multimode operation. The oscillation signal was dependent on the excitation frequency. For the excitation frequency of 1.99 GHz, the excitation was possible with a very low power, of only -37 dBm. In this case, after excitation signal was turned off, the oscillation frequency was 1.976 GHz, with output power of -29 dBm (Fig. 6 (a)). The oscillation was possible for a bias voltage between 0.54 V and 0.60 V, and the excitation in somewhat smaller bias range. The bias voltage of 0.64 V is necessary to bias all four diodes in the middle of the NDR region. For the excitation frequency of 2.05 GHz, much larger excitation power was required, of -7 dBm. In this case, the oscillation frequency was 2.015 GHz, with output power of -27 dBm (Fig. 6 (b)). The oscillation was possible for a bias voltage from 0.56 V to 0.615 V, and the excitation in a somewhat smaller bias range. It is possible that only three diodes oscillated in a four diode oscillator, specially in a lower frequency mode.

Active antenna oscillators with three and four diodes were tested as well. The experimental findings for the active antenna configuration will be described elsewhere [9].

CONCLUSIONS

Oscillators with three and four packaged tunnel diodes connected in series were designed and tested. Due to the diode separation, it is difficult to calculate the impedance of the series connection accurately. Because of the considerable length of the series connection, four-diode oscillator exhibits circuit level power combining behavior, such as multimode operation. A series integrated device, such as proposed in [3], should not be affected by these problems, since diodes can be placed very close to each other. Therefore, connecting

more than two packaged diodes in series does not provide insight into behavior of a series integrated device.

ACKNOWLEDGMENT

We would like to thank Carl W. Pobanz for measurement assistance and Siou Teck Chew for helpful discussions. This work is supported by Joint Services Electronics Program, through AFOSR F49620-92-C-0055.

REFERENCES

- [1] E. R. Brown, J. R. Soderstrom, C. D. Parker, L. J. Mahoney, K. M. Molvar, and T. C. McGill, "Oscillations up to 712 GHz in InAs/AlSb resonant-tunneling-diodes," *App. Phys. Lett.*, vol. 58, pp. 2291-2293, May 1991.
- [2] Y. I. Vorontsov and I. V. Polyakov, "Study of oscillatory processes in circuits with several series-connected tunnel diodes," *Radio Eng. Electron. Phys.*, vol. 10, pp. 758-763, May 1965.
- [3] C. C. Yang and D. S. Pan, "Theoretical investigations of a proposed series integration of resonant tunneling diodes for millimeter-wave power generation", *IEEE Trans. Microwave Theory and Tech.*, vol. 40, pp. 434-441, March 1992.
- [4] M. P. DeLisio, J. F. Davis, S. J. Li and D. B. Rutledge, " A 16-element tunnel diode grid oscillator," submitted to the 1995 *AP-S International Symposium*.
- [5] S. Nogi, J. Lin and T. Itoh, "Mode analysis and stabilization of a spatial power-combining array with strongly coupled oscillators," *IEEE Trans. Microwave Theory and Tech.*, vol. 41, pp. 1827-1837, October 1993.
- [6] O. Boric-Lubecke, D. S. Pan and T. Itoh, "Large signal quantum-well oscillator design", *Proc. of 23rd European Microwave Conf.*, Madrid, Spain, Sept. 1993, pp. 817-818.
- [7] O. Boric-Lubecke, D. S. Pan and T. Itoh, "RF Excitation of an oscillator with several tunneling devices in series," *IEEE Microwave and Guided Wave Lett.*, vol. 4, no. 11, pp. 364-366, November 1994.
- [8] O. Boric-Lubecke, D. S. Pan and T. Itoh, "Fundamental and subharmonic excitation for an oscillator with several tunneling diodes in series," Special Issue on Space Terahertz Technology of *IEEE Trans. Microwave Theory Techn.*, vol.43, no.4, April 1995.

- [9] O. Boric-Lubecke, D. S. Pan and T. Itoh, "Quasi-optical RF excitation of an active antenna with two tunnel diodes in series," submitted to the *25th European Microwave Conference*, 1995.

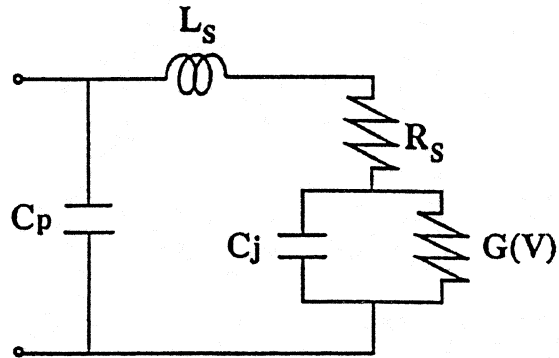


Fig. 1. Packaged tunnel diode equivalent circuit model

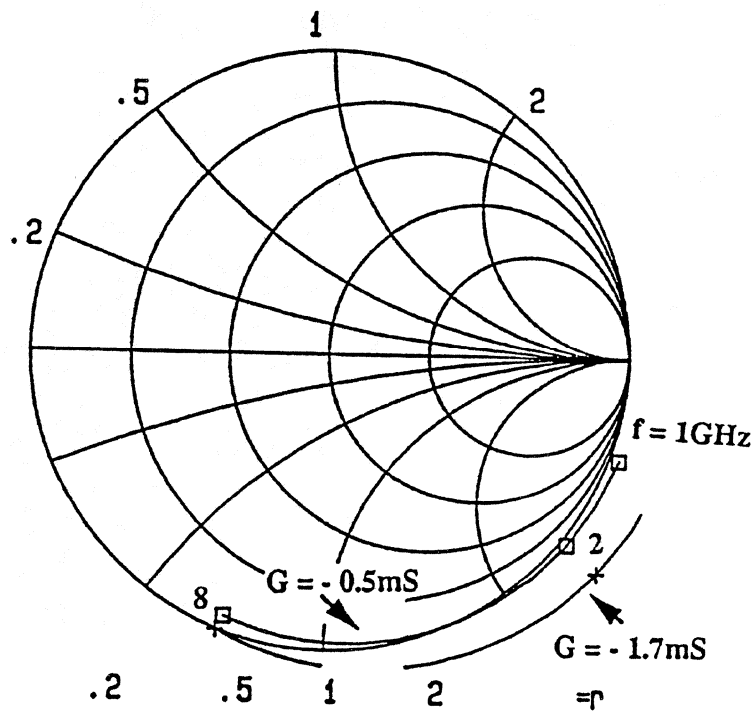


Fig. 2. Tunnel diode impedance for $G = -0.5\text{ mS}$ and $G = -1.7\text{ mS}$, from 1 to 8 GHz.

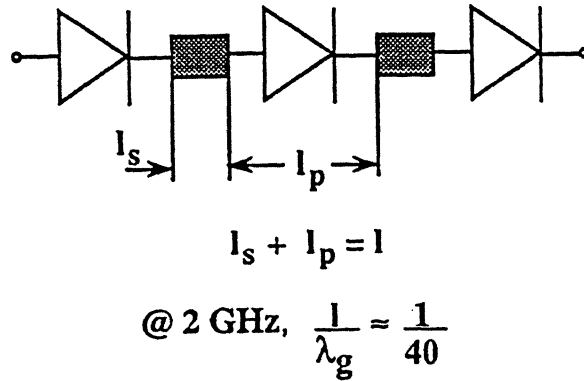


Fig. 3. Series connection; diode package length l_p is 2.25 mm, and separation between packages l_s 0.75 mm.

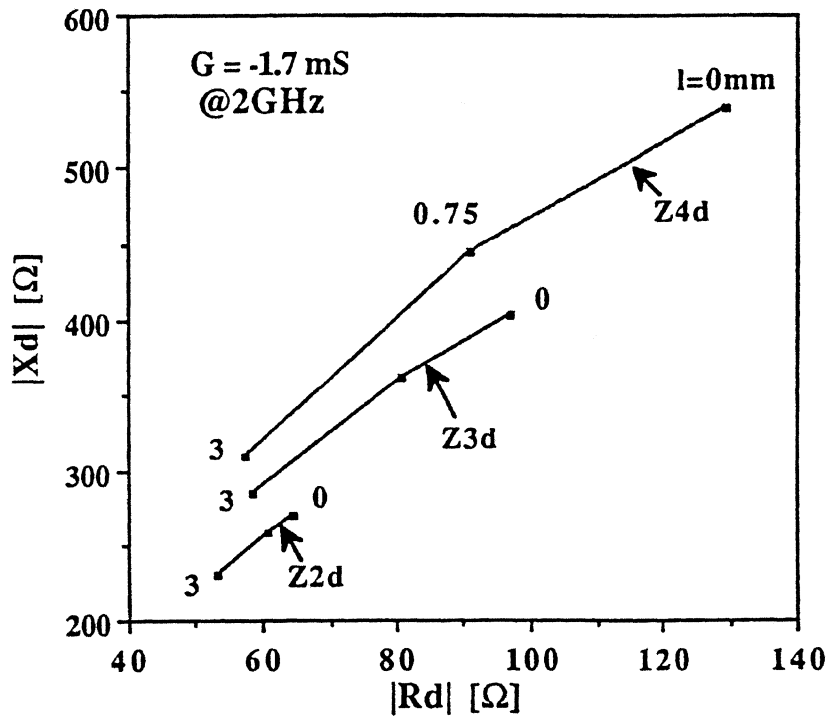


Fig 4. Impedance of the series connection of two, three and four diodes, for separation of 0, 0.75 and 3 mm.

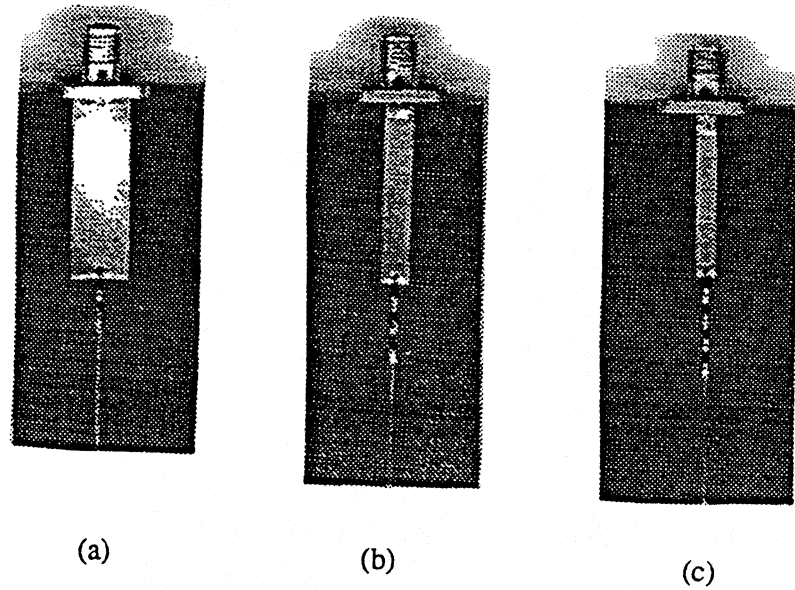


Fig. 5. One-port oscillators with two (a), three (b) and four (c) tunnel diodes, designed for the oscillation amplitude of 0.176 V.

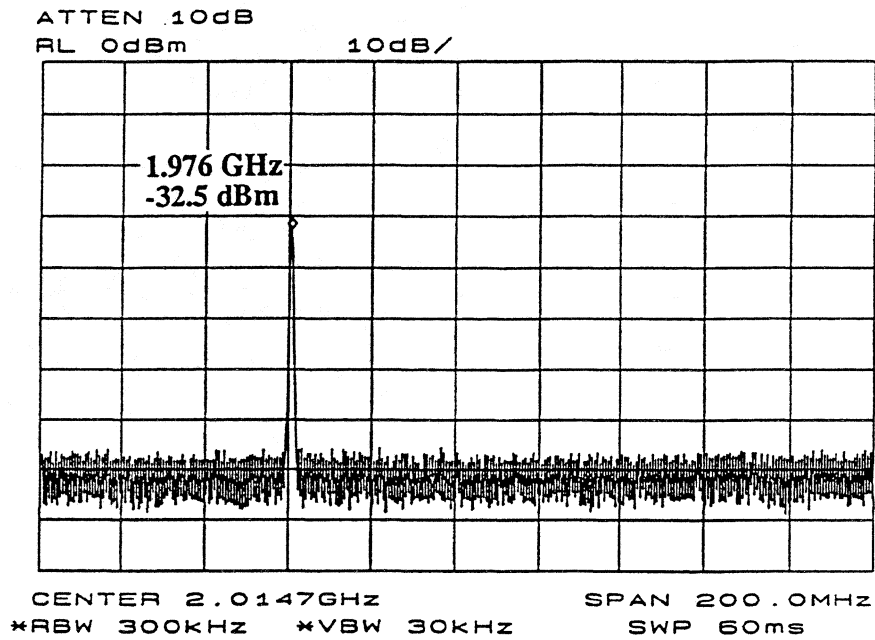
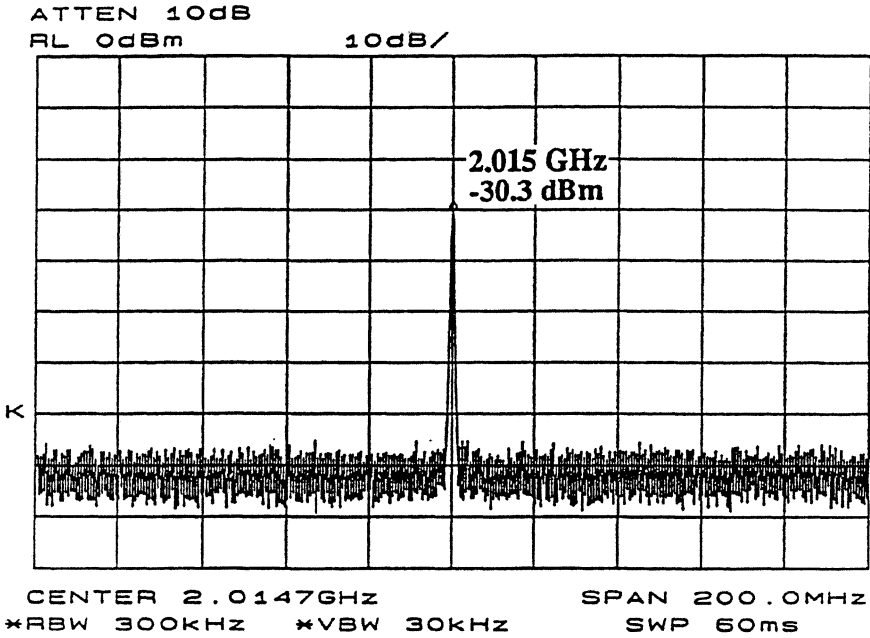


Fig. 6 (a)



(b)

Fig. 6. Output spectrum of four-diode oscillator for excitation frequency of 1.99 GHz (a), and 2.05 GHz (b).

HOT-ELECTRON BOLOMETER MIXERS FOR SUBMILLIMETER WAVELENGTHS: AN OVERVIEW OF RECENT DEVELOPMENTS

William R. McGrath

Center for Space Microelectronics Technology, Jet Propulsion Laboratory,
California Institute of Technology, Pasadena, CA 91109

INTRODUCTION

In the past couple of years there has been a resurgence of interest in bolometers as heterodyne mixers at submillimeter wavelengths. This is due primarily to two new, and different, innovative concepts [1,2] which result in bolometers with response times fast enough to allow for intermediate frequencies (IF) of 1 GHz - 10 GHz, as well as low mixer noise temperatures. These IF's are high enough for practical spectroscopy applications and thus these bolometers need to be seriously considered as heterodyne sensors. In this paper I will review briefly the basics of bolometer mixers. Then an overview will be given of the basic operation of the new high speed bolometers. The advantages and potential limitations of each approach will be discussed. A few recent results which demonstrate the performance will be given. Finally, the role these sensors may be expected to fulfill will be discussed. I should emphasize that this paper is meant to provide an introduction to these new bolometer mixers, and reference will be made to the recent literature for the interested reader who wishes to delve more deeply into the details. However, this is not a review article, but rather an overview of recent developments, so no attempt is made to give a complete listing of results and publications.

BOLOMETER MIXERS

Bolometers have been used occasionally over the years as heterodyne mixers. This is because bolometer mixers have several important advantages: 1) High frequency operation: bolometers can be designed and optimized to work at millimeter wavelengths, submillimeter wavelengths, and of course, on out to infrared wavelengths and beyond. 2) Bolometers can have very high sensitivity and near-quantum limited noise. 3) Bolometers are simple square-law or total power detectors. There is no instantaneous response at the rf as with an electronic mixer, such as a Schottky diode or SIS tunnel junction. There is also no harmonic response. The principle disadvantage of the bolometer mixer is the slow thermal response time. This limits the IF to low values, usually of order MHz. In general this is too low to be useful for many remote-sensing applications involving molecular line spectroscopy such as radioastronomy, atmospheric chemistry, and planetary science. The limitation placed on the IF by the thermal response time can be understood by considering the basic operation of a bolometer mixer as discussed below.

The two basic elements of a bolometer are shown in figure 1. There is an element which absorbs the incident rf power. This can be an absorbing film or other lossy material. The absorber has a thermal heat capacity C , and as it absorbs power its temperature T increases. The absorber is connected to a thermal bath temperature T_{bath} by a thermal conductance G . The thermal response time is given by $\tau_{\text{th}} = C / G$, and represents the characteristic time over which the temperature of the bolometer can change for a sudden change in incident rf power.

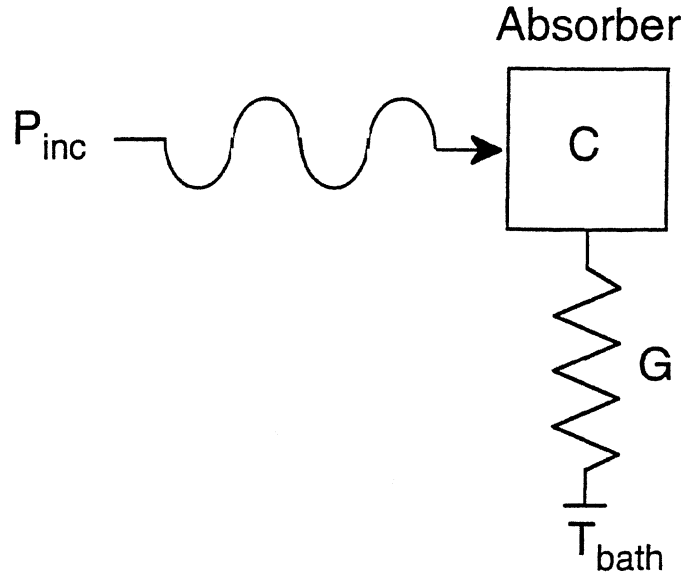


Fig. 1: Basic elements of a bolometer. C is the heat capacity of the absorber, typically a thin film. G is the thermal conductance to the bath temperature. P_{inc} is the incident rf power.

To operate the bolometer in a heterodyne mode, a local oscillator (LO) voltage at frequency ω_{LO} and a signal voltage at frequency ω_s are applied to the absorber:

$$V(t) = V_{LO} \cos(\omega_{LO} t) + V_s \cos(\omega_s t) \quad (1)$$

For simplicity, we take the absorber to be a thin resistive film of total resistance R_n . Then the power dissipated in the film is:

$$P(t) = V(t)^2 / R_n \quad (2)$$

Substituting eqn (1) into eqn (2) yields:

$$P(t) = P_{LO} + P_s + 2(P_{LO} P_s)^{1/2} \cos(\omega_{IF} t) \quad (3)$$

where $\omega_{IF} = \omega_{LO} - \omega_s$ is the IF frequency, and $P_{LO} = (V_{LO}^2 / 2R_n)$ and $P_s = (V_s^2 / R_n)$ are the LO power and signal power respectively dissipated in the bolometer. The bolometer is not fast enough to follow the rf, so the power dissipated at these frequencies is the time averaged value. However, if the IF is low enough, the bolometer can follow this variation, so there can be a time dependent term at this frequency. The *Voltage Responsivity*, S , of the bolometer [3] gives the change in voltage across the bolometer for a change in absorbed power, and hence can be used to estimate the IF voltage amplitude:

$$V_{IF} = S \cdot 2(P_{LO} P_s)^{1/2} \quad (4)$$

The responsivity is given by:

$$S = I (dR / dT) / [G \cdot (1 + \omega_{IF}^2 \tau_{th}^2)^{1/2}] \quad (5)$$

where I is the bias current through the resistive film, and dR/dT is the derivative of film resistance with temperature. Thus for low enough IF, that is $\omega_{IF}^2 \tau_{th}^2 < 1$, the bolometer can follow the IF power swing; but for $\omega_{IF}^2 \tau_{th}^2 > 1$, the IF voltage will decrease and hence the conversion efficiency of the mixer will decrease. As mentioned above, τ_{th} for many conventional bolometers is long enough that the IF is limited to undesirably low values. However, the two new bolometer concepts discussed below address this issue.

NEW APPROACHES

Recently, two new approaches [1,2] have been proposed for bolometers with very short thermal response times and hence a high IF rolloff frequency. Both bolometers utilize the resistive transition in a superconductive thin film which results in a large dR/dT and hence high responsivity. What is new however, is that these devices make use of very thin films: about 10 nm for Nb or NbN. Such thin films have a very high scattering rate due to surface effects and hence a short electron mean free path ℓ , which is about 1 nm - 10 nm. In these films, it is found that the electron-electron interaction is enhanced, resulting in a short electron-electron interaction time: $\tau_{ee} \propto \ell$; and the electron-phonon interaction is weakened: $\tau_{ep} \propto \ell^{-1}$ [2]. Hence the electrons can reach thermal equilibrium at a temperature different from the lattice temperature. Thus when absorbing rf power, the electrons can warm up relative to the lattice temperature. The electrical resistance in the film depends on the electron temperature and such a device is known as a hot-electron bolometer. Since only the electrons are heated, the heat capacity C can be very small, especially for a submicron-sized device. In addition, the hot-electron bolometer mixers discussed below employ novel mechanisms for cooling the electrons which results in a high thermal conductance and hence an overall short thermal relaxation time.

Before describing the details of the bolometers, it is useful to list the important advantages of these novel devices:

- 1) The thermal response time is very fast: ≈ 10 's ps. Thus IF's of 1 GHz - 10 GHz can be achieved.
- 2) These bolometer mixers should operate well to very high frequency: several THz. There is no energy gap limitation as in an SIS mixer. In fact, rf power is absorbed more uniformly above the energy gap frequency.
- 3) The mixer noise temperature is very low: near-quantum limited.
- 4) Very low LO power is required: nW's - μ W's. This is comparable to the requirements for SIS mixers and is an important issue at high submillimeter wave frequencies where LO power is difficult to generate.
- 5) The rf impedance of the device is essentially resistive and is determined by the geometry of the film; that is, the number of squares in a small strip. Typical values range from 20 Ω to 200 Ω . This greatly simplifies the rf circuit design. Unlike a Schottky diode or SIS

tunnel junction, there are no parasitic reactances to tune out. The real rf resistance of the bolometer should be independent of frequency from about the energy gap frequency up to a frequency corresponding to the inverse electron-electron elastic scattering time (about 10^{-15} sec) which is approximately 160 THz.

- 6) In addition, these devices make use of existing materials and fabrication techniques: Nb, NbN, YBCO; micron-scale photolithography, and/or submicron E-beam lithography.

DIFFUSION-COOLED HOT-ELECTRON BOLOMETER MIXER

Figure 2 shows the basic geometry of this bolometer mixer which was proposed by D. Prober in 1993 [1]. The unique feature of this device is that it uses the rapid diffusion of hot electrons out of a submicron length strip of superconductor (or microbridge) into normal metal contacts as the cooling mechanism, or thermal conductance. In order for diffusion to dominate, over electron-phonon interactions, as the cooling mechanism, it is necessary for the microbridge to be short. The appropriate length L can be estimated from the expression:

$$L \approx 2 (D \tau_{ee})^{1/2} \quad (6)$$

where D is the diffusion constant, and τ_{ee} is the electron-electron inelastic ("energy sharing") interaction time. Basically when an electron absorbs energy from an rf photon, it shares its energy in a time τ_{ee} and also diffuses a distance $L/2$. A hot electron in the middle of the bridge can thus go $L/2$ left or right. At that point, it encounters the normal metal contact which serves as a heat sink. These pads at the end of the microbridge must be normal metal since Andreev reflection [4] at the energy gap in a thick superconducting film would trap the hot-electrons inside the microbridge and substantially slow the response of the device. The electron-electron interaction time can be estimated from [5]:

$$\tau_{ee} \approx (10^8 R_s T_c)^{-1} \quad (7)$$

where R_s is the surface resistance and T_c is the transition temperature of the thin film. For the very thin (dirty limit) film used here, R_s is larger and T_c is smaller than the bulk values. For a 10 nm Nb film for example, $R_s \approx 20 \Omega/\text{sq}$, $T_c \approx 5$ K, and the width of the transition is $\Delta T_c \approx 0.5$ K. Substituting these values into eqn (6) and eqn (7), yields a length $L \approx 0.2 \mu\text{m}$. The microbridge can be somewhat longer (with a corresponding increase in τ_{th}), but should be less than $2(D \tau_{ep})^{1/2}$ where τ_{ep} is the electron-phonon interaction time. For this length and longer the electrons will remain in the bridge long enough to produce phonons which can then warm the lattice and slow the device response time.

The thermal response time can be calculated from the usual expression:

$$\tau_{th} = C / G \quad (8)$$

The thermal capacitance is given by the electron specific heat [6]:

$$C = \gamma T V \quad (9)$$

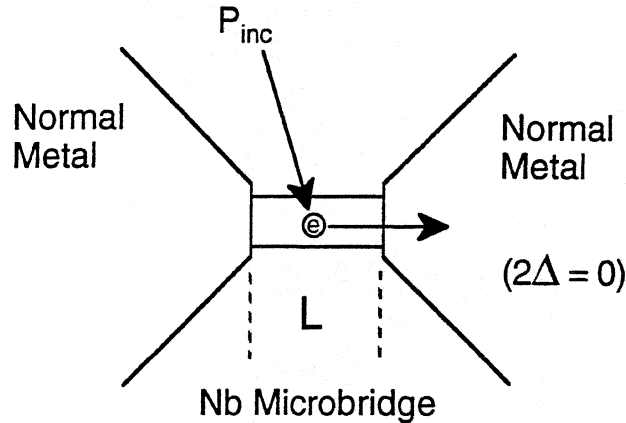


Fig. 2: Basic geometry of the diffusion-cooled hot-electron bolometer mixer.

where $\gamma = 700 \text{ J/K}^2\text{m}^3$ for Nb, T is the electron temperature (which is always about T_c in a transition edge device), and V is the device volume. The thermal conductance G is given by the Wiedemann-Franz Law [6]. This law states that the ratio of thermal conductance to electrical conductance is proportional to temperature, if the electrons carry both the electrical current and the thermal current, which is the case for the diffusion-cooled microbridge. Thus:

$$G = (\pi^2/3) (k_B / q_e)^2 (T / R_{eff}) \quad (10)$$

where k_B is Boltzman's constant, q_e is the charge on the electron, T is the temperature ($\approx T_c$) and R_{eff} is the effective electrical resistance of the microbridge: $R_{eff} \approx R_n / 12$ [1]. R_n is the DC resistance of the microbridge for $T > T_c$, or equivalently it is the rf resistance for frequencies above the gap frequency. The factor 1/12 arises because heat flows symmetrically out both ends of the microbridge.

For an actual bridge [7] with dimensions width = $0.14 \mu\text{m}$, length = $0.28 \mu\text{m}$, thickness = $0.01 \mu\text{m}$ and $R_n = 30 \Omega$, the estimated response time is 30 psec. The 3 dB IF rolloff frequency for the mixer gain is then given by:

$$IF_{roll\ off} = (2 \cdot \pi \cdot \tau_{th})^{-1} \quad (11)$$

which is about 5 GHz in this case. However, due to self-heating effects [3] (and to a lesser extent by IF impedance mismatch effects [8]) the thermal conductance is reduced to a lower effective value:

$$G_{eff} = G (1 - A) \quad (12)$$

where typically $0.1 < A < 0.9$ for thermally stable operation. Thus the value of $IF_{roll\ off}$ can actually be in the range of about 2-5 GHz. This allows for an IF commonly used in heterodyne instruments.

Now we will estimate the mixer conversion efficiency η , the double-sideband receiver noise temperature $T_R(\text{DSB})$, and the LO power P_{LO} following the approach given by

Prober [1]. The conversion can be estimated using the voltage responsivity of the bolometer and the IF power amplitude. The result is:

$$\eta = P_{IF} / P_{rf} = [I^2 (dR/dT)^2 / G^2] \cdot [P_{LO} / 2R] \quad (13)$$

(note that this expression is valid for $\omega_{IF} \tau_{th} < 1$, otherwise there would be another factor of $[1 / (1 + \omega_{IF}^2 \tau_{th}^2)]$ multiplying the above expression). For equal DC power ($P_{DC} = I^2 R$) and LO power dissipated in the bolometer, then $\eta(SSB) = 1/8 = -9$ dB (see references 8 and 9 for a detailed formulation of bolometer-mixer conversion efficiency). It can be shown that the conversion efficiency in this case is independent of L, the length of the microbridge [1]. However, the response time $\tau_{th} \propto L^2$, thus $IF_{roll-off} \propto 1 / L^2$. Hence, as expected for a device that relies on diffusion out the ends, shorter is better for high speed. However, there is no sacrifice in conversion efficiency. While decreasing L will increase G and hence reduce the bolometer responsivity, in the heterodyne mode this can be compensated by increasing the LO power. Thus it is possible to have a bolometer mixer which is both *fast* and *sensitive*.

The LO power can be readily approximated by:

$$P_{LO} \approx \Delta T_c G \quad (13)$$

This expression simply states that enough LO power must be applied to increase the temperature of the bolometer up through the range of ΔT_c , the temperature range over which the resistance of the bolometer varies strongly. In practice, the bolometer is thermally biased at a temperature somewhat below T_c , then a combination of DC and LO power is used to heat the electrons up to T_c . The best optimization of DC and LO power is a topic of current discussion (see reference 10, for example), but eqn(13) gives a good first-order estimate. (Actually, since the typical operating temperature is about T_c which is in the middle of the range ΔT_c , the required LO power may be 1/2 to 1/4 of the value given by eqn(13)). For the Nb bolometer discussed here, the required LO power is about 10 nW: a very low value.

It is currently accepted that the main contributions to the noise in a bolometer mixer are due to Johnson noise and electron temperature fluctuation noise [11]. The latter being dominant. The Johnson noise temperature is, of course, T_c and arises from the film resistance at the transition temperature. The electron temperature fluctuation noise arises from the thermodynamic energy fluctuations in an electron gas at an average thermodynamic temperature T_c . The RMS electron temperature fluctuation can be expressed as [8]:

$$\Delta T_e = 4 k_B T^2 / G \quad (14)$$

The resulting DSB receiver noise temperature can be expressed as [1]:

$$T_R (DSB) = [(T_c^2 / \Delta T_c) + T_c + T_{IF}] / \eta \quad (15)$$

where T_{IF} is the IF amplifier system noise temperature. Thus for $T_c = 5$ K, $\Delta T_c = 0.5$ K, $T_{IF} = 4$ K, and $\eta(DSB) = -7$ dB (ie: 6 dB intrinsic mixer conversion loss and 1 dB of receiver optical path loss), we get $T_R(DSB) = 295$ K. However, reducing T_c just 1 K (a slightly thinner film) yields $T_R(DSB) = 200$ K. This performance becomes competitive with current state-of-the-art SIS receivers near frequencies of 500 GHz - 600 GHz. However, for the bolometer mixer there is no inherent frequency dependence of the performance above the

energy gap frequency (except of course for the linear frequency dependence set by the quantum limit [12]). The same noise temperature, 200 K, should be possible at 0.5 THz or several THz (mechanisms which may ultimately limit the high frequency performance will be briefly discussed below).

To date, the diffusion-cooled hot-electron bolometer mixer has been rapidly developed by the Jet Propulsion Laboratory in collaboration with Yale University [7,13] (no other groups have yet reported results on this new device). Figure 3 shows an SEM photo of a Nb bolometer with a length of 0.28 μm . In fig. 4, a typical resistance-vs-temperature curve shows T_c and ΔT_c . These bolometers were tested in a waveguide mixer mount in a receiver at an LO frequency of 530 GHz (see references 7 and 14 for a complete discussion of these results). This LO frequency is well above the gap frequency of ≈ 390 GHz for this thin Nb film with $T_c \approx 5$ K. The DSB receiver noise temperature is 650 K at an IF of 1.4 GHz. The estimated DSB mixer noise temperature is 560 K and mixer conversion efficiency is about -11 dB. The predicted receiver noise temperature is 570 K - 750 K (depending on the exact choice of ΔT_c from the R-T curve), and similarly the predicted mixer conversion efficiency efficiency is about -10 dB to -15 dB. Thus the calculated values agree well with experiment. The IF rolloff frequency was measured to be about 2 GHz, making this the fastest bolometer ever reported. It is thus clear from these results that this device works well as a submillimeter wave heterodyne mixer.

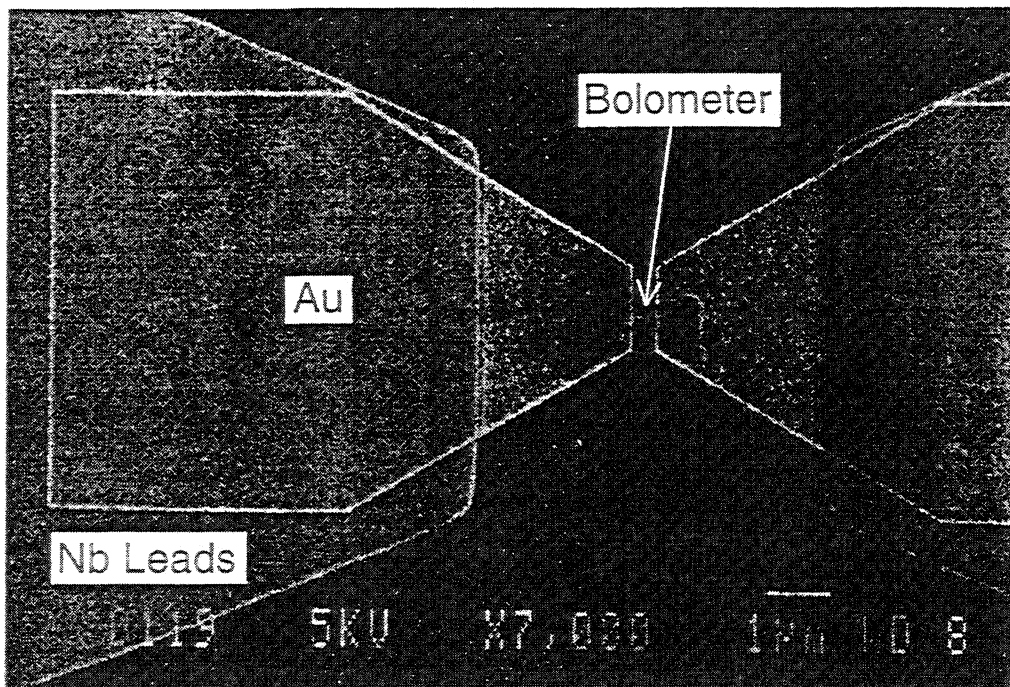


Fig. 3: SEM photo of a diffusion-cooled bolometer mixer.

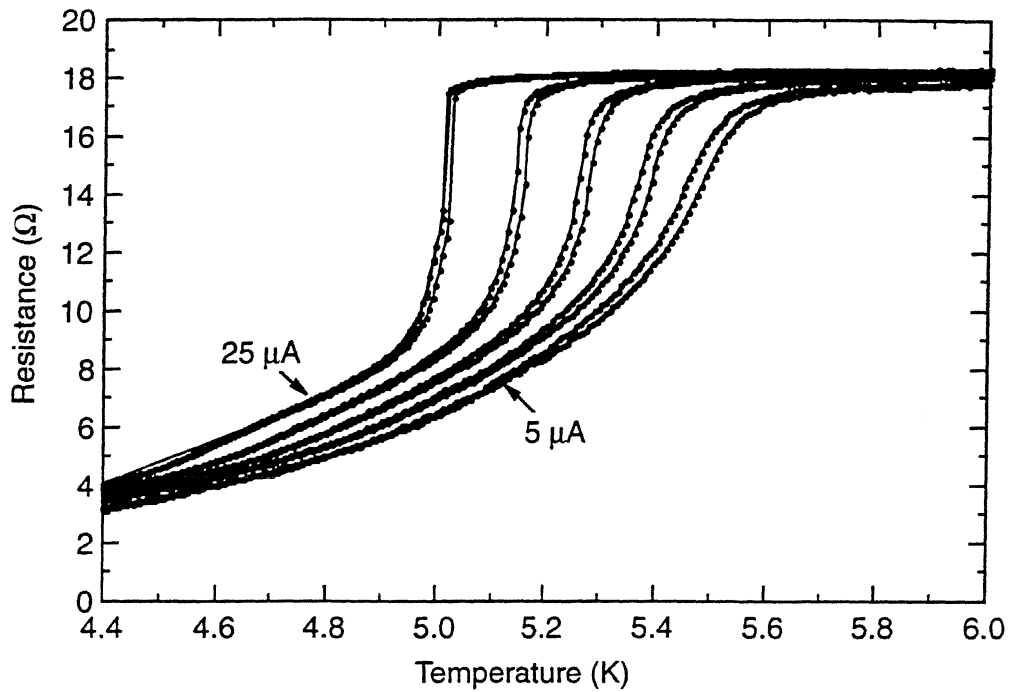


Fig. 4: Resistance versus temperature for a Nb microbridge. The different curves are for different DC currents through the device to measure its resistance. The resistive transition sharpens due to self-heating by the larger currents. The T_c is around 5.4 K and the width is about 0.5-1 K (see 5 μA curve)

ELECTRON-PHONON COOLED HOT-ELECTRON BOLOMETER MIXER

Figure 5 shows the basic geometry of this bolometer which was proposed by E. Gershenzon, et al in 1990 [2]. The geometry is similar to the diffusion-cooled bolometer except that it does not use normal metal at the ends of the microbridge since it employs electron-phonon interactions to the substrate, rather than diffusion to out the ends, to cool the hot electrons (perhaps it is more correct to say that the geometry of the diffusion-cooled bolometer resembles the electron-phonon cooled bolometer since it was proposed first). The basic operation of this bolometer can be understood from fig. 5(b). An incident rf photon imparts its energy to an electron in the film. In a short time τ_{ee} this electron shares its energy with other electrons. The cumulative effect of absorbed rf power and the energy sharing process (ie: the enhanced electron-electron interaction) in these ultra-thin films is to create a hot-electron distribution. Then in a time τ_{ep} a hot electron creates a phonon which then escapes ballistically, for a sufficiently thin film, to the substrate in a short time τ_{ES} . In order for the hot-electron bolometric mechanism to proceed in this manner, there are some constraints which must be met. First $\tau_{ee} \ll \tau_{ep}$ to allow the electrons to heat up from absorbed power. This is usually satisfied for a thin (dirty limit) film at low temperatures $T < 10$ K ($\tau_{ee} \approx 10^{-10}$ sec to 10^{-12} sec) [15]. Next it is important for $\tau_{ES} \ll \tau_{pe}$, where τ_{pe} is the phonon-electron interaction time. That is, the phonons must escape to the substrate before they interact back with other electrons. This requires that the film be very thin since [2,15,16]:

$$\tau_{ES} = 4 d C_e / (v \alpha C_{ph}) \quad (16)$$

where d is the film thickness, C_e and C_{ph} are the electron and phonon specific heats respectively, v is the velocity of sound, and α is the coefficient of transmission of a phonon through the film-substrate interface. The thermal response time of the bolometer can then be written as:

$$\tau_{th} = \tau_{ep} + \tau_{ES} \quad (17)$$

Thus the limiting speed of this type of bolometer is set by τ_{ep} (this limit requires $\tau_{ES} \ll \tau_{ep}$ and thus the films should be thin, the phonon transmission at the substrate interface high, and the thermal conductivity of the substrate should also be high so that it remains a constant temperature bath). This electron-phonon thermal response time can be estimated from C/G where $C = \gamma T V$ is the electron specific heat (see eqn (9)) and:

$$G = 4 A T^3 V \quad (18)$$

is the phonon thermal conductance (A is a constant $\approx 10^4$ W cm⁻³ K⁻⁴ for thin Nb films [2]) Thus [17]:

$$\tau_{ep} = \gamma / (4 A T^2) \quad (19)$$

For a Nb bolometer, $\tau_{ep} \approx 1$ ns and hence $IF_{rolloff} \approx 160$ MHz, which is higher than most bolometer mixers but still too low for many practical applications. For NbN operated at 7 K - 8 K, $\tau_{ep} \approx 15$ ps and hence $IF_{rolloff} \approx 10$ GHz. This is of course high enough to be of practical value.

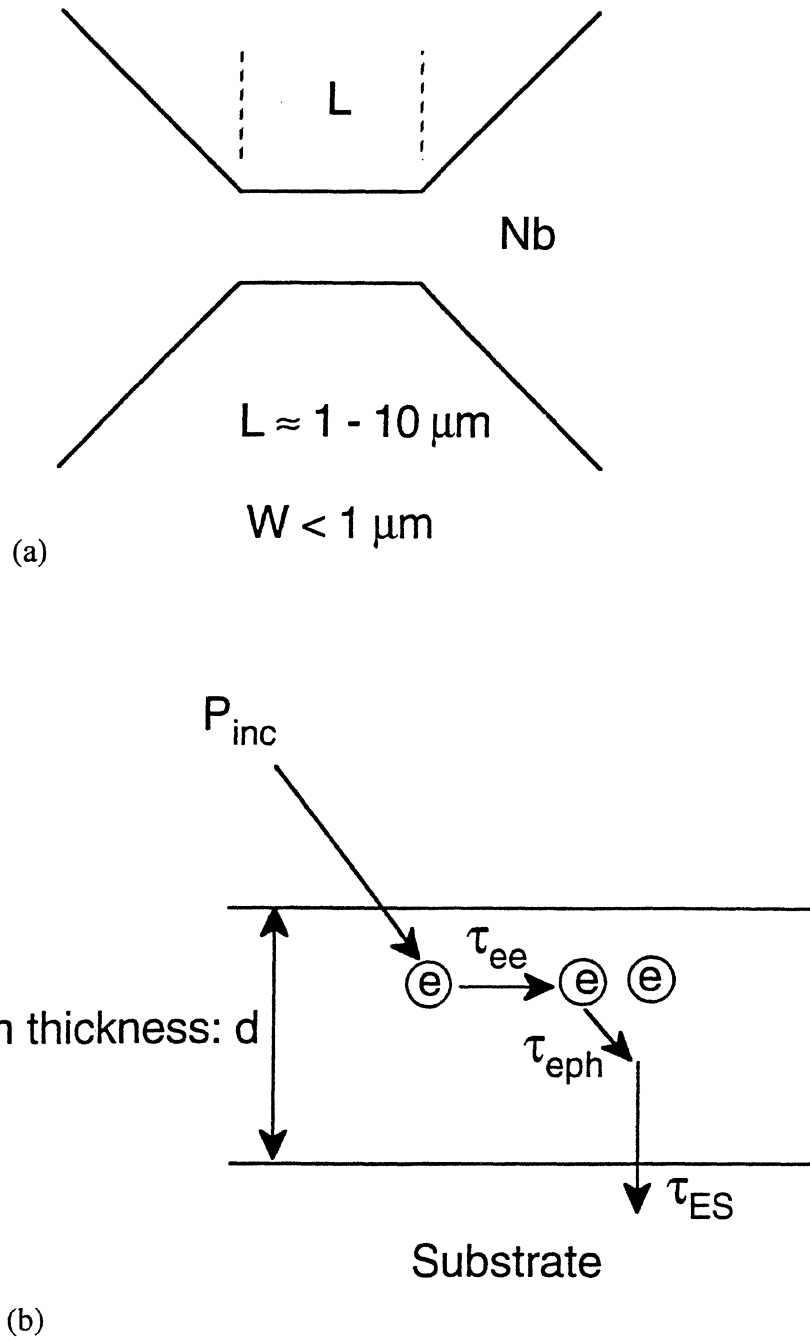


Fig. 5: Basic geometry of electron-phonon cooled bolometer mixer. (a) Top view showing geometry of microbridge. (b) cross sectional view showing schematically the electron-phonon interactions described in the text.

The LO power requirements can be estimated in the same way as for the diffusion-cooled bolometer mixer using eqn. (13), except G is now given by eqn.(18). It should be noted that G in this case depends on the volume of the microbridge and thus it is advantageous to keep the volume small. The width of the microbridge should be less than about $1\ \mu\text{m}$ to avoid a backflow of phonons from the substrate [2]. Then for a given film surface resistance R_s the length is chosen to give the appropriate resistance for an rf match to the mixer embedding circuit (waveguide, planar antenna, etc...). A typical size is $1\ \mu\text{m} \times 5\ \mu\text{m}$. The LO power then required for a Nb bolometer mixer is about 50-70 nW ($T_c = 4\ \text{K}$ and $\Delta T_c = 0.5\ \text{K}$); and for NbN, $P_{LO} \approx 0.5\text{-}1\ \mu\text{W}$ ($T_c = 7\ \text{K}$ and $\Delta T_c = 0.5\ \text{K}$). These are extremely low and therefore very desirable for submillimeter operation.

The mixer noise temperature and conversion efficiency are calculated in the same way as for the diffusion-cooled bolometer mixer. However, the more detailed analysis in [8] suggests that under certain conditions, conversion efficiency greater than unity is possible. Also, as mentioned above, the exact choice of DC and LO power to optimize the mixer is still being theoretically analyzed.

Recent results have shown that the electron-phonon cooled bolometer mixer performs very well. Measurements on a Nb bolometer mixer [8] at an LO frequency of 20 GHz gave conversion efficiencies between -1 dB and -7 dB, an IF rolloff of 80-100 MHz, and an LO power of about 40 nW. These results are in close agreement with expected values. The noise measurements were less certain, but gave a DSB mixer noise temperature of 80 K - 450 K. This may seem high for 20 GHz, but it should be kept in mind that the performance should be independent of frequency, and thus this would be excellent performance at submillimeter wavelengths. Measurements on an NbN bolometer mixer at 100 GHz [18] gave $\eta = -10\ \text{dB}$, $\text{IF}_{\text{rolloff}} \approx 700\ \text{MHz}$ to 1 GHz, $T_R(\text{DSB}) \approx 1000\ \text{K}$, and $P_{LO} \approx 1\ \mu\text{W}$. This is also good performance, except that the IF rolloff is somewhat lower than might be expected. This is probably due to the fact that the phonons did not readily escape into the substrate due to a poor film-substrate interface. This issue is currently being addressed; see the NbN bolometer mixer papers in this conference proceedings for the latest results.

DISCUSSION

The recent innovations in transition-edge hot-electron bolometers (micron and submicron sized, thin, dirty films) have led to ultra-fast, sensitive devices which are competitive as heterodyne mixers. Recent measurements (see particularly this conference proceedings) have proven the concepts and even shown competitive performance. However, the measurement to date have been mainly below 1 THz (there are some recent results on a high- T_c YBCO hot-electron bolometer mixer at an LO wavelength of $1.8\ \mu\text{m}$ [19], but I have not discussed them here) where there already exist state-of-the-art SIS receivers with very low noise. These new bolometer mixers will play an important role at frequencies well above 1 THz where SIS and Schottky receivers become either extremely difficult or impossible (ie: above the energy gap frequency of NbN for example) to operate. In addition, a high- T_c version will be useful in applications where sensitivity can be traded off against cooling requirements, as in a space-based mission.

Important development issues must be addressed for each bolometer. The diffusion-cooled bolometer will need improved submicron definition and alignment of the normal metal contacts. Also, low-resistance normal-to-superconductor contacts are required. For the electron-phonon cooled bolometer, the phonon reflection at the film substrate interface must be minimized. This will be particularly important for materials like NbN (which have a high

upper limit to the IF rolloff) which can react strongly with common rf substrates such as quartz, thereby producing a poor interface. In addition, both types of bolometers are resistive at the rf, so a very broadband match, to a planar antenna for example, should be easily achieved. The rf bandwidth can however be so broad that the mixer will be easily saturated. Unlike the common situation for an electronic mixer with reactive parasitics where the goal is to achieve a broadband rf match, these bolometer mixers may require band-limiting rf filters.

Finally, since the likely role for these bolometer mixers will be at very high frequencies, it is important to test as soon as possible the prediction that the performance is independent of frequency. If they do not perform well at frequencies beyond a THz, their application may be limited. Certain mechanisms may affect the high frequency performance. A high energy rf photon (several THz) will produce a high energy electron in the superconductive film. This hot electron can then either share its energy with other electrons, or break Cooper pairs, or produce hot phonons. In any case, the film will absorb rf power, but if the energy escapes, for example by the hot phonons rapidly leaving the film, before it is shared with the electron gas, then the electrons will not heat as efficiently and the sensitivity of the mixer will decrease. The expectation is that the performance will not degrade until at least several THz. Assuming this is true, these detectors should have a significant impact on the field of THz heterodyne sensors.

ACKNOWLEDGEMENTS

This overview would not have been possible without the generous and fruitful discussions with the many researchers working on these detectors, and in related areas. I wish in particular to thank Bruce Bumble, Peter Burke, Hans Ekstrom, Eugene Gershenson, Gregory Gol'tsman, Sigfrid Yngvesson, Boris Karasik, Rick LeDuc, Tom Phillips, Dan Prober, Rob Schoelkopf, Anders Skalare, Lianne Verheijen, and Jonas Zmuidzinas (who also suggested I give this talk).

The research described in this paper was performed by the Center for Space Microelectronics Technology, Jet Propulsion Laboratory, California Institute of Technology, and was sponsored by the National Aeronautics and Space Administration, Office of Space Access and Technology.

REFERENCES

- [1] D.E. Prober, "Superconducting terahertz mixer using a transition-edge microbolometer", *Appl. Phys. Lett.* **62** (17), pp. 2119-2121 (1993).
- [2] E.M. Gershenson, G.N. Golt'sman, I.G. Gogidze, Y.P. Gusev, A.I. Elantev, B.S. Karasik, A.D. Semenov, "Millimeter and submillimeter range mixer based on electronic heating of superconductive films in the resistive state", *Superconductivity* **3** (10), pp. 1582-1597 (1990).
- [3] P.L. Richards, "Bolometers for infrared and millimeter waves", *J. Appl. Phys.* **76**, pp. 1-23 (1994).
- [4] A.F. Andreev, *Sov. phys. JETP* **19**, 1228 (1964).
- [5] P. Santhanam and D.E. Prober, "Inelastic electron scattering mechanisms in clean aluminum films", *Phys. Rev B* **29**, pp. 3733-3736 (1984).
- [6] C. Kittel, *Introduction to Solid State Physics*, 5th edition, John Wiley & Sons, Inc. New York (1976).
- [7] A. Skalare, W.R. McGrath, B. Bumble, H.G. LeDuc, P.J. Burke, A.A. Verheijen, D.E. Prober, "A heterodyne receiver at 533 GHz using a diffusion-cooled superconducting hot electron bolometer mixer", to appear in *IEEE Trans. Appl. Superconductivity* (March 1995).
- [8] H. Ekstrom, B. Karasik, E. Kollberg, K.S. Yngvesson, "Investigation of a superconducting hot electron mixer", *Proc. 5th Int'l. Symp. on Space Terahertz Technology*, Univ. of Michigan, pp. 169-188 (1994).
- [9] F. Arams, C. Allen, B. Peyton, E. Sard, "Millimeter mixing and detection in bulk InSb", *Proc. IEEE* **54**, pp. 308-318 (1966).
- [10] B.S. Karasik and A.I. Elantev, "Analysis of the noise performance of a hot-electron superconducting bolometer mixer", *This conference proceedings*.
- [11] J.C. Mather, "Bolometer noise: nonequilibrium theory", *Appl. Optics* **21**, p.1125 (1982).
- [12] C.M. Caves, *Phys. Rev D* **26**, p. 1817 (1982).
- [13] A. Skalare, W.R. McGrath, B. Bumble, H.G. LeDuc, P.J. Burke, A.A. Verheijen, D.E. Prober, "A superconducting hot-electron bolometer mixer for 530 GHz", *Proc. 5th Int'l. Symp. on Space Terahertz Technology*, Univ. of Michigan, pp. 157-168 (1994).
- [14] A. Skalare, W.R. McGrath, B. Bumble, H.G. LeDuc, P.J. Burke, A.A. Verheijen, D.E. Prober, "Noise temperature and IF bandwidth of a 530 GHz diffusion-cooled hot-electron bolometer mixer" *This conference proceedings*.
- [15] E.M. Gershenson, M.E. Gershenson, G.N. Gol'tsman, A.M. Lyul'kin, A.D. Semenov, and A.V. Sergeev, "On the limiting characteristics of high-speed superconducting bolometers", *Sov. Phys. Tech. Phys.* **34**, pp. 195-201 (1989).
- [16] G.N. Gol'tsman, A.I. Elant'iev, B.S. Karasik, and E.M. Gershenson, "Antenna-coupled superconducting electron-heating bolometer", unpublished.
- [17] E.M. Gershenson, G.N. Gol'tsman, B.S. Karasik, G.Ya. Lugova, N.A. Serebryakova, and E.V. Chinkova, "IR radiation detectors based on electronic heating of films made from conventional superconductors in the resistive state", *Superconductivity* **5**, pp.1126-1137 (1992).
- [18] O. Okunev, A. Dzardanov, H. Ekstrom, S. Jacobsson, E. Kollberg, G. Gol'tsman, and E.M. Gershenson, "NbN hot electron waveguide mixer for 100 GHz operation", *Proc. 5th Int'l. Symp. on Space Terahertz Technology*, Univ. of Michigan, p.214 (1994).
- [19] M. Lindgren, M.A. Zorin, V. Trifonov, M. Danerud, D. Winkler, B.S. Karasik, G.N. Gol'tsman, and E.M. Gershenson, "Optical mixing in a patterned YBa₂Cu₃O₇ thin film", *Appl. Phys. Lett.* **65**, pp.3398-3400 (1994).

Analysis of the Noise Performance of a Hot–Electron Superconducting Bolometer Mixer

B.S. Karasik and A.I. Elantev

*Department of Physics, Moscow State Pedagogical University,
Moscow 119435, Russia*

Abstract

A theoretical analysis for the noise temperature of hot–electron superconducting mixer has been presented. The contributions of both Johnson noise and electron temperature fluctuations have been evaluated. A set of criteria ensuring low noise performance of the mixer has been stated and a simple analytic expression for the noise temperature of the mixer device has been suggested. It has been shown that an improvement of the mixer sensitivity does not necessarily follow by a decrease of the bandwidth. An SSB noise temperature limit due to the intrinsic noise mechanisms has been estimated to be as low as 40–90 K for a mixer device made from Nb or NbN thin film. Furthermore, the conversion gain bandwidth can be as wide as is allowed by the intrinsic electron temperature relaxation time if an appropriate choice of the mixer resistance has been made. The intrinsic mixer noise bandwidth is of 3 GHz for Nb device and of 5 GHz for NbN device. An additional improvement of the theory has been made when a distinction between the impedance measured at high intermediate frequency (larger than the mixer bandwidth) and the mixer ohmic resistance has been taken into account.

Recently obtained experimental data on Nb and NbN bolometer mixer devices are viewed in connection with the theoretical predictions.

The noise temperature limit has also been specified for the mixer device where an outdiffusion cooling mechanism rather than the electron–phonon energy relaxation determines the mixer bandwidth. A consideration of the noise performance of a bolometer mixer made from YBaCuO film utilizing a hot–electron effect has been done.

I. Introduction

During past several years the sensitivity of SIS submillimeter mixers has been increasingly improved. By now a DSB noise temperature of about 4–5 times of the quantum limit has been reached for both waveguide and quasi-optical mixers up to about 700 GHz frequencies corresponding to the bandgap in Nb [1-7]. The rapid progress in the development of low noise submillimeter heterodyne receivers faced the researchers to the problem of the further advance towards THz frequencies where the SIS mixers has not been demonstrated yet to perform very well.

Today, perhaps the most promising device which can probably compete to the SIS mixer, is a hot electron superconducting bolometer (HEB) mixer proposed in [8]. Recent experimental studies of the mixer device noise temperature [9,10] as well as of the intrinsic noises [11] have demonstrated a possibility of low noise performance

of the HEB mixer at microwaves and submillimeter waves. A rapid progress in the improvement of the HEB mixer sensitivity is raising an interest in the limiting parameters of such devices.

A theory of HEB mixer was given for the first time by Arams et al. [12]. Despite the only semiconductor InSb mixer device was considered the expression for the mixer gain is useful for superconductor HEB device, as well. More recently this approach was specified for Nb HEB mixer at 20 GHz [9]. The noise temperature of the mixer device was studied using numerical model calculations by Gershenson et al. [8]. As low as a 40 K SSB mixer noise temperature along with a 40 MHz mixer bandwidth has been predicted for Nb device. Since then new superconducting materials such as NbN [13-16] and YBaCuO [17] are used for the development of HEB mixers. Also a new approach has been proposed [18] when an outdiffusion cooling mechanism rather than electron-phonon relaxation should limit the bandwidth of HEB mixer. Here we present a generalized analytic theory for the noise performance of the HEB superconducting mixer applicable for different materials and electron cooling mechanisms.

The paper is designed as follows. In Section II we give a background which is needed for the consequent derivations, i.e. heat balance equation, model of current-voltage (I-U) characteristic and relationship between the voltage responsivity and conversion gain. In Section III the derivations for the mixer intermediate frequency (IF) impedance, voltage responsivity, conversion gain and time constants are given. The expressions for mixer noise temperature due to Johnson noise and thermal fluctuation noise are obtained in Section IV. A brief summary of the noise measurements in HEB mixers known to date is also presented. The peculiarities of the noise performance for novel HEB devices, namely outdiffusion cooled mixer and high- T_c mixer are discussed in Section V.

II. Heat balance equation and basic relationships

The HEB mixer device is a thin superconducting strip on dielectric substrate cooled below its critical temperature T_c . Different external factors [e.g. magnetic field, transport current, local oscillator (LO) power] may partially destroy superconductivity and create a resistive state where the film resistance depends on the electron temperature. Depending on the film and substrate materials, and ambient temperature the relaxation of the electron temperature can be different. Thus, in low temperature limit the electron specific heat c_e is typically much larger than the phonon one c_p . In this case the electron temperature relaxation is governed by a single time constant τ_θ [19]. For a relatively long film when a temperature spatial distribution is fairly uniform the electron temperature relaxation time is given by $\tau_\theta = \tau_{e-ph} + \tau_{esc} c_e / c_p$, where τ_{e-ph} is the electron-phonon energy relaxation time, τ_{esc} is the time for phonons to escape to the substrate. When the film is made very thin (thickness $d \leq 10$ nm) $\tau_\theta = \tau_{e-ph}$. For very short bridges which length $L \ll \sqrt{D \tau_{e-ph}}$ the value for τ_θ is given by $\tau_{diff} = (L/4)^2 / D$ [18] (D is the electron diffusivity). For higher temperatures when $c_p \geq c_e$ the relaxation of the electron temperature is determined by several time constants like e.g. for YBaCuO film. The consideration of this case is given in Section V.

If one assumes the distribution of the electron temperature along the film to be uniform ("lumped" bolometer) the following heat balance equation is valid:

$$c_e V \frac{\partial \theta}{\partial \tau} = -\Pi(\theta, T) + \mathcal{W} + \alpha P_{rad}. \quad (1)$$

Here $\Pi(\theta, T)$ is the flow of heat from electrons to surrounding, I is the bias current, U is the voltage across the film, P_{rad} is the incident radiation power, V is the mixer volume and α is the radiation coupling factor. A certain form of $\Pi(\theta, T)$ function depends on material and device geometry. For instance, for lumped Nb hot-electron bolometer [20]:

$$\Pi(\theta, T) = AV(\theta^4 - T^4), \quad (2)$$

where $A \approx 10^4 \text{ W cm}^{-3} \text{ K}^{-4}$.

In order to derive the mixer characteristics as functions of IF the heat balance equation should be supplemented with a certain relationship between voltage U and current I which, in general, can not be stated *a priori*. The formal equation is

$$U = U(\theta, I) \quad \text{and} \quad dU = \frac{\partial U}{\partial \theta} \frac{d\theta}{dI} dI + \frac{\partial U}{\partial I} dI \quad (3)$$

For frequencies $f \gg \tau_\theta^{-1}$ the electron temperature does not respond to the current change therefore the relationship between U and I is set through $\partial U / \partial I$. The very common assumption is $\partial U / \partial I = R$ (R is the device dc resistance). However, as it has been shown in [21], this is not necessarily true for HEB superconducting devices. Due to the particular resistivity mechanism (e.g. vortex flow) the I-U characteristic can be non-linear even at high frequencies. This fact has also been mentioned in [22] as rather common for various types of infrared bolometers. A $\partial U / \partial I$ value [denoted in [22] $Z(\infty)$] must be found experimentally in each particular case. In terms of impedance one can say that the impedance of superconducting HEB decreases with frequency from dc differential resistance dU/dI to $Z(\infty)$. The difference $dU/dI - Z(\infty)$ appears because of the electron heating and, consequently, reflects the device sensitivity. The proper relationship between the impedance and the voltage responsivity is given in Section III.

The next important step is an equation coupling the mixer conversion gain η and the voltage responsivity S in the detector mode. It has been obtained by several authors [8,12,18] that an alternating voltage generated in the mixer load at intermediate frequency $\omega = 2\pi f$ is given by

$$U_{IF}(\omega) = 2S(\omega) \sqrt{P_s P_{LO}} e^{j\omega t + \varphi}. \quad (4)$$

Here P_{LO} and P_s are the LO and signal powers respectively. Then the conversion gain is given

$$\eta(\omega) = \frac{|P_{IF}|}{|P_s|} = \frac{2|S(\omega)|^2 P_{LO}}{R_L}. \quad (5)$$

III. Characteristics of the mixer

IF impedance.

The derivation of the formula for the device IF impedance can be done basing on the assumption stated in previous Section, i.e. the impedance contains both frequency dependent and frequency independent components.

From Eq. 3 we can obtain for the dc impedance:

$$Z(0) = \frac{dU}{dI} = \frac{\partial U}{\partial \theta} \frac{d\theta}{dI} + Z(\infty) = I \frac{\partial R}{\partial \theta} \kappa(0) + Z(\infty), \quad (6)$$

where the function $d\theta/dI$ is denoted κ . It is obvious that $\kappa \rightarrow 0$ when $\omega \rightarrow \infty$. In the above expression we assume the device operates in constant current mode which is important for a definition of the impedance. Then, in complex form:

$$Z(\omega) = I \frac{\partial R}{\partial \theta} \kappa(\omega) + Z(\infty). \quad (7)$$

Small variation of the current $\Delta I = \Delta I_0 e^{j\omega t}$ produces the corresponding variation of the electron temperature $\Delta \theta = \Delta \theta_0 e^{j(\omega t + \varphi)}$. The relationship between these variations is given using Eq. 1:

$$j\omega c_e V \Delta \theta = -G \kappa(\omega) \Delta I + U \Delta I + I Z(\omega) \Delta I. \quad (8)$$

Here $G(\theta) = d\Pi/d\theta$ is the thermal conductivity between the electrons and the heat sink. From Eq. 8 we obtain the following equation for complex function $\kappa(\omega)$:

$$j\omega c_e V \kappa(\omega) = -G \kappa(\omega) + U + I Z(\omega). \quad (9)$$

Since $\tau_\theta = c_e V/G$ then from Eqs. 7 and 9 we finally obtain:

$$Z(\omega) = \frac{CR + Z(\infty)}{1-C} \frac{1 + j\omega \frac{\tau_\theta Z(\infty)}{Z(\infty) + CR}}{1 + j\omega \frac{\tau_\theta}{1-C}}, \quad (10)$$

where $C = I_0^2 (\partial R / \partial \theta) / G$ is the dimensionless self-heating parameter. Denoting $\bar{\tau} = \tau_\theta (1-C)^{-1}$, $\tau_0 = \tau_\theta Z(\infty) [Z(\infty) + CR]^{-1}$, and $Z(0) = [CR + Z(\infty)](1-C)^{-1}$ we can reduce Eq. 10 to

$$Z(\omega) = Z(0) \frac{1 + j\omega \tau_0}{1 + j\omega \bar{\tau}}, \quad (11)$$

which coincides with the expression used in [21].

In particular case $Z(\infty) = R$ (see [9,12]):

$$Z(0) = R \frac{1+C}{1-C}, \quad (12)$$

$$\tau_0 = \frac{\tau_\theta}{1+C} \quad (12a)$$

Voltage responsivity.

Using a similar approach one can derive the expression for the voltage responsivity [22]:

$$S(\omega) = \frac{\alpha}{I} \frac{Z(0)/Z(\infty) - 1}{[Z(0)/R_L + 1][R/Z(\infty) + 1]} \frac{1}{1 + j\omega \bar{\tau}}. \quad (13)$$

Here R_L is the load resistance, τ^* is the apparent time constant given by

$$\tau^* = \frac{[Z(\infty) + R_L][Z(0) + R]}{[Z(0) + R_L][Z(\infty) + R]} \tau_\theta. \quad (14)$$

Using parameter C Eqs. 12 and 13 can be written as follows:

$$S(\omega) = \frac{\alpha}{I} \frac{C}{1+C} \frac{R_L}{\frac{R-R_L}{Z(\infty)+R_L}} \frac{1}{Z(\infty)+R_L} \frac{1}{1+j\omega\tau^*} \quad (15)$$

$$\tau^* = \frac{\tau_\theta}{1+C \frac{R-R_L}{Z(\infty)+R_L}}. \quad (15a)$$

If $Z(\infty) = R$ then

$$S(\omega) = \frac{\alpha}{I} \frac{C}{1+C} \frac{R_L}{\frac{R-R_L}{R+R_L}} \frac{1}{R+R_L} \frac{1}{1+j\omega\tau^*} \quad (16)$$

$$\tau^* = \frac{\tau_\theta}{1+C \frac{R-R_L}{R+R_L}} \quad (16a)$$

One should point out that the difference between τ^* and $\bar{\tau}$ arises because of the electro-thermal feedback through the load. If $R_L \rightarrow \infty$ then $\tau^* = \bar{\tau}$.

Mixer conversion gain.

Here we can give a general expression for the mixer conversion gain. Equations (5) and (15) give

$$\eta(\omega) = 2\alpha C^2 \frac{R_L R}{[Z(\infty) + R_L]^2} \frac{\alpha P_{LO}}{P_{DC}} \frac{1}{\left(1+C \frac{R-R_L}{Z(\infty)+R_L}\right)^2} \frac{1}{1+(\omega\tau^*)^2}, \quad (17)$$

where $P_{DC} = I^2 R$ is the Joule power dissipated in the device.

Returning to the particular case $Z(\infty) = R$ one can obtain the well known expression previously derived in [9,12]:

$$\eta(\omega) = 2\alpha C^2 \frac{R_L R}{(R+R_L)^2} \frac{\alpha P_{LO}}{P_{DC}} \frac{1}{\left(1+C \frac{R-R_L}{R+R_L}\right)^2} \frac{1}{1+(\omega\tau^*)^2}. \quad (18)$$

The analysis of the above expression (e.g. given in [9]) and also numerical calculation in [8] show that the conversion gain is theoretically limitless. To ensure this the unpumped I-U characteristic of the mixer must have a

branch with negative differential resistance that in turn can be attained if the bath temperature T is much lower than the critical temperature T_c . One more necessary condition to reach high conversion gain is $C \approx 1$. This corresponds to the point of the bolometer thermal runaway and the differential resistance of the mixer is very large (see Eq. 12 and Fig. 3). Very often an appearance of large conversion gain is supposed to be followed by the drastic decrease of the mixer bandwidth. It is true only for $R_L \gg R$ when $\tau^* \approx \bar{\tau} \rightarrow \infty$ if $C \rightarrow 1$. If R_L value is chosen to be equal R no significant change of the bandwidth is expected comparing to $\Delta f = (2\pi\tau_\theta)^{-1}$ set by the bolometer material and its electron temperature. Thus if $R = R_L$ then $\tau^* = \tau_\theta$ even for $C=1$ and for $\alpha \approx 1$ we obtain

$$\eta(0) = \frac{P_{LO}}{2P_{DC}}. \tag{19}$$

Local oscillator and Joule powers are coupled through the heat balance equation. One can show that if $T \ll T_c$ and the superconducting transition width is small $\Delta T \ll T_c$ the conversion gain in Eq. 19 is larger than 1. More details are given in the next Section.

IV. Noise in HEB mixer

The conventional mechanisms for bolometer detector noise should be dominating in case of mixer. As much as it concerns an intrinsic noise mechanisms the contributions of Johnson noise and thermal fluctuation noise to the mixer noise temperature have to be evaluated. An important issue is the significant non-equilibrium caused by the LO pumping.

A nonequilibrium theory of the bolometer detector noise has been given by Mather [23]. Mather introduced a dynamic equivalent circuit of the bolometer where the intrinsic reactance in the bolometer response was presented by an equivalent inductance. Similar circuit for more general case $Z(\infty) \neq R$ is shown in Fig. 1a.

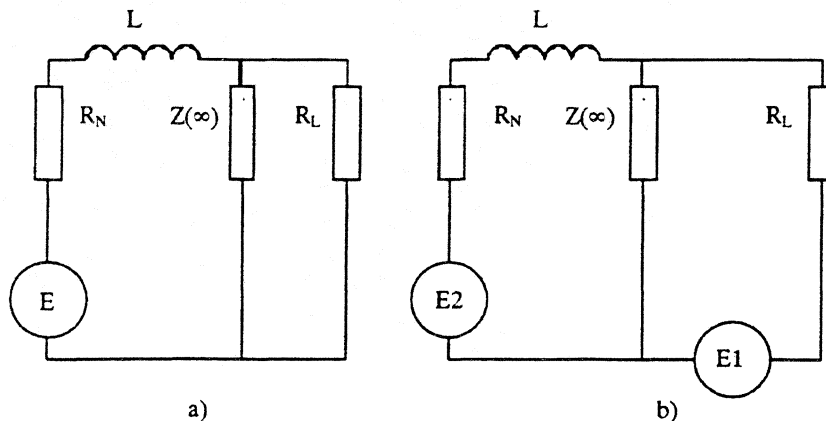


Fig. 1. Equivalent circuits for the HEB. E , $E1$, and $E2$ are the equivalent sources of the detected signal or intrinsic noises.

If the circuit parameters are

$$R_N = \frac{Z(0)Z(\infty)}{Z(\infty) - Z(0)}, \quad (20)$$

$$L = \frac{R + Z(0)}{Z(\infty) - Z(0)} \frac{Z(\infty)^2}{R + Z(\infty)} \tau_\theta = -\frac{\tau_\theta}{C} \frac{Z(\infty)^2}{R + Z(\infty)}, \quad (20a)$$

then the output impedance of the circuit is given by Eq. 11. To represent the responsivity correctly the equivalent voltage source must be chosen as

$$E = -\frac{\alpha P_{\text{rad}}}{I_0} \frac{Z(\infty)}{R + Z(\infty)}. \quad (21)$$

To calculate the modification of the noise by the bolometer self-heating one should place the corresponding noise source appropriately in the circuit and find the noise voltage across the load.

Johnson noise.

Following Mather [23] we assume the classical Johnson noise source $e_J = \sqrt{4k_B Z(\infty)\theta}$ must appear twice in the bolometer equivalent circuit (see Fig. 2b). Source E1 acts simply as a voltage source in series with the bolometer impedance $Z(\omega)$. Mather used $E2 = -e_J/2$, however in more general case when $Z(\infty) \neq R$ $E2 = -e_J Z(\infty)/[Z(\infty) + R]$ is placed to take into account the output noise enhancement caused by the detection of the Johnson noise in the bolometer. Both sources give an actual noise output voltage in the load of

$$e_J^*(\omega) = e_J(\omega) \frac{Z(0) + R}{Z(0) + R_L} \frac{R_L}{R + Z(\infty)} \frac{1 + j\omega\tau_\theta}{1 + j\omega\tau^*}. \quad (22)$$

Hence, the output HEB mixer noise temperature due to Johnson noise is:

$$T_{\text{out}}^J(\omega) = \frac{|e_J^*(\omega)|^2}{k_B R_L} = \frac{4Z(\infty)R_L\theta}{[R_L + Z(\infty)]^2} \frac{1}{\left[1 + C \frac{R - R_L}{Z(\infty) + R_L}\right]^2} \frac{1 + (\omega\tau_\theta)^2}{1 + (\omega\tau^*)^2}. \quad (23)$$

Finally, the SSB mixer noise temperature contribution is given by:

$$T_m^J(\omega) = T_{\text{out}}^J(\omega)/\eta(\omega) = \frac{2\theta P_{DC}}{\alpha^2 C^2 P_{LO}} \frac{Z(\infty)}{R} \left[1 + (\omega\tau_\theta)^2\right]. \quad (24)$$

Thermal fluctuation noise.

This noise is very common for any kind of bolometer having a temperature dependent parameter. The physical cause of the noise are thermal fluctuations of the electron temperature $\langle \Delta\theta \rangle_\omega = \sqrt{4k_B\theta^2/G} (1 + j\omega\tau_\theta)^{-1}$ producing

the noise voltage across the load. The contribution of this noise source can be given using the circuit in Fig. 2a with E representing the equivalent noise source:

$$e_{TF}(\omega) = -G(\Delta\theta)_\omega \frac{Z(\infty)}{I[Z(\infty) + R]} = -\frac{\sqrt{4k_B\theta^2G}}{I} \frac{Z(\infty)}{Z(\infty) + R} \frac{1}{1 + j\omega\tau_\theta}. \quad (25)$$

After a number of transformations one can get an output noise voltage across the load:

$$e_{TF}^*(\omega) = \frac{\sqrt{4k_B\theta^2G}}{I} \frac{C}{1 + C} \frac{R - R_L}{Z(\infty) + R_L} \frac{R_L}{Z(\infty) + R_L} \frac{1}{1 + j\omega\tau^*}. \quad (26)$$

Consequently, the output noise temperature is:

$$T_{out}^{TF}(\omega) = \frac{|e_{TF}^*|^2}{k_B R_L} = \frac{4\theta^2G}{I^2} \frac{C^2}{\left[1 + C \frac{R - R_L}{Z(\infty) + R_L}\right]^2} \frac{R_L}{[Z(\infty) + R_L]^2} \frac{1}{1 + (\omega\tau^*)^2}. \quad (27)$$

Using Eq. 17 this results in the following mixer noise:

$$T_m^{TF} = \frac{2\theta^2G}{\alpha^2 P_{LO}}. \quad (28)$$

Effective noise bandwidth.

An interesting consequence of Eqs. 24 and 28 is that whereas the T_m^J value increases at intermediate frequencies larger than $(2\pi\tau_\theta)^{-1}$, the thermal fluctuation noise temperature does not depend on IF. Thus, the equivalent bandwidth of the mixer device is given by:

$$\Delta f = (2\pi\tau_\theta)^{-1} \sqrt{1 + \frac{T_m^{TF}}{T_m^J}}. \quad (29)$$

Broken-line transition model.

For further analysis it is useful to simplify the model assuming that the $R(T)$ characteristic of the bolometer has a broken-line shape [18] (see Fig. 2). Then, using a steady state heat balance equation for the electron temperature

$$AV(\theta^n - T^n) = P_{DC} + \alpha P_{LO}, \quad (30)$$

we can obtain $G(\theta) = nAV\theta^{n-1}$, where n is the material dependent constant ($n = 4$ for Nb) Since $\theta = T_c$ and $R = R_n/2$ then $C = 2P_{DC} / (nAVT_c^{n-1}\Delta T_c)$.

One can see from Eqs. 24 and 28 that the increase of both P_{LO} and C leads to the decrease of the noise temperature. At the same time P_{DC} decreases since both θ and T are fixed (see Eq. 30). The most favorable regime

of operation is when $C = 1$, which corresponds to $P_{DC} = nAV T_c^{n-1} \Delta T_c / 2$. To ensure this condition the applied LO power has to heat the device up to the temperature point $\theta^* = T_c - \Delta T_c / 2$, just below the superconducting transition edge (see Fig. 2). The LO power is then given by $P_{LO} = \alpha^{-1} AV (T_c^n - T^n - nT_c^{n-1} \Delta T_c)$. The I-U characteristic for this case is shown in Fig. 3.

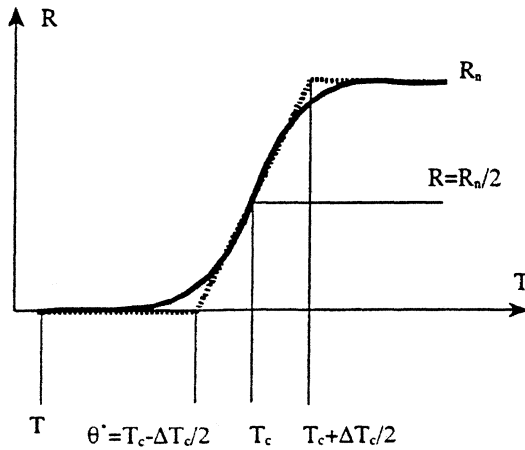


Fig. 2. $R(T)$ curve and "broken-line transition".

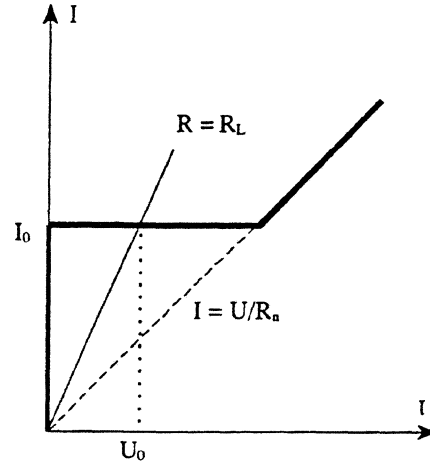


Fig. 3. Pumped I-U curve for $C = 1$.

Finally, we obtain

$$T_m^J = \frac{\alpha^{-1} n T_c^n \Delta T_c}{T_c^n - T^n - n T_c^{n-1} \Delta T_c} \quad \text{and} \quad T_m^{TF} = \frac{2 \alpha^{-1} n T_c^{n+1}}{T_c^n - T^n - n T_c^{n-1} \Delta T_c} \tag{31}$$

It is seen that a larger difference between T_c and T provides a lower noise temperature, therefore when $T_c^n \gg T^n$ and the superconducting transition is very narrow ($\Delta T_c \ll T_c$) the noise temperatures are given by

$$T_m^J = n \Delta T_c / \alpha \quad \text{and} \quad T_m^{TF} = 2 n T_c / \alpha \tag{32}$$

The noise bandwidth of the device is in turn given by

$$\Delta f = (2\pi \tau_\theta)^{-1} \sqrt{1 + \frac{2 T_c}{\Delta T_c}} \tag{33}$$

We would like to point out that the minimum noise temperature due to thermal fluctuation noise does not depend on the superconducting transition width, but ΔT_c must be made very small in order to reach this minimum. For the particular case considered by Prober, $P_{LO} = P_{DC} = G(T_c) \Delta T_c / 4$ Eq. 28 gives $T_m^{TF} = 8 \alpha^{-1} T_c^2 / \Delta T_c$, which is similar to the corresponding formula in [18].

The conversion gain can be given for the "broken-line transition" model using Eq. 18:

$$\eta(0) = \frac{\alpha}{n} \frac{T_c}{\Delta T_c} \frac{R_L}{R} \tag{34}$$

The apparent time constant τ^* for the conversion gain is given by

$$\tau^* = \frac{\tau_\theta}{2} \left(1 + \frac{R_L}{R} \right). \quad (35)$$

It is seen from Eqs. 34 and 35 that the increase of the ratio R_L/R can ensure a very large conversion gain, $\eta(0) > 1$, but along with this the gain bandwidth can degrade significantly. However, a gain as large as $\eta(0) \approx 1$ can be obtained even if $R_L = R$, that also gives $\tau^* \approx \tau_\theta$. This is important if one wants to increase the gain bandwidth and, hereby reduce the noise contribution of IF circuit at higher intermediate frequencies. The contribution to the noise temperature from the mixer itself does not depend on IF load.

The estimations from Eqs. 32 and 33 for typical materials currently used for fabrication of hot electron mixers and $\alpha = 1$ are presented in Table I. One can see that an excellent noise performance can be expected for both Nb and NbN superconducting HEB mixers.

Table I. Theoretical limits for the noise performance of HEB mixers.

Material	T_c [K]	ΔT_c [K]	n	T_m^J [K]	T_m^{TF} [K]	τ_θ [ns]	Δf [GHz]
Nb	5	0.1	4	0.4	40	0.5 ^a	3.2
NbN	12	0.5	3.6	1.8	86	0.2 ^b	5.0

^a These data are taken from [24] assuming the electron diffusivity to be $1 \text{ cm}^2/\text{s}$.

^b We use the experimental data recently obtained in mixing experiments at 100 GHz [13–15] and at 300–350 GHz [11,16]. They are different from the results of τ_{e-ph} measurements performed in equilibrium conditions in [25].

The most important formulas obtained above are summarized in Table II.

Related experiments.

The HEB responsivity and impedance have been studied in [20] and [21] respectively. A good agreement with the frequency dependence given by Eqs. 11 and 15 has been obtained for Nb device placed in a strong magnetic field. The value of τ_θ has been studied as a function of P_{DC} and P_{LO} .

More recently the similar study has been performed for Nb HEB mixer at 20 GHz with no magnetic field applied [9]. The validity of Eq. 18 for conversion gain has been checked. Also Eq. 11 for impedance and Eq. 16a for the

Table II. Equation summary

Voltage responsivity	$S(\omega) = \frac{\alpha}{I} \frac{C}{1+C} \frac{R_L}{\frac{R-R_L}{Z(\infty)+R_L}} \frac{1}{Z(\infty)+R_L} \frac{1}{1+j\omega\tau^*}$
Apparent time constant	$\tau^* = \frac{\tau_\theta}{1+C} \frac{R-R_L}{Z(\infty)+R_L}$
Impedance	$Z(\omega) = \frac{CR+Z(\infty)}{1-C} \frac{1+j\omega\tau_0}{1+j\omega\bar{\tau}}$
Impedance time constants	$\bar{\tau} = \frac{\tau_\theta}{1-C}, \tau_0 = \frac{\tau_\theta Z(\infty)}{Z(\infty)+CR}$
Conversion gain	$\eta(\omega) = 2\alpha C^2 \frac{RR_L}{[Z(\infty)+R_L]^2} \frac{1}{\left[1+C \frac{R-R_L}{Z(\infty)+R_L}\right]^2} \frac{1}{1+(\omega\tau^*)^2}$
Johnson output noise temperature	$T_{\text{out}}^J(\omega) = \frac{4Z(\infty)R_L\theta}{[Z(\infty)+R_L]^2} \frac{1}{\left[1+C \frac{R-R_L}{Z(\infty)+R_L}\right]^2} \frac{1+(\omega\tau_\theta)^2}{1+(\omega\tau^*)^2}$
Thermal fluctuation output noise temperature	$T_{\text{out}}^{\text{TF}}(\omega) = \frac{4\theta^2 G}{I^2} \frac{C^2}{\left[1+C \frac{R-R_L}{Z(\infty)+R_L}\right]^2} \frac{R_L}{[Z(\infty)+R_L]^2} \frac{1}{1+(\omega\tau^*)^2}$
Johnson mixer noise temperature	$T_m^J(\omega) = T_{\text{out}}^J(\omega)\eta(\omega) = \frac{2\theta P_{\text{DC}}}{\alpha^2 C^2 P_{\text{LO}}} \frac{Z(\infty)}{R} \left[1+(\omega\tau_\theta)^2\right]$
Thermal fluctuation mixer noise temperature	$T_m^{\text{TF}} = \frac{2\theta^2 G}{\alpha^2 P_{\text{LO}}}$
Effective noise bandwidth	$\Delta f = (2\pi\tau_\theta)^{-1} \sqrt{1 + \frac{T_m^{\text{TF}}}{T_m^J}}$

apparent time constant were found to work well. Noise measurements indicated a device output noise temperature of about 50 K and SSB mixer noise temperature below 250 K. There are also a number of measurements done with a waveguide 100 GHz receiver [14,15] where a receiver noise temperature (DSB) has been measured to be ≤ 1000 K along with a 1 GHz bandwidth. Similar data have been obtained for quasioptical (double-dipole antenna on substrate lens) receiver at 350 GHz [11]. The receiver noise temperature (DSB) was around 3000 K whereas a mixer noise temperature could be as small as 400 K. For outdiffusion cooled mixer recent experiments [10] indicated a noise temperature as low as 600 K along with about 2 GHz bandwidth.

Experiments with NbN devices revealed a physical phenomenon preventing a good mixer performance at higher IF. At temperatures $T \ll T_c$ in the films longer than the thermal diffusion length the resistive state created by transport current is, usually, spatially non-uniform because of the normal domain formation. A significant fraction of the radiation power is absorbed in the normal metal parts of the film and then diffuses through the N-S boundaries in the film (domain edges), giving an indirect contribution to the bolometer response. The latter process slows down the relaxation process as whole which, moreover, can not be described by a single time constant [16]. As a result, the necessary LO power is determined by the smaller effective thermal conductivity for the slower process, similar to that given by Eq. 30. The fast process, responsible for mixing at higher IF, is thereby "underpumped". For instance, for a NbN HEB mixer made of ~ 20 nm thick film, when pumping was done with 300–350 GHz radiation, a uniform resistive state appeared only when $T = 7.5\text{--}8$ K whereas $T_c \sim 9$ K [16]. However, even in this case the thermal fluctuation noise dominated, giving about 400 K SSB contribution to the mixer noise temperature [11]. The output mixer noise temperature has been measured as a function of IF. It has been found that the corresponding time constant agrees well with that for conversion gain. The value of the output noise temperature due to thermal fluctuations also agrees with Eq. 27. The Johnson noise contributed as little as 40 K, hence the effective noise bandwidth of the device given by Eq. 13 could be 2–2.5 GHz ($\tau_{\theta} = 230$ ps). The influence of the domains can be hopefully reduced at higher radiation frequencies where the absorption of radiation is more uniform.

V. Novel HEB devices

HEB exploring outdiffusion cooling.

When the device length is made very short ($L \ll \sqrt{D \tau_{e-ph}}$) then the diffusion of hot electron into the contacts becomes more effective cooling mechanism than the electron-phonon interaction. This mechanism has been suggested for terahertz HEB mixer by Prober [18] to solve the problem of narrow band in Nb devices. Recent experiments [10] have demonstrated that as wide as 2 GHz bandwidth can be attained if the device length is made 0.2–0.3 μm . The efficiency of such cooling mechanism in nanoscale metal structures has been recently demonstrated in [26]. The crossover between the electron-phonon energy relaxation and the electron diffusion transport was experimentally observed in $\text{Au}_{60}\text{Pd}_{40}$ alloy wires at temperatures below 1.5 K.

It is likely that this type of distributed HEB can, nevertheless be considered as lumped to some extent. Since electron-electron inelastic time τ_{ee} for similar Nb films at 5 K is ~ 20 ps [27,28] the electron temperature relaxation length $l_{\theta} = \sqrt{D \tau_{ee}} = 40\text{--}70$ nm ($D = 1\text{--}3$ $\text{cm}^2 \text{ s}^{-1}$ [24,29]) is shorter than the sample length. This allows to describe such type of HEB to some extent in terms of electron temperature using the noise theory given above. Numerical modeling [30] shows that the relaxation of electron temperature can be well approximated by single time constant $\tau_{diff} \approx (L/4)^2/D$. Under such conditions the main contribution to the mixer noise temperature is given by Eq. 28 where $G = c_e V / \tau_{diff}$. However, because of the distributed heat link a modification of the thermal fluctuation noise has to be taken into account [23]. If thermal conductivity G relates to the highest temperature point (T_c), the noise temperature given by Eq. 28 should be multiplied by factor

$$\Gamma = \frac{\int_T^{T_c} \left[\frac{t\chi(t)}{T_c\chi(T_c)} \right]^2 dt}{\int_T^{T_c} \frac{\chi(t)}{\chi(T)} dt}, \quad (36)$$

where $\chi(T)$ is the thermal conductivity of the film. Considering that the thermal conductivity in the resistive state of the bolometer is close to that for normal metal ($\chi \propto T$). The Γ value can be obtained in the following form:

$$\Gamma = \frac{2}{3} \frac{T_c^3 - T^3}{T_c^2 - T^2}. \quad (37)$$

The largest reduction of noise $\Gamma = 2/3$ is achieved if $T \ll T_c$.

High- T_c mixer.

Thin films made of high- T_c superconductors are interesting for terahertz HEB mixer applications since they offer a very short electron-phonon relaxation time $\sim 10^{-12}$ s. For the first time this fact was emphasized in [31] and more thoroughly studied in a series of papers [32-34]. Recently the fast response of picosecond duration to optical and FIR laser pulses has been found in $\text{YBa}_2\text{Cu}_3\text{O}_{7-\delta}$ thin ($d < 100$ nm) films. The data both of kinetic inductance response and pure resistive response have been obtained [35-41]. The latter can be reasonably well described in terms of hot-electron phenomena in high- T_c film [41]. The most essential difference from the low temperature case is that the non-equality $c_e \gg c_p$ does not hold no longer if the working temperature is about 90 K. According to the literature data on YBaCuO phonon and electron heat capacities $c_p = (25-30)c_e$. In such case the heating of lattice is unavoided at low IF. To describe the situation more properly the heat balance equation (Eq. 1) has to be supplemented with a similar equation for the phonon temperature T_p , which now is different from bath temperature T . The characteristics of the high- T_c HEB can be obtained from the following equations:

$$c_e V \frac{\partial \theta}{\partial t} = -\Pi(\theta, T_p) + \mathbb{W} + \alpha P_{\text{rad}} \quad (38)$$

$$c_p V \frac{\partial T_p}{\partial t} = -\Psi(T_p, T) + \Pi(\theta, T_p) \quad (38a)$$

For the case when both functions Π and Ψ can be linearized, i.e. $\Pi(\theta, T_p) = c_e(\theta - T_p)/\tau_\theta$ and $\Psi(T_p, T) = c_p(T_p - T)/\tau_\infty$ the solution for the alternating part of electron temperature $\Delta\theta$ was given in [19]:

$$\Delta\theta = \alpha P_{\text{rad}} \frac{\tau_{e-ph} + (c_e/c_p)\tau_\infty}{c_e} \frac{1 + j\omega\tau_\phi}{(1 + j\omega\tau_1)(1 + j\omega\tau_2)}. \quad (39)$$

Three time constants in Eq. 38 can be found as follows:

$$\tau_{1,2}^{-1} = \tau_{+,-}^{-1} = \frac{1}{2\tau} \left[1 \pm \sqrt{1 - 4 \frac{\tau^2}{\tau_{es}\tau_{e-ph}}} \right], \tau^{-1} = \tau_{es}^{-1} + \tau_{e-ph}^{-1} (c_e/c_p + 1), \text{ and } \tau_\phi^{-1} = \tau_{es}^{-1} + \tau_{e-ph}^{-1} c_e/c_p. \quad (40)$$

Since for YBaCuO films τ_{e-ph} is quite short then as a rule $\tau_{es} \gg \tau_{e-ph}$ even for thin films. This condition together with the non-equality $c_p \gg c_e$ allows to simplify Eq. 38:

$$\Delta\theta = \alpha P_{rad} \frac{\tau_{e-ph} + (c_e/c_p)\tau_{es}}{c_e} \frac{1 + j\omega\tau_{e-ph}c_p/c_e}{(1 + j\omega\tau_{es})(1 + j\omega\tau_{e-ph})}. \quad (41)$$

Such frequency dependence has been recently demonstrated in optical mixing experiment ($\lambda = 1.55 \mu\text{m}$) performed up to IF = 18 GHz [17] (see Fig. 4). It is seen from the modelled curves that a decrease of the film thickness makes the frequency dependence more flat which is useful for reducing of the conversion loss at higher IF's.

A simple way to estimate the mixer noise temperature is the introduction of frequency dependent thermal conductivity:

$$G_\omega^{-1} = \frac{\tau_{e-ph} + (c_e/c_p)\tau_{es}}{c_e} \frac{1 + j\omega\tau_{e-ph}c_p/c_e}{(1 + j\omega\tau_{es})(1 + j\omega\tau_{e-ph})} \quad (42)$$

and its use at high IF's of interest ($\tau_{e-ph}^{-1} c_e/c_p \ll \omega < \tau_{e-ph}^{-1}$). Within this region ("second plateau") the thermal conductivity can be reduced to

$$G_2 = \frac{c_e^2 \tau_{es}}{(\tau_{e-ph} + c_e \tau_{es}/c_p) \tau_{e-ph} c_p}. \quad (43)$$

At the same time the self-heating parameter C is determined by the thermal conductivity taken at dc:

$$G_0 = \frac{c_e}{\tau_{e-ph} + (c_e/c_p)\tau_{es}}. \quad (44)$$

For example, for thin films used in [41] ($d = 60 \text{ nm}$) on MgO substrates $\tau_{es} = 2 \text{ ns}$, $\tau_{e-ph} = 1.5\text{-}2 \text{ ps}$ giving $G_0 \approx 40G_2$.

P_{DC} and P_{LO} can be estimated as

$$P_{LO} = \frac{g_e g_p}{g_e + g_p} (T_c - T) \quad \text{and} \quad P_{DC} = \frac{g_e g_p}{g_e + g_p} \frac{\Delta T_c}{2}, \quad (45)$$

where $g_e \equiv c_e/\tau_{e-ph}$, $g_p \equiv c_p/\tau_{es}$. With typical practically interesting parameters $T = 77 \text{ K}$, $T_c = 90 \text{ K}$ we obtain the "conversion gain at dc"

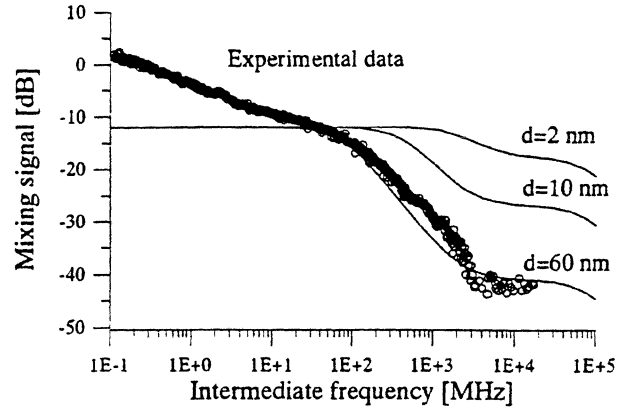


Fig. 4. Optical mixing data obtained with $YBa_2Cu_3O_{7-x}$ thin film [17] and fitting (solid lines) to two-temperature model with different film thickness'. The "excessive" signal below 50 MHz is because of the heat diffusion in the substrate.

$$\eta_{DC} = \frac{P_{LO}}{2P_{DC}} = \frac{T_c - T}{\Delta T_c} \approx 20 \quad (46)$$

and thermal fluctuation noise temperature

$$T_m^{FL} \approx \frac{2T_c^2}{T_c - T} \approx 800K. \quad (47)$$

To estimate the Johnson noise contribution one can use the conversion gain within "second plateau"

$$\eta_2 = \frac{T_c - T}{\Delta T_c} \frac{\tau_{e-ph} C_p}{\tau_{\infty} C_e} \approx 0.25 \quad (48)$$

and, finally, the noise temperature is given $T_m^J = T_c / \eta_2 = 360K$.

Conclusion

In conclusion, we have derived the analytic expressions describing an ideal hot-electron bolometer mixer performance. It has been shown that the noise temperature limit is determined by the thermal fluctuations and SSB noise temperature can as low as several T_c 's. An equivalent noise bandwidth can be theoretically very wide even for the devices made of material with a relatively long electron-phonon relaxation time. The bandwidth depends on the superconducting transition width (Johnson noise contribution) and also on the contribution of IF amplifier. Even for presently available Nb films the bandwidth set by the intrinsic noises is estimated to be about a few GHz. The present theory has passed a partial experimental verification and, hopefully, can be useful for description and prediction of the characteristics of various hot-electron mixers.

Acknowledgment

We thank E. Gershenzon and G. Gol'tsman for interest to this research, D. Prober and K.S. Yngvesson for stimulating discussions on the origin of HEB noises. BSK is grateful to E. Kollberg for the hospitality at Chalmers University of Technology and numerous discussions on the mixing mechanism in bolometric devices. The cooperation with H. Ekström was very fruitful and stimulated the formulating of many statements in this paper.

This research was made possible in part by Grant No. NAF000 from the International Science Foundation. We also acknowledge the support from Russian Council on High- T_c Problem under Grants No. 93169 and No. 94043.

References

- [1] G. de Lange, C.E. Honingh, J.J. Kuipers, H.H.A. Schaeffer, R.A. Panhuyzen, T.M. Klapwijk, H. van de Stadt, and M.M.W.M. de Graauw, "Heterodyne Mixing with Nb Tunnel Junctions Above the Gap Frequency," *Appl. Phys. Lett.*, vol. 64(22), pp. 3039-3041, 30 May 1994.
- [2] J. Zmuidzinas, H.G. LeDuc, J.A. Stern, and S.R. Cypher, *IEEE Trans. on Microwave Theory and Techniques*, vol. 42, p. 698, 1994.
- [3] P. Febvre, W.R. McGrath, P. Batelaan, B. Bumble, H.G. LeDuc, S. George, and P. Feautrier, "A Low-Noise Receiver Measured from 480 GHz to 650 GHz Using Nb Junctions with Integrated RF Tuning Circuits," *Int. J. IR and MM Waves*, vol. 15(6), pp. 943-965, June 1994.
- [4] K.-F. Schuster, A.I. Harris, and K.H. Gundlach, "A 691 GHz Receiver for Radio Astronomy," *Int. J. IR and MM Waves*, vol. 14(10), pp. 1867-1887, October 1993.
- [5] H. Rothermel, K.H. Gundlach, and M. Voss, "A 350 to 700 GHz Open Structure SIS Receiver for SubMM. Radioastronomy," *Colloque C6 Supplement au J. de Physique III*, vol. 4, pp. 267- 272, June 1994.
- [6] J.W. Kooi, C.K. Walker, H.G. LeDuc, P.L. Schaffer, T.R. Hunter, D.J. Benford, and T.G. Phyllips, "A Low Noise 665 GHz SIS Quasi-Particle Waveguide Receiver," *IEEE Trans. on Microwave Theory and Techniques*, vol. 42, p. 750, 1994.
- [7] J. Zmuidzinas, N.G. Ugras, D. Miller, M. Gaidis, H.G. LeDuc, and J.A. Stern, "Low-Noise Slot Antenna SIS Mixers," *IEEE Trans. on Appl. Supercond.*, in press.
- [8] E.M. Gershenzon, G.N. Gol'tsman, I.G. Gogidze, Y.P. Gusev, A.I. Elant'ev, B.S. Karasik, and A.D. Semenov, "Millimeter and submillimeter range mixer based on electronic heating of superconducting films in the resistive state," *Sverhprovodimost' (KIAE)*, vol. 3(10), pp. 2143-2160, October 1990 [*Sov. Phys. Superconductivity*, vol. 3(10), pp. 1582-1597, 1990].
- [9] H. Ekström, B.S. Karasik, E. Kollberg, and K.S. Yngvesson, "Investigation of a superconducting hot electron mixer," Proc. of the Fifth Int. Symp. on Space Terahertz Technology (May 10-12, 1994, Ann Arbor, Michigan), pp. 169-188; "Conversion gain and noise of niobium superconducting hot-electron-mixers," *IEEE Trans. on Microwave Theory and Techniques*, in press.
- [10] A. Skalare, W.R. McGrath, B. Bumble, H.G. LeDuc, P.J. Burke, A.A. Verheijen, and D.E. Prober, "A heterodyne receiver at 533 GHz using a diffusion-cooled superconducting hot electron bolometer mixer," *IEEE Trans. on Appl. Supercond.*, in press.

- [11] H. Ekström and B. Karasik, "Electron temperature fluctuation noise in hot-electron superconducting mixer," *Appl. Phys. Lett.*, in press; H. Ekström, B. Karasik, E. Kollberg, G. Gol'tsman, and E. Gershenzon, "350 GHz NbN hot electron bolometer mixer," *this issue*.
- [12] F. Arams, C. Allen, B. Peyton, and E. Sard, "Millimeter mixing and detection in bulk InSb," *Proc. IEEE*, vol. 54, pp. 308-318, 1966.
- [13] A. Dzardanov, H. Ekström, E. Gershenzon, G. Gol'tsman, S. Jacobsson, B. Karasik, E. Kollberg, O. Okunev, B. Voronov, and S. Yngvesson, "Hot-electron superconducting mixers for 20–500 GHz operation," *Proc. SPIE*, vol. 2250, pp. 236-238, 1994.
- [14] O. Okunev, A. Dzardanov, H. Ekström, S. Jacobsson, E. Kollberg, G. Gol'tsman, and E. Gershenzon, "NbN hot electron waveguide mixer for 100 GHz operation," *Proc. of the 5th Int. Symp. on Space Terahertz Technology* (May 10–12, 1994, Ann Arbor, Michigan), pp. 214-224.
- [15] G.N. Gol'tsman, B.S. Karasik, O.V. Okunev, A.L. Dzardanov, E.M. Gershenzon, H. Ekström, S. Jacobsson, and E. Kollberg, "NbN hot electron superconducting mixers for 100 GHz operation," *IEEE Trans. on Appl. Supercond.*, in press.
- [16] B.S. Karasik, G.N. Gol'tsman, B.M. Voronov, S.I. Svechnikov, E.M. Gershenzon, H. Ekström, S. Jacobsson, E. Kollberg, and K.S. Yngvesson, "Hot electron quasioptical NbN superconducting mixer," *IEEE Trans. on Appl. Supercond.*, in press.
- [17] M. Lindgren, M.A. Zorin, A.V. Trifonov, M. Danerud, D. Winkler, B.S. Karasik, G.N. Gol'tsman, and E.M. Gershenzon, "Optical mixing in a patterned $\text{YBa}_2\text{Cu}_3\text{O}_{7-x}$ film," *Appl. Phys. Lett.*, vol. 65(26), pp. 3398-3400, 26 December 1994.
- [18] D.E. Prober, "Superconducting terahertz mixer using a transition-edge microbolometer," *Appl. Phys. Lett.* vol. 62(17), pp. 2119-2121, 26 April 1993.
- [19] N. Perrin and C. Vanneste, "Response of superconducting films to a periodic optical irradiation," *Phys. Rev.* vol. B28, pp. 5150-5159, 1 November 1983.
- [20] E.M. Gershenzon, G.N. Gol'tsman, A.I. Elant'ev, B.S. Karasik, and S.E. Potoskuev, "Intense electromagnetic radiation heating of electrons in the resistive state," *Fiz. Nizk. Temp.* vol. 14(7), pp. 753-763, July 1988 [*Sov. J. Low. Temp. Phys.*, vol. 14(7), pp. 414-420, 1988].
- [21] A.I. Elant'ev and B.S. Karasik, "Effect of high frequency current on Nb superconducting film in the resistive state," *Fiz. Nizk. Temp.*, vol. 15(7), pp. 675-683, July 1988 [*Sov. J. Low Temp. Phys.*, vol. 14(7), pp. 379-383, July 1988].
- [22] J.C. Mather, "Electrical self-calibration of nonideal bolometer," *Appl. Opt.* vol. 23(18), pp. 3181-3183, 15 September 1982.
- [23] J.C. Mather, "Bolometer noise: nonequilibrium theory," *Appl. Opt.* vol. 21(6), pp. 1125-1129, 15 March 1982.
- [24] E.M. Gershenzon, M.E. Gershenzon, G.N. Gol'tsman, A.M. Lyul'kin, A.D. Semenov, and A.V. Sergeev, "Electron-phonon interaction in ultrathin Nb films," *Zh. Eksp. Teor. Fiz.*, vol. 97, pp. 901, 1990 [*Sov. Phys. JETP*, vol. 70, pp. 505-511, March 1990].

- [25] Yu.P. Gousev, G.N. Gol'tsman, A.D. Semenov, E.M. Gershenson, R.S. Nebosis, M.A. Heusinger, and K.F. Renk, "Broadband ultrafast superconducting NbN detector for electromagnetic radiation," *J. Appl. Phys.*, vol. 75, pp. 3695-3697, April 1994.
- [26] M. Kanskar and M.N. Wybourne, "Crossover between dissipative and nondissipative electron transport in metal wires," *Phys. Rev. Lett.*, vol. 73(15), pp. 2123-2126, 10 October 1994.
- [27] B.J. Dalrymple, S.A. Wolf, A.C. Enrlich, and D.J. Gillespie, "Inelastic electron lifetime in niobium films," *Phys. Rev.*, vol. B33(11), pp. 7514-7519, 1 June 1986.
- [28] M.E. Gershenson, V.N. Gubankov, and Yu.E. Zhuravlev, "Quantum effects in two-dimensional films of superconductors at $T > T_c$," *Zh. Exp. Teor. Fiz.*, vol. 85(1), pp. 287-298, July 1983.
- [29] J.W.P. Hsu and A. Kapitulnik, "Superconducting transition, fluctuation, and vortex motion in two-dimensional single-crystal Nb film," *Phys. Rev.*, vol. B45(9), pp. 4819-4835, March 1992.
- [30] D. Prober, private communication.
- [31] E.M. Gershenson, M.E. Gershenson, G.N. Gol'tsman, B.S. Karasik, A.D. Semenov, A.V. Sergeev, "Light-induced heating of electrons and the time of the inelastic electron-phonon scattering in the YBaCuO compound," *JETP Lett.*, vol. 46(7), pp. 226-228, 1987.
- [32] E.M. Gershenson, G.N. Gol'tsman, I.G. Goghidze, A.D. Semenov, and A.V. Sergeev, "Processes of electron-phonon interaction in thin YBaCuO films," *Physica C*, vol. 185-189, pp. 1371-1372, 1991.
- [33] A.D. Semenov, G.N. Gol'tsman, I.G. Goghidze, A.V. Sergeev, E.M. Gershenson, P.T. Lang, and K.F. Renk, "Subnanosecond photoresponse of a YBaCuO thin film to infrared and visible radiation by quasiparticle induced suppression of superconductivity," *Appl. Phys. Lett.*, vol. 60(7), pp. 903-906, 1992.
- [34] E.M. Gershenson, G.N. Gol'tsman, A.D. Semenov, and A.V. Sergeev, "Mechanism of picosecond response of granular YBaCuO films to electromagnetic radiation," *Solid State Commun.*, vol. 76(4), pp. 493-496, 1990.
- [35] M. Johnson, "Nonbolometric photoresponse of YBCO film," *Appl. Phys. Lett.*, vol. 59(11), pp. 1371-1373, 1991.
- [36] L. Shi, G.L. Huang, C. Lehane, J.P. Zheng, and H.S. Kwok, "Temporal relaxation measurements of photoinduced nonequilibrium in superconductor," *Appl. Phys. Lett.*, vol. 61(4), pp. 489-491, 1992.
- [37] N. Bluzer, "Temporal relaxation of nonequilibrium in Y-Ba-Cu-O measured from transient photoimpedance response," *Phys. Rev.*, vol. B44(18), pp. 10222-10233, 1991.
- [38] F.A. Hegmann, J.S. Preston, "Origin of the fast photoresponse of epitaxial $\text{YBa}_2\text{Cu}_3\text{O}_{7-x}$ thin films," *Phys. Rev.*, vol. B48(21), pp. 16023-16039, 1993.
- [39] F.A. Hegmann, R.A. Hughes, J.S. Preston, "Picosecond photoresponse of epitaxial $\text{YBa}_2\text{Cu}_3\text{O}_{7-x}$ thin films," *Appl. Phys. Lett.*, vol. 64(23), pp. 3172-3174, 1994.
- [40] A. Ghis, S. Pfister, J.C. Villegier, M. Nail, and J.P. Maneval, "Ultra fast non bolometric photoresponse of $\text{YBa}_2\text{Cu}_3\text{O}_{7-x}$ thin films," *IEEE Trans. Appl. Superconductivity*, vol. 3(1), pp. 2136-2139, 1993.
- [41] M. Lindgren, V. Trifonov, M. Zorin, M. Danerud, D. Winkler, B.S. Karasik, G.N. Gol'tsman, and E.M. Gershenson, "Transient resistive photoresponse of $\text{YBa}_2\text{Cu}_3\text{O}_{7-x}$ films using low power 0.8 and 10.6 μm laser radiation," *Appl. Phys. Lett.*, vol. 64(22), pp. 3036-3038, 30 May 1994.

Performances of Hot-Electron Superconducting Mixer for Frequencies Less than the Gap Energy: NbN Mixer for 100 GHz Operation

O. Okunev, A. Dzardranov, G. Gol'tsman, and E. Gershenzon
Moscow State Pedagogical University, 119435 Moscow, Russia

Abstract

The possibilities to improve the parameters of the 100 GHz NbN HEB superconducting waveguide mixers have been studied. The device consists of a signal strip 1 μm wide by 2 μm long made of 40 \AA thick NbN film. The best operation point was found at 5 K, where the mixer bandwidth made up 1.5-2 GHz and the total loss diminished down to 8 dB. The critical current density has been increased up to $\sim 10^6$ A/cm², the noise temperature of the receiver (DSB) has reduced down to 450 K and the local oscillator power has decreased down to ~ 0.1 μW .

1 Introduction

Hot electron bolometric (HEB) mixers based on thin superconducting films have been given intensive consideration recently [1-5]. The purpose of such studies is to significantly reduce the noise temperature of the Terahertz waverange mixers. Since no visible results of these studies in the waverange higher than 1 THz have been achieved so far (which is due to considerable technical difficulties), it is essential that experimental studies aimed at defining the maximum achievable parameters of such mixers under lower frequencies be continued.

In [2] we reported the results of a study into HEB superconducting mixers based on thin NbN films in the 100 GHz waverange. The following characteristics were obtained: the noise temperature of the receiver $T_n \approx 1000$ K, the intermediate frequency band $\Delta f_{IF} \approx 0.6$ GHz, the optimal local oscillator power $P_{LO} \approx 1$ μW , the total conversion loss ~ 10 dB. For a typical mixer chip, the latter value included a 2 dB loss in the transmitting waveguide, a 5 dB loss in the mixer block and a 3 dB loss in the mixer itself. Meanwhile, the theoretically calculated parameters for coupling factor $\alpha=1$ for typical properties of NbN thin films currently used for fabrication of HEB mixers are as follows: the conversion gain +8 dB, $T_n \approx 70$ K, $\Delta f_{IF} \approx 5$ GHz. Although the calculated and the experimentally achieved characteristics differ quite significantly, one cannot pinpoint any one main factor which would account for these differences. Their analysis [2] helped define several possible ways to improve the characteristics.

One of the ways is connected with using quartz substrates being the most convenient for the commonly used mixer block design. The fact is that the thermal boundary resistance between the NbN film and the quartz substrate is greater and the quality of the NbN film is worse than those of sapphire or silicon. The former leads to a decrease

in the intermediate frequency range, since a limited heat flow into the substrate for the films used gives an approximate equality of the time of phonon escape into the substrate $\tau_{e,s}$ and the time of electron-phonon interaction τ_{eph} at 4.2 K. The latter decreases the critical current density and consequently the bias current and the optimal local oscillator power, which does not allow to increase significantly the electron temperature above the lattice temperature and limits not only the IF bandwidth, but also the internal conversion gain. The greatest influence upon the loss is, however, exerted by the coupling factor. It is difficult to match an HEB mixer under the frequencies $f < 2\Delta/h$ (where 2Δ is the energy gap) because it is impossible to calculate the superconductor film impedance in the resistive state under the nonequilibrium conditions with significant P_{LO} and bias current density. It seems that the only feasible way for these frequencies is to experimentally select the film geometry in order to achieve the best matching of the mixer block.

In the present work, we have made progress in all the directions mentioned.

2 Experimental

2.1 Design of Mixers and the Experimental Installation

The studied mixer structures were manufactured from thin NbN films made by reactive magnetron sputtering of Nb target in an argon-nitrogen mixture onto polished crystalline quartz substrates. The film quality is primarily defined by the gas pressure and the temperature of the substrate. The film thickness was checked by a profilometer-profilograph with a $\pm 10 \text{ \AA}$ precision. A scanning electron microscope with a 100 \AA resolution was used to make sure that there are no granules or heterogeneities. The mixers were produced as single NbN film strips. The contact pads and microwave filters were produced on the same substrate by photolithography. The mixer configuration and the design of the mixer block are shown in Fig. 1. The element produced was fastened in the centre of the 100 GHz waveguide. The film plane coincided with the E-plane of the waveguide. One contact pad was grounded in a mixer block. The IF signal through the microwave filter was removed from the mixer using a coaxial cable, which was also used to supply the constant bias current.

The parameters of the mixers were studied in the 100 GHz waverange using a setup whose block diagram is shown in Fig. 2. The working temperature of the mixer block could be varied between 4.2 K and 9 K. The RF power loss in the waveguide between the cryostat input and the input of the mixer block did not depend on the frequency in the 80–120 GHz range and amounted to 2 dB. A backward wave oscillator (BWO) was used as local oscillator. A discharge tube with noise temperature of 6000 K was used as a signal source. The local oscillator power and the radiation of the signal were combined into one channel using a directional coupler. The local oscillator power, previously measured with a thermistor, was varied by calibrated attenuators. A DC bias supply with an internal resistance of 50 Ohm produced a bias current through the sample.

While measuring the bandwidth of the mixers, a wideband amplifier with an am-

plifying range of 1-2000 MHz was included into the IF circuit. The IF signal amplitude after it was amplified by 50 dB was measured by a spectrum analyser. The noise temperature T_N of the device was measured in a waverange of 1.3-1.7 GHz using a low-noise amplifier. The amplifier and the isolator were placed near the mixer block with the same working temperature.

The setup allowed to measure the IV-curves using the 2-point scheme, the value and the IF-frequency dependence of the conversion gain, as well as the noise temperature of the mixers under working temperatures from 4.2 K to 9 K.

2.2 Results

Fig. 3 and Fig. 4 respectively show the IV-curves of the mixers No 1 and No 2 under LO power. HEB mixer No 1 was made of a NbN film of higher quality than those described in paper [2]. With the same film thickness of 50 Å the critical current and the bias current in the optimal working point are practically identical with the respective currents of multistrip mixer elements mentioned in [2], since the critical current density of the superconducting strip was now greater almost by an order of magnitude and amounted to $5 \cdot 10^6$ A/cm². The superconducting transition temperature is higher than 11 K, and the temperature transition width is lower than 0.3 K. The film of the HEB mixer No 2 is still thinner: ~ 40 Å. Despite the decrease of the critical current density ($\sim 10^6$ A/cm²), the IV-curve still has, in the absence of microwave radiation power, an N-shape with a peculiar nonstable interval. The series resistance between the film and the contact pads is reduced and is now less than 2 Ohm.

Under LO power the resistance of mixer strips increases and the IV-curves shift to the area of weaker currents and higher voltages. The IV-curve of mixer chip No 1 loses its N-shape under the power radiation higher than -25 dBm. The local oscillator power, optimal for the conversion gain, amounts to -29 dBm. At the same time the optimal bias working point is located near the current unstability on the IV-curve. The differential resistance R_d in the operating point for mixer chip No 1 is equal to 95 Ohm. The optimal local oscillator power for mixer chip No 2 is equal to -39 dBm. The IV-curve of this mixer chip loses its breaking character under a power higher than -45 dBm. Thus, the optimal local oscillator power is located on the IV-curve without a negative differential resistance.

The conversion gain measurements in the IF waverange from 1 MHz to 2 GHz have shown a decrease of no more than 3-5 dB for both mixer chips. Thus, the frequency range of the mixers under study is 1.5-2 GHz. The conversion loss of the mixer No 1 in the optimal point in respect to local oscillator power and to bias current is 10 dB, and that of the mixer No 2 is 8 dB. The noise temperature of the receiver with the mixer No 2 at an intermediate frequency of 1.7 GHz was equal to 450 K.

The mixer impedance at an intermediate frequency is approximately equal to the differential resistance of the mixer chip. The IF loss of the mixer No 1 associated with this fact is about 1 dB. The remaining losses are distributed among the coupling factor and the internal conversion loss. If one assumes that the strip resistance in the working area of P_{LO} and the bias current is a function of the electron temperature only, the

coupling factor can be calculated as follows:

$$L = \frac{P_{R_a} - P_{R_b}}{P_{DC_b} - P_{DC_a}}$$

where P_{R_a} and P_{R_b} are the microwave powers in the input of the waveguide located in front of the mixer block, P_{DC_a} and P_{DC_b} are Joule powers of the bias current in the points a and b of IV-curves under P_{R_a} and P_{R_b} , corresponding to the same resistance in the DC current. For mixer No 1 the coupling factor values thus received varied from 9 dB at the optimal working point to 7 dB for the increased mixer resistance. Although the above calculation does not take into account the pair-breaking action of the bias current and the microwave power, the estimations obtained in this way show the dominating influence of the coupling factor. A similar estimation in the input of mixer No 2 shows that the losses vary from 10 dB in the optimal point to 7 dB when operating in the area of high resistances of the mixer chips. The conversion loss and the noise temperature mentioned above are obtained under the mixer block temperature of 5 K. As the working temperature approaches the temperature of the superconducting transition, the mixer parameters become worse.

3 Discussion

The unpumped IV-curve of the mixer No 1 can be divided into 4 sections. In the low voltage region the strip is in superconducting state and the resistance observed arises due to the contact pads. The second part of the curve is a region of current instability. Then the curve remains relatively horizontal until the strip enters its normal state. The horizontal fragment of the IV-curve for a homogeneous film under temperature well below T_c takes place due to the formation of a resistive domain region.

As the voltage sinks, the normal section size reduces. When the domain size reaches the thermal length level, its edges draw together, and the film becomes entirely superconducting. The 100 GHz microwave radiation is mostly absorbed by the normal region. The electron heating as a result of P_{LO} and signal radiation causes an intermediate frequency response by shifting the domain edges. The maximal conversion gain is achieved close to the rupture point, where the length of the strip part in normal conducting state reaches its minimum. There the mixer impedance is low, thus increasing the coupling factor. One could expect to reduce it rising the working temperature. This provided, the energy gap narrows while the P_{LO} absorption in the superconducting areas intensifies. Besides, the bias current value at the optimal point and the critical current density diminish. If under higher temperature the latter becomes stronger than the current of depinning vortices in the superconducting regions, the mixer strip in the whole turns into resistive state which takes place because of the viscous flux flow (i.e. more spatially homogeneous). This case must be better described by the hot electron theory. Moreover, it is more convenient to achieve a better matching, since the pumped IV-curves are smooth and the optimal bias region is considerably wide.

The HEB superconducting mixer theory, however, assumes a sharp deterioration of the mixer parameters as the temperature approaches T_c [1]. Whether the situation described above holds already under temperatures not so close to T_c , where the internal conversion loss increases only a little, or this is not the case until very close to T_c , depends on the $hf / 2\Delta$ ratio. The latter must be the case under lower frequencies, i.e. when holds $hf / 2\Delta \ll 1$. Whether the 100 GHz frequency is high enough, can only be found out experimentally, while the appropriate calculation is too complex. The current experiment proves, indeed, that under temperature near 5 K the conversion loss and the noise temperature reach their minimum values.

In order to diminish the coupling factor, a single strip proved useful as the mixer form. Although the resistance in normal state is high and amounts to 1.1 kOhm and 3 kOhm for the mixers No 1 and No 2 correspondingly, their impedance under 100 GHz at the optimal working point (see above) is though significantly lower, but it still seems better matching in the mixer block than the multistrip mixers used in the previous work [2]. Those mixers could be probably more suitable for higher frequencies.

Finally, a reduction of the NbN film thickness together with a certain increase of the working temperature helped expand the IF band up to 1.5-2 GHz.

Acknowledgment

This research was made possible in part by Grant No. NAFOOO from the International Science Foundation. We also acknowledge the support from Russian Council on High-Tc Problem under Grant No. 93169.

References

- [1] E.Gershenson, G.Gol'tsman, I.Gogidze, Y.Gusev, A.Elant'ev, B.Karasik, and A.Semenov, "Millimeter and submillimeter range mixer based on electronic heating of superconducting films in the resistive state", *Sov. Phys. Superconductivity*, vol.3, pp.1582-1597, October 1990.
- [2] O.Okunev, A.Dzardanov, H.Ekstrom, S.Jacobsson, E.Kollberg, G.Gol'tsman, and E.Gershenson, *Proc. of the 5th Int. Symp. on Space Terahertz Technology*, pp.214-224, May 10-12, 1994.
- [3] G.Gol'tsman, S.Jacobsson, H.Ekstrom, B.Karasik, E.Kollberg, and E.Gershenson, *Proc. of the 5th Int. Symp. on Space Terahertz Technology*, pp.209-213a, May 10-12, 1994.
- [4] A.Dzardanov, H.Ekstrom, E.Gershenson, G.Gol'tsman, S.Jacobsson, B.Karasik, E.Kollberg, O.Okunev, B.Voronov, and S.Yngvesson, *Proc. SPIE*, vol.2250, pp.276-278, January 1994.
- [5] A.Scalare, W.R.McGrath, B.Bumble, H.G.LeDuc, P.J.Burke, A.A.Verheijen, and D.E.Prober, *Proc. of the 5th Int. Symp. on Space Terahertz Technology*, pp.157-168, May 10-12, 1994.

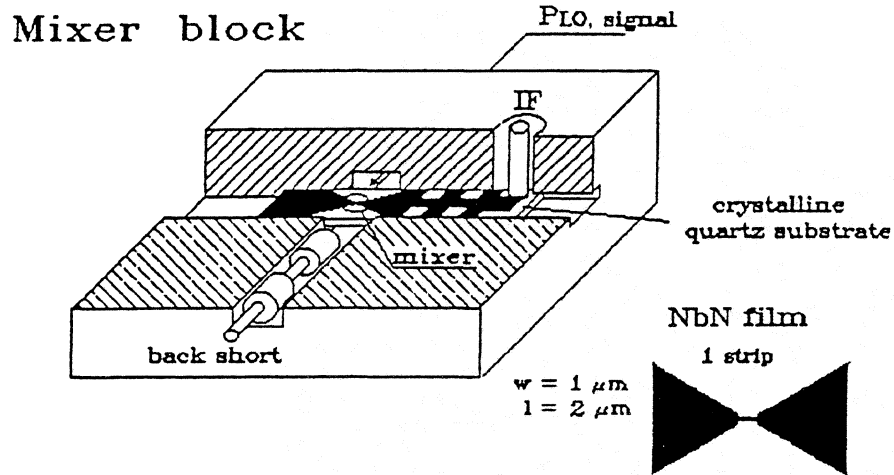


Fig.1. Design of the mixer block and configuration of mixer chip.

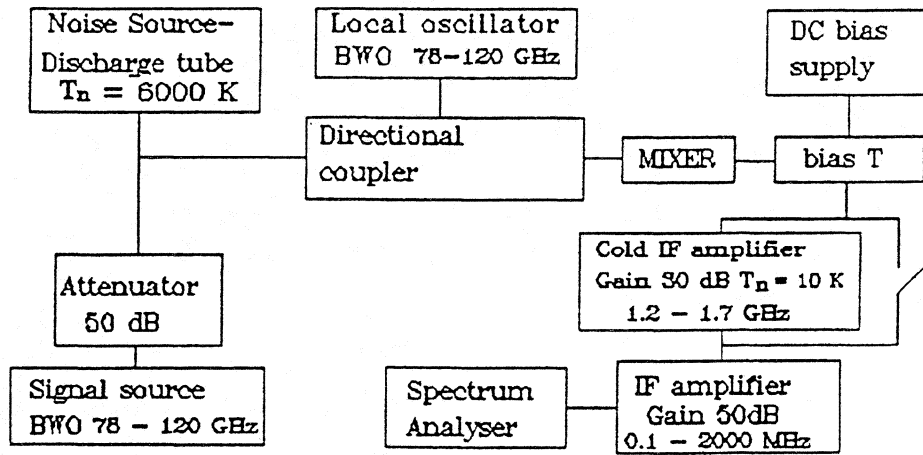


Fig. 2. Experimental set up.

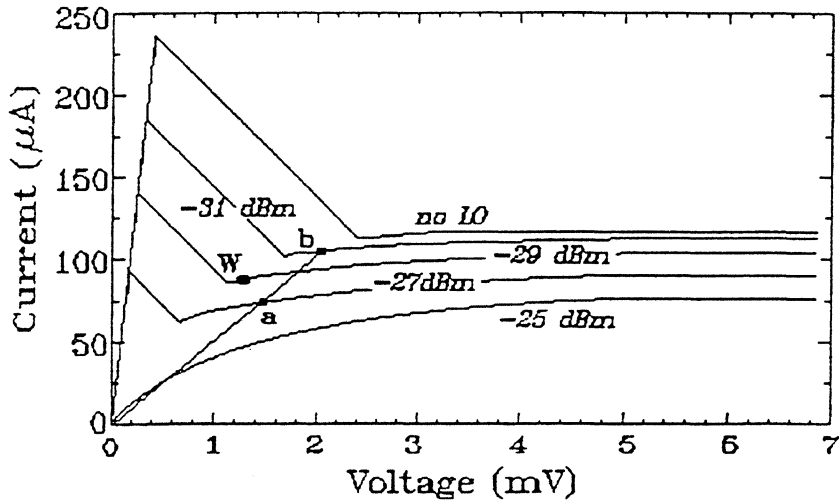


Fig. 3. I-V curves under LO power for sample No. 1.
W - is the optimal bias working point.

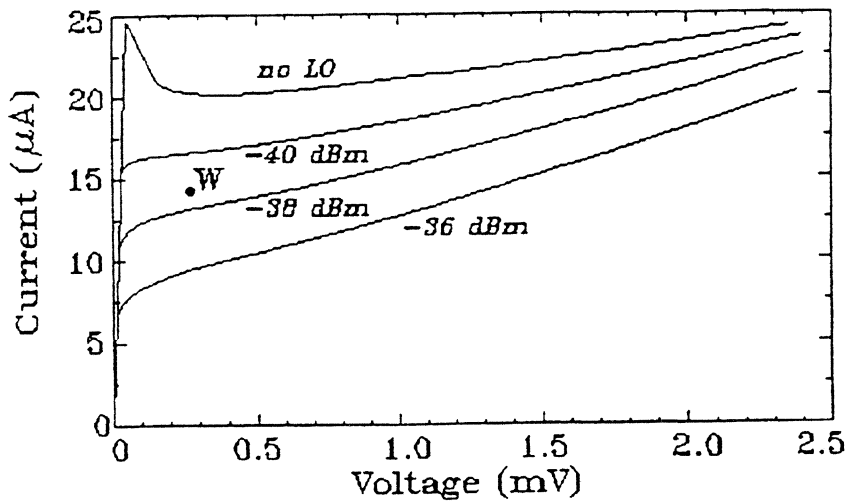


Fig. 4. I-V curves under LO power for sample No. 2.
W - is the optimal bias working point.

NbN Hot-electron Mixer Measurements at 200 GHz

J. Kawamura, R. Blundell, C.-Y. E. Tong
Harvard-Smithsonian Center for Astrophysics
Cambridge, MA 02138

G. Gol'tsman, E. Gershenson, B. Voronov
Moscow State Pedagogical University
Moscow, 119435, Russia

Abstract.

We present noise and gain measurements of resistively driven NbN hot-electron mixers near 200 GHz. The device geometry is chosen so that the dominant cooling process of the hot-electrons is their interaction with the lattice. Except for a single batch, the intermediate frequency cut-off of these mixer elements is ~ 700 MHz, and has shown little variation among other batches of devices. At 100 MHz we measured intrinsic mixer losses as low as -3 dB. We measured the noise temperatures at several intermediate frequencies, and for the best device at 137 MHz with 20 MHz bandwidth, we measured 2000 K; using a low-noise first-stage amplifier at 1.5 GHz with 200 MHz bandwidth, the receiver noise temperature measured 2800 K. We estimate that the noise contribution from the mixer is 500 K and the total losses are -15 dB at 137 MHz.

1. Introduction.

Heterodyne receivers based on the hot-electron mixing mechanism in bulk-semiconductor indium antimonide, InSb, have operated to about 500 GHz, with sensitivity comparable to that of SIS receiver systems[1,2]. However, the instantaneous bandwidth of InSb-based mixers is limited to less than 10 MHz, which limits their practical usefulness. More recently, two-dimensional heterojunction structures with short electron relaxation times have been developed for heterodyne mixing, and GaAlAs structures have been used to demonstrate mixing at 94 GHz with an instantaneous bandwidth of over 1 GHz [3]. Two other candidates for low-noise mixers based on the hot-electron effect utilize superconducting thin films operated in the resistive state. One type chooses a device geometry in which the cooling of hot electrons is dominated by diffusion [4], and recent experiments at submillimeter wavelengths have indicated good noise performance and wide instantaneous bandwidth of about 3 GHz [5]. The other method employs the coupling between the lattice and electrons as the cooling mechanism [6], and the bulk of recent results have come from experiments with Nb devices [7]. Our present work focuses on devices relying on the shorter electron-phonon relaxation time of NbN, for which an instantaneous bandwidth of several GHz is predicted [8]. We report on our initial measurements of NbN hot-electron waveguide mixers at an input frequency of 200 GHz.

2. Experimental Setup.

The mixer elements used in our study consist of ~ 50 angstrom thin-film NbN strips about one micron wide and four microns long, with as many as 50 strips in parallel. The detail in figure (1) illustrates the devices. With these dimensions the dominant cooling process of the heated electrons is believed to be their interaction with the lattice. The devices are fabricated on crystalline quartz using standard reactive sputtering and optical lithography. TiAu pads are evaporated and etched to form low-pass RF block filters, and also serve as electrodes through which DC bias is applied. The substrate is mounted in a reduced-height waveguide mixer block with a single backshort tuner, also illustrated in figure (1). Figure (2) shows a schematic of the mixer block, which is mounted in a helium-cooled laboratory cryostat. The radiation is coupled through a lens-horn combination and the local-oscillator is coupled to the signal outside the cryostat using a wire-grid polarizer.

For gain or impedance measurements the IF is brought directly outside the cryostat using a stainless-steel coax, whereas for receiver noise temperature measurements a first-stage cryogenic low-noise amplifier follows the mixer. In receiver noise measurements, the LO is a frequency-multiplied Gunn oscillator. For gain measurements, a signal is provided by either another frequency-multiplied Gunn oscillator or a harmonic generator driven by a microwave frequency synthesizer. The RF coupling losses were determined using the "isotherm" technique [7]. Receiver noise measurements are made using the standard hot/cold load Y-factor technique.

3. Results.

Figure (3) shows the current-voltage (IV) characteristics typical of a mixer element cooled to above 4.2 K, traced using a voltage source. Three distinct regions are identifiable as the voltage bias is changed: at low bias, below the critical current, the device is superconducting and the series resistance is traced; at an intermediate bias, the device exhibits a "resistive" state; at high bias level, beyond that is traced by the curve in the figure, the device is driven normal. It is in the intermediate region where the device is biased for efficient mixing. The figure also shows a current-voltage curve for the mixer element pumped with 200 GHz radiation. As the device is pumped with higher power, the device is driven normal at all bias levels.

The devices used in our study have room temperature resistances of a few $k\Omega$ per strip, and a contact, or series, resistance from about 3Ω to 50Ω . The quality of the superconducting film varied greatly among the batches, and it has been possible to characterize only some of

the devices because of the limit on available LO power. The amount of LO power required to pump the devices we have studied is about $\sim 1 \mu\text{W}$.

a) IF conversion gain, bandwidth and impedance.

The conversion loss of a mixer is defined as the ratio of the input signal power to that measured at the IF output. Furthermore, conversion losses can be separated into antenna coupling loss, and other losses which usually include the intrinsic loss of the down-conversion process and the IF impedance mismatch. At microwave wavelengths the power levels of the signal and IF are easily measured using standard techniques. At higher frequencies, an indirect technique is used to separate the losses. The signal power coupled to the device is calculated from the amount of heating it produces in the film, relying on the assumption that radiation and DC have the same heating effect on the device. To measure the IF gain curve, the signal is set at a particular frequency and power, and the LO is adjusted in frequency, and in power to reach the operating point.

In figure (4) the conversion loss as a function of IF for a signal frequency of 200 GHz is shown. Also shown is a gain curve measured at 20 GHz, shifted vertically for presentation. The similarity between the microwave and millimeter-wave measurements suggests that microwave measurements, which can be performed using simple apparatus, can be used to preselect good devices for measurements at higher frequencies.

Except for one batch, there is typically very little variation in the roll-off of the gain within and among batches of devices we have fabricated. In our samples of devices, the conversion rolls off in the range 500 to 800 MHz, and the best conversion gain is estimated to be -3 dB. In some batches, there is a rise in the response at very low IF's, indicating bolometric heating of the mixer element, and this is explained by the film being too thick. As shown in figure (5), if the bias or the device temperature is increased, there is a somewhat slight increase in the bandwidth, however, the mixer conversion is poorer. It is not clear whether the bandwidth improvement can be entirely attributed to an actual change in the response time of the detector, or is merely the result of the change in the mixer IF output impedance. Figure (6) shows bandwidth measurements of a mixer element that shows 3 dB conversion roll-off at 2 GHz, measured at a signal frequency of 20 GHz. However, the bandwidth measurements could not be repeated at 200 GHz because the sample was destroyed. An inspection of the mixer elements under an optical microscope revealed that the mask alignment was better for device 1 than for device 2 [referring to figure (6)].

Figure (7) shows the measured IF output impedance for the mixer elements. The impedance of the mixer at its nominal operating point changes smoothly with frequency. At very low IF's (kHz) the impedance is real, and is equal to the differential resistance on the IV curve. At higher frequencies, the device becomes capacitive. At the highest IF (> 5 GHz), the impedance tends towards the series resistance of the mixer element. In figure (7) the IF return loss is also shown for various operating points: nominal operation is ~ 4.2 K and at the lowest stable bias point. Figure (8) shows the IF return loss of the mixer operated at various temperatures.

b) Noise temperature measurement.

The ultimate figure of merit for an astronomical receiver system is its sensitivity. In order to estimate the sensitivity of the mixer, we performed noise temperature measurements at 200 GHz using the standard hot and cold load method. We have measured the receiver noise temperatures at several IF's. The lowest IF band was at 137 MHz, well below the roll-off in the gain of these devices, and the bandwidth was 20 MHz. Here, the best receiver noise temperature was 2000 K. Using a lower noise amplifier at 1.5 GHz, with 200 MHz bandwidth, the receiver noise temperature measured 2800 K. In all these measurements, we ensured that the operating point remained stationary to better than to 0.2% of the current, which was the best we could monitor. Knowing the noise of the amplifiers and the relative conversion losses allowed us to estimate the mixer noise and total losses. The mixer noise is estimated to be ~ 500 K and the total losses to be -15 dB at 137 MHz and -24 dB at 1.5 GHz.

c) Subharmonic mixing.

It is generally assumed that subharmonic mixing is not possible or is an insignificant component in the hot-electron mixing mechanism. It is thought that the device looks linearly resistive at high frequencies, above the instantaneous bandwidth of the mixer. With this in mind, we have tried to measure subharmonic mixing. At microwave frequencies, with an signal frequency of 20 GHz, LO pump frequency of 10.5 GHz, an IF signal appeared, weaker by ~ 6 dB than that obtained by fundamental mixing. With this intriguing result, we tried to and have observed subharmonic mixing at a signal frequency of 460 GHz, subharmonically pumped at about 230 GHz. The LO frequency was varied to measure the mixer gain curve, and the IF response was flat to within 1 dB from 1 MHz to 1.5 GHz. At this point, we are not able to calculate the conversion losses, as we were not able to pump the device at 460 GHz. While

this appears to be an intriguing result, we do not rule out that our result is an artifact of our experimental setup.

4) Summary.

We have performed preliminary mixing experiments using the hot-electron effect in NbN at 200 GHz. We have observed that the mixing mechanism is very efficient, estimated for most devices to be better than -6 dB. The instantaneous bandwidth of these devices is typically 700 MHz, although we have seen a mixer element with a bandwidth of 2 GHz. In our setup, the devices are rather poorly matched; a better match would certainly improve our receiver noise temperature measurements. Our measurements indicate a mixer-noise contribution of 500 K, which is fifty times worse than an SIS mixer working at the same wavelength [9]. However, if a similar performance can be repeated at 1 THz, these mixers may become very important.

References:

- [1] T.G. Phillips and K.B. Jefferts, 'A Low Temperature Bolometer Heterodyne Receiver System for Millimeter-wave Astronomy,' *Rev. Sci. Instr.*, **44**, 1009. (1973)
- [2] R. Padman, private communication.
- [3] S.K. Yngvesson, J.-X. Yang, F. Agahi, R. Brasco, D. Dai, J. Li, W. Grammer, M.A. Tischler and K.M. Lau, 'Electron Bolometric Mixers for the THz Region,' *Proc. 4th Int. Symp. Space Terahertz Tech.*, 555. (April 1993)
- [4] D. Prober, 'Superconducting Terahertz Mixer Using a Transition Edge Microbolometer,' *Appl. Phys. Lett.*, **62**, 2119. (1993)
- [5] A. Skalare, W.R. McGrath, B. Bumble, H.G. LeDuc, P.J. Burke, A.A. Verheijen, D.E. Prober, 'A Superconducting Hot Electron Bolometer Mixer for 530 GHz,' Presented at the Applied Superconductivity Conference, Boston. (Nov. 1994)
- [6] E.M. Gershenson, G.N. Gol'tsman, I.G. Gogidze, Y.P. Gusev, A.I. Elant'ev, B.S. Karasik and A.D. Semenov, 'Millimeter and Submillimeter Range Mixer Based on Electronic Heating of Superconducting Films in the Resistive State,' *Superconductivity*, **3**, 1582. (1991)
- [7] See, for example, H. Ekström, B. Karasik, E. Kollberg and S.K. Yngvesson, 'Superconducting Bolometric Mixers,' *IEEE Microwave and Guided Wave Lett.*, **4**, 253. (1994) or (same authors), 'Investigation of a Superconducting Hot Electron Mixer,' *Proc. 5th Int. Symp. Space Terahertz Tech.*, 169. (May 1994)
- [8] O. Okunev, A. Dzardanov, H. Ekström, S. Jacobsson, E. Kollberg, G. Gol'tsman and E. Gershenson, 'NbN Hot Electron Waveguide Mixer for 100 GHz Operation,' *Proc. 5th Int. Symp. Space Terahertz Tech.*, 214. (May 1994)
- [9] R. Blundell, C.-Y. E. Tong, D.C. Papa, R.L. Leombruno, X. Zhang, S. Paine, J.A. Stern, H.G. LeDuc and B. Bumble, 'A Wideband Fixed-Tuned SIS Receiver for 200 GHz Operation,' *Proc. 5th Int. Symp. Space Terahertz Tech.*, 27. (May 1994)

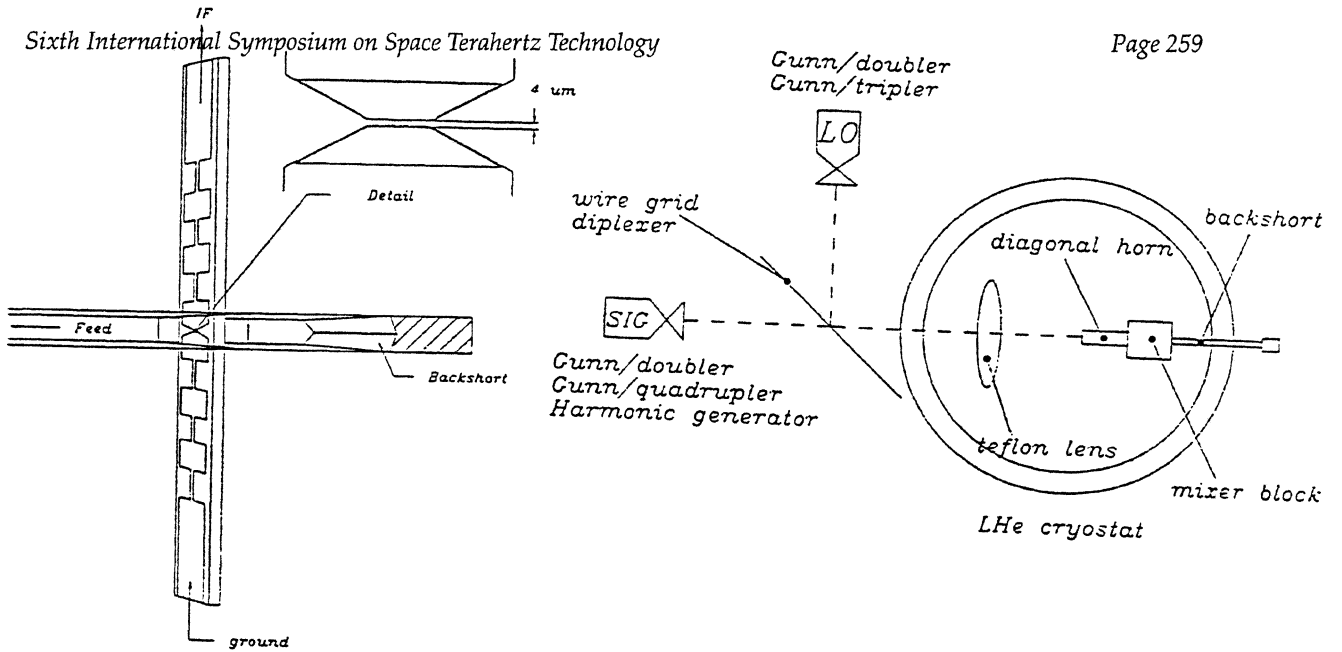


Figure 1. Schematic of waveguide mixer.

Figure 2. Schematic of the experimental setup.

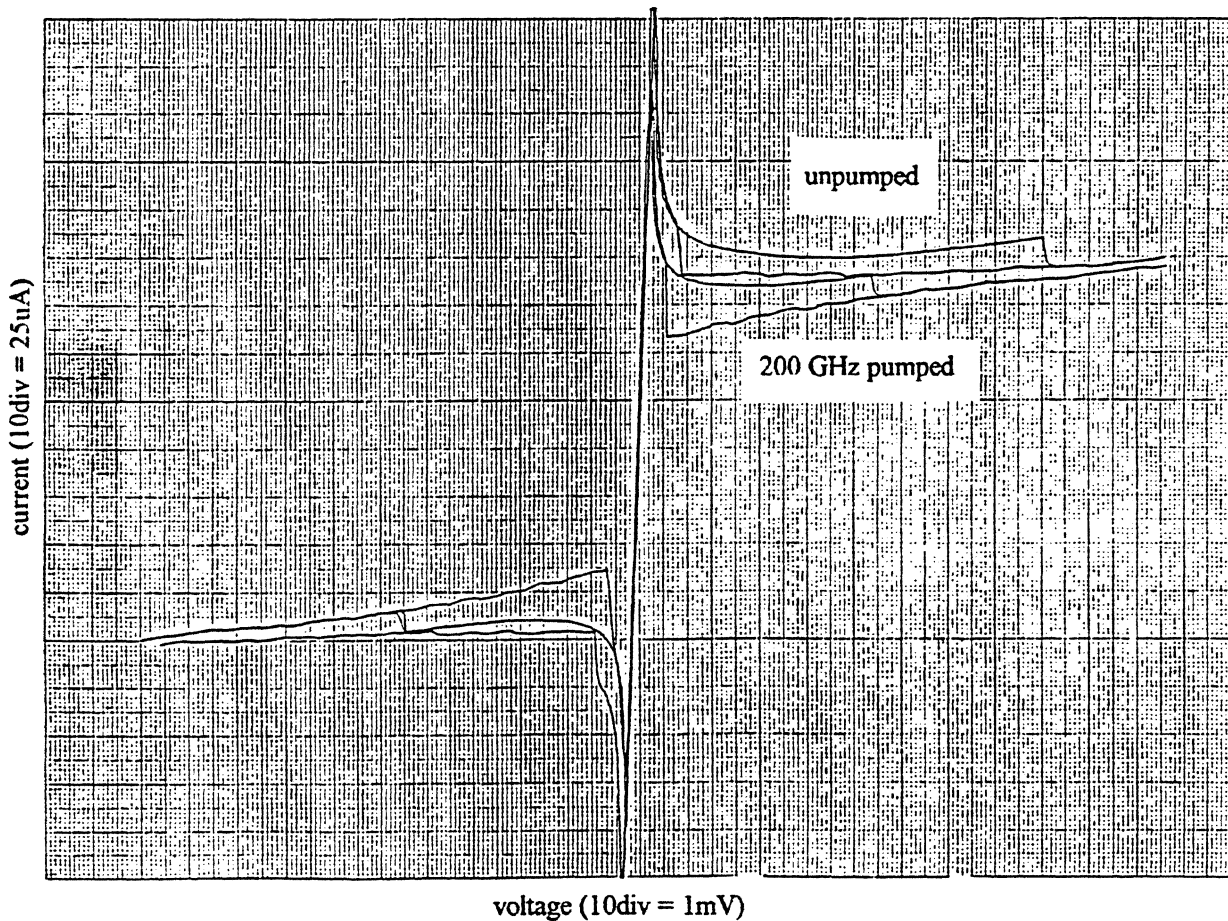


Figure 3. Current-Voltage (IV) characteristics of mixer element.

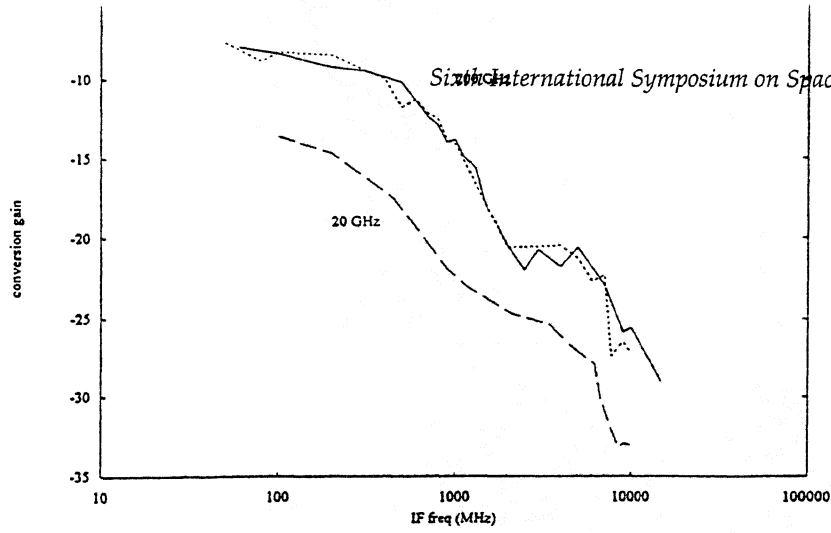


Figure 4. Conversion measurements at 200 GHz

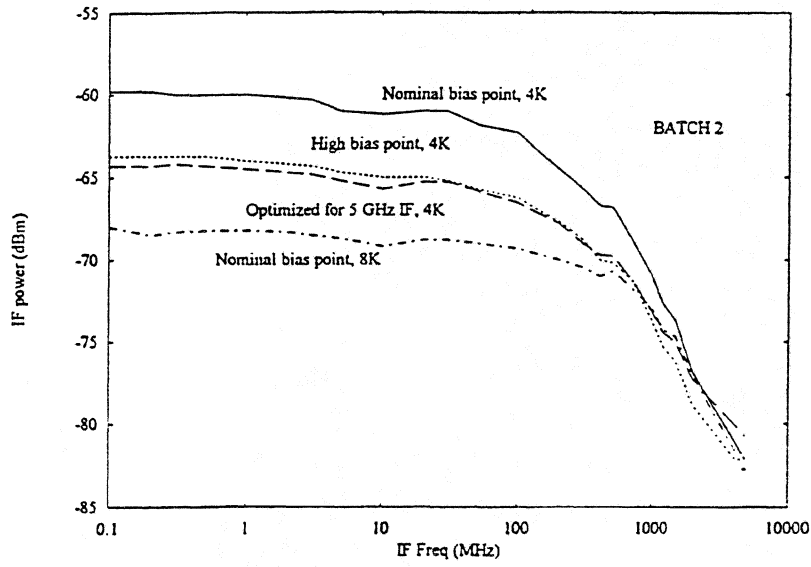


Figure 5. Bandwidth dependence on operating point.

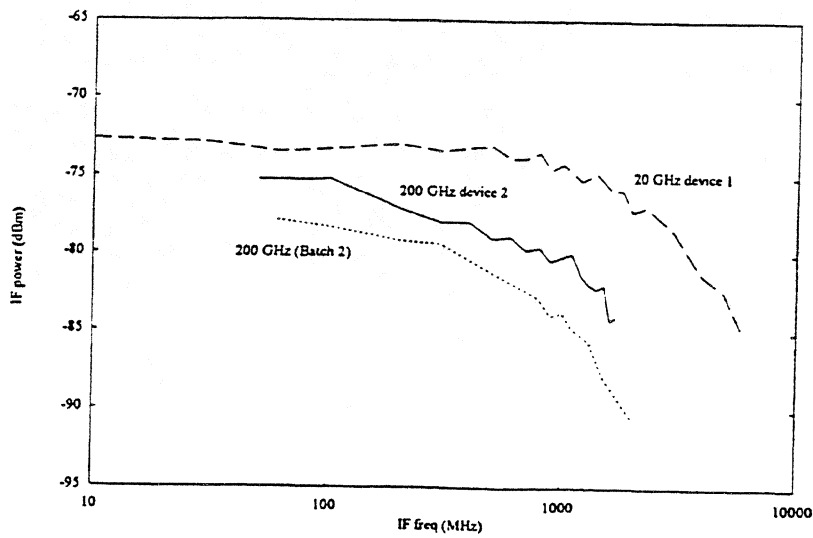


Figure 6. Bandwidth measurement of a mixer element.

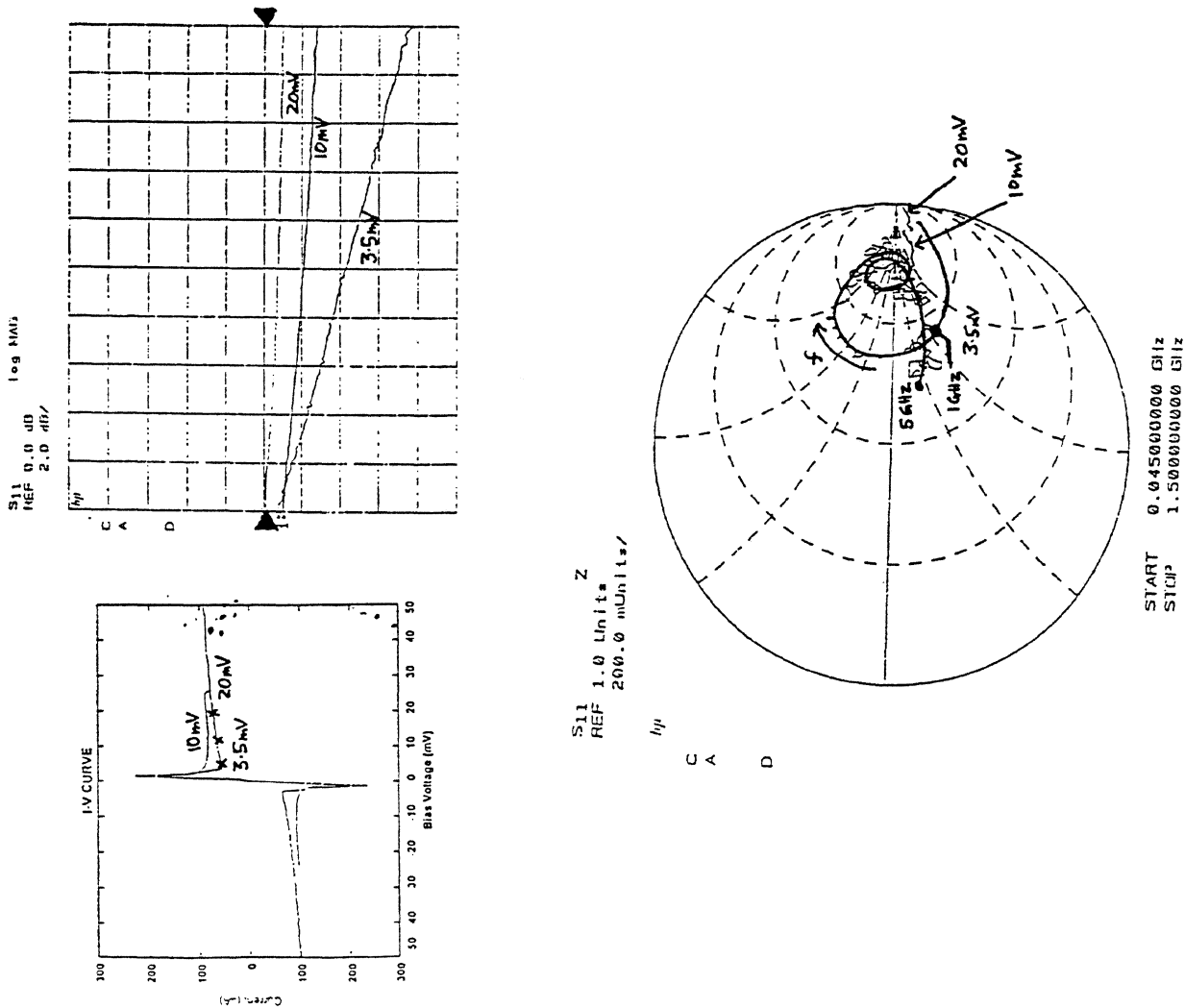


Figure 7. Mixer output impedance at various operating points.

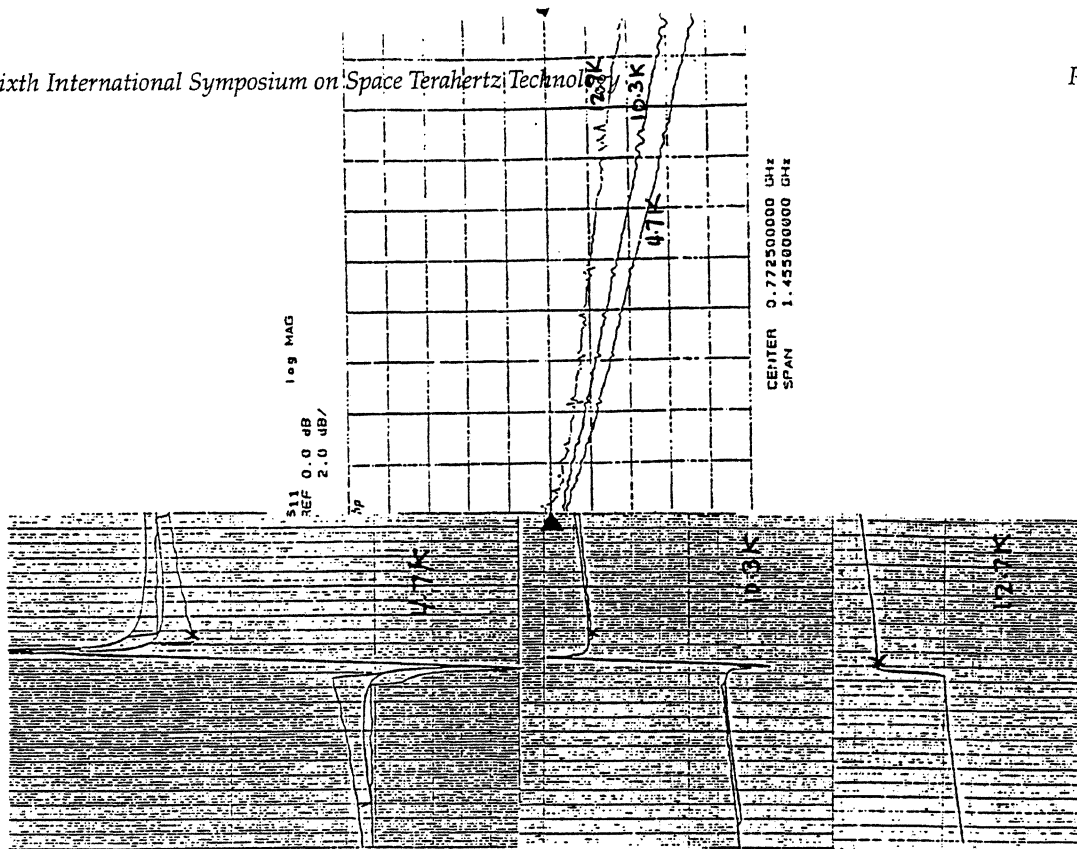


Figure 8. Mixer reflection loss at various operating temperatures.

NOISE TEMPERATURE AND IF BANDWIDTH OF A 530 GHz DIFFUSION-COOLED HOT-ELECTRON BOLOMETER MIXER

A. Skalare, W. R. McGrath, B. Bumble and H. G. LeDuc
Center for Space Microelectronics Technology, Jet Propulsion Laboratory,
California Institute of Technology, Pasadena, CA 91109

P. J. Burke, A. A. Verheijen and D. E. Prober
Dept. of Applied Physics, Yale University, New Haven, CT 06520-8284

Superconducting hot-electron bolometers [1-4] are currently of significant interest for use in heterodyne receivers at frequencies above 1 THz for radioastronomy applications. The mixing process in this type of device relies on heating of the electron gas, which means that, unlike an SIS tunnel junction mixer, the bolometer mixer does not have an upper frequency limit related to the superconductive energy gap (in fact, it absorbs rf power more uniformly for frequencies above the gap frequency). Until recently, hot-electron bolometers have not been extensively developed as heterodyne mixers because of the limitation in intermediate frequency (IF) bandwidth imposed by the thermal relaxation time of the heated electrons in bulk devices. For bulk indium antimonide bolometers, for example, the IF roll-off frequency is around 1 MHz [5], while the typical bandwidth requirement for molecular-line spectroscopy is at least 1 GHz. Recently however, novel hot-electron bolometers using very thin superconductive films have been proposed which can achieve practical IF bandwidths of several GHz [1, 2]. Bolometer mixers using thin NbN films and relying on electron-phonon interactions to cool the electrons have recently demonstrated IF bandwidths near 700 MHz [4].

In this paper we present the first receiver noise and IF bandwidth measurements with a *diffusion-cooled* superconducting niobium hot-electron bolometer mixer, that was first proposed by Prober in 1993 [2, 6]. This device is different from earlier superconducting hot-electron bolometers in that the thermal conductance that cools the heated electrons is provided by rapid electron diffusion rather than phonon emission. To achieve the short electron diffusion time required for a high IF bandwidth the device needs to be very short, less than 0.5 μm . The Nb film must also be very thin (~ 10 nm) to place it in the dirty limit. In this limit the very short ($\approx 1-10$ nm) mean free path enhances the electron-electron interactions relative to the electron-phonon interaction [1]. Thus when absorbing RF power, the electron gas can thermalize at a higher temperature than the lattice. The small electron specific heat, especially for a submicron size device, and the high thermal conductance provided by diffusion result in a very short thermal response time, ≈ 55 ps [7], and hence a 3 dB IF rolloff around 2-3 GHz. The bolometer is contacted at both ends by normal metal films rather than by superconductors, to prevent the occurrence of Andreev reflections which could potentially increase the device response time. See reference [8] for a more detailed description of the device operation.

A more complete description of our measurements will be given elsewhere [9] so they are only briefly described here. The bolometer used in the measurements consists of a 10 nm thick strip of Nb with an approximate width of 0.14 μm and a length of 0.28 μm [6] that

was fabricated on a fused quartz substrate; see Fig. 1. Two 100 nm thick gold films contact the device at both ends, and connect to a waveguide probe and an RF filter circuit patterned from a 110 nm thick niobium layer. The critical temperature T_C of this Nb film is ~ 4.7 K, with a transition width ΔT_C of ~ 1.2 K (in these thin dirty films the T_C is suppressed relative to the bulk value of ~ 9.2 K).

The bolometer chip was mounted into a two-tuner waveguide mixer block designed for 547 GHz [10], which was subsequently placed into a vacuum cryostat and cooled down to 2.2 K by pumping down the pressure in the liquid helium tank. A $\times 2 \times 3$ multiplier chain driven by an 89 GHz Gunn oscillator was used to generate the local oscillator power at 533 GHz, which was coupled into the receiver beam using a folded Fabry-Perot interferometer. A cooled HEMT amplifier [11] together with an isolator was used as the first stage in the intermediate frequency (IF) amplifier chain, which operated at 1.4 GHz and had a total noise temperature of 6 K. A 320 MHz bandpass filter was used to define the IF bandwidth for receiver noise measurements. The receiver sensitivity was determined through Y-factor measurements where 295 K and 77 K blackbody loads were switched into the receiver beam. Fig. 2 shows the best Y-factor response achieved after adjusting the mixer block backshort and E-plane tuner for best coupling of the LO, and optimizing the LO power. As can be seen, the best response is in the resistive branch of the IV curve at a bias voltage just above the "drop-back" voltage. The largest Y-factor was 1.15 dB, corresponding to a double sideband receiver noise temperature of 650 K. The mixer conversion was estimated to -11.4 dB DSB including RF coupling losses. Several tests were made to check for non-heterodyne contributions to the response. Switching between loads with LO power applied and with both loads at 295 K gave no response, which shows that the mixer response is not due to standing waves in the local oscillator path. Switching between 295 K and 77 K loads without LO pump power did not give any output power response. The same switching with LO power applied did not shift the bias voltage of the device measurably ($< 2 \mu\text{V}$) with the bolometer current-biased at DC, indicating that the measured mixer response was not a result of a bias point shift due to heating from the hot and cold loads.

In a separate measurement, an additional Gunn was connected to the multiplier, which thereby generated both power at the local oscillator frequency and a weak signal that could be used as a monochromatic source for mixer experiments. A simple aluminum mirror was used to couple both the local oscillator and signal lines into the receiver, and the intermediate frequency output port was connected to a spectrum analyzer. Measurements were made with the mixer block at 4.3 K and 2.2 K. In both cases the analyzer showed that the mixer output did indeed contain a monochromatic line, which could be tuned over the whole available 1 to 2 GHz IF band by adjusting the frequencies the two Gunn oscillators. A measurement at 2.2 K showed that the difference in IF output power when switching between a hot and a cold blackbody load in the receiver beam showed the same bias voltage dependence as did the output power due to a monochromatic signal source. This fact further supports that the measured Y-factor response is heterodyne. Additionally, a superconducting magnet inside the cryostat was used to apply a magnetic field of approximately 400 Gauss to the bolometer, but was observed to have no effect on the monochromatic IF output power to within the measurement accuracy (0.2 dB).

An important issue for a bolometer mixer is the IF dependence of the conversion efficiency that is set by the thermal response time. Due to significant output power variations with frequency in the multiplier / two-Gunn source, we chose to determine this dependence with

a broadband blackbody RF signal source and with a spectrum analyzer used as a tunable 1 MHz filter after the IF amplifier chain. The IF system of the receiver was also reconfigured with a broadband FET amplifier that was cooled to 77 K in place of the HEMT amplifier. A 25 μm thick Kapton beamsplitter was used to couple the LO power into the cryostat. The measurement was done by switching between a 295 K and a 77 K load in the receiver beam, thereby varying the detected IF output power by $\Delta P_{Out} = \Delta f \cdot k_B \cdot \Delta T_{Load} \cdot \eta_{Mx} \cdot G_{IF}$, where Δf is the 1 MHz filter bandwidth of the spectrum analyzer, η_{Mx} is the DSB conversion efficiency of the bolometer mixer (including RF losses in the optics), G_{IF} is the gain of the broadband (0.5-4 GHz) IF chain (including the spectrum analyzer), and ΔT_{Load} is the difference between the hot and cold load temperatures. $G_{IF}(f_{IF})$ must be carefully calibrated in order to accurately determine the bolometer mixer IF response. This was done by blocking the local oscillator optical path and biasing the bolometer at a high enough DC current to drive it completely into the normal conducting state. Under those conditions the IF output power $P_{Out,Cal}$ was strongly dominated by the IF amplifier system noise term $\Delta f \cdot k_B \cdot T_{IF} \cdot G_{IF}$. However, a small correction was made for the thermal (Johnson) noise contribution of $\Delta f \cdot k_B \cdot T_{Device} \cdot G_{IF}$ of the bolometer, which could be estimated from the slope of the IF output noise versus the DC voltage in this bias regime. The noise temperature of the IF chain was calibrated in a separate measurement using thermal noise from a variable-temperature 50 Ω termination load, and was found to vary from 108 K at 0.5 GHz to 205 K at 4 GHz. The measured IF noise temperature allowed the double sideband mixer

conversion efficiency to be calculated as $\eta_{Mx} = \left(\frac{\Delta P_{Out}}{P_{Out,Cal}} \right) \cdot \left(\frac{T_{IF} + T_{Device}}{\Delta T_{Load}} \right)$. Figure 3

shows the frequency dependency of η_{Mx} at a typically good bias point just above the drop-back voltage. A fitted curve with the expected frequency dependence

$\left(1 + (f_{IF} / f_{Roll-off})^2 \right)^{-1}$ [5] is also shown, where $f_{Roll-off}$ is the intermediate

frequency at which η_{Mx} drops by 3 dB. The roll-off in Fig. 3 occurs at 1.7 GHz, which is close to the expected value, given the level of self-heating in the bolometer. In addition, roll-off frequencies of up to 1.9 GHz were seen at higher DC bias voltages, though the mixer conversion efficiency was lower.

In conclusion, the first Y-factor measurements with a diffusion cooled hot-electron bolometer mixer has yielded a lowest receiver noise temperature of 650 K and an estimated conversion efficiency of -11.4 dB DSB at a local oscillator frequency of 533 GHz. The 3 db roll-off in conversion efficiency in the intermediate frequency band has been measured using a separate broadband IF amplifier system, to be between 1.7 GHz and 1.9 GHz, depending slightly on the DC bias point of the bolometer. The superconducting transition of the device is centered at 4.7 K, with all non-linearity in the IV curve disappearing at 5.3 K. The higher of the two temperature values corresponds to a superconducting gap frequency of 410 GHz, well below that of the mixing experiments. The mixer conversion is not affected by a magnetic field of 400 Gauss.

Acknowledgements

The research described in this paper was performed by the Center for Space Microelectronics Technology, Jet Propulsion Laboratory, California Institute of Technology and by Yale University and was jointly sponsored by the National Science Foundation, the Netherlands Organization for Scientific Research, and the National Aeronautics and Space Administration, Office of Space Access and Technology. Funding for P. J. Burke was provided by a NASA Graduate Student Fellowship as well as a Connecticut High Technology Fellowship.

References

- [1] E. M. Gershenzon, G. N. Gol'tsman, I. G. Gogidze, Y. P. Gusev, A. I. Elant'ev, B. S. Karasik, and A. D. Semenov, "Millimeter and submillimeter range mixer based on electronic heating of superconducting films in the resistive state," *Superconductivity*, vol. 3, pp. 1582-1597, 1990.
- [2] D. E. Prober, "Superconducting terahertz mixer using a transition-edge microbolometer," *Appl. Phys. Lett.*, vol. 62, 1993.
- [3] H. Ekström, B. S. Karasik, E. Kollberg, and K. S. Yngvesson, "Investigation of a superconducting hot electron mixer," presented at the Fifth International Symposium on Space Terahertz Technology, Ann Arbor, MI, USA, 1994.
- [4] O. Okunev, A. Dzardanov, H. Ekström, S. Jacobsson, E. Kollberg, G. Gol'tsman, and E. M. Gershenzon, "NbN hot electron waveguide mixer for 100 GHz operation," presented at the Fifth International Symposium on Space Terahertz Technology, Ann Arbor, MI, USA, 1994.
- [5] F. Arams, C. Allen, B. Peyton, and E. Sard, "Millimeter mixing and detection in bulk InSb," *Proceedings of the IEEE*, vol. 54, pp. 308-318, 1966.
- [6] A. Skalare, W. R. McGrath, B. Bumble, H. G. LeDuc, P. J. Burke, A. A. Verheijen, and D. E. Prober, "A heterodyne receiver at 533 GHz using a diffusion-cooled superconducting hot-electron bolometer mixer," *IEEE Transactions on Applied Superconductivity*, vol. 5 (March), 1995.
- [7] A. Skalare, W. R. McGrath, B. Bumble, H. G. LeDuc, P. J. Burke, A. A. Verheijen, and D. E. Prober, "A superconducting hot electron bolometer mixer for 530 GHz," presented at the Fifth International Symposium on Space Terahertz Technology, Ann Arbor, MI, USA, 1994.
- [8] W. R. McGrath, "Hot-electron bolometer mixers for submillimeter wavelengths: an overview of recent developments," this conference proceedings.
- [9] A. Skalare, W. R. McGrath, B. Bumble, H. G. LeDuc, P. J. Burke, A. A. Verheijen, and D. E. Prober, To be submitted to *Applied Physics Letters*.
- [10] P. Febvre, W. R. McGrath, P. Batelaan, B. Bumble, H. G. LeDuc, S. George, and P. Feautrier, "A low noise SIS receiver measured from 480 GHz to 650 GHz using Nb junctions with integrated RF tuning circuits," *Int. J. Infrared & Millimeter Waves*, vol. 15(6), pp. 943-965, 1994.
- [11] Berkshire Technologies, Telegraph Avenue, Oakland, CA.

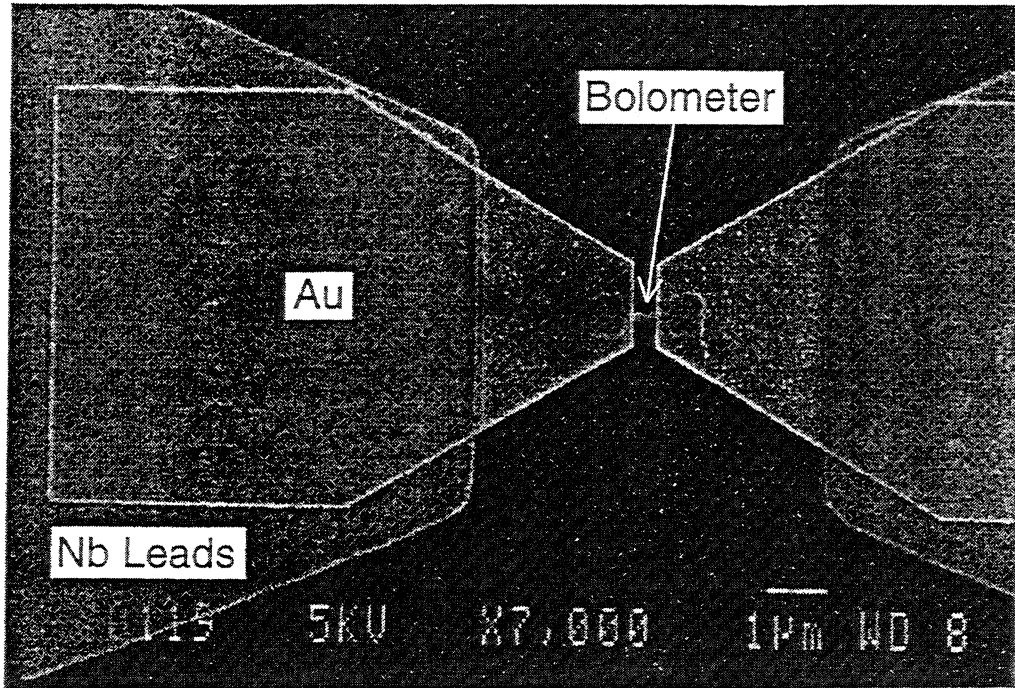


Fig. 1: SEM photo of a diffusion cooled hot-electron bolometer.

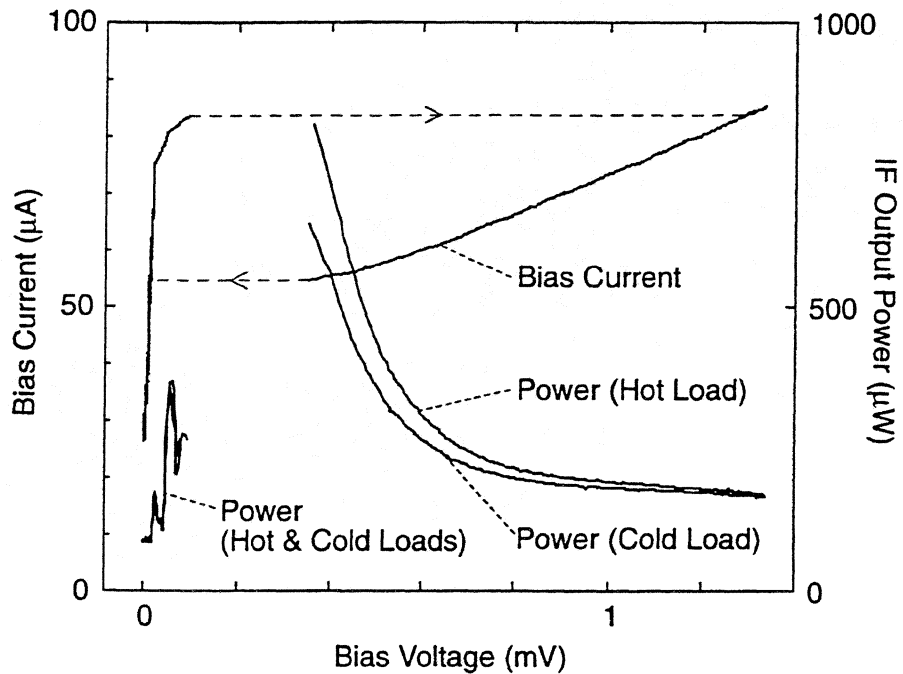


Fig.2: Local oscillator pumped IV curve of the bolometer and output power from the low-noise amplifier chain at the intermediate frequency.

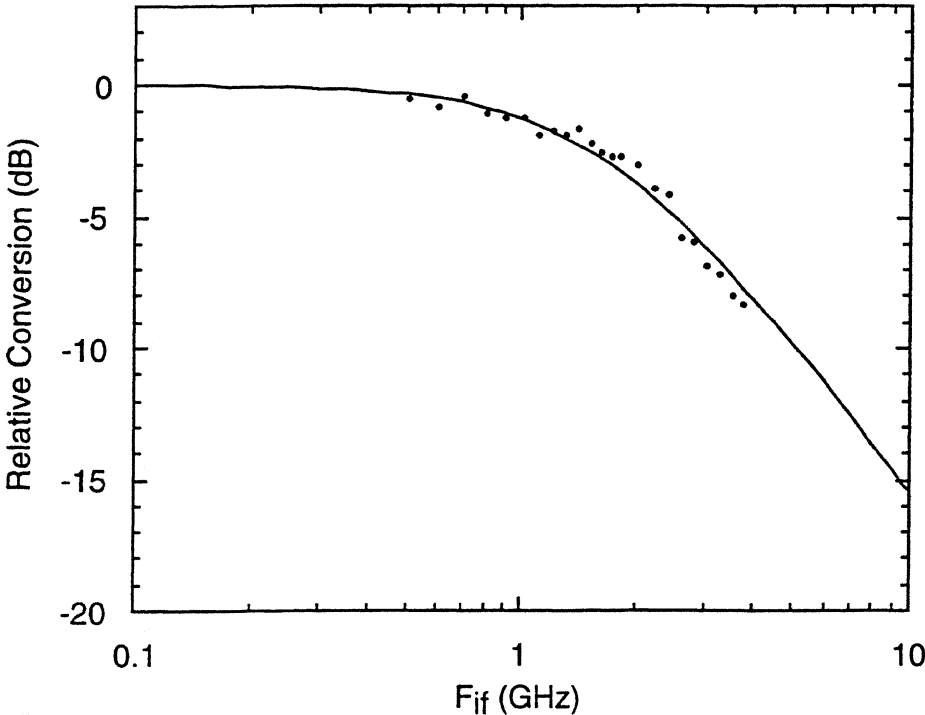


Fig.3: Measured relative conversion versus frequency and a fitted curve.

NOISE TEMPERATURE OF NbN HOT-ELECTRON QUASIOPTICAL SUPERCONDUCTING MIXER IN 200–700 GHz RANGE

G.N. Gol'tsman, B.S. Karasik, S.I. Svechnikov, and E.M. Gershenzon

Department of Physics, Moscow State Pedagogical University, Moscow 119435, Russia

H. Ekström and E. Kollberg

*Department of Microwave Technology, Chalmers University of Technology,
Göteborg S-412 96, Sweden*

The electron heating effect in superconducting films is becoming very attractive for the development of THz range mixers because of the absence of frequency limitations inherent in the bolometric mechanism. However, the evidence for the spectral dependence of the position of optimal operating point has been found recently for NbN thin film devices^{1,2}. The effect is presumably attributed to the variation in the absorption of radiation depending on the frequency. Since the resistive state is not spatially uniform the coupling efficiency of the mixer device with radiation can be different for frequencies larger than $2\Delta/h$ and those smaller than $2\Delta/h$ (Δ is the effective superconducting gap in the resistive state). To study the effect more thoroughly we have investigated the noise temperature of quasioptical NbN mixer device with broken-line tapered slot antenna in the frequency range 200–700 GHz.

The device consists of several (5–10) parallel strips 1 μm wide and 6–7 nm thick made from NbN film on $\text{SiO}_2\text{-Si}_3\text{N}_4\text{-Si}$ membrane. The strips are connected with the gold contacts of the slot-line antenna which serves both as bias and IF leads. We used backward wave oscillators as LO sources and a standard hot/cold load technique for noise temperature measurements.

The frequency dependence of noise temperature is mainly determined by two factors: frequency properties of the antenna and frequency dependence of the NbN film impedance. To separate both factors we monitored the frequency dependence of the device responsivity in the detector mode at a higher temperature within the superconducting transition where the impedance of NbN film is close to its normal resistance. In this case the impedance of the device itself is frequency independent. The experimental results will be reported at the Symposium.

1. G. Gol'tsman, S. Jacobsson, H. Ekström, B. Karasik, E. Kollberg, and E. Gershenzon, "Slot-line tapered antenna with NbN hot electron mixer for 300–360 GHz operation," *Proc. of the 5th Int. Symp. on Space Terahertz Technology*, pp. 209-213a, May 10-12, 1994.
2. B.S. Karasik, G.N. Gol'tsman, B.M. Voronov, S.I. Svechnikov, E.M. Gershenzon, H. Ekström, S. Jacobsson, E. Kollberg, and K.S. Yngvesson, "Hot electron quasioptical NbN superconducting mixer," presented at the ASC'94, submitted to *IEEE Trans. on Appl. Superconductivity*.

350 GHz NbN HOT ELECTRON BOLOMETER MIXER

by

H.Ekström^{a)}, B.Karasik^{b)}, E.Kollberg^{a)}, G.Gol'tsman^{b)}, and E.Gershenzon^{b)}

^{a)}Department of Microwave Technology, Chalmers University of Technology, S-41296 Göteborg, Sweden

^{b)}Department of Physics, Moscow State Pedagogical University, Moscow 119435, Russia

ABSTRACT

Superconducting NbN hot-electron bolometer (HEB) mixer devices have been fabricated and measured at 350 GHz. The HEB is integrated with a double dipole antenna on an extended crystalline quartz hyper hemispherical substrate lens. Heterodyne measurement gave a -3 dB bandwidth, mainly determined by the electron-phonon interaction time, of about 680 and 1000 MHz for two different films with $T_c = 8.5$ and 11 K respectively. The measured DSB receiver noise temperature is around 3000 K at 800 MHz IF frequency. The main contribution to the output noise from the device is due to electron temperature fluctuations with the equivalent output noise temperature $T_{FL} \approx 100$ K. T_{FL} has the same frequency dependence as the IF response. The contribution from Johnson noise is of the order of T_c . The RF coupling loss is estimated to be ≈ 6 dB. The film with lower T_c , had an estimated intrinsic low-frequency conversion loss ≈ 7 dB, while the other film had a conversion loss as high as 14 dB. The difference in intrinsic conversion loss is explained by less uniform absorption of radiation. Measurements of the small signal impedance shows a transition of the output impedance from the DC differential resistance $R_d = dV/dI$ in the low frequency limit to the DC resistance $R_0 = U_0/I_0$ in the bias point for frequencies above 3 GHz. We judge that the optimum shape of the IV-characteristic is more easily obtained at THz frequencies where the main restriction in performance should come from problems with the RF coupling.

INTRODUCTION

There is a continuous need of improved heterodyne receivers for radio astronomy at terahertz frequencies. Mainly one type mixer device is currently in use at and above 1 THz, namely the Schottky diode mixer [1]. The sensitivity is however lower than what is required for several planned projects. The low noise InSb hot-electron bolometer mixers, used up to about 800 GHz [2], have an IF bandwidth of about 2 MHz, which is too narrow for many applications. Nb trilayer SIS quasi-particle tunnel junctions [3] are very sensitive mixer devices, but so far only for frequencies below the energy gap of Nb (≈ 700 GHz). There are however different types of new promising hot-electron bolometric devices under development; 2DEG devices using the temperature dependent mobility of a 2-dimensional electron gas [4], and superconducting hot electron bolometers (HEB) utilizing the electron temperature dependent resistance in superconducting narrow thin film strips [5-7]. The mixer performance of the Nb HEB mixer at 20 GHz is promising [6], however the bandwidth of Nb devices, determined by the electron-phonon interaction time, τ_{e-ph} , is narrow (≈ 90 MHz). An improved bandwidth of Nb mixers is obtained in very short devices [8]. The response or hot electron temperature relaxation time is reduced when the electron diffusion time out from the device is shorter than the electron-phonon interaction time. A bandwidth of about 2 GHz has been measured [7] in this type of device. It is also possible to obtain a larger bandwidth with materials with shorter τ_{e-ph} . We show here that it is possible to have a bandwidth larger than 1 GHz with NbN devices. NbN has a larger energy gap than Nb, why a larger signal frequency is required to get uniform absorption in the film at low temperatures, which is required for optimum mixer performance. At THz frequencies this is fulfilled, i.e. the energy gap $\Delta_{NbN}(T) < h\nu/2$. However, for the current measurements at 350 GHz, the device has to be heated up to within 1 K below T_c to obtain $\Delta < h\nu/2$. For the heated sample, measured noise, conversion gain and impedance agrees reasonably well with theory. Improved agreement is expected at higher signal frequencies.

THE NbN HEB DEVICE

The HEB devices are made of NbN films, either 100 or 200 Å thick. The films are patterned to form 11 parallel, 1.5 μm wide and 5 μm long strips. The devices are integrated with double dipole antennas [9] on extended hemispherical crystalline-quartz substrate lenses [10]. The NbN-films are DC magnetron sputtered [11] on non-heated substrates and patterned by conventional photo-lithography and plasma etching (30 sccm He + 10 sccm CF₄ (incl. 8% O₂)). The antenna and contacts are made of 3000 Å Nb + a 1500 Å thick layer of Au, patterned by lift-off. We have tested two film of different

quality. Devices made from the first 200 Å thick film, represented by the typical device #A, has lower T_C , critical current I_C , unpumped resistive state current I_{00} , and surface resistance R_s , than device #B, made from a much thinner (≈ 100 Å) film of higher quality, see table I. However, together with the improved I_{00} and T_C , is a degradation of the superconducting transition width ΔT_C , see Fig. 1. This figure also shows that device #B has a foot structure in the $R(T)$ curve. Future devices will be made on Si substrates with contacts made of ≈ 3000 Å thick Au without the additional Nb layer. This will improve the film quality with respect to transition width, and prevent possible degradation by Andreev reflections [12] in the NbN-Nb interface, which could be important if the devices are made much shorter .

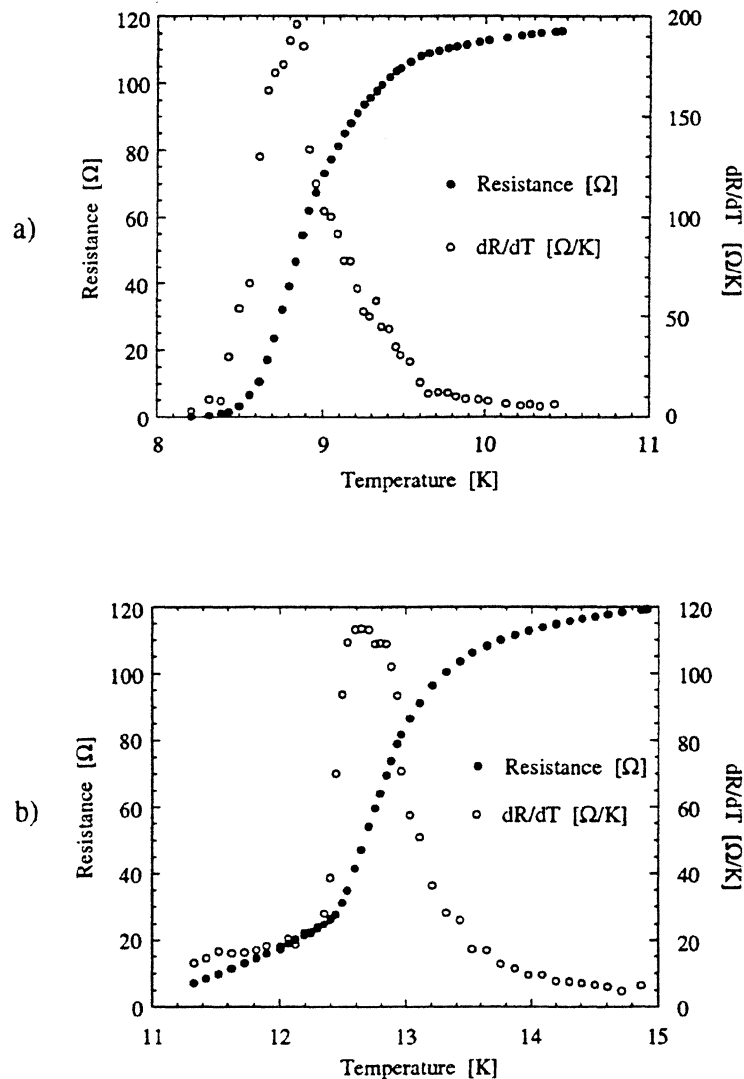


Fig. 1. Plot a) shows $R(T)$ and dR/dT for device #A, and plot b) shows the same for device #B.

TABLE I

#	d [Å]	R _s ¹⁾ [Ω]	R _N ¹⁾ [Ω]	dR/dT [Ω/K]	T _c ²⁾ [K]	T _c ³⁾ [K]	ΔT _c [K]	I _c [μA]	I _∞ [μA]
A	200	390	122	190	8.5	8.8	0.5	1900	600
B	100	500	150	110	11	12.6	1 ⁴⁾	3150	1130

¹⁾ At room temperature

²⁾ At onset of resistance

³⁾ At maximum dR/dT

⁴⁾ Excluding the foot structure.

MEASUREMENT SET-UP

The measurements are made with the mixer mounted in a LHe cooled vacuum cryostat. Attached to the mixer mount are a resistive heater and a thermometer for temperature control. Signal and LO are combined with a 50 μm thick Mylar beamsplitter and fed to the mixer through a Teflon window and Fluorogold IR shield in the cryostat wall. The LO source is a 310-370 GHz BWO (Carcinotron), and the signal is obtained from a SBV quintupler pumped by a 70 GHz Gunn oscillator. Bandwidth and output noise measurements are made with a wideband (0.02-4 GHz) room temperature IF amplifier, while for mixer noise measurements a cooled 680 to 920 MHz balanced low noise amplifier¹ together with a cooled bias²-T are included in the IF chain. The output IF signal is registered on a spectrum analyser. Alignment of the set-up was done with the device in detection mode. The LO path was adjusted to obtain maximum reduction of bias current, while the signal path was adjusted using a lock-in amplifier to observe the response to the low-frequency modulated signal.

We have estimated the losses on the RF-side to be roughly about 5-7 dB. See Table II.

TABLE II

	loss [dB]
Mylar beamsplitter	1
Teflon window	0.5
Fluorogold IR shield	1
Quartz lens	2
Back lobe	1
Beam coupling	0.5
TOTAL loss	≈ 6 dB

¹ Supplied by R.Brady, NRAO; Noise temperature ≈6 K and ≈17 dB gain at 14 K.

² Radiall R44353533000-9437 bias-T, 0.1-1.5 GHz

BIAS POINTS

Fig. 2 shows typical IV-characteristics for the device with optimum bias points. Depending on the physical temperature of the device and frequency of the IF output signal, it is possible to find different optimum bias points. For low temperatures the IV-characteristic has a hysteretic behaviour with a critical current $I_c \neq 0$. In this case, for output frequencies not too far above the IF bandwidth the optimum bias point is found just beside the unstable region at the transition from the resistive state to the superconducting state. At these low temperatures and relatively large DC-powers, it is reasonable to believe that resistive domains are responsible for the resistive state, where also the main part of radiation is absorbed.

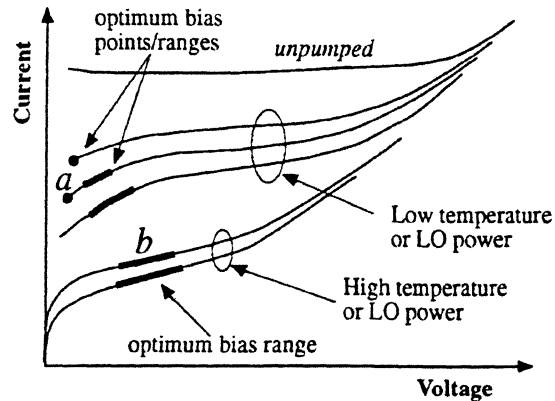


Fig. 2. Schematic of the optimum bias points and ranges for different temperatures and LO-powers for device #A. *a* shows the optimum bias point for low f_{IF} at low temperatures, and *b* shows the optimum bias range at high temperatures. This difference is probably valid only as long as the signal frequency ν at low temperatures is less than $2\Delta/h$. For higher ν the conversion should not be improved by an increased temperature (reduced Δ) for f_{IF} close to the IF bandwidth.

For IF frequencies a few times the IF bandwidth a shift of the optimum bias is observed. The optimum no longer found in "one point" for the lowest bias voltages, but there is instead an optimum bias-range at higher voltages (Fig. 2). For higher temperatures, when the supercurrent is suppressed, $I_c \approx 0$, the same kind of shift in optimum bias is found. At these higher temperatures the energy gap is reduced, and the radiation can be more uniformly absorbed over the whole film. A shift of optimum bias can also be found when the superconductivity is suppressed by increased LO-power instead of thermal heating. Moreover, for a certain range of temperatures or LO power, it is possible to find two optimum biases, one point just at the instability and one wide region for higher bias.

We believe there are two different mixing modes at high and low temperatures, i.e. at the bias point close to the instability and in regions of higher bias. We have also seen that the mixing mechanism dominating for larger bias has a wider bandwidth. A possible explanation is that at higher temperatures the resistive state is most likely due to vortex flow (more uniform), while at lower temperatures a slow motion of the domain walls contributes to the signal at low f_{IF} .

MIXER CONVERSION AND BANDWIDTH

The mixer conversion gain is given by Eq. 1 [6, 13].

$$G = 2(C_o I_o)^2 \frac{\chi^2 P_{LO} R_L}{(R_L + R_o)^2} \left(1 - C_o I_o^2 \frac{R_L - R_o}{R_L + R_o}\right)^{-2} \left(1 + (\omega \tau_{mix})^2\right)^{-1} \quad (1)$$

where χP_{LO} , R_L , R_o is the absorbed LO-power, load resistance, and bolometer DC-resistance respectively, and

$$C = C_o I_o^2 = \frac{dR}{dP} I_o^2 = \frac{dR}{d\theta} \frac{I_o^2}{G_e} = \frac{R_d - R_o}{R_d + R_o} \quad (2)$$

C is sometimes called the self-heating parameter, θ is the electron temperature, G_e the thermal conductivity between the electron system and the lattice, and R_d the DC differential resistance. Since the response of the HEB as bolometer is the same to DC and RF-power, these two can be compared in the IV-characteristic, and an estimation of the absorbed LO power and conversion gain can be made [6].

The two HEB devices described above have been compared in heterodyne measurements at 350 GHz. The IF bandwidth of device #B, with a larger T_c , shows an improved bandwidth (1000 MHz) compared to #A (680 MHz) (Fig. 3 and 4). This agrees qualitatively with the experimental data on the temperature dependence of the electron-phonon relaxation time [14] since

$$Bandwidth^{-1} = 2\pi\tau_{mix} \propto \tau_{e-ph} \propto \theta^{-1.6} \approx T_c^{-1.6} \quad (3)$$

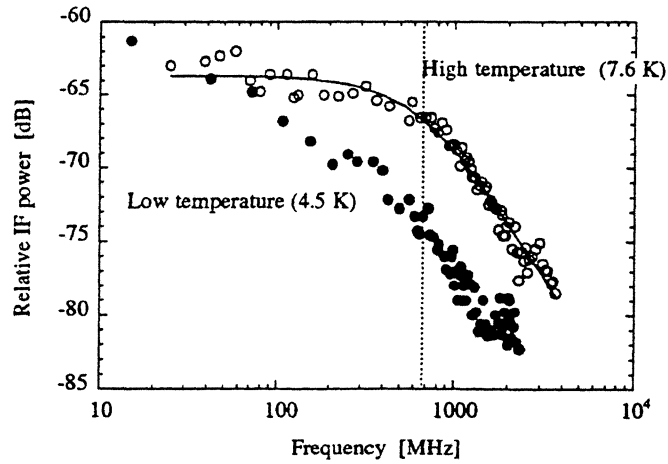


Fig. 3. IF response of sample #A at 4.5 K and 7.6 K.

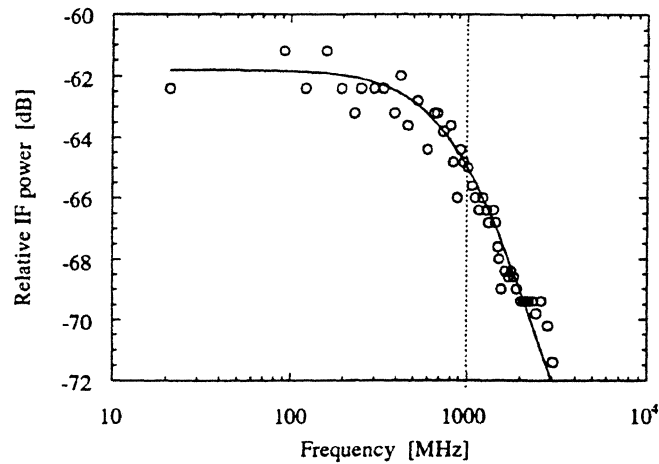


Fig. 4. IF response of sample #B at 11.6 K.

According to Eq. 1 and 2, a film of higher quality with a narrower transition width ΔT_c , i.e. larger $dR/d\theta$ at T_c , should have better conversion gain since it will give a larger self-heating parameter C . Device #A had an intrinsic conversion gain of -7 to -8 dB, estimated by Eq. (1), with an optimum absorbed LO power of $2 \mu\text{W}$, while the conversion gain of device #B (with larger I_c) was estimated to be -14 dB with an optimum absorbed LO power of $15 \mu\text{W}$. In both cases the physical temperature had to be adjusted to obtain the largest possible bandwidth since the photon energy of the pump-power was not high enough to be uniformly absorbed at low temperatures. The physical temperature was therefore within 1 K below T_c . The reduced gain for sample #B can be explained by the shape of the IV-characteristic (Fig. 5).

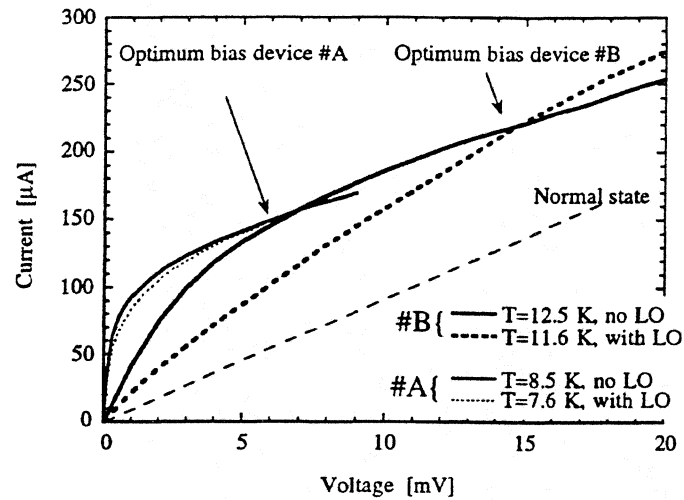


Fig. 5. Pumped and unpumped IV-characteristics for device #A and #B, with optimum bias points for $f_{IF} = 800$ MHz. For device #B the difference between the curves thermally heated and heated by LO is much larger than for device #A.

The difference between the pumped and thermally heated IV-curve is large. The pumped curve for device #B has a smaller differential resistance, which is not much larger than R_0 and gives a smaller self heating parameter C (Eq. 2), and thus smaller gain (Eq. 1). Moreover, film #B, with smaller maximum dR/dT , has a foot structure extending about 1 K below T_c (Fig. 1b), making the transition width even larger. This could be a reason for the degraded IV-characteristic. The value for C which is obtained from R_0 and dR/dT (Fig. 1b and Eq. 6) is larger than one which is obviously not correct as it indicates that there should be a negative differential resistance ($dU/dI < 0$) of the DC IV-characteristic in the bias point. We therefore make the conclusion that neither is the electron temperature given by T_c , i.e. the electrons are not uniformly heated. The quality of NbN film on quartz substrates are worse (e.g. foot structure) than the films made on sapphire or silicon. We expect to obtain improved results with film made on such substrates.

One possible reason for a smaller bandwidth, or increased response at low frequencies for low temperatures (Figs. 3 and 4), when radiation is only absorbed in resistive domains, could be the slow heat redistribution within the domain. At low temperatures the estimated conversion gain is as high as -1 dB. This value for the gain is only valid in the low frequency limit, i.e. for zero IF frequency, and decreases rapidly with frequency. Above a certain frequency the gain at low temperatures will be less than the gain at high temperatures. Thus estimations of conversion gain for $f_{IF} \neq 0$ with Eq. 1 is only possible when the IF response is flat below the IF bandwidth, defined by $f_{max} = (2\pi\tau_{mix})^{-1}$. This is not the case for NbN at low temperatures. For Nb

$f_{\max} \approx 90$ MHz, much less than f_{\max} for NbN, and more or less coincide with the increased response at low frequencies. An estimation of the gain at low temperatures for $f_{IF} \neq 0$ is therefore more correct in the case of Nb films. However, it is predicted that the IF response should always be flat when the signal frequencies $f_s > 2\Delta/h$, i.e. one has uniform heating. Thus there will be a flat response even at the lowest temperature when the signal frequency is large enough.

IMPEDANCE

An attempt has been made to measure the small-signal IF output impedance in the frequency range between 1 MHz and 5 GHz for sample #A at a temperature of about 1 K below T_c (Fig. 6). It was possible to detect a small influence on the HEB from the measurement signal of the network analyser, why this measurement should only be used as a guide of the general behaviour of the output impedance of the HEB. The temperature and bias of the operating point is chosen to give the maximum IF signal at 800 MHz (centre frequency of IF amplifier). In the low frequency limit up to about 100 MHz, the impedance is real and approximately equal to the DC differential

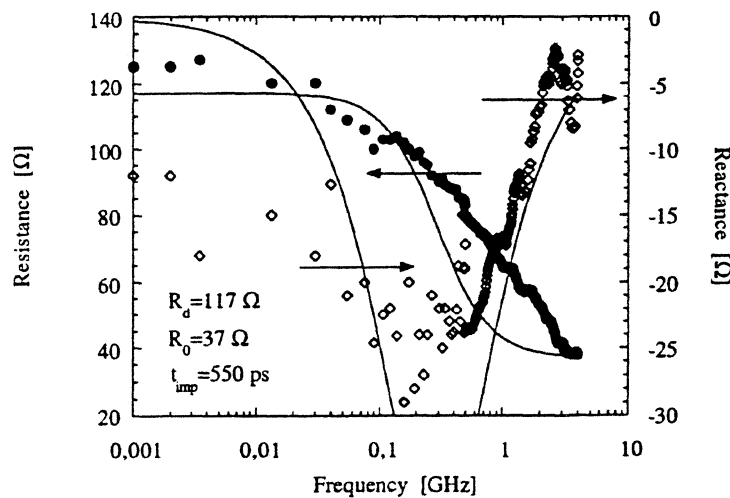


Fig. 6. A rough measurement to show the general behaviour of the resistive and reactive parts of the NbN HEB small signal IF impedance. The measurement was done in the optimum bias point with respect to the conversion gain at 800 MHz IF frequency. The solid lines are fitted curves obtained from Eq. (4). The values used for R_d , R_0 , and τ_{imp} are inserted in the plot.

resistance in the bias point (115 Ω). At 1 GHz the real part of the impedance is about 65 Ω and for frequencies above 3 GHz it equals the DC resistance in the bias point (37 Ω). At about 300 MHz the reactive part of the impedance is maximum and about

-40 Ω . For frequencies above 2 GHz (and below 300 MHz) it is close to zero. A rough estimation of the impedance time constant $\tau_{imp}=550$ ps can be made, taken as an average of the two time constants given by the measured resistive and reactive parts of the impedance, Eq. (4) [15].

$$Z(\omega) = R_d \frac{1 + j\omega\tau_{imp} \frac{R_o}{R_d}}{1 + j\omega\tau_{imp}} \quad (4)$$

where R_d is the DC differential resistance, i.e. $R_d=Z(0)$.

The impedance time constant can as well be derived from the mixing time constant, $\tau_{mix}=240$ ps ($f_{IF}=680$ MHz) as

$$\tau_{imp} \equiv \frac{\tau_{\theta}}{1-C} = \frac{\tau_{mix} \left(1 - C \frac{R_o - R_L}{R_o - R_L} \right)}{1-C} \quad (5)$$

where τ_{θ} is the electron temperature relaxation time.

It is seen that τ_{imp} depends strongly on the self-heating parameter C , which can be obtained in different ways according to

$$C = I_o^2 \frac{dR/d\theta}{V \cdot c_e} \cdot \tau_{\theta} = 0.58 \quad (6)$$

or

$$C = \frac{dU/dI - R_o}{dU/dI + R_o} = 0.59 \quad (7)$$

Eq. 5 gives $\tau_{imp}=640$ ps or 660 ps with C from Eq. (6) and (7) respectively. Considering the large uncertainty in the impedance measurements (the measured time constant for the resistance is three times shorter than the time constant obtained from the reactance, $\tau_{imp,Im}=3 \cdot \tau_{imp,Re}$) the excellent agreement between the measured τ_{imp} and τ_{mix} is probably more or less a coincidence, as the accuracy of the measured τ_{imp} is only within a factor of 3-4. At low temperatures the low frequency impedance increases as the differential resistance increases but we never obtain a measured value larger than 300 Ω , even for a larger differential resistance. This demonstrates that a slow relaxation is important for the low temperature resistive state and contributes even more at frequencies below 1 MHz.

NOISE

The output noise of the mixer as well as the DSB receiver noise has been measured for device #A and #B. The output noise temperature, T_{out} , was measured by comparing the noise levels obtained on a spectrum analyser connected to the IF port of the mixer,

for the device biased in the point for maximum output power, with the noise level in normal state at a temperature well above T_c . Thus

$$\frac{P_{noise,opt}}{P_{noise,normal}} = \frac{T_{out}(1-L) + T_{IF}}{T_J(1-L) + T_{IF}} \quad (8)$$

where T_{IF} is the noise contribution from the room temperature IF amplifier + bias-T etc., T_J is the Johnson noise from the device in normal state working as an ordinary resistor, and

$$L = \left(\frac{R_o - R_d}{R_o + R_d} \right)^2 \quad (8b)$$

is the corresponding mismatch loss, which is the same in normal state and in the bias point since $R_N \approx R_d (\approx 115 \Omega)$ for #A. T_{IF} was measured by comparing the output noise levels for the device in normal state at two temperatures, 77 and 300 K.

The output noise consists mainly of temperature fluctuation noise and Johnson noise, i.e. $T_{out} \approx T_{FL} + T_J$. When the radiation is uniformly absorbed ($\nu > 2\Delta/h$) the electrons have an equivalent temperature $\theta \approx T_c$, and T_J is approximately given by T_c . The temperature fluctuation noise of #A has been measured over the frequency range 20 MHz to 2 GHz at a temperature 7.6 K (about 1 K below T_c) [16], and at 6.8 K. This type of noise has the same output frequency dependence as the IF signal. At 7.6 K it has an equivalent output temperature $T_{FL} \approx 100$ K within the IF band. At the lower temperature 6.8 K, where still $I_c = 0$, there is an overall increase of noise particularly towards lower frequencies (Fig. 7).

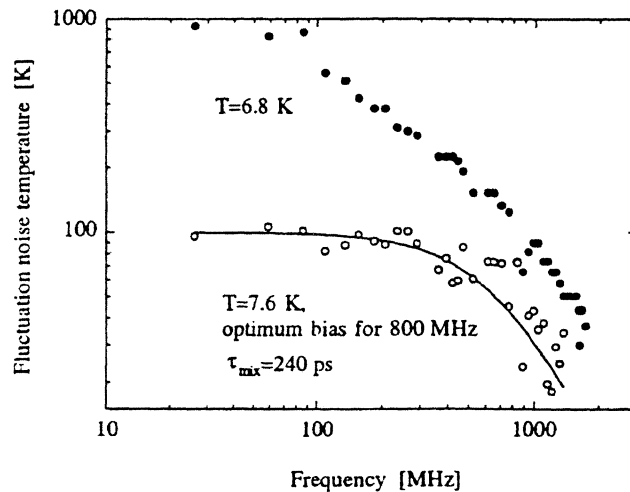


Fig. 7. Output noise temperature due to thermal fluctuation of the electron temperature for sample #A. At 7.6 K this noise shows the same frequency dependence as the IF signal and is about 100 K within the IF band, while for lower temperatures, the noise increases, particularly at lower frequencies.

Fig. 8 gives a general idea of how the output noise is reduced with bias and through heating of the film by different levels of pump power as the film approaches the normal state. The physical temperature is 5 K, well below the temperature when the output noise is flat within the IF-band. From the inset in Fig. 8 it is seen that heating by LO power at this low temperature gives an IV-characteristic with much lower differential resistance than what is obtained by thermal heating of the device. The heating is thus not uniform. We can say very little on the origin of the enhanced noise towards lower temperatures, where we meet a domain contribution, Figs. 7 and 8. It is probably different from the equilibrium thermal fluctuation mechanism and can not be described by the same formulas as the thermal fluctuation noise temperature [17].

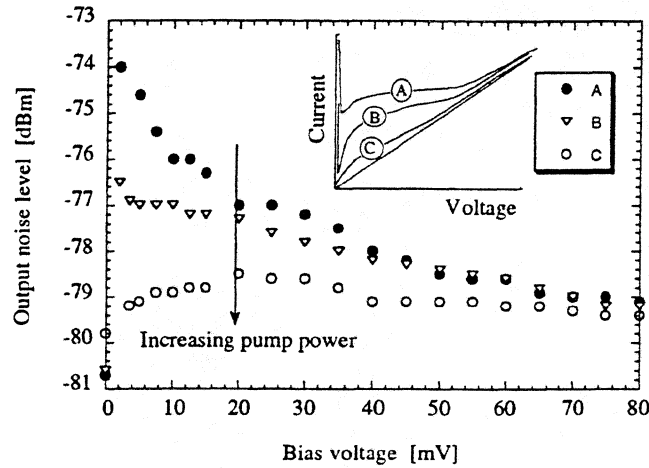


Fig. 8. Output noise level as a function of bias voltage and pump power. The insert shows the IV-characteristics for the different pump levels A, B and C. level A<B<C.

The contribution from $T_{FL}+T_J$ to the double sideband receiver noise temperature within the IF band is given by

$$T_{mix,DSB} = \frac{1}{2G}(T_{FL} + T_J)(1 - L) \approx 200 \text{ K}, \tag{9}$$

where G is the estimated intrinsic conversion gain including IF losses $\approx -6.5 \pm 1$ dB.

Measurements of sample #A with a hot/cold (295/80 K) load facing the input signal port, gave a DSB receiver noise temperature of about 3000 K. These measurements were made within the band of the cooled IF-amplifier (680-920 MHz). This is outside the maximum -3 dB bandwidth of device #A ($f_{IF}=680$ MHz). From Fig. 3 it is seen that in the middle of the amplifier band (800 MHz), and for a physical temperature about 1 K below T_c , the mixer conversion is reduced to about $L_{BW} \approx 4$ dB below the conversion at low frequencies $L_{int} \approx 7$ dB (given by Eq. 1). In Fig. 7 it is seen that also the noise contribution from temperature fluctuations has decreased, from 100 K to about 50 K at

800 MHz. $R(800) \approx 70 \Omega$, thus L is reduced from 0.155 to ≈ 0.05 (Fig.5). From Eq. 9 we then obtain $T_{mix,DSB} = 360 \text{ K}$ at 800 MHz. *Comparing this with the DSB noise temperature obtained from hot/cold measurements, 3000 K, gives that we have an additional loss on the RF side and in the mixer itself of about 8 dB. In TABLE I we have estimated the RF losses to about $L_{RF} \approx 6 \text{ dB}$, about $\frac{3}{2}$ dB below this value.

The noise contribution of the IF chain with the cooled amplifier was again measured using the mixer device as a resistive load. The device is thus heated to its normal state in a temperature range 3-10 degrees above the critical temperature T_c , where the output noise level was measured for several temperatures. No bias current is applied to be sure there will be no noise contribution from the device other than the Johnson noise. The output power had the expected linear dependence on temperature, and gave a noise contribution from the IF chain equal to 12 K.

With sample #B it was possible to measure the mixer noise within the bandwidth of the mixer $f_{max} \approx 1 \text{ GHz}$. The DSB receiver noise temperature was as high as 4700 K but the output noise temperature due to thermal fluctuations was not more than $T_{FL} \approx 50 \text{ K}$. However, as was said previously, the intrinsic conversion gain was much worse for sample #B, -14 dB compared to #A. With $R_d = 100 \Omega$, $T_c = 11 \text{ K}$ we obtain $T_{mix,DSB} \approx 700 \text{ K}$ from Eq. (9). *Comparing this value with $T_{rec,DSB} = 4700 \text{ K}$ obtained from hot/cold measurements, we have an additional loss of about $\frac{3}{7}$ dB on the RF-side.

Notice that an error is introduced in the calculation of the output noise (Eq. 8) for sample #A outside the IF bandwidth and for sample #B, since here R_d is not equal to R_N . Noise data is summarised in TABLE III.

TABLE III

#	R_d [Ω]	R_d^* [Ω]	R_N [Ω]	G [dB]	G^* [dB]	T_{FL} [K]	T_{FL}^* [K]	T_J [K]	$T_{mix,DSB}$			L_{RF} [dB]
									T_{DSB} [K]	T_{DSB}^* [K]	$T_{DSB}^{(1)}$ [K]	
A	115	80	120	7	11	100	50	8.5	200	360	3000	$\frac{3}{8}$
B	-	100	150	-	14	-	50	11	-	700	4700	$\frac{3}{7}$

* At the IF frequency 800 MHz.

(1) Hot/cold measurement, receiver noise temperature

CONCLUSIONS

With heterodyne measurements of NbN HEB devices integrated with double dipole antennas on quartz substrate lenses, we have shown that it is possible to obtain a bandwidth larger than 1 GHz, and a conversion loss about 7 dB. The output noise is

* Including T_{IF} (12K) and

dominated by electron temperature fluctuations, and has an equivalent temperature of about 100 K, with the same frequency dependence as the IF response. Hot/cold measurements gives a DSB receiver noise temperature of about 3000 K. The small signal IF impedance has been measured and we obtained an impedance time constant in good accuracy with the mixing time constant. The measured low and high frequency impedance equals the values obtained from the IV-characteristic. We have seen indication of two different mixing regimes at low temperatures and high temperatures when the signal frequency $\nu > 2\Delta/h$.

The performance of the NbN HEB device can be improved in many ways. The RF coupling losses should be possible to reduce by several dB. NbN films on quartz are of worse quality than films on sapphire or silicon. Thus we expect improved results for NbN devices on the latter substrates, where a sharp superconducting transition (dR/dT is large) can be obtained also for films with higher T_c . More experiments have to be performed to find out if it is possible to obtain both the low output noise of sample #B with the better conversion of sample #A. Further improvement is also expected for signal frequencies $\nu > 2\Delta/h$.

ACKNOWLEDGEMENT

We are greatly thankful to B. Voronov and V. Siomash for manufacturing of NbN films. This work was supported by the Swedish National Board of Industrial and Technical Development (NUTEK), and by the Russian Council on High-Tc Problems under Grant no. 93169. The research was made possible in part by Grant no. NAF000 from the International Science Foundation.

REFERENCES

- [1] T. W. Crowe, R. J. Mattauch, H. R. Röser, W. L. Bishop, W. C. B. Peatman, and X. Liu, "GaAs Schottky Diodes for THz Mixing Applications," *Proc. IEEE*, vol. 80, pp. 1827-1841, 1992.
- [2] E. R. Brown, J. Keene, and T. G. Phillips, "A Heterodyne Receiver for the Submillimeter Wavelength Region Based on Cyclotron Resonance in InSb at Low Temperatures," *Int. J. Infrared Millimeter Waves*, vol. 6, pp. 1121-1138, 1985.
- [3] M. J. Wengler, "Submillimeter-Wave Detection with Superconducting Tunnel Diodes," *Proc. IEEE*, vol. 80, pp. 1810-1826, 1992.
- [4] J. X. Yang, F. Agahi, D. Dai, C. F. Musante, W. Grammer, K. M. Lau, and K. S. Yngvesson, "Wide-bandwidth electron bolometric mixers: a 2DEG prototype and potential for low-noise THz receivers," *IEEE Trans. Microwave Theory Tech.*, vol. 41, pp. 581-589, 1993.
- [5] E. M. Gershenson, G. N. Gol'tsman, I. G. Gogidze, A. I. Elant'ev, B. S. Karasik, and A. D. Semenov, "Millimeter and submillimeter range mixer based on electronic heating of superconducting films in the resistive state," *Sov. Phys. Superconductivity*, vol. 3, pp. 1582-1597, 1990.
- [6] H. Ekström, B. Karasik, E. Kollberg, and S. K. Yngvesson, "Conversion Gain and Noise of Nb Superconducting Hot Electron Mixers," *IEEE Trans. Microwave Theory Tech.*, vol. 43, 1995. (in press)

- [7] A. Skalare, W. R. McGrath, B. Bumble, H. G. LeDuc, P. J. Burke, A. A. Verheijen, and D. E. Prober, "A Heterodyne Receiver at 533 GHz using a Diffusion-Cooled Superconducting Hot Electron Bolometer Mixer," *IEEE Trans. Appl. Superconductivity*, vol. 5, 1995. (in press)
- [8] D. E. Prober, "Superconducting terahertz mixer using a transition-edge microbolometer," *Appl. Phys. Lett.*, vol. 62, pp. 2119-2121, 1993.
- [9] A. Skalare, H. van de Stadt, T. de Grau, R. A. Panhuyzen, and M. M. T. M. Dierich, "Double dipole antenna SIS receivers at 100 and 400 GHz," presented at 3rd Int. Symp. on Space THz Technology, 1992.
- [10] D. F. Filipovic, S. S. Gearhart, and G. M. Rebeiz, "Double-slot antennas on extended hemispherical and elliptical silicon dielectric lenses," *IEEE Trans. Microwave Theory Tech.*, vol. 41, pp. 1738-1749, 1993.
- [11] B. M. Voronov, G.N.Gol'tsman, E. M. Gershenson, L. A. Seidman, T. O. Gubkina, and V. D. Siomash, "Superconducting properties of ultrathin NbN films on different substrates," *Superconductivity: Physics, Chemistry, Engineering*, vol. 7, pp. 1097-1102, 1994. (in Russian)
- [12] A. F. Andreev, *Sov. Phys. JETP*, vol. 19, pp. 1228, 1964.
- [13] F. Arams, C. Allen, B. Peyton, and E. Sard, "Millimeter Mixing and Detection in Bulk InSb," *Proc. IEEE*, vol. 54, pp. 308-318, 1966.
- [14] Y. P. Gousev, G.N. Gol'tsman, A. D. Semenov, E. M. Gershenson, R. S. Nebosis, M. A. Heusinger, and K. F. Renk, "Broadband ultrafast superconducting NbN detector for electromagnetic radiation," *J. Appl. Phys.*, vol. 75, pp. 3695-3697, 1994.
- [15] A. I. Elant'ev and B. S. Karasik, "Effect of high frequency current on Nb superconducting film in the resistive state," *Sov. J. Low Temp. Phys.*, vol. 15, pp. 369-383, 1989.
- [16] H. Ekström and B. Karasik, "Electron Temperature Fluctuation Noise in Hot-Electron Superconducting Mixers," *Appl. Phys. Lett.*, accepted.
- [17] B. S. Karasik and A. I. Elantev, "Analysis of the Noise Performance of a Hot-Electron Superconducting Bolometer Mixer," presented at 6th Symp. on Space Terahertz Tech., Pasadena, USA, 1995.

HOT ELECTRON DETECTION AND MIXING EXPERIMENTS IN NbN AT 119 MICROMETER WAVELENGTH

E. GERECHT, C.F. MUSANTE, R. SCHUCH, C.R. LUTZ, JR., AND K.S. YNGVESSON

Department of Electrical and Computer Engineering, University of Massachusetts at Amherst,
Amherst, MA 01003

E.R. MUELLER AND J. WALDMAN

Submillimeter Technology Laboratory, University of Massachusetts at Lowell Research Foundation,
Lowell, MA 01854

G.N. GOL'TSMAN, B.M. VORONOV, AND E.M. GERSHENZON

Department of Physics, Moscow State Pedagogical University, Moscow 119882, Russia

ABSTRACT

We have performed preliminary experiments with the goal of demonstrating a Hot Electron Bolometric (HEB) mixer for a 119 micrometer wavelength (2.5 THz). We have chosen a NbN device of size 700 x 350 micrometers. This device can easily be coupled to a laser LO source, which is advantageous for performing a prototype experiment. The relatively large size of the device means that the LO power required is in the mW range; this power can be easily obtained from a THz laser source. We have measured the amount of laser power actually absorbed in the device, and from this have estimated the best optical coupling loss to be about 10 dB. We are developing methods for improving the optical coupling further. Preliminary measurements of the response of the device to a chopped black-body have not yet resulted in a measured receiver noise temperature. We expect to be able to complete this measurement in the near future.

I. INTRODUCTION

The on-going development of Hot Electron Bolometric (HEB) mixers [1,2,3,4] is ultimately justified by the fact that such mixers are predicted to achieve lower receiver noise temperatures than existing receivers, starting at frequencies of about 1 THz. SIS mixers are now the lowest-noise receivers up to about 700 GHz, and are making progress in achieving lower receiver noise temperatures between 700 GHz and 1 THz (see Figure 1). At 1 THz and above, the thin film superconductor version of the HEB mixer will have the advantage of not being limited to frequencies below or close to the bandgap frequency

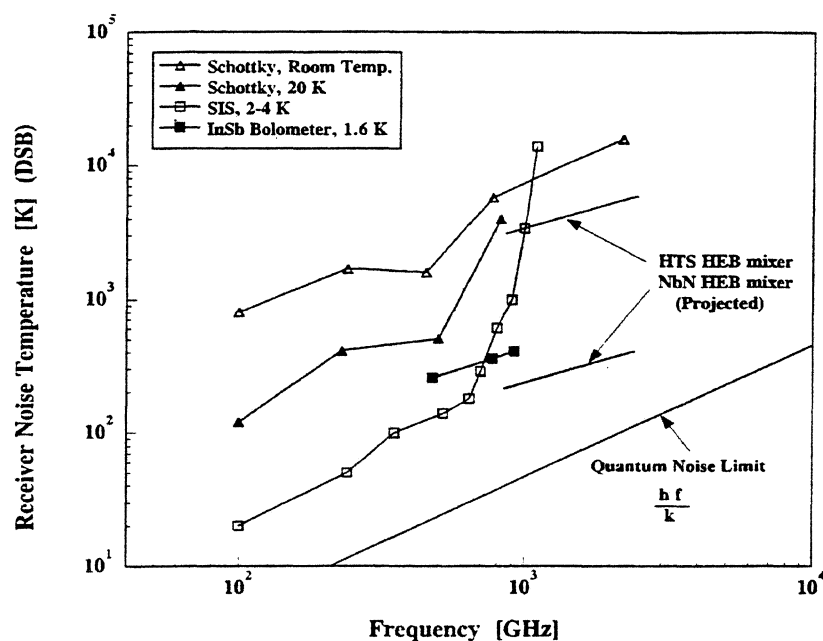


Figure 1: Receiver noise temperature for receivers in the THz frequency range.

of the superconductor. It is appropriate that the initial exploration of HEB mixers takes place at frequencies up to a few hundred GHz, until enough has been learned about the properties of hot electrons (quasi-particles) in thin film superconductors, but at some point an actual THz HEB mixer need also be explored. This paper describes the initial phase of this type of an investigation. We chose to work with NbN films, which have demonstrated IF bandwidths close to 1 GHz as reported in earlier papers; two papers presented at this conference describing millimeter wave NbN HEBs now report IF bandwidths of 2 GHz [5,6], and further studies are likely to improve on this number. The IF bandwidth of NbN HEB mixers thus is now in the range where it can be expected to meet the requirements of practical THz receivers. Additionally, the receiver noise temperature of NbN HEB mixers is predicted to be in the same range as that demonstrated in Nb HEB mixers [3,4]. These facts identify NbN as the most promising HEB material in which the hot electrons in the device are cooled by emission of phonons to the substrate [2].

Submillimeter gas lasers, pumped by CO₂-lasers, can produce output powers of a few mW to 100 mW or more at discrete frequencies from 1 to several THz. They are thus ideal laboratory sources of LO power for initial experiments with NbN HEB mixers. We have chosen to work with the 118.83 micrometer wavelength line of methanol (a frequency of 2.52 THz), using a modified Apollo laser, making it possible to utilize direct focusing of the laser onto a device of size 700 micrometers by 350 micrometers as shown in Figure 2. The device consists of about 175 strips of NbN, which have a width of 1 micrometer and are spaced by 1 micrometer. Since the strips are very narrow compared with the wavelength, the device

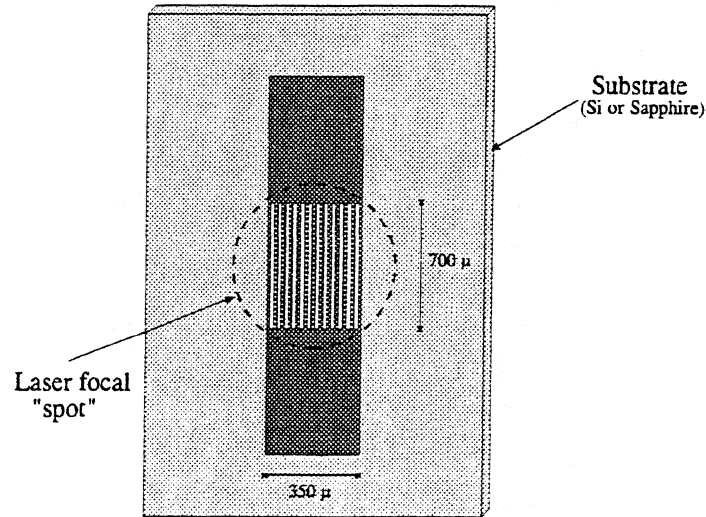


Figure 2: NbN device for 2.5 THz mixer.

absorbs THz power as a uniform resistive sheet. The device size was chosen to match the size to which the laser beam could easily be focused.

We have demonstrated strong detection in this device at 2.5 THz. We have also developed methods for obtaining good optical coupling to a large device of this type, even when the equivalent surface resistance of the film is quite high (several $k\Omega/\text{square}$). The theoretical coupling has been derived and agrees with our preliminary measurements. Further experiments will be performed in the near future which are expected to demonstrate improved coupling. We also describe our preliminary attempts at measuring the receiver noise temperature of the mixer and our plans for future experiments.

II. DEVICE FABRICATION

The devices were fabricated from NbN films which were from 30 to 70 Å thick. The NbN films are DC magnetron sputtered on substrates of either silicon or sapphire. We chose these substrates since it had been shown [7] that thin NbN films on these substrates have high critical temperatures (T_c) and a sharp transition (ΔT_c). Theory indicates that the highest conversion gain is obtained for films with small ΔT_c . In contrast, almost all other work on NbN HEB mixers has been performed with NbN on quartz substrates which generally results in lower T_c values and a wider transition. Typical films on sapphire have T_c of about 14 K for $t = 70$ Å and 12.5 K for $t = 50$ Å. The transition width may be as narrow as 0.2 K for 70 Å films and 0.35 K for 50 Å films. Surface resistance values for the films vary from 220 Ω/square for 70 Å thickness to 420 Ω/square for 50 Å. The devices should have a surface resistance of about twice these values due to the 50% filling factor. Transition temperatures for films on silicon are slightly lower, and ΔT_c 's slightly wider compared with films of the same thickness on sapphire. The NbN

films remain superconducting down to 30 Å thickness, with T_c values above 4.2 K. The particular range of thicknesses was chosen in anticipation of achieving bandwidths of 1-2 GHz. Generally, the thinner films have wider bandwidths until a limit is reached, for which the bandwidth becomes independent of the thickness. The critical thickness for which this happens is known for Nb, but not for NbN, on the above substrates. The quality of the films is also important for good mixer performance and has been steadily improved in the last couple of years. We are in the process of measuring the bandwidth of devices with different film thickness in a microwave setup [8]. Experience with microwave measurements on other HEB mixers indicates that the bandwidth measured is close to that found in actual mm-wave mixers [6].

The devices are contacted by pressing indium onto the contact regions. They are then mounted onto a copper post, which is connected at the other end to the cold plate of an IRLABS liquid helium dewar. A heater and temperature sensor are also attached to the copper post close to the device.

III. OPTICAL COUPLING TO LARGE DEVICES

In order to calculate the optical coupling to one of our devices, we use a plane wave approach. Plane wave propagation in the different media involved is modeled by TEM transmission lines of the appropriate impedance with the help of a commercial software package (Hewlett-Packard's MDS). We have studied three configurations, as shown in Figure 3a, 3b and 3c. The configuration in Figure 3a is the NbN film on a substrate, which has thickness of about 0.5 mm. The fraction of optical power coupled to an infinite film as a function of the surface resistance of the film is plotted in Figure 4 (the dotted curve). Note that the surface resistance of the film at 2.5 THz is equal to or a little less than the normal state surface resistance, since the frequency is well above the bandgap frequency.

Improved coupling can be obtained by forming a $\lambda/4$ coating on the back side of the substrate as indicated in Figure 3b and Figure 4 (the full drawn curve). The radiation should then be incident from the coated side. We have produced a film of the required thickness (16 μ m) by spin coating with the polymer PPQ (polyphenylquinoxalin)¹. Three consecutive spinings are required. PPQ has a refractive index of 1.76, measured in the visible region. Its exact THz properties will be measured in the near future, but are not expected to differ very much.

A second method for matching THz power to a large device can be used in the case of silicon substrates (see Figure 3c). This method consists of etching a well in the silicon substrate behind the device to a depth such that the remaining thickness is $\lambda/4\sqrt{\epsilon_r} \approx 8.7\mu$ m and then covering this well with conducting metal. The well forms a "back-short" behind the device which is particularly effective in improving the coupling to a thin film device, as demonstrated in Figure 4 (the dash-dot curve). We are presently experimenting with techniques for etching such back-shorts. The calculations in Figure 4 have been done for silicon substrates; very similar results would be obtained for the sapphire case, since the dielectric constants are quite close. There will also be another factor involved in the optical coupling to the actual device which can be obtained by convoluting the (gaussian) form of the laser focal spot with the shape of the device. This factor is roughly 50% or a little larger.

¹ PPQ is a trade name of the CEMOTA Corp., Vernaison, France

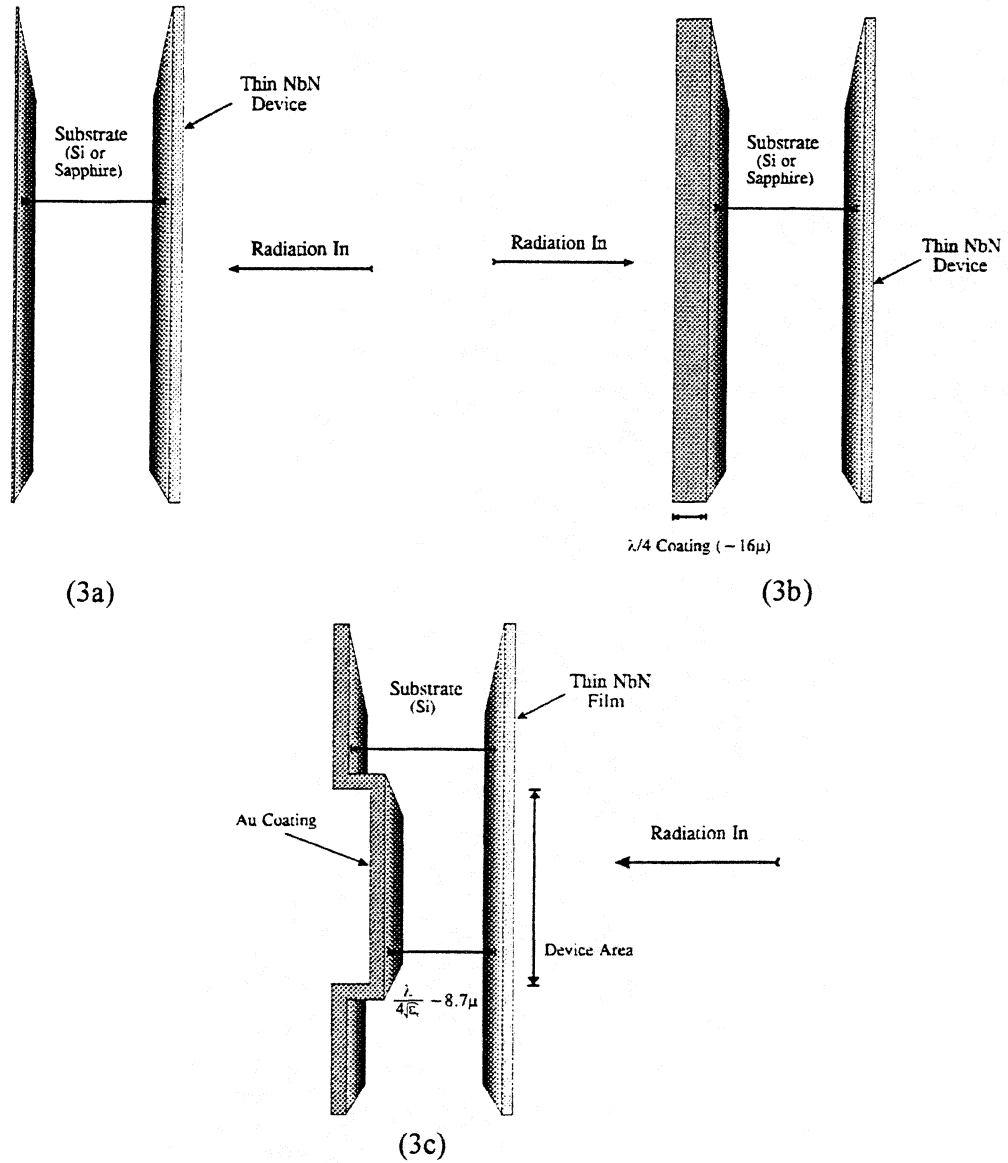


Figure 3: Different configurations for 2.5 THz NbN mixers: a) with no matching layer. b) with PPQ matching layer. c) with etched "back-short".

IV. OPTICAL SETUP

The optical setup is arranged as shown in Figure 5. The THz laser has a maximum output power of 100 mW (CW) on the 119 μ m line. The laser power output was increased to this level by utilizing a capacitance grid type uniform output coupler [9]. A mylar beam splitter transmits 40% of the laser power, while diverting 60% into a matched load. The laser beam is then focused by an off-axis paraboloidal mirror through a 0.75 mm polyethylene widow into the dewar. Shorter IR wavelengths are further

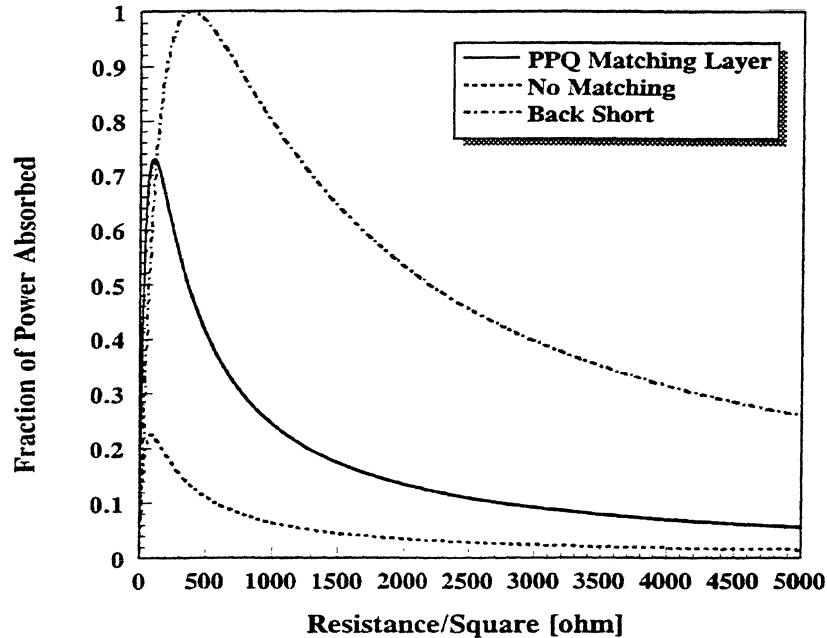


Figure 4: Power coupling to NbN device for different configurations.

attenuated by a sheet of black polyethylene at 77 K. The beamsplitter allows radiation from a hot-cold load to be directed into the beam path. This blackbody radiation is derived by chopping between a room temperature absorber and a liquid nitrogen bath. The device is biased through a cold bias tee connected through an isolator to a broadband cooled HFET amplifier with close to 30 dB gain and about 90 K noise temperature (including isolator losses). The IF system bandwidth is limited by the circulator to 950 - 1400 MHz. After further amplification, the IF power is measured with a microwave detector followed by a lock-in amplifier with its reference derived from the chopper.

The setup is aligned by using the HEB device itself as a detector and observing the signal through the bias port. The device is biased close to T_c for maximum responsivity, which is of the order of 10's of V/W. This makes it easy to find the detector position and maximize the detected signal for alignment.

V. EXPERIMENTAL RESULTS AND DISCUSSION

We have detected the effect of the laser power on the IV-characteristics of two devices: Device A with R/square of 5 k Ω and device B with R/square of 1 k Ω . These initial devices have somewhat lower T_c 's and also a higher resistance. The predicted optical coupling factors for the two devices are about 1.5% and 7%, respectively. The actual coupled power can be measured on the I-V curves by using the assumption that DC and RF power have identical effects in terms of heating the electrons [3]. An example

of measured I-V curves is given in Figure 6. The laser power incident outside the dewar window was measured with a large area power meter. In the recording of Figure 6, the power absorbed by the device was 2 mW while the power measured in front of the offset paraboloid mirror was 20 mW. We can thus estimate a total optical coupling loss of 10 dB, which includes small losses in the window and the black polyethylene sheet. Similar measurements for device A gave 20 dB total optical loss. These values agree quite well with theoretical predictions. The coupling loss may be improved slightly with the range of resistance values that are possible with films of thicknesses up to 70 Å. However, a more substantial improvement can be obtained by using the matching techniques described in Section III. From Figure 4 we can predict coupling loss of 4 to 5 dB by using the PPQ layer, and better than 1 dB with the backshort technique. We are in the process of preparing for such experiments.

With the present optical coupling loss of 10 dB, it should be possible to measure the receiver noise temperature. The first such measurements have resulted in extraneous signals in which a fraction of the laser power is diverted toward the chopper and gives rise to a modulation of the power at the detector, which in turn changes its impedance and sends a chopped signal through the IF amplifier. Further

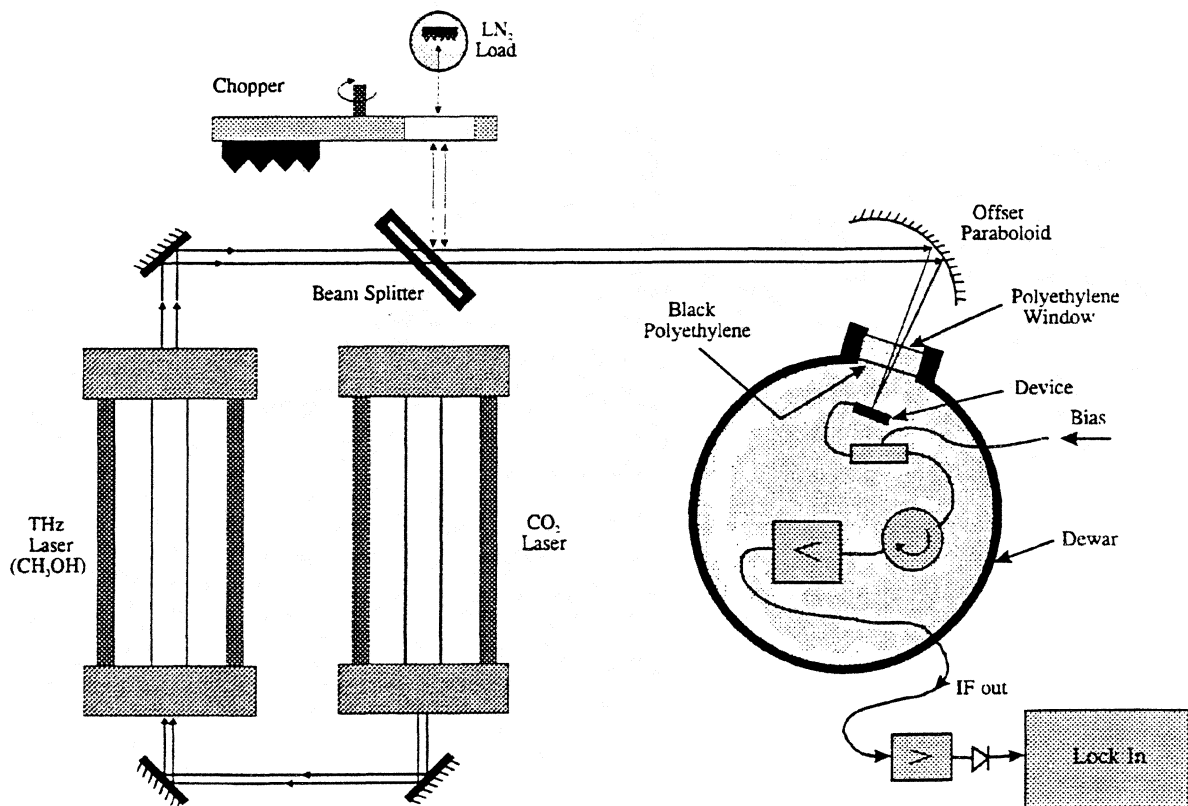


Figure 5: Optical layout of the noise temperature measurements.

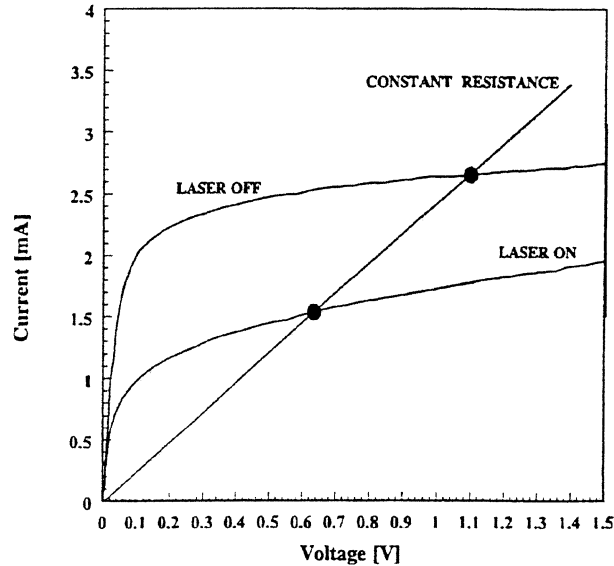


Figure 6: IV curves for NbN device at 11.3K. ($T_c = 11.8K$)

refinements in the system will eliminate such extraneous signals and allow us to measure the noise temperature of the mixer.

A more convenient method of measurement for THz mixers involves the use of two laser sources. This can be accomplished by using laser lines from different gases which have accidental near-coincidences. A more elegant technique utilizes a sideband generator such as the one described by Mueller and Waldman [10]. This configuration is illustrated in Figure 7. In our future experiments we also plan to focus the laser and blackbody power through an extended hemispherical lens and couple a device to a log-periodic antenna behind this lens. The LO power required will then decrease to the μW level, due to much smaller size of the device in this case.

VI. CONCLUSION

We have shown that 2.5 THz laser power can be coupled to a large (700 x 350 micrometer) NbN HEB device with a best coupling loss of about 10 dB. The changes induced by the laser power on the I-V curve of the device are similar to those obtained in efficient NbN mixers operated at lower frequencies, which leads us to believe that we should be able to demonstrate mixing in this device. Experiments are under way to improve the optical coupling further and to measure the receiver noise temperature.

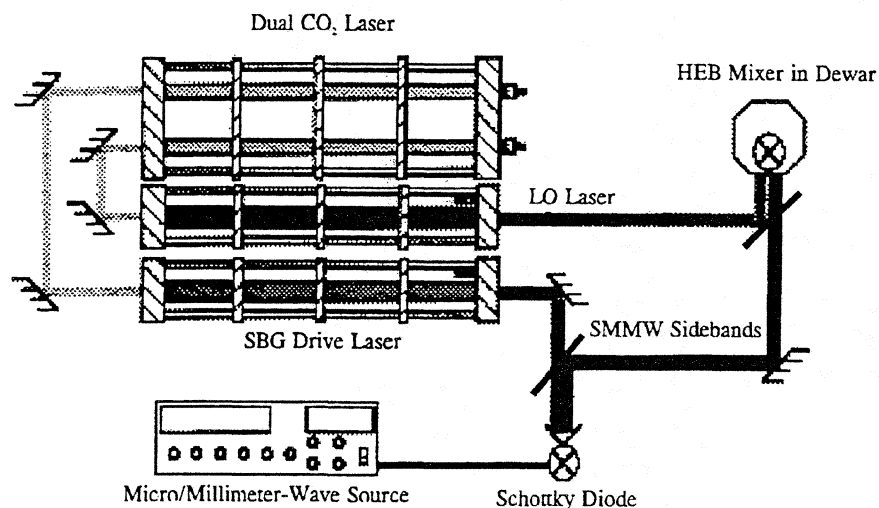


Figure 7: Configuration of a sideband-generator.

VII. ACKNOWLEDGMENTS

We acknowledge support from NSF International Programs grant ECS-9313920 and a University of Massachusetts Faculty Research Grant. We also would like to thank Professors Neal Erickson, Department of Physics and Astronomy, University of Massachusetts, Amherst, for lending us equipment, and Professor Andrew Harris from the same Department for equipment loans and fruitful discussions on the topic of THz receivers.

VIII. REFERENCES

- [1] E.M. Gershenzon, G.N. Gol'tsman, I.G. Gogidze, Y.P. Gousev, A.I. Elant'ev, B.S. Karasik, and A.D. Semenov, "Millimeter and Submillimeter Range Mixer Based on Electronic Heating of Superconducting Films in the Resistive State," *Soviet Physics: Superconductivity*, 3, 1582 (1990).
- [2] O. Okunev, et al., "NbN Hot Electron Waveguide Mixer for 100 GHz Operation," *Proc. Fifth Int. Symp. Space THz Technology*, Ann Arbor, MI, p 214 (May 1994).
- [3] H. Ekstrom et al., "Conversion Gain and Noise of Niobium Superconducting Hot-Electron Mixers," *IEEE Trans. MTT*, in press (1995).

- [4] D.E. Prober, "Superconducting Terahertz Mixer Using a Transition-Edge Microbolometer," *Appl. Phys. Lett.*, 62, 2119 (1993). Also see Skalare et al., "Heterodyne Detection at Submillimeter Wavelengths Using Diffusion-Cooled Hot-Electron Bolometric Mixers," this conference.
- [5] O. Okunev et al., "Performance of Hot-Electron Superconducting Mixer for Frequencies Less Than the Gap Energy: NbN Mixer for 100 GHz Operation," this conference.
- [6] J. Kawamura et al., "NbN Hot-Electron Mixer Measurements at 200 GHz," this conference.
- [7] B.M. Voronov, G.N. Gol'tsman, E.M. Gershenzon, L.A. Seidman, T.O. Gubkina, and V.D. Siomash, "Superconducting Properties of Ultrathin NbN Films on Different Substrates," *Superconductivity: Physics, Chemistry, Engineering*, vol. 7, pp. 1097-1102, 1994. (In Russian)
- [8] J. Bergendahl, Honors Project, Department of Electrical and Computer Engineering, University of Massachusetts (1995).
- [9] R. Densing et al., "Effective Far Infrared Laser Operation with Mesh Couplers," *Infrared Physics*, 33, 219 (1992).
- [10] E.R. Mueller, and J. Waldman, "Power and Spatial Mode Measurements of Sideband Generated, Spatially Filtered, Submillimeter Radiation," *IEEE Trans. Microw. Theory Techniques*, MTT-42, 1892 (1994).

ANALYTICAL TREATMENT AND OPTIMUM PARAMETERS FOR DSB SIS RECEIVERS

Pascal FEBVRE

DEMIRM - Observatoire de PARIS
61, avenue de l'Observatoire - 75014 PARIS - FRANCE

ABSTRACT

The quantum theory of mixing developed by Tucker [1] has been widely used to predict SIS mixer performance using either the three or five-frequency approximations. Most of the current SIS receiver developments above 500 GHz use matching circuits to resonate the SIS intrinsic parasitic capacitance at the operating frequency. The three-frequency approximation is then a good assumption since the harmonics of signal, image and Local Oscillator (LO) frequencies are shunted by the SIS specific capacitance which is not resonated any more by the matching circuit. Moreover the SIS mixer is operated as a Double Side-Band (DSB) mixer as long as the Intermediate Frequency (IF) is much lower than the instantaneous RF bandwidth at the resonance frequency of the matching circuit (low IF limit). With these two assumptions the IF output impedance of the mixer and the conversion gain can be calculated analytically [1].

It has been already shown [2] that the contours of constant IF conductance are circles in the RF source admittance plane (G_s , B_s). With some additional assumptions the contours of constant DSB conversion gain are also circles [2]. We present here the full analytical formalism including contours of constant mixer and receiver noise temperature. We then derive analytically the minimum receiver (and mixer) noise temperature and the source admittance associated to it. Also all the parameters (bias voltage, LO power, RF admittance, IF conductance) for minimum receiver and mixer noise are given versus LO frequency. We discuss the location of the minimum mixer noise admittance in the (G_s , B_s) plane and the way SIS receivers can be optimized above the gap frequency.

- [1] J.R. Tucker and M.J. Feldman, Rev. Mod. Phys. **57**, 1055 (1985)
- [2] P. Febvre, Proc. 5th THz Conf., Univ. of Michigan, May 1994.

A Fixed Tuned Low Noise SIS Receiver for the 600 GHz Frequency Band

**C.-Y.E. Tong, R. Blundell, D.C. Papa, J.W. Barrett
S. Paine, and X. Zhang**

Harvard-Smithsonian Center for Astrophysics,
60 Garden St., Cambridge, MA02138.

J.A. Stern, and H.G. LeDuc

Jet Propulsion Laboratory,
Pasadena, CA 91109.

Abstract

A fixed tuned waveguide receiver has been designed and tested in the 600 GHz frequency band. This receiver is a scaled version of the 200 GHz fixed tuned receiver reported previously [1]. Equipped with a corrugated horn, the receiver operates at an IF of 5 GHz. The mixing element is an Nb/AlO_x/Nb SIS junction. Nominal junction size is about 1 μm². On-chip tuning is provided by a 2-section microstrip transformer in series with a short inductor section containing the device. Preliminary measurements show that this receiver has a low noise performance. Using a Martin-Puplett interferometer as the local oscillator diplexer, the DSB receiver noise temperature is about 275 K over most of the 600 GHz frequency band. Further work is under way to perfect the performance of the receiver.

I. Introduction

Fixed tuned waveguide receivers incorporating SIS junctions for the Smithsonian Astrophysical Observatory Sub-Millimeter Array (SMA) have been demonstrated to possess wide-band low-noise performance at frequencies up to 500 GHz [1,2]. Recently, we have scaled the original design for operation in the 600 GHz frequency band. In this report, we shall present the major features of this 600 GHz receiver as well as preliminary test results.

II. Mixer Block Design

Fig. 1 is a detailed drawing of the central portion of the 600 GHz mixer block. Its dimensions are essentially one third of the corresponding dimensions of the 200 GHz mixer block from which it is derived. As in the original design, the reduced height waveguide section (0.373×0.091 mm) is created by mechanical punching. This shorted waveguide section, which forms the fixed backshort tuner of the mixer, measures 0.124 mm in depth. This mechanical layout together with the low-pass IF filters produce a driving point impedance of about 35Ω at the waveguide feed point over the required operating bandwidth.

The mixer block is fitted with an electro-formed corrugated feed horn section that includes a transition from reduced height guide to corrugated guide. The semi-flare angle of the horn is about 11° . The quartz mixer chip, measuring $0.165 \times 0.050 \times 2$ mm, is clamped between the horn section and the mixer block back piece, in a suspended microstrip line configuration parallel to the E-plane of the waveguide. The chip is contacted on both the IF connector side and the ground side by gold plated beryllium copper wire, 0.125 mm in diameter. Since the contact pads on the chip are overlaid with a thin gold layer, no indium is needed to maintain the mechanical contact.

Two grooves are milled on each side of the block along the H-plane of the waveguide. They allow a pair of magnetic pole pieces to come into close proximity of the junction.

III. Junction Design and Tuning

At the center of the mixer chip is the waveguide to thin film microstrip transition. A thin film microstrip coupling network has been designed to couple the junction to the driving point impedance of 35Ω of the waveguide circuitry. As in the lower frequency receivers, the design employs a 2-section transformer plus a short inductive lead in front of the junction.

The insulator of the thin film microstrip line is the 200 nm layer of SiO used to define the size of the Nb/AlO_x/Nb junction. Reproducibility and tolerance considerations dictate a minimum line width of about $2 \mu\text{m}$, implying a maximum characteristic impedance of about 16Ω . This sets a ceiling to the target source impedance of the junction. We have chosen a value of 13Ω , consistent with previous designs. Since the frequency is around the gap frequency of niobium, we assume that the optimum source resistance for the junction is simply its normal state resistance R_N . Therefore, the target value of R_N is also 13Ω .

The ωCR product of the junction is determined by the current density of the junction. A higher current density yields a lower ωCR product and therefore a potentially broader operating band width with the appropriate tuning. We have chosen a target current density of $12 \text{ kA}/\text{cm}^2$. This corresponds to an ωCR product of 4.25 at 650 GHz assuming a junction specific capacitance of $65 \text{ fF}/\mu\text{m}^2$. Considering that the atmospheric window in this frequency band runs from 600 to 720 GHz, corresponding to about 18% bandwidth, it is possible to design a tuning circuit to cover this entire window [3]. At the target current density, a junction size of $1.1 \times 1.1 \mu\text{m}$ is required to give an R_N of 13Ω .

There has been some doubt concerning the losses of niobium thin film microstrip transformer at frequencies approaching the gap frequency. In our case, the total length of the tuning circuit is only about $\lambda_g/2$. The coupling loss is estimated to be less than 0.5 dB.

At the IF frequency, the low impedance section of the transformer behaves as a lumped capacitor and tends to reduce the IF coupling efficiency. The IF of the SMA is 5 GHz, which is considerably higher than the more popular 1.5 GHz IF of most SIS receivers. Consequently, it is important to minimize the IF output capacitance. Instead of having a quarter-wave low impedance section, we have used

a low impedance section with an electrical length of 70° . Even in this configuration the wider section still makes up about half of the total IF output capacitance, which is about 0.3 pF. This is equivalent to a reactance of 100Ω at 5 GHz.

In the lower frequency SMA receivers, the junction is located on a $5 \times 5 \mu\text{m}$ wiring pad. This is necessary for aligning the final wiring layer to the junction in the fabrication process. In the 600 GHz frequency band, this pad corresponds to an additional line of about 10° in electrical length. This length is comparable to the length of the inductive lead in front of the junction. Furthermore, the microstrip width discontinuity between the inductive lead and the wiring pad also adds non-negligible reactance to the tuning circuitry. Therefore, instead of a $2 \mu\text{m}$ wide lead, we have employed a $4 \mu\text{m}$ wide lead, wide enough to align the junction directly on it. The $4 \mu\text{m}$ wide lead is lower in characteristic impedance and is better suited to tune out high capacitive junctions in the 650 GHz frequency range. The predicted return loss of the coupling network is given in Fig. 2.

III. Receiver Noise Measurement

The mixer block is installed in a liquid helium dewar for laboratory noise temperature measurements. The atmospheric window is a 0.5 mm thick Teflon sheet. This is followed by a thin Zitex sheet on the radiation shield as an infrared block. A 90-degree offset parabolic mirror mounted on the cold plate focuses the beam emerging from the corrugated feed onto the local oscillator diplexer. Two additional layers of Zitex infrared filters are inserted in front of the aperture of the corrugated feed horn to ensure that the mixer chip is not heated by infrared radiation focused by the optical grade parabolic mirror.

Local oscillator power is provided by solid state multipliers pumped by a Gunn oscillator. A cascaded doubler-tripler covers most of our frequency band, from 620 to 710 GHz, with a peak available power of about $100 \mu\text{W}$ at some frequencies. A Martin-Puplett diplexer provides LO/signal diplexing. At frequencies where there is abundant local oscillator power, a wire grid polarizer has also been used for LO injection purposes.

Double-side-band noise temperatures are measured using the standard hot (295 K) and cold (77 K) load method. Linear noise temperatures are computed

from the experimental Y-factor with correction for Planck's radiation law. No corrections has been made for losses in the optics. The IF amplifier has a noise temperature of about 8 K. Measurements are made with a 1 GHz IF bandwidth.

IV. Results and Discussion

The junctions used in the laboratory tests have current densities of around 8 kA/cm^{-2} , lower than the design value. Their normal resistances are in the 20Ω range. At 4.2 K, the gap voltage is typically 2.85 mV, corresponding to a gap frequency of 690 GHz. The subgap to normal state resistance ratio (R_{sg}/R_N) is typically 12.

The lowest noise comes from a junction that is 20% smaller than the nominal size. The measured noise temperature is plotted in Fig. 3. The receiver performs best at around 580 GHz. Noise temperature is generally around 275 K from 625 GHz to 680 GHz. When the junction temperature is lowered to 2.5 K, the receiver noise temperature is reduced by about 30 K at around 600 GHz and by more than 50 K towards 700 GHz. This is clearly related to the proximity to the gap frequency. The use of a polarising grid as LO injector also improves the performance. The lowest noise temperatures measured at 4.2 K are 142 K at 580 GHz and 225 K at 675 GHz.

Fig. 3 also shows a breakdown of the measured noise temperature into input noise (losses in the optics), mixer noise and multiplied IF noise at selected frequencies. It can be seen that input noise contribution is about 100 K or more. This explains why the use of a polarising grid injector considerably reduces the receiver temperature. The possible reasons for the relative high input losses are:

- (a) The 0.5 mm Teflon vacuum window is $1.5\lambda_d$ thick at about 620 GHz. The bandwidth over which its transmission is close to unity is fairly narrow. In fact, at 690 GHz, the power transmission coefficient is only 90%.
- (b) The off-axis parabolic mirror might generate a high level of cross-polarisation. A Martin-Puplett LO diplexer terminates this cross polarisation content at LO port, effectively introducing a room temperature loss.
- (c) The polarising grids used in the LO diplexer may have losses of up to 3% per reflection at 700 GHz. In our setup, the signal beam undergoes 3 reflections in the diplexer.

(d) Misalignment of the diplexer also contributes to the input noise.

In general, the response curve of the receiver shifts in frequency with junction size. The fact that the performance is optimal with a smaller device and that the receiver performs best at the lower part of the band suggests that the value of the junction capacitance ($65 \text{ fF}/\mu\text{m}^2$) used in the design process is too small. Another possibility is that the magnetic penetration depth used in the design may be different from that of the actual value. That is particularly important given that the operating frequency is close to the gap frequency.

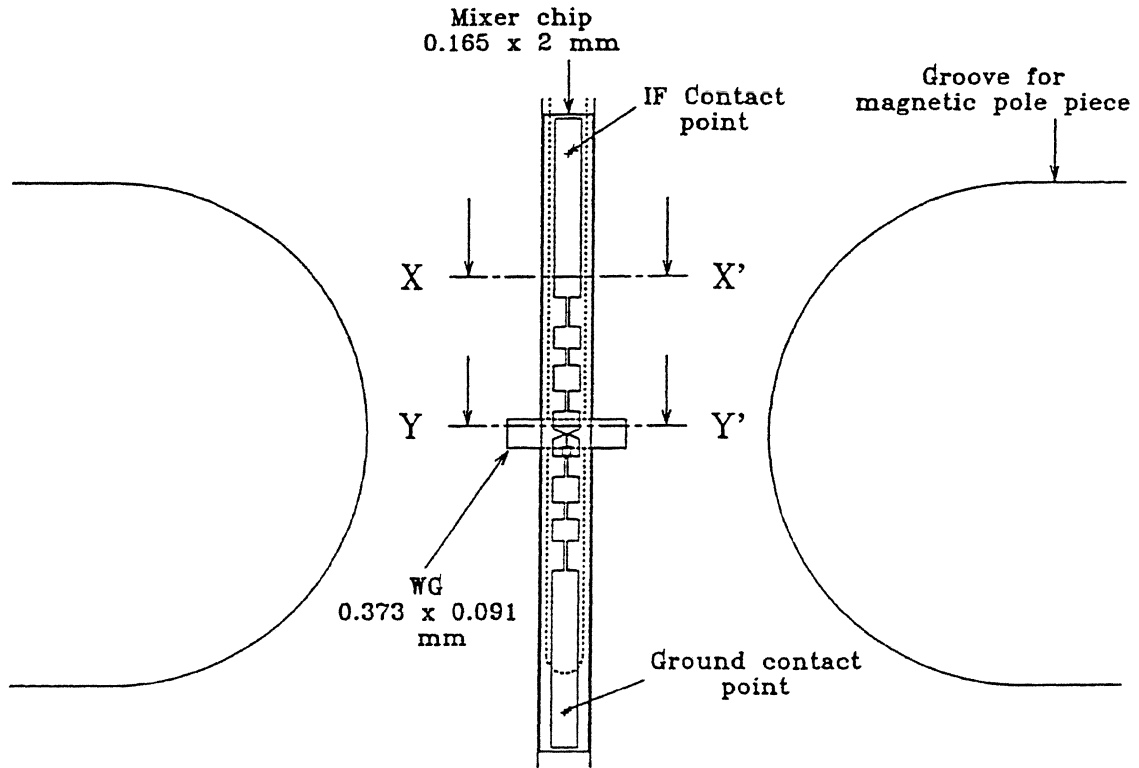
In this receiver, a small resonance is always apparent at around 650 GHz. This feature is fairly independent of junction size. A possible explanation for this is the onset of a surface wave mode in the substrate carrying the junction. In the 200 GHz design, the substrate thickness was 0.125 mm. A strict scaling would require a thickness of $40 \mu\text{m}$ for operation in the 600 GHz frequency band. However, since the thinnest commercially available substrate is $50 \mu\text{m}$, we have decided to forego a lapping step and to use the thicker substrate for simplicity. In practice, the substrate used was $54 \mu\text{m}$ thick. Therefore, the suspended microstrip line is probably not monomode over the entire frequency band. Nevertheless, the effect of the surface wave mode is not prohibitively damaging.

V. Conclusion

Preliminary tests have been made on a 600 GHz fixed tuned receiver employing a niobium SIS junction with an integrated tuner. The receiver has a double-sideband noise temperature of around 275 K over most of the 600 - 700 GHz frequency band. Input losses account for about 100 K of the total noise. We are currently making improvements to the receiver optics and we are also working on an improved tuner to reduce the noise temperature of the system.

Acknowledgement

We would like to thank Mr. Michael Smith for his superior technical assistance in the fabrication of the mixer block.



SMA 660 GHz Mixer Block

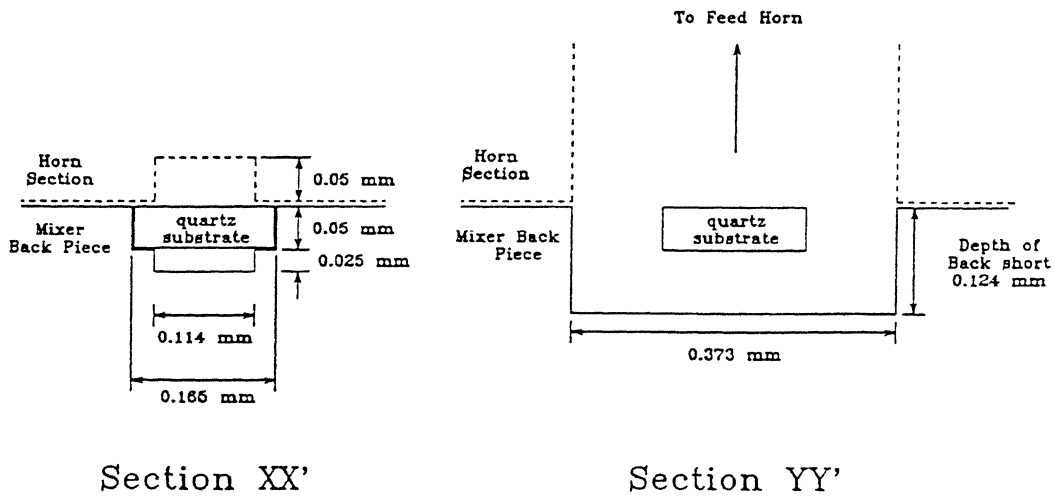


Fig. 1 Details of the central portion of mixer block showing mixer chip

Reference

- [1] R. Blundell *et al*, A wideband fixed-tuned SIS receiver for 200 GHz operation, *Proc. 5th Intl. Symp. Space THz Tech.*, pp. 27-37.
- [2] R. Blundell *et al*, A fixed tuned SIS receiver for the 400 GHz operation, *these proceedings*.
- [3] A.R. Kerr, Some fundamental and practical limits on broadband matching to capacitive devices and the implications for SIS mixer design, *IEEE Trans. Microwave Theory & Tech.*, vol. 43, pp. 2-13, 1995.

Theoretical Performance of Integrated Tuner of 660 GHz SIS Mixer

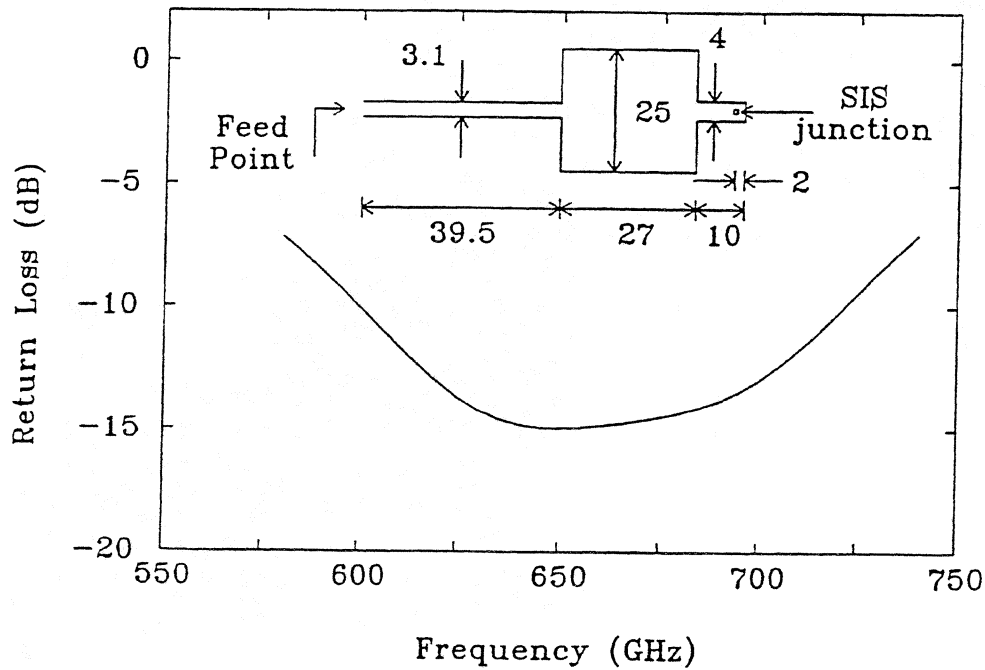


Fig. 2 Predicted return loss of tuning circuit for a junction with $R_N = 13\Omega$ and $C_J = 80$ fF.

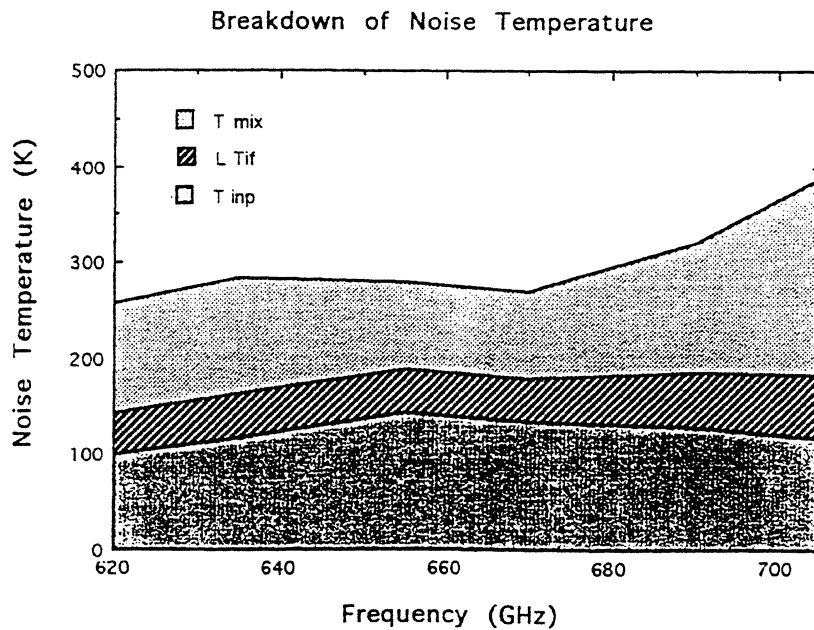
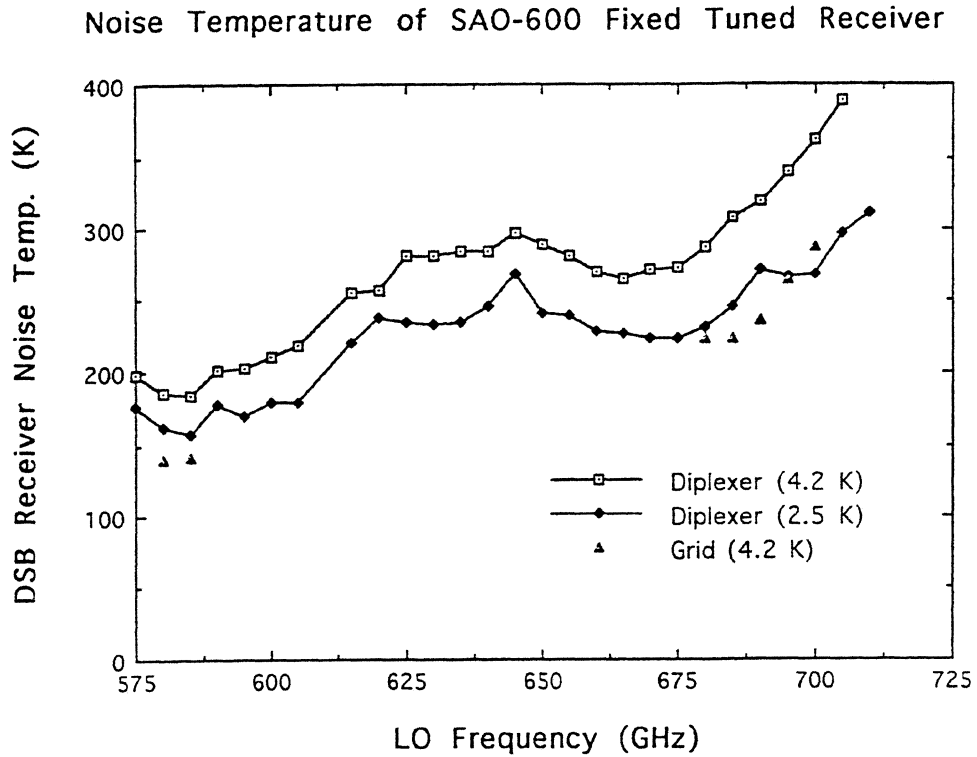
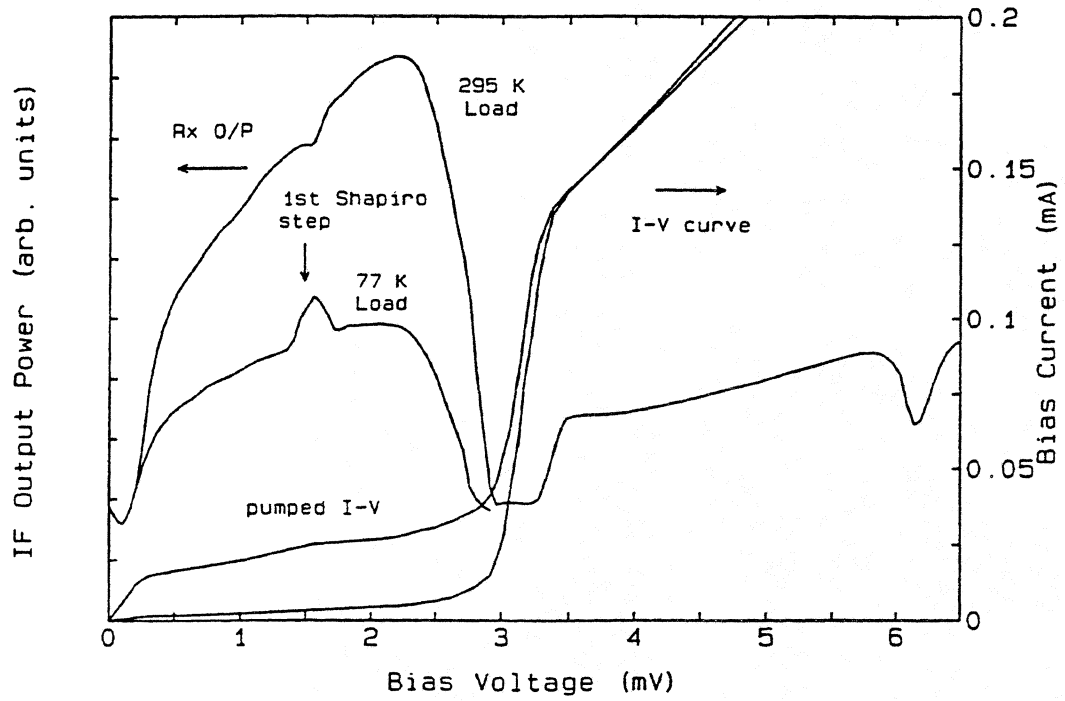


Fig. 3 DSB noise Temperature of the receiver as a function of LO frequency and its composition at selected frequencies. The breakdown is given for the case in which a Martin-Puplett LO diplexer is used, the device being at 4.2 K.

Fig. 4 Quasi-Particle Mixing with LO at 690 GHz



DESIGN AND CHARACTERIZATION OF TWO-JUNCTION TUNING CIRCUITS FOR SUBMILLIMETER SIS MIXERS

M.C. Gaidis, M. Bin, D. Miller, J. Zmuidzinas
George W. Downs Laboratory of Physics, 320-47
California Institute of Technology, Pasadena, CA 91125

H.G. LeDuc, J.A. Stern
Jet Propulsion Laboratory, 302-231, Pasadena, CA 91109

Abstract

We report on the continuing development of submillimeter quasi-optical slot antenna SIS mixers which use two-junction tuning circuits [1]. The mixers use 10 kA/cm^2 Nb/Al-Oxide/Nb junctions and Nb wiring, and have generated DSB receiver noise temperatures around $5h\nu/k_B$ to 700 GHz, and $16h\nu/k_B$ (620 K) at 798 GHz. We present Fourier-transform spectrometer (FTS) measurements and heterodyne measurements on several such devices. In general, the measured response at frequencies below the gap of Nb is in good agreement with the predicted performance.

Introduction

SIS mixers with Nb-trilayer tunnel junctions offer excellent performance at frequencies below 800 GHz, and should perform competitively at frequencies as high as 1.4 THz [2-5]. Our goal is to develop a suite of ultra-low-noise SIS mixers which cover frequencies from ≈ 400 GHz to more than 1 THz.

At frequencies below the Nb gap (< 700 GHz), existing devices perform quite well [6], but further improvements in noise temperatures remain important. In addition, it is quite useful to be able to predict device performance given the design parameters. One can then optimize the device design for a particular frequency band, and confirm that we indeed understand the physics of the device. Progress in the design and operation of devices in this frequency range is presented below.

At frequencies above the Nb gap, RF photons can break Cooper pairs, resulting in greater signal loss and higher receiver noise temperatures. The loss is particularly important in the slender microstrip lines used to resonate the junction capacitance and to transform the antenna impedance down to the RF junction impedance. However, the actual coupling of radiation into Nb junctions above the gap should still be reasonably efficient -- more than 30% at 800 GHz [7]. In addition to RF loss, one is also affected by increased dispersion at frequencies near the gap. The Nb microstriplines have therefore been carefully designed to ensure the desired bandpass is achieved. We demonstrate for the first time that all-Nb SIS receivers can have substantially better performance than GaAs Schottky receivers for the astronomically important CI ($^3P_2 - ^3P_1$) and CO (7-6) transitions near 810 GHz.

Receiver Configuration

Since waveguide mixers become difficult to construct at short submillimeter wavelengths, we have adopted a quasi-optical approach. Here, lenses take the place of waveguide horns, and the incoming radiation is collected by a planar antenna on the SIS mixer substrate [8]. This offers several other advantages, such as on-chip broad-band

lithographic tuning elements, straightforward scaling to yet higher frequencies, and natural adaptation to focal-plane imaging arrays.

A macroscopic view of the receiver is presented in Figure 1; the microscopic description of the mixer chip follows in the next section. The local oscillators (LO) used for our measurements are compact, solid-state, tunable Gunn oscillators with varactor multipliers. The signal and LO are combined with 10 or 25 μm mylar beamsplitters, which couple approximately 8% or 23% (92% or 77%) of the LO (signal) power into the device, respectively, at 810 GHz. Low LO power levels available from our oscillator chain at the higher frequencies often dictates the use of the thicker (25 μm) beamsplitter. Although convenient, the beamsplitter can significantly increase the measured receiver noise temperature.

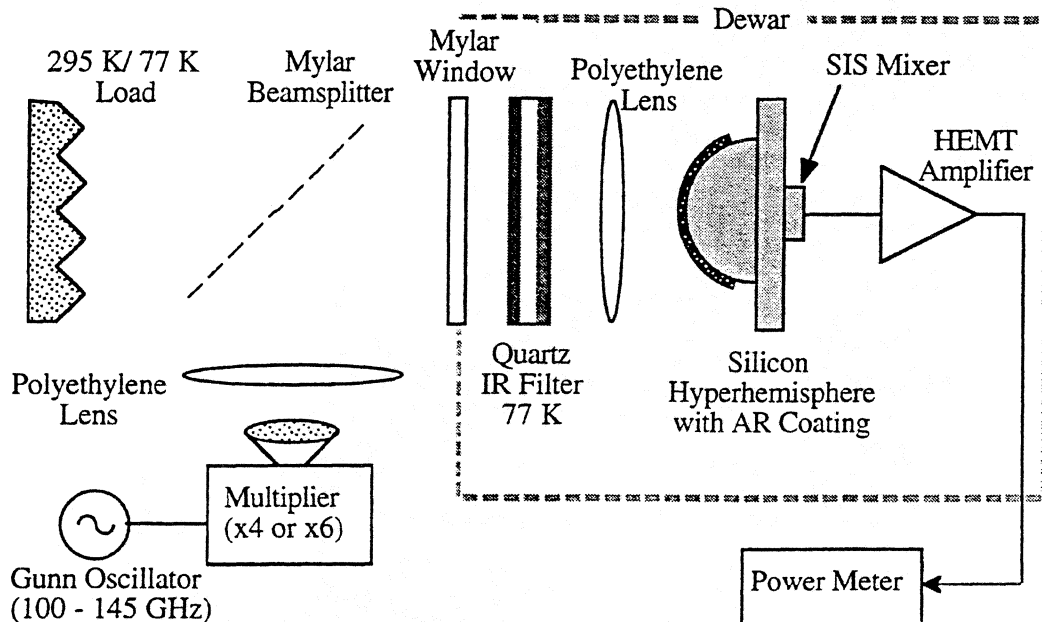


Figure 1: Simplified receiver layout.

The combined signal and LO travel into the vacuum dewar through a 25 μm mylar window at room temperature, followed by a 2.5 mm thick, z-cut quartz IR filter at 77 K. In the 800 GHz band experiments to be discussed below, both sides of this quartz had an additional antireflection (AR) coating which was optimized for ≈ 820 GHz. This coating consists of a ≈ 10 μm thick black Xylan primer sprayed on the quartz, followed by clear Teflon FEP to the thickness required for optimal AR performance [9]. The window and coating withstand repeated thermal cycling, and are quite durable. We have not measured the IR transmission properties, but we note that the dewar helium hold time is limited by thermal conduction along the electronic wiring, rather than radiation through the optical path. For a similar IR filter, with AR coating optimized for 590 GHz, the RF loss (including reflection and absorption loss) was measured at less than 5% at 690 GHz. The normal to the quartz IR filter used in the 800 GHz band experiments is also tilted at a $\approx 5^\circ$ angle with respect to the beam in an effort to suppress Fabry-Perot resonances. (In the 550 GHz band measurements, the quartz IR filter is perpendicular to the beam.)

A polyethylene lens and a silicon hyperhemisphere, AR coated with alumina-loaded epoxy [6,10], transform the $\approx F/17$ input beam to match the broad pattern of the twin-slot

planar antenna. In the near future, we will replace the polyethylene lens with teflon-coated quartz, which should give $\approx 10\%$ gain in coupling efficiency.

The IF output from the mixer is fed to a low-noise amplifier which has a bandwidth of $\approx 1.25 - 1.75$ GHz and a specified noise temperature of 3 K [11]. The amplifier output is sent to room temperature amplifiers and a diode detector which measures the total power in the 500 MHz IF bandwidth.

Mixer Design and Fabrication

The detailed design of the twin-slot planar antenna and the two-junction SIS mixer tuning circuit has been presented elsewhere [1,6]. Figure 2 is a diagram representative of the mixers used in this work. The present mixers are quite similar to earlier designs, except for several right-angle bends in the transformer sections. These bends allow us to better optimize the impedance match between the antenna ($\approx 30 \Omega$) and the tunnel junctions ($\approx 10 \Omega$). We have written a computer program to simulate and optimize the device design. Our circuit model includes the frequency-dependent impedance of the antennas, striplines, and tunnel junctions. The properties of the superconducting microstrip lines are calculated using our previously described method [8], which includes the frequency-dependent surface impedance given by the Mattis-Bardeen theory in the local limit. Future work on the simulator will include RF loss in the antenna.

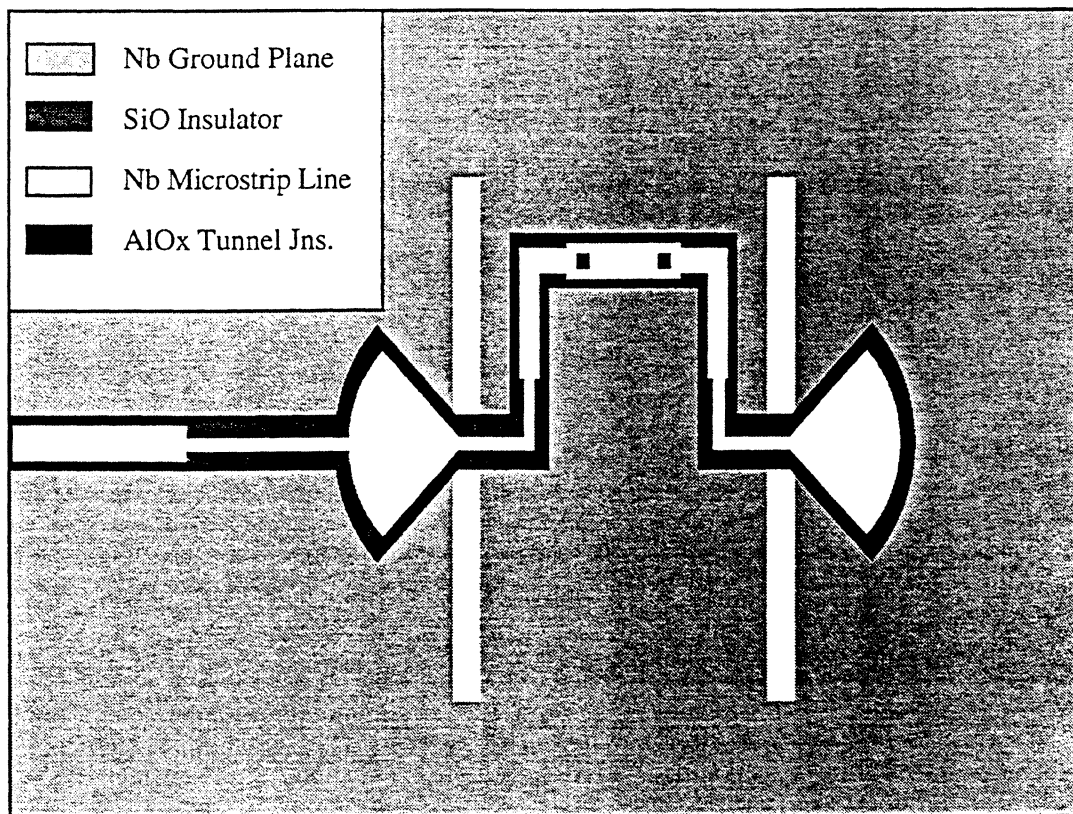


Figure 2: Twin-slot antenna, two-junction SIS mixer design (top view).

The use of antisymmetrically driven tunnel junction pairs simplifies the inductive tuning necessary to resonate the junction capacitance. The resonating inductance for each junction is simply one-half the total inductance joining the two junctions, as the antisymmetric feed creates a virtual ground halfway between the two junctions [1]. Because the junctions are defined in the same lithographic step, misalignment between lithography layers cannot significantly affect the tuning inductance. A misalignment will primarily produce a minor phase difference between the two slot antennas, which results in a very slightly tilted beam -- approximately 2° per μm misalignment, compared to the beam FWHM of 48° .

The low antenna impedance promotes good impedance matching to even relatively low-resistance tunnel junctions. Therefore, we design with junction areas between $1.2 \mu\text{m}^2$ and $2.3 \mu\text{m}^2$, and can utilize JPL's all-optical-lithography junction fabrication process [1,8]. These large area junctions are easier to fabricate than e-beam devices, can be less sensitive to static discharge, and offer adequate bandwidths ($\omega RC \approx 7$ at 700 GHz). One drawback of large junctions is the need for higher LO power -- as much as a factor of 4 more than for typical e-beam defined junctions.

Device designs were generated with the simulation program to cover the frequency range from ≈ 400 GHz to ≈ 800 GHz. To allow for parameter variation, particularly in the junction areas and specific capacitance, we have included three different nominal junction sizes ($1.2 \mu\text{m}^2$, $1.7 \mu\text{m}^2$, and $2.3 \mu\text{m}^2$) for each tuning structure design. Design specifications for the two devices discussed below are presented in Table 1. Note that the design of the 1995 mixers is also adjusted to reduce overall capacitance for broadband IF output (to > 4 GHz).

Parameter	Device 623 (1993)	Device 73 (1995)
Ground Plane	2000 Å Nb	2000 Å Nb
Wiring	2000 Å Nb	2000 Å Nb
RF Choke (IF Output)	Nb microstrip	Nb coplanar
90° Radial Stub Radius	29 μm	36 μm
Slot Antenna Size	154 μm x 7.7 μm	133 μm x 6.7 μm
Slot Spacing	77 μm	67 μm
First Transformer Section (WxL)	3 μm x 25 μm	5.8 μm x 15 μm
Second Transformer Section (WxL)*		3.3 μm x 15 μm
SiO Thickness: Transformer Microstrip	2000 Å	4000 Å
Junction Area	0.9 μm^2	2.3 μm^2
Junction Specific Capacitance	85 fF/ μm^2	65 fF/ μm^2
Junction Resistance–Area Product	15.6 $\Omega \mu\text{m}^2$	26.1 $\Omega \mu\text{m}^2$
Inductor (Between Jn. Centers) (WxL)	6 μm x 22.4 μm	5 μm x 7 μm
SiO Thickness: Inductor Microstrip	2000 Å	2000 Å

*For the 623 device, only one transformer section was used. Neither of these devices utilized right-angle bends in the transformer section. All devices used a 2.5 micron length of microstrip (width equal to inductor width) to connect the last transformer with the inductor.

Table 1: Design parameters for two representative devices.

Receiver Performance

Receiver response as a function of frequency was measured using an FTS system (built in-house) using the mixer as a direct detector. Although we cannot yet reliably measure the absolute response using the FTS, the *shape* of the relative response vs. frequency is quite reliable. The absolute response of different devices is best compared by performing heterodyne measurements. We find that the variation of the noise temperature with frequency correlates well with the response measured on the FTS, so that we can rely heavily on FTS data to select useful devices from a given fabrication run.

Figure 3 illustrates the accuracy with which we can predict mixer response at present. The simulation curves give the fraction of the power received by the antenna which is dissipated in the junction resistances. The vertical scale of the FTS data is arbitrarily adjusted to give the best match to the simulation. This is considered valid, as coupling differences between FTS runs should be frequency-independent.

In general, the agreement is quite good, given the nonidealities present in the measurement: strong water absorption lines at 557 and 752 GHz, and Fabry-Perot resonances from the quartz IR filter spaced approximately 50 GHz apart. (The only correction for optics in the data is for the efficiency of the mylar beamsplitter in the FTS. The frequency-dependent quantum responsivity of the detector, $\propto 1/\nu$, is also corrected for in the figures.) The FTS data presented for device "623" was obtained with a poor-quality black polyethylene A/R coating on the IR filter, and shows considerable Fabry-Perot resonances. The "73" device results are not so affected, presumably because of the more effective teflon A/R coating discussed above, and because of a 10° angle to the IR filter. The deviation between FTS data and simulation at higher frequencies is not well understood at present, but can be partially attributed to antenna losses which were not included in the simulation.

More than ten different device designs have been tested in this manner to date, and all agree with simulations to the degree shown in Figure 3, thus indicating that the simulation method is reasonably reliable. For a given fabrication run, the junction capacitance is the only variable parameter. When this is fixed by FTS data from one device, the FTS data from remaining devices in the batch will match the simulations with no fittable parameters (other than the arbitrary amplitude scaling). Junction capacitance has been our largest uncertainty, possibly being affected by small amounts of high-dielectric-constant Nb oxides in the tunnel barrier. It appears, however, that a recent change in the fabrication process -- using DC sputtering for the Al junction barrier layer, rather than RF sputtering -- has resulted in somewhat more reproducible results. The typical junction specific capacitance for the new devices is ≈ 65 fF/ μm^2 . This is determined from FTS measurements of the device bandpass, as compared with simulations (below the Nb gap), and is adjusted for junction area variations through the use of test die on the device wafer. The (minor) observed variations in junction resistance have only a small effect on the overall bandwidth.

The rather unconventional shapes of the response curves have different origins for the two devices. The older "623" design (1993) was originally optimized to give relatively flat, $>90\%$ response in the 600 to 700 GHz band. However, the capacitance of the fabricated junctions appears to be $\approx 25\%$ higher than assumed for the design, and this, combined with an error in the microstrip circuit design, has skewed the passband and shifted it to lower frequency. The theoretical curve shown in Figure 3 has been adjusted for these deviations. Even with the nonideal bandpass, the device exhibits respectable heterodyne noise temperatures, as presented below. The more recent "73" design was optimized for a center frequency of 750 GHz. The design optimization incorporates response above the Nb gap, where losses are very important. This explains the relatively low peak response and the odd shape of the theoretical curve. This 1995 photomask design also includes devices optimized for passbands of 400 – 500 GHz, 500 – 600 GHz, and 600 – 700 GHz. These devices have been designed for high response ($>90\%$), flat

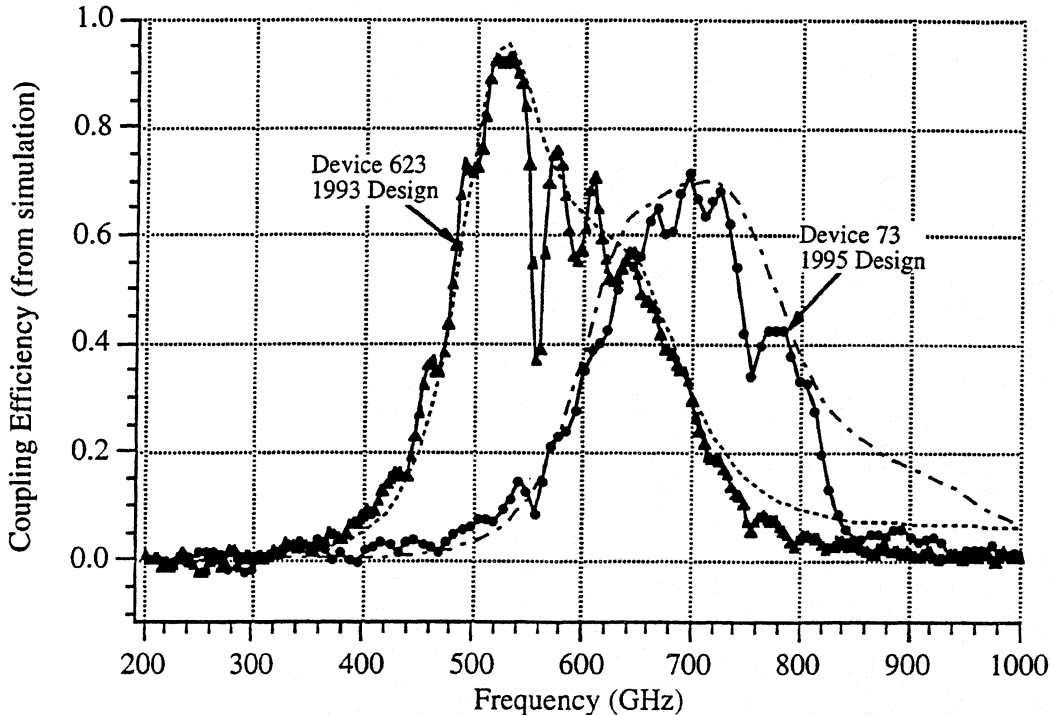


Figure 3: FTS measured response (solid lines) vs. mixer simulation (dashed lines) for two representative devices.

passbands. Preliminary measurements on the 600 – 700 GHz device are quite encouraging.

We have measured the noise temperatures of several devices, including those in Figure 3, using the Y-factor method. Our noise temperatures are referred to the input of the beamsplitter; unless otherwise noted, no corrections have been made for the beamsplitter or other optical losses. Figure 4 shows the DC current-voltage characteristics of the "73" device characterized in Figure 3. The pumped (798 GHz) and unpumped I-Vs are shown for a bath temperature of 4.2 K. The photon step from the nonlinearity at $V = -2\Delta/e \approx -2.85$ mV appears at $V \approx +0.45$ mV, as expected from the 798 GHz LO input ($h\nu/e \approx 3.3$ mV). Also shown in Figure 4 are the total IF output power in a 500 MHz bandwidth when room temperature and 77 K absorbers are placed at the receiver input. The curves are relatively smooth, indicating good suppression of Josephson noise. With no mechanical tuning elements -- simply adjustment of the magnetic field, bias, and LO power -- this device gives a DSB receiver noise temperature of 787 K at the 798 GHz LO frequency.

Figure 5 displays receiver noise temperatures as a function of frequency for several of our best devices. Interesting to note from the plot are the noise temperatures of the "73" device when cooled to 2.5 K. The noise temperatures decrease by as much as 100 K, in part due to a slightly higher Nb gap at the lower temperatures, and the correspondingly lower stripline losses. The lower ambient temperature also decreases the shot noise from the dark current, which is $\approx 40\%$ of the total (pumped) bias current at 4.2 K. Receiver noise temperatures are adversely affected by the relatively low output power typical of our LO chain configuration, and the situation is further degraded by our power-hungry large junction areas ($2.25 \mu\text{m}^2$ for this particular device). The use of thicker beamsplitters to couple in more LO power does not improve the receiver noise temperature, as a greater portion of the signal is reflected away from the mixer. The device would offer

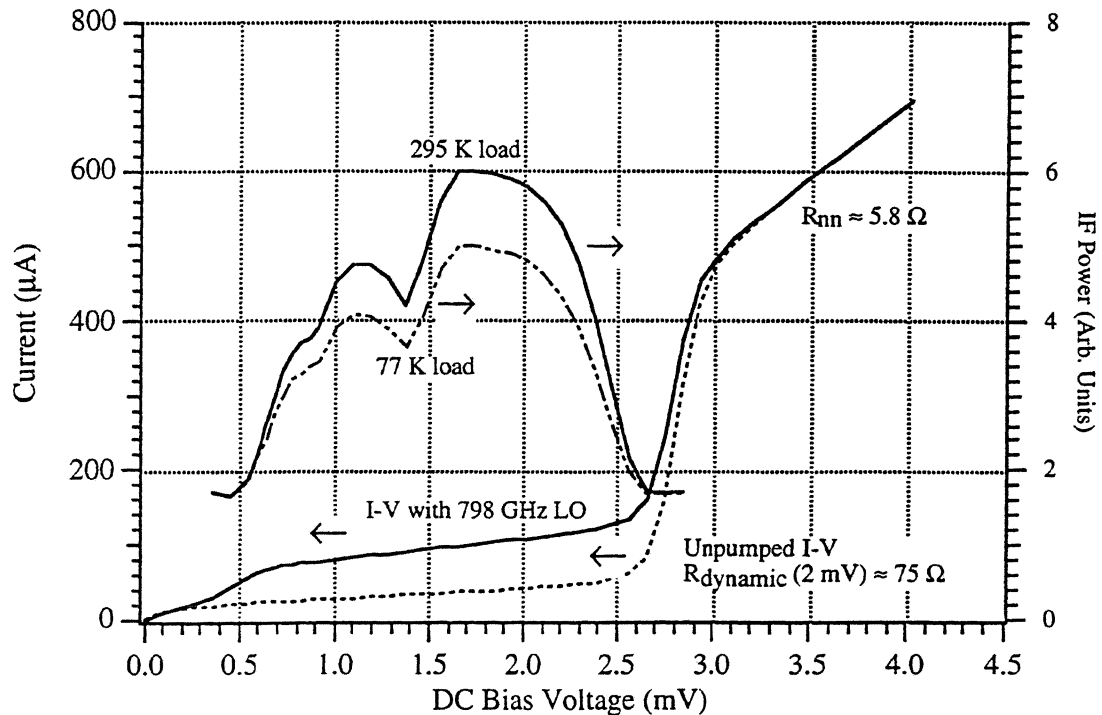


Figure 4: Current vs. voltage trace and IF power vs. voltage bias for device "73" at 4.2 K. The LO frequency is 798 GHz, and the DSB receiver noise temperature is 787 K.

significantly lower noise temperatures if a stronger LO source with thinner beamsplitter were employed. (Correcting for present beamsplitter losses would improve the 798 GHz, 2.5 K receiver noise temperature from 617 K to below 450 K.)

To our knowledge, the (uncorrected) results presented in Figure 5 are the best reported to date for any broadband heterodyne receiver at 800 GHz. To highlight the usefulness of our low-noise SIS receiver, we compare with state-of-the-art Schottky corner-cube receivers -- offering DSB receiver noise temperatures no better than 1500 K (after correcting for the $\approx 50\%$ corner-reflector antenna efficiency) [12].

Conclusion and Outlook

We have demonstrated quasi-optical low-noise SIS receivers with *predictable* performance at frequencies up to ≈ 800 GHz. The measured receiver noise temperatures are low enough to perform exciting astronomy in the $\lambda = 350 \mu\text{m}$ atmospheric window. Our device simulation program can accurately predict the experimentally observed performance, giving us the ability to reliably design broadband, high sensitivity devices over our frequency range of interest, 400 – 800 GHz. Preliminary results on other devices in the series further supports this claim, giving expected bandwidths, and respectable receiver noise temperatures (for example, 180 K DSB at 690 GHz).

We have initiated a program to replace the Nb antenna and stripline with lower loss normal-metal Al films. We expect these devices to have useful response at frequencies exceeding 1 THz. Reuter-Sondheimer theory has been used to predict the surface impedance of Al in this regime of the anomalous skin effect. The Al device response does not approach that of lower frequency fully-superconducting devices, but we expect to achieve receiver noise temperatures below 10 hv/k at 1 THz. We believe the Al device

predictions to be reasonably accurate, judging from experiments with non-optimized Al-wiring devices at lower frequencies: the existing Nb-wiring device masks were used to establish the Al-wiring device fabrication process, and the resulting devices were tested on our FTS. Although these devices have 550 – 650 GHz bandwidths, our success with all-Nb devices above the Nb gap indicates that it is reasonable to expect Al-wiring devices will extend the useful frequency range of our mixers beyond 1 THz.

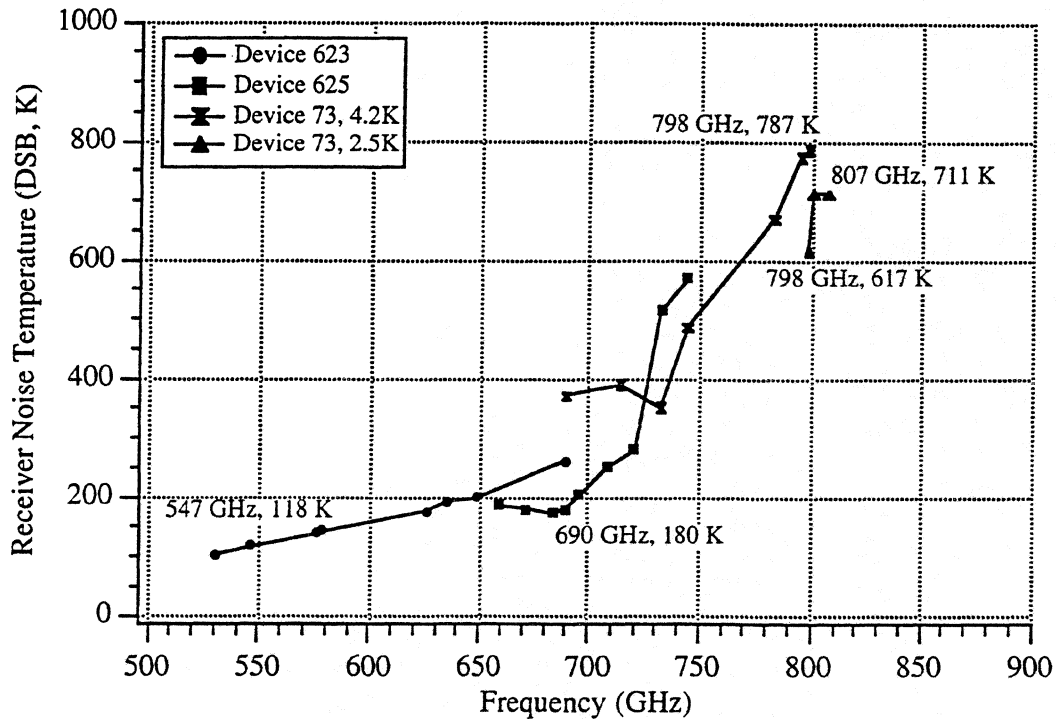


Figure 5: Noise temperatures of selected devices. $2\Delta/h \approx 700$ GHz for our Nb films.

Acknowledgements

We thank N.G. Ugras, A. Clapp, J. Ward, J. Kooi, R. Schoelkopf, and T. Büttgenbach for their contributions to the laboratory work and for helpful advice. This work was supported in part by grants from NASA (NAGW-107 and NAG2-744), NASA/JPL, and a NSF PYI grant to J.Z. The junction fabrication was performed at the Center for Space Microelectronics Technology, Jet Propulsion Laboratory, California Institute of Technology and was sponsored by the National Aeronautics and Space Administration, Office of Space Access Technology.

References

- [1] J. Zmuidzinas, H.G. LeDuc, J.A. Stern, and S.R. Cypher, "Two Junction Tuning Circuits for Submillimeter SIS Mixers," *IEEE Trans. Microwave Theory Tech.* **42**, 698-706 (1994).
- [2] G. DeLange, C.E. Honingh, J.J. Kuipers, H.H.A. Schaeffer, R.A. Panhuyzen, T.M. Klapwijk, H. Van de Stadt, and M.M.W.M. de Graauw, "Heterodyne Mixing with Nb Tunnel Junctions Above the Gap Frequency," *Appl. Phys. Lett.* **64**, 3039-3041 (1994).
- [3] D. Winkler and T. Claeson, "High Frequency Limits of Superconducting Tunnel Junction Mixers," *J. Appl. Phys.* **62**, 4482-4498 (1987).
- [4] M.J. Wengler and D.P. Woody, "Quantum Noise in Heterodyne Detection," *IEEE J. Quantum Electronics* **23**, 613-622 (1987).
- [5] W.C. Danchi and E.C. Sutton, "Frequency Dependence of Quasiparticle Mixers," *J. Appl. Phys.* **60**, 3967-3977 (1986).
- [6] J. Zmuidzinas, N.G. Ugras, D. Miller, M. Gaidis, H.G. LeDuc, and J.A. Stern, "Low-Noise Slot Antenna SIS Mixers," to appear in the proceedings of the Applied Superconductivity Conference, Boston, MA, 1994.
- [7] R. Pöpel, "Electromagnetic Properties of Superconductors," pp. 44-78 in V. Kose, ed., *Superconducting Quantum Electronics*, Springer-Verlag: Berlin, 1989.
- [8] J. Zmuidzinas and H.G. LeDuc, "Quasi-optical Slot Antenna SIS Mixers," *IEEE Trans. Microwave Theory Tech.* **40**, 1797-1804 (1992).
- [9] Thermech Engineering Corp, 1773 W. Lincoln Ave, Bldg. K, Anaheim, CA 92801.
- [10] Janos Technology, Inc., HCR #33, Box 25, Route 35, Townshend, VT 05353-7702.
- [11] Berkshire Technologies, Inc., 5427 Telegraph Ave., Suite B2, Oakland, CA 94609; model L-1.5-30HI.
- [12] A.I. Harris, J. Stutzki, U.U. Graf, and R. Genzel, "Measured Mixer Noise Temperature and Conversion Loss of a Cryogenic Schottky Diode Mixer Near 800 GHz," *Int. J. Infrared and Millimeter Waves* **10**, 1371-1376 (1989).

A CIRCULAR WAVEGUIDE SIS RECEIVER FOR 600-720 GHz

P. A. Jaminet¹, J. A. Stern², H. G. LeDuc²,
C.-Y. E. Tong¹, S. Shepard³, J. Kawamura¹, X. Zhang¹

ABSTRACT

We have designed a 600-720 GHz SIS receiver which uses a novel fixed-tuned, circular waveguide mixer block mount. We describe the design, and discuss its advantages and disadvantages compared to more conventional rectangular-waveguide mounts. Also, we describe a new technique for making durable anti-reflection coatings for quartz optical elements, including lenses.

Introduction

SIS receivers using rectangular waveguide mixer mounts have provided very impressive performance through the Niobium gap frequency, slightly above 700 GHz [5, 6, 7, 8]. However, at very high frequencies there may be grounds for considering circular waveguide mounts as a competing technology.

Circular waveguides have intrinsically lower loss than rectangular waveguides, and can be matched to corrugated feed horns with slightly shorter transition sections, so that waveguide losses will be slightly lower. Also, non-contacting backshorts can be made more effectively in circular waveguide than rectangular waveguide: the best rectangular waveguide backshorts at high frequencies use circular sections to produce a reflective filter [4], just as non-contacting backshorts in circular waveguide do, but the range of impedances in the filter sections is more restricted. Against this must count a few deficiencies of circular waveguide mounts. First, because of the increased density of modes in circular waveguide, the receiver bandwidth is somewhat reduced; tunerless designs have achieved 40% bandwidth in rectangular waveguide [1], whereas the design we will describe here achieves roughly 25% bandwidth. This need not be a crippling consideration at high frequencies, as the atmospheric windows above 500 GHz are less than 20% wide. Second, circular waveguides have no intrinsic polarization selectivity. Therefore, much more than rectangular waveguide mounts, they are vulnerable to losing power into a cross-polar component which does not couple to the receiver

¹Smithsonian Astrophysical Observatory, 60 Garden St., Cambridge, MA 02138.

²Jet Propulsion Laboratory, Center for Space Microelectronics Technology, Pasadena, CA 91109.

³Harvard University, Division of Applied Sciences, McKay Laboratory, Cambridge, MA 02138.

optics.

As the waveguide and backshort losses tend to rise rapidly with frequency, while the polarization losses probably do not rise so rapidly with frequency, at sufficiently high frequencies circular waveguide mounts may be competitive with (or superior to) rectangular waveguide mounts. At frequencies above the Niobium energy gap, the improved backshort performance may make it possible to tune close to the edge of the Smith chart, and thereby match to untuned junctions. Furthermore, to our knowledge, before this work there was no existing circular waveguide mixer mount design which is known to be capable of giving performance comparable to that of rectangular waveguide mounts. Thus, we thought it both interesting and worthwhile to investigate circular waveguide designs.

Design of the RF Block

Because this design was intended to operate at short wavelengths ($\lambda < 500 \mu\text{m}$), where junction chips can become fragile, some attention was given to developing a design which makes the junction chips mechanically robust. This requires, first, a small aspect ratio between the long and small dimensions; as well as minimizing the length of the chip, this leads to the use of a chip with a nearly square cross-section.

Additionally, because very fine dicing tolerances are difficult to meet, a design was sought in which the width of the substrate was not critical. These conditions, for thick substrates and loose constraints on the substrate width, led us away from suspended stripline designs, and to a "microstrip-in-a-box" configuration.

Figure 1 presents the design of the IF transmission line (RF block) in our 600-720 GHz mixer block. With the parameters shown, the effective dielectric constant is about 1.44 at the IF. At the time the RF filter structure was designed, we were considering both the use of thicker substrates and a smaller airgap, and using some dielectric to fill in the airgap. For this reason the filter section lengths are optimized for a somewhat higher effective dielectric constant. As a result the filter sections (shown in Figure 3) are shorter than optimal for blocking the 600-720 GHz TEM mode transmission down the line. However, these filter lengths should still work adequately well.

Scale Model Tests

We performed scale model tests on a 2.0 inch diameter circular waveguide mount. For this waveguide diameter, cutoff of the desired TE_{11} mode is at 3.46 GHz, cutoff of the TM_{01} mode is at 4.52 GHz, and the onset of higher order modes begins at 5.74 GHz. The TM_{01} mode has radial electric fields with a null in the electric field at the center of the waveguide; thus symmetric designs, which place the antenna feed point at the center of the guide, do not couple

to this mode. This arrangement makes possible moderately wideband circular waveguide mixers.

Figure 2 is a Smith chart showing the best results we obtained from a scale model. For a fixed-tuned mount matching to a detector impedance of 40Ω , performance is reasonably good from 3.88 GHz to 5.46 GHz, a bandwidth of 40%. However, it is best from about 4.2 to 5.3 GHz; in this range the reflection coefficient from a 40Ω detector is less than 5%. This corresponds to a bandwidth of 25%, slightly wider than the high-frequency atmospheric windows. Using this band would lead to a scaling factor of 140 for the 600-720 GHz window. However, we chose a slightly larger scaling factor, as the lower end of the 3.88-5.46 GHz frequency band was less sensitive to parameter changes in the substrate, antenna pattern, RF block, and backshort position. For instance, for the same scale model test shown in Figure 2, a small change in backshort position produces a good fixed-tuned match from 4.0 to 4.9 GHz at 43Ω .

600-720 GHz Receiver

A mixer block of design closely similar to the optimal scale model design was acquired from Custom Microwave [2]. There were a few slight deviations. The most significant occurs in the RF block. The smallest available slitting saw for cutting the slot for the RF block was 0.004 inch wide (0.102 mm). The slitting saw blades could be ground down to the proper size; however, at the time of ordering the vendor was reluctant to do this and we chose instead to receive a 0.102 mm wide slot and solder indium to the sides and bottom to reduce it to approximately the proper dimensions. This seems to have worked fairly well, at least in mechanical terms: by using a junction chip we have formed a rectangular slot of the appropriate size. The extra RF loss due to the indium walls of the slot actually improves the RF block.

The mixer block and junction chip layout of the 600-720 GHz mixer are shown in Figure 3. The waveguide is 0.326 mm in diameter; the RF block is 0.318 mm long. The design is not perfectly symmetric, as an indium press contact to ground is made just outside the waveguide wall on one side of the waveguide. However, this alteration did not seem to affect results in scale model tests, perhaps because the attenuation length in the RF block is relatively short (e-folding length less than $85 \mu\text{m}$ for non-TEM modes). This deviation from a symmetric design reduces the length of the junction chip, improving its mechanical strength, and also improves the thermal grounding of the junction. After passing through the RF block, the junction makes another indium press contact to an IF transmission line which is also a superconducting microstrip line. The substrate metallization faces the backshort.

AR-Coated Crystalline Quartz Lenses

Another novel feature of this receiver is its use of crystalline quartz lenses and windows AR-coated with a novel material, Teflon AF 1600 Fluoropolymer [3]. Teflon AF is a Teflon variant which is soluble in an inert solvent (we use Fluorinert FC-75, made by 3M and sold by DuPont). In solution, it can be spray- or drip-coated, and after baking (up to 300 C), it forms a strongly adhering film. We have cycled an AR-coated lens between nitrogen temperature and room temperature with no loss in adhesion. The coatings do not peel, even under scraping by a razor blade. However, they can be easily removed by overnight soaking in the solvent.

AR-coated quartz has some advantages over the competing technology of grooved plastic lenses. The anti-reflection grooves are difficult to machine at short wavelengths because the plastic deforms and does not cut cleanly. The plastics have a lower dielectric constant and consequently cannot reach focal lengths as short as quartz can. They have low thermal conductivity, and under radiative load are difficult to cool. The favorite material from a machinist's point of view, teflon, becomes lossy at high frequencies; while polyethylene, which has low loss, is more difficult to machine.

Crystalline quartz, on the other hand, has high thermal conductivity; lens surfaces can be polished to very high tolerances; and it has modest submillimeter loss even at room temperature and negligible loss at cryogenic temperatures. It is transparent to visible light, which is convenient. The loss due to birefringence in z-cut crystalline quartz is very small as long as all significant power lies in rays making an angle to the quartz optical axis of less than 10 degrees, which is easily achieved for typical receiver designs. (The loss due to birefringence goes as the fourth power of the angle to the optical axis.) Its liabilities, compared to plastic lenses, are the need to make an AR-coating, and the losses due to spherical aberration if (inexpensive) spherical surfaces are obtained from an optical lens maker. (Plastic lenses can very readily be machined to non-spherical surfaces.) The use of Teflon AF obviates the problem of AR-coating the quartz.

The calculated transmission through a 1.5 mm thick (two inch diameter) vacuum window AR-coated for 600-720 GHz is shown in Figure 4. It may be possible to reduce the thickness, which provides a somewhat conservative safety margin against rupture. Typical absorption losses are 3% at 660 GHz, while reflection losses are on the order of 1% within the band.

Reflectivity from a single AR-coated crystalline quartz surface was measured in a Fourier Transform Spectrometer. The reflectivity was nearly uniform at about 1.5 - 2% over a 40% band. Using indices of 1.38 for Teflon and 2.107 for z-cut crystalline quartz, one would expect a minimum reflectivity of 0.25% rising to 2% over a nearly 50% band from a perfect coating. We attribute the washing out of the resonance to nonuniformity in the Teflon film. When baked at 300

C, the Teflon film is a viscous fluid and can slowly flow to make a more uniform coating. However, if the substrate is not parallel to the ground, the Teflon also tends to flow toward the lower gravitational potential. To preserve the coating uniformity to within 10% (.008 mm) over a 2 inch aperture requires a flatness of 30 arcseconds, which is difficult to achieve. For this reason, it may be best to use relatively short bakes for very high-frequency coatings, in which case the coatings must be applied with a uniform spray-coating. An alternative we intend to investigate is using a lathe to machine down a thick coating to the proper thickness.

Conclusion

As we write, the receiver is very nearly complete and mixer measurements should begin shortly. Testing has been delayed by several problems typical when a new design, and receiver, are used for the first time. In addition to standard problems such as a backshort which froze up upon first cooldown, and the need to improve thermal conduction from the helium cold can to the mixer block, there were a few unexpected difficulties. A notable one was the poor mechanical robustness of the indium press contact on the IF transmission line in the mixer block. This superconducting line was made of niobium with a gold contact layer, and the gold was easily stripped from the niobium even by gentle nudges to the indium soldered to it. We are remaking the circuit with a niobium-aluminum-chrome-gold layering to improve the adhesion.

We expect to obtain mixing results within a few weeks. We expect that these will show that a circular waveguide mount can provide comparable performance to rectangular waveguide mounts, and can give us evidence of the utility of circular waveguide mounts at still higher frequencies.

References

- [1] R. Blundell, C.-Y. E. Tong, D. C. Papa, R. L. Leombruno, X. Zhang, S. Paine, J. A. Stern, H. G. LeDuc, B. Bumble, *Fifth International Symposium on Space Terahertz Technology*, "A Wideband Fixed-Tuned SIS Receiver for 200 GHz Operation".
- [2] Custom Microwave, Inc., 940 Boston Avenue, Longmont, CO 80501, USA.
- [3] Du Pont Specialty Polymers, P. O. Box 80713, Wilmington, DE 19880.
- [4] A. R. Kerr, *NRAO Electronics Division Internal Report*, No. 280, "An Adjustable Short-Circuit for Millimeter Wavelengths".

- [5] J. W. Kooi, C. K. Walker, H. G. Leduc, P. L. Schaffer, T. R. Hunter, D. J. Benford, and T. G. Phillips, *International Journal of Infrared and Millimeter Waves*, **15**, 477 (1994).
- [6] Morvan Salez, Pascal Febvre, William R. McGrath, Bruce Bumble, and Henry G. Leduc, *International Journal of Infrared and Millimeter Waves*, **15**, 349 (1994).
- [7] K.-F. Schuster, A.I. Harris, and K.-H. Gundlach, *International Journal of Infrared and Millimeter Waves*, **14**, 1867 (1993).
- [8] C.-Y. E. Tong, R. Blundell, D. C. Papa, J. W. Barrett, S. Paine, X. Zhang, J. A. Stern, and H. G. LeDuc, *Sixth International Symposium on Space Terahertz Technology*, "A Fixed Tuned Low Noise SIS Receiver for the 600 GHz Frequency Band".

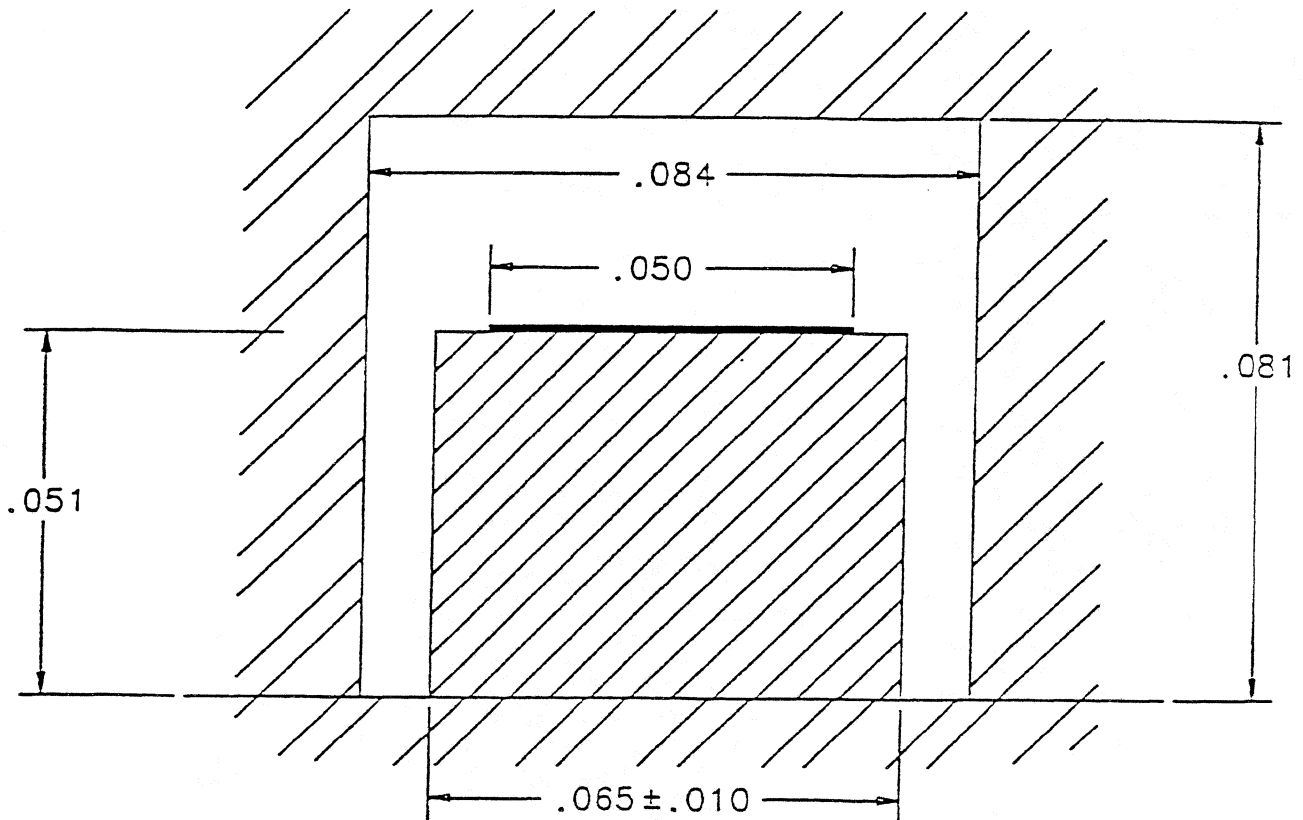


Figure 1: A cross-section of the RF block and IF transmission line used in the 600-720 GHz receiver. Dimensions are in millimeters. On a fused quartz substrate are filter sections alternately $2\ \mu\text{m}$ and $50\ \mu\text{m}$ wide. The cutoff frequency for non-TEM modes in this line is nearly 1.5 THz, well above the RF.

MARKER 1

3.88 GHz

$43.3 - j15.1 \Omega$

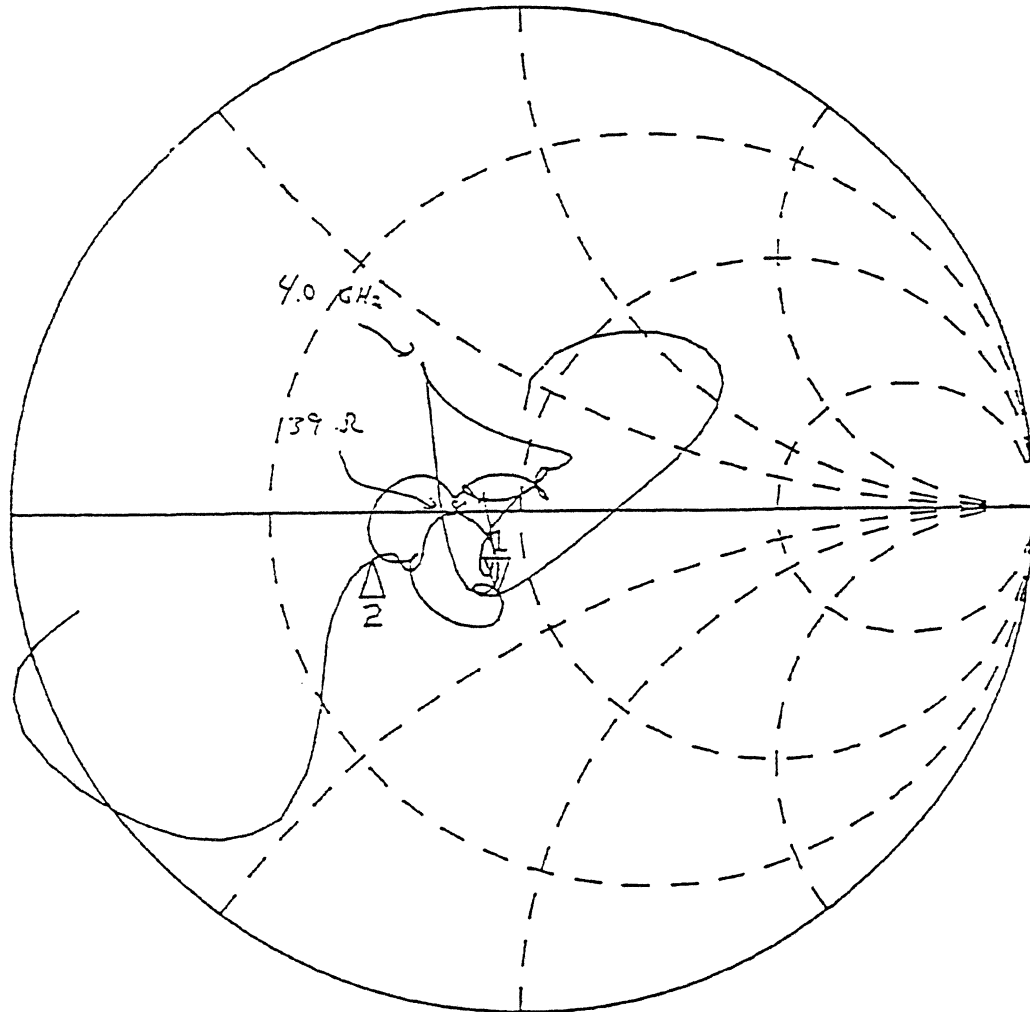
MARKER 2

5.46 GHz

$27 - j5 \Omega$

$$4.2 - 5.3 \text{ GHz} \times 140 = 588 - 742 \text{ GHz}$$

$$R < 57\% \text{ to } 40 \Omega$$



START 3.700000000 GHz
 STOP 5.700000000 GHz

Figure 2: A Smith chart of the embedding impedance seen at the antenna feed point in the best scale model mixer mount. An impedance of 40Ω makes a good match to the radiation over a nearly 40% bandwidth, and an excellent match over a 25% bandwidth.

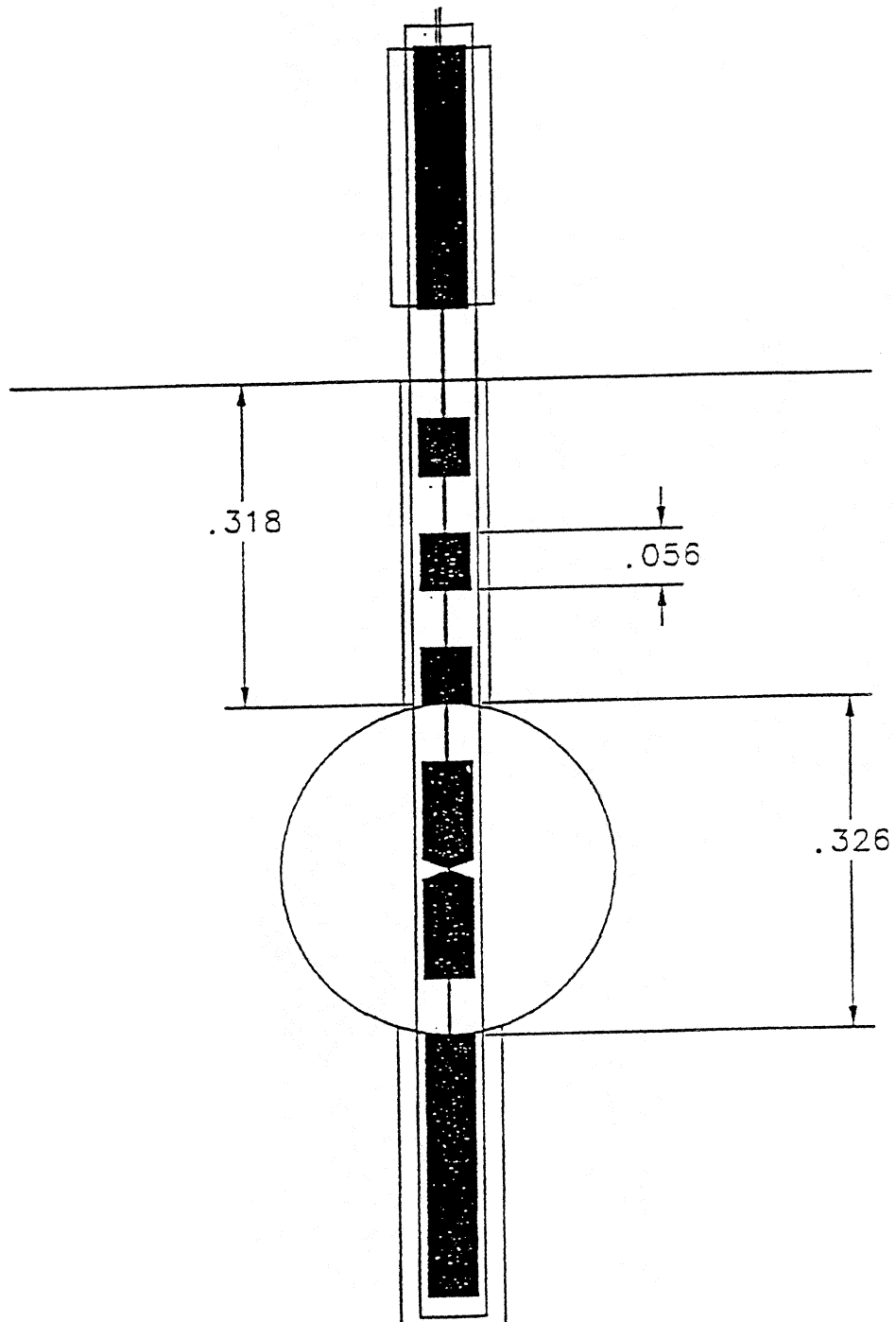


Figure 3: The layout of the 600-720 GHz mixer block and the junction chip metallization pattern. Dimensions are in millimeters. The junction chip makes indium press contacts at each end: at bottom, to ground; at top, to a superconducting microstrip IF transmission line.

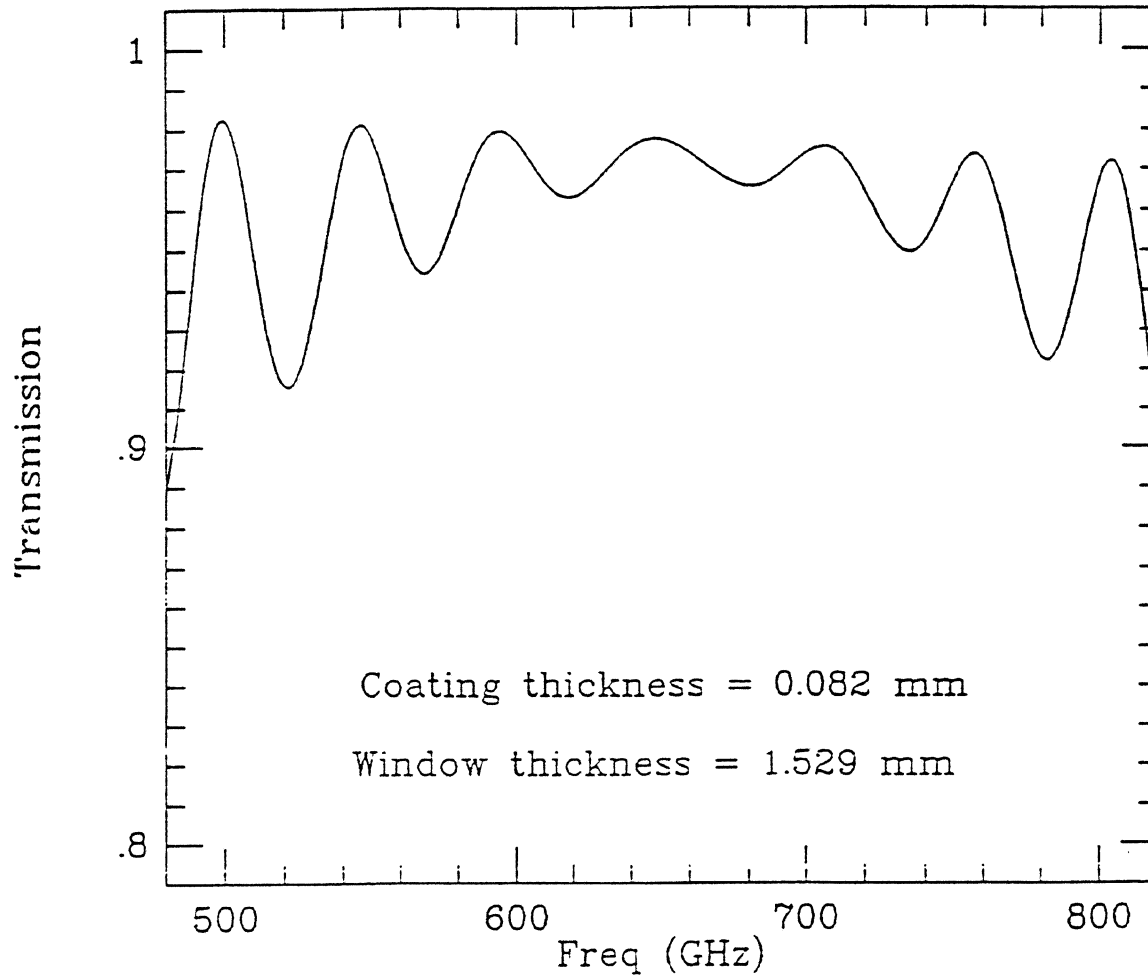


Figure 4: Calculated transmission through a 1.529 mm thick z-cut crystalline quartz vacuum window AR-coated with 0.082 mm layers of Teflon AF 1600 Fluoropolymer. Absorption losses are larger than reflection losses throughout the 600-720 GHz band.

A Superconducting Planar Integrated Receiver for the Frequency Range 430-480 GHz

S. V. Shitov, V. P. Koshelets, A. M. Baryshev, I. L. Lapitskaya, L. V. Filippenko,
Institute of Radio Engineering and Electronics, Russian Academy of Sciences,
103907 Moscow, Russia,

and

Th. de Graauw, H. Schaeffer, H. van de Stadt, W. Luinge
Groningen Space Research Laboratory,
P.O. Box 800, 9700 AV Groningen, the Netherlands

Abstract

A planar receiver comprising a Josephson flux-flow oscillator (FFO), a double dipole antenna and a SIS mixer integrated on a single chip within an area of 3 x 3 mm has been realised in the frequency range of 400-500 GHz. RF tests have been performed at temperatures between 2 K and 4.2 K. A best DSB noise temperature of $595 \text{ K} \pm 20 \text{ K}$ at 465 GHz was obtained for the receiver with the mixer pumped by the FFO. The width of the antenna beam has been measured referred to the input window of the cryostat and was about ± 4 degrees at the power level of about -20 dB. The power consumption of the whole device is estimated to be $20 \mu\text{W}$.

Introduction

Recent developments in the field of superconducting thin film technology and RF design resulted in sensitive SIS mixers for heterodyne receivers in both the mm and the submm wavelength regions (1). In addition, a number of important RF components such as two types of oscillators based on synchronous arrays of lumped Josephson junctions (2-4) and long Josephson junctions (5-8), SIS attenuators (9) and *dc* SQUID RF amplifiers (10), have been developed or improved recently and can be used in combination with SIS-mixers. New superconducting RSFQ elements (11) could also be used, for example, in a digital correlators for data processing. All these devices are fast enough and have very low power dissipation. Integration of these elements on a single chip to create a small size and low power consumption receiving system for airborne/ spaceborne astronomy and environmental monitoring at mm and submm wavelengths, is an important step to be done.

In order to realise a fully integrated receiver in the submm region one has to put close together an antenna feed, mixer element, local oscillator including a power injection system, IF-amplifier and preferably also a back-end spectrometer. It is clear that such a complicated device will consist of a number of chips. For example, the front end including the antenna, mixer and LO source could be on a single chip. There is no doubt that an SIS mixer must be used in an integrated receiver. However, the choice of the best suitable LO between existing superconducting oscillators still has to be made.

Both types of superconducting oscillators mentioned above are voltage tuneable sources according to the Josephson relation $f = V/\Phi_0$; $\Phi_0 = h/2e$. For the first type, the synchronous array, reasonable output powers (up to $40 \mu\text{W}$) have been obtained at frequencies of about 400 GHz in a matched load (3); but no linewidth narrower than 10 MHz has been measured for a Josephson 10-junctions array (4). The synchronous array with a number of junctions of $N \sim 10^3$ could provide a linewidth of about 100 kHz, but the device seems rather complicated and it has not been tested yet. The distance between adjacent junctions (or between compact groups of junctions) in the array

should be equal to the wavelength λ in order to provide phase synchronisation; so the overall dimension of such a device is rather large. Another disadvantage of the synchronous arrays is its narrow range of frequency and power tuning.

For the second type of Josephson oscillator, the long tunnel junction, two different modes of oscillation can be used as a microwave source: i) resonant soliton motion (at weak magnetic field applied to the junction with low damping), whence this device is called the soliton oscillator; ii) unidirectional and viscous magnetic flux flow (at relatively large applied magnetic field) in a junction with high damping. The soliton oscillator has very narrow linewidth (5), and its frequency is strictly determined by the junction length. Only a relatively small power can be delivered to the load in this case.

At large magnetic field the unidirectional flow of the fluxons (flux quanta Φ_0) occurs in a long Josephson junction (6-7). Long means that the junction length $L \gg \lambda_j$, while the width of the junction $W \leq \lambda_j$, where λ_j is the Josephson penetration depth. Under the influence of bias current and magnetic field H fluxons are created at one end of the junction. These fluxons form a Josephson vortex array that is driven to the opposite end by Lorentz force due to bias current. The fluxons annihilate at the end of the junction creating pulses of electromagnetic energy. This kind of fluxon motion manifests itself as a current step in the dc I-V curve, the so-called Flux Flow Step (FFS), at the voltage:

$$V_{\text{FFS}} = f_{\text{FFS}} \Phi_0 = vN\Phi_0/L = v\Lambda H, \quad (*)$$

where v - the propagation velocity of electromagnetic waves in the Josephson junction (Swihart velocity), typically 1-2 % of the light velocity in the vacuum; N is a number of fluxons in the junction and $\Lambda = (\lambda_L + \lambda_L + t)$ is the magnetic thickness of the junction (λ_L is London penetration depth). It is possible to explain qualitatively the appearance of the FFS by an interaction of the oscillating Josephson current with the travelling electromagnetic pulses of the same frequency.

Using (*) one can see that the FFS voltage, and consequently the oscillation frequency of the Flux-Flow Oscillator (FFO) is directly proportional to the applied magnetic field. The FFO frequency can be tuned over a wide frequency range and is limited only by the superconducting gap frequency (6-8). Moreover, in the case of a strong enough field, the FFO provides a nearly sinusoidal output with low content of higher harmonics and sufficient power to pump a SIS array mixer. The phase-locking of the FFO with external oscillator seems to be possible (12). In summary, this is why the FFO seems the best choice for the local oscillator for submm integrated receiver.

Since all proposed components have *compatible fabrication processes*, the next step in the research of an integrated receiver is the development of new interfaces that make all components *compatible on the same substrate*. For example, the FFO integrated on the same chip with SIS mixer has to be controlled by a relatively weak magnetic field. But the strong field usually applied to a micron size SIS-junction by an external coil could disturb the operation of the FFO. The use of local magnetic fields concentrated near each device seems to be necessary in the case of a submm SIS-mixer and FFO integrated on a chip.

The injection of LO power can be realised not only by quasioptical coupling of the beam to the antenna, but also via an integrated interface (transmission line) connected to the SIS-junction (or the array of SIS junctions). It should be mentioned that a SIS array usually needs more LO power. Significant losses of the incoming signal into the LO path could happen in case of strong coupling between the FFO and the mixer. However, reduction of LO coupling by more than -10 dB could cause lack of the mixer pump since the power available from the experimental FFO is of the order of 0.3 μW . An estimate of FFO power at bias point ($I_{\text{FFO}}, V_{\text{FFO}}$) is $kI_{\text{FFO}} \cdot V_{\text{FFO}}$, where $k \approx 0.15$, that

has been evaluated from the experimental data (13),(14). Because of mentioned limitation of available LO power, a single junction design of SIS mixer looks more attractive.

Description of the experimental chip

The well-developed concept of a double-dipole antenna SIS-mixer (15) has been chosen as a basic approach. The point symmetry of the double-dipole design allows us to use additional leads as an interface between the mixer and other parts of the integrated receiver. A drawing of the central part of the experimental chip of full size $4 \times 4 \times 0.2$ mm is presented in Fig.1. The SIS mixer comprises double dipole antenna and tuned $1 \mu\text{m}$ size SIS junction Nb-AlO_x-Nb. The FFO is on the same chip, but separated from the mixer by a choke structure that prevents leakage of the RF input signal from the antenna. The microstrip transmission line connecting the LO and the mixing junction lies on top of the choke structure. A simplified equivalent diagram of the device is presented in Fig.2.

A. SIS mixer

The single junction SIS mixer of an original design is featured by tuning strips used as the control line for the "internal" magnetic field. An SIS junction is placed in the center of the $3 \mu\text{m}$ wide strip which is connected to both dipole antennas ($210 \times 10 \mu\text{m}$ each) via two $\lambda/4$ microstrip transformers. The control current of the line I_{c1} produces the magnetic field applied to the junction. The size of the dipole antenna was chosen such that no counter reflector needs to be used. Of course, it is a compromise between sensitivity and simplicity of the device that was accepted for the first experiments. The use of both a movable backshort and a counter reflector is planned for a future development. Four contacts on the chip are used to control the SIS-mixer. Two of them, as usually, provide the bias current and pick-up the IF output signal, the two others are connected to the control line to suppress the Josephson noise (see Fig.1,2).

We use a quasi-optical mount containing two lenses. The sample is mounted on the flat back side of a fused quartz hyper hemispherical lens ($R = 5$ mm) with the double-dipole antenna being in the center. The hyper hemispherical lens is illuminated by a primary quartz lens ($F \cong 65$ mm, $D = 20$ mm, effective) coated with antireflection Teflon film $100 \mu\text{m}$ thick. 8 pads on the chip and 10 pin contacts of the mounting are used to control the whole device. The mount is placed in vacuum on the cold plate behind an RF transparent window in cryostat with liquid helium.

SIS mixers with an "internal" magnetic field source passed preliminary RF tests that were performed in a mixer block of similar design and demonstrated good suppression of *ac* Josephson effect (Shapiro steps) when operated at 400-450 GHz. Receiver DSB noise temperature of about 300 K were measured with an external LO source (carcinotron) at 430 GHz (16).

B. Local oscillator

The FFO in the tested samples are designed in overlap geometry with length $L = 450 \mu\text{m}$ and width $W = 3 \mu\text{m}$. The Josephson penetration depth was estimated to be $\lambda_j \cong 4 \mu\text{m}$. It is known that the "idle" overlapping strongly affect the FFO properties, i.e. the propagation velocity (17). We minimised the idle overlapping to 6-10 μm in the present design.

To avoid the self field effect that leads to inclination of the FFS, the bias current should be distributed in the same manner as supercurrent in the tunnel junction (6, 8). The improved bias is realized by employing a "tail" without direct current injection at the end of the junction where

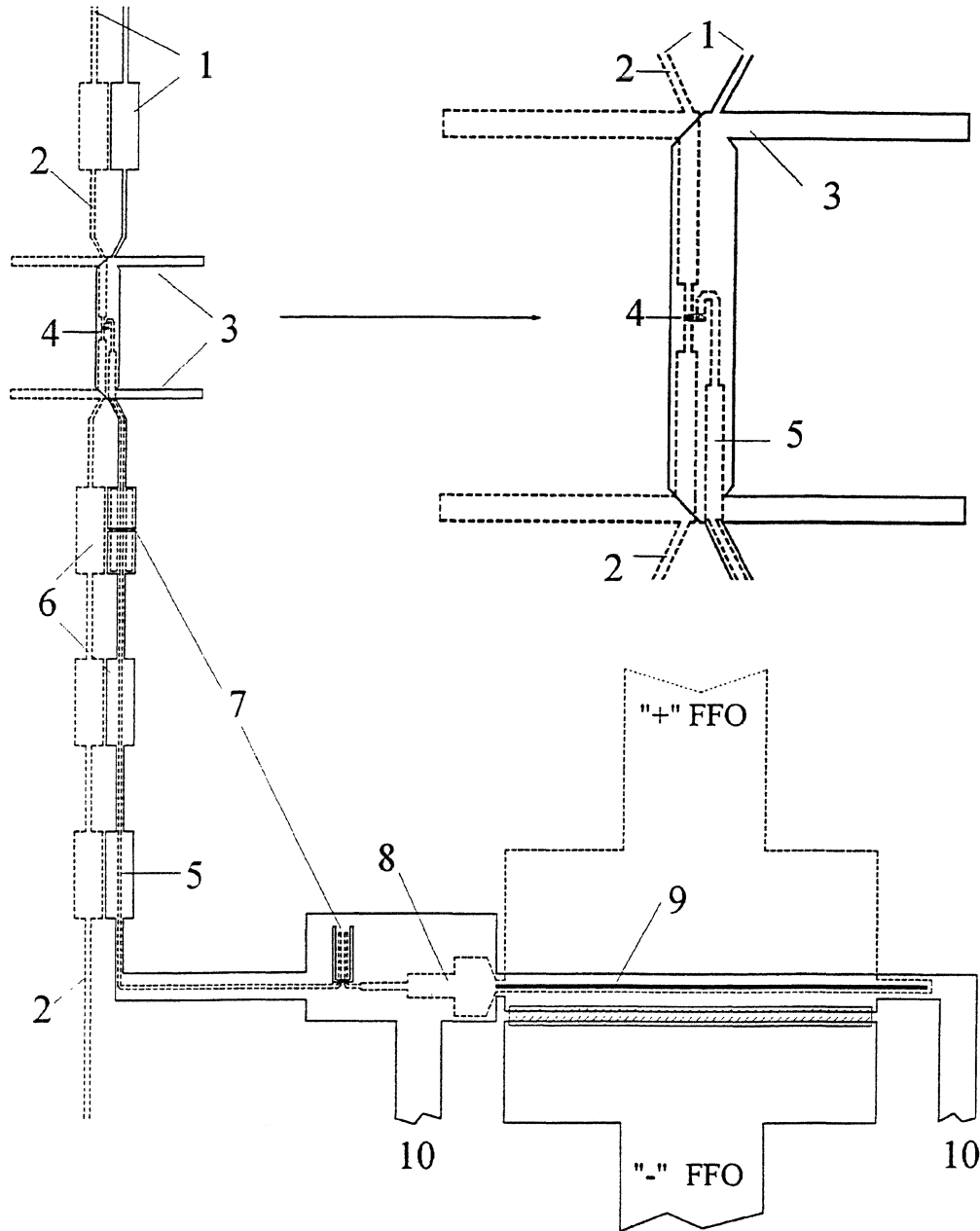


Fig.1 Drawing of the central part of the chip. Numbers in the figure are: 1- IF/DC leads; 2- SIS-mixer H-field control line, 3- double dipole antenna; 4- SIS junction; 5- LO feed line; 6- choke filters; 7- *dc* blocks; 8- Chebyshev transformer; 9- FFO junction; 10- FFO H-field control line.

fluxons are nucleated. The length of the unbiased tail was selected to be about $12\lambda_j$ (about 50 μm) for the optimal operation near 500 GHz.

To obtain uniform bias current injection along the junction, the finger-type *dc* feed with series resistors is used (18). The wide strip feed with spread resistor has been tested also for comparison. The resistors in the finger-type feed are intended to avoid trapping of the magnetic field near the junction. They also allow the junction base electrode to be used as a control line. To reduce the parasitic heating due to resistors, they are designed to be "vertical", i.e., the current is passing them in vertical direction. The nominal value of one resistor of size 10 x 10 μm was estimated as 0.01 Ω . Since no significant influence on the FFO operation has been found, the wide strip with the spread series resistor could be recommended as more simple to fabricate.

C. Matching circuits

The FFO output impedance to be matched to the SIS-mixer was assumed as the characteristic impedance of a Josephson transmission line with size of the junction. The value of the FFO output impedance about 0.4 Ohm was estimated. Three stages impedance transformer is used to couple the FFO output power to the microstrip line of 4 μm wide. The calculated characteristic impedance of the microstrip line is 14 Ohm. The Chebyshev three stages transformer has a compensated first (widest) section which is tapered with the angle of 120 degrees. To reduce the width of the first section, thinner insulating SiO layer of 230 nm is used.

Two *dc* blocks (breaks) are incorporated into the microstrip transmission line to separate the bias currents of the mixer and FFO and prevent leak of IF signal due to the capacitance of the matching circuit. Since FFO is intended to be frequency locked on harmonics of pumping source, the band-pass filter of high order (not shown in Fig.1) has to be used to prevent a leakage of the fundamental frequency to the mixer. The phase-locked 10 GHz and 70 GHz sources are planned to be used in future experiments around 500 GHz. The low loss performance of the band-pass filter has been proven within this frequency range experimentally.

A new design for *dc* block in a microstrip line using only two layers has been developed. The design principle has been verified successfully with a scale model in the frequency range 1-1000 MHz. In Fig.3 schematic pictures of the *dc* blocks as well as measured and calculated transmission of the design from Fig.3a are presented. The *dc* blocks are band-pass filters that use a combination of resonant microstrips and slots. The break from Fig.3a has been designed on a base of the folded slot line antenna. Because of high mutual inductance of the two half-slots excited in antiphase, the radiation loss in the *dc*-block is very low.

The LO power is coupled from the transmission line to the mixing junction via the two stages transformer situated inside the mixer. The transformer raises the impedance of the LO source up to 50-60 Ω . The mismatch between the LO source and the mixer is used to get the LO coupling at the level of 25-30%. A small 2 Ω resistor is used at the place of connection of the LO circuit to the SIS junction. This resistor is to prevent decrease of current density in the mixer control line near the SIS junction.

Experimental Data and Discussion

To make the technological run shorter and more reliable, both the mixing and FFO junctions have been formed on the base of the same trilayer Nb-AlO_x-Nb (19, 20) on a crystalline quartz substrate. Because of good thermal conductivity of the crystalline quartz, better heat sink of the chip can be achieved in the vacuum cryostat. The substrate 15x24x0.2 mm contains 8 chips of slightly different design and two well-defined SIS junctions of size about 20 μm^2 which are used to check

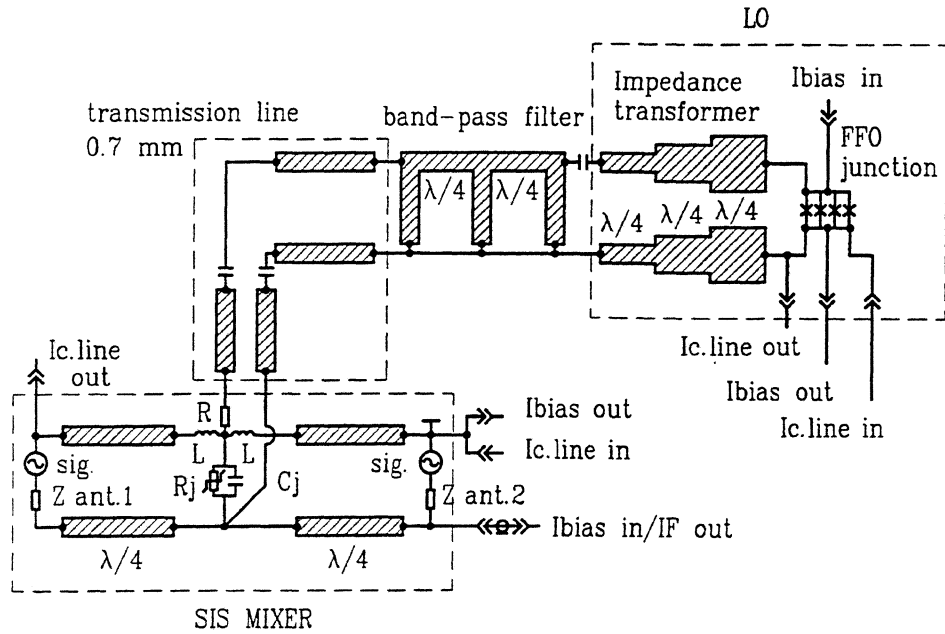


Fig. 2 Simplified equivalent diagram of the integrated receiver.

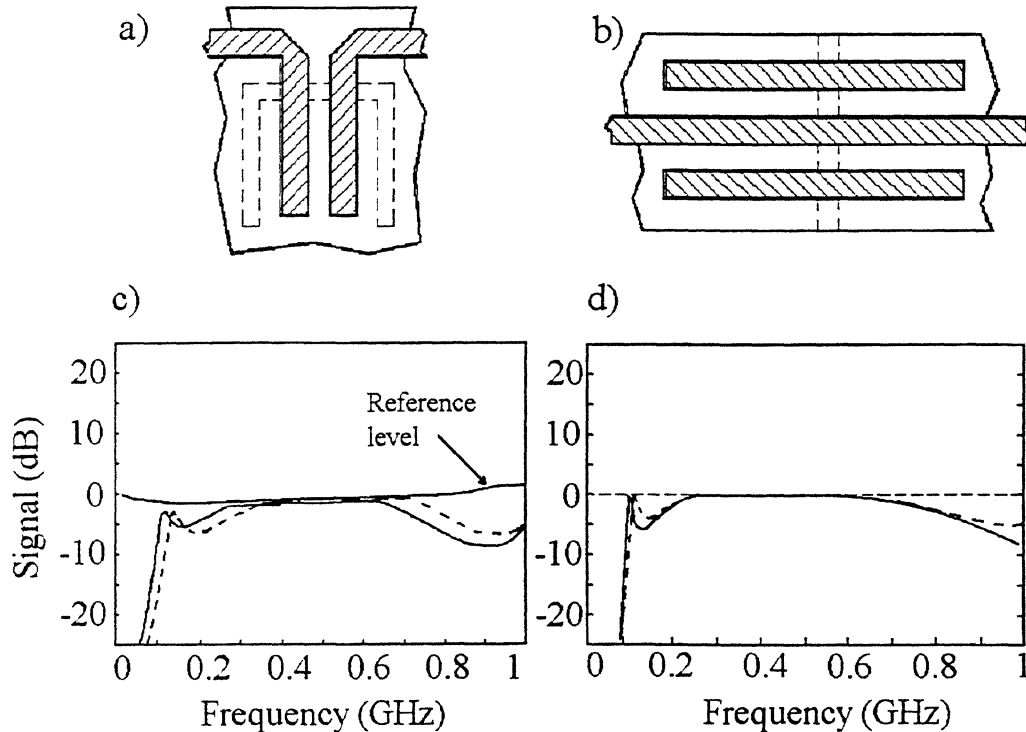


Fig.3 The dc-blocks in the micro strip line use only two metal layers: a) dc-break in the line; b) dc-break in the ground; c) measured transmission with scale model (1:1000) for different length of the microstrip stubs; d) calculated transmission for two cases: lossless slot-line (dashed) and radiative slot-line (solid).

the current density and size of small mixing junctions. High current density $j_c=5-8 \text{ kA/cm}^2$ of the trilayer was used. The $R_n A$ product (R_n is the normal state resistance of SIS junction; A is its area) could be treated as the most natural τ -parameter to characterise a quasiparticle mixer since specific capacitance C_s varies slightly in comparison to R_n (1). The $R_n A$ in the range of $25 - 40 \text{ } \Omega \cdot \mu\text{m}^2$ was used and $C_s \cong 80 \text{ fF}/\mu\text{m}^2$ was assumed for the samples tested. The mixing junctions have an area of $1-1.2 \text{ } \mu\text{m}$. The cross-windows process is used to fabricate the junctions of $1 \text{ } \mu\text{m}$ size with high definition using standard optical lithography (20). Two layers of SiO (230 nm and 140 nm) are used. The FFO junction is formed with single 230 nm thick insulating layer of SiO.

The Ti film with the surface resistance of $5 \text{ } \Omega$ is used to form the resistors in the FFO *dc* feed and LO injection circuit. Contact pads are gold plated. The full technological process uses 8 layers.

A. Dipstick tests

The experimental SIS-mixers integrated with FFO have been tested first at *dc* in a dipstick to select candidates for the real RF experiment. The typical IV-curve of the mixing junction is presented in Fig.4. The specific resonance at the IV-curve at about $800 \text{ } \mu\text{V}$ indicates tuning frequency of the mixing junction around 400 GHz . In the inset of the Fig.4 a control line characteristic is presented. It was found that the control current through the tuning strips of the SIS mixer produces a magnetic field that is strong enough to suppress Josephson supercurrent down to the second minimum in the $1 \text{ } \mu\text{m}$ size junction.

To realise viscous flux flow state in the long Josephson junction (i.e. FFO regime), one should avoid the resonant soliton oscillations by increasing the junction length and damping that is inversely proportional to the quality factor Q_j :

$$Q_j = \{ \alpha_{qp} + \beta (f_{FFS} / f_p)^2 \}^{-1}, \quad (**)$$

where β is surface loss of the films; f_p is plasma frequency of the junction. In Fig.5 the IV-curve of typical FFO is presented. The estimated quasiparticle losses α_{qp} is very low for our junctions (typically $\alpha_{qp} \sim 0.01$) and we have no "pure" flux flow regime below $V = 900 \text{ } \mu\text{V}$. Because of insufficient damping the IV-curve in this voltage region consists of a number of small amplitude Fiske resonances, excited by electromagnetic waves reflected from the ends of the junction. At higher voltages (higher frequency) the surface losses β become dominant. The "tail" geometry of the junction seems to be efficient since steady and near vertical FFS at $V \geq 900 \text{ } \mu\text{V}$ are obtained (see Fig.5). The linewidth of the FFO estimated with an external carcinotron (mutual linewidth of two oscillators, actually) did not exceed 1 MHz as measured with a spectrum analyser.

The horizontal bars on the IV-curve indicate regions where pumping of the mixing SIS junction with $\alpha > 1$ has been obtained in the dipstick measurements. As it was expected, the efficient pump takes place around tuning frequency of the SIS mixer. The vertical branches at voltages above 0.8 mV are the repeatedly recorded traces of FFS that moves with the magnetic field changed. The tuning range of about $200-750 \text{ GHz}$ is available with the control current adjusted from 4 to 15 mA for the most normally operated FFO.

B. RF tests in vacuum cryostat

The RF tests in the vacuum cryostat usually started with Fourier Transform Spectrometer (FTS) in video detection mode to check frequency of the best sensitivity of the SIS mixer. Typical RF response obtained in FTS experiment as well as calculated coupling of the signal and LO power to the SIS mixer are presented in Fig.6. Reasonable agreement between the experimental and the

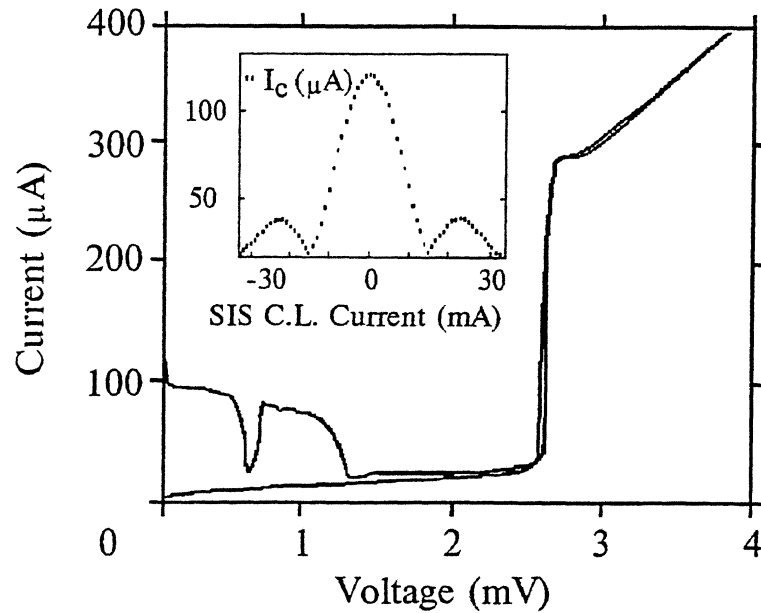


Fig.4 IV-curve of the mixing junction. The two curves are with and without magnetic field applied. The resonance feature at about $V=0.8\text{mV}$ is due to the tuning structure. The dependence of the critical current I_c on the current through the control line is presented in the inset

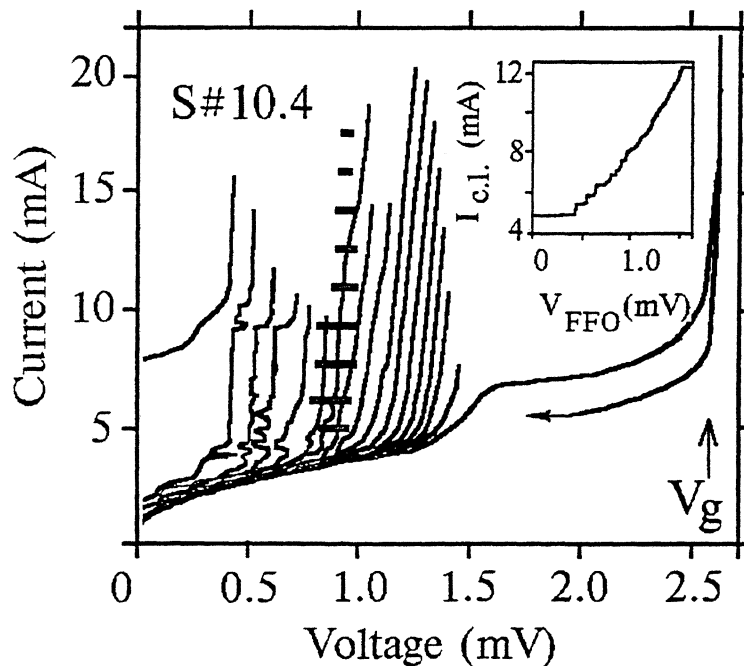


Fig.5 IV-curves of flux-flow oscillator (FFO) for different values of the control current. The horizontal bars show regions of efficient pump of SIS mixer. The dependence of the bias voltage V_{FFO} (oscillator frequency) on the current through the control line $I_{c.l.}$ is presented in the inset.

calculated data is seen. However, the horizontal bar, which is the experimental low estimation for the SIS mixer pump over tuning range of the FFO, was obtained in a dipstick experiment since the pump is significantly lower in the case of vacuum cryostat. A clear overheating of the FFO junction as well as decrease of the mixing junction gap voltage from 2.75 mV to 2.5 mV was observed in the vacuum cryostat at 4.2 K. Moreover, the pump levels for the cases of the dipstick (4.2 K) and the extra cooled vacuum cryostat (about 2 K) were still different. This effect is probably due to a local overheating of both the FFO junction and the nearest interface because of insufficient heat sink. The details of the problem are not clear yet. As a result the RF tests were performed at the temperature of LHe bath about 2 K.

In Fig.7 the experimental IV-curve of the SIS mixer pumped by FFO and the response for hot/cold antenna at IF = 1.5 GHz are presented. It is clearly seen that Shapiro steps are completely suppressed with the magnetic field produced by the control line. In Fig.8 the summary for the integrated receiver tuned with FFO frequency in the range of 404-490 GHz is plotted. On the top of the Fig.8 the integrated receiver noise temperature T_r is presented for two cases of internally and externally pumped SIS mixer. On the bottom the bias current of the mixing SIS junction is plotted for the same two cases. It is necessary to mention that the T_r obtained with the external LO are corrected for the beam splitter loss, but no correction should be done for T_r of integrated receiver since no beam splitter is used in front of the window of the cryostat.

One can see that the closest values of T_r take place for the closest pumping currents of the mixer (see Fig.8). The region of the lowest T_r within frequency range 460-470 GHz is rather an exception. In this specific region the gain of the mixer is arbitrary high and T_r is much less dependent on the pumping level. The shift between the region of the lowest T_r and highest pumping level could be explained by the difference in tuning frequencies of the mixer and the output transformer in LO coupling interface. Nevertheless the receiver has demonstrated wide band operation with DSB noise temperature <1500 K in the frequency region 428-482 GHz.

C. Power consumption analysis

Four separate bias sources have been used in the experimental tests. A voltage source was used to bias the SIS mixer. Three current sources were used for bias the FFO, its control line and the control line of the SIS mixer. It is important to mention that the main heat production is originated from the FFO. Typical values for the power dissipation loading the helium bath are summarised in Table 1.

Table 1 Power consumption of some elements of the integrated receiver.

element of integrated receiver	bias current, mA	bias voltage, mV	power dissipation, μ W
SIS mixer	0.005-0.012	1.5-2.5	0.0075-0.03
control line of SIS mixer	15-50	0 (superconducting)	0
Flux-Flow oscillator (FFO)	5-20	0.8-1	4-20
resistor(s) in FFO bias circuit	5-20	0.01-0.04	0.05-0.8
control line of FFO	5-20	0 (superconducting)	0

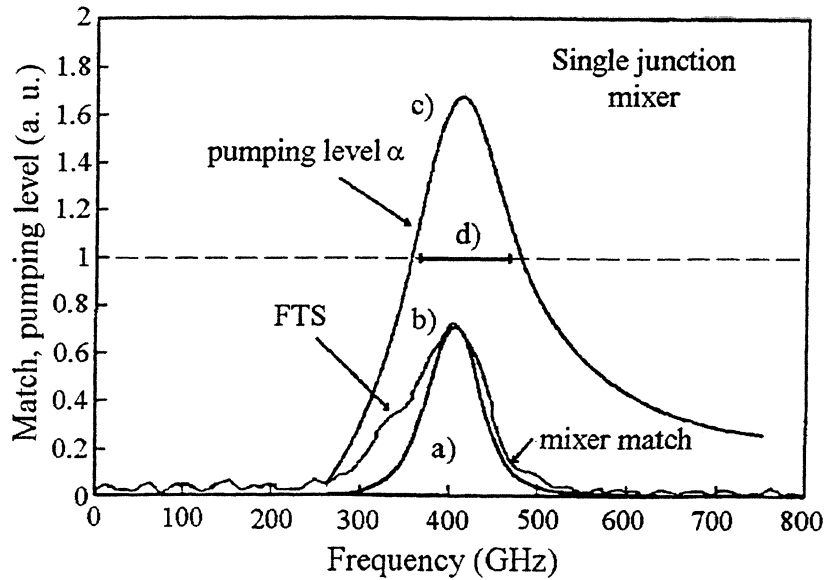


Fig.6 Coupling parameters for the integrated receiver: a) calculated match to the mixing junction; b) fitted to the video response of the mixer obtained with Fourier transform spectrometer; c) predicted pump level $\alpha=V_{RF}/hf$; d) the horizontal bar presents the region of pump level exceeding $\alpha=1$ (estimated from dipstick measurements).

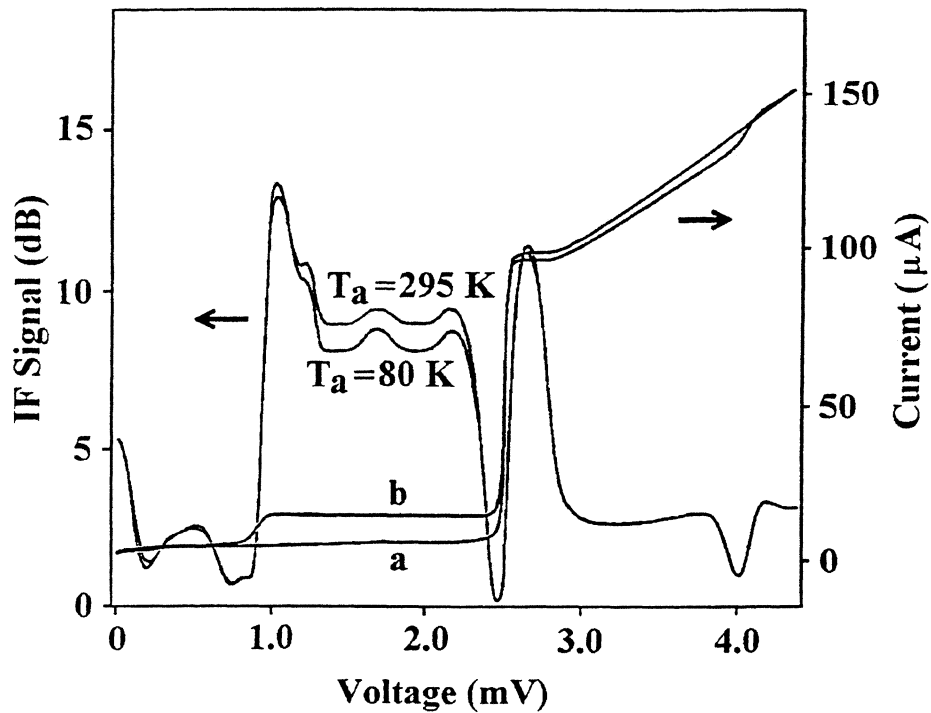


Fig.7 IV-curve of the unpumped mixer (a) and the pumped mixer (b). The IF power output at IF=1.5 GHz is given for blackbody radiators with temperatures of 80 K and 295 K.

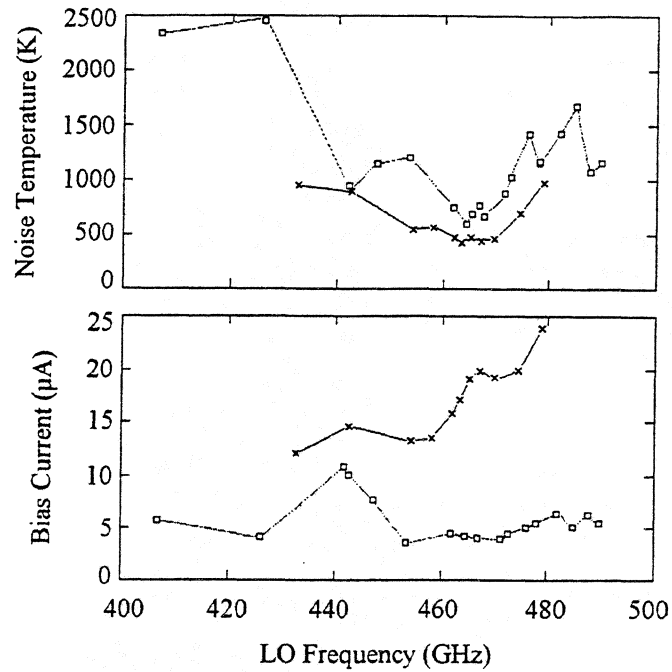


Fig.8 Noise temperatures of the integrated receiver and the LO induced bias current through the junction. Crosses refer to the use of an external oscillator, boxes refer to the use of the FFO.

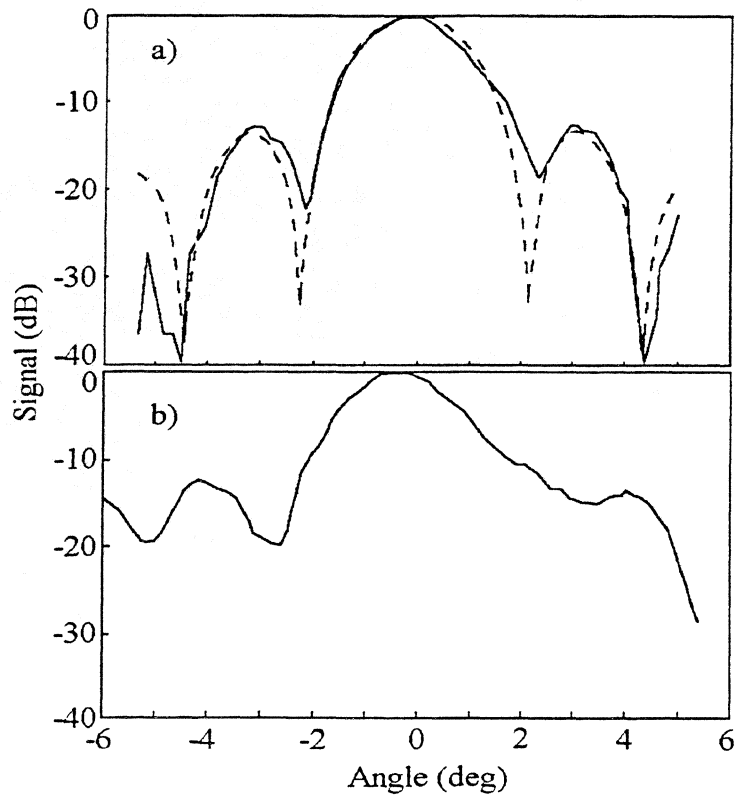


Fig. 9 Antenna beam patterns of the integrated receiver: a) in horizontal plane (solid); b) in vertical plane. The dashed line in a) is a calculated diffraction limited pattern.

D. Antenna beam

The antenna beam pattern of the receiver is presented in Fig.9. The data have been obtained in the video detection mode of the externally chopped CW signal at 465 GHz by tilting the cryostat around the phase center of the beam. The measured beam has width ± 4 degrees at the level of -20 dB in the horizontal plane (the dipoles of the antenna are vertical). The comparison between the experimental data and calculated diffraction pattern demonstrates that the size of the fitted diffraction hole is $R = 9.7$ mm. It is in reasonable agreement with the size of the primary lens ($R = 10$ mm). However, the beam is less symmetric in the vertical plane. The most probable explanation is the effect of asymmetric feed of the antenna because the central part of the mixer is large enough and the connection to the antennas is realised via asymmetric microstrip line.

Conclusion

A planar receiver consisting of a double dipole antenna, SIS mixer and a flux flow Josephson oscillator as LO integrated on a single chip, has been tested successfully in the frequency range of 400-500 GHz. Extensive experimental and numerical studies have been performed to match the FFO and the SIS mixer on the same chip. The data of the experimental test are in good agreement with predicted parameters of the integrated receiver that confirm the numerical method used for design and analysis of the device.

To avoid interference between the mixer and LO, novel integrated control lines have been used to produce the two localised magnetic fields for suppression of the Josephson noise in the mixer and for tuning the frequency of the FFO. High efficiency of the mixer control line is demonstrated by a second order minimum of the Josephson supercurrent in $1 \mu\text{m}$ size SIS junction. Hence the compatibility of SIS mixer and FFO in the submm region has been proven experimentally.

The integrated LO of the receiver has demonstrated good tuneability over the frequency range 400-500 GHz by adjusting the magnetic field applied to the FFO. The intrinsic linewidth of the free-running FFO is estimated experimentally as 1 MHz.

A number of original wide-band dc-breaks, impedance transformers and filters have been developed especially for the integrated receiver that allow to use only two metal layers. Hence the whole device has been fabricated with a reduced number of superconducting layers: one trilayer Nb- AlO_x -Nb and only one superconducting wiring layer. The single chip receiver has demonstrated wide band operation with DSB noise temperature < 1500 K over the frequency range of 428-482 GHz and a minimum of $T_f = 595 \pm 20$ K at 465 GHz.

Acknowledgements

The authors thank A. V. Ustinov for fruitful discussions, H. Golstein and H. Ode' for the help in the experiment. The work was supported in part by the International Science Foundation (Grant No.MCH000), the Russian Program of Fundamental Research (contract 92-02-3484), the Russian State Scientific Program "Superconductivity" (contract No.91009) and ESA TRP contract No.7898/88/NL/PB/SC.

References

- (1) J.R.Tucker, M.J.Feldman, "Quantum Detection at Millimeter Wavelengths," *Rev. of Mod. Phys.*, vol 4, pp. 1055-1113, 1985. G. de Lange, C. H. Honingh, M. M. T. M. Dierichs, H. H. A. Schaeffer, R. A. Panhuyzen, T. M. Klapwijk H. van de Stadt, Th. de Graauw. "A Low Noise 410-495 GHz Nb/AlOx/Nb SIS Waveguide Mixer", *IEEE Trans., on Appl. Supercond.*, vol. 3, No. 1, pp. 2613-2616, 1993. J. Zmuidzinas, N. G. Urgas, H. G. LeDuc, J. A. Stern, "Low-noise slot antenna SIS mixers", was presented on ASC-94, Boston, USA, report ER-2, (1994). Will be published in *IEEE Trans. on Appl. Supercond.*, No 3, 1995. A. Karpov, J. Blondel, B. Lazareff, M. Voss, and K.H. Gundlach, "Four photons sensitivity heterodyne detection of submillimeter radiation with superconducting tunnel junctions ", was presented on ASC-94, Boston, USA, report EUC-5 (1994). Will be published in *IEEE Trans. on Appl. Supercond.*, No.3, 1995.
- (2) A. K. Jain, K. K. Likharev, J. E. Lukens and J.E.Sauvageau, "Mutual phase-locking in Josephson junction arrays", *Physics Reports*, vol **109**, No 6, pp. 309-426, 1984.
- (3) S. Han, B. Bi, W. Zhang, A. H. Worsham, and J. E. Lukens, "High Power Submillimeter Wave Source using Series Biased Linear Josephson Effect Array", *Proc. Fourth Int. Symp. on Space Terahertz Techn.*, pp. 474-476, March 30 - April 1, UCLA, Los-Angeles, USA, 1993.
- (4) B. Bi, S. Han, and J. E. Lukens, "Distributed Josephson Junction Arrays as Local Oscillators", *IEEE Trans. on Appl. Superconduct.*, vol. **3**, No. 1, pp. 2303-2306, 1993.
- (5) E. Joergensen, V. P. Koshelets, R. Monaco, J. Mygind and M. R. Samuelsen, "Thermal Fluctuations in Resonant Motion of Fluxons on a Josephson Transmission Line, Theory and Experiment", *Phys. Rev. Let.*, vol **49**, No. 15, pp 1093-1096, 1982.
- (6) T. Nagatsuma, K. Enpuki, F. Irie, and K. Yoshida, "Flux-Flow type Josephson oscillator for millimeter and submillimeter wave region", *J. Appl. Phys.*, vol **54**, p. 3302, 1983; see also Pt. II: *J. Appl. Phys.*, vol **56**, p 3284, 1984; Pt. III: *J. Appl. Phys.*, vol **58**, p. 441, 1985; Pt. IV: *J. Appl. Phys.*, vol **63**, p. 1130, 1988.
- (7) A. V. Ustinov, T. Doderer, R. P. Huebener, J. Mygind, V. A. Oboznov, and N. F. Pedersen, "Multi-Fluxon effects in long Josephson junctions", *IEEE Trans. on Appl. Supercond.*, vol. **3**, No. 1, pp. 2287-2294, 1993.
- (8) Y. M. Zhang, D. Winkler, and T. Claeson, "Linewidth measurements of Josephson flux-flow oscillators in the band 280-330 GHz," *Appl. Phys. Lett.*, vol. **62**, p. 3195, 1993, see also *Proc. Fourth Int. Symp. on Space Terahertz Techn.*, pp. 485-499, March 30 - April 1, UCLA, Los-Angeles, USA, 1993.
- (9) V.P. Koshelets, S.V. Shitov, A.V. Shchukin, A.M. Baryshev, L.V. Filippenko, G.M. Fisher and J. Mygind, "Josephson tunnel junction attenuator", *Appl. Phys Lett.*, vol. 63, No. 23, pp. 3218-3220, 1993.
- (10) C. Hilbert and J. Clarke, "DC SQUID as a radiofrequency amplifier", *J. Low Temp. Phys.*, vol. 61, No. 3/4, pp. 263-280, 1985. M. Tarasov, V. Belitsky, and G. Prokopenko, "DC SQUID RF amplifier", *IEEE Trans. Appl. Supercond.*, vol. 2, pp. 79-83, Feb. 1992

- (11) K. K. Likharev and V. K. Semenov, "RSFQ logic/memory family: a new Josephson junction technology for sub teraHertz clock frequency digital systems", *IEEE Trans. on Appl Supercond.*, v. 1, p. 3, 1991. V. P. Koshelets, "Single Flux Quantum Digital Devices", *Supercond. Sci. Technol.*, vol. 4, pp. 555-560, 1991.
- (12) V. P. Koshelets, A. V. Shchukin, and I. L. Lapitskaya, and J. Mygind, "Spectral linewidth of autonomous and injection locked flux flow oscillators", Submitted for *Phys. Rev. B. Rapid Comm.* - February, 1994; see also *Proc. of ASC-94*, Boston, USA, report EQA-4, (1994), will be published in *IEEE Trans. on Appl. Supercond.*, 1995.
- (13) V. P. Koshelets, A.V. Shchukin, S.V. Shitov, and L.V. Filippenko, "Superconducting millimeter wave oscillators and SIS mixers integrated on a chip," *IEEE Trans., on Appl. Supercond.*, vol. 3, No. 1, pp. 2524-2527, 1993.
- (14) V. P. Koshelets, S. V. Shitov, A. M. Baryshev, I. L. Lapitskaya, L. V. Filippenko, H. van de Stadt, J. Mess, H. Schaeffer, T. de Graauw, "Integrated Submm Wave Receivers" was presented on ASC-94, Boston, USA, report ER-3, (1994). Will be published in *IEEE Trans. on Appl. Supercond.*, No 3, 1995.
- (15) A. Skalare, M. M. T. M. Dierichs, J. Mees, H. van de Stadt, R.A. Panhuyzen, T. de Graauw, T. M. Klapwijk, "SIS mixers using endfire and broadside double dipole antennas at 435 and 480 GHz", *Proc. Fourth Int. Symp. on Space Terahertz Techn.*, Los Angeles, USA, pp. 639-651, 1993.
- (16) S. V. Shitov, V. P. Koshelets, A. V. Shchukin, A. M. Baryshev, I. L. Lapitskaya, L. V. Filippenko, Th. de Graauw, J. Mees, H. Schaeffer, H. van de Stadt, "Experimental Study of a Superconducting Integrated Receiver at Submillimeter Wavelengths", in *Digest of the 19th international conference on Infrared and millimeter waves*, Report M7.11, pp. 122-123, Sendai, Japan, October 17-20, 1994
- (17) G.S Lee, A.T. Barcnecht, "Geometric and material dispersion in Josephson transmission lines", *IEEE Trans. on Appl. Supercond.*, vol. 2, No. 2, pp. 67-72, (1992). N. Thyssen, H. Kohlstedt, A. V. Ustinov, S. Pagano, J. G. Caputo, N. Flytzanis, "Experimentally study of fluxon resonances in window-type long Josephson junctions", was presented on ASC-94, Boston, USA, report EQA-9, (1994), will be published in *IEEE Trans. on Appl. Supercond.*, No.3, 1995.
- (18) J. Mygind, V.P. Koshelets, A.V. Shchukin, S.V. Shitov, and I.L. Lapytskaya, "Properties of the autonomous and injection locked Flux-Flow Oscillators" was presented on ASC-94, Boston, USA, report EQA-4 (1994)), will be published in *IEEE Trans. on Appl. Supercond.*, No.3 (1995).
- (19) M. Gurvich, M. A. Washington, and H. A. Huggins, "High quality refractory Josephson tunnel junctions utilizing thin Al layers", *Appl. Phys. Lett.*, v.42, pp. 472-474, 1983
- (20) V. P. Koshelets, S. A. Kovtonyuk, I. L. Serpuchenko, L.V. Filippenko, and A.V. Shchukin, "High quality Nb-AlO_x-Nb tunnel junctions for microwave and SFQ logic devices", *IEEE Trans. on Magn.*, vol. 27, No 2, pp. 3141-3144, 1991.

A 16-ELEMENT SIS-RECEIVER FOR 455 - 495 GHz FOR THE HEINRICH HERTZ TELESCOPE

**M.A. Scherschel^{a)}, G.A. Ediss^{a)}, R. Güsten^{a)},
K.H. Gundlach^{b)}, H. Hauschildt^{a)}, C. Kasemann^{a)},
A. Korn^{a)}, D. Maier^{b)}, and G. Schneider^{a)},**

a) Max-Planck-Institut für Radioastronomie, Auf dem Hügel 69,
D-53121 Bonn, Germany

b) Institut de Radio Astronomie Millimetrique, 300 Rue de la Piscine,
38406 Saint-Martin-d'Herès Cedex, France

Abstract

The development status of the 455 - 495 GHz SIS-receiver array is presented. The array consists of 16 elements arranged in subgroups of 2:4:2. The mixer elements are $1 \mu\text{m}^2$ Nb/AlO_x/Nb-junctions grown on fused quartz substrates together with the IF-filter and the integrated tuning circuit. The mixers use corrugated feed horns, reduced-height waveguides and a sliding backshort which, in addition to the integrated tuning circuit is required to achieve a broad band response. The junction fabrication technique is summarized. Receiver noise temperatures below 180 K between 430 and 480 GHz have been obtained. The receiver noise does not depend on the frequency at which the backshort is optimized.

Introduction

The need for the efficient use of radiotelescopes has led to the construction of focal plane arrays of receivers at centimeter and, more recently, at millimeter wavelengths [1, 2]. Due to the costs and technological effort at submillimeter wavelengths, telescopes above 300 GHz are currently operating with a maximum of two channels at a given frequency. The 16-element array of 455 - 495 GHz SIS receivers requires particular attention to the design of mixers and SIS-elements. In addition the waveguide mixers must be 22 mm apart between centres, so that all connections (backshorts, IF's, bias and coil currents) must emerge from the rear of the mixers. The separation of the individual elements is limited by the permissible truncation of the lenses preceding the feed horns.

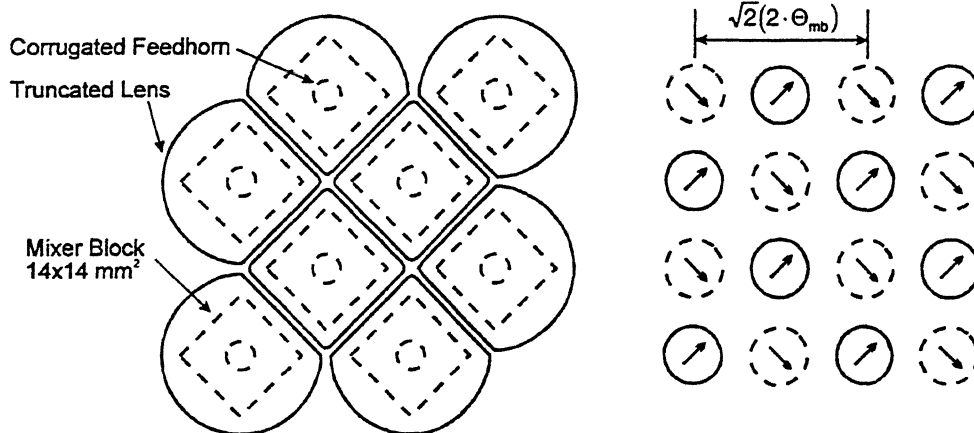


Figure 1: Lens-mixer layout of one subarray (left) and beam patterns of the SIS-array on the sky (right). Circles mark the half-power beamwidth ($\Theta_{MB} = 16''$). Arrows denote beams from the two different interleaved subarrays.

To bring the sky-beams closer together, two interleaving subarrays (of 8 elements each) are employed (Fig. 1), with perpendicular polarisations to one another: for a single array the beams are separated by $2 \cdot \Theta_{MB}$, so that interleaving gives a sky-beam separation $\sqrt{2} \cdot \Theta_{MB}$ for all 16 elements. The lens-horn-mixer units are arranged in a 2:4:2 configuration (Fig. 1). For a facility instrument with so many elements, it is necessary to utilise broad band SIS-structures and to tune each mixer only once in the laboratory: thereafter no further mechanical tuning will be possible.

The noise temperature target for all channels is less than 150 K, including losses due to coupler, window and IR-filters, and IF noise.

Horn and Mixer

Scalar-feeds are used, due to their superior beams and larger bandwidths. The circular horn throat is transformed to a 4:1 reduced-height waveguide with dimensions $480 \times 60 \mu\text{m}$. A contacting backshort (BS) is used which will be fixed after initial tuning.

Mixers and feed horns were fabricated by Radiometer Physics, and IF matching-structures (160 to 50Ω for 2 - 4 GHz IF) were designed and constructed in house.

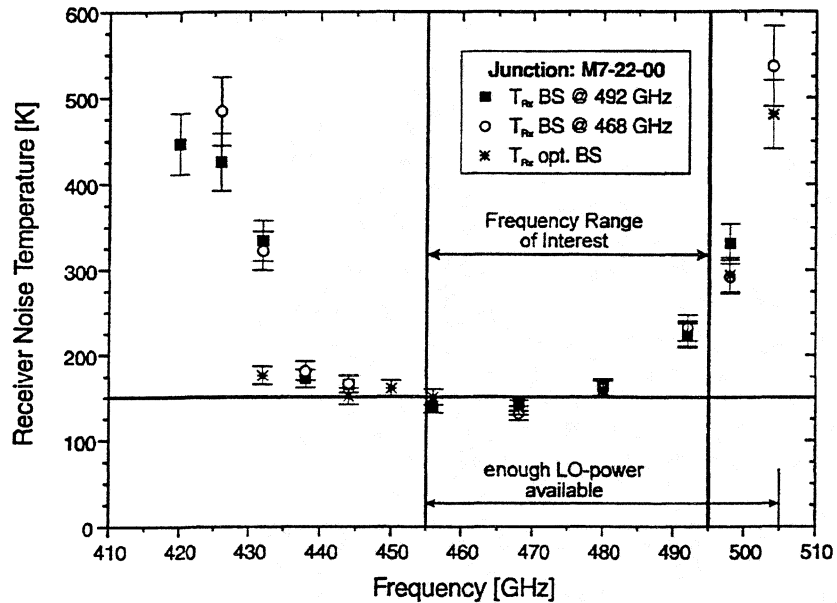


Figure 4: Receiver noise temperature T_{Rx} for a junction with microstrip transformer tuning circuit in the frequency range of our LO. The backshort was optimized at 492 GHz and thereafter kept fixed (closed squares). The open circles denote T_{Rx} vs. frequency for the backshort optimized at 468 GHz and the stars represent T_{Rx} at the optimum backshort position for each frequency.

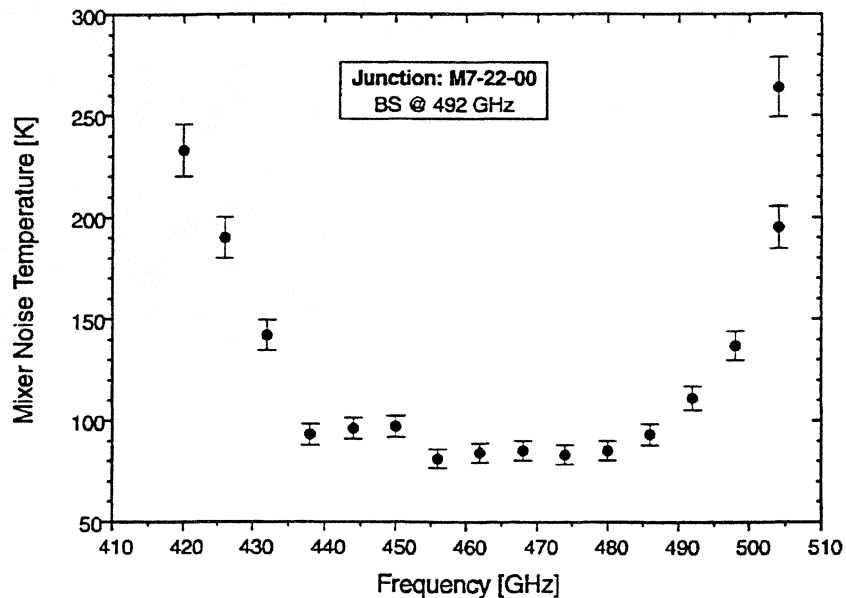


Figure 5: Mixer noise temperature T_M for a junction with microstrip transformer tuning circuit in the frequency range of our LO. The backshort was optimized at 492 GHz and thereafter kept fixed.

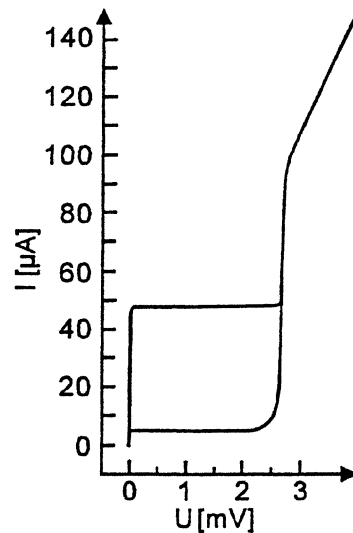


Figure 3: Typical IV-curve of a $1\mu\text{m}^2$ junction.

Results

The best receiver noise results were achieved with the integrated microstrip transformer tuning structure [4]. Radial stub tuning circuits were also used, but yielded worse results. The radial stub mixers displayed a negative differential resistance below the gap and therefore no stable operation was possible. The total receiver noise temperature T_{Rx} for a microstrip transformer tuning circuit in the frequency range of our LO is presented in Fig. 4. The BS was optimized at 492 GHz and thereafter kept fixed (closed squares). In Fig. 4 we also show T_{Rx} vs. frequency for the BS optimized at 468 GHz (open circles) and at the optimum BS-position for each frequency (stars). In all three cases the receiver noise temperature in the frequency range 435 - 480 GHz hardly changes within the experimental error (± 10 K) and is well below 180 K.

The mixer noise temperature (T_{M}) was extracted from the measured receiver noise by subtracting the IF-noise temperature (T_{IF}) and the losses in coupler, window and filters. T_{M} is shown in Fig. 5 as function of LO-frequency and varies from 80 to 100 K between 435 and 480 GHz.

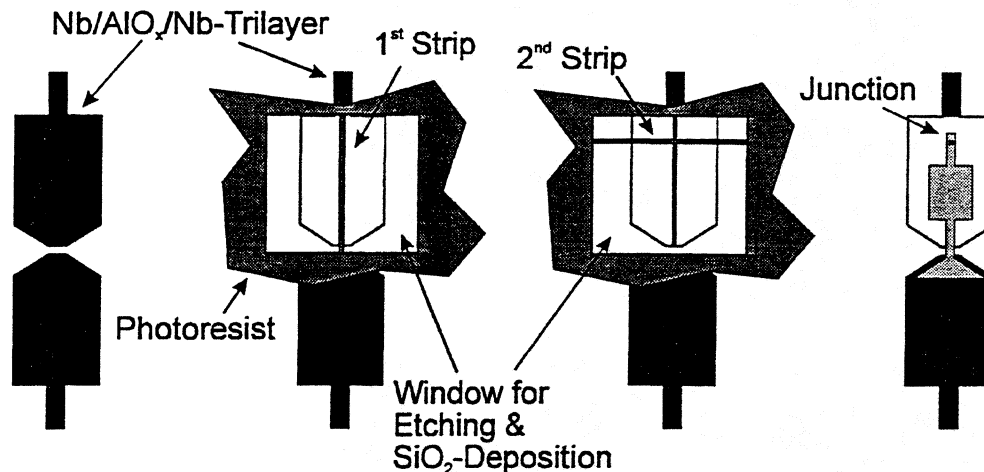


Figure 2: Schematical fabrication of SIS-junctions by means of the SNAP-technique (see text for more details) .

Junction Fabrication

The SIS-junctions were fabricated by means of a slightly modified SNAP-technique (Selective Niobium Anodization Process) [3] (see Fig. 2). In a first step the Nb/Al/AIO_x/Nb-multilayer is deposited in situ into a photoresist stencil. After removing the photoresist by lift-off the antenna structure and the low-pass IF-filter remain on the 200 μm-thick quartz substrate. In the second step a photoresist line is patterned onto the multilayer. The upper Nb-Layer is then removed by RIE followed by anodization, SiO₂-deposition and lift-off. The second production step is the repeated with a photoresist line perpendicular to the first one. In order to optimize the RF match of the junction, a superconductive microstrip circuit is deposited in the fourth production step. The Nb-tuning structure also provides the electrical contact to the upper Nb-layer of the junction, and to the antenna.

We produced junctions of 0.5 μm² and 1 μm². Typical junction parameters are:

- critical current: 7 - 9 kA/cm²
- quasiparticle current at 2 mV: 3 - 5 μA/μm²
- gap parameter: $2\Delta = 2.6$ meV
- normal state resistance: $R_N = 25 - 35 \Omega$

Fig. 3 shows a typical IV-curve of a 1 μm² junction. The relatively low gap parameter is presumably due to the thickness of the upper Nb layer of 30 nm. We tried to keep the upper Nb layer as thin as possible in order to minimize the etching time. This should reduce the underetching of the structure protected by the photoresist and therefore increase the homogeneity of the junction shape.

Conclusions

A 16-element SIS-receiver array is being developed at MPIfR. After the first junction production run at IRAM receiver noise temperatures less than 180 K were achieved over the frequency range 435 - 480 GHz. Based on the evaluation of these first results the calculation of the tuning structure will be optimized in order to improve the broad band RF impedance match of the junctions in the frequency range of interest. The second junction production run is scheduled for April 1995.

Acknowledgements

We acknowledge many helpful discussions with N. Keen.

We would like to thank IRAM (Grenoble) for support, especially D. Billon, T. Lehnert, P. Pasturel, and B. Plathner.

The project was supported in part by *Verbundforschung* under Grant no. 05 2BN734 (0).

References

- [1] J.M. Payne, *Rev. Sci. Instr.*, **59**, 1911, (1988).
- [2] N.R. Erickson, P.F. Goldsmith, G. Novak, R.M. Grosslein, P.J. Viscuso, R.B. Erickson, and C.R. Predmore, *IEEE Trans. MTT*, **40**, 1, (1992).
- [3] M. Voss, A. Karpov, and K.H. Gundlach, *Supercond. Sci. Technol.*, **6**, 373, (1993).
- [4] P. Febvre, W.R. McGrath, P. Batelaan, H.G. LeDuc, B. Bumble, M.A. Frerking, and J. Hernichel, *Proceedings of the IEEE MTT-S International Microwave Symposium*, June 14-18, 1993.

Low noise mixer with the Nb-Al Oxide-Al-Nb tunnel junctions for a multibeam 345 GHz receiver

A. Karpov*, D. Maier*, J. Blondel*, B. Lazareff*, K. H. Gundlach*

* IRAM, 300 rue de la Piscine, F - 38406 St. Martin d'Hères, France.

Abstract

In this work we present for the first time a low-noise submillimeter receiver with a mixer using Superconductor-Insulator-Normal metal-Superconductor (SINS) junctions. Junctions containing a normal metal layer may be free of the Josephson current and of the related perturbations of mixer operation specific for the standard SIS mixers. This SINS mixer quality is important for the application in the multibeam receiver. The SINS mixer stability of operation and independence on the magnetic field have been confirmed in our experiment. Minimum SINS receiver noise in the 290 - 330 GHz band is about 135 K when the junction $R_N\omega C$ is about 30. Noise, conversion gain and thermal properties of the SINS mixer have been studied and compared with the SIS mixers. The limit of SINS mixer operation improvement is discussed in the end of the work.

Introduction

Improvement of the modern receivers used in radioastronomy at the submillimeter wavelength is based on the progress of the mixers with the Superconductor-Isolator-Superconductor (SIS) quasiparticle tunnel junctions [1, 2]. Quasiparticle current and pair current exist in this type of junctions. Problems related to the pair current in the SIS mixers are well known (instability, excessive noise)[3]. With the commonly used Nb-Al Oxide-Nb SIS junctions this problem is more pronounced at the submillimeter wavelength, where the low order Shapiro steps interfere with the first Tien-Gordon step. Magnetic field is normally used to suppress the pair current but in practice it is difficult to remove it completely. Even after adjustment of magnetic field the stability of operation may be lost due to the magnetic flux quanta trapping or simply to the instability of the magnetic field. Necessity of the periodical adjustment of the magnetic field in the numerous SIS mixers may be an important handicap of the multibeam SIS receiver at the submillimeter wavelength.

A Superconductor-Isolator-Normal metal (SIN) junction may be used as a version of the quasiparticle tunnel junction alternative to the SIS. Absence of the pair current in SIN junction simplifies the device behavior. It makes possible to avoid the Josephson effects related perturbations in the SIN devices and to use the mixer without applying the magnetic field to the tunnel junctions.

Up to now only few papers were published on the receivers with the SIN mixers. The best result is 220 - 300 K DSB receiver noise temperature in the 220-230 GHz range [4].

Theoretical analysis of a mixer performance with a tunnel SIN junction [5] is normally based on the same approach as the analysis of the SIS mixers [6], where the mixer performance is calculated using the Kramers-Kronig transform of the I-V curve. The I-V curve of a SIN junction is more

smooth than that of the SIS junction resulting in the lowest mixer conversion gain [5]. Gap voltage of a SIN junction is a half of the gap of the SIS junction with the same superconductor. Nevertheless a gain about - 5 dB may be predicted for a SIN mixer [7].

Analysis of the experiments with the SIN mixers shows importance of the loss in the normal conductor electrode. At the submillimeter wavelength a tunnel junction typical resistance is well below 1 Ohm and a parasitic resistance of the same order of magnitude [4] may reduce in a few time conversion gain of a SIN mixer. Even a small loss in a parasitic resistance associated with a low conversion gain in a SIN junction degrades the receiver performance.

The idea of this work is to ameliorate performance of the mixer using a SINS junction instead of a SIN. In SINS junction the two electrodes are made in superconductor and the loss in a short Al layer is not important. At the same time the pair current through the SINS junction may be close to zero without an external magnetic field.

We introduce also an L-C impedance transformer integrated with the junction to prevent the degradation of the mixer gain related to the loss in the circuit.

Below we present an experiment in 290 - 330 GHz band with a low noise mixer with an Nb-Al Oxide-Al-Nb junction; we discuss the noise properties and the gain of the mixer, the thermal behavior of the mixer and the limit of the mixer optimization.

SINS junctions

The SINS junction was produced according to the method presented in [8]. Base electrode of the junction is in Nb 90 nm thick, the Al layer is 30 nm thick and the counter electrode is in Nb 300

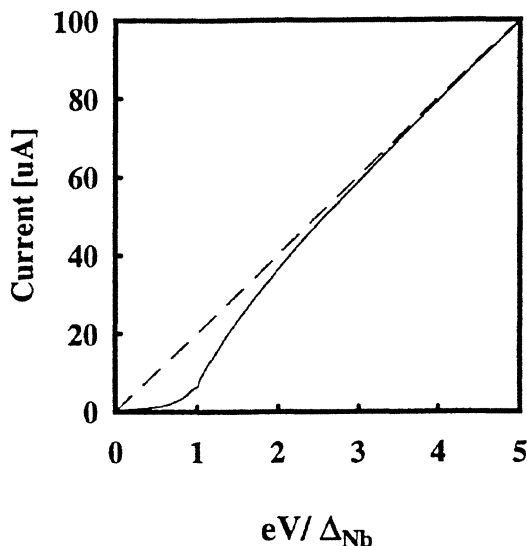


Figure 1. I-V characteristic of the SINS junction used in a mixer. Bias voltage is normalized to Δ_{Nb}/e . Junction is at 3 K. A dashed line corresponds to the normal resistance of the junction.

nm thick. In the mixer we use an array of two junctions. Junction technology is in progress and up to the moment only few were accessible for the test. Junction definition is done with a mask with few different junction areas and with the same matching circuit. Only the junctions with the biggest area were usable. Junctions available for the test have the area $1.6 \times 1.6 \mu m^2$ and the individual normal resistance 72 Ohm resulting in a relatively important $R_N \omega C \approx 30$.

Gap voltage of a tunnel junction is important for the estimation of the frequency limit of the operation of a mixer $f_{MAX} \approx 2Vg/eh$ [6]. It is known that in SIN junctions $Vg = \Delta_S/e$ resulting in $f_{MAX} \approx 700$ GHz for Nb superconductor electrode; for the SIS junctions the gap voltage is two times larger $Vg = 2\Delta_S/e$ with $f_{MAX} \approx 1400$ GHz for Nb. The SINS junctions have some intermediary properties and a limit frequency is between 700 and 1400 GHz.

Theoretical and experimental consideration of the Nb\Al junctions with a similar structure presented in [9] gives the gap voltage for the different thickness of the Al layer. When Al layer is about 30 nm thick a gap voltage according to [9, 10] is $V_g \approx 1.48\Delta_{Nb}/e$ mV at 4.2 K and $V_g \approx 1.52\Delta_{Nb}/e$ at 1.6 K. Using this data one can expect the limit frequency of our SINS mixer as $f_{MAX} \approx 1000$ GHz convenient for the application at the submillimeter wavelength. In practice the junction gap voltage depends strongly on the conductivity of the metals in the Nb and Al layers and on the interface between the layers and so on the technology of the junction fabrication.

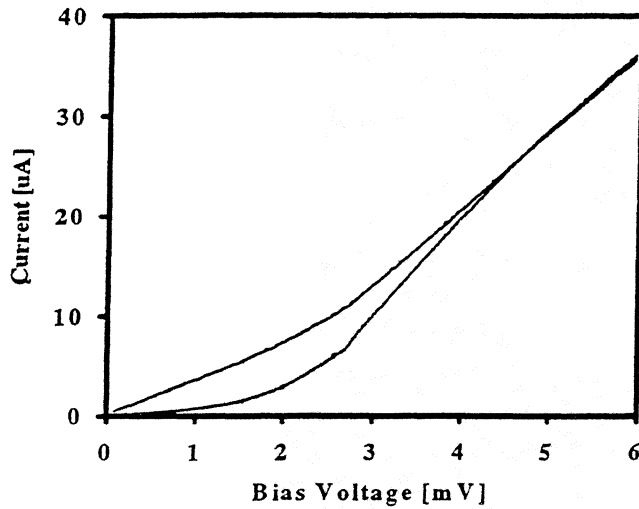


Figure 2. The details of the I-V characteristics of the SINS junction without local oscillator power (below) and with the local oscillator at 300 GHz.

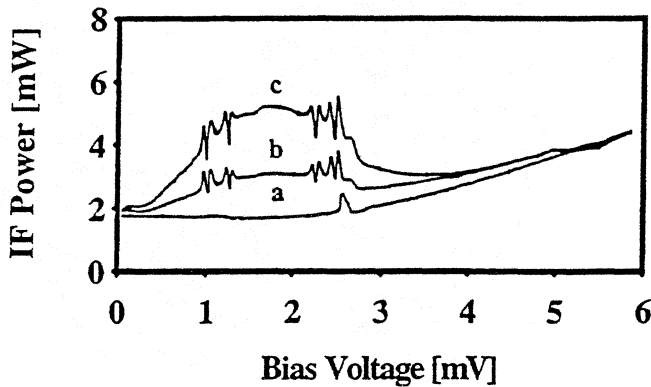


Figure 3. Receiver output power at the intermediate frequency 1.5 GHz a) without the local oscillator power P_{LO} , b) with the P_{LO} and with the nitrogen temperature load in front of the receiver, C) with P_{LO} and with the ambient temperature loads.

Experimental I-V characteristic of a SINS junction measured in our mixer at 3 K temperature is presented in Fig. 1. Bias voltage of the two junction array is divided by 2 and than normalized to $\Delta_{Nb}/e = 1.4$ mV; a dashed line corresponds to the normal resistance of the junction. Critical Josephson current in this junction was not observed. The I-V curve is very smooth. Gap voltage of the junction may be referred to the on-set of the current situated just behind Δ_{Nb}/e . Normally a knee-like structure on the I-V curve specific for the proximity effect in the SINS tunnel junctions exceeds the line of the junction normal resistance on the I-V plane. In I-V characteristic of our junction knee-like structure is not visible in a broad round slop behind the gap voltage. In the terms of [9] this I-V curve corresponds to the case of the a large proximity parameter of the SINS junction electrodes related with a low conductivity of the Nb layer. An other possible explication of this smooth I-V curve is a low transparency of the Nb/Al interface [9]. Small structure just below the gap voltage may be referred to a small gap induced in Al through an additional barrier between the top Nb electrode and Al layer, produced accidentally before deposition of the

top electrode. Smooth form of this structure indicates the simultaneous existence of both effects - low transparency of the Al/Nb interface and reduced conductivity of Nb electrode. One can conclude that junction used in our experiment is nearly SIN contact with a gap voltage corresponding to the frequency limit of the mixer about $f_{MAX} \approx 700$ GHz.

Characteristics of an array of the two SINS junctions with and without local oscillator radiation at 300 GHz are presented in Fig. 2. Receiver output power at the intermediate frequency 1.5 GHz (P_{IF}) is presented in Fig. 3. Curve a) in Fig. 3 is measured without local oscillator power (P_{LO}). Curve b) is measured with P_{LO} and with a nitrogen load in front of the receiver. Curve c) is measured with P_{LO} and with an ambient temperature load. Mixer is at 3 K temperature; no magnetic field is applied to the junction. Pair currents are very small in this junction. No traces of the critical Josephson current or of the Schapiro steps are visible on the I-V curve. Only at the curve of the output power of the receiver one can mentioned some structures related to the excessive power generation by the Josephson effects at the I-V curve regions with a larger dynamic resistance. The amplitude of these perturbations is of the same order of magnitude as may be currently observed with an SIS mixer after optimization of the magnetic field. The presence of these structures does not restrain to use the mixer in the receiver. With the central voltages 1.24 mV and 2.48 mV the structures correspond to the voltage of the first and the second Schapiro steps on the I-V curve of the junction irradiated at 300 GHz. Separation of this structures in the two substructures may be explained by a 15-20% difference in the individual junction area.

A structure at the output power curve without local oscillator power (Fig. 3 a) at 2.7 mV may be explained by the increase of the differential resistance just below the current on-set at the I-V characteristic of the junction. An other smooth maximum at the curve a) Fig. 3 may be mentioned around 1.3 mV. It may be associated with the traces of the two particles tunneling structure.

The Tien-Gordon steps are not obvious at a very smooth I-V curve of the SINS junction when the local oscillator power is applied. However in the dependence of the IF power versus bias voltage a structure corresponding to the quantum step with the size about $2\hbar v/e = 2.5$ mV is visible. It confirms the existence of the quantum assisted tunneling in the tested junctions.

Mixer design

Mixer design is based on our experience with the SIS junctions [11]. It is a single backshort mixer

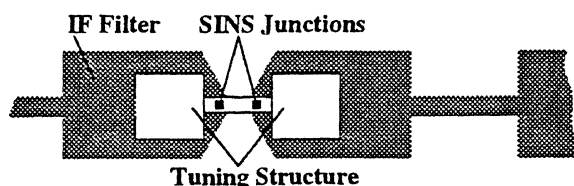


Fig. 4. SINS junctions with the individual tuning structures. An L-C microstrip circuit is used to compensate the junction capacity.

with a reduced height waveguide. An L-C resonant microstrip impedance transformer is integrated with the each junction as a part of the interconnection layer in the junction fabrication process (Fig. 4). Printed circuit of the mixer was optimized for the individual junction normal resistance about 30 Ohm, the junction capacitance 0.15 pF and $R_N\omega C \approx 9$. This mixer design with a relatively large $R_N\omega C$ product of

the junctions presumes the adjustment of the backshort position at each frequency.

Coupling loss between the mixer input port and the junction depends on the junction impedance, frequency, position of the backshort in the mixer and the loss in the circuit. A mixer model [12] was used for the estimation of the minimum coupling loss for the expected junction parameters ($R_N=30$ Ohm, $C=0.15$ pF) and for the junction used in the experiment ($R_N=72$ Ohm, $C=0.22$ pF) in the 290 - 360 GHz band (Fig. 5). Minimum coupling loss of the junction used in this experiment is expected about 7 dB in the band 290 -320 GHz and degrades quickly out of this range (black line in Fig. 5). With a lower junction area and a larger current density minimum coupling loss may be expected 0.5 - 1 dB in a 30 GHz band around 345 GHz (gray line in Fig. 5).

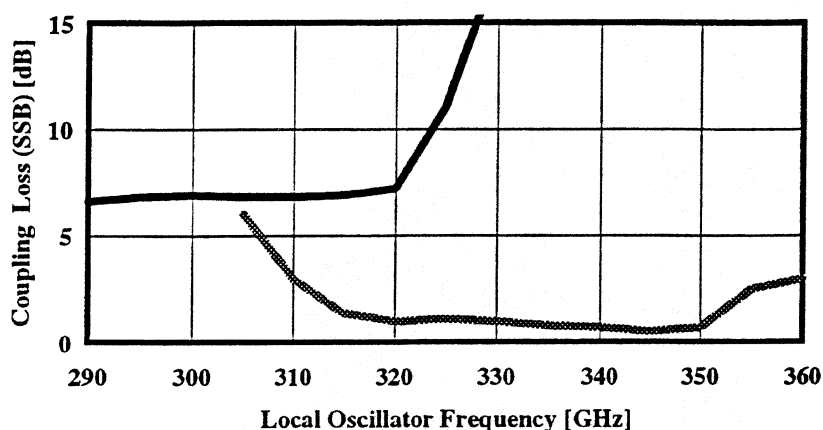


Fig 5 Coupling loss between the junction and the mixer input port calculated for the actual junction area and normal resistance (black line) and for the parameters used for the design of the mixer (gray line).

Experimental set-up

Experiments with the SINS mixer were held in the receiver developed for the SIS Nb mixers. Receiver comprises an Infrared Laboratory liquid helium cryostat, SINS mixer, cooled HEMT IF amplifier, ambient temperature amplifier and the local oscillator. Local oscillator consists of the Carlstrom Gunn oscillator and Millitech quadrupler. Local oscillator power is injected at the mixer input by a cooled waveguide coupler. Receiver input window is in polyethylene and an infrared filter fixed at the 77 K shield is made in expanded polystyrene form.

Receiver operation

Receiver noise temperature was measured in the standard ambient and nitrogen loads experiments. Minimum DSB receiver noise temperature 135 K was measured at 312 GHz when the junction was at 2.7 K temperature. An example of the receiver noise dependence on the local oscillator power is given in the Fig. 6. In this experiment the bias voltage is constant (1.8 mV) and the P_{LO} varied. This leads to a variation of the junction bias current. Current induced in the junction may be expected to be proportional to the LO power. One can mention an excellent 50 % allowance to the local oscillator power around the optimum noise point. Independence of the SINS receiver noise on the P_{LO} may give in the multibeam receiver a good tolerance to the coupling of the

different mixers with a common LO source.

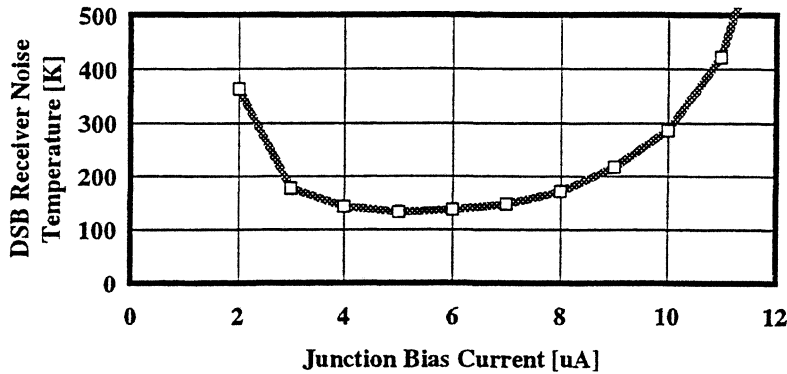


Figure 6. SINS DSB receiver noise for the different levels of the local oscillator power at 312 GHz. Bias voltage is fixed at 1.8 mV and the current in the junction follows the local oscillator power.

In the 290 - 320 GHz band measured DSB receiver noise temperature is quite uniform with the minimum about 135 K and the average level of 150 K (Fig. 7). SINS Mixer was tuned at each frequency to the minimum receiver noise. The frequency band of the low noise receiver operation is shifted to the lower frequency due to the junction large capacitance. It is the first demonstration of the low noise operation of a SIN mixer at the submillimeter wavelength.

Contributions of the different sources to the DSB receiver noise T_{Rec} may be discussed using a standard relation:

$$T_{Rec} = T_{RF} + \frac{T_M}{G_{RF}} + \frac{T_{OUT} + T_{IF}}{2G_M \cdot G_{RF}} \tag{1}$$

Here T_{RF} , T_M , T_{OUT} and T_{IF} are respectively the noise temperatures of the receiver input section, of the mixer, the output mixer temperature and the IF amplifier temperature. Terms G_{RF} and $G_M = G_C G_J$ denote the gains of the receiver input section and the mixer respectively; G_C and G_J the coupling of the junction with the mixer input and the junction conversion gain respectively. Receiver conversion gain is $G_R = G_{RF} G_M$.

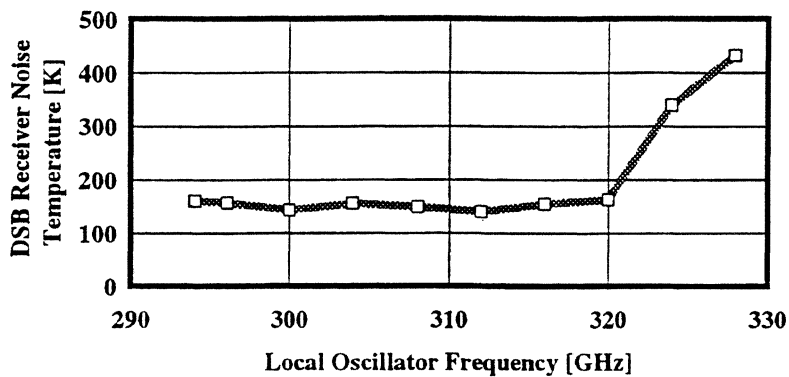


Figure 7. Measured DSB receiver noise temperature.

We measured receiver conversion gain and IF amplifier noise temperature in situ using the junction at the bias voltage behind the gap as a noise source for the calibration of the circuit [13]. Intermediate frequency chain noise temperature in the 1.25-1.75 GHz band is about 4 K. Maximum measured receiver conversion gain between the receiver input port and the IF port of the mixer is about -12 dB.

Measured SSB receiver conversion gain versus frequency dependence $G_{\text{Rec}}(F)$ between the reference plane at the cryostat window and the IF port of the mixer is presented in Fig. 8 by a black line. Receiver conversion gain in the 290 -320 GHz band is $-12 \div -13$ dB. Out of this band the mixer matching circuit is no more efficient and the reflection loss and loss in the mixer circuit becomes too important. The gray line in this figure is a calculated coupling gain G_C between the RF input of the mixer and the junction from the Fig. 5. Junction capacitance is included in the mixer circuit. Calculated variation of the coupling explains well the measured frequency dependence of the gain. One can note a nearly constant difference of 5 - 6 dB between the experimental data and the model prediction of the coupling. We may estimate the available mixing conversion gain $G_J = G_{\text{Rec}} / (G_C G_{\text{RF}})$ in the SINS junction as $-5 \div -5.5$ dB expecting the loss in the input section of this receiver $G_{\text{RF}} \approx -0.5$ dB. This estimation of the mixer conversion gain is in a good agreement with the $G_J = -6$ dB at 320 GHz predicted in [7] for a SIN junction with a similar I-V characteristic. However the noise of our receiver is larger than 10 K minimum predicted at 320 GHz in the same work.

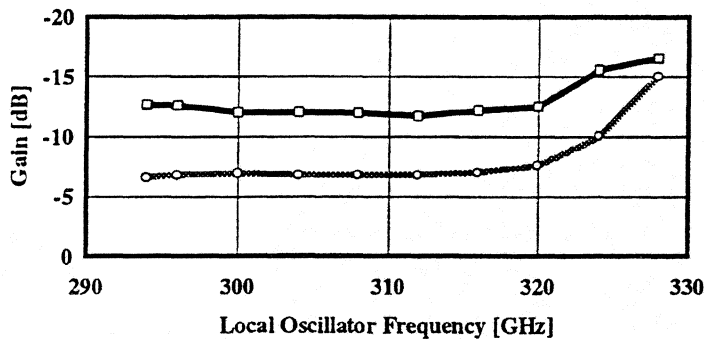


Figure 8. Measured receiver conversion gain (black line) and calculated coupling loss between the mixer waveguide input flange and the SINS junction RF resistance (gray line). The difference between this gain let us estimate the available conversion gain of about -6 dB in the SINS junction.

junction predicted in [16].

Relation between the receiver gain $G_{\text{Rec}} = G_M G_{\text{RF}}$ and T_{Rec} measured with SINS mixer at 312 GHz is presented in Fig. 9. Receiver noise versus junction bias current for this experiment is given in Fig. 6. As with the SIS mixer the SINS mixer experimental $T_{\text{Rec}}(1/G_{\text{Rec}})$ may be well explained by linear function up to the local oscillator amplitude providing the minimum receiver noise temperature (135 K). Black line in Fig. 9 is a linear fit of $T_{\text{Rec}}(1/G_{\text{Rec}})$. Intersection of this line with the T_{Rec} axis gives $T_{\text{RF}} + T_M / G_{\text{RF}} = 30$ K. In experiment with SIS mixer in the same receiver we find a similar value of $T_{\text{RF}} + T_M / G_{\text{RF}}$. All this confirms the validity of the methods proposed in [14, 15] for the case of the SINS mixer.

The first term of expression (1) $T_{\text{RF}} + T_M / G_{\text{RF}}$ is determined by a method proposed by R. Blundell et al [14] and Qing Ke and M. Feldman [15] for an SIS mixer. Receiver input section contribution in the receiver noise $(T_{\text{RF}} + T_M / G_{\text{RF}})$ is evaluated as a constant component in the linear relation between the SIS receiver noise and the receiver gain at a low level of the local oscillator power. This rule is based on the independence of the mixer output noise from the local oscillator amplitude at the tunnel

Output noise of the SINS mixer is determined according (1) with the measured $T_{RF}+T_M/G_{RF}$, T_{IF} and $G_R = G_{RF}G_M$. Output noise measured at the different frequencies is presented in Fig. 10. In a good agreement with prediction in [16] it is almost frequency independent. Moderate level of the SINS mixer output noise measured in our experiment ~ 13 K is very encouraging for the use of this devices in the low noise receivers.

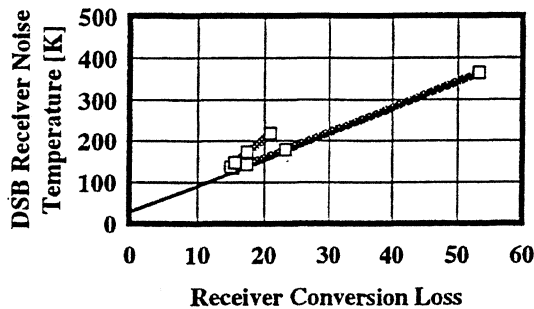


Figure 9. Measured SINS receiver DSB noise temperature versus receiver conversion loss. Noise to loss dependence is nearly linear at the local oscillator power below optimum.

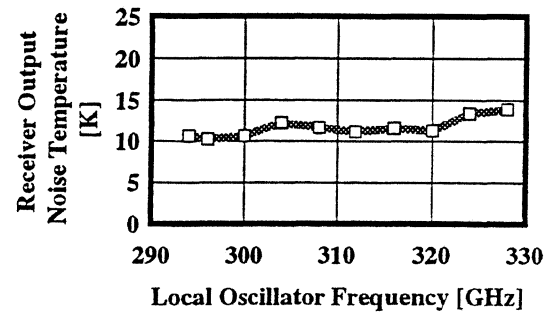


Figure 10. Measured receiver output noise temperature versus frequency. In a mixer with SINS junction T_{OUT} is nearly frequency independent when the mixer is tuned at the minimum of the receiver noise.

Comparison of the different components of the SINS receiver noise measured in our experiments shows that the SINS receiver noise is dominated by the term depended on the mixer output noise and receiver conversion gain. If the SINS mixer output noise is comparable with that of the SIS mixers, the receiver conversion gain may be improved. Actually the 135 K receiver noise comprises a dominate contribution of about 100 K produced by the output noise and multiplied by the receiver loss. Even a moderate reduction of the receiver loss may give an important improvement of the receiver noise. With the optimum SINS junction area and with a lower normal junction resistance the coupling loss and the receiver loss may be reduced for about 5 dB (Fig. 8). In these conditions the SINS receiver with the noise of about 60 K will be competitive with the best SIS receivers.

Thermal behavior of an SINS mixer

Thermal properties of the SINS junction are substantial for the use of the mixer with this device. In the absence of the pair current is a clear advantage of SINS against the SIS, an operation temperature well below 4.2 K normally used in SIN receiver [4] is a serious handicap. Architecture of a receiver with the cryogenics providing the temperature below the liquid helium temperature is complex and its use on the radiotelescope is more difficult.

For the best understanding of the optimum temperature for the SINS receiver operation the performance of a SINS mixer was studied in the 2.7 - 5.5 K range experiments. This range corresponds to the possible conditions in cryostats with and without He pumping. In all the 290 - 330 GHz frequency range it has been found that the receiver noise temperature strongly depends on the temperature.

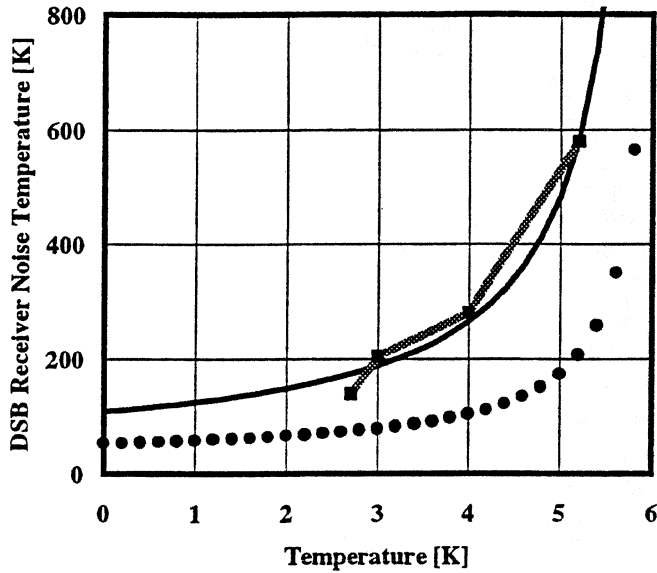


Figure 11. SINS Receiver DSB noise temperature at 312 GHz versus temperature of the junction. Experimental data (gray line) are in a good accord with the model (black line). Junction used in experiment has $R_N\omega C=30$. Dotted line is the model estimation of the receiver was noise with a better SINS junction with $R_N\omega C=9$. Note a smaller difference in the receiver noise temperature expected at 3 K and 4.2 K after optimization of the junction $R_N\omega C$.

conversion gain temperature dependence is presented in Fig. 13. In the 2.7 - 5.5 K range $G(T)$ dependence is quasi linear function. This understanding of the SINS mixer temperature behavior is illustrated in Fig. 11. In this figure we compare the measured DSB receiver noise temperature (gray line) and the receiver noise evaluated according (1) using a linear interpolation for $G(T)$, a constant value for the mixer output noise temperature $T_{OUT}=14$ K, $T_{IF}=4$ K and a constant contribution of the receiver front-end section $T_{RF}+T_M/G_{RF} = 30$ K (black line). Interpolation is in a good agreement with experimental $T_{Rec}(T)$.

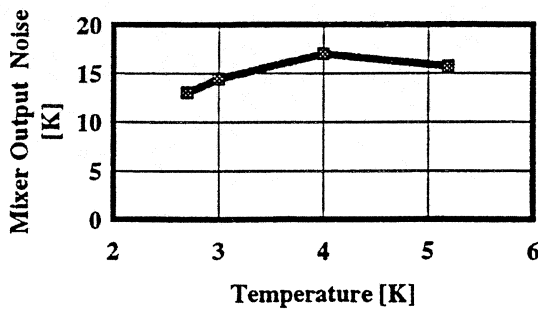


Figure 12. SINS mixer output noise temperature versus temperature of the junction at 312 GHz.

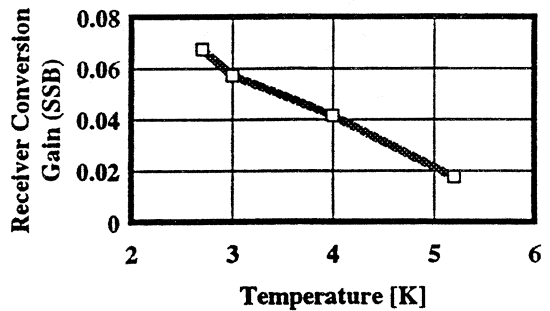


Figure 13. SINS receiver conversion gain versus junction temperature at 312 GHz.

In more details we present a typical temperature behavior of the SINS mixer measured in experiment at 312 GHz (Fig. 11). Mixer tuning and P_{LO} were optimized at each temperature in this test. In a 2.7 - 5.5 K temperature range DSB receiver temperature varied between 600 K and 135 K. The sources of this 450% receiver noise variation may be classified in terms of parameters of equation (1).

Receiver input section noise, receiver conversion gain and the SINS mixer conversion gain were measured at each temperature. Input section contribution is constant about 30 K except 2.7 K point where infrared filter was changed and RF loss in the filter reduced. Output noise of the SIN mixer has been found in this temperature range almost temperature independent (Fig. 12). The most part of the receiver noise temperature variation may be explained by the thermal dependence of the SINS mixer conversion gain. Mixer

Estimation of the SINS mixer possible thermal behavior with improved junction area definition ($R_N\omega C \approx 9$) is presented by a dotted line in Fig. 11. We expect the same quality of the I-V curve and the same thermal dependence of the mixer noise and gain as in our experiment. As before (Fig. 8) receiver conversion gain is expected to be improved by 5 dB after improvement of the junction $R_N\omega C$. In this conditions the SINS receiver noise is no more dominated by the term depended from the receiver conversion gain. Receiver noise thermal dependence with $R_N\omega C \approx 9$ may be less pronounced than in our experiment with $R_N\omega C \approx 30$ where the receiver gain is the main source of the receiver noise variation with the temperature. In Fig. 11 receiver noise calculated for a SINS junction with an improved $R_N\omega C$ is nearly the same at the liquid helium temperature (4.2 K) and at 3 K temperature. Improvement of the junction $R_N\omega C$ may not only reduce the SINS receiver noise but also may allow to use the SINS mixers at the liquid helium temperature without losing the receiver sensitivity.

Conclusion

A low noise mixer with the SINS quasiparticle Nb/Al Oxide/Al/Nb junction is prepared and tested in the 290 -330 GHz band. Minimum DSB receiver noise temperature with the new mixer is about 135 K. No magnetic field was necessary to suppress the pair currents in the junction. Mixer operations may be stable, without Josephson effect related perturbations.

Available conversion gain of the RF signal in the tested junctions has been found to be close to -6 dB in a good accord with the theoretical predictions in literature for the mixer with a similar I-V characteristic [7].

SINS mixer output noise has been found to be constant and to be quite low (~13 K). Combination of a low output noise and a moderate conversion loss in the SINS mixer may allow to built the low-noise submillimeter receivers with the SINS mixers.

Junction technology is in progress and only the SIN junction with a quite large $R_N\omega C \approx 30$ was accessible for the test. With the SIN junctions having a moderate $R_N\omega C$ about 8-9 one can expect a significant improvement of the receiver performance up to 60 K DSB receiver noise temperature. Improvement of the SIN junction parameters may allow to built a low noise receiver with the SINS mixer at the liquid helium temperature.

Low noise operations of the SINS mixers at the submillimeter wavelength and the absence of the Josephson related perturbations are promising for the use of these mixers in the radioastronomy multibeam receivers in the 300 - 700 GHz range.

References:

1. G. Philips and J. Keene, "Submillimeter astronomy", Proceedings of the IEEE, Vol. 80, No. 11, pp. 1662-1678, Nov. 1992.
2. R. Blundell and C.-Y. E. Tong, "Submillimeter receivers for radioastronomy", Proceedings of the IEEE, Vol. 80, No 11, pp. 1702-1720, November 1992.
3. G. Jablonski and M. W. Henneberger, "Influence of Josephson currents on superconductor-insulator-superconductor mixer performance", J. Appl. Phys., Vol. 58, pp. 3814-3821, Nov. 1985.

4. R. Blundell and K. H. Gundlach, "A quasiparticle SIN mixer for the 230 GHz frequency range", *Int. J. IR & MM Waves*, Vol. 8, pp. 1573-1580, 1987
5. M. Chernin and R. Blundell, "Harmonic mixing in a superconductor-insulator-normal metal tunnel junction", *J. Appl. Phys.*, Vol. 69, pp. 2682-2683, Feb. 1991.
6. R. Tucker and M. J. Feldman, "Quantum detection at millimeter wavelengths", *Reviews of Modern Physics*, Vol. 57, No. 4, pp. 1055-1113, Oct. 1985.
7. M. Chernin, R. Blundell, C.-Y. Tong and R. E. Miller, "Fundamental and harmonic mixing at 500 GHz using a superconductor-insulator-normal metal junction", *J. Appl. Phys.*, Vol. 72, pp. 3829-3831, 1992.
8. T. Lehnert and K. H. Gundlach, "Fabrication and properties of superconductor-insulator-normal metal tunnel junctions", *J. Vac. Sci. Technol. A*, Vol. 10, No. 1, pp. 110-114, Jan/Feb 1992.
9. A. Golubov et al, "Proximity effect in superconductor-insulator-superconductor Josephson tunnel junctions: Theory and experiment", *Physical Review B*, Vol. 51, No. 2, pp. 1073-1089, January 1995.
10. P. Houwman et al, "Proximity effect in Nb/Al, AlOxide, Al/Nb Josephson tunnel junctions", *IEEE Transactions on Applied Superconductivity*, Vol. 3, No. 1, pp. 2170-2173, March 1993.
11. A. Karpov, J. Blondel, M. Voss and K. H. Gundlach, "Four photon sensitivity heterodyne detection of the submillimeter radiation with superconducting tunnel junctions", *IEEE Transactions on Applied Superconductivity*, Vol. 5, March 1995.
12. A. Karpov, M. Carter, B. Lazareff, D. Billon-Pierron, K. H. Gundlach, "Modeling and performance of Nb SIS mixers in the 1.3 mm and 0.8 mm bands", *Proceedings of the third International Symposium on Space Terahertz Technology*, Ann Arbor, MI, USA, pp. 244-250, 24-26 March 1992.
13. Woody, R. E. Miller and M. J. Wengler, "85-115 GHz receivers for radio astronomy", *IEEE Trans. Microwave Theory Tech.*, vol. MTT-33, pp. 90-95, 1985.
14. R. Blundell, R. E. Miller, and K. H. Gundlach, "Understanding noise in SIS receivers", *Int. J. IR and MM waves*, Vol 13, No 1, pp. 3-26, 1992.
15. Q. Ke, and M. Feldman, "A technique for accurate noise temperature measurements for the superconducting quasiparticle receiver", in *Proceedings of the Fourth International Symposium on Space Terahertz Technology*, 1993, Los Angeles, US, pp. 33-40.
16. Q. Ke, and M. Feldman, "Constant output noise temperature of the superconducting quasiparticle mixer", *IEEE Transactions on Applied Superconductivity*, Vol. 3, No. 1, pp. 2245-2249, March 1993.

**180-500 GHz LOW NOISE SIS WAVEGUIDE RECEIVERS
EMPLOYING TUNED Nb/AIO_x/Nb TUNNEL JUNCTIONS**

*J. W. Kooi¹, M. Chan³, B. Bumble²,
H. G. LeDuc², M. Bin¹, and T.G. Phillips¹*

1- Caltech Submillimeter Observatory
Division of Physics, Mathematics and Astronomy
California Institute of Technology, Pasadena, California 91125

2- Center for Space Microelectronics Technology, Jet Propulsion Laboratory

3- Casio Manufacturing Corporation

Abstract

We report recent results on two full height waveguide receivers that cover the 180-300 GHz and 380-510 GHz atmospheric windows. The receivers are part of the facility instrumentation at the Caltech Submillimeter Observatory on Mauna Kea in Hawaii. Receiver noise temperatures range from 30K-50K DSB for the 180-325 GHz band, and 80-100K DSB for the 380-510 GHz atmospheric band.

A 50% operating bandwidth is achieved by using a RF compensated junction mounted in a two-tuner full height waveguide mixer block. The 0.49 μm^2 Nb/AIO_x/Nb tunnel junctions use an "end-loaded" tuning stub with two quarter-wave transformer sections to tune out the large junction capacitance.

Fourier Transform Spectrometer (FTS) video measurements of the 230- and 492 GHz tuned junctions (designed for waveguide mixers) mounted in a quasi-optical system show good agreement with the measured heterodyne waveguide response. This method has proved to give quick and accurate information on the frequency response of the waveguide mixers.

A Self-Biased Anti-parallel Planar Varactor Diode

Neal R. Erickson
Department of Physics and Astronomy
University of Massachusetts
Amherst, MA 01003

Abstract

A set of design criteria are presented which are required of varactor diodes for use in practical wideband circuits. These include: high power handling, low in-circuit Q, tolerance to input power variations and reasonably high real impedance. To better meet these criteria, a modified planar varactor diode is proposed, in which the varactor junction is dc isolated from the circuit so that it will self-bias to the correct operating point. The required structure may be made as a simple modification to a conventional planar varactor, by replacing the ohmic contact with a Schottky contact. This diode is ideally suited for anti-parallel operation in tripler circuits. The behavior of the diode in a wideband circuit is discussed, as well as various means to characterize devices which can not be measured at dc.

Varactor Design Criteria

A large number of novel varactor diodes have been proposed recently with antisymmetric CV curves intended for use in tripler circuits [1,2]. In most cases, the design has been based solely on the predicted efficiency in an optimized embedding circuit. Depending on the application there are many possible criteria that may be required for varactor diodes. Not all of these are relevant in every case, but the important point is that there is a lot more to consider than just a cutoff frequency. This list should make it clear that there needs to be a synthesis between the user, the circuit designer and the device fabricator. A particular point which must be made about evaluating the properties discussed below is that the in-circuit behavior of nonlinear devices can not be assessed without the use of a large signal circuit simulator. In the case of back to back devices, this simulation is particularly critical, because the rf pump produces a CV characteristic which may be very different from that measured at dc.

1. Efficiency at a useful power level. For nearly all devices it is easy to make a low power device by simply reducing the junction area. Since this has the effect of raising the effective impedance level, it presents no problem to the circuit designer. High power devices are much more difficult to make. Simply increasing the area will work, but large area diodes have

very low impedances and make matching difficult. Power handling may also be increased by raising the breakdown voltage of the diode, but this also raises the series resistance. Making devices in series tends to be the most effective way to handle high power. Most devices are also prone to carrier velocity saturation at some power level (or frequency) and this must also be considered.

2. Conservative design. Most devices work best near the upper end of their power range, but this should not be right on the edge of destruction. Heat sinking should be a part of the design. The desired input power should not drive the device into breakdown, although rf breakdown appears to be less of a problem than circuit simulators would predict.

3. Wideband impedance matching. The device should have a low Q (ratio of reactance to resistance) at both the input and output frequency for best bandwidth. The in-circuit impedance values must be derived from a nonlinear circuit simulator, and have little relation to R_s and $C_j(0)$. A Q of 3 at the input and 1.5 at the output is typical for a tripler under optimum load, although these Q values tend to increase significantly under nonoptimized conditions. Any higher optimum Q will seriously degrade the performance of full waveguide band multipliers.

4. Reasonably high real part to the optimum embedding impedance. Depending on frequency, this should be at least 25 ohms and even higher for submillimeter devices.

5. Efficiency and impedance level over a reasonable power range. In order to make real multipliers for system applications, there should be at least a factor of two power range for nearly optimum operation, and over this range the optimum circuit impedances should not change significantly.

6. For planar diodes the device package should include enough inductance for matching at the output. The package parasitic capacitance must be very small compared to the average junction capacitance for best bandwidth. While for general applications, a low level of integration on a chip is desirable, a highly integrated approach may be necessary for really wide band circuits.

7. A device with a voltage tunable junction capacitance is very helpful because it may be tuned to fit the mount. A nontunable device forces higher standards on the mount, and this may make fabrication very difficult. The absence of a bias port simplifies the mount and in some applications this may be very valuable.

8. The advantage of antisymmetric devices is primarily in the ease of fabricating triplers with wide bandwidth. In narrow band triplers it is fairly easy to provide the correct second harmonic terminations without much extra complexity. Antisymmetric devices also may permit the fabrication of quintuplers with only one idler. This would be a real advantage in the submillimeter even if the circuit has narrow bandwidth.

Schottky Varactor Advantages and Limitations

In reviewing this list, it appears that the conventional abrupt junction varactor still compares favorably to all other devices considered so far. It is a proven device; high power and efficiency have been achieved with practical planar devices, and moderate bandwidth ($\Delta f/f_c = 0.2$) circuits have been built successfully. Its limitations tend to be of the same sort as with other types of devices, and include the need to provide very different inductances

at the various circuit harmonics, and the need for idlers in higher order multipliers.

One of the primary drawbacks to conventional Schottky varactor diodes has been the need to provide bias to the diode. Under typical operating conditions this bias is $\sim .3 - .4$ times the breakdown voltage, applied in the reverse direction. Providing bias requires dc connections to the diode, with appropriate filtering, adding complexity as well as loss to the circuit. While bias is frequently applied by an external voltage source, under sufficient drive power a varactor will develop enough forward current flow to self-bias given the proper dc load, which is typically a high impedance.

In some cases such bias connections are only a minor problem, and may be incorporated somewhat naturally into the circuit. One such case is the balanced doubler [3], in which the pair of diodes have the same polarity with respect to the coupling line to the output circuit, and in which it is fairly easy to decouple the rf output from the bias. In other cases, the need for bias complicates the circuit sufficiently to make it quite difficult to implement.

The balanced tripler using an anti-parallel pair of diodes is a particularly good example of this problem. This circuit is quite desirable because it produces odd harmonics only, but the parallel connected diodes must be provided with equal and opposite bias. This means that while they are rf connected they must be dc isolated, and that two separate bias ports must be provided. While practical circuits may be built, they are complex and require split or overlaid rf lines to introduce bias, and such circuits become very difficult to build in the submillimeter range. Because this circuit is free of even order harmonics, and because the required second harmonic idler current circulates within the loop of the two diodes (independent of any external circuitry), it is particularly suitable for wide band triplers. It has little advantage in narrow band applications, in which a single diode can work very well, and bias circuitry is not very complex.

Planar Diode Modifications

This paper suggests a rather simple modification to the processing of planar varactors which can provide internal bias to the diode, so that the dc terminal voltage is zero yet the varactor operates at optimum bias. The basic concept is to add a second diode with the opposite polarity in series with the varactor, as shown in Fig. 1. This second diode has a very large area relative to that of the varactor, so that its effect on the rf circuit is negligible,

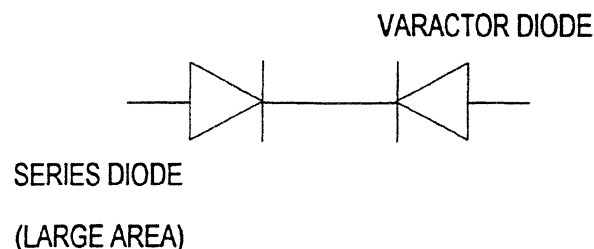


Fig.1. Varactor diode with large area diode in series to allow varactor to self-bias.

but it changes the dc behavior of the circuit. Assume that the dc voltage across the pair of diodes is constrained to be zero. With rf power applied, initially both diode junctions are at zero bias. The rf voltage across the varactor can cause forward current flow only, so the charge on the terminal between the diodes is depleted, and the varactor becomes reverse biased. Since this reverse biases the second junction, no charge can return via this route, either. This second junction has negligible rf voltage across it because of its high capacitance. Eventually, the reverse bias voltage reaches a steady state when nearly the entire rf voltage swing across the varactor is in the reverse direction. One extreme is at a small forward voltage to just balance the reverse leakage. The operating point which is achieved is almost optimal for varactor operation, because the bias seeks the point where no forward current flows. If the rf power continues to increase, the voltage swing will eventually reach reverse breakdown. At this point the bias will stabilize at the point where equal forward and reverse currents flow. This is not necessarily desirable, because typical varactors can not handle significant reverse current flow. It is also hard to predict the exact power level where this will occur, so there is no easy way to avoid over driving the diode.

It is preferable to operate the varactor with a fixed voltage bias, which is chosen for optimum performance at a given power level, and which keeps the circuit working in a similar fashion over a range of power. If this voltage is set to about $0.35 V_b$, then optimum pump will fully modulate the diode between forward conduction and reverse breakdown, while the reverse current will increase slowly for higher power levels, since the voltage swing instead is forced to go into forward conduction. It is easy to achieve this constant bias operation by causing the series diode to have a breakdown voltage of $\sim 0.35 V_{b(\text{varactor})}$. This diode will begin to conduct at this voltage and will let charge back into the isolated terminal, preventing it from going more negative. Except that this diode is internal to the circuit, the behavior is the same as that with an external bias zener diode.

It is remarkable that the structure required to achieve this behavior is very easily built. It can be made with only a small modification of the standard processing involved with a planar varactor. Consider the typical planar diode shown in Fig. 2. The junction itself is a small metallized pad on top of a thin moderately doped epi-layer, which is in turn on top of a heavily doped, highly conducting layer. This active junction is surrounded by a much larger metal pad which is connected to the highly doped layer through an ohmic contact. The ohmic contact is a graded junction which is made by thermally diffusing a high concentration of carriers into the semiconductor in such a way that no barrier is created, so that the metal

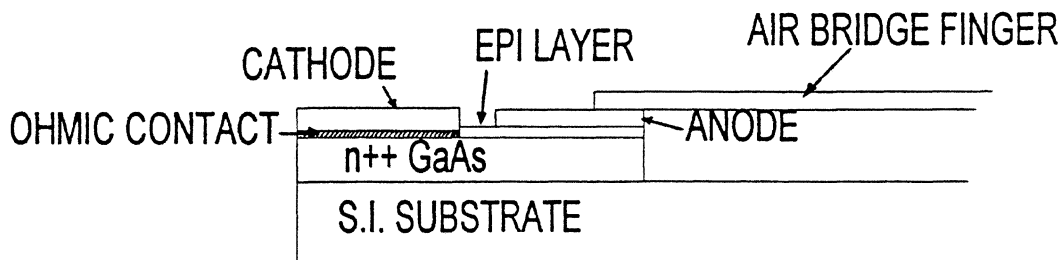


Fig. 2. Typical planar diode cross section.

pad is effectively connected to the highly doped layer. Ohmic contacts are a limitation to the fabrication of planar diodes because they require a minimum area to achieve a sufficiently small resistance, and creating them is a somewhat poorly understood process. Ohmic contacts have traditionally been required on all diodes, because the usual application has been in mixers, where substantial bias current must flow, and where intermediate frequencies may be very low compared to the signal and LO frequencies. This method of fabrication has been carried over into varactor diodes without much consideration as to whether it is still necessary.

If the ohmic alloying step were eliminated, the large area junction would become a second Schottky diode, creating the situation described above. If nothing else were done, this junction would have the same breakdown voltage as the varactor, and the questions about the operating bias would remain. However, the epitaxial material may be thinned so that this junction breaks down at a lower voltage, and this thinning is very easily controlled, since this type of processing is used in all diode fabrication. It appears that this new structure would be nearly ideal, except that the I/V curve of the varactor can no longer be measured at dc. This may not be entirely bad, since dc characterization frequently is misleading, although it does serve as a convenient means to screen out really bad diodes. There are a number of ways to measure R_s at microwave frequencies, and one possible probe configuration is described later.

This diode still requires a dc connection between the terminals to maintain them at the same voltage. This occurs naturally in some circuits, so it is not always a problem, and in the case of the antiparallel diode tripler, the diodes provide their own dc connection. This is because the internally developed bias currents have opposite polarities, and thus flow entirely within the loop formed by the two diodes. Assuming that the diodes are identical, they receive equal power from the pump, and so the bias currents will be the same. In this ideal case, the end terminals remain at the same voltage. The bias remains stable against reasonable variations in diode parameters. Even if one diode is larger and receives more of the input power, the voltage swing across it will be the same as that of its mate. Thus reverse breakdown through the bias diodes begins at the same power level, but the current through the larger varactor increases faster. This current imbalance forces the bias voltage on the larger diode to increase, and that on the smaller one to decrease until the currents are in balance. This situation is stable because with this distribution of voltages the larger diode is driven to lower capacitance, while the smaller diode is driven to higher capacitance, and the power coupled tends to become more equal. The final state will have some voltage across the terminals, which is not inherently bad if it is small relative to V_b .

Requirements for the Bias Junction

We now need to define the actual requirements for the bias junction. The most important is its capacitance relative to that of the active junction. From a circuit standpoint, the bias junction should have a reactance very small relative to that of the active junction so that it does not raise the Q of the varactor circuit. This is particularly important for wideband applications. This requires that the bias junction at reverse breakdown have a capacitance ~ 30 times that of the time averaged capacitance of the varactor. Typical varactors have a

time averaged capacitance 0.4 times $C_j(0)$, while the rather thin bias junction is biased to its minimum value. For such a thin junction this is not much less than that at zero bias (let us assume $\sim 0.7 C_j(0)$). Then to maintain a factor of 30 ratio, the area of the bias junction should be ~ 17 times the varactor area, which is a very modest constraint.

A second constraint is that the bias junction must be able to carry enough current in breakdown to stabilize the bias without being damaged in the process. While some multipliers operate with very low bias current, this is not the rule, and particularly in the case of very wideband devices, best operation tends to occur with ~ 1 mA of bias current. The reason for this is that operation slightly into the forward bias region lowers the time averaged reactance of the diode, lowering its Q , while the power lost in the bias circuit is not serious for a current of up to ~ 1 mA. This bias current is really only this large at relatively low frequencies (< 150 GHz input), and will become smaller as less input power is available. There is little data on the ability of Schottky diodes to carry continuous avalanche currents, and the damage usually occurs at areas of current concentration. It is routine to test the breakdown of $1\mu\text{m}$ diameter diodes at $1\mu\text{A}$ without apparent damage, so in principal, a $30\mu\text{m}$ diameter anode should be able to carry $\sim 1\text{mA}$. However, the fabrication of diodes to carry this current safely may require special care in processing.

These constraints appear to be less restrictive than the present requirement for the area of ohmic contacts, and have the advantage that the required area drops with increasing frequency. This is particularly important in the submillimeter, because ohmic contacts of the conventional size become inconveniently large even by 300 GHz.

Measurements of Diode Properties

It is essential to have some means of testing diodes outside of the complete circuit. Without independent tests, there is no way to determine how well the circuit is actually performing. Diode pairs present problems in isolating the quality of the individual elements, while the dc isolated diodes proposed here present additional problems. Let us first consider the problems in characterizing single diodes with dc isolation.

Measuring capacitance is little different than with conventional diodes. Since the bias junction is so large, it may be ignored in the capacitance measurement. Its only effect is to add its forward voltage to the total voltage across the device in the measurement of the C/V characteristic. The bias junction becomes reverse biased when the varactor is forward biased, but by using current bias, the forward region may be safely measured.

The series resistance is critical, and can not be measured at dc through the bias diode since its breakdown characteristic is not well known, and this junction may not be able to handle sufficient current in any case to permit accurate determination of R_s . This leaves rf measurements as the only practical means. This is a problem for on-wafer tests, so some diodes on a wafer could have ohmic contacts in order to check the process. In principal, the complete diode parameters can be determined through one port measurements using a vector network analyzer with conventional 50Ω wafer probes at some high microwave frequency, but in fact, the accuracy will be poor because the impedance is so highly reactive. It is essential to tune out the reactance of the diode in order to achieve reasonable accuracy. This could be done by adding an inductance at the end of the probe line, or by otherwise modifying the

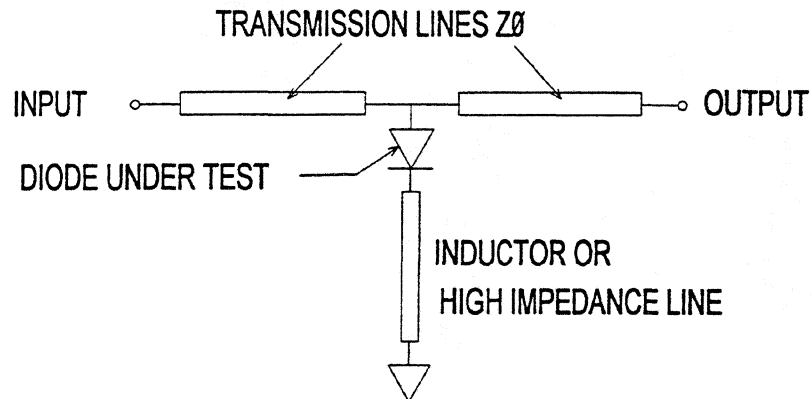


Fig.3. Schematic diagram of DeLoach fixture for testing varactor diodes.

probe to improve the match into a capacitive load.

One variation on this approach is the DeLoach fixture [4], in which a diode plus a suitable inductance are placed in shunt across a transmission line, as shown in Fig. 3. The frequency is swept over a wide band, and one measures the transmitted power on the resonance of the diode with the circuit, where it best shorts out the line. Any parasitic capacitance of the diode will somewhat alter the measured resistance, and require some interpretation of the data. While such measurements may require some special test fixtures, they have the advantage that R_s may be measured at a high enough frequency to be meaningful for predicting performance. In fact, a fixture in the 75-110 GHz band seems quite practical, and has the advantage that the diode is measured at a frequency near that of its actual use.

Evaluation of Anti-parallel Diodes

Anti-parallel diodes present special challenges in measurement, in order to determine the match between the properties of the diodes. The average resistance and capacitance at zero bias may be measured exactly in the way that they would be for a single diode. The match in properties may be determined if the measurement is made with bias applied with opposite polarities at a level sufficient to slightly forward bias each junction in turn. In measurements of R_s with a DeLoach fixture, this bias causes the capacitance of one junction to be much larger than that of the other, so that its resistance dominates the measurement. Some modeling is required to interpret the measurements, but the needed data is available.

The match in junction capacitance may also be derived from these measurements, using the change in resonant frequency with bias, but the same data may be as easily obtained with conventional capacitance bridge measurements. The total capacitance of the pair can be measured and a correction for fringing fields applied by measuring a sample with broken contact fingers. The interpretation of this measurement requires some modeling. There is no way to accurately measure the capacitance-voltage characteristic of the pair since the voltage distribution across the series diodes is not uniquely determined except for a bias voltage high

enough to breakdown one of the bias diodes, and in this case the capacitance is dominated by that of the forward biased diode. The interesting capacitance in the reverse direction is poorly measured, but can be measured at the batch level by breaking the contact finger on one diode of the pair.

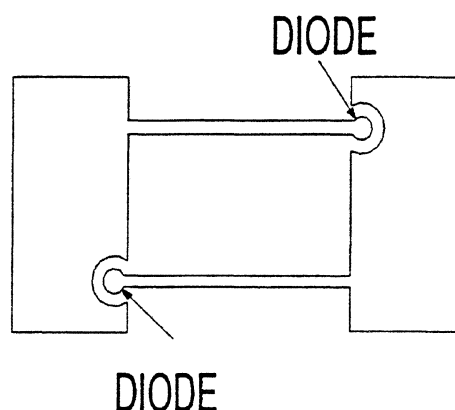


Fig. 4. Simplest circuit for a pair of varactors connected in anti-parallel.

Circuit Requirements for Tripler

All varactor circuits require inductive terminations at all harmonics, with the effective diode capacitance nearly the same at all harmonics. If the optimum inductances at the first three harmonics are defined as L_1 , L_2 and L_3 : $L_1 = 4L_2$, and $L_3 = 0.44L_2$. The second harmonic currents are critical to operation of a tripler, so the idler inductance must be near optimum. Since the optimum real parts of the input and output impedances are less than their respective reactances, providing these correct inductances is also critical.

A major design challenge is to include enough inductance for the idler without increasing the circuit reactance at the output. Since the idler currents with anti-parallel diodes circulate in a loop, this loop must have the correct inductance. The simplest circuit shown in Fig.4 has problems in this respect. In this circuit, the mutual inductance of the parallel lines causes the inductance for odd harmonics to be greater than for even. To minimize this effect, the lines must be widely separated, and providing this separation in a microstrip or stripline environment is impossible. If the situation is accepted, then it is necessary to add capacitance in series with the output to tune out the excess capacitance, which decreases the circuit bandwidth. If we reverse the direction of the coupled lines, the situation changes. Now the inductance for odd harmonics is less than for even, and it becomes possible to provide optimized second and third harmonic reactance simultaneously. However, the circuit realization is not simple, as shown in Fig. 5. This layout requires a crossover, and extensive analysis in order to work out a feasible geometry. A preliminary study shows that such a layout is practical, but further work is required.

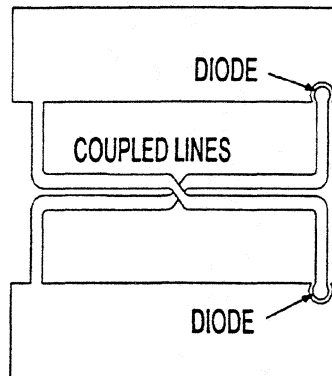


Fig. 5. Anti-parallel diode pair using mutual inductance of coupled lines to increase second harmonic inductance.

Conclusions

A modified construction of a planar diode is presented which eliminates the need for an external bias circuit for varactor applications. This diode must be tested at microwave frequencies, but various means are available to do this. The new diode is particularly well suited for anti-parallel operation in tripler circuits, but a suitable circuit still needs to be developed.

Acknowledgments

The author thanks Tom Crowe, Richard Bradley and Peter Smith for helpful discussions. This work was supported by JPL under contract 959206.

References

- [1] Frerking, M.A. and East, J., "Novel Heterojunction Varactors," Proc. of IEEE, vol. 80, pg. 1853, 1991.
- [2] Nilsen, S.V., Grönquist, H., Hjelmgren, H., Rydberg, A., and Kollberg, E.L., "Single barrier varactors for submillimeter wave power generation," IEEE Trans. Microwave Theory Tech., vol. 41, pg. 572, 1993.
- [3] Erickson, N.R., "High efficiency submillimeter frequency multipliers," 1990 IEEE MTT-S Int'l. Microwave Symp. Digest, pg. 1301 (Dallas, TX).
- [4] DeLoach, B.C., "A new microwave measurement technique to characterize diodes....," IEEE Trans. Microwave Theory Tech., vol. 12, pg. 15, 1964.

Monolithic Nonlinear Transmission Line

W-M. Zhang, Xiaohui Qin

Dept. of Electrical Engineering, University of California, Los Angeles, CA 90024

F. Jiang, G. Song, Y. Li, C.W. Domier, N.C. Luhmann, Jr.

Dept. of Applied Science, University of California, Davis, CA 95616

[ABSTRACT]

Superlattice Schottky Quantum Barrier varactors have been employed as nonlinear elements in nonlinear transmission line circuits. Short pulses with <37ps fall time have been detected in initial proof-of-principle experiments in good agreement with theoretical predictions leading confidence in the predictions of <20ps fall time for the next generation of NLTLs. The HP HFSS EM and MDS simulation codes have been employed to optimize the circuit layout and to provide an accurate device level equivalent circuit model. The resultant accurate EM model is utilized for transmission line equivalent circuit simulations.

This work is supported by the Department of Energy under contract DE-FG03-95ER94295, the Joint Services and Electronics Program under contract F4962092-C-0055 and the Lawrence Livermore National Laboratory LDRD program under contract LLNL-W-740J-ENG-48.

[INTRODUCTION]

A nonlinear transmission line (NLTL) is comprised of a transmission line loaded with varactors, where the nonlinearity arises from the variable depletion layer width which depends both on the DC bias voltage and on the AC voltage of the propagating wave. Monolithic NLTLs have been made by several groups utilizing coplanar wave guide and GaAs Schottky diodes for short pulse generation [1,2]. The output power and pulse duration are limited by the device breakdown voltage and the diode cut-off frequency. Ultrashort pulses have been obtained by compromising peak pulse voltages. Pulses with higher peak voltages were generated albeit with longer pulse duration. The trade-off between breakdown voltage and the cut-off frequency of Schottky diodes makes it difficult to simultaneously achieve high output voltage and ultrashort pulse width. In the present work, Superlattice Schottky Quantum Barrier (SSQBV) Varactors (SSQBV) are employed as nonlinear elements[3-5]. The MBE wafer doping profile of the SSQBV varactors is illustrated in Fig. 1, where superlattice barriers have been utilized to reduce the leakage current associated with standard quantum barriers. With modern MBE technology, devices are stacked vertically to provide high power handling capability. The cut-off frequencies of these devices are predicted to exceed 2THz. By using a back-to-back layout configuration, the SSQBV varactors have symmetric C-V curves, and therefore can be utilized to generate pulses with both polarities.

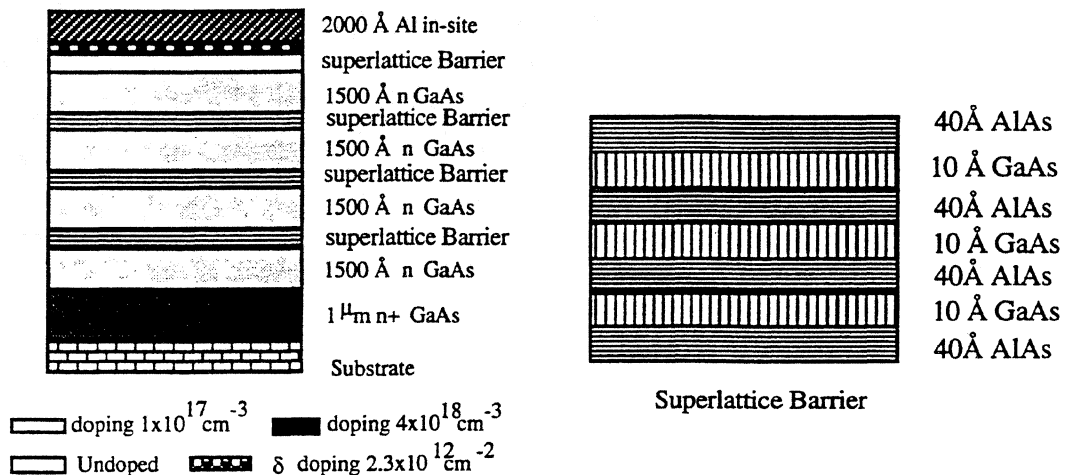


Fig. 1 GaAs SSQBV Wafer Doping Profile

[EM SIMULATION]

The HP high frequency structure simulator (HFSS) electromagnetic code has been utilized to optimize the diode layout and to reduce parasitic capacitance as well as series resistance. In the modelling, a back-to-back diode resides inside a waveguide and on top of the GaAs substrate. With properly defined electric and magnetic walls, the waveguide supports the TEM mode. As shown in Fig. 2, an embedded resistive layer under the metal fingers is utilized to simulate the n+ region.

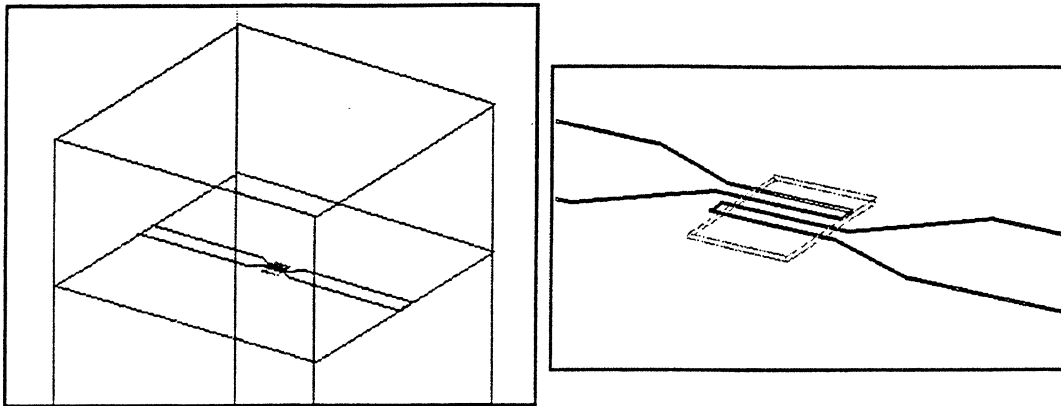


Fig. 2 The 3-D model for the HP HFSS Code

Frequency	S ₁₁	S ₁₂ /S ₂₁	S ₂₂
30.4 GHz	0.647 -178.79	0.761 -111.87	0.642 -137.19
31.4 GHz	0.659 -178.91	0.751 -116.64	0.654 -127.46
32.4 GHz	0.673 -178.99	0.738 -121.62	0.667 -117.33

Table 1. S Parameters from HFSS Simulation

Table 1 shows the S parameters obtained from the HFSS simulations. Using these S parameters, an accurate EM equivalent circuit model has been generated by utilizing the HP MDS simulation tool. The equivalent circuit model is shown in Fig. 3. For a typical diode with $4\mu\text{m} \times 20\mu\text{m}$ finger dimensions and $4\mu\text{m}$ finger spacing, the series resistance from the n+ layer is $1.5\ \Omega$ while C_{min} is $14.1\ \text{fF}$ which corresponds to $4.5\ \text{fF}$ parasitic capacitance. These simulation results are consistent with our previous experimental results.

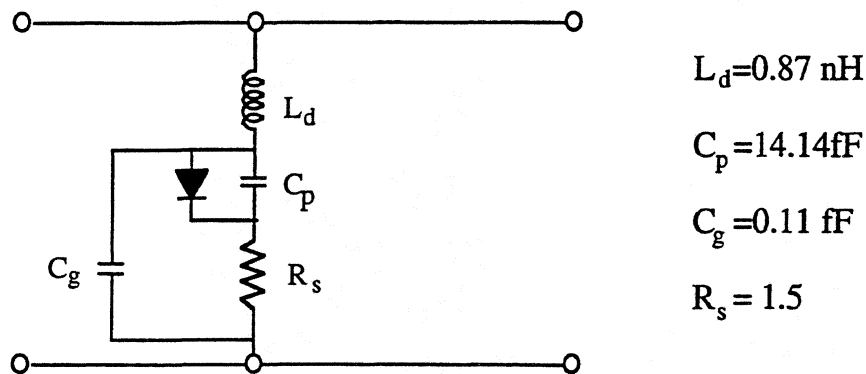


Fig. 3. Simulation Model Utilized by the HP HFSS EM Code

[EXPERIMENTAL RESULTS]

Monolithic NLTLs have been fabricated on SSQBV wafers grown by Quantum Epitaxial Designs. DC characteristic measurements have been performed with a HP4140B pA meter (I-V) and a HP4279CV meter. With this three superlattice barrier structure, the breakdown voltage is 17.5V, and $C_{\text{max}}/C_{\text{min}}$ is ~ 3.9 .

An initial test system has been configured, as shown in Fig. 4, which includes Cascade WPH-405 Microwave Probes (DC-65GHz), an Avtech impulse generator (350 ps FWHM pulses) and a Tektronix 11802A digital sampling oscilloscope equipped with a 50GHz plug-in. A portion of the pulse signal from the Avtech pulse generator is utilized as a trigger signal for the sampling scope.

A hybrid NLTL is employed to precompress the input pulse, which has been fabricated utilizing MA46580-992 GaAs beam-lead varactor diodes. The output signal from the hybrid NLTL is a shock wave with ~ 100 ps fall time. The first proof-of-principle SSQBV based NLTL was only designed to generate pulses with ~ 26 ps fall time and 15.0 V peak voltage, so that they could be accurately measured by our current test system. This transmission line is not designed for the highest performance (ultrashort pulse) but for the purpose of providing an accurate model.

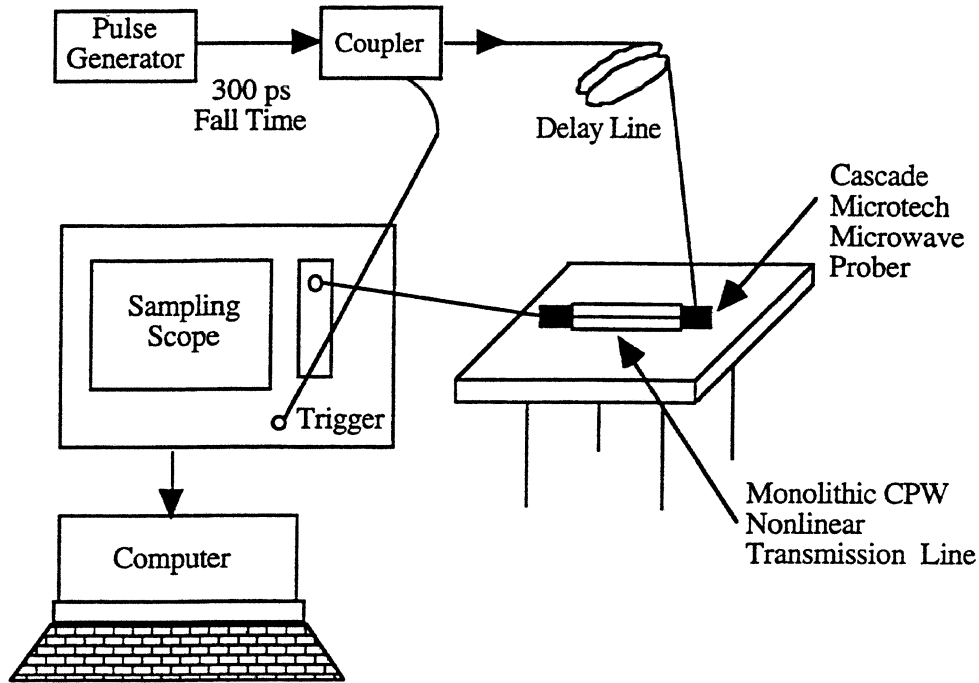


Fig. 4. Transmission Line Test Set-up

Both experimental and simulation (employing actual device and circuit parameters) results are shown in Fig. 5. Pulses with peak-to-peak voltage levels of 11.2 V and <37ps fall time were measured. It should be noted that a second pulse is also formed (albeit not separated from the first one), which indicates that this NLTL is not sufficiently long to fully compress the pulses.

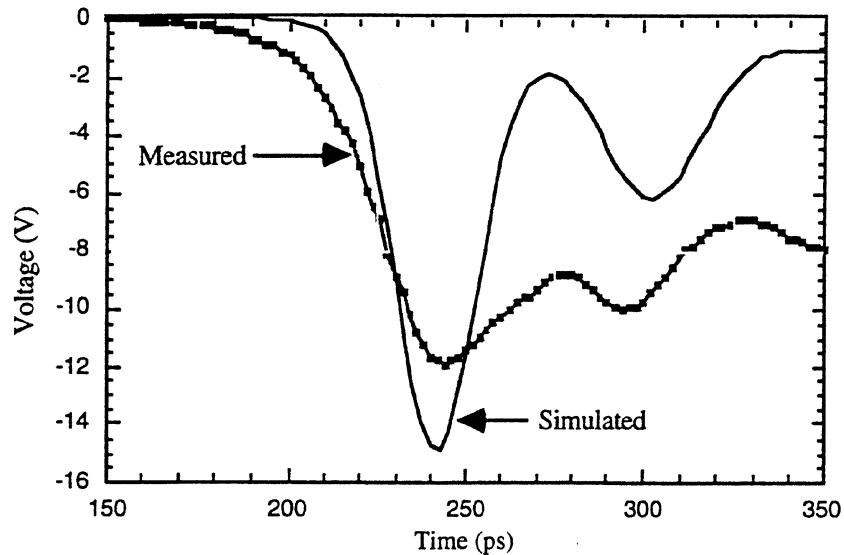


Fig.5. Comparison of Experimental and Simulation Results

[DISCUSSION]

Two new transmission lines have been designed and fabricated to generate >15V with ~20ps and ~10ps fall times, respectively. These two lines are currently under test. New wafer profiles have been designed to increase the power handling capability of quantum barrier devices by vertically stacking more than six barriers together. Lateral stacking techniques can be utilized to further increase the breakdown voltage, and varactors with >50 V breakdown voltages and >300GHz cut-off frequencies appear to be readily achievable.

[REFERENCES]

- [1] E. Carman, M. Case, M. Kamegawa, R. Yu, K. Gilboney and M. Rodwell, *IEEE Trans. on Microwave Theory and Techniques*, Vol. 40, 819, (1992)
- [2] D. W. Van Der Weide, J. S. Bostak, B. A. Auld, and D. M. Bloom, *17th International Conference on Infrared and Millimeter Waves, Pasadena, 97*, (1992)
- [3] C. Raman, J. P. Sun, W. L. Chen, G. Munns, J. East, G. Haddad, *Third International Symposium on Space Terahertz Technology*, 146 (1992)
- [4] H-X. Liu, L. B. Sjogren, N. C. Luhmann, Jr., D. B. Rutledge, *International Journal of Infrared and Millimeter Waves*, Vol. 13, 251, (1992)
- [5] W-M. Zhang, X. Qin, J. Y. Liao, R. P. Hsia, R. W. Geck, F. Jiang, Y. Li, C. W. Domier and N. C. Luhmann, Jr. *Fifth International Symposium on Space Terahertz Technology* 324 (1994)

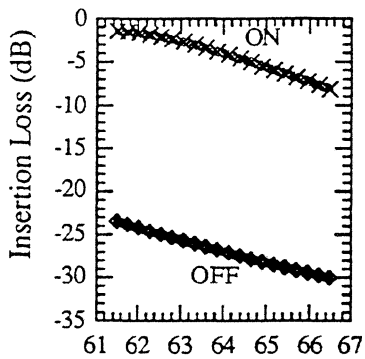
Submit to: Sixth International Symposium on Space Terahertz Technology, May 10-12, 1995, Pasadena

60 GHZ MONOLITHIC SCHOTTKY VARACTOR TRANSMISSION BEAM SWITCHING ARRAY

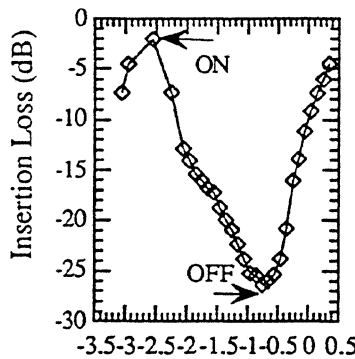
Xiaohui Qin*, W-M. Zhang*, C.W. Domier**, N.C. Luhmann, Jr.**,
W. Berk†, S. Duncan† and D.W. Tu†

Millimeter wave switches may be used in a variety of radar applications including millimeter wave imaging systems, (e.g. for airport runways), and collision avoidance systems for automotive vehicles. High speed switches can also be used in fusion plasma diagnostics. Both transmitters and receivers are needed, with high speed electronic scanning and high power capabilities highly desirable. Monolithic integrated diode grid beam controllers can perform switching and amplitude modulation functions at high power levels. EM modeling using HFSS has been performed, which allows one to analyze the switch grid using actual geometry, and to determine the circuit parameters including parasitics. In our design, a single grid with an optimum unit cell size can provide a contrast ratio of 24 dB with a minimum insertion loss of 1.5 dB, and 50 dB contrast ratio and a minimum insertion loss of 2 dB with a stacked grid pair.

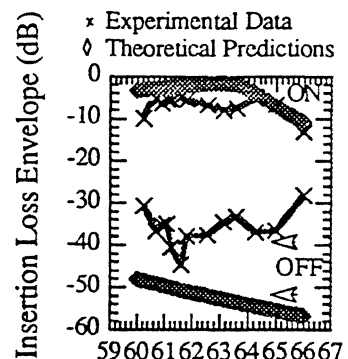
Four beam control arrays have been fabricated (courtesy of Martin Marietta laboratories) on 3" diameter GaAs substrates. Experimental results have been achieved with a contrast ratio of 24 dB with a single grid and 40 dB contrast ratio with a grid pair. Figure 1 illustrates the comparison of simulated and experimental results for a single grid transmission switch at 62 GHz. Similarly, figure 2 shows the comparison for a grid pair transmission switches as a function of frequency.



(a) Frequency (GHz)



(b) Bias Voltage (V)



Frequency (GHz)

Fig. 1 Comparison of the predicted (a) and experimental (b) results of transmission switches with a single grid at 62 GHz.

Fig. 2 Comparison of the predicted and experimental results of for a grid pair transmission switches as a function of frequency.

This project is supported by the Department of Energy under contract DE-FG03-86-ER53225 and the Joint Services and Electronics Program under contract F4962092-C-0055.

*Dept. of Electrical Engineering, University of California, Los Angeles, CA 90024

**Dept. of Applied Science, University of California, Davis, CA 95616

†Martin Marietta Laboratories, 1450 S. Rolling Road, Baltimore, Maryland 21227

Micromachined Millimeter-wave SIS-mixers

Gert de Lange, Brian R. Jacobson, Arifur Rahman, and Qing Hu

Department of Electrical Engineering and

Research Laboratory of Electronics,

Massachusetts Institute of Technology, Cambridge, Massachusetts 02139.

A heterodyne mixer with a micromachined horn antenna and a superconductor-isolator-superconductor tunnel junction as mixing element is tested in the 75-115 GHz frequency range. Experimental results show that the SIS mixers can be operated on thin Si_3N_4 membranes in a vacuum environment, and that the micromachined horn antenna can withstand repeated thermal cycling. A lowest DSB receiver noise temperature of 70 K is measured at 102 GHz with a 3-dB bandwidth of 15 GHz. Analysis of the noise measurements shows that the receiver noise is mainly limited by the reflection loss due to the capacitance of the tunnel junctions and therefore can be further improved by the use of integrated tuning elements.

1 Introduction

Micromachined integrated horn antennas consist of a dipole antenna suspended on a thin ($\sim 1 \mu\text{m}$) Si_3N_4 dielectric membrane inside a pyramidal cavity etched in silicon [1]. In the construction of this type of antenna, standard whole-wafer Si photolithography and well established anisotropic etching processes are used. We investigate the combination of micromachining with Nb-based fabrication technology and cryogenic operations, for the development of superconducting heterodyne receivers for millimeter and sub-millimeter wavelengths.

Several reasons make a micromachined horn-antenna attractive in comparison with conventional waveguide and open-structure antennas. (a) The feasibility of micromachined horn antennas for imaging array applications, (b) the relative ease (and low cost) of fabrication of very accurate (sub-)millimeter-wave cavities, (c) the use at frequencies above 1 THz, where machined waveguides become inconveniently small and difficult to fabricate and open structure

antennas will suffer from substrate losses, (d) the possibilities of integrating a mixing element with (super- or semi-conducting) electronics, for example SQUID IF-amplifiers or Flux-Flow oscillators.

The development of heterodyne receivers with room-temperature semiconductor GaAs Schottky diode detectors for use at millimeter and sub-millimeter wavelengths [2] has shown the feasibility of micromachined integrated horn receivers. A similar design is used in this work in the construction of micromachined millimeter-wave heterodyne mixers using superconducting tunnel junctions (SIS-junctions) as mixing elements. Heterodyne receivers based on SIS-junctions are the most sensitive receivers for frequencies from 36 GHz up to 840 GHz, both in waveguide [3] and quasi-optical designs [4], with noise performance limited by fundamental quantum-noise limits. The current state-of-the-art waveguide and quasi-optical receivers for the 90-115 frequency range have DSB noise temperatures of 20 K and 35 K, respectively [5, 6, 7, 8, 9].

This paper reports on the first measurements of a micromachined SIS mixer for the 75-115 GHz frequency range. Section 2 describes the receiver design. The fabrication process of the SIS-junctions and the micromachined horns is described in Section 3. Results of cryogenic testing, a Fourier Transform Spectrometer measurement and actual receiver noise measurements of a 75-115 GHz mixer are given in Section 4.

2 Receiver Design

The geometry and main dimensions of the horn-aperture and the dipole antenna are shown in Figs. 1 and 2, where the dimensions are expressed in units of wavelength of the design frequency. The 70° opening angle of a horn cavity, inherent to the [111] crystal planes of Si, is far too large for direct application in single-element or array receivers. To improve the wide beam pattern due to the large flare angle, an electroformed horn section with a 9° flare angle is placed in front of the micromachined section. Measurements on this quasi-integrated horn show a 97% Gaussian beam-coupling, a 34° 10-dB beam-width and a -27 dB side lobe level [10]. The actual dimensions of the micromachined horn-antenna used in this work (based on the work in [2] and [11]) are shown in Table 1. The dipole length and distance from the apex of the pyramidal horn are chosen to give a 35 Ω antenna impedance at a center frequency of 90 GHz. The co-planar stripline used to bias the SIS-junction and to couple the IF-signals (Fig. 2) has a RF blocking capacitor of ~ 0.4 pF placed at 1/4 λ away from the antenna center. This capacitor is formed by a Nb₂O₅ dielectric layer and the overlap area of a 17 μm wide crossbar on top of the 20 μm wide coplanar striplines.

The stack of 5 Si-wafers forming the micromachined horn section is glued with cyanobond

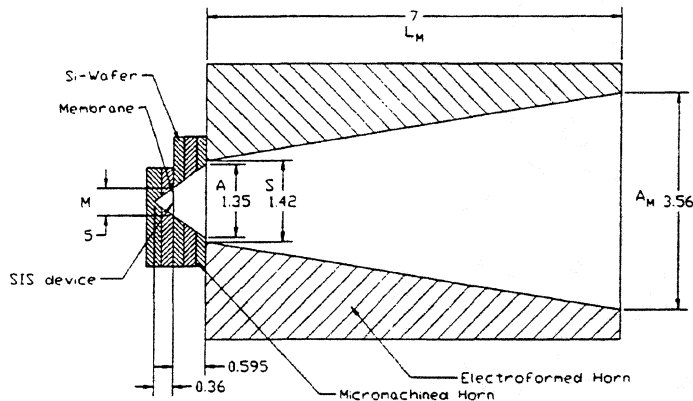


Figure 1: Geometry of the micromachined horn structure. Dimensions are given in units of wavelength at the designed frequency.

to the backplate of the mixer mount. The backplate also holds a bias-tee, made of chip capacitors and coil inductors. The machined horn section is placed in front of the backplate, mounted in an xyz-stage which allows the alignment with the micromachined section. The electrical connection from the junction-chip to the bias circuit is made by pressing two stiff wires into two indium contacts on the chip.

The mixer block and cold stage of the IF-amplification chain are mounted in an Infrared Laboratories HD3-8 dewar. The cold-plate of the dewar also holds a 1000-turn superconducting magnet for suppression of Josephson-currents. The signal and LO-power are combined by a 97% transmission beam splitter and enter the cryostat via a 25- μm thick polypropylene vacuum window of 3 cm diameter. On the 77 K radiation shield a 750- μm thick quartz plate covered with black polyethylene serves as a cooled low-pass filter. A $F=28$ mm TPX-lens is placed at focal length in front of the horn.

The IF-chain consists of the bias-tee circuit in the mixer block, a Pamtech LTE 1268K isolator, and a Berkshire Technologies L-1.5-30HI IF-amplifier (40 dB). A further amplification of 60 dB is provided by room-temperature amplifiers outside the dewar. The IF-power is measured in

Table 1: Dimensions (in mm) of the quasi-integrated horn antenna. See Fig. 1 for definitions of lengths.

f (GHz)	A	S	L	M	L_M	A_M
95	4.3	4.3	1.2	1.6	22.1	11

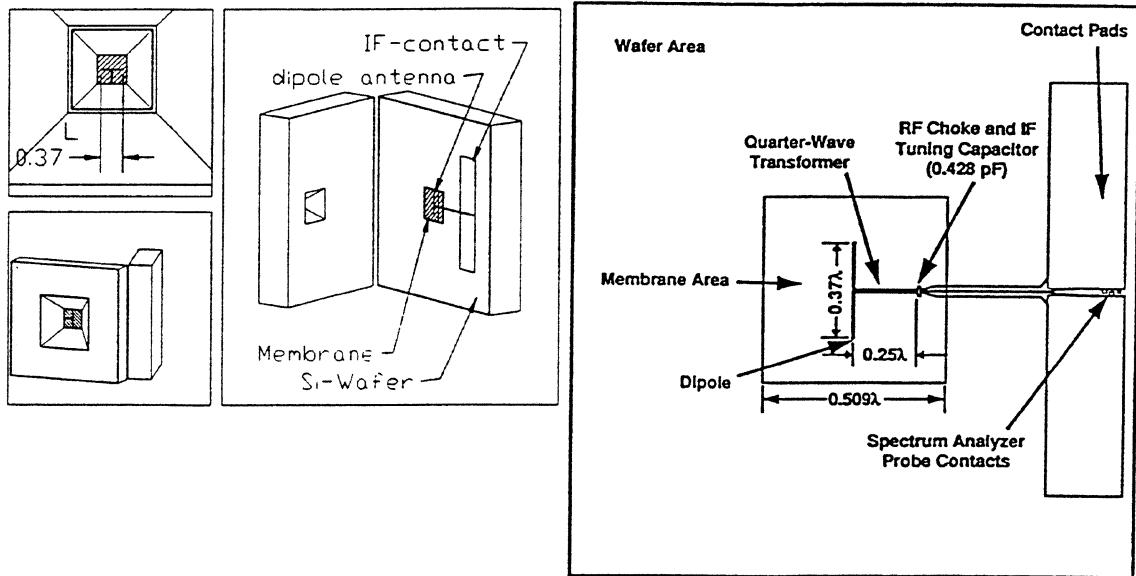


Figure 2: (a) Details of a micromachined mixer before bonding the wafers together. (b) Details of the device wafer, showing the dipole antenna and the DC-bias/IF-output connections

a 35 MHz bandwidth with an HP-436A power sensor at a center frequency of 1.5 GHz (set by a tunable bandpass filter).

3 Fabrication

Previous work in our group has shown that high-quality Nb/Al₂O₃/Nb SIS junctions can be fabricated on thin SiN membranes [12]. The process steps currently used differ slightly from the one described in [12] and are outlined below. The different stages of the fabrication process are shown in Fig. 3.

3.1 Junction Fabrication

The fabrication starts with the chemical vapour deposition (at the Center for Integrated Systems at Stanford University) of 1- μ m thick low-stress SiN membranes on both sides of a 0.38 mm-thick and (100)-oriented silicon wafer. The 4-inch diameter silicon wafer is double-side polished and has a high resistivity $> 2000 \Omega\text{cm}$. The high resistivity is currently required for room temperature testing of the IF-circuitry, but will in future be replaced by low resistivity Si since free carriers will be frozen out at LHe temperatures. The junction fabrication is performed at MIT Lincoln Laboratory using a selective niobium anodization process (SNAP). Several

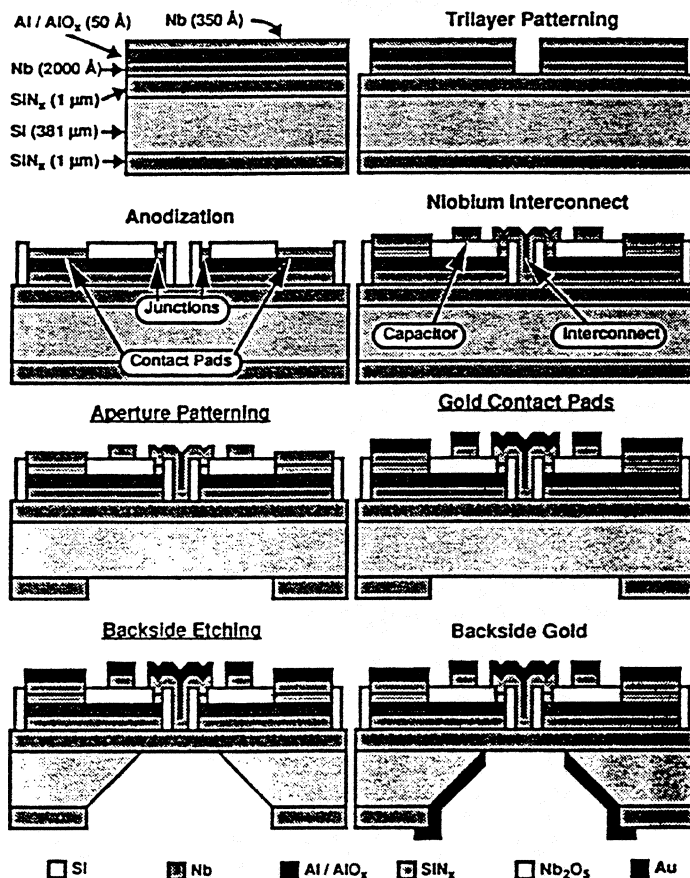


Figure 3: Illustration of the fabrication process of SIS junctions on a Si_3N_4 membrane and the aperture etching for the horn antenna.

trilayers for junction fabrication have also been supplied by Ron Miller at AT&T Bell Labs. The details of the fabrication process are similar to the process described by Bhushan and Macedo [13]. The junction fabrication starts with the deposition of a trilayer by dc-magnetron sputtering at a base pressure $< 5 \times 10^{-4}$ mTorr. The 200-nm Nb base electrode is deposited at a power of 1500 watts and an argon pressure of 10 mTorr. After the substrate is allowed to cool down, a 5-nm Al layer is deposited at a power of 150 watts and a pressure of 2 mTorr and this layer is subsequently oxidized at an oxygen pressure of 10 mTorr. Finally a 35-nm counter electrode is deposited at the same conditions as the base electrode.

The trilayers are patterned by plasma etching the Nb layers with CF_4 and a wet etch of the Al layer. Care should be taken that the pattern is properly aligned with the crystallographic

axes of the silicon wafer, since otherwise the aperture hole (which is aligned later with the trilayer pattern) will end up rotated with respect to the crystallographic axes and will have a rough surface. The junctions are defined by the standard anodization process and a 300-nm Nb counter electrode is deposited and patterned to connect the junctions. After the infrared-alignment (described below) the same pattern is used again for the E-beam evaporation of 400-nm thick Au bonding pads. Currently the mask contains 9 device definitions for the 85-105 GHz and 170-210 GHz frequency range. The junction sizes are designed to be $1.6 \times 1.6 \mu\text{m}^2$.

The patterned trilayer now serves as an alignment mark for an infrared alignment, in which the antenna apertures have to be defined on the *opposite* side of the wafer. To protect the trilayer during this patterning, the device wafer is placed face-down on a Si backing wafer and bonded to it with FSC-M. Although the backing wafer somewhat blurs the image in the infrared alignment, an accuracy of $\pm 5 \mu\text{m}$ can be achieved. After patterning, the silicon nitride is etched (with an approximate etch rate of 100 nm/min) in a mixture of freon-23 with 4 % oxygen at a power level of 100 W.

The chip is now mounted in a Teflon KOH etching mount shown in Fig. 4 which isolates the front and backside of the wafer by sandwiching the wafer between two O-rings [14, 15]. Extreme care should be taken to avoid any contact between the KOH and the frontside of the wafer, otherwise the Nb devices will be completely destroyed. The space on the device side of the wafer is slightly overpressurized with nitrogen gas, to prevent KOH leakage through pinholes in the Si_3N_4 membranes. The freestanding membrane is formed by etching the silicon in a solution which contains 20% KOH by weight at 80 °C for 4-5 hours and another hour of etching at 60 °C. The last step is used to create smoother sidewalls of the aperture.

The final fabrication step is the deposition (with E-beam evaporation) of a 400-nm Ti/Au layer on the sidewalls of the aperture through a ceramic shadowmask. The shadowmask (which was patterned by cutting with an excimer laser) is used to avoid the deposition of gold on the membrane.

3.2 Horn Apertures

The micromachining of the horn apertures is similar to the etching process described above. In the patterning of these apertures a mask with circular hole definitions is used. Because of the highly anisotropic etching rate these holes will end up as square holes with an area as large as the smallest rectangle that encloses the circular holes (Fig. 4). The advantage of this method is that the alignment to the crystallographic axes of the wafer is not important. After the etching, the SiN layers on the wafers are stripped in 160 °C H_3PO_4 and a 400-nm Ti/Au layer is deposited on the sidewalls.

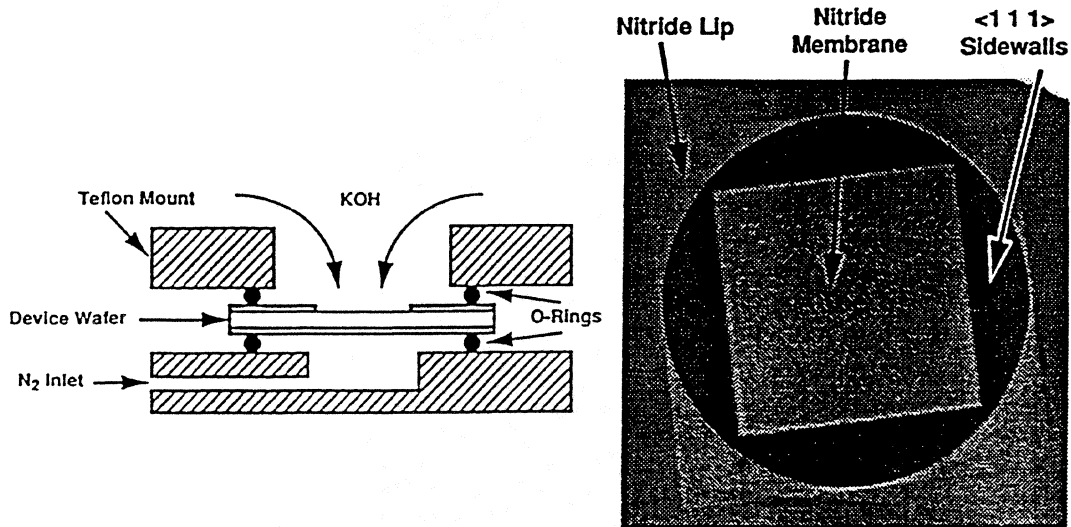


Figure 4: (a) Mount used in the KOH etching of the apertures in the device wafer. (b) SEM picture of the circular aperture in the Si_3N_4 membrane and the pyramidal cavity formed by the anisotropic etch.

3.3 Mounting

The separate parts of the horn aperture are aligned under a microscope and bonded together with UV- and heat-curing Norland optical Glue and Crazy Glue Cyanobond. The accuracy of this alignment is within $20\ \mu\text{m}$. The parts forming the horn section can be permanently bonded with the optical glue, but for repeated use of this horn section, the device wafer is glued with a cyanobond glue that dissolves easily in acetone.

4 Results

4.1 Cooling and mechanical ruggedness

A possible drawback in the use of thin freestanding membranes with superconducting devices could be that due to the high thermal resistance of the Si_3N_4 membrane, the cooling of the superconducting devices is not sufficient.

Measurements shown in Fig. 5 demonstrate that the superconducting junctions can be adequately cooled. In Fig. 5, three measurements of the same device are shown, where the device

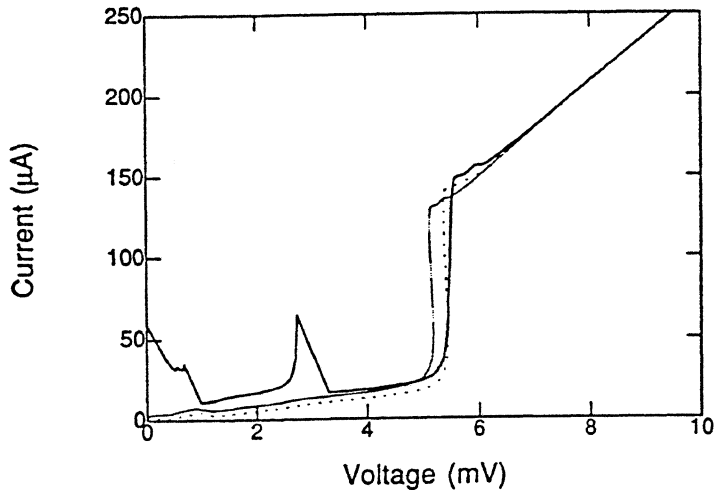


Figure 5: DC I-V characteristics of device HEN52 measured immersed in liquid helium (solid line) and in the vacuum dewar at a mixer mount temperature of 4.6 K and 2.74 K (dashed and dotted line).

was either immersed in liquid Helium (solid line), or mounted in the vacuum dewar with a mixer mount temperature of 4.6 K (dashed line) or 2.74 K (dotted line). The measurements show that the gap voltage of the two junction array decreases from 5.45 mV in the liquid Helium dewar ($T=4.2$ K) to 5.19 mV when the device is mounted in the vacuum dewar. This 0.13 mV decrease in gap voltage (per junction) corresponds to a temperature increase of 1 K. It will be shown next that this increase in temperature deteriorates the mixer performance somewhat, but even at the elevated temperature a good mixing performance is still achievable.

By pumping the He bath of the vacuum dewar the mixer mount temperature is reduced to 2.74 K. As can be seen in Fig. 5 this increases the gap voltage to a value similar to the measurement in the liquid helium dewar. Since the gap voltage of a superconducting tunnel junction is nearly independent of temperature for temperatures below half the critical temperature (9.2 K for Nb), this measurement shows that by pumping the He bath an optimum operating temperature can be reached.

The steep and even somewhat backbending current rise near the gap of the devices mounted in the vacuum dewar, which is not observed in the measurement in the liquid He dewar, indicates that the power dissipated by the DC tunnel current at the gap voltage increases the junction temperature (thereby decreasing the gap voltage). Although this bias current dependent temperature is inconvenient for a comparison of measured data with mixer theory, we do not expect that it influences the mixer performance in a very strong way, since for mixer operation the bias current of a device will be approximately one third of the total current increase at the gap voltage ($\approx 50 \mu\text{A}$ for this junction) and the temperature increase will be only marginal.

The observed temperature increase of the devices when mounted in the vacuum dewar is

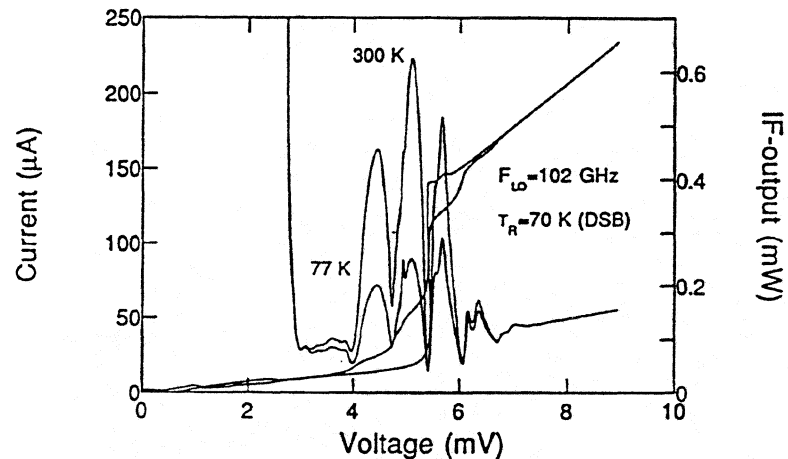


Figure 6: Pumped and unpumped I-V characteristics of device HENS2 at a LO frequency of 102 GHz and the measured IF-output power with a 295 and 77 K input load.

expected to be less for higher frequency designs, since the membrane size decreases with the wavelength.

Glueing the device wafer with the Si_3N_4 membrane to the wafers that form the apex of the horn cavity forms a sealed air-filled cavity and the pressure difference between this closed cavity and the dewar vacuum will cause bending of the membrane. Several devices have been mounted and used in the vacuum dewar and all the membranes withstand the pressure differences. Also, the thermal cycling between room temperature and 4.2 K does not degrade the device characteristics.

4.2 Noise measurements

The results for a heterodyne measurement on an array of two junctions, which gave the best noise temperature measured thus far, is shown in Fig. 6. The array has a normal state resistance of $R_N = 37 \Omega$ and each junction has an area of $2.6 \mu\text{m}^2$ (the critical current density is $J_c = 4.9 \text{ kA/cm}^2$). Fig. 6 shows the DC I-V curve measured with and without the 102 GHz local oscillator radiation applied (at a mixer mount temperature of 2.74 K) and the IF-output power with a 77 K and 295 K blackbody input signal.

The maximum Y-factor (measured at the first photonstep below the gap voltage) is 3.94 dB, which results in a 70 K DSB receiver noise temperature (without any correction). For a mixer mount temperature of 4.7 K the DSB noise temperature is 80 K, showing that although there is a clear decrease in gap voltage (see Fig. 5) the noise temperature increases only 10 K. The measured noise temperature as a function of frequency is shown in Fig. 7. The 3 dB bandwidth

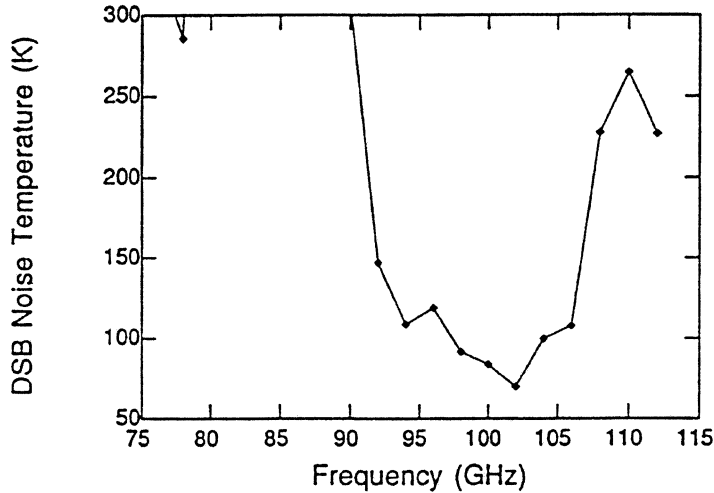


Figure 7: Noise temperature as a function of frequency. The 3 dB bandwidth is 15 GHz.

of the mixer is ≈ 15 GHz.

Our first results are within a factor of 3.5 and 2 in comparison with the best waveguide and quasi-optical SIS mixers for this frequency range, respectively. As will be shown next the present level of the noise temperature is mainly caused by the large reflection of signal power due to the capacitance of the tunnel junction. The waveguide and quasi-optical mixers have overcome this problem by use of (external or integrated) tuning elements, or by use of sub-micron area tunnel junctions.

For a possible further optimization of the micromachined receiver, the various noise and gain contributions of the receiver are analyzed. The total measured receiver noise temperature, expressed in terms of noise and gain of the rf, Mixer and IF components, is given by:

$$T_{\text{REC}} = T_{\text{RF}} + \frac{T_{\text{MIX}}}{G_{\text{RF}}} + \frac{T_{\text{IF}}}{G_{\text{RF}}G_{\text{MIX}}} \quad (1)$$

The noise contribution T_{IF} and the gain of the IF-chain are found by using the shot noise of the unpumped I-V curve as a calibrated noise input for the IF-chain. The values thus found are $T_{\text{IF}} = 3.6$ K and $G_{\text{IF}} = 100.3$ dB. Once the IF gain is known, the product $G_{\text{RF}}G_{\text{MIX}}G_{\text{IF}}$ is found from the difference in output power δP_{out} caused by the 295 K and 77 K input signals, since $\delta P_{\text{out}} = \delta P_{\text{in}}G_{\text{RF}}G_{\text{MIX}}G_{\text{IF}}$ (where $\delta P_{\text{in}} = kB(295 - 77)$, k = Boltzmann's constant, B = IF filter bandwidth). At the biasvoltage with the optimum noise performance, $G_{\text{RF}}G_{\text{MIX}} = -5.1$ dB, which results in a noise contribution of 11.6 K from the $T_{\text{IF}}/G_{\text{RF}}G_{\text{MIX}}$ term in Eq. 1. The noise contribution of the RF input is caused by the loss of the beamsplitter (97 % transmission), the dewar window (97 % transmission) and the quartz heat filter (≈ 100 % transmission at 100

GHz) and amounts up to 16 K. Losses in the lens and the machined and micromachined horn sections do not contribute to the RF noise temperature, since those losses are at 4.2 K.

The unknown parameters in Eq. 1 are the separate mixer and RF loss G_{RF} , G_{MIX} and the mixer noise temperature T_{MIX} . We estimate the resistive loss of the micromachined horn section to be 1-2 dB, based on the scale model measurements described in [16]. Main cause of this loss is the partly uncovered sidewall of two wafers of the pyramidal horn section. A part of the sidewall is not covered with gold, to avoid shorting of the coplanar IF-output/DC-bias lines. With a total RF input loss of 1.3-2.3 dB, the mixer gain is -3.8– -2.8 dB and the mixer noise temperature is 28 ± 12 K.

The mixer gain and noise are also calculated with the quantum mixer theory. For an accurate calculation a precise knowledge of the embedding admittances at the LO, USB (upper side band) and LSB (lower side band) is necessary and from an analysis of the pumped I-V curve these embedding impedances can be found. As was already pointed out, the current dependent temperature near the gap voltage makes it difficult to obtain a very accurate value for the embedding admittances. Furthermore we observed that the shape of the pumped I-V curves does not change very much if the frequency is changed. Very flat or even negative slopes on the first photonstep below the gap were not observed, indicating that the embedding admittance is mainly determined by the junction capacitance and also that the embedding will change slowly as a function of frequency. Analysis of the pumped curve shown in Fig. 6 yielded a calculated LO embedding admittance of $Y_{emb} = 0.75 + j2.5$ (scaled to the normal state admittance $Y_N = (37 \Omega)^{-1}$). This capacitive embedding results in a -5 dB coupling coefficient to the 35Ω antenna impedance. If we ignore the influence of any reactive antenna admittance, the embedding admittance from the parallel connection of the antenna admittance, the parasitic capacitance due to the overlap of the electrodes (~ 30 fF) and the junction capacitance ($55 \text{ fF}/\mu\text{m}^2$, with a junction area of $2.6 \mu\text{m}^2$) we find a scaled embedding admittance of $1 + 2j$ at 100 GHz, in reasonable agreement with the value found from the analysis of the pumped curve.

The mixer noise and gain are calculated with the value for Y_{emb} found from the analysis of the pumped curve. Assuming the same embedding admittance at the LO, USB and LSB frequencies the calculated mixer gain and noise are $G_{MIX} = +1.5$ dB and $T_{MIX} = 16$ K. The calculations therefore overestimate the gain and underestimate the mixer noise, which we attribute to the error margins in the determination of the embedding impedances.

4.3 FTS measurements

The frequency response of the micromachined horn antenna is measured with a Fourier Transform Spectrometer. In these measurements the SIS junction array is biased at a voltage just below the gap voltage and used as a video detector, with a frequency dependent responsivity $R = \Delta I / \Delta P \approx e / h\nu$.

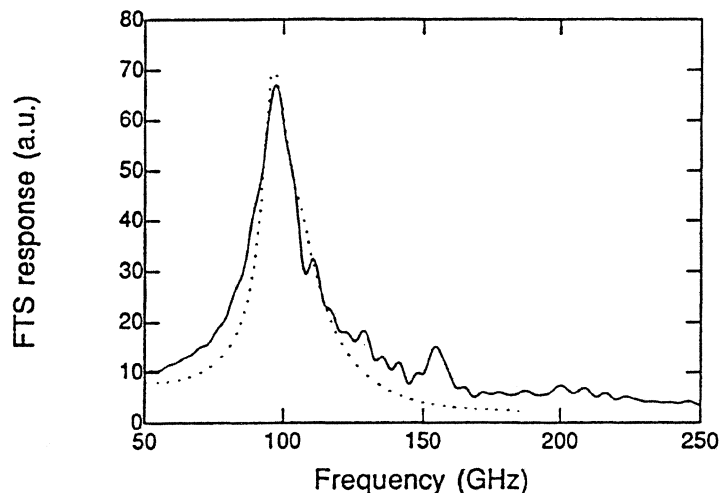


Figure 8: *Frequency dependent coupling measured with a Fourier Transform spectrometer (solid line) and the calculated coupling (dotted line).*

Fig. 8 shows the result of the frequency dependent coupling measured with the FTS, together with a calculated coupling, to be discussed later. The maximum coupling is measured just above 100 GHz, in agreement with the noise temperature measurement.

The dotted line shown in Fig. 8 shows a calculated frequency dependent coupling (scaled to the maximum measured coupling) of which the general behaviour is in good agreement with the measured frequency response. In the calculations we used the dipole antenna impedance measured in a scale model and added in parallel the capacitance from the two junction SIS array. The original impedances and the impedance after adding the junction capacitance are shown in Fig. 9, together with the embedding impedance found from the analysis of the pumped curve. The displayed curve of the calculated coupling in Fig. 8 is shifted +5 GHz in frequency to make the measured and calculated peak couplings coincide. Since the scale model differs somewhat from our actual design, slight differences between the measured and calculated coupling are to be expected. The maximum coupling calculated from this model is -4.9 dB, which is nearly the same as the coupling calculated with the calculated embedding impedance although the actual admittances differ significantly.

5 Conclusion

In summary we have shown for the first time the operation of a micromachined SIS mixer for the 75-115 GHz range. The feasibility of micromachined SIS-mixers is demonstrated: the complete micromachined mixer is robust and can be thermally cycled in a cryogenic vacuum environment, the tunnel junctions can be sufficiently cooled, and noise measurements are performed. The measured minimum noise temperature of 70 K DSB is very encouraging and is expected to

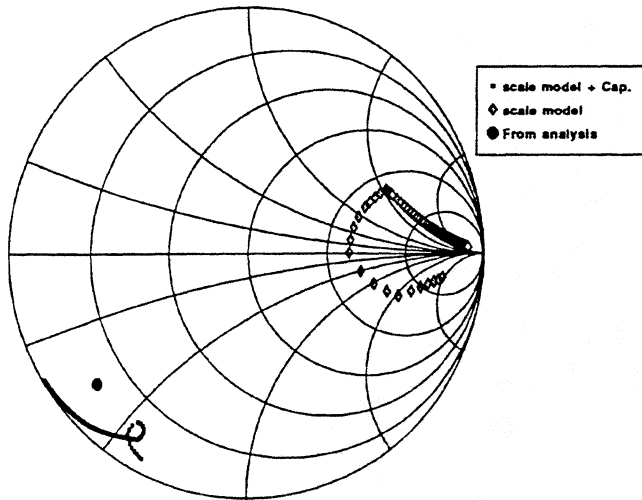


Figure 9: Smith chart showing the impedance at the dipole antenna terminals measured from a scale model, and the impedance after adding a parallel capacitance of the tunnel junction array. Also shown is the embedding impedance calculated from the pumped I-V curve.

be further improved by future designs in which the junction capacitance is tuned out by an integrated tuning element.

Acknowledgment

We would like to thank Earl Macedo, Janen Deneeno and Dan Baker at MIT Lincoln Laboratory for their technical assistance during the fabrication of the SIS devices. This work was supported by NASA under grants No, NA G2-693 and 959705.

References

- [1] G.M. Rebeiz, D.P. Kasilingam, P.A. Stimpson, and D.B. Rutledge, "Monolithic millimeter-wave two-dimensional horn imaging arrays," *IEEE-Transactions Antennas Propag.*, vol. AP-38, pp. 1473–11482, Sept. 1990
- [2] W.Y. Ali-Ahmad, and G.M. Rebeiz, "A 335 GHz integrated Schottky receiver," *IEEE-Microwave and Guided Wave Letters*, vol. 4, pp. 37–39, Feb 1994.
- [3] G. de Lange, C.E. Honing, J.J. Kuipers, H.H.A. Schaeffer, R.A. Panhuyzen, T.M. Klapwijk, H. van de Stadt, and M.W.M. de Graauw "Heterodyne mixing with Nb tunnel junctions above the gap-frequency," *Appl. Phys. Lett.* vol. 64 pp. 3039–3042, July 1994.

- [4] J. Zmuidzinas, H.G. LeDuc, J.A. Stern, and S.R. Cypher, "Two junction tuning elements for submillimeter SIS mixers," *IEEE Trans. Appl. Superconductivity* vol. 42, 698–671 May 1994
- [5] Gordana Pance and Michael J. Wengler, "Broadband quasi-optical SIS mixers with large area junctions," *IEEE Trans. MTT* vol. 42, 750–752 April 1994
- [6] T.H. Büttgenbach, R.E. Miller, M.J. Wengler, D.M. Watson, and T.G. Phillips, "A broadband, low-noise SIS receiver for submillimeter astronomy," *IEEE Trans. MTT* vol. 36, 1720–1726 May 1988
- [7] A.R. Kerr, S.K. Pan, A.W. Lichtenberger, F.L. Lloyd, and N. Horner, "A new SIS mixer for the 2-mm band," *Proceedings of the Fourth International Symposium on Space Terahertz Technology*, March 1994
- [8] S.V. Shitov, V.P. Koshelets, S.A. Kovtonyuk, An B Ermakov, N.D. Whyborn and C-O Lindström, "Ultra-low-noise 100 GHz receiver based on parallel biased SIS arrays," *Superconducting Sci. Technol.* vol. 4, 406–408 1991
- [9] H. Ogawa, A. Mizuno, H. Hoko, H. Ishikawa, and Y. Fukui, "A 110 GHz SIS receiver for radio astronomy," *Int. Journal of Infrared and Millimeter waves* vol. 6, 717–725 1990
- [10] G.V. Eleftheriades and G.M. Rebeiz, "Analysis and design of millimeter-wave quasi-integrated horn antennas," *IEEE-Transactions MTT*, vol. 41, pp. 954–965, 1993
- [11] G.V. Eleftheriades, W.A. Ali-Ahmad, L.P. Katehi, and G.M. Rebeiz, "Millimeter-wave integrated horn antennas: Part I: theory," *IEEE-Transactions Antennas Propag.*, vol. AP-39, pp. 1575–1581, Nov. 1991
- [12] Edouard Garcia, Brian R. Jacobson, and Qing Hu, "Fabrication of high-quality superconductor-insulator-superconductor junctions on thin SiN membranes," *Appl. Phys. Lett.*, vol. 63, pp 1002–1004, August 1993.
- [13] M. Bhushan and E.M. Macedo, "Nb/AlO₂/Nb trilayer process for the fabrication of submillimeter Josephson junctions and low-noise dc SQUIDS," *Appl. Phys. Lett.*, vol. 58, pp. 1323-1325, August 1991.
- [14] Brian R. Jacobson, *Masters Thesis MIT*. May 1994, unpublished.
- [15] J.T. Kung, A.N. Karanicolas, and H. Lee "A compact, inexpensive apparatus for one-side etching in KOH and HF," *Sensors and Actuators A*, vol. 29, 1991.

- [16] W.Y. Ali-Ahmad, G.V. Eleftheriades, L.P. Katehi and G.M. Rebeiz, "Millimeter-wave integrated horn antennas:PartII: Experiment," *IEEE-Trans Antennas and Propagation*, vol. AP-39, pp. 1582–1586, Nov 1991.

Integrated Silicon Micromachined Waveguide Circuits For Submillimeter Wave Applications

John A Wright¹, Svetlana Tatic-Lucic, Yu-Chong Tai
William R. McGrath*, B. Bumble*, H. LeDuc*

1. Author to whom correspondence should be addressed at Department of Electrical Engineering, California Institute of Technology, Pasadena, CA 91125

* Center for Space Microelectronics Technology, Jet Propulsion Laboratory, California Institute of Technology, Pasadena, CA 91109

Abstract --Rectangular waveguides are commonly used as circuit elements in heterodyne sensor systems at millimeter wavelengths. However, conventional machining techniques for such components operating above a few hundred GHz, are complicated and costly. Previously we reported on the development of silicon micromachining techniques for fabricating silicon-based waveguide circuits which can operate up to high submillimeter wave frequencies. Continuing this work, we have used (110) silicon wafers as a substrate and fabricated WR-4 (170 - 260 GHz) waveguides. The new capability of placing a nitride membrane that runs the length of the waveguide's central axis has been developed and demonstrated. Submicron SIS tunnel junctions have also been successfully fabricated on nitride membranes which will allow them to be integrated into the waveguide design. This eliminates the traditional mounting problems of thin substrates for high frequencies. Low temperature, selective metallization techniques (electroless nickel) have been developed which coat the silicon waveguide walls but leave the nitride membranes untouched. By avoiding a high temperature metallization process, integration of the temperature sensitive Superconductor-Insulator-Superconductor (SIS) junctions with the waveguide channels is made possible. Insertion loss measurements of WR-4 waveguide sections show performance comparable to conventional metal waveguides.

I. Introduction

Rectangular waveguides are used in a variety of rf components and circuits. In particular, heterodyne radiometers use waveguide circuits at millimeter wavelengths and even recently at submillimeter wavelengths [1]. Conventional machining techniques for metallic waveguides become time consuming, costly, and difficult for frequencies above a few hundred GHz. Waveguide dimensions are comparable to the wavelength, which is $\lambda = 0.3$ mm at 1000 GHz for example. In addition, mounting small dielectric substrates with devices such as mixer diodes, filters and planar probes in these waveguides is difficult.

We are developing and adapting silicon micromachining techniques [2, 3] to create waveguide circuits which can operate up to high submillimeter wave frequencies. Silicon micromachined waveguide components have several advantages, as previously discussed [4], including precise tolerance control, atomically smooth walls, rapid turnaround for

optimization, and the inclusion of membranes as integrated substrates for planar devices and circuits. Initial efforts have produced straight waveguide sections for WR-10 band (75-115 GHz) [4]. In this work, the focus has been on higher frequencies (170-260 GHz), improved metallization techniques (electroless nickel), and incorporation of thin ($\approx 2 \mu\text{m}$) silicon nitride membranes which can support planar devices and circuits.

II. Fabrication Process

Overview - The major steps of the fabrication process for the half sections with emphasis on the cross section is shown in Fig. 1.

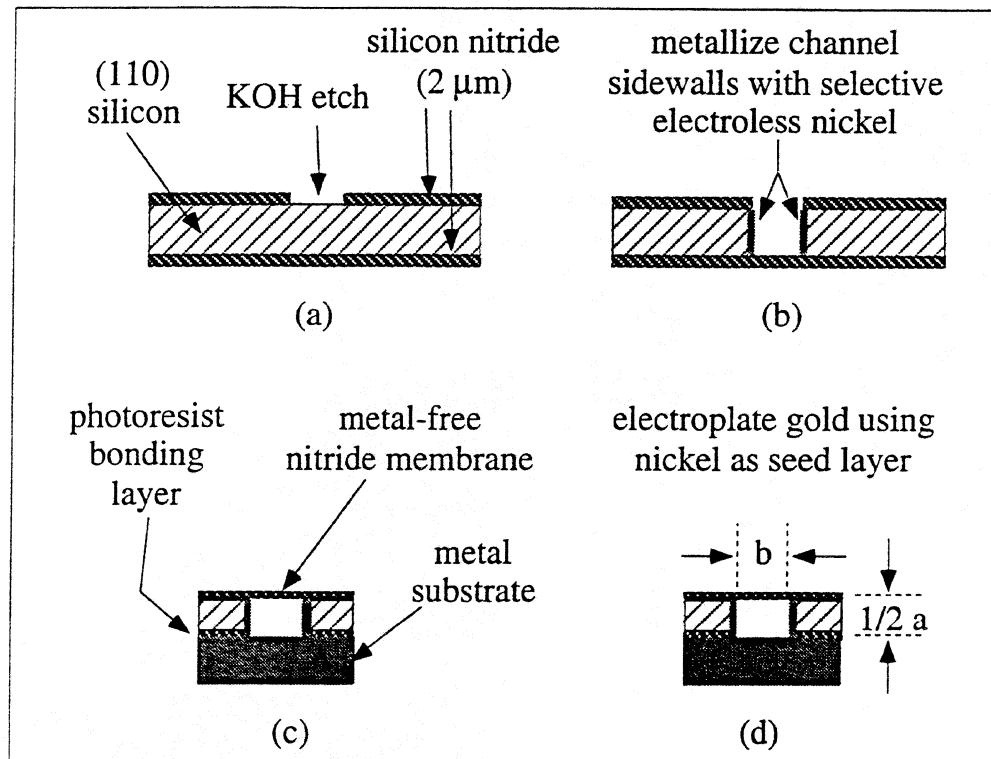


Fig. 1. A cross section view of the fabrication process. (a) Si_3N_4 mask defines the waveguide height. (b) Wafer is etched completely through and the channel sidewalls are metallized (c) Wafer with waveguide channels is bonded to a smooth metal substrate which forms the floor of the half-channel. (d) Completed half-section of waveguide with gold plating. Two of these sections are mated to form the waveguide. "a" is the waveguide width and "b" is the height.

Double-side polished silicon wafers with (110) surface orientation and 0.0215 inches thick are used. A thick ($\approx 2 \mu\text{m}$) layer of Low Pressure Chemical Vapor Deposited (LPCVD) silicon nitride (Si_3N_4) is deposited on both sides of the wafer. Photoresist is used to pattern windows in the Si_3N_4 on the backside of the wafer with an SF_6 plasma. These windows define b, the waveguide height, shown in Fig. 1(d). The wafer is put in a reflux system and etched in a water based solution of potassium hydroxide (KOH) to form the channel. Figure 1(b) shows the wafer after it has been etched completely through to form half of the waveguide. Not only does the etch create waveguide half-channels but it also forms the nitride on the front side of the wafer into a membrane as it

removes silicon from behind. Metallization is done using a selective nickel plating bath, and a photoresist bonding technique is used to glue the channels to a smooth metal substrate, as shown in Fig. 1(c), to form the third wall of the half-channel. After patterning of the nitride membranes, the wafer is diced into individual waveguide halves 25.4 mm in length as shown in Fig. 1(d). Further metallization is done to reduce rf conduction losses by electroplating gold to a thickness of $\sim 3 \mu\text{m}$.

Channel Formation - As noted above, a water based solution of KOH is used to etch the channels into the silicon wafer. We are using a continuously stirred 40% solution heated to 80°C . As we reported previously [4], the etching rate of (110) silicon by this solution is $2 \mu\text{m}/\text{min}$ and the etching ratio of (110):(111) planes is 170:1. It is the large etching ratio that makes this etchant attractive. A (110) wafer has its (111) planes perpendicular to its surface. When etched by KOH, the (111) planes are effectively not etched when compared to the other planes. As a result, channels with vertical sidewalls can be obtained. If alignment to the (111) crystal plane is very accurate ($\approx 0.1^\circ$), the walls of the channels will be atomically smooth. Figure 5 shows how smooth the (111) defined sidewalls can be when compared to the planes that are being etched down to form the channel. The figure shows a partially etched channel spanned by a patterned "air bridge." The sidewalls are extremely smooth as compared to the rough bottom which needs to be etched further. (Note the abrupt transition between the rough, wood-like texture of the bottom and the smooth sidewalls.)

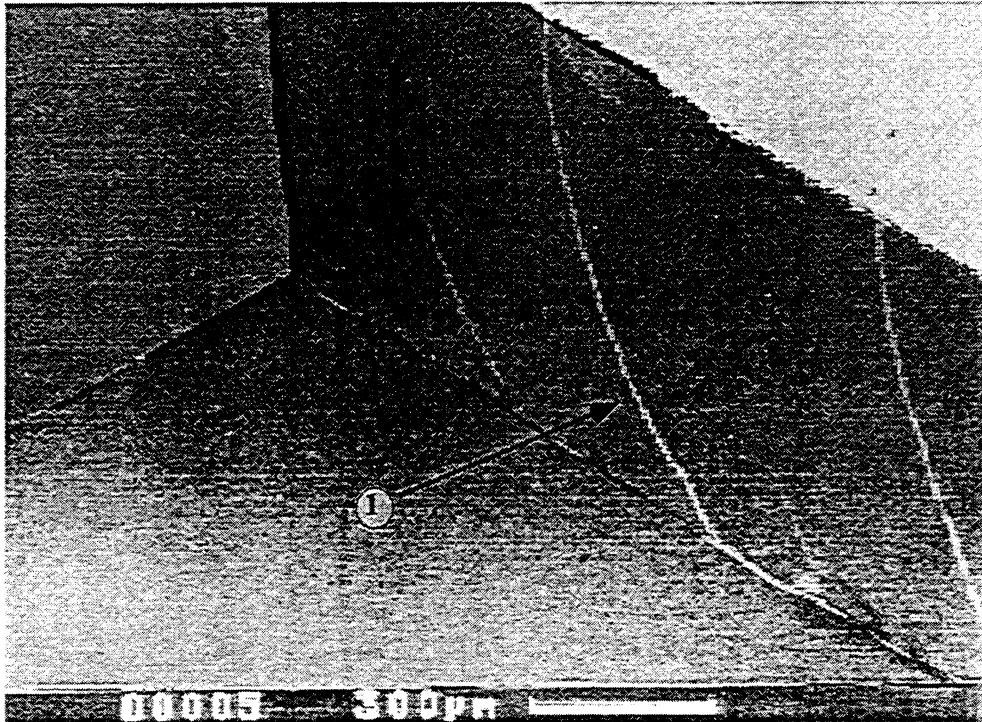


Fig. 2 SEM photo of a channel's sidewall. (1) indicates one of the curved steps that were formed during the KOH etching. They are caused by poor alignment to the (111) plane.

Since extremely smooth sidewalls are desired, especially to minimize rf losses at higher frequencies, accurate alignment of the channel masks to the (111) crystal plane is

required. The wafers used have their major flats cut along the (111) plane but alignment to this alone is insufficient to assure featureless sidewalls. Wafer specifications state that major flat alignment to the designated plane is only to within $\pm 1^\circ$. We have found that alignment to the (111) plane must be within a $\pm 0.25^\circ$ in order to avoid producing ridges in the sidewalls during etching (see fig. 2.)

Fine alignment to the (111) plane is achieved by KOH etching a fan pattern into the wafer before the channels are defined. The fan pattern consists of an array of lines with each line rotated 0.1° with respect to its neighbor. These fans consist of fifty one lines which allows for a correction of $\pm 2.5^\circ$. The KOH etching of the fan pattern is short in comparison to the etch that creates the waveguide channels, being only about 30 minutes. This is sufficient to generate significant undercut in those lines that are poorly aligned to the (111) crystal while negligible undercut occurs in the well-aligned lines. The pair of lines deemed to have the least amount of undercut is then used as the alignment marks for the exposure with the channel mask.

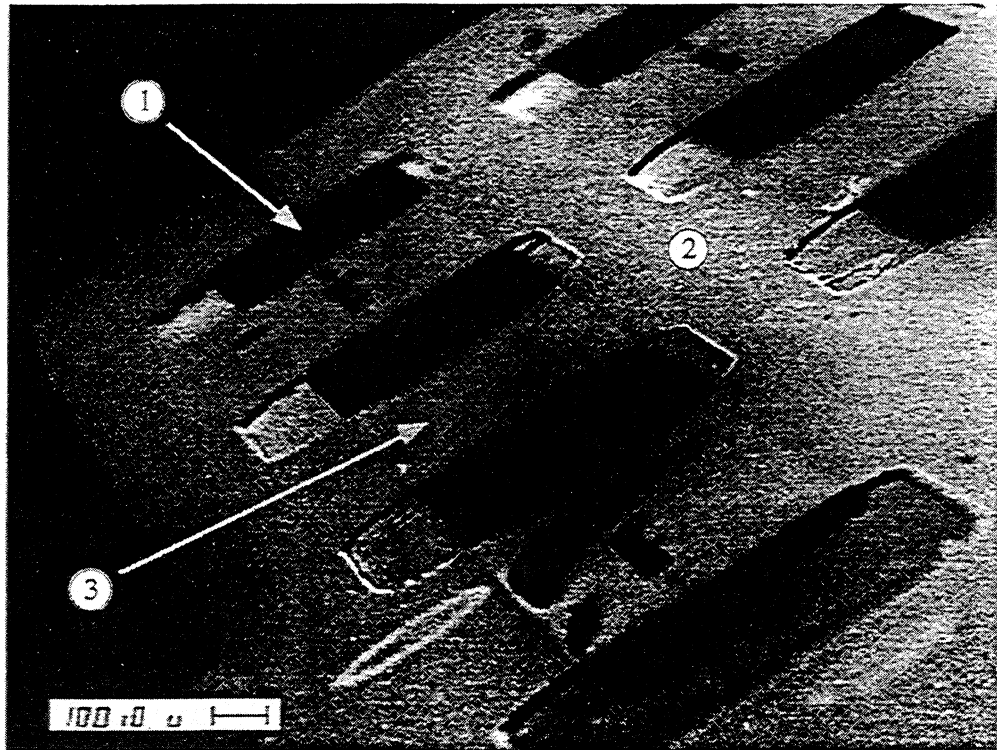


Fig. 3 SEM photo of a silicon waveguide channel spanned by three nitride air bridges, $2\mu\text{m}$ thick. (1) show the channel, (2) shows the silicon substrate that is the channel's sidewall and (3) shows the one of the nitride air bridges. The front nitride air bridge has fractured. Both the front and back nitride air bridges are inscribed with a name. A portion of a second, neighboring channel can be seen in the upper right corner of the photo.

Membranes - Of particular interest is the development of a technique which permits thin membranes of dielectric material (such as silicon nitride) to be fabricated across the waveguide channels. As noted in the channel fabrication section, this is done by coating the wafer with a relatively thick layer ($\approx 2\mu\text{m}$) of nitride and etching away the silicon from one side of the wafer. This permits the entire channel to be spanned by silicon

nitride and if desired, allows further processing to be performed on the wafer. This provides for the possibility (but not the requirement) of fabricating SIS junctions and planar tuning circuits on the membranes after the channels have been created. The membranes can be patterned into air bridges if desired to limit the amount of dielectric crossing the channel. Figure 3 shows waveguide spanned by three nitride air bridges. The front and back air bridges have a name inscribed in them. The front bridge is fractured due to handling but is still mainly intact. Figure 4 shows a close-up of a single air bridge spanning the channel.

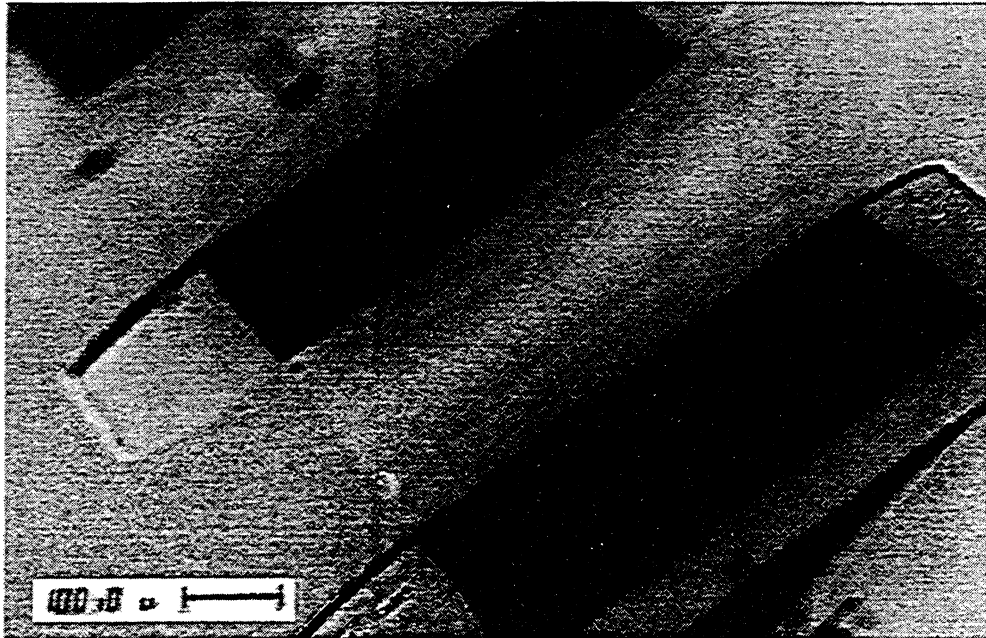


Fig. 4 Close-up of the blank air bridge identified in figure 3

A second method for fabricating air bridges has been demonstrated which allows the channels to be etched from the membrane side of the wafer as opposed to the backside as used to produce the 200GHz waveguides. Figure 5 shows an air bridge spanning a partially etched channel. The diamond holes in the nitride are needed to ensure that the silicon beneath the air bridge is removed. An improvement on this process which involves adding a sacrificial oxide layer beneath the nitride should eliminate the need for such holes but it has yet to be demonstrated.

Metallization - Metallization of silicon waveguides is a crucial step in fabricating components that show comparable insertion losses to conventional waveguides. Because the bulk material from which the channels are produced is a semiconductor and not metal, RF losses are extremely high. In previous work, evaporated metal, deposited at varying angles, was used to coat the walls of the silicon waveguides [4]. Followed by an electroplated gold step, this technique was shown to produce waveguides with good performance. Evaporation, however, cannot be used when nitride air bridges span the channels. Evaporation is not conformal, i.e. it is a directional deposition, and thus areas beneath the air bridges are "shadowed" and will not be metallized. Furthermore, the nitride membranes will themselves be metallized rendering any junctions or tuning

circuitry on them useless. A final issue involved with evaporated metal is temperature. During the deposition the temperature of the wafer, and particularly the nitride air bridges, can easily exceed 150°C which will result in the destruction of sensitive devices such as SIS tunnel junctions.

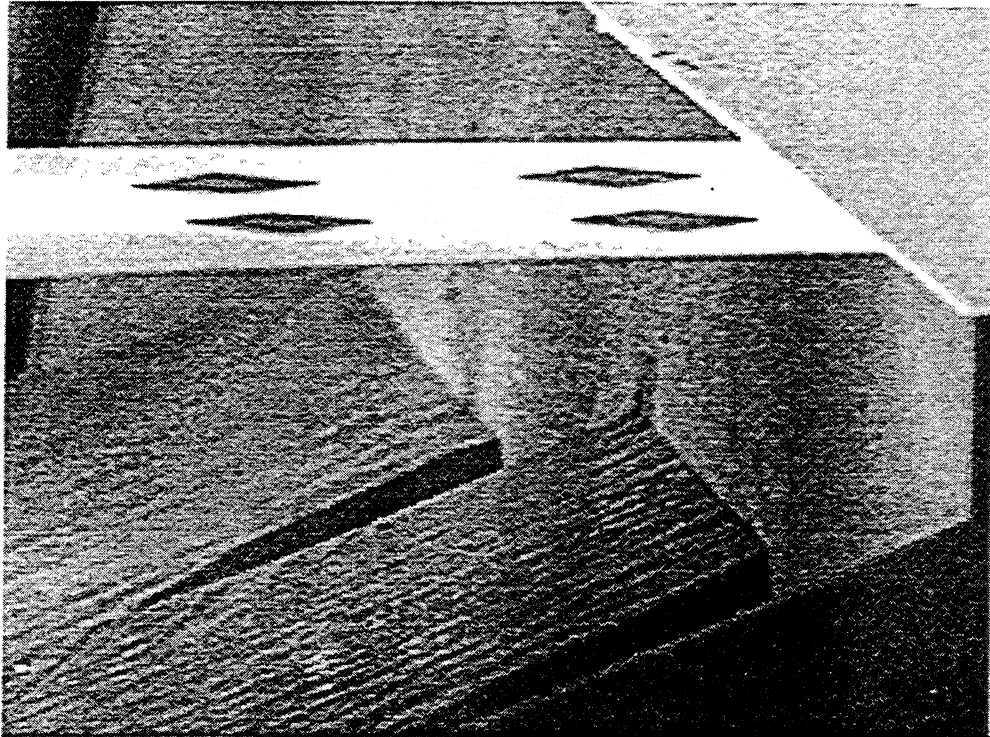


Fig. 5 SEM photo of a partially etched waveguide spanned by a silicon nitride air bridge. Note the smoothness of the sidewalls as compared to the rough etched floor. The change from rough floor to smooth sidewalls is very abrupt.

One process we investigated that would have addressed most of these issues is LPCVD tungsten. In this process, tungsten metal selectively deposits on any exposed silicon surface. It is expected that even silicon "hidden" beneath air bridges can be coated. After a thin layer of metal is deposited it can act as a seedlayer for a subsequent electroplated gold layer. Unfortunately, the deposited tungsten layer has an very high intrinsic stress, too high it turns out to permit coating a continuous surface area as great as the sidewalls of the waveguide channels. Extensive flaking of the tungsten film occurred after the deposition and the final metallization of the channels was spotty at best. If the stress in the film could be reduced, this may be a viable process for future waveguides. One additional constraint that must be observed if this process is used is that SIS junctions must be fabricated after the tungsten deposition since they will be destroyed by the high temperature used in the metallization technique.

The process finally developed that addresses all of the aforementioned issues is a selective, electroless nickel deposition. The plating solution used is an alkaline bath, pH 8 - 10, reported in [5]. This bath was chosen for its many attractive qualities which include selective plating of silicon, high quality, and excellent adherence (see fig. 6). Because plating occurs in a liquid bath, issues of shadowing due to air bridges are no

longer a concern. This process is also SIS junction compatible as the plating temperature is $< 95^{\circ}\text{C}$.

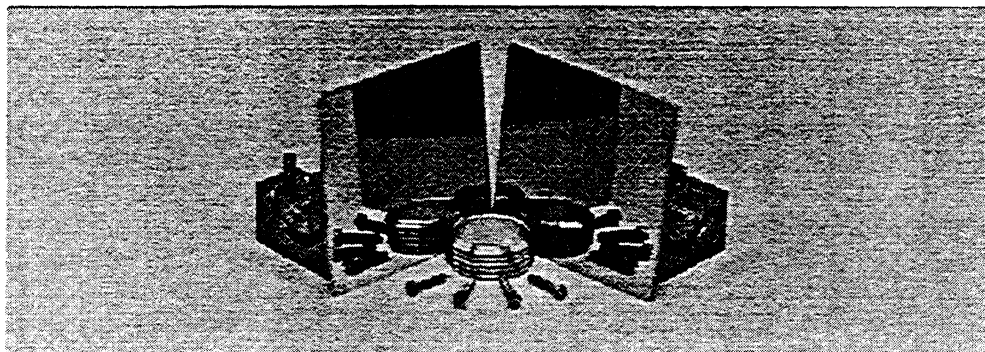


Fig. 6 The photo shows two square, mirror-like samples positioned to create a reflective corner. The sample on the right is bare, polished silicon and on the left is a similar silicon sample onto which electroless nickel has been plated. The two samples are nearly indistinguishable.

Selectivity in the nickel plating is the main attraction of this process. Nickel is deposited only on those surfaces that are non-insulating. Thus for the waveguide components, only the silicon sidewalls will be plated by the bath. Nitride, however, being an insulator will remain metal free. This permits the nitride air bridges to be left unprotected during the metallization. Simultaneously, the silicon beneath such structures will be plated guaranteeing that there will be continuous metallization down the length of the channel.

It should be noted that the plated nickel will not be the final metal lining the channels. The layer deposited, while not necessarily thin, is kept thin for this process. As an RF conduction material, this nickel is relatively poor. It can, however, perform more than adequately as a seed layer upon which high quality gold or copper can be electroplated. Measurements indicate that 25.4 mm long channels metallized by nickel alone have an insertion loss on the order of -10dB. Once covered by electroplated gold, the losses become comparable to commercial waveguides as described in the following section. For gold electroplating we used AU125 by Selrex [6] which is an acidic bath that is heated to 60°C and continuously stirred.

Wafer Bonding - Due to the relatively large dimensions of the 200 GHz channels and size limitations of the silicon processing equipment, it is not possible to fabricate the half channels in a single silicon wafer. The present process relies on the wafer into which the channels are etched to be as thick as the half-width, $a/2$, of the target waveguide. This means that once fabricated, the channels must be bonded to a substrate which forms the third wall, or bottom of the channel. The method of bonding is relatively unimportant as long as: 1) it is strong enough to withstand the processes which follow it, 2) the thickness of any adhesive layer used is negligible compared to the waveguide dimensions and 3) after bonding, gold can be plated onto the "third wall." Preferably the gold plate can electrically connect the bottom to the sidewalls.

We chose to use photoresist to bond the channels to the substrate. The main reason being ease of use. Since photoresist is a part of almost every major step in silicon processing, it is a well characterized, easily deposited material. Its bonding strength is adequate for our needs and it can withstand both dicing and gold electroplating steps. Of

particular importance is the fact that it can be deposited in a very thin layer (1 to 2 μm) and it can be selectively removed after exposure to UV light.

Bonding with the photoresist is a very straightforward process. We first choose the substrate. The main requirement is that it is conductive. A silicon wafer coated with a layer of evaporated gold is used. A thin layer of positive photoresist (AZ1350J @ 3500RPM) is then spun onto the wafer. Immediately following the spinning step, the wafer into which channels have been etched and metallized is placed onto the photoresist coated wafer, membrane side up. The two bonded wafers are then soft baked at 100°C for half an hour. Following the bake, the two wafers are globally exposed with UV light and developed. This removes the photoresist from the bottom of the channels while leaving the resist involved in the actual bonding intact. The end result is two wafers bonded together to form half channels. The distance between the sidewalls and the bottom is $\approx 2\mu\text{m}$ which should be easily covered by a 3 μm thick gold plate, the final step in the waveguide fabrication process.

Photoresist is, of course, not the only option for the bonding step. Previously we have used polyimide as the bonding material which, in this process, is simply a more rugged form of photoresist [4]. Other bonding options include anodic bonding, metal-to-metal pressure bonding and common glue or epoxy bonding. There are benefits and drawbacks associated with each of these depending on the specific application for the waveguide component. Photoresist, however, is preferable for rapid turnaround development work. As a final note, for waveguides with target frequencies of 350 GHz and higher, wafer bonding will no longer be necessary. Instead, silicon-on-insulator (SOI) wafers can be used which are essentially two wafers bonded together with a layer of oxide between them.

IV. Experimental Results

In order to perform insertion loss measurements, a pair of brass mounting blocks was designed and fabricated as shown in figures 7 and 8. The two waveguide half-sections are put in the brass mounting blocks and mated together. This allows the silicon waveguide to be connected to microwave test equipment using conventional waveguide round mini-flanges for WR-4 band. The silicon waveguides are rugged and can be firmly clamped to metallic flanges. The insertion loss of the WR-4 waveguide was measured over a frequency range of 200 GHz to 255 GHz in ≈ 10 GHz steps using a backward wave oscillator as a swept-frequency source and a direct detector. For each frequency a reference measurement was first taken without a waveguide section present, and then measurements with the commercial and silicon waveguides were made. These steps were

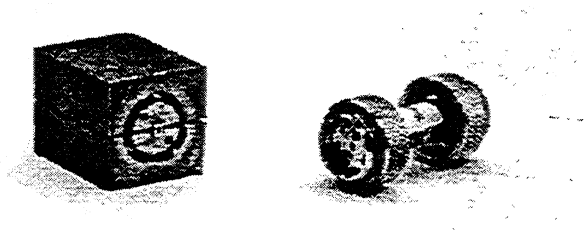


Fig. 7 On the right is a 25.4 mm, commercial WR-4 waveguide section. On the left is our silicon micromachined WR-4 waveguide section. Two fabricated silicon half-channels are assembled in the mounting block to form a functional waveguide.

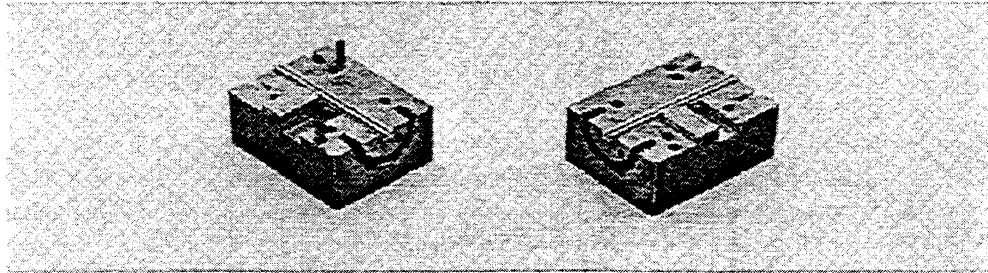


Fig. 8 The photo shows our waveguide mounting block split into its two halves. A waveguide half-channel is mounted in each of the two mounting block pieces.

repeated several times to reduce any variation from the frequency source itself. The insertion loss measurements for a one inch long section of waveguide is shown in Fig. 9. The measured loss is about -0.80 dB across the band for both the commercial and silicon waveguides.

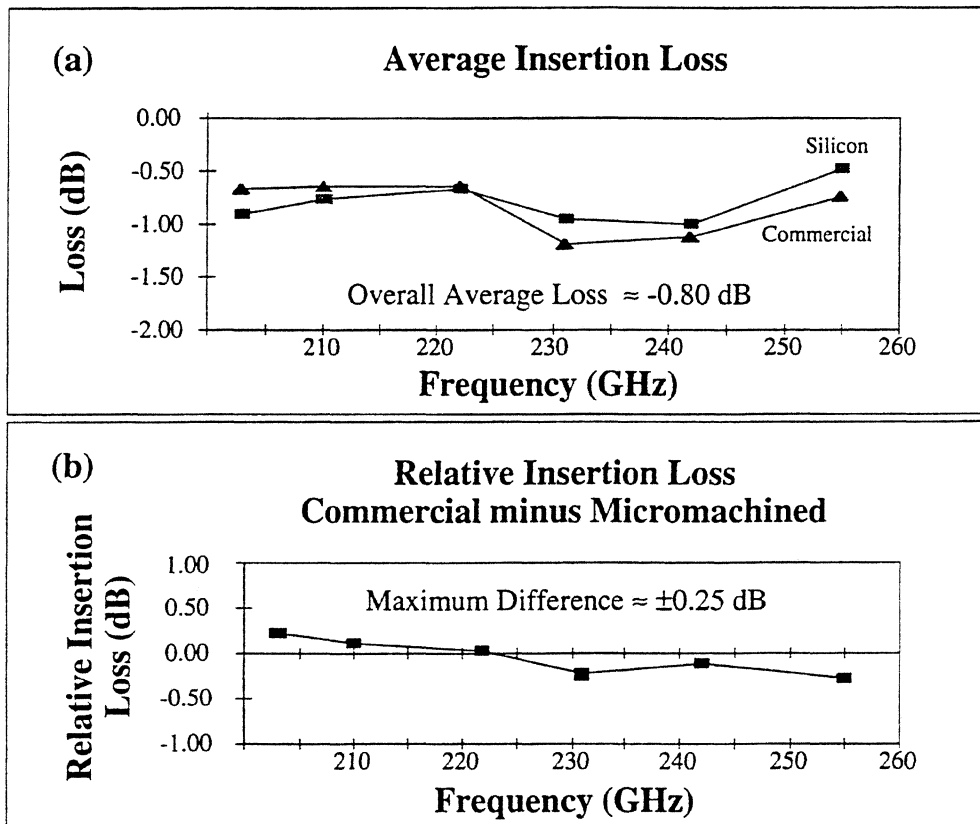


Fig. 9 (a) Measured loss of a 25.4 mm long section of a silicon and a commercial WR-4 waveguide. The surface of the silicon was electroplated with gold to reduce rf losses. (b) Relative loss comparison between silicon and commercial waveguides showing maximum deviation between the two as $< \pm 0.25$ dB.

Assuming bulk copper as the wall material, calculations predicts a loss of ≈ -0.30 dB. The difference between theory and experiment is most probably due to differences in the quality of the gold plated surfaces and bulk copper. Calculations show that the metal coating the channels of both the commercial and silicon waveguides has $\approx 1/12$ the conductivity of bulk copper which is reasonable for electroplated gold. A comparison between the two types of waveguides shows that the relative losses are $< |0.25|$ dB. The data shows that the commercial channel performs better for the lower frequencies while the silicon guide performs better at the higher frequencies. We believe that this apparent trend is an artifact of the measurement since the differences are within the experimental error, rather than it reflecting actual changes in performance. Regardless, these results show that there is little discernible difference in the performance of the two types of waveguides.

VI. Summary

We have improved upon a new approach in fabricating waveguide circuits using silicon micromachining technology. In particular, we have fabricated a 200 GHz silicon rectangular waveguide spanned by $\approx 2\mu\text{m}$ thick silicon nitride air bridges. A new technique for metallizing the waveguide channels using an electroless nickel plating bath has been introduced to the fabrication process which produces a high quality, selectively deposited film. The plated nickel acts as a seed layer for a subsequent layer of electroplated gold. The measured insertion losses of the fabricated devices are found to be ≈ -0.80 dB which is comparable to losses incurred in commercially available, conventional waveguides. The present fabrication process is fully compatible with the integration of SIS junctions and planar RF tuning circuits with the devices.

Acknowledgments

The research described in this paper was performed by the Center for Space Microelectronics Technology, Jet Propulsion Laboratory, and the Dept. of Electrical Engineering, California Institute of Technology. It is jointly sponsored by the National Aeronautics and Space Administration, Office of Space Access and Technology and the JPL Director's Discretionary Fund.

References

- [1] Morvan Salez, Pascal Febvre, William R. McGrath, Bruce Bumble, Henry G. LeDuc, "An SIS Waveguide Heterodyne Receiver for 600 GHz - 635 GHz", *International Journal of Infrared and Millimeter Waves*, vol. 15, pp. 349-368, February 1994.
- [2] L.-S. Fan, Y.-C. Tai, and R. S. Muller, "Integrated Movable Micromechanical Structures for Sensors and Actuators," *IEEE Trans. on Electron Devices*, vol. 35, pp. 724-730, June 1988.
- [3] M. Mehregany, K. J. Gabriel, and W. S. N. Trimmer, "Integrated Fabrication of Polysilicon Mechanisms," *IEEE Trans. on Electron Devices*, vol. 35, pp. 719-730, June 1988.
- [4] W. McGrath, C. Walker, M. Yap, and Y.C. Tai, "Silicon Micromachined Waveguides for Millimeter-Wave and Submillimeter-Wave Frequencies," *IEEE Microwave and Guided Wave Letters*, Vol 3, pp. 61-63, March 1993.
- [5] M. V. Sullivan and J. H. Eigler. "Electroless Nickel Plating for Making Ohmic Contacts to Silicon," *Journal of the Electrochemical Society*, vol. 104, No. 4, pp. 226-229, April 1957.
- [6] Enthone - OMI Inc., 2779 El Presidio, Long Beach, CA 90810. (310) 537-0288.

TOLERANCE ANALYSIS OF A 500 GHz AMPLITUDE HOLOGRAM

Taavi Hirvonen, Jussi Tuovinen, Antti V. Räsänen,
Radio Laboratory, Helsinki University of Technology,
Otakaari 5A, FIN-02150 Espoo, Finland

ABSTRACT

The antenna of the Odin satellite is planned to be tested with a hologram type of a compact antenna test range (hologram CATR) at 119 GHz and 500 GHz. The quiet-zone field is analysed theoretically by using an exact near-field aperture integration method. Main focus of this paper is on the hologram pattern errors parallel to the surface of the hologram. Also the surface flatness requirement is discussed. Due to fabrication errors the slots of the hologram are wider or narrower than in an ideal case, which is shown as increased amplitude and phase ripple in the quiet-zone. Large holograms have to be fabricated by joining several pieces together. A possible displacement of the pieces causes an inclination to the amplitude and phase in the quiet-zone. Also the effect of a frequency change has been simulated; the effect is the inclination of the phase, i.e., the plane wave leaves the hologram in a different angle than at the design frequency.

INTRODUCTION

Odin is an international, mainly Swedish satellite project for monitoring aeronomical and astronomical spectral lines. On the astronomy side the main purpose of the satellite is to perform detailed studies of the physics and the chemistry of the interstellar medium by observing emission from key species. The main targets for observations are giant molecular clouds, nearby dark clouds, comets, planets, circumstellar envelopes and nearby galaxies. Molecular lines of Cl, H₂¹⁸O, H₂O, H₂S, NH₃, H₂CO, O₂, CS, ¹³CO, H₂CS, SO and SO₂ are of interest. On the aeronomy side the stratospheric ozone depletion and the vertical exchange of green house effect gases are of interest. Molecular lines of ClO, CO, NO₂, N₂O, H₂O₂, HO₂, H₂O, H₂¹⁸O, NO, N₂O, HNO₃, O₃ and O₂ will be observed by limb sounding.

The Odin satellite will carry on board a millimeter and submillimeter wave radio telescope and an optical spectrometer. The radio telescope has an offset reflector antenna. The main reflector diameter is 1.1 m. This antenna is meant to operate with heterodyne receivers at frequencies 119, 422, 488, 553 and 575 GHz. The antenna is planned to be tested with a hologram type of a compact antenna test range (hologram CATR).

In this paper, the idea of a hologram CATR is described and the manufacturing process of the hologram is explained. Also the theoretical basis and the results of the tolerance analysis are presented. In this case the tolerance analysis includes the effect of the fabrication error of the hologram pattern on the field in the quiet-zone. Also, the effect of the displacement of the different parts of the hologram when the hologram is joined together from two pieces is analyzed. The analysis is based on an exact near-field aperture integration method.

A HOLOGRAM CATR

A hologram is an interference pattern of two wave fronts. One of the interfering wave fronts can be recreated by illuminating the hologram with the other one of the original fields. The idea of a hologram CATR is described in reference [1]. Figure 1 shows the principle of the hologram CATR. The feed horn transmits a spherical wave, which is transformed into a plane wave with a planar, computer generated amplitude hologram structure. The antenna under test (AUT) is illuminated with this plane wave. The area where the plane wave meets its requirements is called the quiet-zone and it has to be larger than the antenna under test. The quality of the quiet-zone is characterized by the amplitude and phase ripple, amplitude and phase taper, crosspolarization level, spurious reflections and multiple reflections in the area [2]. In this paper, the amplitude and phase ripple as well as the amplitude and phase taper are considered.

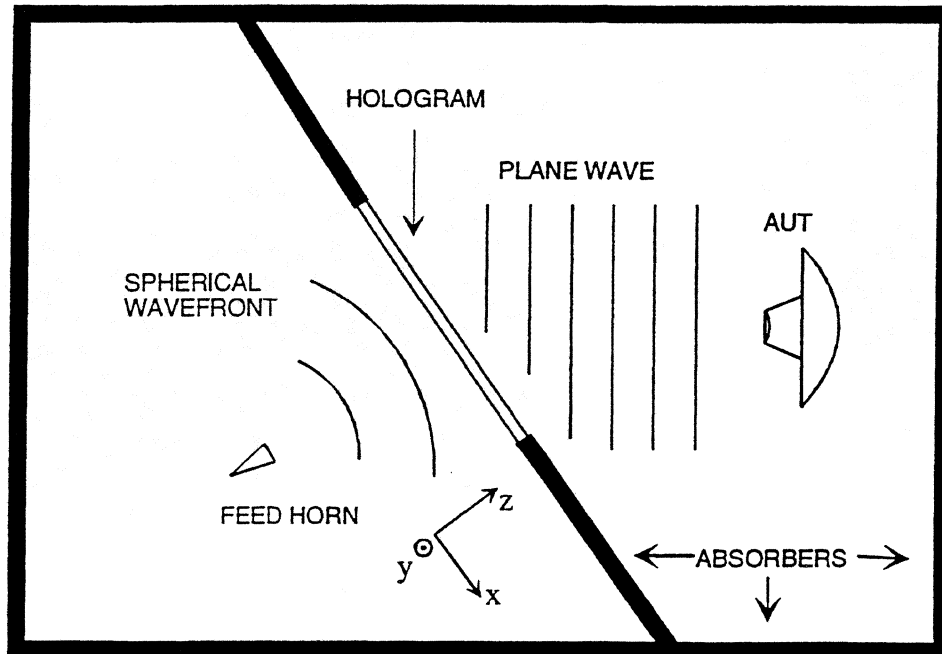


Figure 1. A hologram type of a compact antenna test range.

FABRICATION OF THE HOLOGRAM

In many practical applications holograms are synthesized by computational methods (computer generated hologram, CGH). The hologram pattern is determined by calculating numerically the structure required to change the known input field (feed horn) into the desired output field. Due to fabrication limitations, the structure of the hologram has to be quantized in some way. This is called the coding scheme of the CGH. The two most widely used schemes are the binary phase and the binary amplitude quantizations, in which either the phase or amplitude transmittance (or reflectance) of the hologram is limited to have only two different discrete values. Different coding techniques have been reviewed in reference [3].

The discretized pattern of the hologram is printed on a film with a high precision plotter. This film is used as a mask when the pattern is transferred to a copper plated dielectric sheet covered with a photoresist. Finally, the extra copper is removed with a wet chemical etching process. The manufacturing procedure is similar to that used for making printed circuits. The manufacturing errors which affect the field in the quiet-zone are due to inaccuracies of the plotter, pattern transfer and etching. In this case the inaccuracy of the plotter is about 7 μm . The inaccuracy of the pattern transfer is 5–10 μm with collimated light and 50–100 μm with uncollimated light. Usually the thickness of the copper layer is a good estimation for the inaccuracy of the etching process. A dielectric sheet with a 5 μm copper layer is available. Therefore, the achievable inaccuracy of the widths of the slots of the hologram is about 40–200 μm depending on the pattern transfer.

THEORETICAL ANALYSIS OF A HOLOGRAM CATR

The transmittance of an amplitude hologram is [3,4]

$$T(x', y') = \frac{1}{2} [1 + a(x', y') \cos \Psi(x', y')], \quad (1)$$

where $a(x', y')$ is the relation between the output and input amplitudes so that the hologram compensates the amplitude variation of the input field and adds a cosine amplitude taper to the amplitude of the output field. The phase term is $\Psi(x', y') = \varphi(x', y') + 2\pi\nu x'$, where ν denotes the spatial carrier frequency, which separates the diffraction orders produced by this hologram. The desired output field leaves the hologram in an angle of

$$\theta = \arcsin(\nu\lambda). \quad (2)$$

The normalized phase of the input field (feed horn) in the plane of the hologram is $\varphi(x, y)$. The coordinates in the plane of the hologram are x' and y' . The transmittance of the corresponding binary-amplitude coded hologram is given by the formula

$$T_B(x', y') = \begin{cases} 0, & 0 \leq \frac{1}{2}[1 + \cos \Psi(x', y')] \leq b, \\ 1, & b \leq \frac{1}{2}[1 + \cos \Psi(x', y')] \leq 1, \end{cases} \quad (3)$$

where $b = 1 - (1/\pi) \arcsin a(x', y')$. In this case, the desired output field is a plane wave with a cosine amplitude taper and the plane wave is designed to leave the hologram in an angle of 33° . In binary-amplitude coding, the phase is stored in the locations of the slots and the amplitude information is recorded in the variations of slot widths. The main effect of the binarization is the redistribution of energy between the various diffraction orders of the hologram [5]. Figure 2 shows an example of a binary amplitude hologram.

The field in the quiet-zone is calculated by using an exact near-field aperture integration (physical optics). The formula for the quiet-zone field is [6,7]

$$\mathbf{E}(x, y, z) = \iint_S E_a \frac{1 + jkR}{2\pi R^3} e^{-jkR} [\mathbf{u}_y(z - z') - \mathbf{u}_z(y - y')] dS', \quad (4)$$

where $R = \sqrt{(x - x')^2 + (y - y')^2 + (z - z')^2}$ is the distance from a point in the aperture (hologram) to a point in the quiet-zone. In this case, the aperture field is $E_a(x', y') = T_B(x', y')E_{\text{feed}}(x', y')$, where $E_{\text{feed}}(x', y')$ is the complex field of the feed horn in the plane of the hologram. In this analysis, the aperture field is assumed to be linearly polarised in \mathbf{u}_y -direction. However, the polarization effects of a hologram structure are not included in these analyses, i.e., the incoming wave is only modulated by a scalar T_B function.

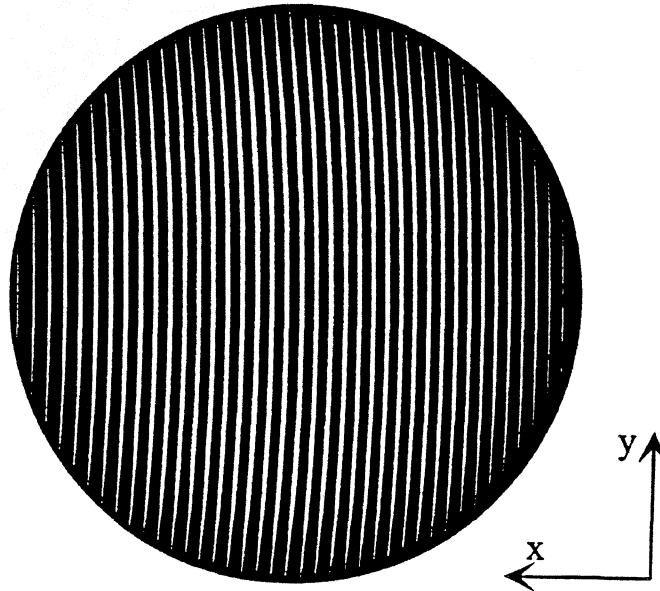


Figure 2. An example of a binary amplitude hologram.

RESULTS

In order to keep the simulation time reasonable, the diameter of the hologram in these analyses was 200 mm at 500 GHz. Cray X-MP EA/464 and Silicon Graphics Onyx were used in the analyses. The grid spacing in the numerical integration was $20 \mu\text{m}$ ($\approx \lambda / 30$), which was found to be small enough. All the results in this paper have been calculated for the angle of 33° and the distance of 500 mm from the center of the hologram. Also, the results that are shown here are calculated in the xz -plane in the quiet-zone so that the u_z -component of the electric field is zero because of the symmetry.

The widths of the slots of the hologram depend on the frequency, the distance of the feed horn from the hologram and the function $a(x', y')$. In this case the widths of the slots vary between 5 and $365 \mu\text{m}$ (or actually between 20 and $360 \mu\text{m}$ because of the grid spacing in the calculation). Naturally, in this case the $5 \mu\text{m}$ slot can not be fabricated. The effect of the fabrication error was simulated by changing the widths of the slots of the hologram in steps of $40 \mu\text{m}$. Figure 3 shows the ideal situation and situation where the slots are $120 \mu\text{m}$ wider than in the ideal case. The amplitude and phase ripple inside the quiet-zone is 0.3 dB and 1.3° in the ideal case and 0.7 dB and 3.0° with the $120 \mu\text{m}$ wider slots. Table 1 shows the resulting amplitude and phase ripple in the quiet-zone. In the figures and tables the quiet-zone is the area $\rho \leq 50 \text{ mm}$.

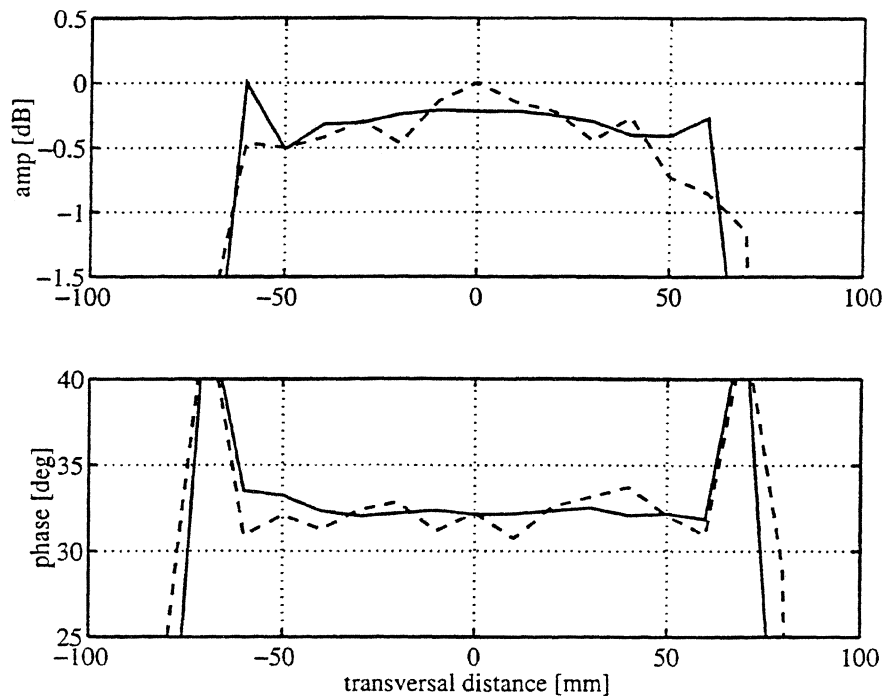


Figure 3. The amplitude and phase ripple in the quiet-zone: ideal case (solid line), slots are $120 \mu\text{m}$ larger than in ideal case (dashed line).

Table 1. The amplitude and phase ripple in the quiet-zone, when the widths of the slots (w) are changed.

Δw [μm]	amplitude ripple [dB]	phase ripple [deg]
-80	0.35	2.0
-40	0.25	2.0
0	0.30	1.3
40	0.40	1.0
80	0.55	2.0
120	0.70	3.0
160	1.0	4.0
200	1.3	5.0

The hologram which will be used in the testing of the Odin antenna will have to be fabricated by joining several pieces together. The displacement of the pieces has an effect on the field in the quiet-zone. This is simulated here by cutting the hologram from the middle into two pieces and displacing the parts 60, 100, 140 and 180 μm from each other. The cut is in the x -direction as shown in Figure 4. The effect of the displacement (d) is the inclination of amplitude and phase in quiet-zone in xz -plane. In y -direction there is no effects in the quiet-zone field. Figure 5 shows the worst case which was calculated (180 μm displacement) compared to the ideal case. The results are presented in Table 2.

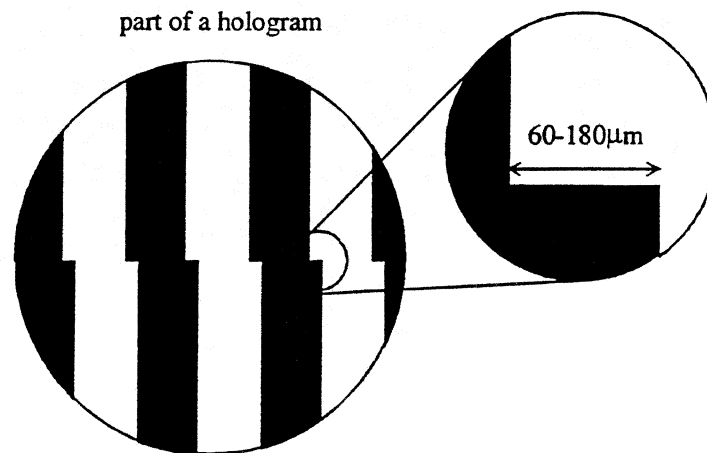


Figure 4. The displacement of the two different parts of the hologram.

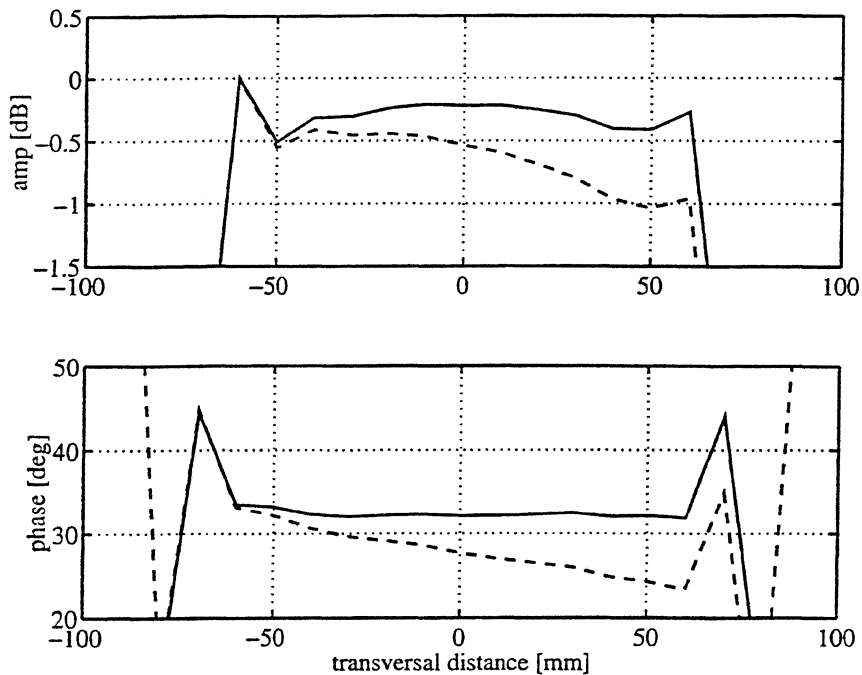


Figure 5. The amplitude and phase inclination in the quiet-zone caused by the displacement ($d = 180 \mu\text{m}$) of the different parts of the hologram (dashed line). Solid line shows the situation without any displacement.

Table 2. The amplitude and phase inclination in the quiet-zone caused by the displacement (d) of the different parts of the hologram.

d [μm]	amplitude inclination [dB]	phase inclination [deg]
0	0	0
60	0.05	4
100	0.2	5
140	0.4	6.5
180	0.6	8

Unavoidably, a hologram is a frequency dependent component, because the locations of the slots is determined by the phase of the incoming field. This was simulated by coding the hologram at 500 GHz and then calculating the field in the quiet-zone at different frequencies. The effect of the frequency change is the inclination of the phase front in xz -plane of the output field of the hologram. Figure 6 shows the situation when the frequency is changed from 500 GHz to 501 GHz. In Figure 6 the amplitude is almost unchanged and the phase changes 77° in the quiet-zone area, which means that instead of 33° the plane wave leaves the hologram in an angle of 32.93° . The angle can be calculated by using Equation (2). Similar results were obtained at 502 and 510 GHz. Only difference was the that the direction of the plane wave deviated more from 33° . The useful bandwidth of a hologram is case-specific, i.e.,

it depends on the actual center frequency and hologram size compared to the distance from the feed horn to the hologram. Logically, the field in y -direction is not affected by the frequency change.

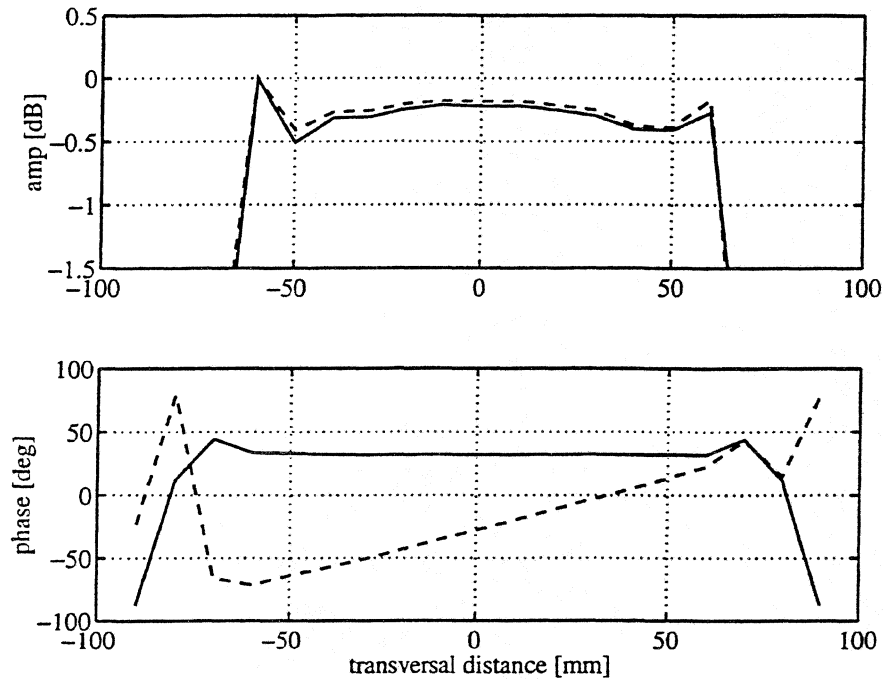


Figure 6. The field in the quiet-zone at frequencies 500 GHz (solid line) and 501 GHz (dashed line), when the hologram is coded at 500 GHz.

Main focus of this paper is on the hologram pattern errors parallel to the surface of the hologram. Obviously the quality of the quiet-zone is also effected by the flatness errors of the hologram, i.e. errors perpendicular to the surface of the hologram. The main advantage of an amplitude hologram is that inherently the surface errors of this structure have much less effect than those of a reflector. Figure 7 schematically enlightens this situation. The lower part of the figure, a hologram with surface error, shows that distances r_1 and r_2 have become shorter, but the shortening of these electrical lengths is partly compensated, because the incoming wave travels a longer way on the other side. Furthermore, because this is a transmission type of focusing element, we can have twice the surface error compared to the reflector. Due to this reasoning the planarity error is not assumed to be the main problem, but it will be studied more carefully during the project.

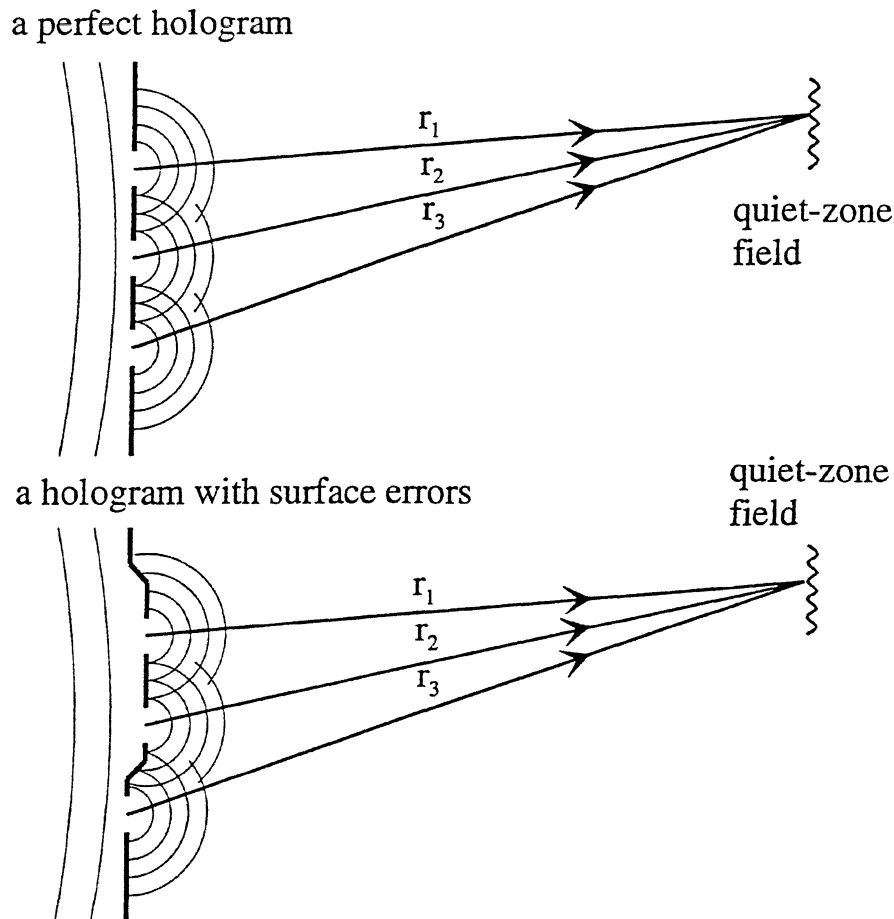


Figure 7. A side view of a perfect hologram and a hologram with surface errors.

CONCLUSIONS

A hologram CATR is a new method for testing antennas at millimeter- and submillimeter wavelengths. According to the simulations carried out here for an ideal hologram it is possible to achieve a field in the quiet-zone which has a tolerable amplitude and phase ripple: 0.3 dB and 1.3 degrees. Due to fabrication errors the slots of the hologram are wider or narrower than in the ideal case, which increases the amplitude and phase ripple in the quiet-zone. However, with reasonable values of fabrication error the quality of the quiet-zone is not degraded decisively (Table 1). The effect of the displacement of the different parts of the hologram is the inclination of amplitude and phase in quiet-zone (Table 2). In the latter case the undesirable feature is the amplitude inclination, because together with the amplitude ripple caused by the fabrication error, the quality of the quiet-zone may degrade too much. The phase inclination caused by the displacement of the different parts of the hologram or a change in frequency is not a problem, because it only means that the plane wave leaves the hologram in a different angle than in the ideal case.

ACKNOWLEDGEMENTS

The authors would like to thank Mr. Jyrki Louhi and Mr. Timo Haiko for useful discussions during this work.

REFERENCES

- [1] Tuovinen, J., Vasara, A., Räisänen, A.: A new type of compact antenna test range. *Proceedings of the 22nd European Microwave Conference*, Espoo, 1992, pp. 503–508.
- [2] Aurinsalo, J., Karhu, S., Koivumäki, A., Pitkäaho, R., Lehto, A., Räisänen, A., Tolmunen, T., Tuovinen, J.: Test methods and ranges for testing the millimeter wave sounder of the Meteosat second generation satellites. Final report, ESTEC contract no. 7966/88/NL/PB(SC), March 1990.
- [3] Lee, W-H.: Computer-generated holograms: techniques and applications. In *Progress in Optics XVI*, Wolf, E., ed., North-Holland, 1978, pp. 119–232.
- [4] Burch, J., J.: A computer algorithm for the synthesis of spatial frequency filters. *Proceedings of the IEEE*, Vol. 55, 1967, pp. 599–601.
- [5] Vasara, A., Turunen, J., Friberg, A., T.: Realization of general nondiffracting beams with computer-generated holograms. *Journal of Optical Society of America A*, Vol. 6, 1989, pp. 1748–1754.
- [6] Kong, J., A.: *Electromagnetic Wave Theory*, John Wiley & Sons, New York, 1986, 696 p.
- [7] Hirvonen, T., Tuovinen, J., Räisänen, A.: Lens-type compact antenna test range at mm-waves. *Proceedings of the 21st European Microwave Conference*, Stuttgart, 1991, pp. 1079–1083.

Off-Axis Beam Patterns of Extended-Hemispherical Dielectric Lens Antennas: Theory and Experiment at 250 GHz

Gildas Gauthier, Daniel Filipovic, Sanjay Raman, and Gabriel M. Rebeiz

**NASA Center for Space Terahertz Technology
University of Michigan
Ann Arbor, MI 48109-2122**

We report on extensive beam-pattern measurements at 250 GHz of an 11-element array of double-slot antennas placed on an extended hemispherical dielectric lens antenna. The measurements are made for linear arrays spaced in both the E-plane and H-plane directions. The measurements are also done for different extension lengths and for different lens diameters. The measurements are compared to a ray-optics based theory. Antenna gains and Gaussian-coupling efficiencies for different off-axis positions will be measured or extracted from measured patterns. We will finish by showing simple design rules applicable to imaging arrays in extended-hemispherical dielectric-lens antennas.

Effect of voltage modulation on the shape of the depletion layer of a submillimeter wave Schottky varactor

Jyrki T. Louhi and Antti V. Räisänen

Helsinki University of Technology, Radio Laboratory,
Otakaari 5 A, FIN-02150 Espoo, Finland

Abstract

Schottky varactor frequency multipliers are used to generate local oscillator power at millimeter and submillimeter wavelengths. Multiplication efficiency depends on varactor parameters such as capacitance–voltage characteristic and possible current saturation. The aim of this work is to develop the equivalent circuit of the submillimeter wave Schottky varactor in order to model the effect of fast voltage modulation on the three-dimensional shape of the depletion layer. The effect of voltage modulation can be studied by solving the potential and electron conduction currents in the epitaxial layer of the Schottky varactor. In this work the potential and the electron currents have been calculated from device physics by using numerical methods. According to our results the shape of the depletion layer is strongly affected, when the voltage modulation over the pumped varactor is rapid. The dynamic shape of the depletion layer during the voltage sweep affects the junction capacitance as well as the electron velocity saturation. These effects should be included to the equivalent circuit of the Schottky varactor. This can be done by modifying the model obtained by using static equations.

1 Introduction

Frequency multipliers are used to generate the all-solid-state local oscillator power of heterodyne receivers at millimeter and submillimeter wavelengths [1]. These local oscillators are needed in many future scientific satellites (e.g. SWAS, Odin, FIRST and SMIM). At millimeter and submillimeter wavelengths a Schottky varactor is the most commonly used multiplier device, although several novel varactors (SBV, QWD, BNN, bbBNN, HEMV) have been proposed [2].

The aim of this work is to develop the equivalent circuit of the Schottky varactor in order to find a model, which is physically valid at millimeter and submillimeter wavelengths. The most important task is to analyse the shape of the depletion layer during the voltage sweep, when the submillimeter wave frequency multipliers are pumped rapidly. This voltage modulation affects the three-dimensional shape of the transition front so that during a voltage sweep the shape of the front differs from the shape obtained using static solution. This has an effect on the junction capacitance of the Schottky varactor, which means that the correction factor due to the edge effects must be modified compared to the value obtained by using a static solution.

2 Formulation of the problem

A circular metallic anode is assumed to be at the top of the epitaxial semiconductor (GaAs), as shown in Figure 1. The radius of the anode is R_0 and the thickness of the epitaxial layer is t_e . The approximate shape of the depletion layer is shown in Figure 1, when the anode is charged to a static potential $\phi_0 = V - \phi_{bi}$.

At the static situation the electric equilibrium is reached and no currents are flowing in the epitaxial layer. When the potential of the anode is increased (or decreased), the potential of the epitaxial layer has to change, which means that currents*begin to flow

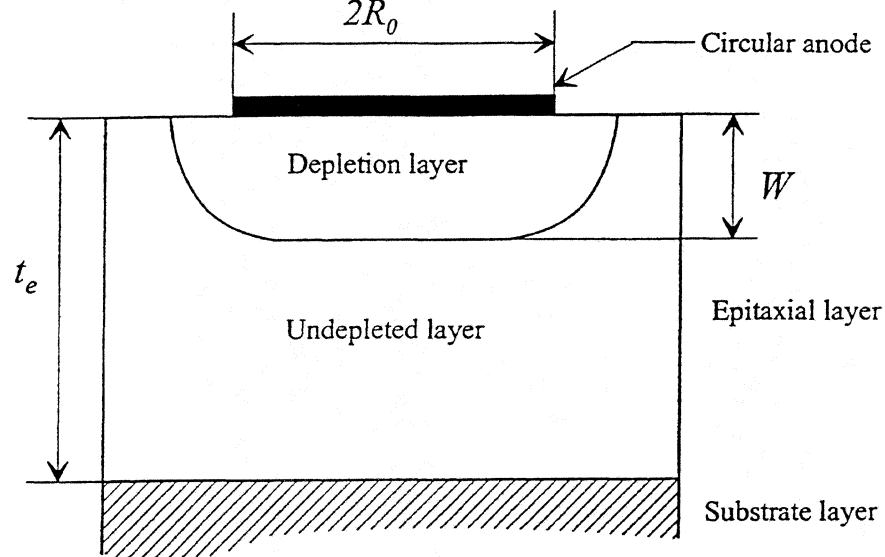


Figure 1: Schematic of the Schottky varactor.

in the undepleted layer. The currents move the transition front between the depleted and undepleted layers. If the potential of the anode is increased very slowly, the shape of the transition front during the transient is equal to the front obtained using the static solution. However, if the potential is increased fast enough, the shape of the transition front is affected by the electron velocity saturation as well as by the edge effects due to the circular anode. The shape of the transition front during the voltage modulation can be determined by using the device equations (Poisson's equation, current continuity equation, etc.) and boundary conditions (potential of anode, potential of substrate, radius of anode, etc.). This two-dimensional problem (actually the problem is three-dimensional but cylindrically symmetric) is non-trivial and the effect of the modulation on the shape of the transition front must be studied by using numerical methods.

Because the problem is very complicated, the following assumptions have been made.

1. Because the conductivity of the substrate is much greater than the conductivity of the epitaxial layer, the substrate layer is assumed to be a perfect conductor and, therefore, the potential of the substrate layer is zero.
2. Because the permittivity of GaAs is greater than the permittivity of air, the normal component of the electric field is assumed to be zero in the air-GaAs interface.

3. Because the Debye length L_D in the epitaxial layer is small, the transition front between the depleted and undepleted layer can be assumed to be abrupt.
4. The radius of the epitaxial layer is assumed to be four times the radius of the anode. This decreases the time required in numerical analyses compared to the case, when the real radius of the epitaxial layer is employed. This assumption can be made because the potential strongly decreases, when the distance from the axis of the cylindrical epitaxial layer increases. The potential is negligible at the distance of 2-3 times R_0 away from the axis.

These four assumptions must be traded against the decreased complexity of the problem as well as the the decreased time required in the numerical simulations.

3 Device equations

3.1 Poisson's equation

The potential ϕ in the epitaxial layer can be found by using the Poisson's equation [3]

$$\nabla^2 \phi = -\frac{\rho}{\epsilon}, \quad (1)$$

where ρ is the net volume charge and ϵ is the permittivity. The electric field is

$$\vec{\mathcal{E}} = -\nabla \phi \quad (2)$$

and the net volume charge is

$$\rho = q(N_D - n), \quad (3)$$

where the q is the charge of the electron and N_D is the doping density. The density of free electrons is

$$n = n_i e^{(E_F - E_i)/kT}, \quad (4)$$

where n_i is the intrinsic electron density, E_F is the Fermi energy level, E_i is the intrinsic Fermi level. k is Boltzmann's constant and T is the temperature. In the undepleted layer

the density of free electrons is equal to N_D and therefore the net volume charge is zero. In the totally depleted layer the density of free electrons is zero and the net charge per unit volume is equal to qN_D . In a static situation (no currents flow in the undepleted layer) the net volume charge depends on the potential as

$$\rho = qN_D(1 - e^{q\phi/kT}). \quad (5)$$

3.2 Current density

The electron current density is the sum of the drift and diffusion components [4, 5]

$$\vec{J}_n = q\mu(\mathcal{E})n\vec{\mathcal{E}} + qD_n\nabla n, \quad (6)$$

where $\mu(\mathcal{E})$ is the electron mobility and the diffusivity D_n is given by the Einstein relation

$$D_n = \frac{kT}{q}\mu(\mathcal{E}). \quad (7)$$

In the depleted layer the density of free electrons is zero and therefore the electron current is also zero. In the undepleted layer the density of free electrons is constant N_D and, therefore, the electron current is

$$\vec{J}_n = q\mu(\mathcal{E})N_D\vec{\mathcal{E}}. \quad (8)$$

Because in the simulation program the transition front is assumed to be abrupt, the diffusion current is always zero. In reality, the diffusion current affects the density of free electrons near the transition front. However, the diffusion current does not affect the conduction current in the epitaxial layer and therefore the diffusion current can be neglected.

As the continuity equation for the electron current is

$$\nabla \cdot \vec{J}_n - q\frac{\partial n}{\partial t} = 0, \quad (9)$$

the velocity of the transition front can be derived to be

$$\vec{v} = -\mu(\mathcal{E})\vec{\mathcal{E}}. \quad (10)$$

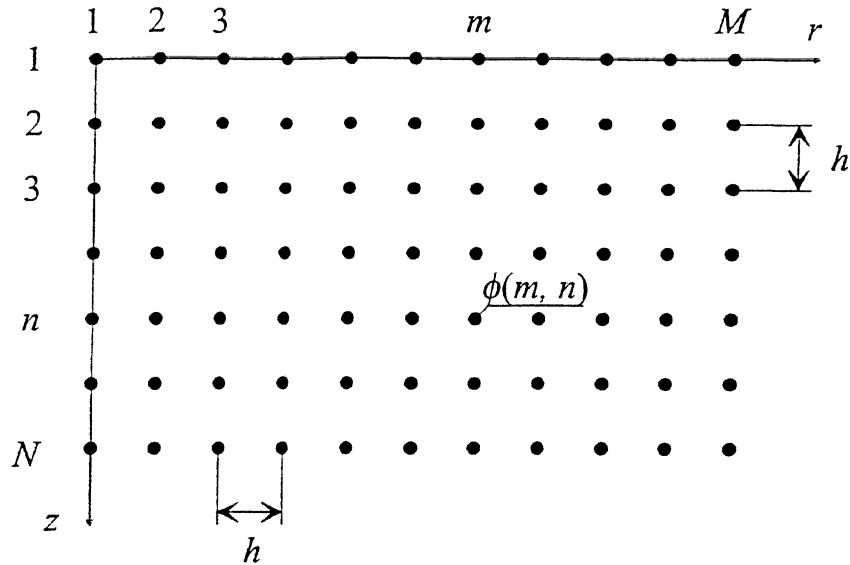


Figure 2: Mesh used in simulations.

4 Numerical method

4.1 Algorithm

Because the problem can not be solved by using analytical methods, the effect of the voltage modulation on the shape of the transition front has been studied by using a numerical method. The Poisson's equation has been solved numerically by using the finite difference method, where the epitaxial layer is divided into a dense mesh of size $M \times N$ as shown in Figure 2. The potential of each mesh point $\phi(m, n)$ is determined by using discrete Poisson's equation and iterative over-relaxation method [6, 7].

The transition front between the depleted and undepleted layers has been modelled by using discrete corner points as shown in Figure 4. The corner points are moved according to the electric field, which is calculated from the potential by using numerical version of equation (2). The net volume charge of each mesh point is determined according to the information of the corner points. If the mesh point is inside the transition front (depleted layer) the net volume charge is N_D and otherwise (undepleted layer) the

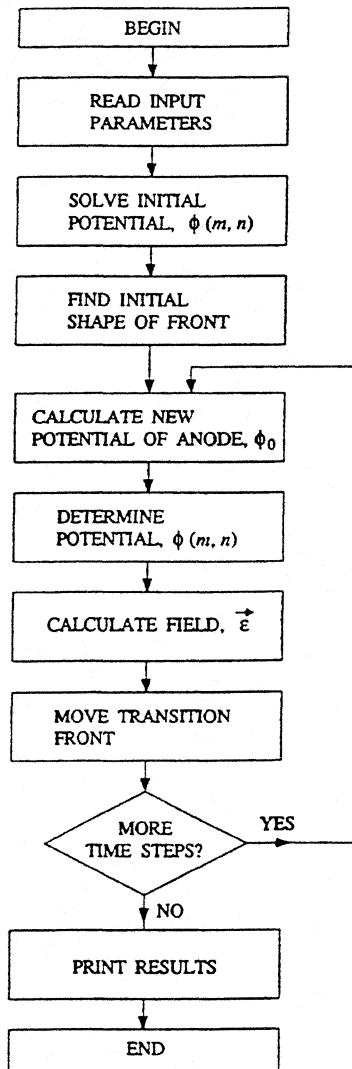


Figure 3: The computer algorithm.

charge is zero at the mesh point.

The computer algorithm of the simulation program is shown in Figure 3. At the beginning of the simulation the potential of the epitaxial layer is determined by using the numerical version of equations (1) and (5) and by using the input parameters (N_D , ϵ_r , R_0 , t_e , etc.) [6, 7]. Then the initial shape of the transition front is determined from this numerically solved potential. The discrete corner points of the transition front are placed smoothly over the transition front so that the vertical (or horizontal) spacing between corner points is equal to the spacing of the initial mesh as shown in Figure 4.

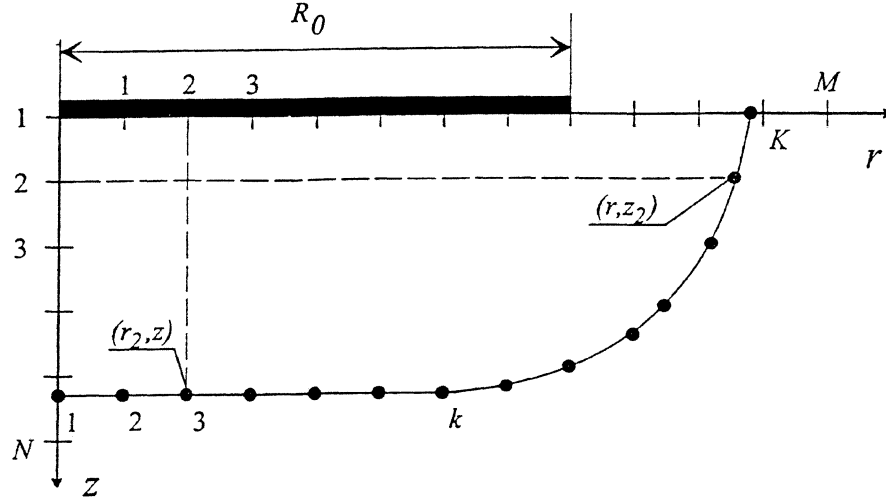


Figure 4: Corner points of the transition front.

At the beginning of each time step, the potential of the anode is determined according to the input parameters of the program. Then the net volume charge of each mesh points is determined from the shape of the transition front (charge is zero in the undepleted layer and equal to qN_D in the depleted layer). After that the potential of each mesh point is calculated numerically by using the iterative over-relaxation method. When the potential is known the electric field is found by using a numerical version of equation (2). Finally the corner points of the transition front are moved according to the electric field. The movement of the corner point is given by

$$\Delta s = -\mu(\mathcal{E}_n)\mathcal{E}_n\Delta t, \quad (11)$$

where Δt is the time step and \mathcal{E}_n is the normal component of the electric field at the corner point.

4.2 Junction capacitance

By using static equations, the junction capacitance of millimeter wave Schottky varactor is given by [7]

$$C_j = \frac{\epsilon A}{W} \gamma_C, \quad (12)$$

where A is the area of anode, W is width of depletion layer and the net correction factor compared to the simple plate capacitance is given by

$$\gamma_C = \left(1 + 1.5 \frac{W}{R_0} + 0.3 \frac{W^2}{R_0^2} \right), \quad (13)$$

where R_0 is the radius of anode.

Because the shape of the depletion layer during a voltage modulation differs from that obtained by using the static equations, the junction capacitance during a transient must be determined by using the net charge of the depletion layer. The net charge can be calculated by using information of the corner points and it is given by the numerical equation

$$Q_{tot} = qN_D \sum_{k=2}^K 2\pi \frac{r_k + r_{k-1}}{2} \frac{z_k + z_{k-1}}{2} (r_k - r_{k-1}), \quad (14)$$

where r_k and z_k are the coordinates of the corner point k . The junction capacitance at the time step t is given by

$$C_j = \frac{\Delta Q}{\Delta V_j} = \frac{Q_{t+1} - Q_{t-1}}{V_{t+1} - V_{t-1}}, \quad (15)$$

where Q_t is the net charge of the depletion layer at the time step t and V_t is the voltage over the depletion layer.

5 Results

The simulation program can be used to analyse any millimeter or submillimeter wave Schottky varactor. Because the time required to analyse the varactor during a single pump cycle is very long (about 10 h), the program can not be integrated to the harmonic balance method. For that reason we have analysed the varactor during a linear voltage sweep, which is a good approximation for the modulation of the anode voltage, when the charge of the depletion layer is loaded or unloaded during the pump cycle [8]. The results have been used to develop the equivalent circuit, which can be employed in the harmonic balance method.

5.1 Shape of the transition front

Because the effect of the voltage modulation depends on the parameters of the varactor as well as on the frequencies and power levels of the multiplier, the actual shape of the depletion front must be analysed separately for each case. As an example we have analysed a very small area Schottky varactor, whose parameters are given in Table 1. The thickness of the epitaxial layer has been optimized for 1 THz operation so that the epitaxial layer is just depleted during the pump cycle [9]. At the beginning of the simulated voltage sweep the applied voltage V is slightly smaller than the contact potential ϕ_{bi} , so that the epitaxial layer is almost totally undepleted. During the simulation the potential of the anode has been decreased by 5 mV/fs. The total time of the voltage sweep is 0.5 ps, which is half of the cycle at the output frequency. This kind of a voltage sweep simulates the situation, where the varactor is pumped with large input power.

Table 1: Parameters of the 1 THz range Schottky varactor.

Radius of the anode	R_0	0.7	μm
Thickness of the epitaxial layer	t_e	0.2	μm
Doping density	N_D	$1.0 \cdot 10^{17}$	cm^{-3}
Series resistance	R_s	12	Ω
Junction capacitance at zero bias	C_0	1.8	fF

The transition front between the depleted and undepleted layer is shown in Figure 5, where time difference between two fronts is 50 fs. At the beginning of the voltage sweep the epitaxial layer is almost totally undepleted and the shape of the transition front is equal to the shape which can be obtained by static equations. When the currents begin to flow in the epitaxial layer, the volume of the depleted layer increases. Because the potential of the anode is decreased very fast, the electric field in the epitaxial layer is high and so the transition front moves with the maximum velocity of electrons.

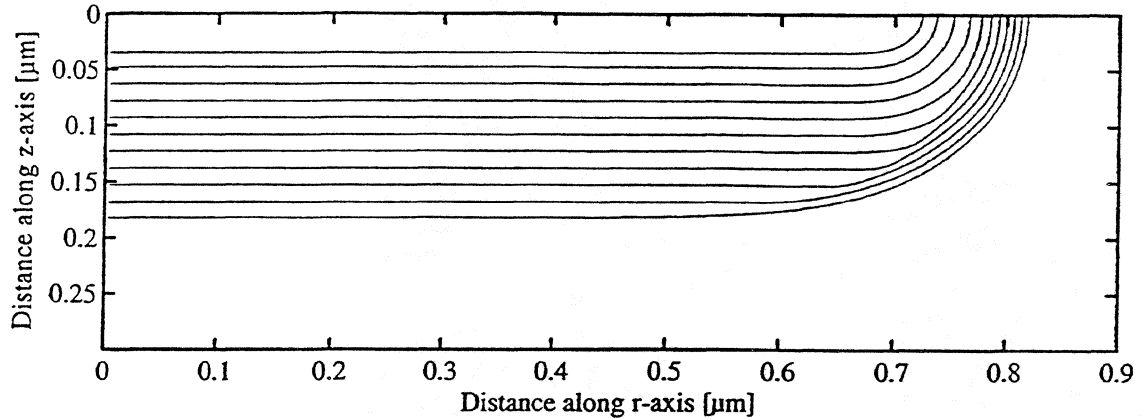


Figure 5: Example of the shape of the transition front during a voltage ramp.

The electric field is extremely high near the edge of the anode, which means that the transition front moves there with the maximum, saturated velocity of electrons. So, the shape of the transition front is almost equal to the shape of a quarter of a circle as shown in Figure 5. This means that the volume of the depletion layer increases faster than can be assumed by using static equations. At the end of the voltage sweep the velocity of the transition front near the center of the anode is still equal to the maximum velocity of electrons. However, near the edge of the anode the velocity of the transition front decreases, because the electric field decreases, as the distance from the edge of the anode increases. This means that at the end of the the sweep the increase of the net charge is slower than can be assumed by using static equations.

5.2 Equivalent circuit

The calculated capacitance of the $R_0 = 0.7 \mu\text{m}$ varactor during a 1 THz voltage sweep is shown in Figure 6. At the beginning of the voltage sweep (applied voltage is almost equal to ϕ_{bi}) the numerically obtained junction capacitance is larger than the static capacitance, because the net volume of the depletion layer increases faster than can be assumed by using static equations. At the end of the voltage sweep (epitaxial layer is almost totally depleted and $V \approx -1.5$) the net volume charge increases slowly and

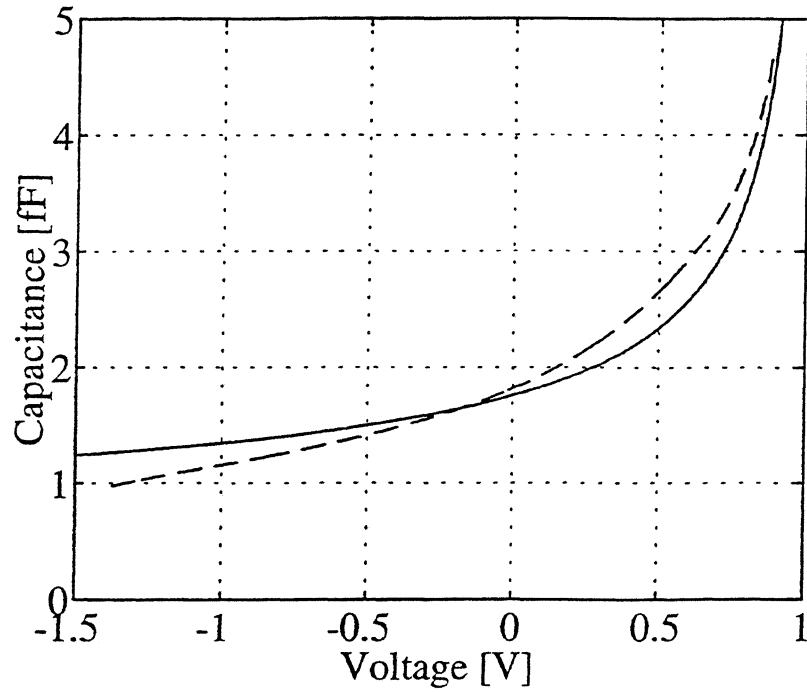


Figure 6: The capacitance of the varactor. Solid line is obtained with static equations and dashed line with a numerical solution using a 1 THz sweep starting from $V = \phi_{bi}$.

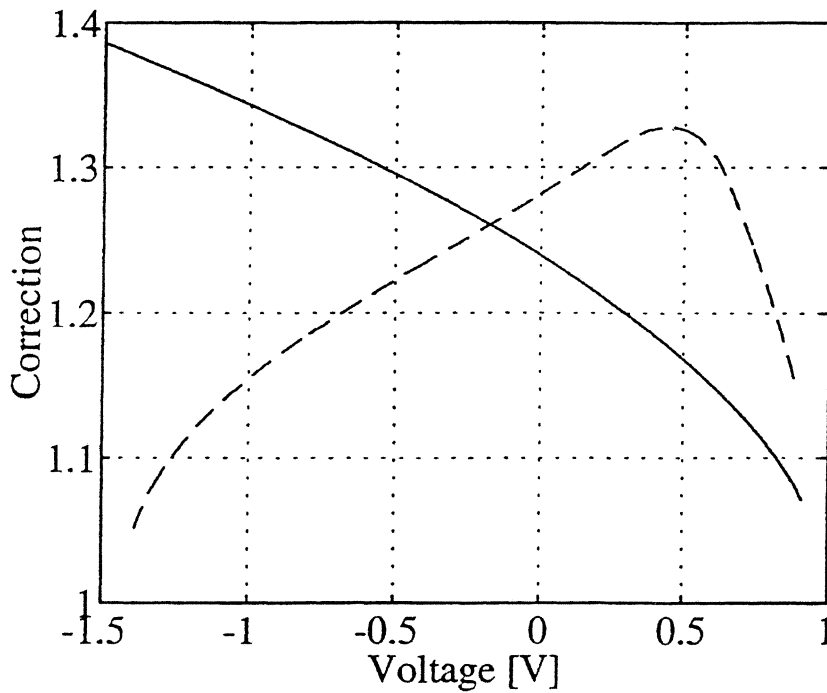


Figure 7: The correction factor γ_C of the varactor. Solid line is obtained with static equations and dashed line with a numerical solution.

thus the numerically obtained capacitance is smaller than the static capacitance. This means that during a fast voltage modulation the C_{max}/C_{min} -ratio is larger than can be assumed by static equation.

At submillimeter wavelengths the maximum output power of the Schottky varactor frequency multiplier is strongly affected by the electron velocity saturation [10]. The saturation effect can be included in the model of the varactor by limiting the electron conduction current to the value of the maximum current [9]

$$i_{max} = AN_D q v_m \gamma_C, \quad (16)$$

where v_m is the maximum velocity of electrons. The net correction factor γ_C can be calculated from the numerically obtained capacitance by using equation (12). As shown in Figure 7, at the beginning of the voltage sweep the numerically obtained correction factor is larger than the static value. However, at the end of the voltage sweep the numerically obtained correction factor is small. This means that at the beginning of the voltage sweep the electron conduction current may be much larger than can be assumed by using static equations. This helps to pump the varactor more effectively.

5.3 Doubler for 1 THz

As an example we have simulated a doubler for 1 THz. At small input power levels the effect of voltage modulation is small and thus the capacitance-voltage characteristic derived using static equations can be used. However, when the input power increases, the effect of voltage modulation increases and the numerically obtained capacitance characteristic should be used. According to our results the theoretical output power without circuit losses at 1 THz is about 200 μ W, when a doubler is pumped with 2.0 mW input power at 500 GHz. This is 1.5 dB higher than the simulated output power obtained by using the static equations. However, the output power is still much smaller than the power obtained, if the electron velocity saturation is omitted.

Above we have used a very small area Schottky varactor ($R_0 = 0.7\mu\text{m}$), in which case the edge effects are shown clearly. If the area of the varactor is larger than assumed above, the edge effects are smaller. This means that the effect of voltage modulation is not as large as above. Therefore, in the case of large area Schottky varactor the static equations can be employed.

6 Conclusions

The shape of the transition front between the depleted and undepleted layer in a small area Schottky varactor is strongly affected by the fast voltage modulation during the pump cycle of a submillimeter wave frequency multiplier. The effect can be studied by numerically solving the device equations. According to our results the C_{max}/C_{min} -ratio of the junction capacitance is larger than can be assumed by static equations. In addition, the electron conduction current is larger than derived from static equations, which helps to pump the Schottky varactor more effectively at THz range. These two effects together result in simulations in higher output powers than those obtained with static equations including the electron velocity saturation.

Acknowledgements

This work was financially supported in part by Academy of Finland and European Space Agency. The author would like to thank Professor Juha Sinkkonen and Dr. Tapani Närhi for useful discussions.

References

- [1] A.V. Räisänen, "Frequency multipliers for millimeter and submillimeter wavelengths," *Proceedings of the IEEE*, vol. 80, no. 11, pp. 1842-1852, 1992.
- [2] M.A. Frerking and J.R. East, "Novel heterojunction varactors," *Proceedings of the IEEE*, vol. 80, no. 11, pp. 1853-1860, 1992.
- [3] S.M. Sze, *Physics of Semiconductor Devices*, New York, Wiley, 1981.
- [4] T. Adachi, A. Yoshii and T. Sudo, "Two-dimensional semiconductor analysis using finite element method", *IEEE Transactions on Electron Devices*, vol. ED-26, no. 7, pp. 1026-1031, 1979.
- [5] H. Hjelmgren, "Numerical modeling of hot electrons in n-GaAs Schottky-barrier diodes", *IEEE Transactions on Electron Devices*, vol. 37, no. 5, pp. 1228-1234, 1990.
- [6] E. Wasserstrom and J. McKenna, "The potential due to a charged metallic strip on a semiconductor surface," *The Bell System Technical Journal*, May-June, pp. 853-877, 1970.
- [7] J.T. Louhi, "The capacitance of a small circular Schottky diode for submillimeter wavelengths," *IEEE Microwave and Guided Wave Letters*, vol. 4, no. 4, pp. 107-108, 1994.
- [8] J.T. Louhi and A.V. Räisänen, "Cooled Cascaded Frequency Multipliers at 1 THz," *Proceedings of the 22nd European Microwave Conference*, Espoo, 1992, pp. 597-602.
- [9] J.T. Louhi and A.V. Räisänen, "On the modelling and optimization of Schottky varactor frequency multipliers at submillimeter wavelengths," *IEEE Transactions on Microwave Theory and Techniques*, vol. 43, no. 4, 1995.
- [10] E.L. Kollberg, T.J. Tolmunen, M.A. Frerking and J.R. East, "Current saturation in submillimeter wave varactors," *IEEE Transactions on Microwave Theory and Techniques*, vol. 40, no. 5, pp. 831-838, 1992.

SELF-CONSISTENT PHYSICS-BASED NUMERICAL DEVICE/HARMONIC-BALANCE CIRCUIT ANALYSIS OF HETEROSTRUCTURE BARRIER AND SCHOTTKY BARRIER VARACTORS INCLUDING THERMAL EFFECTS

J. R. Jones, S. H. Jones, and G. B. Tait[†]

Department of Electrical Engineering, University of Virginia, Charlottesville, VA 22903

[†]Department of Electrical Engineering and Computer Science, United States Military Academy, West Point, NY 10996

Abstract

In order to effectively design millimeter and submillimeter wave frequency multipliers, both the electrical and thermal properties of the device and circuit must be analyzed in a fully self-consistent manner. To facilitate a self-consistent analysis of Heterostructure Barrier Varactor (HBV) and Schottky Barrier Varactor (SBV) frequency multipliers, large-signal time- and temperature-dependent numerical device simulators, with excellent computational speed and convergence properties, have been developed for generic GaAs/InGaAs/AlGaAs HBV and conventional GaAs SBV structures having arbitrary doping profiles. The numerical device simulators are based on the first two moments of the Boltzmann transport equation coupled to Poisson's equation, and combine current transport through the device bulk with thermionic and thermionic-field emission currents imposed at the Schottky interface or heterojunction interfaces. Given the importance of both the active device and its embedding circuit in the design of frequency multipliers, the numerical device simulators have been combined with a novel and efficient harmonic-balance circuit analysis technique to provide unified computer-aided design environments for entire HBV or SBV multiplier circuits. The steady-state thermal properties of frequency multipliers are analyzed based on the amount of power dissipated in the active region of the device and the thermal resistance to heat flow presented by the various elements that make up the circuit. From these quantities, the average temperature across the active region of the varactor can be estimated for use in the appropriate device simulator. The thermal model presented here uses simple geometrical expressions for the various thermal resistances of circuits utilizing both planar and whisker-contacted diode geometries assuming the ambient air is a perfect insulator. For planar diodes, the thermal resistance of the diode substrate is calculated using a three-dimensional finite-element heat flow analysis to account for the substrate's irregular heat flow geometry. Using the numerical device/harmonic-balance circuit simulators, an investigation is undertaken to determine the frequencies at which the widely used quasi-static equivalent circuit varactor models fail, and for what reasons these models fail. A comparison is made between published experimental results and a full analysis, including both electrical and thermal properties, of frequency multipliers utilizing the UVA 6P4 GaAs SBV and a single barrier GaAs/Al_{0.7}Ga_{0.3}As HBV.

I. Introduction

In order to effectively design highly nonlinear circuits such as large-signal amplifiers, frequency converters, and oscillators, both the electrical and thermal properties of the active device and its embedding circuit must be analyzed in a fully self-consistent manner. To achieve such a self-consistent analysis, the electrical interaction between the nonlinear active device and its linear

embedding circuit is typically determined using a harmonic-balance circuit analysis technique. The active device is usually modelled analytically by a lumped quasi-static equivalent circuit. The use of such an equivalent circuit model for the active device, however, has limited validity at high device operating frequencies and power levels, requires significant insight into the operation of the active device in order to develop an accurate equivalent circuit topology, and requires a laborious and often non-unique procedure to determine the elements of the equivalent circuit as functions of bias, frequency, and temperature. The validity of such an active device model is particularly suspect at the millimeter and submillimeter wavelengths where the large-signal nonstationary high frequency dynamics of carrier transport begin to dominate device operation. With this in mind, the development of reliable and efficient circuits operating into the terahertz frequency range clearly requires a much more accurate approach to nonlinear circuit analysis and design.

Our approach to the analysis and design of high frequency nonlinear circuits is to utilize a physics-based numerical device model in conjunction with a harmonic-balance circuit analysis technique. This paper details the simulation and analysis of Heterostructure Barrier Varactor (HBV) and Schottky Barrier Varactor (SBV) frequency multipliers using such an analysis and design approach. To facilitate a fully self-consistent analysis of HBV and SBV frequency multipliers, large-signal time- and temperature-dependent numerical device simulators, with excellent computational speed and convergence properties, have been developed for generic GaAs/InGaAs/AlGaAs HBV and conventional SBV structures having arbitrary doping profiles. The numerical device simulators have been combined with a novel and efficient harmonic-balance circuit simulation technique specifically designed to facilitate the inclusion of a numerical device simulator. The combined numerical device/harmonic-balance circuit simulators provide unified computer-aided design environments for entire HBV or SBV frequency multiplier circuits so that such circuits can be co-designed from both a device and a circuit point of view. Such co-design requires the user to specify the device geometry, doping profile, and alloy composition profile, as well as the parasitic device impedances and embedding impedances of the circuit. In conjunction with the combined numerical device/harmonic-balance circuit analysis, the steady-state thermal properties of frequency multipliers are analyzed based on the amount of power dissipated in the active region of the device and the thermal resistance to heat flow presented by the various elements that make up the circuit. From these quantities the average temperature across the active region of the varactor can be estimated for use in the appropriate device simulator.

The remainder of the paper is outlined as follows. The transport equations, interface conditions, and numerical solution approach used in the large-signal time- and temperature-dependent device simulators are presented in Section II. An overview of the novel harmonic-balance circuit analysis technique and its integration with the numerical device simulator is also given in Section II. Section II ends with a discussion of the frequency-dependent parasitic impedances of whisker-contacted HBV and SBV diodes. Section III details the thermal model used to calculate the average active region temperature of whisker-contacted and planar geometry varactor diodes. A comparison between the thermal properties of a standard whisker-contacted varactor diode and an equivalent planar varactor diode is also presented in Section III. Using the harmonic-balance circuit analysis technique coupled to both the numerical device simulators and lumped quasi-static equivalent circuit models derived from the DC results of the numerical device simulators, we examine at what frequencies the widely used quasi-static equivalent circuit models fail and why they fail in Section IV. A comparison is also made in Section IV between published experimental results and a full analysis, including both electrical and thermal properties, of

frequency multiplier circuits utilizing the UVA 6P4 GaAs SBV and a single barrier GaAs/Al_{0.7}Ga_{0.3}As HBV. Finally, conclusions are given in Section V.

II. Numerical Device/Harmonic-Balance Circuit Simulation Approach

A. Physics-Based Numerical Device Simulation Technique

Carrier transport through the bulk region(s) of an HBV or SBV has been described[1-3] by a set of one-dimensional coupled nonlinear differential equations for electrons based on the first two moments of the Boltzmann transport equation and Poisson's equation. The resulting equations governing DC and time-dependent transport are

$$\frac{\partial n(x, t)}{\partial t} = \frac{1}{q} \frac{\partial J_n(x, t)}{\partial x}, \quad (1)$$

$$J_n(x, t) = -q\mu_n(x) n(x, t) \frac{\partial \phi_n(x, t)}{\partial x}, \quad (2)$$

and

$$\frac{\partial}{\partial x} \left[\epsilon(x) \frac{\partial \psi(x, t)}{\partial x} \right] = q [n(x, t) - N_D(x)], \quad (3)$$

where

$$n(x, t) = n_{i,ref} \exp \left[\frac{q}{kT} (\psi(x, t) + V_n(x) - \phi_n(x, t)) \right], \quad (4)$$

and where J_n is the electron particle current density, n is the electron density, ϕ_n is the electron quasi-Fermi potential, ψ is the electrostatic potential, k is Boltzmann's constant, q is the electron charge, T is the absolute temperature, $n_{i,ref}$ is the intrinsic electron density in the reference material (GaAs), and V_n , μ_n , m^* , N_D , and ϵ are the spatially-dependent alloy potential[4], electron mobility, electron conductivity effective mass, donor impurity concentration, and dielectric permittivity, respectively. Field-dependent electron mobilities are not considered here since electrons in HBVs, or SBVs below the flat-band voltage, are not being heated by the electric field[5]. Furthermore, electrons can not reach a steady state with the local electric field in the short high field regions of these devices[5]. For longer devices or devices operating above about 300 GHz, it becomes imperative to utilize the drift-diffusion equations presented above, in conjunction with the energy balance equations, so that the electron mobility can vary with the local electron energy.

In order to accurately model the current in heterostructure devices, careful consideration of carrier transport across abrupt material discontinuities is required[6,7]. As such, electron transport across the abrupt heterointerfaces of an HBV has been described by a set of nonlinear electron particle current density equations which take into account thermionic emission and thermionic-field emission of carriers over and through the abrupt barrier[3]. Regardless of bias polarity, one of the two heterointerfaces in a single barrier HBV is above flat-band. For this heterointerface, the semiconductor-semiconductor heterointerface analog[1-3] to the boundary constraint of Adams and Tang[8,9] for metal-semiconductor interfaces at high forward bias has been utilized.

Continuity of the electric displacement, electrostatic potential, and electron particle current density complete the set of interface conditions required for a self-consistent solution at a given heterointerface. A complete description of the boundary conditions for HBVs, including tunneling through the barrier, is given in [3]. As a result of this simulation approach, current transport through the heterostructure bulk is self-consistently combined with thermionic and thermionic-field emission currents imposed at the heterointerfaces.

For SBVs, a similar simulation approach is utilized to self-consistently combine current transport through the device bulk with thermionic and thermionic-field emission current imposed at the metal-semiconductor contact in a manner analogous to the analytical thermionic-emission/diffusion theory of Crowell and Sze[10]. Following the work of Adams and Tang[8,9], we have adopted a current density boundary constraint at the metal-semiconductor interface which is derived under the assumption of a drifted Maxwellian electron distribution at the interface. The use of this boundary constraint allows us to avoid the unphysical accumulation of electrons at the Schottky contact above the flat-band voltage. The resulting metal-semiconductor current density interface constraint at $x = 0$ is

$$J(0) = qv_{r,n}[n(0) - n_0] \quad (5)$$

where $n(0)$ is the electron density at the metal-semiconductor interface and n_0 is the equilibrium electron density at this interface. The effective surface recombination velocity for electrons, $v_{r,m}$, is given by

$$v_{r,n} = v_d + \sqrt{\frac{2kT}{\pi m^*}} \left\{ \frac{\exp\left[-v_d^2 \left(\frac{2m^*}{kT}\right)\right]}{1 + \operatorname{erf}\left(v_d \sqrt{\frac{2m^*}{kT}}\right)} \right\} \quad (6)$$

where m^* is the electron effective mass at the metal-semiconductor interface, and the amount of drift in the electron distribution at the metal-semiconductor interface is modelled as

$$v_d = \frac{J(0)}{qn(0)}. \quad (7)$$

The electrostatic potential at the metal-semiconductor interface, assuming the metal is maintained at a potential of zero, is

$$\psi(0) = \frac{\chi_{ref} - \Phi}{q} + \frac{kT}{q} \ln\left(\frac{N_{C,ref}}{n_{i,ref}}\right) \quad (8)$$

where χ_{ref} is the electron affinity in the reference material, Φ is the metal work function, and $N_{C,ref}$ is the total effective conduction band density of states in the reference material. The first term in this equation is the barrier height, ϕ_b , at the metal-semiconductor interface divided by the electronic charge. To account for the image-force lowering of the metal-semiconductor barrier, the barrier height is modified by an amount

$$\Delta\phi_b = \sqrt{\frac{q|\xi(0)|}{4\pi\epsilon(0)}} \quad (9)$$

where ξ is the electric field at the metal-semiconductor interface.

In order to develop robust numerical device simulators which could be efficiently combined with a harmonic-balance circuit analysis technique, careful consideration has been given to developing device simulators with excellent numerical convergence and accuracy properties. Potential problems and inefficiencies have been minimized by the use of finely subdivided, nonuniform mesh structures, a fully implicit finite difference time discretization scheme, and the state variables J_n , ϕ_n , ψ , and D . For an HBV, the four resulting carrier transport equations are solved, in the three regions (one barrier and two modulation) of the device, for a given bias value, and subject to the heterointerface constraints and ideal ohmic contact boundary constraints, via the coupled equation Newton-Raphson method. A full discussion of the solution algorithm for HBVs is given in [3]. A similar solution algorithm, with the appropriate metal-semiconductor interface constraints and ideal ohmic contact boundary constraints, has been utilized for SBVs. For SBVs, the algorithm is simplified by the fact there is only one region of interest as opposed to the three regions of an HBV. In order to derive an entire current-voltage (I-V) curve or time-domain current waveform, as well as to obtain information about the internal physics of the device as a function of bias, the DC or time-dependent bias is incrementally changed from the zero-bias condition. For DC simulations, the device static capacitance-voltage (C-V) relationship is derived by calculating the change in charge with respect to the change in applied bias over the depletion side of the device for sufficiently small bias increments. It is important to note that the use of the Adams and Tang metal-semiconductor current density interface constraint allows us to calculate very accurately the forward bias capacitance of SBVs.

B. Harmonic-Balance Circuit Analysis Technique

The novel harmonic-balance circuit analysis technique employed in this work is derived from the multiple-reflection algorithm[11]. The time-domain current through the device active region is calculated by the appropriate numerical device simulator, for one period, as described in the previous section. The harmonic components of the current are extracted from the time-domain current waveform using a discrete fourier transform; for HBVs, thirteen harmonics plus the DC term have been utilized, while six harmonics plus the DC term have been utilized for SBVs. A fixed-point iterative scheme, derived from the robust multiple-reflection algorithm and termed the Accelerated Fixed-Point (AFP) method[12], is then used to update the total voltage applied directly across the active region of the device in terms of the embedding impedances of the circuit, the harmonic components of the current, and the harmonic components of the voltage from previous iterations. In equation form, the new voltage component $V_{n,k+1}$ at the intrinsic device terminals, for harmonic number n and iteration step $k+1$, is

$$V_{n,k+1} = \left(\frac{Z_n^{TL}}{Z_n^{Linear} + Z_n^{TL}} \right) V_n^{Source} + \left(\frac{Z_n^{Linear}}{Z_n^{Linear} + Z_n^{TL}} \right) (V_{n,k} - I_{n,k} Z_n^{TL}) \quad (10)$$

where Z_n^{TL} , Z_n^{Linear} , V_n^{Source} , and $I_{n,k}$ are the fictitious transmission line characteristic impedance, Thevenin equivalent impedance, and source voltage of the linear embedding circuit at harmonic number n , and the device current component for harmonic number n and iteration step k , respectively. This iterative process is applied until the harmonic components of the voltage converge to their steady-state values, or

$$\left| \frac{(V_n - V_n^{Source})}{I_n} \right| / |Z_n^{Linear}| \quad (11)$$

is within a user-specified tolerance factor of unity for all harmonics; this tolerance factor is typically set to about 0.1 percent.

The novelty in the harmonic-balance algorithm utilized here is that, in deriving the fixed-point iterative voltage update expression (equation (10)), we use *a priori* knowledge, from Kirchhoff's voltage law, that the nonlinear device impedance will equal the negative of the linear embedding impedance of the circuit for each of the undriven harmonics in the steady state. This eliminates the computationally intensive and possibly unstable Runge-Kutta numerical time-integration necessary in the original multiple-reflection algorithm[11], and allows us to calculate complex under-relaxation parameters for each harmonic component of the fixed-point iterative voltage update equation. A Steffenson numerical acceleration scheme for iterative equations, derived from the secant methods of numerical analysis[13], is also utilized to greatly increase the computational speed and convergence properties of the harmonic-balance circuit analysis. The new voltage component $V_{n,k+1}$ at the intrinsic device terminals, for harmonic number n and iteration step $k+1$, then becomes

$$V_{n,k+1} = \bar{V}_{n,k+2} + \frac{(\bar{V}_{n,k+2} - \bar{V}_{n,k+1})}{(\bar{V}_{n,k+1} - V_{n,k})} \left(\bar{V}_{n,k+2} - \bar{V}_{n,k+1} \right) \quad (12)$$

where $\bar{V}_{n,k+2}$ and $\bar{V}_{n,k+1}$ are intermediate voltage values calculated from two successive applications of equation (10), starting with $\bar{V}_{n,k} = V_{n,k}$. Overall, the harmonic-balance circuit analysis technique outlined above avoids the laborious numerical calculations needed in Newton-type techniques to assemble Jacobian matrices and solve large linear systems of equations, while maintaining a convergence rate nearly equal to that of Newton-type methods.

Frequency-dependent parasitic impedances, external to the active region of the device and similar to those of [11], are included in the harmonic-balance circuit analysis as additional contributions to the linear device embedding circuit. These parasitic device impedances apply to whisker-contacted geometry diodes, as this geometry is investigated later in the paper. The parasitic impedances utilized here differ from those of [11] as follows: 1) the results of [14] for the purely resistive DC parasitic impedance are used, 2) we include the displacement current and mass-inertial contributions to the parasitic impedance of [15], 3) we include the spreading impedance at the backside ohmic contact as calculated in [16], and 4) the corrected AC spreading impedance expressions given in [17] are used. Given the intrinsic device impedances calculated from the harmonic-balance circuit analysis and the parasitic device impedances, the power generated at each harmonic can, then, be calculated from

$$P_n = \frac{1}{2} \Re e (Z_{n,Device} + Z_{n,Parasitic}) |I_n|^2 \quad (13)$$

where $Z_{n,Device}$ and $Z_{n,Parasitic}$ are the harmonic device and parasitic impedances, respectively, and I_n is the total device current at a given harmonic.

III. Thermal Model of Whisker-Contacted and Planar Varactor Multipliers

In addition to considering the electrical characteristics of HBV and SBV frequency multiplier circuits, the thermal properties of these circuits must also be analyzed due to the large amount of power that can be dissipated in the varactor diode itself. Our analysis of these circuits is a steady-state analysis based on the amount of power dissipated in the active region of the device and the thermal resistance to heat flow presented by the various elements that make up the circuit. From these quantities, the average temperature across the active region of the varactor diode can be estimated for use in the appropriate numerical device simulator.

The thermal model presented here uses simple geometrical expressions for the various thermal resistances of circuits utilizing both whisker-contacted and planar diode geometries assuming the ambient air is a perfect insulator. For heat flow through a bulk section of material surrounded by air (see Figure 1a), the thermal resistance is

$$R_{Thermal} = \frac{t}{\kappa\pi a^2} \quad (14)$$

where t is the thickness of the section, a is an equivalent radius based on the cross-sectional area of the section, and κ is the material's thermal conductivity. Likewise, for heat flow through a heat contact and into a multilayer stack of materials (see Figure 1b), the approximate thermal resistance of the first layer is [18]

$$R_{Thermal} = \frac{t}{\kappa_1\pi((a_1 + a_2)/2)^2} \quad (15)$$

where a_1 is an equivalent radius based on the cross-sectional area of the heat contact through which heat flows into the multilayer stack, and

$$a_2 = a_1 + t \tan \theta. \quad (16)$$

Following [18], the heat flux is assumed to be transmitted within a truncated right circular cone of vertex angle θ , and this angle is taken to be 45° . For heat flow into a semi-infinite heat sink (see Figure 1c), the thermal resistance is given by

$$R_{Thermal} = \frac{1}{4\kappa a} \quad (17)$$

where, again, a is an equivalent radius based on the cross-sectional area of the heat contact through which heat flows into the heat sink.

For planar diodes, the thermal resistance of the diode substrate is calculated using a three-dimensional finite-element heat flow analysis [19] to account for the substrate's irregular heat flow geometry. The substrate thermal resistance is calculated from the amount of power required to generate a 1 K temperature gradient between the input and output heat flow "ports" of the substrate assuming a uniform heat flux into and out of the substrate, a constant substrate thermal conductivity, and perfectly insulating chip boundaries. The planar geometry considered here (see Figure 1d) is that of a planar diode pair, with dimensions that correspond to the δ -doped anti-series SBV of [20]. This geometry is of particular interest as a suitable geometry for planar HBVs. Due

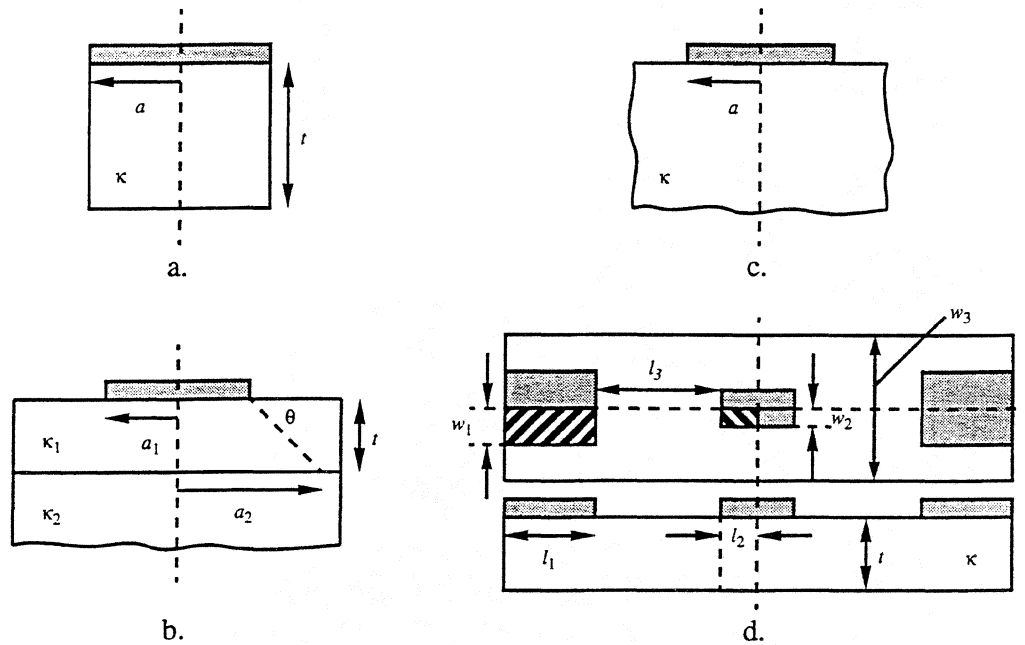


Figure 1. Relevant geometries for constituent elements of multiplier circuits: a. bulk section of material surrounded by air, b. multilayer stack of materials, c. semi-infinite heat sink, and d. planar diode pair substrate configuration (top and side views) with input ($w_1 \times l_1$) and output ($w_2 \times l_2$) heat flow “ports”[20].

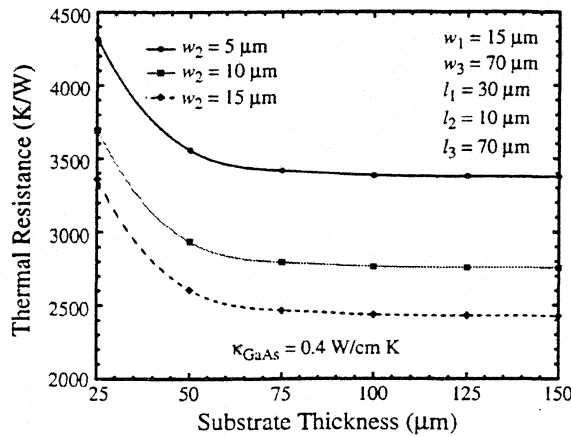


Figure 2a. Thermal resistance versus substrate thickness t and input heat flow “port” width w_2 for half of a planar diode pair.

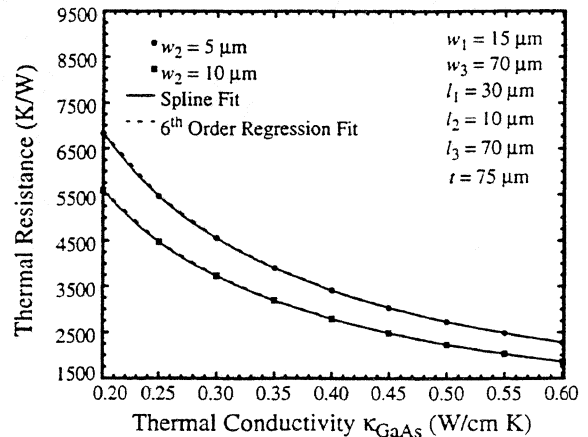


Figure 2b. Thermal resistance versus substrate thermal conductivity and input heat flow “port” width w_2 for half of a planar diode pair

to symmetry considerations, only a quarter of the actual planar substrate is simulated. Figure 2a shows the calculated planar substrate thermal resistance as a function of substrate thickness t and input heat flow “port” width w_2 . The important result to note from this figure is that, to achieve optimum heat sinking with a GaAs substrate and the typical device dimensions shown, the substrate should not be thinned below about 3 mils. Figure 2b shows the calculated planar substrate thermal resistance, as a function of substrate thermal conductivity and input heat flow “port” width

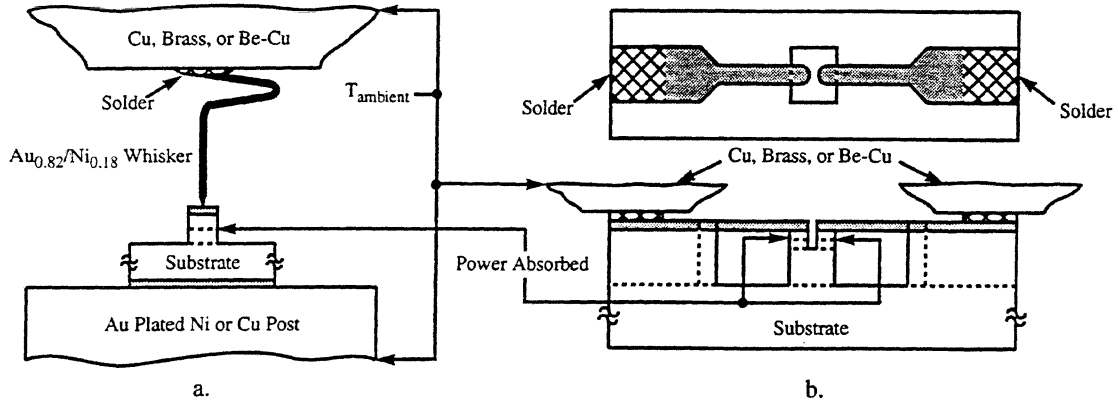


Figure 3. Representative multiplier circuits: a. whisker-contacted geometry and b. planar geometry. Circuit temperature is assumed to reach equilibrium with the ambient air at the locations indicated. The dissipated power is assumed to be absorbed in the center of the diode active region.

w_2 , along with analytical fits to the calculated resistances.

With a known amount of power dissipated in the active region of a varactor multiplier, the steady-state linear temperature gradient across each element of the multiplier circuit is simply the product of the power flowing through the particular element and the thermal resistance of the element. For simplicity, it is assumed that all of the dissipated power is absorbed in the center of the device active region. Representative whisker-contacted and planar multiplier circuits are shown in Figure 3a and 3b. Since these circuits have more than one heat flow path to reach equilibrium with the ambient air, an equivalent circuit representation of the actual circuit's thermal resistances is used to calculate the portion of the total dissipated power that flows through each path of the equivalent circuit. For example, in the planar diode pair configuration, there are four parallel heat flow paths (parallel heat flow through the finger and through the substrate for each diode in the configuration).

To further simplify the analysis, the thermal conductivity of each element in the circuit is taken to be a constant value versus position that is determined by the average temperature across the element. The thermal conductivities of the metallic portions of Figure 3a and 3b vary slowly with temperature; they are essentially equal to their values at 300 K ($\kappa_{\text{Au},300\text{K}} = 3.15 \text{ W/cm K}$, $\kappa_{\text{Ni},300\text{K}} = 0.636 \text{ W/cm K}$, $\kappa_{\text{Cu},300\text{K}} = 3.98 \text{ W/cm K}$, and $\kappa_{\text{Brass/Be-Cu},300\text{K}} = 1.0 \text{ W/cm K}$). On the other hand, the semiconductor portions of Figure 3a and 3b have the largest variation in thermal conductivity with temperature; for GaAs, the thermal conductivity follows a[21]

$$\kappa = \frac{A}{T^{1.2}} \quad (18)$$

law where A varies with doping level. For GaAs doped at $N_D = 1 \times 10^{17} \text{ cm}^{-3}$, $A = 488$ while $A = 366.5$ for highly doped GaAs[21]. Since the thermal conductivity of each element is allowed to vary with the average temperature across the element, the process outlined above is an iterative one. For this work, convergence was achieved when the temperature change, from one iteration to the next and across all of the circuit elements, was less than 0.1 K.

Using this thermal analysis, we examined the thermal properties of two HBV frequency multiplier circuits, one using a whisker-contacted geometry diode (see Figure 3a) and a companion one using a planar geometry diode (see Figure 3b). Both HBV diodes were double barrier

structures (1.5 $\mu\text{m}/\text{barrier}$) with 8 μm diameter anodes and 3 mil thick substrates. The whisker-contacted geometry diode had an n^+ substrate ($A = 488$) while the planar geometry diode had a SI substrate ($A = 544$). The whisker-contacted multiplier circuit utilized a 2.125 mm long, 1 mil diameter $\text{Au}_{0.82}/\text{Ni}_{0.18}$ whisker. Critical dimensions for the planar geometry diode are as follows: n^+ GaAs buffer 4 μm thick, diced chip 220 μm long and 70 μm wide, Au metallized fingers 2.5 μm thick, 50 μm long, and 8 μm wide, and Au metallized bonding pads 2.5 μm thick, 60 μm long, and 30 μm wide. The output heat flow “port” was assumed to be comprised of only half of the bonding pad length and, thus, was assumed to be 30 μm long and 30 μm wide. Figure 4 shows the calculated average active region temperature for these two multiplier circuits. Overall, these initial comparisons of the thermal properties of whisker-contacted and planar geometry varactor diodes indicate that the average active region temperature in planar geometry diodes can be significantly higher than the temperature in whisker-contacted geometry diodes. Such elevated temperatures translate directly into lower carrier mobilities in the device and, thus, lower circuit multiplying efficiencies. Furthermore, for the waveguide-mounted, flip-chip planar diode multiplier circuit configuration considered here, the diode substrate thickness should be no thinner than about 3 mils to insure optimal heat sinking.

IV. Numerical Device and Harmonic-Balance Circuit Simulation Results

In order to investigate the importance of using numerical device simulators in place of the usual lumped quasi-static equivalent circuit device models, the harmonic-balance circuit analysis has been coupled to both the HBV and SBV numerical device simulators, and simple quasi-static device models for HBVs and SBVs. The quasi-static equivalent circuit models have been derived from curve-fits to the DC I-V and static C-V characteristics of the devices as determined by the numerical device simulators. The total device current as an instantaneous function of bias $i(V(t))$ is, thus,

$$i(V(t)) = I_{DC}(V(t)) + C_{Static}(V(t)) \frac{dV}{dt}. \quad (19)$$

While not completely self-consistent and certainly subject to high frequency and high power divergence problems, these quasi-static device models alleviate some of the inaccuracies associated with the device models typically employed in the analysis of frequency multipliers. One such problem is the inaccurate forward bias C-V relationship typically used to describe SBVs operating in a hybrid varactor/varistor mode, i.e. at high frequencies and/or high power levels. For devices such as the HBV, the use of such curve-fit device models is invaluable since the terminal characteristics of such devices are not directly amenable to description by simple analytical expressions. As will be shown below, these vastly improved quasi-static device models still lack complete self-consistency, and do not accurately model the large-signal nonstationary dynamics of carrier transport that dominate device operation at high frequencies and high power levels.

In the remainder of the paper, we examine three specific whisker-contacted frequency multipliers, the UVA 6P4 and UVA 5T1 GaAs SBV doublers of [22], and the single barrier GaAs/ $\text{Al}_{0.7}\text{Ga}_{0.3}\text{As}$ HBV tripler of [23]. The 6P4 SBV has a 1.0 μm , $3.5 \times 10^{16} \text{ cm}^{-3}$ active region, while the 5T1 SBV has a 0.6 μm active region doped at $1.0 \times 10^{17} \text{ cm}^{-3}$. The measured forward DC bias series resistance of the 6P4 (5T1) SBV is 9.5 (5.3) Ω , while the measured zero-bias capacitance is

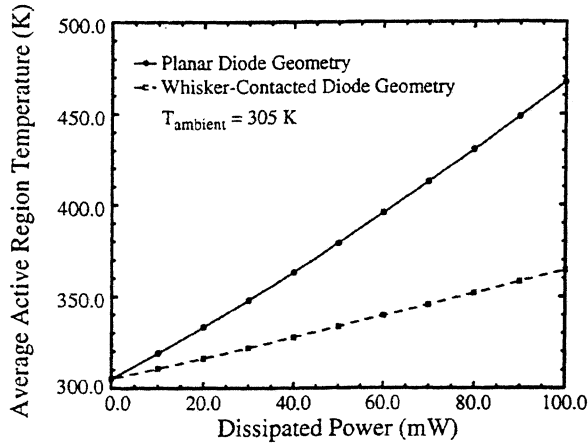


Figure 4. Average active region temperature versus power dissipated in the active region for the whisker-contacted and planar diode geometries of Figures 3a and 3b.

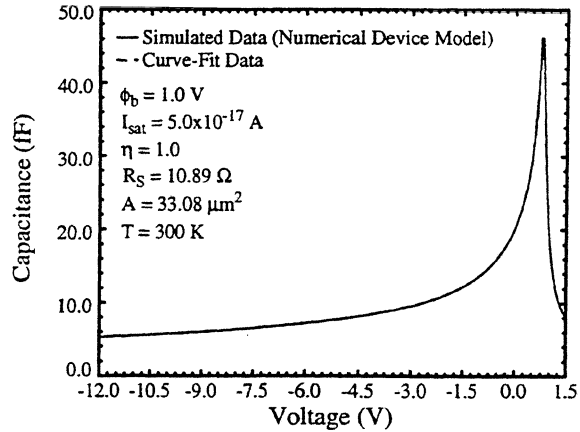


Figure 5. Simulated and curve-fit $C(V)$ characteristics for the UVA 6P4 GaAs SBV of reference [22].

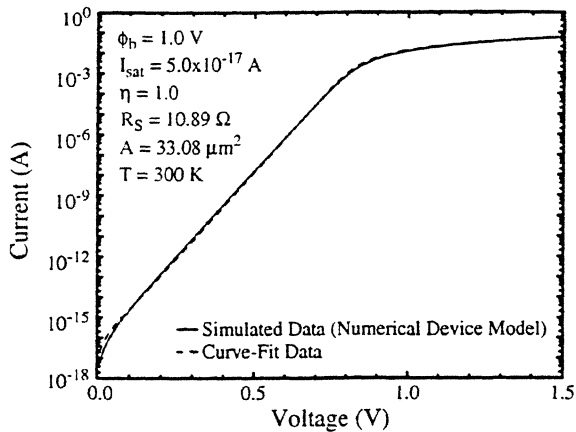


Figure 6. Simulated and curve-fit $I(V)$ characteristics for the UVA 6P4 GaAs SBV of reference [22].

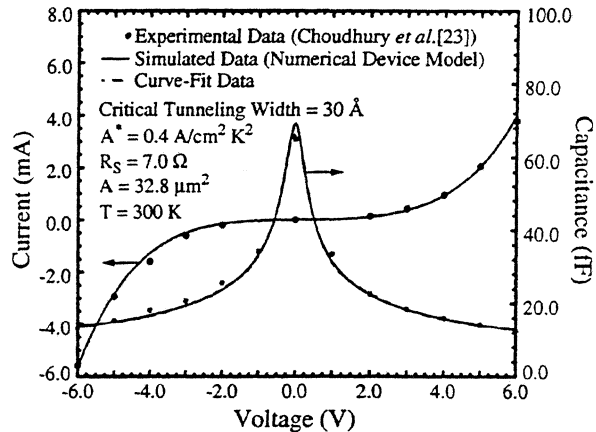


Figure 7. Experimental, simulated, and curve-fit $I(V)$ and $C(V)$ characteristics for the single barrier GaAs/Al_{0.7}Ga_{0.3}As HBV of reference [23].

20.0 (22.0) fF and the measured breakdown voltage is -20.0 (-10.0) V. Again, the quasi-static equivalent circuit model for the SBVs utilized curve-fits to the static $C-V$ characteristics as determined by the SBV numerical device simulator. The static $C-V$ results obtained from the numerical device simulator for the 6P4 SBV are shown in Figure 5 along with the results obtained from the quasi-static equivalent circuit model. Likewise, Figure 6 shows a comparison of the 6P4 SBV DC $I-V$ results obtained from the numerical device and quasi-static equivalent circuit models. Similar results have been obtained for the 5T1 SBV. For the DC $I-V$ characteristics, the quasi-static equivalent circuit model actually utilized the nonlinear diode equation

$$I = I_{sat} \left[\exp\left(\frac{q(V - IR_S)}{\eta kT}\right) - 1 \right] \quad (20)$$

which was solved analytically following the technique of [24]. In this equation, the ideality factor, η , was taken to be unity, the saturation current, I_{sat} , was taken to be 5.0×10^{-17} A, and the series resistance, R_s , was taken to be the calculated resistance of the entire SBV epitaxial layer based on the active layer electron mobility utilized in the numerical device simulator. For the 6P4 SBV, the resistance was 10.89Ω based on a mobility of $4950 \text{ cm}^2/\text{Vs}$; for the 5T1 SBV, the resistance was 4.36Ω based on a mobility of $4200 \text{ cm}^2/\text{Vs}$. A metal-semiconductor barrier height, ϕ_b , of 1.0 V was used in the numerical device simulator for both SBVs. It is important to note that no series resistance term was used in obtaining the numerical device simulator DC I-V results; the correctly simulated linear I-V characteristic in high forward bias is a direct consequence of the resistive nature of a Schottky diode above the flat-band voltage. Furthermore, it should be noted that the forward bias static C-V characteristic of the SBV is properly simulated[8] as a consequence of using the current density-dependent surface recombination velocity in the Schottky contact current boundary constraint.

The Choudhury *et al.*[23] HBV we have investigated consists of a 213 \AA intrinsic $\text{Al}_{0.7}\text{Ga}_{0.3}\text{As}$ barrier surrounded by 53 \AA intrinsic GaAs spacer layers and 5330 \AA n-type ($1 \times 10^{17} \text{ cm}^{-3}$) GaAs modulation layers. The slight asymmetry evident in the experimental HBV data has been modelled via a slight asymmetry in the modulation layer doping concentrations; one side of the device was assumed to have a doping concentration of $1.0 \times 10^{17} \text{ cm}^{-3}$, while the other side was assumed to have a doping concentration of $1.125 \times 10^{17} \text{ cm}^{-3}$. In the numerical device simulator, the active layer electron mobility was assumed to be $4200 \text{ cm}^2/\text{Vs}$, while an effective Richardson constant of $0.4 \text{ A/cm}^2\text{K}^2$ was assumed for the heterointerface current density boundary constraints[1-3]. The quasi-static equivalent circuit model for this HBV was derived entirely from curve-fits to the DC I-V and static C-V results obtained from the numerical device simulator. Excellent correlation has been obtained between the HBV numerical device simulator and experimental DC I-V and static C-V characteristics[23]. Figure 7 shows the experimental DC I-V and static C-V characteristics of this HBV along with the simulated characteristics from the numerical device and equivalent circuit models. The measured series resistance of 7.0Ω has been utilized in calculating the simulated and curve-fit DC I-V and static C-V characteristics.

For all of the simulations to follow, current waveforms are generated by the numerical device simulators and the quasi-static equivalent circuit models based solely on the harmonic voltages given to them. Although the quasi-static equivalent circuit models utilize a constant "series resistance" that limits the forward conduction of the diode, only the numerical device simulator self-consistently accounts for the bias-dependent parasitic impedance of a simulated device's undepleted epitaxial layer.

A. Large-Signal Sinusoidal Results

Before examining results from the harmonic-balance circuit analysis technique coupled to the numerical device and quasi-static equivalent circuit models, it is instructive to examine results from these two models when the device under investigation is subject to pure sinusoidal large-signal voltage excitations, i.e. in the absence of harmonic voltages impressed on the device as a consequence of its nonlinear interaction with the embedding circuit. Figures 8a and 8b show the current and voltage waveforms for the 5T1 SBV DC biased at -4.0 V and subject to a 5.0 V sinusoidal excitation voltage at 50 GHz and 100 GHz , respectively. Likewise, Figures 9a and 9b show the current and voltage waveforms for the Choudhury *et al.* HBV DC biased at 0.0 V and subject to a 2.0 V sinusoidal excitation voltage at 10 GHz and 100 GHz , respectively. For the 5T1

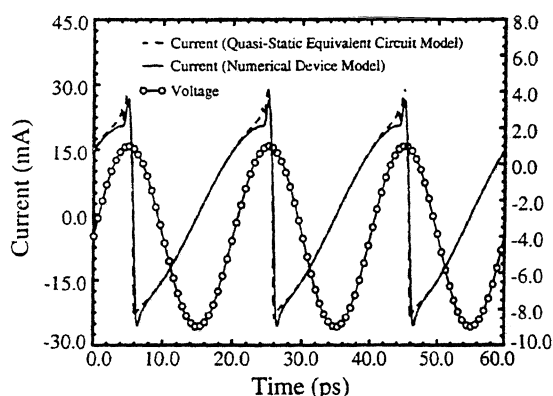


Figure 8a. Current waveforms for the UVA 5T1 GaAs SBV of reference [22] DC biased at -4.0 V and subject to 50 GHz, 5.0 V sinusoidal excitation.

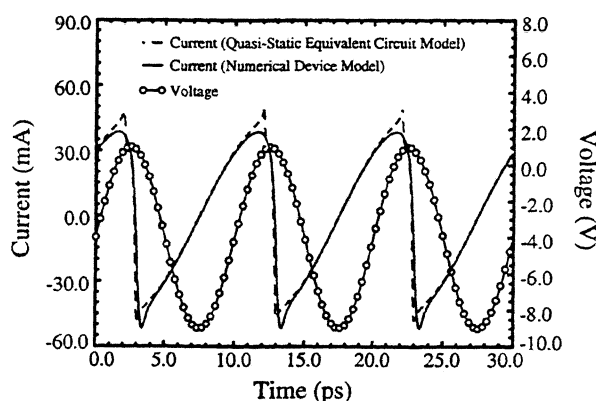


Figure 8b. Current waveforms for the UVA 5T1 GaAs SBV of reference [22] DC biased at -4.0 V and subject to 100 GHz, 5.0 V sinusoidal excitation.

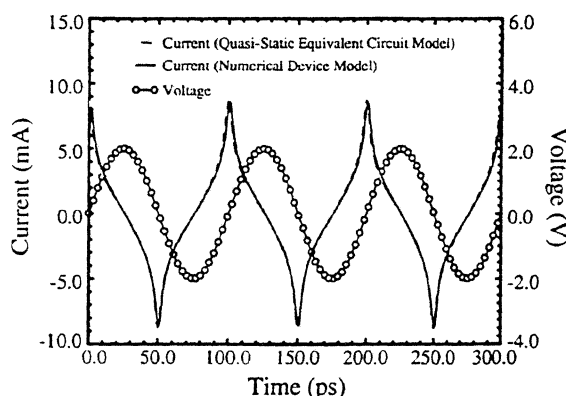


Figure 9a. Current waveforms for the GaAs/ $\text{Al}_{0.7}\text{Ga}_{0.3}\text{As}$ HBV of reference [23] DC biased at 0.0 V and subject to 10 GHz, 2.0 V sinusoidal excitation.

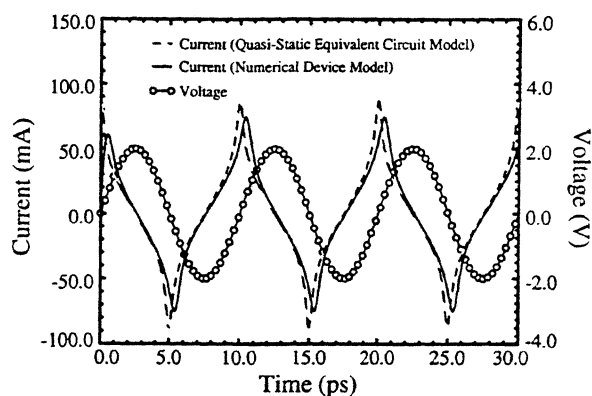


Figure 9b. Current waveforms for the GaAs/ $\text{Al}_{0.7}\text{Ga}_{0.3}\text{As}$ HBV of reference [23] DC biased at 0.0 V and subject to 100 GHz, 2.0 V sinusoidal excitation.

SBV subject to the specified drive level, the current waveforms from the two device models begin to deviate at about 50 GHz with the deviations increasing with increasing frequency. For the Choudhury *et al.* HBV subject to the specified drive level, the current waveforms from the two device models begin to deviate at about 10 GHz with the deviations, again, increasing with increasing frequency.

At low frequencies (below about 10 GHz in the SBV and about 1 GHz in the HBV), when the current throughout the device is dominated by conduction current, small discrepancies between the results of the two models are observed. These discrepancies are attributed to errors in the curve-fits to the numerical device DC I-V and static C-V results. At higher frequencies, the current is dominated by displacement current in high field regions of the device (near the Schottky barrier or heterostructure barrier) and by conduction current in low field regions of the device (near the ohmic contacts). In the numerical device simulator, the conduction and displacement currents are balanced throughout the device in a self-consistent manner so that the total current versus position is constant. In the quasi-static equivalent circuit model, however, these currents are not self-

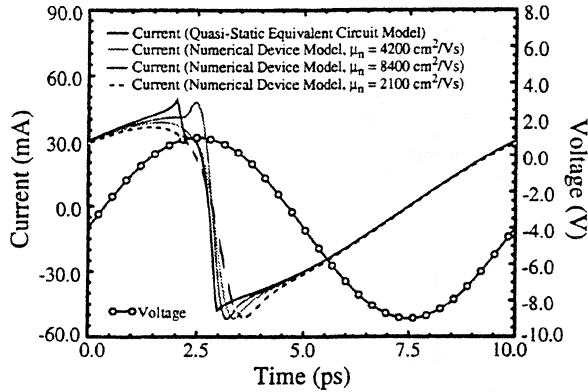


Figure 10. Current waveforms (one steady-state period) for the UVA 5T1 GaAs SBV of reference [22] DC biased at -4.0 V and subject to 100 GHz, 5.0 V sinusoidal excitation. The active region electron mobilities have been varied in the numerical device model as shown in the figure.

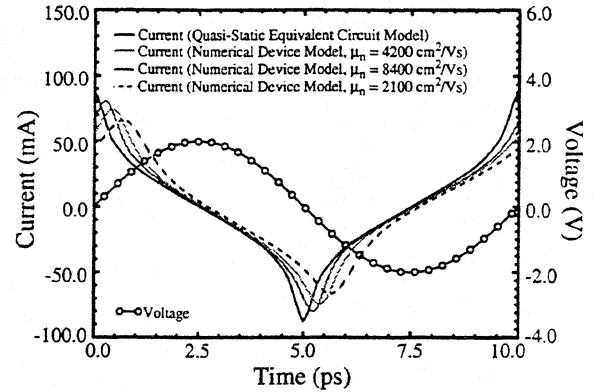


Figure 11. Current waveforms (one steady-state period) for the GaAs/Al_{0.7}Ga_{0.3}As HBV of reference [23] DC biased at 0.0 V and subject to 100 GHz, 2.0 V sinusoidal excitation. The active region electron mobilities have been varied in the numerical device model as shown in the figure.

consistently balanced. As a result, the displacement current in the high field regions of the device can greatly exceed the sustainable conduction current in the (relatively) low field regions of the device. As a result, the increasing current waveform deviations that we have observed with increasing frequency are a direct consequence of the current saturation phenomenon described in [25] and [22]. These deviations also increase with increasing drive level. Although attempts have been made to compensate for this lack of self-consistency in the quasi-static equivalent circuit models [26,27], the resulting models are device-specific, and require empirical fitting parameters and/or an analytical understanding of the device's internal physics.

In essence, the standard quasi-static equivalent circuit models assume an infinite electron mobility such that there is no limit to the allowable displacement current in the device. To further examine this concept, we have compared the quasi-static equivalent circuit models for the 5T1 SBV and the single barrier GaAs/Al_{0.7}Ga_{0.3}As HBV with their respective numerical device models assuming an active region mobility of μ_{n0} , twice μ_{n0} , and one half μ_{n0} . The results are shown in Figures 10 and 11 for drive levels identical to those previously specified. Clearly, as the active region mobility is increased from μ_{n0} , the current waveform from the numerical device simulator approaches that of the quasi-static equivalent circuit model. Alternately, as the active region mobility is decreased from μ_{n0} , the differences between the numerical device simulator current waveform and that of the quasi-static equivalent circuit model increase.

It is important to remember that the phenomenon described here is strictly a current saturation phenomenon. Since a constant, field-independent electron mobility has been utilized, saturation of the electron drift-velocity has not been accounted for. For long diodes, where a field-dependent electron mobility is justified, drift-velocity saturation could be directly incorporated in the numerical device models presented here. A better approach would be to utilize the drift-diffusion equations in conjunction with the energy balance equations to accurately account for saturation of the electron drift-velocity, even in relatively short diodes.

B. Harmonic-Balance Results

The differences in the sinusoidally pumped results, presented in the last section for the quasi-static equivalent circuit and numerical device models, are relatively small, at least below 100 GHz for the specified drive levels. Again, it is important to note that the differences increase with increasing frequency and drive level, and can be quite substantial above about 150 GHz. These relatively small differences, however, are magnified by the nonlinearity of the device when it is embedded in a circuit.

We investigate this phenomenon for the UVA 6P4 GaAs SBV doubler pumped at 100 GHz and the single barrier GaAs/Al_{0.7}Ga_{0.3}As HBV tripler pumped at 64 GHz using the harmonic-balance circuit analysis technique in conjunction with the two device modelling approaches[28-30]. Parasitic impedances for these frequency multipliers, external to the active regions of the devices, have been calculated using estimated chip parameters (ohmic contact resistivities of $2 \times 10^{-6} \Omega \text{cm}^2$, total device thickness of 4 mils, and square chip side lengths of 250 μm). For the 6P4 SBV doubler pumped at 100 GHz, the DC impedance is 0.614 Ω and the impedances at the fundamental and second-harmonic frequencies are $1.491 + j1.016 \Omega$ and $1.924 + j1.549 \Omega$, respectively. For the HBV tripler pumped at 64 GHz, the DC impedance is 7.021 Ω and the impedances at the fundamental and third-harmonic frequencies are $7.685 + j0.788 \Omega$ and $8.298 + j1.537 \Omega$, respectively.

At the incident pump powers of interest, near-optimum fundamental and third-harmonic circuit impedances for the zero DC biased HBV tripler have been estimated from [23] for a device DC parasitic impedance of 7.0 Ω . The optimum fundamental impedances vary from $8.75 + j46.75 \Omega$ to $19.25 + j92.50 \Omega$ for incident pump powers ranging from 0 mW to 40 mW; the optimum third-harmonic impedances vary from $10.75 + j15.75 \Omega$ to $17.50 + j35.50 \Omega$ over the same pump power range. For the 6P4 SBV doubler, experimental DC bias values have been utilized[31]. Near-optimum fundamental and second-harmonic circuit impedances have been obtained for this doubler from the harmonic-balance circuit simulator coupled to the quasi-static 6P4 SBV equivalent circuit model. For simplicity, these SBV doubler circuit impedances have been optimized subject to the following constraints: 1) the real parts of the two harmonic impedances are equal and 2) the imaginary part of the second-harmonic impedance is half of the impedance at the fundamental. The optimized fundamental impedances vary from $23.5 + j207.0 \Omega$ to $48.0 + j223.0 \Omega$ for incident pump powers ranging from 7.5 mW to 47.0 mW. For both frequency multipliers, the high order harmonic circuit impedances are set to short-circuit impedances of $0.001 + j0.0 \Omega$. For the 6P4 SBV simulations, a DC circuit impedance of 1.0 Ω has also been utilized.

The steady-state current and voltage waveforms for the 6P4 SBV doubler subject to a 100 GHz, 18.8 mW pump excitation are shown in Figure 12; similar waveforms for the HBV tripler subject to a 64 GHz, 20 mW pump excitation are shown in Figure 13. As previously noted, the relatively small differences in the results obtained from the two device modelling approaches are magnified by the nonlinearity of the device when it is embedded in a circuit. This is clearly evident from the harmonic-balance results shown in these figures. Although the current and voltage waveforms generated by the two device models have the same general shape, the sharpness, magnitudes, and phases of the waveforms differ substantially. As a result, the predicted absorbed powers, output powers, and multiplying efficiencies are substantially overestimated by the quasi-static equivalent circuit/harmonic-balance circuit simulation approach. For the 6P4 SBV doubler,

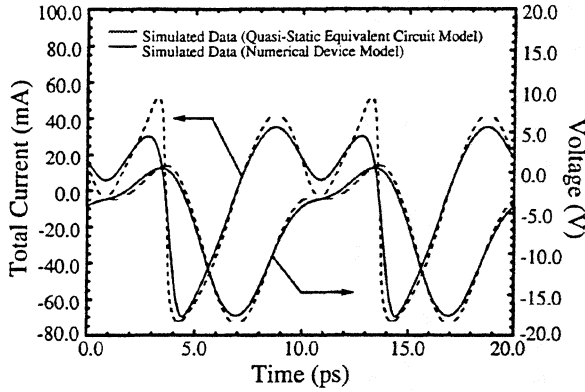


Figure 12. Steady-state harmonic-balance current and voltage waveforms for the UVA 6P4 GaAs SBV doubler of reference [22] DC biased at -7.03 V and subject to 100 GHz, 18.8 mW pump excitation.

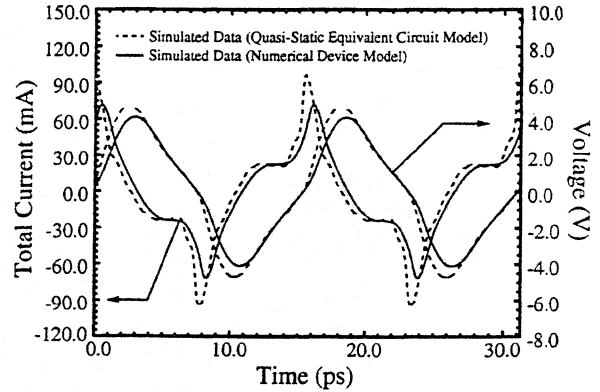


Figure 13. Steady-state harmonic-balance current and voltage waveforms for the single barrier GaAs/Al_{0.7}Ga_{0.3}As HBV tripler of reference [23] DC biased at 0.0 V and subject to 64 GHz, 20 mW pump excitation.

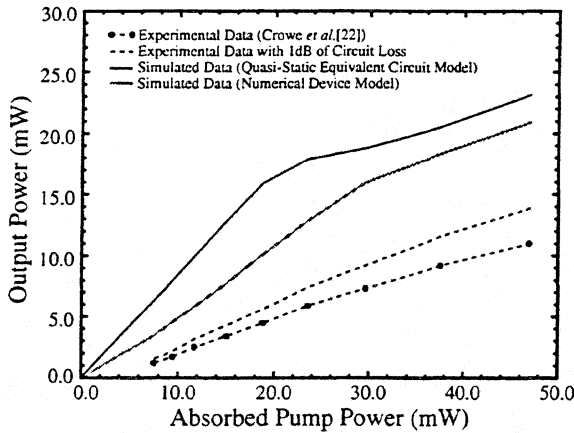


Figure 14. Experimental and simulated output power versus absorbed pump power results for the UVA 6P4 GaAs SBV doubler reference [22] subject to 100 GHz pump excitation.

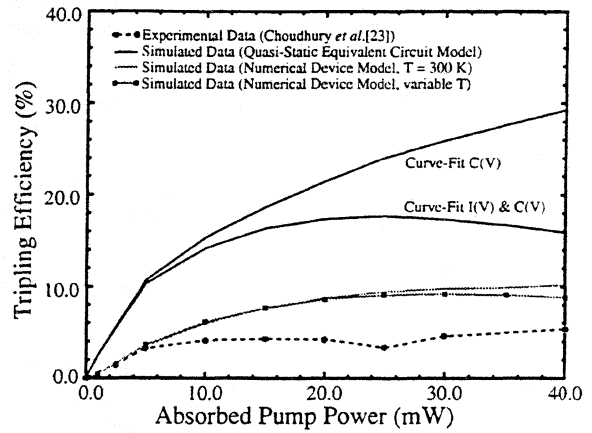


Figure 15. Experimental and simulated tripling efficiency versus absorbed pump power results for the single barrier GaAs/Al_{0.7}Ga_{0.3}As HBV tripler of reference [23] DC biased at 0.0 V and subject to 64 GHz pump excitation.

this can be seen clearly in Figure 14. This figure shows the experimental output power versus absorbed pump power results for this circuit, along with the simulated results obtained from the harmonic-balance circuit simulator coupled to the two device models. Similarly, Figure 15 shows the experimental tripling efficiency versus absorbed pump power results for the HBV tripler, along with the two simulated results. Also shown in Figure 15 is simulated data that includes thermal effects. For this particular whisker-contacted HBV tripler, the average active region temperature was estimated to be about 332 K at an incident pump power of 40 mW; this temperature translates into an active region electron mobility of about 3850 cm²/Vs which is about 92 percent of the 300 K mobility. Simulations including thermal effects have not been undertaken for the 6P4 SBV doubler since the average active region temperature was only found to reach about 320 K at an incident pump power of 50 mW. It is important to note that circuit losses have been incorporated

into the experimental tripling efficiency data shown in Figure 15[23]. For the 6P4 SBV doubler, the raw output power data has been plotted along with output power data assuming 1 dB of circuit loss. For all of the harmonic-balance simulations presented here, neither the breakdown voltage nor the critical breakdown field has been exceeded. For the 5T1 SBV doubler, however, it was found that the breakdown voltage is exceeded at relatively low incident pump power levels when near-optimum circuit impedances are assumed. This result indicates that careful modelling of avalanche breakdown may be required to accurately simulate the performance of the 5T1 SBV doubler.

Overall, the harmonic-balance results presented here indicate that the physics-based numerical device models for SBVs and HBVs provide significantly improved correlation to experimental data when compared to typical quasi-static equivalent circuit models. The remaining discrepancies between simulation and experiment are attributed mainly to the inaccurate assumption that the multiplier circuits present optimum impedances to the active devices. The accurate determination of active device embedding impedances would be of great benefit to the analysis and design of frequency multipliers as well as other highly nonlinear circuits.

V. Conclusions

In conclusion, accurate and efficient simulations of the large-signal time- and temperature-dependent characteristics of SBV and HBV frequency multiplier circuits have been obtained by combining a novel harmonic-balance circuit analysis technique with physics-based numerical device simulators. This approach to the analysis and design of highly nonlinear millimeter and submillimeter wave circuits allows for the careful examination of the internal physical phenomena occurring in a wide array of highly nonlinear active devices. This is particularly important at high frequencies and for devices whose terminal characteristics are not amenable to description via analytical expressions. Even when such an analytical description is possible or when curve-fit DC results from a physics-based numerical device simulator are utilized, the resulting quasi-static equivalent circuit model lacks self-consistency and neglects important high frequency nonstationary carrier dynamic effects. Only the general approach presented in this paper adequately addresses these issues and allows for the accurate and self-consistent modelling of phenomena such as current saturation, the bias-dependent parasitic impedance and shunting capacitance of device undepleted regions, electron velocity saturation, and electron mass-inertial effects[25]. It is our belief that analysis and design approaches as advocated in this paper are essential to the development of efficient and reliable circuits operating into the terahertz frequency range.

Acknowledgments

J. R. Jones is supported by a United States Air Force Laboratory Graduate Fellowship under the sponsorship of the Solid-State Directorate, Wright Laboratory, WPAFB, OH. This work is also partially supported by NSF Grant #ECS-9412931. The authors thank M. F. Zyburra and Dr. T. W. Crowe of the University of Virginia, and Dr. R. F. Bradley of the National Radio Astronomy Observatory for stimulating technical discussions relevant to this work.

References

1. J. R. Jones, G. B. Tait, and S. H. Jones, "DC and Large-Signal AC Electron Transport Properties of GaAs/InGaAs/AlGaAs Heterostructure Barrier Varactors," *Proc. 1993 Int. Semiconductor Device Research Symp.*, Charlottesville, VA, Dec. 1-3, 1993, pp. 389-392.
2. J. R. Jones, S. H. Jones, and G. B. Tait, "GaAs/InGaAs/AlGaAs Heterostructure Barrier Varactors for Frequency Tripling," *Proc. Fifth Int. Symp. Space Terahertz Technol.*, May 10-12, 1994, Ann Arbor, Michigan, pp. 497-513.
3. J. R. Jones, G. B. Tait, and S. H. Jones, "DC and Large-Signal Time-Dependent Electron Transport in Heterostructure Devices: An Investigation of the Heterostructure Barrier Varactor," to appear, *IEEE Trans. Electron Dev.*, Vol. 42, No. 6, June 1995.
4. M. S. Lundstrom and R. J. Schuelke, "Numerical Analysis of Heterostructure Semiconductor Devices," *IEEE Trans. Electron Dev.*, Vol. 30, No. 9, Sept. 1983, pp. 1151-1159.
5. H. Hjelmgren, "Numerical Modeling of Hot Electrons in n-GaAs Schottky-Barrier Diodes," *IEEE Trans. Electron Dev.*, Vol. 37, No. 5, May 1990, pp. 1228-1234.
6. K. Horio and H. Yanai, "Numerical Modeling of Heterojunctions Including the Thermionic Emission Mechanism at the Heterojunction Interface," *IEEE Trans. Electron Dev.*, Vol. 37, No. 4, Apr. 1990, pp. 1093-1098.
7. G. B. Tait and C. R. Westgate, "Electron Transport in Rectifying Semiconductor Alloy Ramp Heterostructures," *IEEE Trans. Electron Dev.*, Vol. 38, No. 6, June 1991, pp. 1262-1270.
8. J. Adams and T. W. Tang, "A Revised Boundary Condition for the Numerical Analysis of Schottky Barrier Diodes," *IEEE Electron Dev. Lett.*, Vol. 7, No. 9, Sept. 1986, pp. 525-527.
9. J. G. Adams and T. W. Tang, "Computer Simulation of Boundary Conditions for Schottky Barrier Diodes," *Elec. Lett.*, Vol. 25, No. 16, Aug. 1989, pp. 1098-1100.
10. C. R. Crowell and S. M. Sze, "Current Transport in Metal-Semiconductor Barriers," *Solid-State Electron.*, Vol. 9, No. 11/12, Nov./Dec. 1966, pp. 1035-1048.
11. P. H. Siegel, A. R. Kerr, and W. Hwang, "Topics in the Optimization of Millimeter-wave Mixers," *NASA Tech. Papers*, No. 2287, Mar. 1984.
12. G. B. Tait, "Efficient Solution Method for Unified Nonlinear Microwave Circuit and Numerical Solid-State Device Simulation," *IEEE Microwave Guided Wave Lett.*, Vol. 4, No. 12, Dec. 1994, pp. 420-422.
13. J. Ortega and W. Rheinboldt, *Iterative Solution of Nonlinear Equations in Several Variables*, New York, New York: Academic Press, 1970.
14. L. E. Dickens, "Spreading Resistance as a Function of Frequency," *IEEE Trans. Microwave Theory Tech.*, Vol. 15, No. 2, Feb. 1967, pp. 101-109.
15. K. S. Champlin and G. Eisenstein, "Cutoff Frequency of Submillimeter Schottky-Barrier Diodes," *IEEE Trans. Microwave Theory Tech.*, Vol. 26, No. 1, Jan. 1978, pp. 31-34.
16. J. A. Calviello, J. L. Wallace, and P. R. Bie, "High Performance GaAs Quasi-Planar Varactors for Millimeter Waves," *IEEE Trans. Electron Dev.*, Vol. 21, No. 10, Oct. 1974, pp. 624-630.
17. U. Bhapkar, "An Investigation of the Series Impedance of GaAs Schottky Barrier Diodes," M.S.E.E. Thesis. University of Virginia, May 1990, pp. 25-28 and 31-34.
18. L. H. Holway, Jr. and M. G. Adlerstein, "Approximate Formulas for the Thermal Resistance of IMPATT Diodes Compared with Computer Calculations," *IEEE Trans. Electron Dev.*, Vol. 24, No. 2, Feb. 1977, pp. 156-159.
19. ABAQUS, Hibbitt, Karlsson, & Sorensen, Inc.
20. B. J. Rizzi, K. K. Rausch, T. W. Crowe, P. J. Koh, W. C. B. Peatman, J. R. Jones, S. H. Jones, and G. B. Tait, "Planar Varactors Diodes for Submillimeter Applications," *Proc. Fourth Int. Symp. Space Terahertz Technol.*, March 30-April 1, 1993, Los Angeles, California, pp. 297-311.

21. *Properties of Gallium Arsenide* (second edition), London, United Kingdom: INSPEC, The Institution of Electrical Engineers, 1990.
22. T. W. Crowe, W. C. B. Peatman, R. Zimmermann, and R. Zimmermann, "Consideration of Velocity Saturation in the Design of GaAs Varactor Diodes," *IEEE Microwave Guided Wave Lett.*, Vol. 3, No. 6, June 1993, pp. 161-163.
23. D. Choudhury, M. A. Frerking, and P. D. Batelaan, "A 200 GHz Tripler Using a Single Barrier Varactor," *IEEE Trans. Microwave Theory Tech.*, Vol. 41, No. 4, Apr. 1993, pp. 595-599.
24. T. A. Fjeldly, B. Moon, and M. Shur, "Analytical Solution of Generalized Diode Equation," *IEEE Trans. Electron Dev.*, Vol 38, No. 8, Aug. 1991, pp. 1976-1977.
25. E. L. Kollberg, T. J. Tolmunen, M. A. Frerking, and J. R. East, "Current Saturation in Submillimeter Wave Varactors," *IEEE Trans. Microwave Theory Tech.*, Vol. 40, No. 5, May 1992, pp. 831-838.
26. J. East, E. Kollberg, and M. Frerking, "Performance Limitations of Varactor Multipliers," *Proc. Fourth Int. Symp. Space Terahertz Technol.*, March 30-April 1, 1993, Los Angeles, California, pp. 312-325.
27. J. T. Louhi and A. V. Räsänen, "On the Modelling of the Millimeter Wave Schottky Varactor," *Proc. Fifth Int. Symp. Space Terahertz Technol.*, May 10-12, 1994, Ann Arbor, Michigan, pp. 426-436.
28. J. R. Jones, S. H. Jones, G. B. Tait, and M. F. Zybura, "Heterostructure Barrier Varactor Simulation Using an Integrated Hydrodynamic Device/Harmonic-Balance Circuit Analysis Technique," *IEEE Microwave Guided Wave Lett.*, Vol. 4, No. 12, Dec. 1994, pp. 411-413.
29. J. R. Jones, S. H. Jones, G. B. Tait, and M. F. Zybura, "Correction to 'Heterostructure Barrier Varactor Simulation Using an Integrated Hydrodynamic Device/Harmonic-Balance Circuit Analysis Technique,'" *IEEE Microwave Guided Wave Lett.*, Vol. 5, No. 2, Feb. 1995, p. 62.
30. M. F. Zybura, J. R. Jones, S. H. Jones, and G. B. Tait, "Simulation of 100-300 GHz Solid-State Harmonic Sources," to appear, *IEEE Trans. Microwave Theory Tech.*, Vol. 43, No. 4, Apr. 1995.
31. T. W. Crowe, private communication.

Monte Carlo Simulation of Schottky Barrier Mixers and Varactors

J. East¹

Center for Space Terahertz Technology
The University of Michigan
Ann Arbor, Michigan 48109

Abstract

Current saturation effects can be an important limitation on the performance of Schottky barrier mixers and multipliers. This effect was first discussed at this conference in 1991 with additional results in 1993 and 1994. These earlier results are all based on a static or equilibrium description of the device. This paper will describe a large signal Monte Carlo simulation of Schottky barrier mixers and varactors. The simulation is a time dependent particle field Monte Carlo simulation with ohmic and Schottky barrier boundary conditions included. The simulation will be used to point out some important time constants in GaAs and to describe the effects of current saturation due to valley transfer in GaAs varactors and inductive delay and current saturation effects in very high frequency mixers.

I. Introduction

Schottky barrier diodes are critical components in millimeter and submillimeter wave receiver systems. They are used in multipliers with input and output frequencies of hundreds of GHz and in receivers to THz frequencies. Mixer and multiplier modeling is needed to better understand the performance of these devices and to design circuits. Several modeling tools are available¹⁻³. The modeling is usually a combination of a linear frequency domain description of the circuit and a nonlinear time domain description of the device. The approaches use harmonic balance or multiple reflection techniques. They start with an approximation for the voltage waveform across the devices and frequency domain information about the circuit and time evolve to a final approximation for the voltage and current waveforms at the device terminals. These techniques require a description of the active device. A lumped element model with voltage dependent elements is typically used. Measured low frequency data or calculated information for the capacitance and current vs. voltage can be used. The performance also depends on the series resistance which

¹This work was supported by the Center for Space Terahertz Technology under contact No. NAGW-1334

be either calculated or measured. The series resistance is sometimes also frequency dependent. This approach has been used to study mixer and multiplier performance over a wide range of frequencies. The match between theory and experiment is encouraging at lower frequencies. However, as the frequency or power levels go up the predicted powers and efficiencies are typically lower than experimental results. There are several possible explanations. High frequency circuits are small and difficult to fabricate. Skin effect and backshort losses both go up with frequency. These losses can be taken into account in the simulation, but the required loss values tend to be relatively large when compared with other information about waveguide and mount loss. The impedance presented to the device by the circuit is sometimes inferred from scale model measurements at much lower frequencies. As the operating frequency increases mechanical tolerance limitations and loss make it much more difficult to predict operating conditions from scale models. Another problem is the nonlinear circuit used to describe the diode. Another problem is the lump element model for the nonlinear device.

A simple lumped element equivalent circuit can have problems representing the device operation at high frequencies. A paper by Kollberg et al⁴ described saturation effects in varactors using a lumped element representation for the varactor with elements that depended on the current level. This approach was also used by to model multipliers by Louhi and Raisanen⁵ and experimentally to design varactors by Crowe et. al.⁶ A paper by East et. al.⁷ described a more detailed physical model for the saturation effects. That paper used a static velocity vs. electric field electron transport model to investigate saturation. A Monte Carlo based device simulation to further investigate device operation will be described in this paper.

The paper is organized as follows. The next section will discuss the implementation of a Monte Carlo simulation of Schottky barrier mixers and varactors. Several characteristic times that are important for varactor and mixer operation will be discussed. Section III will describe the Monte Carlo simulation of varactors. Section IV will describe THz mixer simulation. The paper will be summarized in Section V.

Monte Carlo Device Simulation

The effects under investigation occur at the high frequencies and electric field levels where the lumped element circuit approximation for the semiconductor device no longer applies. This section will describe a Monte Carlo based device simulation that can be used to investigate a range of frequencies and RF drive levels in order to get a better physical understanding of the device operation. A Monte Carlo simulation follows the motion of a collection of individual electrons as they move in a

semiconductor as a function of position and time. The details of the electron transport are represented by random variables with distributions that match the underlying physics of the transport. A Monte Carlo simulation typically follows the motion of many electrons to obtain average values for variables of interest. Descriptions of the Monte Carlo technique are given by Fawcett⁸ and by Hochney and Eastwood⁹. The advantage of the Monte Carlo technique is a better physical description of the device operation and the disadvantage is the large amount of computer time needed. A Monte Carlo Schottky barrier device simulation has been written and will be discussed next.

A particle field Monte Carlo simulation has been modified to investigate the varactors and mixers of interest in this paper. The code uses a two valley parabolic band approximation for the GaAs. The details of the physics are taken from Fawcett⁸. The simulation steps the electrons and the solution of Poissons' equation as a function of time to obtain terminal characteristic. The code has been modified to investigate Schottky barrier devices. The boundary conditions have been modified to approximate a Schottky barrier diode. Electron flow out of the Schottky barrier end of the device during a time step. These electrons, along with the ones that flow out of the ohmic contact are available to be reintroduced at the ohmic contact at the end of each time steps. Electron in equilibrium with the contact field are added or eliminated from the contact to form a charge neutral ohmic contact at the start of each time step. Thus the number of electrons in the structure is a function of time. This simulation is an approximation to more complete codes that better describe the transport physics and the details of emission over the thermionic barrier¹⁰. However, it allows full device simulations with reasonable amounts of computer time. A typical simulation involving 10,000 initial electrons for 10 picoseconds corresponding to 100 GHz operation takes about several minutes per RF period. Fourier transforms of information for successive RF periods are compared until steady state results are obtained. to decay .

There are several characteristic times for semiconductor materials that effect the operation of mixers and multipliers. Before the details of the Monte Carlo results are described, it is informative to discuss these time scales, and the resulting nonequilibrium effects that modify device performance. The nonequilibrium effects include velocity saturation, valley transfer delays and inductive delays in the electron motion for rapidly changing electric fields. Varactors are usually operated as reverse biased diodes with relatively large RF voltage levels across the device. Frequency multipliers have input frequencies in the several hundred GHz range with corresponding time scales of one to ten picoseconds. Velocity saturation and valley transfer delays are important effects in these devices. Mixers are needed into the THz range, with corresponding time scales between several picoseconds and a fraction of a picosecond. They are usually forward biased with much lower RF power levels than

varactors. Inductive effects are important for these devices, with velocity saturation and valley transfer effecting the very high frequency operation. The Monte Carlo program can be used to investigate these characteristic times in a bulk GaAs structure.

One important time scale is the energy relaxation time or valley transfer time. Valley transfer occurs when electrons are heated by moderate electric fields. The time response of electrons in GaAs to an electric field switching slowly between one and twenty 20 KV/cm square wave is shown in Fig. 1. Fig. 1a shows the fraction of the electrons in the high mobility Γ valley as a function of time for the field shown in Fig. 1b. There are two important times, the time required to heat the electrons up enough to transfer to the upper valley and the corresponding cooling time required to relax again. The heating time is relatively short, a fraction of a picosecond, but the cooling time is about 2.75 picoseconds for GaAs. This corresponds to a frequency of about 60 GHz in GaAs. If the time scale is reduced, the electrons do not return to the Γ valley. This is shown in Fig. 1c and 1d for a total simulation time of twenty picoseconds. These valley transfer delays are well understood in the operation of Gunn devices and are a major limitation in their high frequency operation^{11,12}. In a Gunn device a rapid transfer of electrons from valley to valley under a changing electric field is needed. The frequency response of GaAs based Gunn devices is limited to frequencies below 80 - 100 GHz because of the slow return of electrons from the upper valley. These valley response times also limit the performance of GaAs based varactors. A varactor consists of a depletion region and a bulk quasi-neutral region. The terminals of the device are pumped with a changing RF voltage which changes the width of the depletion region forming a nonlinear capacitance. The motion of the depletion layer edge depends on the motion of the electrons in the bulk quasi-neutral region. The goal is to have high mobility high velocity electrons in the region. This is the typical condition at lower frequencies and RF voltages where the amount of displacement current that the bulk region must support is reasonable. However, as the RF frequency increases for the same RF drive level, the peak fields in the bulk increase and electron begin to transfer to the upper valley during a portion of the RF cycle and do not have enough time to transfer back during the remaining portion of the cycle. This leads to a decrease in the average velocity of the bulk electrons, a saturation of the velocity through the bulk region and a decrease in the multiplier efficiency. Details of this effect will be described in more detail in section III.

An inductive delay occurs in a material when the electron motion can not follow a rapidly changing electric field. The delay effect can be illustrated with a balance equation relating the time rate change of an electron's velocity as a result of an electric field and a simple momentum relaxation term

$$dv/dt = qE/m^* - v/\tau_m, \quad (1)$$

where v is the velocity, q is the electronic charge, E is the applied field, m^* is the effective mass and τ_m is the momentum relaxation time. Under steady state conditions, the time derivative is zero, and the equation becomes

$$\mu = v/E = q\tau_m/m^* \quad (2)$$

where μ is the carrier mobility. For GaAs the effective mass is $0.068m_0$ and μ is $8500 \text{ cm}^2/\text{Vsec}$ for lightly doped material giving τ_m around 0.32 picoseconds. The current vs. time through a piece of bulk GaAs in response to a 1000 volt per cm peak to peak sin wave at 500 GHz is shown in Fig. 2. The response of the current to the sinusoidal drive is inductive. GaAs is a useful material for devices because it's high mobility gives a low resistance. However, at frequencies above 500 GHz, the inductive nature of the electron motion or current becomes important. This inductive effect will be discussed further in section IV.

Monte Carlo Simulation of Varactors

The Monte Carlo device simulation described in the last section has been used to study the operation of varactors and mixers. A description of these results will be given in this section. The structures are chosen to illustrate the saturation effects under consideration.

The first device is a GaAs Schottky barrier varactor diode with an epitaxial layer doping of $3 \times 10^{16}/\text{cm}^3$, an epitaxial layer length of 1.25 μmeter and a 0.25 μmeter long contact doped at $10^{17}/\text{cm}^3$. These parameters correspond to a relatively low frequency, high breakdown voltage device. All the plots are normalized to an area of one cm^2 . The voltages all refer to voltages across the semiconductor excluding the built-in voltage of the Schottky barrier, so zero volts corresponds to flat band. The Monte Carlo device is pumped with a single frequency RF voltage with a DC bias and the resulting device conditions are investigated.

The "capacitance" of the varactor as a function of RF phase for a DC bias of -10.5 volts, RF voltages of 2,4,6,8 and 10 volts and frequencies of 100 and 200 GHz is shown in Fig. 4a and Fig. 4b and the fraction of Γ electrons is shown in Fig. 4c and Fig. 4d. The "capacitance" is defined using the depletion layer approximation. The number of electrons in the device changes as a function of time. The number of missing electrons corresponds to an effective depletion layer thickness, and to a "capacitance". An additional "capacitance" associated with the time varying field and out of phase current in the neutral region will add an additional capacitance to the terminal characteristics.

The device capacitance vs. time at 100 GHz is similar to results that would be obtained using under static conditions. The fields in the undepleted portion are low enough that valley transfer doesn't occur for the first four RF voltage levels. Valley

transfer effects due to high electric fields begin to occur for the 10 volt RF voltage case. Cool contact electrons are pulled into the device in the first half of the RF cycle and heated. These heated electrons are then pushed out between 180 and 360°. The maximum time derivative of the terminal voltage is at 270°, so the valley fraction is smaller there. There is reasonable valley fraction modulation. The 100 GHz frequency under consideration corresponds to a period of 10 picoseconds. There is enough time for the electrons that have transferred in the second half of the cycle to relax to the Γ valley for the following lower voltage bias conditions.

The results are different for 200 GHz modulation. Since the frequency is higher a simple scaling would require twice as much current. However, the light doping in the undepleted region will not support the required current. Valley transfer occurs during a portion of the RF cycle. This reduces the velocity and the depletion layer width modulation. Since the depletion layer is narrower than in the 100 GHz case, the neutral region fields are higher. This causes additional transfer. The upper valley electrons do not have time to return to the higher mobility lower valley in the 5 picosecond time scale. These valley transfer effects increase the ohmic loss in the structure. Fig. 4 shows the loss $\frac{1}{2\pi} \int I(t)V(t)dt$ for the two frequencies. The rapid increase in the ohmic loss is due to the higher resistive loss in the lightly doped material.

One way to overcome some of these problems is to increase the doping. Capacitance results for a varactor doped at $9^{16}/cm^2$ with an epitaxial layer $0.8\mu m$ long is shown in Fig. 5a and b and the corresponding valley fraction results are shown in Fig. 5c and d. This structure works much better, but there is still a reduced valley fraction for the 200 GHz modulation. Again, electrons in the neutral region that transfer to upper valleys do not have enough time to transfer back, so there is a buildup of low mobility electrons over several RF periods. Careful characterization will be needed to optimize structures for different RF drive levels and frequencies.

Monte Carlo Simulation of Mixers

The Monte Carlo simulation has also been to start an investigation of limitations in mixers. Mixers are needed at higher frequencies than multipliers, they are usually operated in forward bias, so the capacitance per unit area is higher, and the structure must support both the displacement and injected current. A simulation of a mixer diode with a doping of $1 \times 10^{17}/cm^3$ and a $0.1\mu m$ long epitaxial layer is shown in Fig. 6. It is driven with a 0.5 volt RF voltage at a -0.5 volt bias point. The 180° phase point corresponds to “flatband”. The terminal current vs. phase is shown in Fig. 6a. There is a strong inductive effect in this plot, with the inductive delay of the electrons in the neutral region resonating with the depletion layer capacitance. The resulting injected current, or electron current across the Schottky barrier is shown in Fig. 6b. The injected current is delayed about 45° from the “flatband” bias point at 180°. The

peak current is limited by the supply of electrons through the neutral region. The electron energy vs. phase is shown in Fig. 6c. The electrons are being heated by the high electric fields in the device, even though the total voltage across the device is modest. The peak energy of almost 100 milli electron volts occurs near the 270 ° phase point where the current is largest. The time derivative of the terminal voltage is largest at the 90° and 270° phase point. At 90° cool electrons are being pulled into the device from the contact. At 270° hotter electrons are being pushed out. Even with low bias voltages, the electrons are being heated enough to allow valley transfer, as shown in the Fig. 6d. The electrons are heated over several RF cycles, with slow energy loss.

Some of the results in Fig. 6 occur because the structure limits the current. Results for a similar structure with a doping of $2 \times 10^{17}/\text{cm}^3$ are shown in Fig. 7. The injected current peak is much higher, but is still shifted by the inductive delay. Since the doping is higher, the resistance in the neutral region is smaller, and there is less damping of the terminal current waveform. The electron energies are smaller and the valley fraction is larger.

Conclusions

This paper has briefly discussed the Monte Carlo simulation of Schottky barrier varactors and mixers. This description shows several important limitations in the operation of these devices beyond the saturation effects discussed in earlier literature. GaAs varactors operating about 100 GHz are limited by valley transfer effects. There is an accumulation of hot electrons in the neutral region of the device in the high voltage portion of the RF cycle. These electrons do not have enough time to thermalize in the remaining portion of the cycle. This will increase the resistance and reduce the performance. The problem can be reduced but not overcome with increased doping. GaAs mixers also have current saturation effects. The bulk region of the device must support both the injected and the displacement current. In addition, an inductive current delay causes an under damped resonant current flow at the device terminals. This current flow heats the electrons and causes valley transfer, increasing the device resistance. These effects will modify the device performance in circuits. The next step is to include these physical effects into a device model that can be used in a nonlinear circuit simulation.

List of Figures

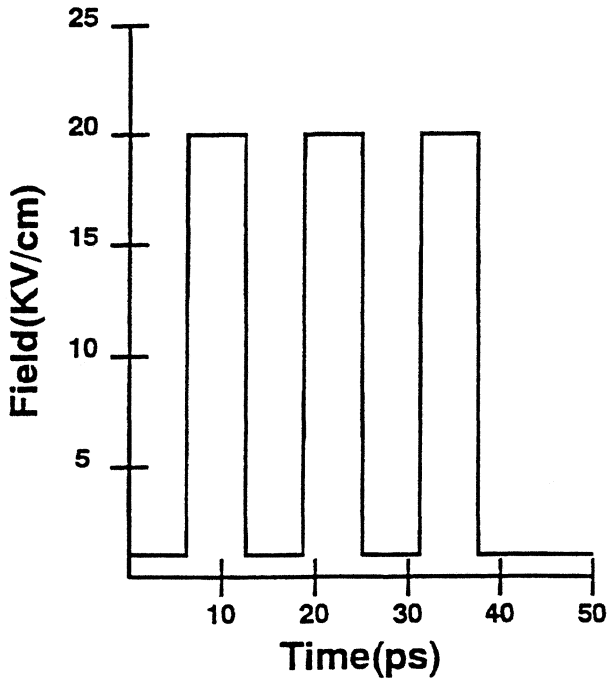
1. Fig. 1 a. Time Response of Electron Γ valley Fraction, b. Electric Field vs. Time for 50 picosecond simulation, c. Time Response of Electron Γ valley Fraction, d. Electric Field vs. Time for 20 picosecond simulation.
2. Fig. 2a. Electric field vs. time b., Current vs. Time for 500 GHz simulation.
3. Fig. 3 a. 100 GHz capacitance vs. time for RF voltages of 2,4,6,8 and 10 volts, b. 200 GHz capacitance vs. time for RF voltages of 2,4,6,8 and 10 volts, c. 100 GHz valley fraction vs. time and d. 200 GHz valley fraction vs. time for $3 \times 10^{16}/cm^3$ structure.
4. Fig. 4 Ohmic loss vs. RF voltage at 100 and 200 GHz.
5. Fig. 5 a. 100 GHz capacitance vs. time for RF voltages of 2,4,6,8 and 10 volts, b. 200 GHz capacitance vs. time for RF voltages of 2,4,6,8 and 10 volts, c. 100 GHz valley fraction vs. time and d. 200 GHz valley fraction vs. time for $9 \times 10^{16}/cm^3$ structure.
6. Fig 6 a. 1 THz terminal current, b. Injected current c. Electron energy and d. Valley fraction for a $1 \times 10^{17}/cm^3$ doped Schottky barrier mixer with RF voltage of 0.5 volts and bias of -0.5 volts.
7. Fig 7 a. 1 THz terminal current, b. Injected current c. Electron energy and d. Valley fraction for a $1 \times 10^{17}/cm^3$ doped Schottky barrier mixer with RF voltage of 0.5 volts and bias of -0.5 volts.

References

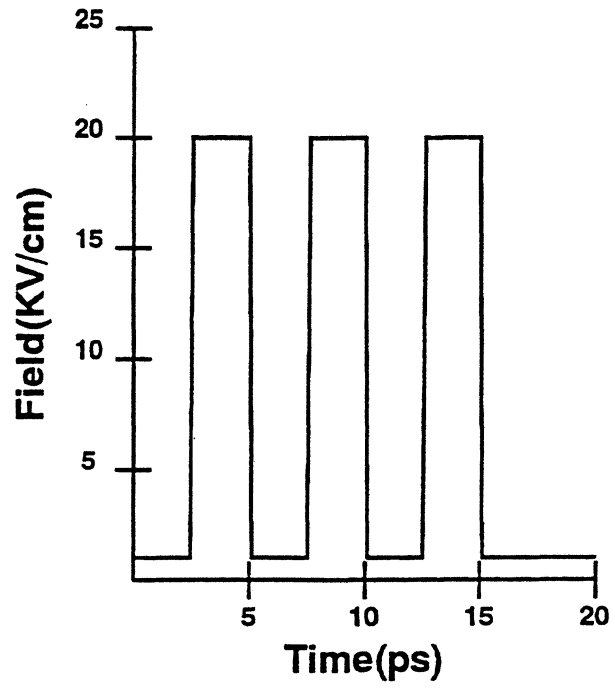
1. Siegel, P., Kerr, A, and Hwang,W. ,“Topics on the Optimization of Millimeter Wave Mixers,” NASA Technical Paper 2287, March 1984.
2. Microwave Mixers, S.A. Maas, Artech House, 1986.
3. Commerical software includes Harmonica, a product of Compact Software and Libra, a product of HP/EESOF.
4. “Current Saturation in Submillimeter Wave Varactors,” by E.Kollberg, T. Tolmunen, M. Frerking and J.East presented at the Second International Conference on Space Terahertz Technology, Pasadena, California, March 1991 with an extended version in *IEEE Trans. on Microwave Theory and Techniques*, Vol. MTT-40, pp. 831-838, 1992..

5. "On the Modeling and Optimization of Schottky Varactor Frequency Multipliers at Submillimeter Wavelengths," by J. Louhi and A. Raisanen, presented at the Fifth International Conference on Space Terahertz Technology, Ann Arbor, Michigan, May, 1994.
6. Crowe, T., Peatman, W., Zimmermann, R. and Zimmermann, R., "Consideration of Velocity Saturation in the Design of GaAs Varactor Diodes," *IEEE Microwave and Guided Wave Letters*, vol. 3, No. 6, pp 161-163, June, 1993.
7. "Performance Limitations of Varactor Multipliers," by J. East, E. Kollberg and M. Frerking presented at the Fourth International Conference on Space Terahertz Technology, Los Angeles, California, March 1993.
8. Non-Ohmic Transport in Semiconductors by W. Fawcett in *Electrons in Crystalline Solids*, International Atomic Energy Agency, Vienna 1973.
9. *Computer Simulation Using Particles* by R. Hockney and J. Eastwood, McGraw Hill, 1981.
10. U. Bhapkar and R. Mattauch, "Time-Dependent Monte Carlo Simulation of Schottky Diodes at Terahertz Frequencies," 1993 International Semiconductor Device Research Symposium, Charlottesville, Virginia, Dec. 1993, pp 381-384.
11. Bosch, R. and Thim, H., "Computer Simulation of The Transferred Electron Effect Using the Displaced Maxwellian Approach," *IEEE Trans. on Electron Devices* Vol. ED-21, No. 1 pp 16, Jan. 1974.
12. Kroemer, H., "Hot-Electron Relaxation Effects in Devices," *Solid State Electronics*, Vol. 21, pp 61-67, 1978.

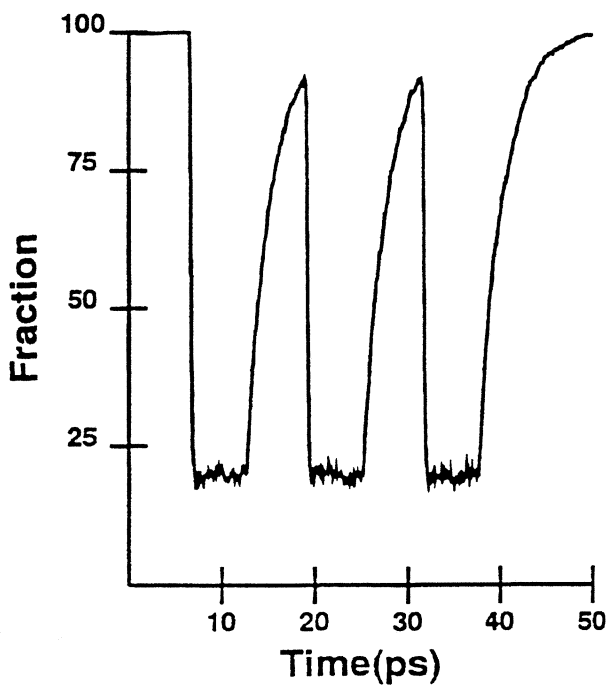
(a) Field vs. long time



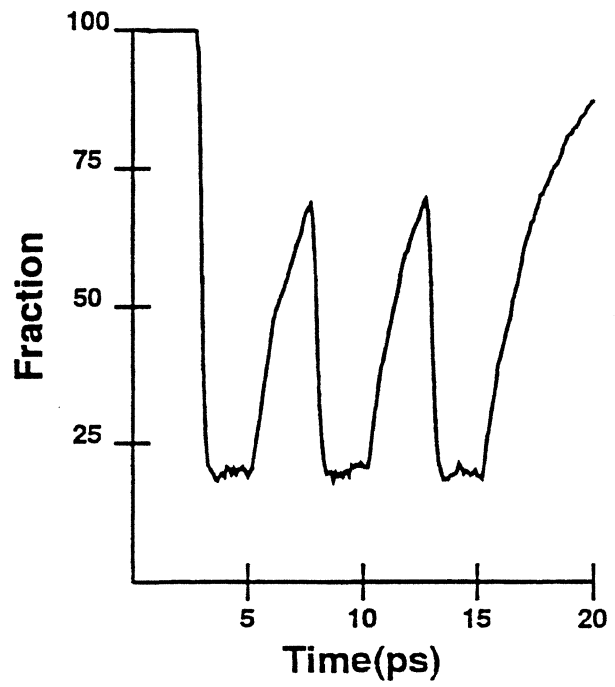
(c) Field vs. short time



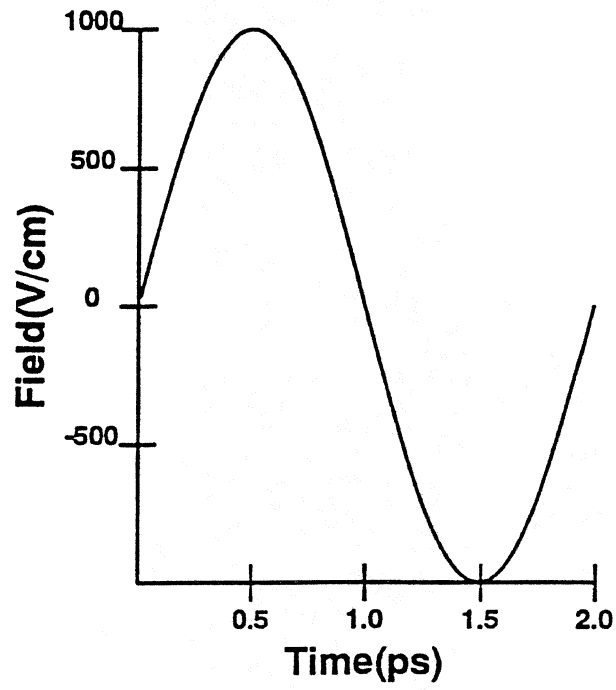
(b) Valley fraction vs. long time



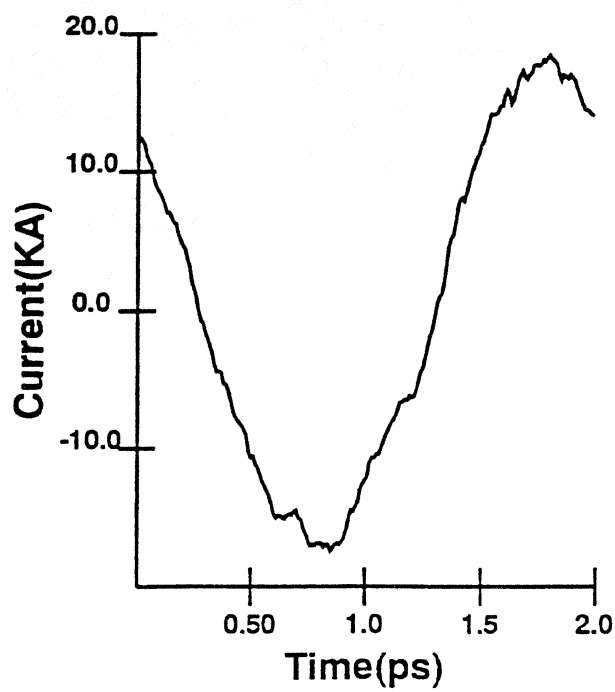
(d) Valley fraction vs. short time



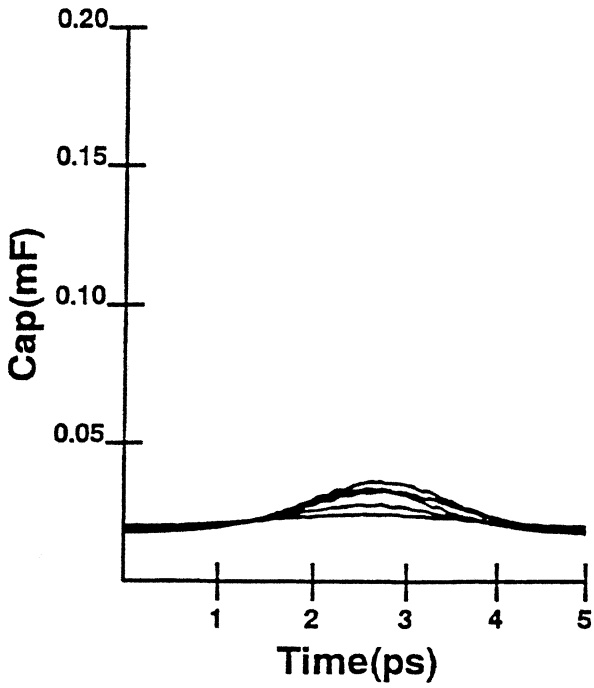
(a) Field vs. time



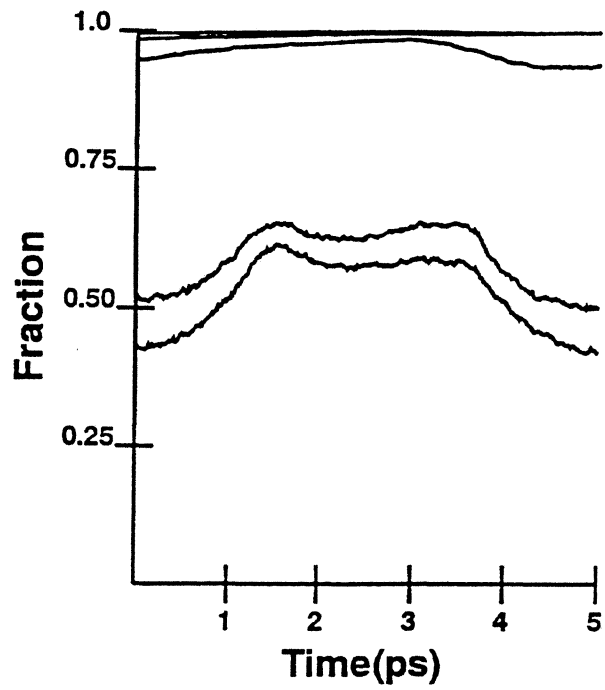
(b) Current vs. time



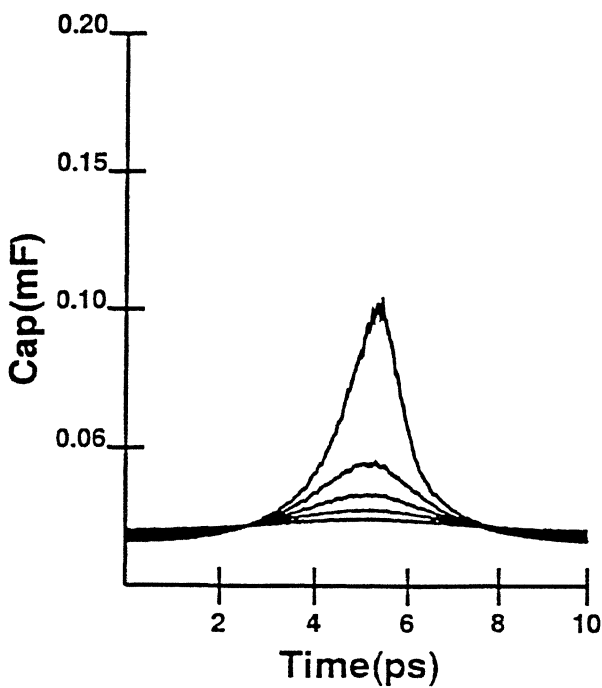
(b) 200 GHz capacitance



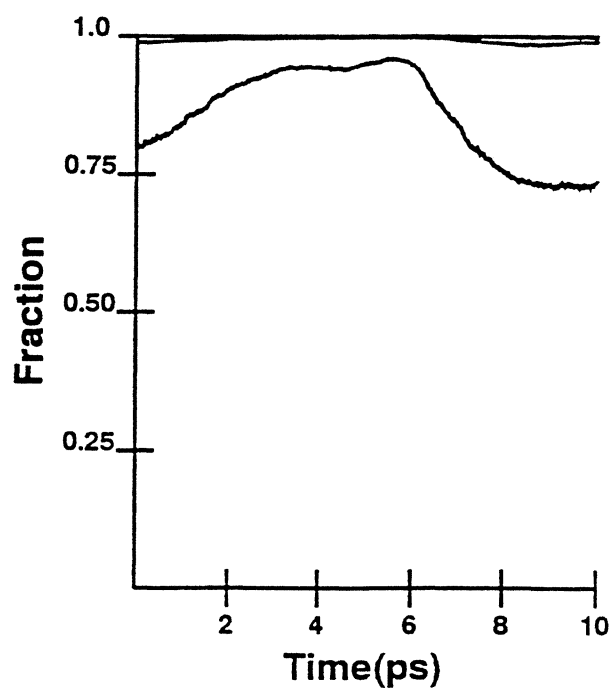
(d) 200 GHz fraction



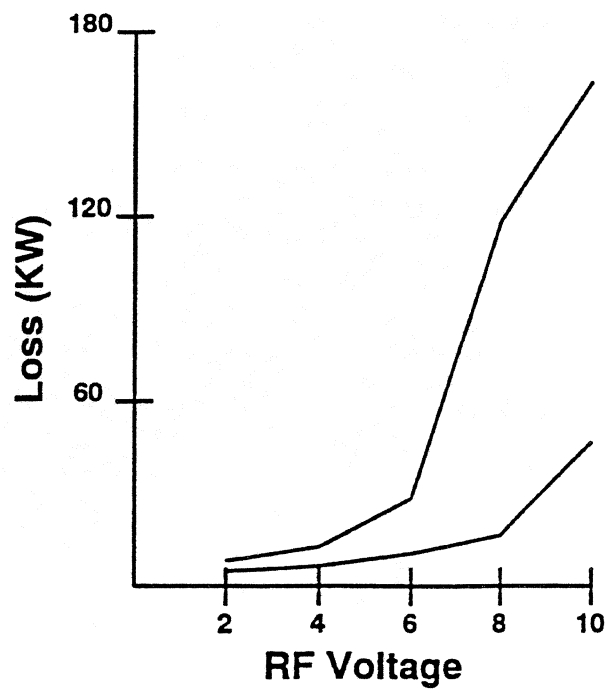
(a) 100 GHz capacitance



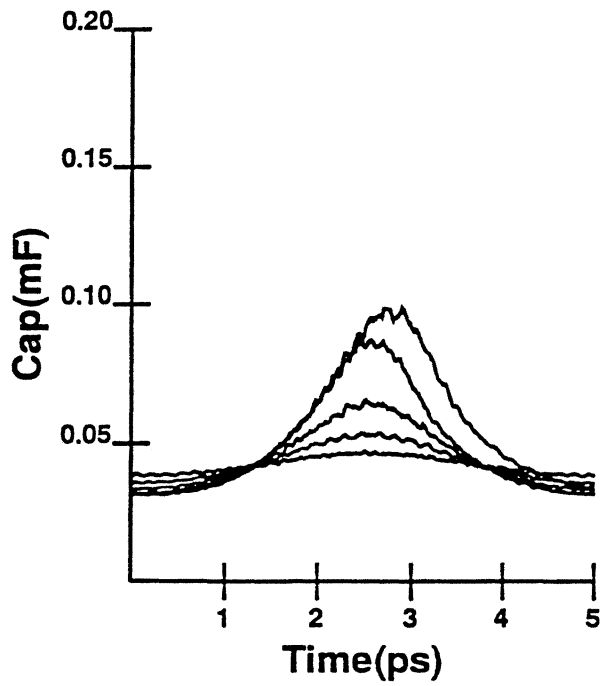
(c) 100 GHz fraction



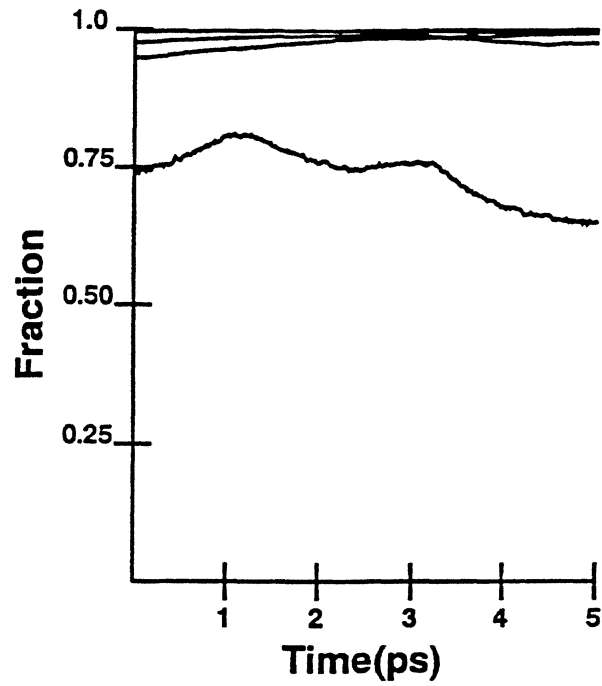
ohmic loss vs. drive level



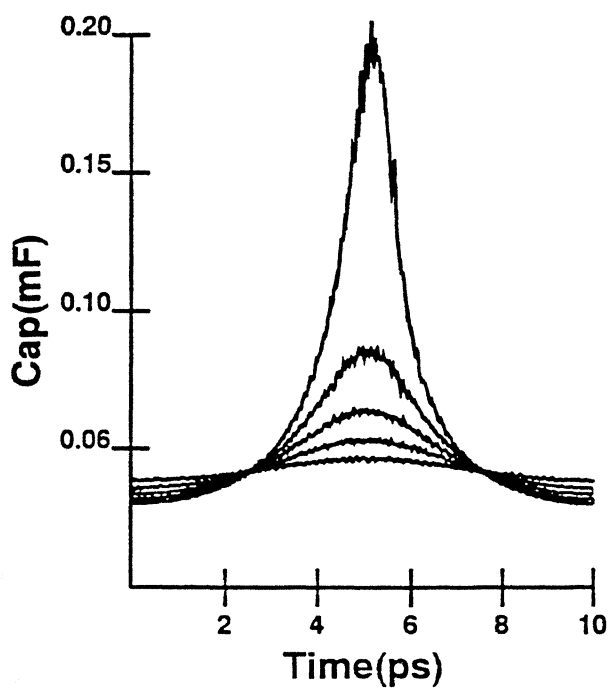
(b) 200 GHz capacitance



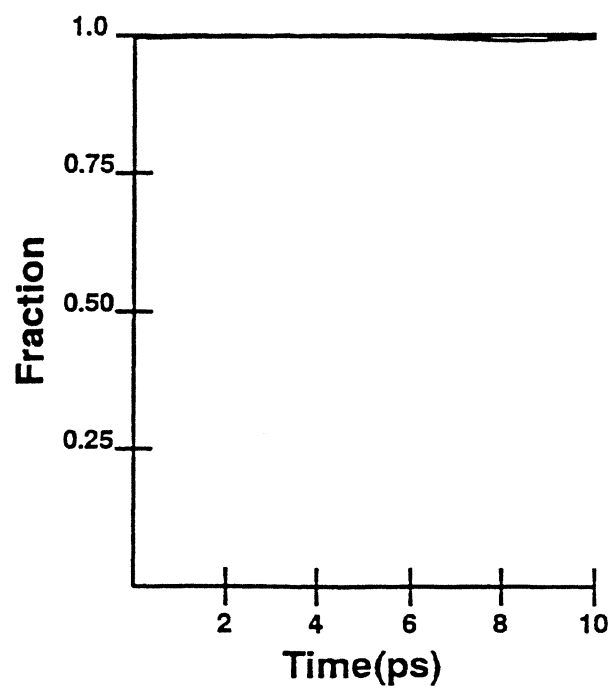
(d) 200 GHz fraction



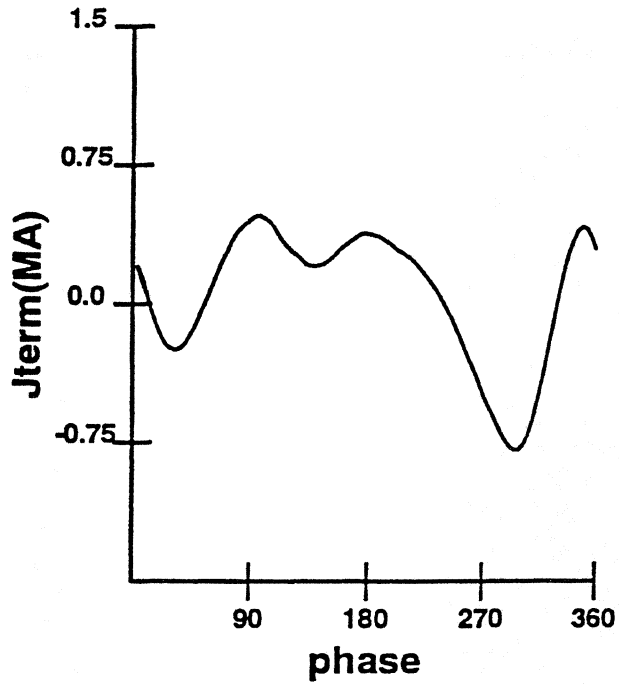
(a) 100 GHz capacitance



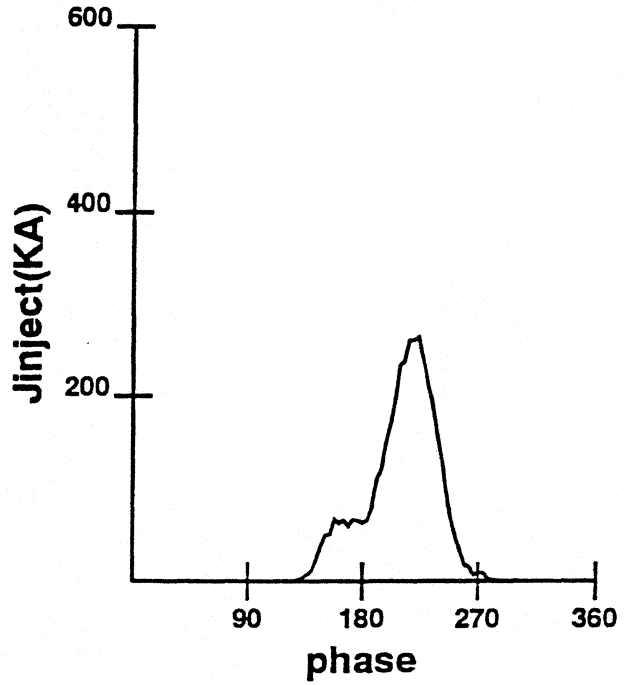
(c) 100 GHz fraction



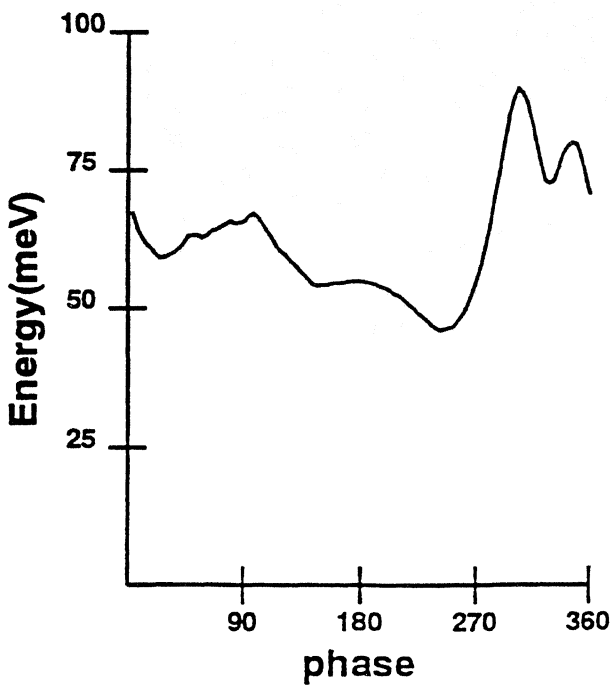
(a) 1 THz terminal current vs. phase



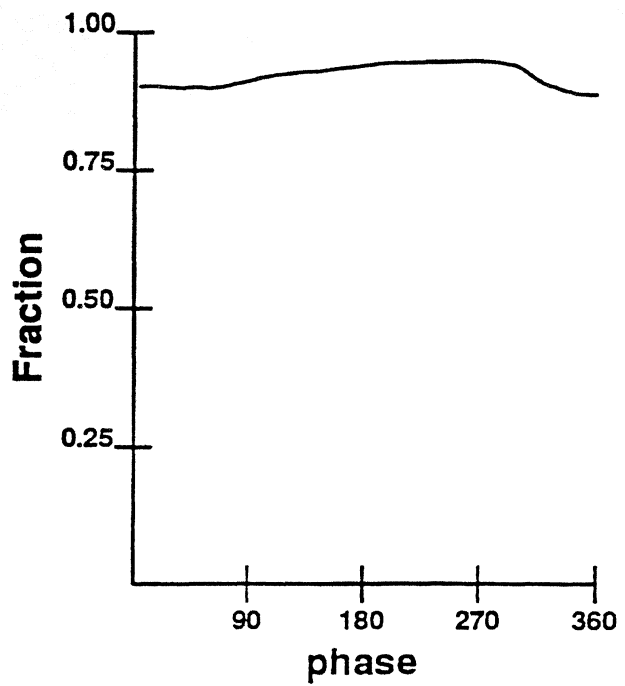
(b) 1 THz injected current vs. phase



(c) 1 THz energy vs. phase

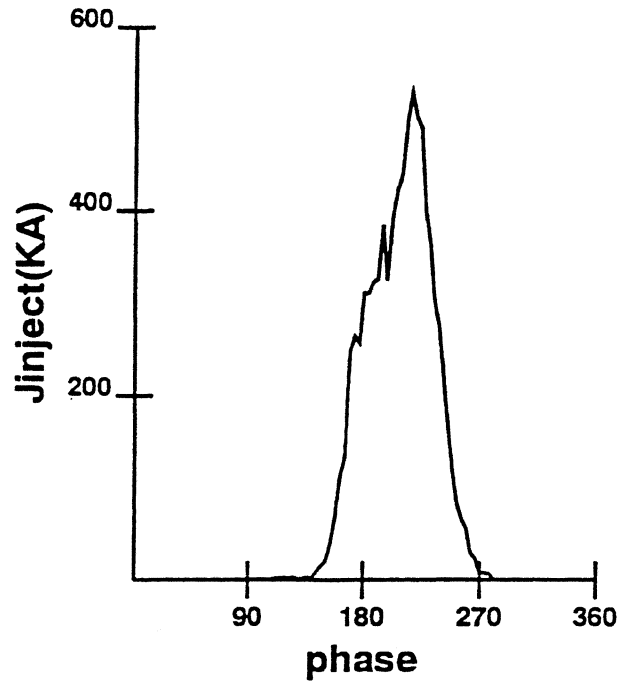
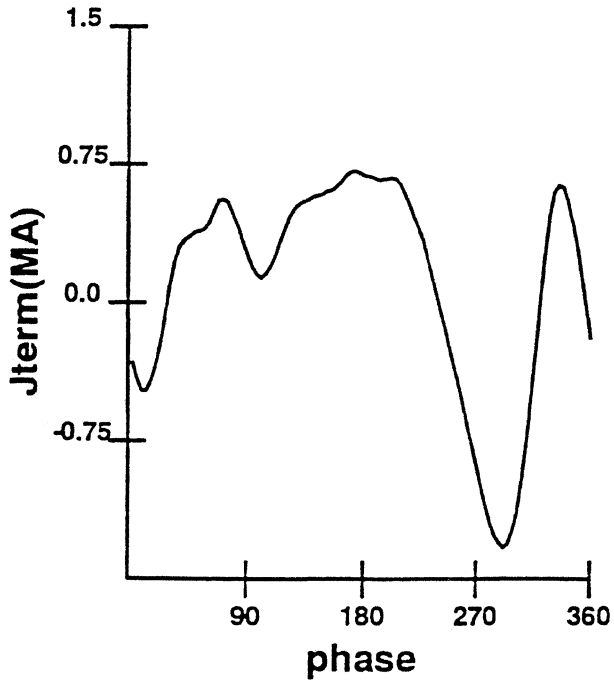


(d) 1 THz fraction vs. phase



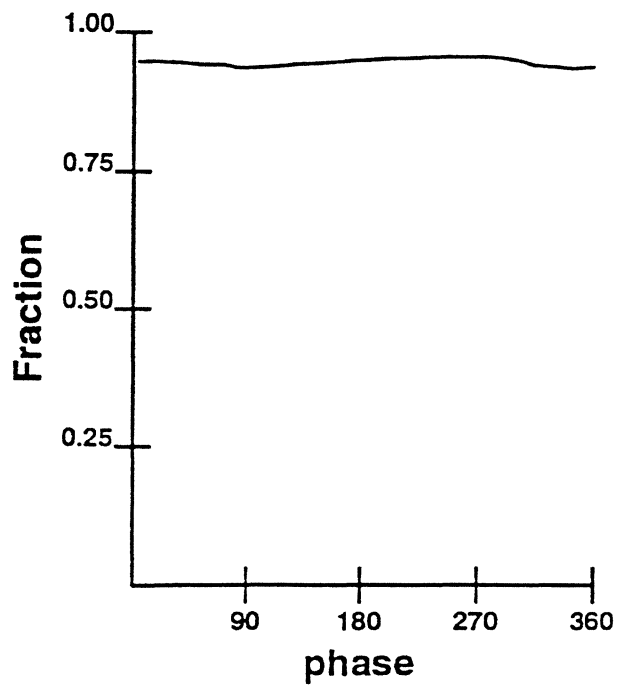
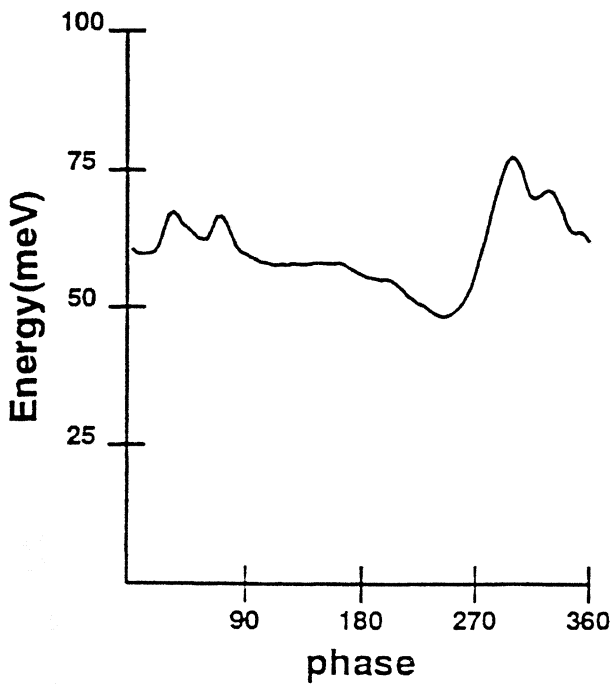
(a) 1 THz terminal current vs. phase

(b) 1 THz injected current vs. phase



(c) 1 THz energy vs. phase

(d) 1 THz fraction vs. phase



Submicron Schottky-Collector AlAs/InGaAs Resonant Tunnel Diodes

S.C. Martin, R.E. Muller, K. Nummila*, and R.P. Smith
Center for Space Microelectronics Technology
Jet Propulsion Laboratory/California Institute of Technology
4800 Oak Grove Drive, Pasadena, CA 91109

M. Reddy, M.J. Mondry, and M.J.W. Rodwell,
Department of Electrical and Computer Engineering,
University of California, Santa Barbara, CA 93106.

D.H. Chow and J.N. Schulman
Hughes Research Laboratories
Malibu, CA 90265.

Introduction

Resonant tunnel diodes (RTDs) are currently the widest bandwidth semiconductor devices useful for high frequency oscillators and picosecond pulse generators [1], [2]. 712 GHz oscillators [2] and 1.7 ps pulse generators [3], fabricated with 1.0 THz bandwidth InAs/AlSb RTDs, are some examples of high speed RTD applications. Here, we report the fabrication and the dc and microwave characteristics of AlAs/In_{0.53}Ga_{0.47}As Schottky-collector resonant tunnel diodes (SRTDs) with deep submicron Schottky collectors and an estimated intrinsic maximum frequency of oscillation f_{max} of 2.2 THz. The process is planar, so monolithic integration of single devices with matching circuitry for waveguide-based LO's or of many SRTDs into quasi-optical oscillator arrays is possible.

Schottky-Collector RTDs

RTD bandwidths are currently limited by parasitic resistance from the ohmic contacts. In Schottky-collector RTDs, the ohmic-contacted collector of a conventional RTD is replaced with a direct Schottky contact to the space-charge layer (Fig. 1), eliminating the top contact

series resistance[4]. The remaining series resistance components are minimized by scaling the Schottky-collector to deep submicron dimensions. This reduced series resistance leads to an increased maximum frequency of oscillation, f_{max} . 0.1 μ m AlAs/GaAs SRTD's have been previously reported with an estimated f_{max} =900 GHz [5].

AlAs/In_{0.53}Ga_{0.47}As SRTDs should yield further increases in f_{max} owing to the superior material properties of this system [6].

RTD electrical characteristics when biased in the negative-differential-resistance (NDR) region [1] are represented by the parasitic series resistance, R_s , the space charge layer capacitance, C, the negative resistance, R_n , and a quantum well inductance, L_{qw} (see inset of Fig. 2). $L_{qw} = -\tau_{qw}R_n$ (negative in the NDR region), where τ_{qw} is the electron lifetime in the quantum well. f_{max} is the frequency at which the network's admittance, $Y(\omega)$ has a zero real component. Inclusive of the quantum well lifetime τ_{qw} and assuming that

$$\tau_{qw} \gg C(R_n R_s)^{-1/2},$$

the expression for calculating f_{max} is

$$f_{max} = 1/(2\pi)(\tau_{qw})^{-1/2}(R_n C)^{-1/4}(R_s C)^{-1/4} \quad (1).$$

* Current address: Nokia Research Center, PO Box 45, FIN-00211 Helsinki, Finland

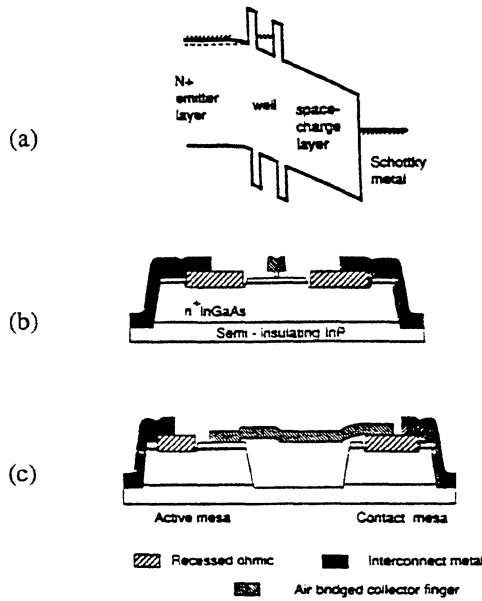


Fig. 1: (a) Band diagram, (b) and (c) perpendicular cross sections of a submicron AlAs/In_{0.53}Ga_{0.47}As SRTD.

Improvements in f_{max} are obtained by decreasing R_sC , R_nC and τ_{qw} . Thin barriers result in both small τ_{qw} and a high current density which reduces R_nC . Reduction in τ_{qw} and R_nC through the use of very thin barriers is ultimately limited by degradation in the current peak-to-valley ratio (PVR) and by high device power dissipation. R_s can be reduced by employing a Schottky collector of submicron width; the resulting increase in f_{max} is shown in Fig. 2. Compared to 0.1 μm AlAs/GaAs SRTDs

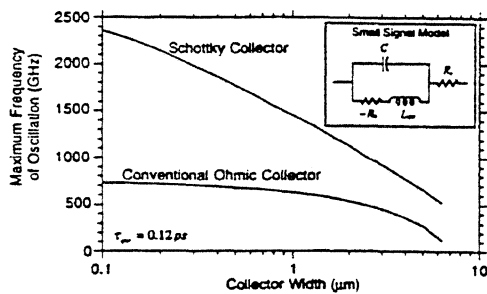


Fig. 2: Comparison of a conventional RTD to a Schottky-Collector RTD using measured values of R_n and C from the 5 ML AlAs/In_{0.53}Ga_{0.47}As SRTD, inclusive of the effects of τ_{qw} . The inset shows the small signal equivalent circuit model of an RTD biased in the negative differential resistance region.

[4], AlAs/In_{0.53}Ga_{0.47}As SRTDs have slightly smaller τ_{qw} and substantially smaller R_s and R_nC and therefore should attain higher f_{max} .

Fabrication

Molecular beam epitaxial growth of the RTD layer structure started with a 1.0 μm , $10^{19}/\text{cm}^3$, Si doped, In_{0.53}Ga_{0.47}As buried N+ contact layer on the [100] InP substrate at a temperature of 540^o C. This was followed by a 50nm, $10^{18}/\text{cm}^3$, Si doped, In_{0.53}Ga_{0.47}As emitter and a 10nm, undoped, In_{0.53}Ga_{0.47}As spacer layer. The last 10 nm of the emitter and the entire spacer layer were grown at a substrate temperature of 320^o C to minimize out diffusion of Si dopants into the double barrier structure. 1.4 nm or 1.7 nm (5 or 6 monolayers), undoped AlAs form the barriers on either side of a 4.7 nm, undoped, In_{0.53}Ga_{0.47}As quantum well. Growth interruptions were used before and after the low temperature growth to stabilize the substrate temperature. The rest of the structure, grown at 510^o C, consisted of a 25 nm, undoped, In_{0.53}Ga_{0.47}As space-charge layer and 10 nm, $5 \times 10^{18}/\text{cm}^3$, Be-doped, In_{0.53}Ga_{0.47}As p-type cap layer.

Due to the approximately 0.1 eV - 0.3 eV potential barrier at the air-semiconductor interface there is significant free charge in the space charge region of the uncontacted regions surrounding the Schottky collector. Parasitic surface leakage currents will arise if this sheet charge is significant. Assuming a 0.2 eV potential barrier at the air-semiconductor interface, the calculated electron free charge density is $10^{11}/\text{cm}^2$ without the p-type cap and is reduced to $10^9/\text{cm}^2$ with the cap. The cap layer, an extension of the space charge region, is fully depleted. Within the SRTD, the fully depleted cap increases the forward voltage by an estimated 0.4 V. This increased forward voltage can be eliminated by a self-aligned recess etch through the p-type cap before deposition of the Schottky metal. Experiments with a recess etch were abandoned due to difficulties in controlling the etch uniformity in very small area devices - while working devices were fabricated, the uniformity required for the parameter extraction described in the following section could not be accomplished. The total space charge layer thickness is 35 nm which minimizes space-charge transit time.

Acknowledgements

The work at U.C.S.B. was supported by ONR under contract # N00014-93-1-0378, NSF/PYI, and a JPL President's Fund. The work at JPL was performed by the Center for Space Microelectronics Technology, Jet Propulsion Laboratory, California Institute of Technology, and was sponsored by the National Aeronautics and Space Administration, Office of Advanced Concepts and Technology, and by the Innovative Science and Technology Office of BMDO through an agreement with NASA.

References

1. E.R. Brown, J.R. Soderstrom, C.D. Parker, L.J. Mahoney, K.M. Molvar, and T.C. McGill, *Appl. Phys. Lett.*, 58, 2291 (1991).
2. E.R. Brown, T.C.L.G. Sollner, C.D. Parker, W.D. Goodhue, and C.L. Chen, *Appl. Phys. Lett.*, 55, 1777 (1989).
3. E. Ozbay, D.M. Bloom, D.H. Chow, and J.N. Schulman, *IEEE Electron Dev. Lett.* 14, 400 (1993).
4. Y. Konishi, S.T. Allen, M. Reddy, M.J.W. Rodwell, R.P. Smith and J. Liu, *Solid-State Electronics*, 36, 1673 (1993).
5. R.P. Smith, S.T. Allen, M. Reddy, S.C. Martin, J. Liu, R.E. Muller, and M.J.W. Rodwell, *IEEE Electron Dev. Lett.*, 15, 295 (1994).
6. D.H. Chow, J.N. Schulman, E. Ozbay, and D.M. Bloom, *Appl. Phys. Lett.*, 6, 1685 (1992).
7. R.E. Muller, S.C. Martin, R.P. Smith, S.T. Allen, M. Reddy and M.J.W. Rodwell, *The 38th International Symposium on Electron, Ion and Photon Beams*, New Orleans, Louisiana, June 1994; *J. Vac. Sci. Technol. B* (to be published).

Sixth International Symposium on Space Terahertz Technology
Registered Participants

1. Dr. P. Batelaan, Jet Propulsion Laboratory, 4800 Oak Grove Drive, MS 168-314, Pasadena, CA 91009-8099.
Phone: (818) 354-4797 *E-mail:*
2. Dr. V. Yu. Belitsky, Department of Microwave Technology, Chalmers University of Technology, Rännvägen 6, S-412 96 Göteborg, Sweden.
Phone: +46 31 7721898 *E-mail:* ire@ep.chalmers.se
3. Mr. D. Benford, Caltech MS 320-47, Pasadena, CA 91125.
Phone: (818) 395-3741 *E-mail:* dbenford@tacos.caltech.edu
4. Dr. A. L. Betz, University of Colorado, CB 446, Boulder, CO 80309-0446.
Phone: 303-492-4880 *E-mail:* betz@spot.colorado.edu
5. Ms. Mei Bin, Caltech MS 320-47, Pasadena, CA 91125.
Phone: (818) 395-4868 *E-mail:* mei@tacos.caltech.edu
6. Dr. R. Blundell, Harvard Smithsonian Center for Astrophysics, 60 Garden St., MS 42, Cambridge, MA 02138.
Phone: (617) 496-7667 *E-mail:* rblundell@cfa.harvard.edu
7. Ms. O. Boric-Lubecke, c/o Prof. T. Itoh, University of California Los Angeles, School of Engineering and Applied Science, Electrical Engineering Department, 405 Hilgard Avenue, Los Angeles, CA 90024-1595.
Phone: (310) 206-1024 *E-mail:* boric@ee.ucla.edu
8. Dr. E. Bründermann, DLR, Institute for Space Sensor Technology, Rudower Chaussee 5, D-12489 Berlin, GERMANY.
Phone: 49 30 69 545 593 *E-mail:* ws2t@arzvs1.rz.ba.dlr.de
9. J. Bruston, Jet Propulsion Lab, MS 168-314, 4800 Oak Grove Drive, Pasadena, 91009-8099.
Phone: *E-mail:*
10. Mr. Bruce Bumble, Jet Propulsion Laboratory, 4800 Oak Grove Drive, MS 302-231, Pasadena, CA 91009-8099.
Phone: *E-mail:*
11. Mr. Peter Burke, Yale University, 217 Prospect St., New Haven, CT 06511.
Phone: *E-mail:*
12. Mr. J.-C. Chiao, California Institute of Technology, MS 116-81, Pasadena, CA 91125.
Phone: (818) 395-4846 *E-mail:* jcchiao@cco.caltech.edu
13. Ms. D. Choudhury, Millitech Corp., South Deerfield Research Park, South Deerfield, MA 01373.
Phone: *E-mail:*
14. Prof. Tah-Hsiung Chu, National Taiwan University, Dept. of Electrical Engineering, Taipei, Taiwan, R. O. C..
Phone: *E-mail:*
15. Dr. A. Clapp, Caltech MS 320-47, Pasadena, CA 91125.
Phone: (818) 395-4601 *E-mail:* andre@ra.caltech.edu

47. Mr. J. R. Jones, University of Virginia, Dept. of Electrical Engineering, Thornton Hall, Charlottesville, VA 22903.
Phone: (804) 924-3960 *E-mail:* jrj2h@virginia.edu
48. Dr. S. Jones, University of Virginia, Dept. of Electrical Engineering, Thornton Hall, Charlottesville, VA 22903.
Phone: (804) 924-6080 *E-mail:* shj2n@virginia.edu
49. Dr. B. S. Karasik, Jet Propulsion Laboratory, 4800 Oak Grove Drive, MS 168-314, Pasadena, CA 91009-8099.
Phone: 818 393-4438 *E-mail:* boris.s.karasik@jpl.nasa.gov
50. Dr. A. Karpov, Institut de Radioastronomie Millimetrique, 300 rue de la Piscine, Domaine universitaire de Grenoble, ST. Martin d'Herès, F-38406, France.
Phone: (33) 76 82 49 00 *E-mail:* karpov@iram.grenet.fr
51. Mr. J. Kawamura, Harvard Smithsonian Center for Astrophysics, 60 Garden St., MS 75, Cambridge, MA 02138.
Phone: (617) 496-7667 *E-mail:* jkawamura@cfa.harvard.edu
52. Dr. Liam Kelly, Prospect Row, NMRC University College, Cork, IRELAND, .
Phone: 353 21 904094 *E-mail:* kelly@nmrc.ucc.ie
53. Dr. A. R. Kerr, National Radio Astronomy Observatory, 2015 Ivy Road, Suite 219, Charlottesville, VA 22903.
Phone: *E-mail:*
54. Dr. Timothy Koch, Jet Propulsion Laboratory, MS 169-506, 4800 Oak Grove Drive, Pasadena, CA 91109-8099.
Phone: (818) 354-8469 *E-mail:* tim@kuiper.jpl.nasa.gov
55. J. W. Kooi, Caltech MS 410-47, Pasadena, CA 91125.
Phone: (818) 395-4286 *E-mail:* kooi@tacos.caltech.edu
56. Mr. Erik Kollberg, Department of Microwave Technology, Chalmers University of Technology, Rännvägen 6, S-412 96 Göteborg, Sweden.
Phone: +46 31 7721898 *E-mail:*
57. Dr. Carl A. Kukkonen, Jet Propulsion Laboratory, 4800 Oak Grove Drive, MS 180-604, Pasadena, CA 91009-8099.
Phone: *E-mail:* carl.a.kukkonen@jpl.nasa.gov
58. Dr. Gert de Lange, RLE, Rm. 36-491, Massachusetts Institute of Technology, 77 Massachusetts Avenue, Cambridge, MA 02139.
Phone: (617) 253-2532 *E-mail:* gert@mit.edu
59. Dr. H. G. LeDuc, Jet Propulsion Laboratory, 4800 Oak Grove Drive, MS 302-231, Pasadena, CA 91009-8099.
Phone: *E-mail:* rleduc@vaxeb.jpl.nasa.gov
60. Dr. K. Lee, Jet Propulsion Laboratory, 4800 Oak Grove Drive, MS T-168-314, Pasadena, CA 91009-8099.
Phone: *E-mail:*

61. Dr. T. Lee, Jet Propulsion Laboratory, 4800 Oak Grove Drive, 168-314, Pasadena, CA 91009-8099.
Phone: *E-mail:*
62. Mr. Frank Li, University of Virginia, Dept. of Electrical Engineering, Thornton Hall, Charlottesville, VA 22903.
Phone: *E-mail:*
63. Dr. Jyrki T. Louhi, Helsinki University of Technology, Otakaari 5A, FIN-02150 Espoo, FINLAND.
Phone: +358 0 4512248 *E-mail:* jlo@radio.hut.fi
64. Mr. P. Marsh, University of Michigan, 1301 Beale, Ann Arbor, MI 48109.
Phone: (313) 747-1778 *E-mail:*
65. Dr. R. N. Martin, SMTO/Steward Observatory, University of Arizona, Tuscon, AZ 85721.
Phone: 602-621-4031 *E-mail:* rmartin@as.arizona.edu
66. Dr. R. J. Matlack, University of Virginia, Dept. of Electrical Engineering, Thornton Hall, Charlottesville, VA 22903.
Phone: *E-mail:*
67. Dr. W. R. McGrath, Jet Propulsion Laboratory, 4800 Oak Grove Drive, MS 168-314, Pasadena, CA 91009-8099.
Phone: (818) 354-8542 *E-mail:* rob@rob-mac.jpl.nasa.gov
68. Dr. I. Mehdi, Jet Propulsion Laboratory, 4800 Oak Grove Drive, MS 168-314, Pasadena, CA 91009-8099.
Phone: *E-mail:*
69. Dr. G. Melnick, Center for Astrophysics, 60 Garden Street, Cambridge, MA 02138.
Phone: 617-495-7388 *E-mail:* gmelnick@cfa.harvard.edu
70. Mr. D. Miller, Caltech MS 320-47, Pasadena, CA 91125.
Phone: (818) 395-3668 *E-mail:* davem@occat.caltech.edu
71. Dr. Tapani Närhi, ESA/ESTEC/XRM, PO Box 299, 2200 AG Noordwijk, The Netherlands .
Phone: *E-mail:* tnarhi@vmprofs.estec.esa.nl
72. Dr. S. Padin, Owens Valley Radio Observatory, Caltech, P.O. Box 968, Big Pine, CA 93513.
Phone: (619) 938-2075, x101 *E-mail:* spad@caltech.edu
73. Dr. S. Paine, Harvard Smithsonian Center for Astrophysics, 60 Garden St., MS 78, Cambridge, MA 02138.
Phone: (617) 496-7667 *E-mail:* spaine@cfa.harvard.edu
74. Dr. T. G. Phillips, Caltech MS 320-47, Pasadena, CA 91125.
Phone: (818) 395-4278 *E-mail:* phillips@tacos.caltech.edu
75. Mr. X. Qin, 228 Walker Hall, Applied Science, U.C. Davis, Davis, CA 95616.
Phone: (916) 752-4201 *E-mail:* qin@ece.ucdavis.edu
76. Dr. A. Räisänen, Radio Laboratory, Helsinki University of Technology, Otakaar 5A, FIN-02150 Espoo, FINLAND.
Phone: *E-mail:*

77. Dr. G. Rebeiz, NASA Center for Space Terahertz Technology, Dept. of Electrical Engineering and Computer Science, University of Michigan, Ann Arbor, MI 48109-2122.
Phone: (313) 764-3354 *E-mail:* rebeiz@engin.umich.edu
78. Prof. Hans Peter Röser, DLR, Institute for Space Sensor Tech, Rudower Chaussee 5, Berlin 12489, GERMANY.
Phone: 49 30 69 545 500 *E-mail:*
79. Dr. H. Rothermel, Max Planck Institut für Extraterrestrische Physik, Postfach 1602, Garching 85740, Germany.
Phone: *E-mail:*
80. Prof. David B. Rutledge, Caltech, MS 116-81 Pasadena, CA 91125.
Phone: (818) 395-4806 *E-mail:* rutledge@systems.caltech.edu
81. Dr. M. Salez, Jet Propulsion Laboratory, MS 168-314, 4800 Oak Grove Drive, Pasadena, CA 91109-8099.
Phone: (818) 354-6082 *E-mail:* msalez@jplsp.jpl.nasa.gov
82. Dr. Virendra Sarohia, Jet Propulsion Laboratory, 4800 Oak Grove Drive, MS 180-604, Pasadena, CA 91009-8099.
Phone: (818) 354-6758 *E-mail:*
83. M.A. Scherschel, Max-Planck-Institut für Radioastronomie, Auf dem Hügel 69, D-53121 Bonn, Germany.
Phone: (49) 228 525 232 *E-mail:* sersel@mpifr-bonn.mpg.de
84. Dr. Robert Schoelkopf, Yale University, 429 Becton, 15 Prospect St., New Haven, CT 06520.
Phone: (203) 432-4289 *E-mail:* rob_schoelkopf@quickmail.cis.yale.edu
85. Dr. E. Serabyn, Caltech MS 320-47, Pasadena, CA 91125.
Phone: (818) 395-6664 *E-mail:* serabyn@tacos.caltech.edu
86. Dr. S. V. Shitov, Institute of Radio Engineering and Electronics, Russia Academy of Sciences, Mokhovaya st. 11, 103907 Moscow, RUSSIA.
Phone: +7 (095) 2032784 *E-mail:* sergey@stron.rug.nl; IREE235@glas.apc.org
87. Dr. P. Siegel, Jet Propulsion Laboratory, 4800 Oak Grove Drive, MS 168-314, Pasadena, CA 91009-8099.
Phone: (818) 354-9089 *E-mail:* phs@merlin.jpl.nasa.gov
88. Dr. A. Simon, TH Darmstadt, Institut für Hochfrequenztechnik, Merckstr. 25, 64283 Darmstadt, Germany.
Phone: +49 6151 16 2662 *E-mail:*
89. Dr. A. Skalare, Jet Propulsion Laboratory, MS 168-314, 4800 Oak Grove Drive, Pasadena, CA 91109-8099.
Phone: (818) 354-9383 *E-mail:* anders@lolita.jpl.nasa.gov
90. Dr. P. Smith, Jet Propulsion Laboratory, MS 302-306, 4800 Oak Grove Drive, Pasadena, CA 91109-8099.
Phone: (818) 354-4424 *E-mail:* r.peter.smith@jpl.nasa.gov

91. Dr. H. van de Stadt, Space Research Organization of the Netherlands, P. O. Box 800, 9700 AV Groningen, The Netherlands.
Phone: +31 50 634074 *E-mail:* herman@sron.rug.nl
92. Dr. A. Stark, Harvard Smithsonian Center for Astrophysics, 60 Garden St., MS 78, Cambridge, MA 02138.
Phone: (617) 496-7648 *E-mail:* aas@cfastark.harvard.edu
93. Dr. J. A. Stern, Jet Propulsion Laboratory, 4800 Oak Grove Drive, MS 302-231, Pasadena, CA 91009-8099.
Phone: *E-mail:* jstern@vaxeb.jpl.nasa.gov
94. Dr. P. A. Stimson, Jet Propulsion Laboratory, 4800 Oak Grove Drive, MS 168-314, Pasadena, CA 91009-8099.
Phone: (818) 354-7092 *E-mail:*
95. Dr. R. Titz, DLR, Institut für Optoelektronik, Postfach 1116, D-82230 Wessling, Germany.
Phone: 8153 282779 *E-mail:* titz@dlr.de
96. Dr. E. Tong, Harvard Smithsonian Center for Astrophysics, 60 Garden St., MS 42, Cambridge, MA 02138.
Phone: (617) 496-7667 *E-mail:* etong@cfa.harvard.edu
97. Dr. J. Tuovinen, Radio Laboratory, Helsinki University of Technology, Otakaari 5A, FIN-02150 Espoo, FINLAND.
Phone: *E-mail:*
98. Dr. N. Wang, Caltech MS 320-47, Pasadena, CA 91125.
Phone: (818) 395-6610 *E-mail:* nwang@tacos.caltech.edu
99. Mr. J. Ward, Caltech MS 320-47, Pasadena, CA 91125.
Phone: (818) 395-3740 *E-mail:* ward@ocat.caltech.edu
100. Dr. M. J. Wengler, Electrical Engineering Department, University of Rochester, Rochester, NY 14627.
Phone: (716) 275-9402 *E-mail:* wengler@ee.rochester.edu
101. Mr. Perry Wood, University of Virginia, Dept. of Electrical Engineering, Thornton Hall, Charlottesville, VA 22903.
Phone: *E-mail:*
102. Dr. D. P. Woody, Owens Valley Radio Observatory, Caltech, 100 Observatory Rd., P.O. Box 968, Big Pine, CA 93513.
Phone: (619) 938-2075 *E-mail:* dwoody@caltech.edu
103. Dr. Dwight Woolard, Army Research Laboratory - EPSD, ARL-EPPO, Fort Monmouth, NJ 07703-5601.
Phone: 908-544-2647 *E-mail:* dwoolard@arl.mil
104. Mr. J. Wright, Caltech, MS 116-81, Pasadena, CA 91125.
Phone: (818) 395-4861 *E-mail:* jaws@touch.caltech.edu
105. Dr. S. Yngvesson, Dept. of Electrical & Computer Engineering, University of Massachusetts, Amherst, MA 01003.
Phone: (413) 545 0771 *E-mail:* yngvesson@ecs.umass.edu

